Magmatic response to the evolving New Zealand Margin of Gondwana during the Mid-Late Cretaceous

---

A thesis submitted in partial fulfilment

of the requirements for the degree

of

DOCTOR OF PHILOSOPHY IN GEOLOGICAL SCIENCES

at the

University of Canterbury

by

Vanessa E Tappenden

University of Canterbury

2003

Abstract

The Mount Somers Volcanic Group (MSVG) and Mandamus Igneous Complex (MIC) are the magmatic manifestations of the transition from convergence to extension at the Gondwana margin, which culminated in the separation of New Zealand from Australia and Antarctica. The MIC has been correlated both geochemically and temporally with the Central Marlborough Igneous Province (CMIP).

The MSVG and CMIP are located in the Eastern Province of New Zealand. The MSVG is restricted to the Rakaia terrane, whereas the CMIP is restricted to the Pahau terrane. The Rakaia and Pahau terranes are thick accretionary complexes, which were strongly deformed as a result of prolonged subduction at the Gondwana margin. The Pahau terrane is the younger of the two and continued to be deposited and deformed until the abrupt cessation of subduction, which in the Marlborough sedimentary record occurred in the Motuan (100 – 105 Ma).

Following the cessation of subduction, after an interval of 2-7 Ma of relative quiescence and subsidence of the Pahau terrane, the MSVG and MIC were erupted/emplaced. The production of MSVG and MIC magmas occurred simultaneously and the activity was of short-lived duration. SHRIMP geochronology yielded crystallisation ages of 97.0 ± 1.5 Ma to 98.0 ± 1.2 Ma from zircons separated from MSVG rhyolites. The SHRIMP ages are within error of the previously published Rb-Sr age for the MIC. The SHRIMP geochronology also confirmed the presence of inherited zircons which yielded ages consistent with their derivation from the Rakaia terrane. Ar-Ar geochronology confirmed the coeval nature of the MSVG and MIC magmatism, but yielded consistently younger ages (94.5 ± 3 Ma for the MSVG and 94.2 ± 1.7 Ma for the MIC). The systematic differences in ages obtained by SHRIMP and Ar-Ar are believed to be method-dependent.

The MSVG comprises a calc-alkaline volcanic assemblage, which ranges in composition from basaltic-andesite lavas (SiO_2 = 54.5%) to high-silica rhyolites and ignimbrites ($SiO_2 \leq$ 78.1%). The MSVG had an original extent of at least 18 000 km^2. The magmas from the MSVG had high LILE/HFSE, high LILE/REE and moderately high LREE/HFSE which are characteristic of subduction derived magmas. Geochemical modelling suggests that the MSVG magmas were formed from partial melting of a subduction-modified mantle wedge, with high degrees of crustal assimilation. The assimilant had an isotopic composition similar to that of the Rakaia terrane, which is consistent with the geological setting of the MSVG. The MSVG has $^{87}Sr/^{86}Sr_i$ from 0.7055 to 0.7100 and $^{143}Nd/^{144}Nd_i$ from 0.51254 to 0.51230 (εNd +0.5 to –4.2), which reflects varying degrees of contamination by Rakaia terrane. Radiogenic isotope modelling suggests that the MSVG end-members were derived from the same parent magma, which evolved through AFC processes from basaltic-andesite to rhyolite. The modelling strongly suggests that assimilation played a lesser role in the petrogenesis of the Malvern Hills magmas than in the petrogenesis of the other units. AFC modelling requires the degree of assimilation to increase as the magmas evolved. Oxygen isotope data are consistent with high degrees of crustal assimilation, and may indicate that the assimilant had higher ^{18}O characteristics than the Rakaia terrane samples analysed.

The MIC is an alkaline suite which ranges in composition from basalt and gabbro to syenite, trachyte and phono-tephrite. The MIC is interpreted to have formed from enriched asthenospheric mantle, with a composition similar to HIMU ($^{206}Pb/^{204}Pb_i$ ranges from 19.2 to 20.3). The samples range in isotopic composition from $^{87}Sr/^{86}Sr_i$ = 0.7030 to 0.7036, $^{143}Nd/^{144}Nd_i$ = 0.51275 to 0.51268 (εNd +4.6 to +3.3). The range in isotopic composition is due to varying degrees of contamination by Pahau terrane, which reaches a maximum of 25% but in most samples is <10%. The MIC is contaminated to a much lesser extent than the MSVG which is interpreted to be related to the thinner nature of the Pahau crust in the mid-Cretaceous. The latest phases of activity in the MIC were subjected to lower degrees of contamination which is interpreted to reflect the passage of magmas through pre-existing pathways.

The onset of MSVG and CMIP magmatism coincided with the initiation of major rift-related depositional basins, and the eruption of the MSVG is demonstrably associated with normal faulting. The tectonic trigger responsible for the sudden onset of magmatism and rifting in the Eastern Province terranes was the detachment of the previously subducting slab following the cessation of subduction due to the arrival of the Hikurangi Plateau at the margin and the subsequent stalling of the Pacific spreading centre. The capture of the Gondwana margin led to the propogation of extension into the margin by the divergent Pacific plate.

The ensuing extension aided the detachment of the subducting slab beneath the Eastern Province terranes. The slab-detachment promoted decompression melting of the sub-lithospheric mantle wedge to produce the MSVG magmas and triggered the ascent of asthenospheric mantle through the slab window, which melted through decompression to produce the CMIP magmatism. The asthenospheric mantle tapped by the slab detachment episode was highly enriched relative to N-MORB and is akin to the similar age HIMU-OIB affinity melts documented from Antarctica and Australia. The short-lived duration of activity is typical of slab-detachment related magmatism which occurs as a passive response to plate reconfiguration.

The similarity in geochemistry of the MIC with OIB-affinity igneous centres in Australia and Antarctica implies an enriched mantle domain of large geographical extent. The distribution of relatively small volumes of OIB magmatism is suggestive of a fossil plume component, which was tapped in response to lithospheric extension producing relatively short-lived HIMU magmatism. The same fossil plume component has previously been implicated in the formation of the Cenozoic West Antarctic Rift System and may be responsible for the late Cretaceous magmatism in the Chatham Islands and Tertiary volcanics of the South Island of New Zealand.

Table of Contents

Chapter 3:

Location of field areas and previous work..... 22

Chapter 4:

Volcanology and temporal evolution of the MSVG 44

Chapter 8:

Geochemistry and Petrogenesis of the MIC 187

Chapter 9:

Tectono-magmatic models for the formation of the MSVG and MIC..... 217

Chapter 10:

Chapter 1:
Introduction and Aims

1.1 Introduction

The mid-Cretaceous was a period of major tectonic change in the southwest Pacific region of the Gondwana margin. During the interval between approximately 110 Ma, to the first appearance of new oceanic crust in the Southern Ocean between New Zealand and Antarctica (Chron 34, 84 Ma), the Gondwana margin underwent a transition from convergence to extension. This culminated in the separation of New Zealand and Australia from Antarctica.

The Rakaia and Pahau terranes of the South Island host the Mount Somers Volcanic Group (MSVG) and the Central Marlborough Igneous Province (CMIP), which is partly comprised of the Mandamus Igneous Complex (MIC) (fig.1.1). The Eastern Province of the South Island (fig.1.2) is composed of a series of accreted terranes. The Rakaia and younger Pahau terrane are both composed of heavily deformed accretionary wedge sedimentary rocks. In the Marlborough area of the South Island, sedimentological evidence suggests that the Gondwana margin was in a convergent regime until the Motuan Stage (105-100 Ma). The magmatism of the MSVG and CMIP is known to be mid-Cretaceous in age and occurred following the cessation of subduction at the margin. The magmatism was broadly coeval with the formation of rift basins in the Eastern Province, and therefore these two igneous suites may provide valuable constraints on the crustal and magmatic processes that occurred during the transition from convergence to extension.

The MSVG is a suite of calc-alkaline volcanic rocks, which are widely distributed throughout the Rakaia terrane in Canterbury and have been geophysically mapped underlying the Canterbury Plains and off the Canterbury coast. The rock types range from basaltic-andesite lava flows to high silica rhyolite flows, domes and ignimbrite deposits. In contrast, the MIC, and CMIP correlatives, are a suite of alkaline volcanic and intrusive rocks, ranging in composition from basalt/gabbro to tephriphonolite and trachyte/syenite. The CMIP is restricted to the Pahau terrane and the igneous centres are distributed throughout the Pahau terrane from north Canterbury to Marlborough (fig.1.1).

The MSVG and MIC are the foci of this research. The thesis study areas are located in the Canterbury region of the South Island of New Zealand (fig.1.1) and extend from the Rangitata Gorge in south Canterbury, to Culverden in north Canterbury.

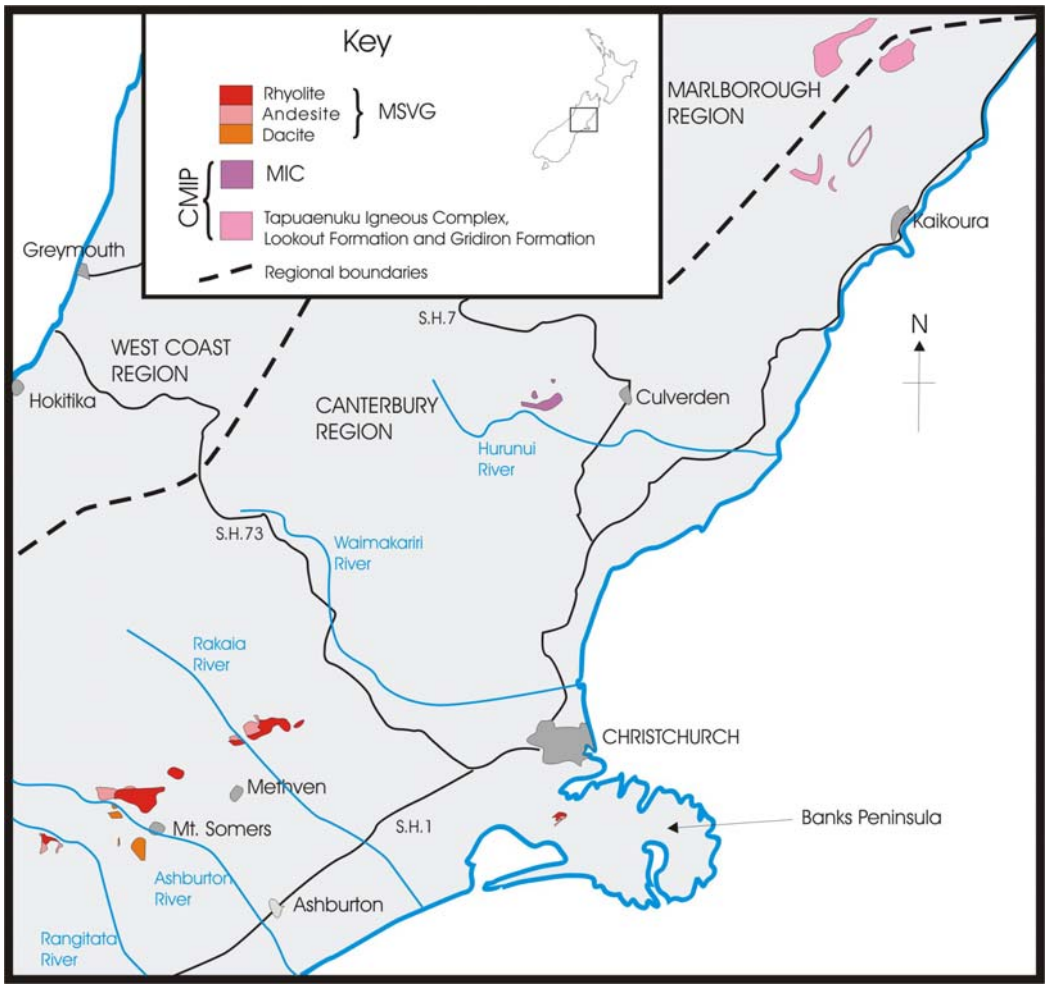

Fig.1.1 Map showing the field areas of the MSVG and MIC.

Also shown on figure 1.1 are other expressions of the CMIP, which outcrop in the Marlborough region. The MIC is part of the CMIP and the similarities between the igneous centres of the CMIP are discussed further in Chapter 8.

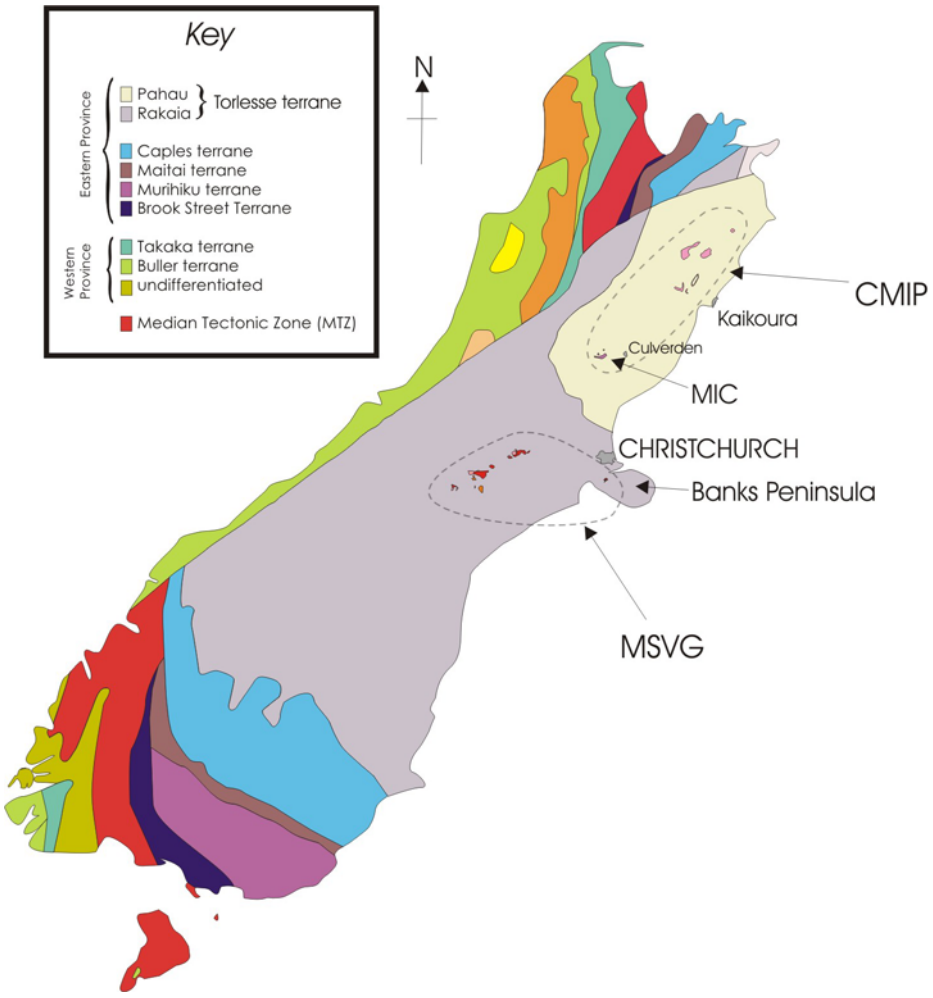

Fig.1.2 Terrane basemap of the South Island of New Zealand with the distribution of the Central Marlborough Igneous Province (CMIP) (which includes the MIC) and Mount Somers Volcanics Group (MSVG) indicated.

1.2 Research aims

This research was undertaken primarily to constrain the timing and nature of crustal and magmatic processes which took place during the mid-Cretaceous New Zealand-Gondwana continental rifting episode. The specific aims of this thesis are as follows:

1. **Evolution of complexes:** To understand the evolution of the MSVG and MIC by means of establishing emplacement mechanisms, relative ages and source areas based on detailed field mapping of all exposures of the MSVG and MIC.

2. **Timing of events:** To determine the age of the MSVG and MIC with the aid of high-precision dating techniques.

3. **Geochemical sampling:** To undertake a systematic and detailed geochemical study of the evolution of the MIC and MSVG using a combination of XRF, ICP-MS and TIMS methods to collate a full array of major, trace, REE and isotopic data. The MIC and MSVG have been examined by other authors, as described in the 'Previous Work' section of Chapter 3. However, neither systematic geochemical studies on the evolution of the two complexes, nor comparitive analyses have hitherto been undertaken.

4. **Parental magmas and crustal processes:** To deduce the nature of the parental magmas and subsequent contamination histories of the MSVG and MIC. To test whether the two suites were derived from the same parent magma and to infer the nature of processes occurring in the underlying mantle at the time.

5. **Relative positions of MSVG and MIC:** To determine why the MIC is restricted to the Pahau terrane of New Zealand and why the MSVG is restricted to the Rakaia terrane of New Zealand. What significance does the apparent geographical restriction of the two suites have?

6. **Generation of a tectono-magmatic model:** To produce a 'best-fit' tectonic scenario, which synthesises the above points to explain the overall geological context and petrogenetic relationship between the MIC and MSVG. The model produced must take into account the broader tectonic picture and work that has been carried out in other areas such as Australia and Antarctica.

1.3 Thesis organization

The thesis is organized into 10 chapters. The following sub-sections provide a guide to the specific abbreviations and terminology used within the text. Complete lists of geochemical, geochronological, isotopic data and petrographic descriptions are found in the appendices. Descriptions of analytical techniques are also provided in the appendices.

1.3.1 Locality and sample numbering system

Each locality and sample collected has a reference number. The prefix to the sample number indicates from which field area the sample was collected and these are listed below.

MS- Mount Somers and Mount Barrosa
MV- McQueens Valley and Gebbies Pass, Banks Peninsula
GD- Gawler Downs
MH- Malvern Hills
RG- Rangitata Gorge
M- Mandamus

Locality numbers are written as follows MS/22, RG/4, GD/22 etc. The locality numbering system differs from the sample numbering system in that the sample numbering system uses a '-' symbol rather than a '/' symbol. For example: "RG/42, RG-30" corresponds to sample number 30 collected from locality number 42 in the Rangitata Gorge mapped area. Where the sample numbers are given a letter suffix e.g. MS-216a, this indicates that a number of samples were collected from the immediate vicinity or outcrop.

The main period of fieldwork was undertaken between January and November 2000.

1.3.2 Sample Treatment

The rock catalogue (Appendix 1) provides a means of cross-referencing the sample number with the locality numbers and grid references. The main purpose of the catalogue is to describe the treatment of each specimen. Each sample was cut and the fresh surface described in order to select samples for more detailed analysis.

Carefully selected samples were thin-sectioned for petrographic investigation and from those samples 190 were selected for XRF analysis. As the analyses progressed, samples were selected for SHRIMP and Ar-Ar geochronology, ICP-MS analysis and radiogenic and stable isotope analysis.

1.3.3 Locality Grid Reference

Eight figure grid references are provided for optimum accuracy in most cases which serves to narrow the locality position to a 10 x 10m area rather than 100 x 100m area in the case of six figure grid references. Each grid reference is prefixed by a map reference e.g. K36/ for ease of relocation by future workers. The map series used is the Land Information 260 1:50 000 scale. For example, K36/ corresponds to : 'Topographic Map 260 K36 METHVEN'. A full list of maps used during the field mapping component of this thesis is listed in table 1.1.

Map Reference Code	Area covered	Reference
K36	METHVEN	(Terralink, 1998)
J36	MOUNT HARPER	(LINZ, 1991)
M36	LINCOLN	(LINZ, 1984)
K35	COLERIDGE	(LINZ, 1998)
L35	WAIMAKARIRI	(Terralink, 1997)
M33	WAIKARI	(LINZ, 1989)

Table 1.1 Maps used in study

1.3.4 New Zealand specific terminology

Due to the problems of using the typical 'northern hemisphere' Cretaceous time-scale, New Zealand workers have developed a New Zealand-specific Cretaceous time-scale which is more applicable to New Zealand research (Edwards *et al*, 1988). A reproduction of the relevant section of the time-scale section can be found in fig. 1.3. Both the international and New Zealand nomenclature are used in this thesis.

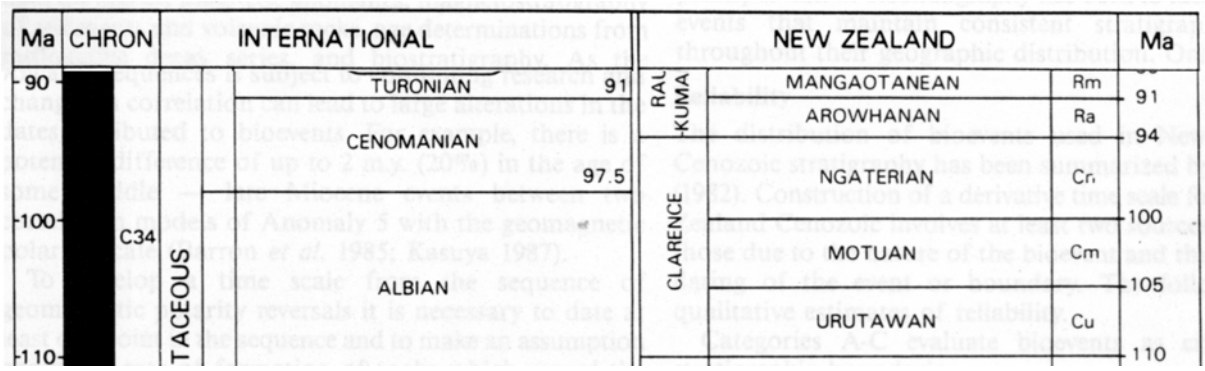

Fig.1.3 New Zealand time-scale, diagram modified from Edwards *et al*, 1988. The Turonian to Maastrichtian time-scale section of the Edwards *et al* time-scale has been removed in the reproduction above because it has been modified (Crampton *et al*, 2000) since the 1988 time scale of Edwards *et al*.

Chapter 2:
New Zealand Geology and Related Rocks

The first section of this chapter describes the present-day geological configuration of tectonostratigraphic terranes in the South Island of New Zealand, together with the offshore components of the New Zealand micro-continent which are pertinent to this study. The following sections provide a summary of the evidence which has been used by previous authors to infer the timing of extension and subsequent rifting.

The present-day configuration of New Zealand is the product of extensive tectonic modifications associated with New Zealand's location along an active plate margin since the Paleocene. Therefore, it must be emphasised that the paleo-configuration of New Zealand terranes immediately prior to break-up, *ca* 100 Ma ago, as described in section 2.1.5, bears at best, only limited resemblance to the present day geology.

2.1 Past and present terrane configuration of the South Island

The South Island can be divided into three super-terranes: the Western Province (WP), Median Tectonic Zone (MTZ) and Eastern Province (EP) (Fig. 2.1).

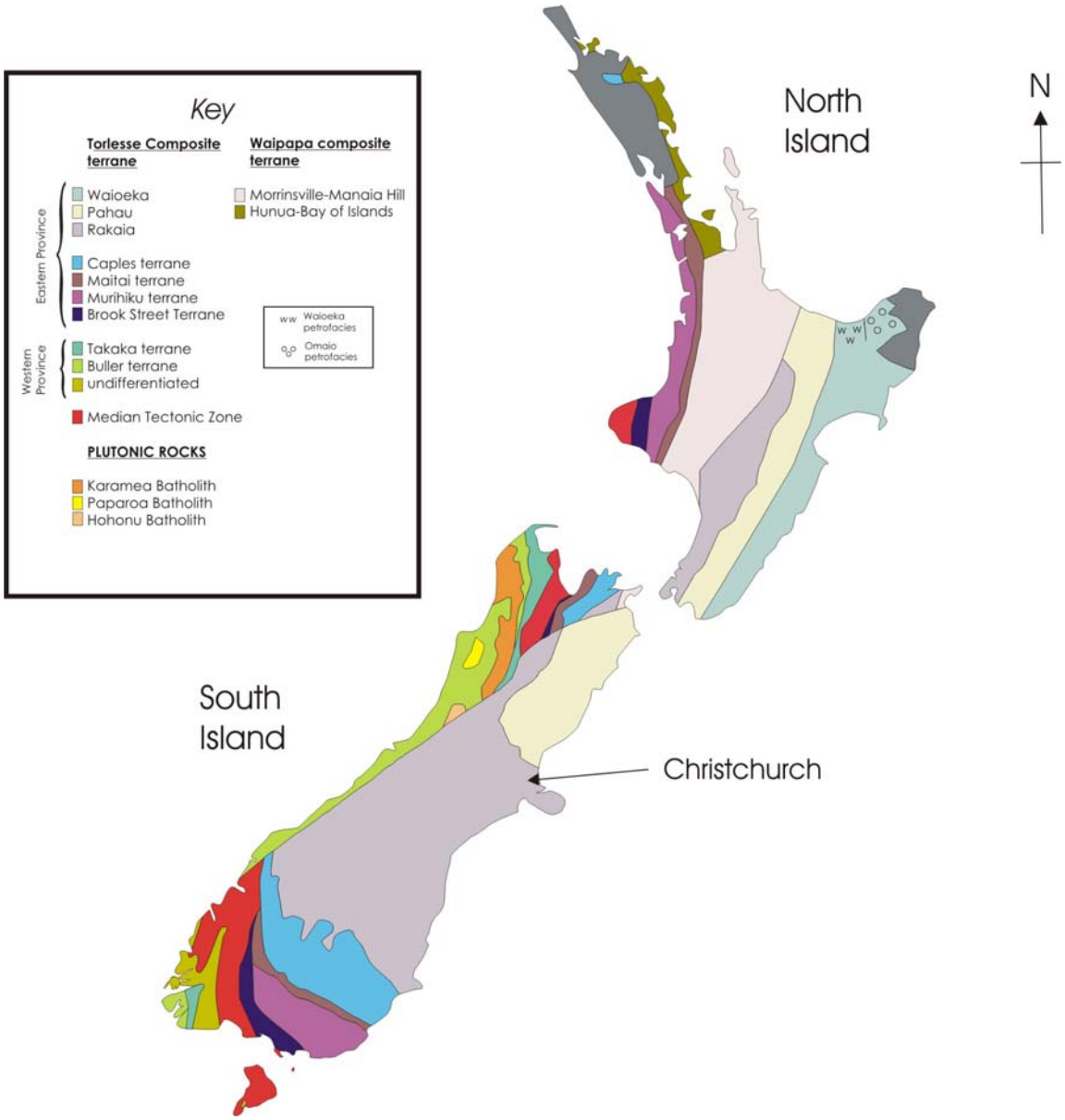

Fig. 2.1 Basement geology of New Zealand, based upon the map of Mazengarb and Speden (2000).

2.1.1 Western Province

The Western Province represents a fragment of the Gondwana Paleozoic margin, comprising Lower Paleozoic quartzose meta-sedimentary rocks cut by Devonian-Carboniferous granitoids, and the remnants of a Cambrian arc.

The Western Province is divided into two terranes, the Takaka and Buller terranes, which are separated by the Anatoki thrust. Both the Takaka and Buller terranes are monotonous sequences of lower Paleozoic metasediments which are cut by predominantly calc-alkaline,

'I' to 'S'-type granitoids of Paleozoic and Mesozoic age (Muir *et al*, 1997). The Buller and Takaka terranes differ with respect to lithology and cover strata. The Buller terrane is composed of quartz-rich sediments and black shales with Devonian cover strata; whereas the Takaka terrane is more variable, consisting of clastics, limestone and volcanics with Permian cover strata. It is widely accepted that the Western Province represents a fragment of Gondwana that had reached continental thickness by the end of the Carboniferous (Bradshaw, 1993).

Correlatives of the Western Province are found in Antarctica, where the Swanson Formation (Ross Province) and Robertson Bay Group (northern Victoria Land) closely resemble the Buller terrane. The Bowers terrane (northern Victoria Land) shows strong similarities to the Takaka terrane (Bradshaw *et al*, 1997). The Lachlan Fold Belt, specifically in the western Victoria area, shows similarities to the Buller terrane (Bradshaw *et al*, 1996), although the terrane boundaries and nomenclature are a topic of on-going research.

2.1.2 Median Tectonic Zone

The MTZ is the dissected remnant of a series of magmatic arcs, sandwiched between the Western and Eastern Provinces. Petrogenetic studies indicate little or no input from continental sources, favouring subduction of oceanic lithosphere and consequent melting of the mantle wedge to produce the predominant I-type granitoids and mafic intrusive bodies (Muir *et al*, 1995; Muir *et al*, 1998; Weaver *et al*, 1997).

Geochronological data suggest that the magmatic arc was active along the paleo-Pacific margin of Gondwana from 247-131 Ma. Activity is concentrated at 226 Ma and from 160 Ma to 131 Ma with a significant break in the Middle Jurassic (Kimbrough *et al*, 1993; Kimbrough *et al*, 1994; Muir *et al*, 1998).

The MTZ has strong similarities with a broader band of arc-magmatism in the Amundsen Province (Bradshaw *et al*, 1996, 1997; Pankhurst *et al*, 1998; Weaver *et al*, 1996), and Thurston Island (Pankhurst *et al*, 1993) in West Antarctica. The Marie Byrd Land equivalent of the MTZ is more intact than the MTZ and reaches a maximum width of 400km (Bradshaw

et al, 1997). The MTZ probably represents a thin sliver of what was a long-lived series of magmatic arcs which developed between the Carboniferous and Cretaceous off the paleo-Pacific margin of Gondwana (Bradshaw *et al*, 1997). Recent studies (Mortimer *et al*, 1999a; Mortimer *et al*, 1999b; Tulloch *et al*, 1999) suggest that the MTZ was an in-situ continental margin magmatic arc because there are instances of plutons intruding the Takaka terrane of the Western Province and '*emerging matches between the chronology of magmatism in the Median Batholith and batholiths in the Western Province*' (Mortimer *et al*, 1999b). These authors favour the re-naming of the MTZ as the 'Median Batholith' due to the predominantly intrusive nature of the contacts (>90%), and their conclusion that the MTZ/Median Batholith developed in-situ rather than being accreted to the Western Province.

2.1.3 The Eastern Province of New Zealand

The Eastern Province is composed of 6 terranes: Brook Street, Murihiku, Maitai, Caples, Torlesse, and Waipapa terranes. The 'Torlesse composite terrane' (Begg & Johnston, 2000) is further subdivided into the Rakaia and Pahau terranes in the South Island, which are separated by the Esk Head Melange. In the North Island, an additional terrane of the Torlesse is recognized as the Waioeka terrane (Leverenz, 2000; Mazengarb & Speden, 2000; Mortimer, 1995).

The boundary between the MTZ and the Eastern Province is the western limit of the Brook Street Terrane (Bradshaw, 1993). The Brook Street terrane contains clasts derived from the MTZ and indicates that the Brook Street terrane was alongside the MTZ in the early to mid-Jurassic (Landis *et al*, 1984; Mortimer *et al*, 1999b; Tulloch *et al*, 1999). The strong provenance relationship between the Brook Street terrane has recently led workers to suggest that the Brook Street terrane might be better placed in the MTZ.

Eastern Province terranes are reported to have correlatives in New Caledonia e.g. Campbell & Grant-Mackie, 2000; Lillie & Brothers, 1970; Sutherland, 1999; and the LeMay Group of central Alexander Island, Antarctica (Tranter, 1991).

2.1.4 Crustal thicknesses

Recent seismic investigations involving the SIGHT programme (South Island GeoPhysical Transect) have revealed that the Rakaia terrane is 30km thick at the east coast of the South Island and thickens to 42km underneath the Southern Alps (Davey *et al*, 1998) (fig.2.2).

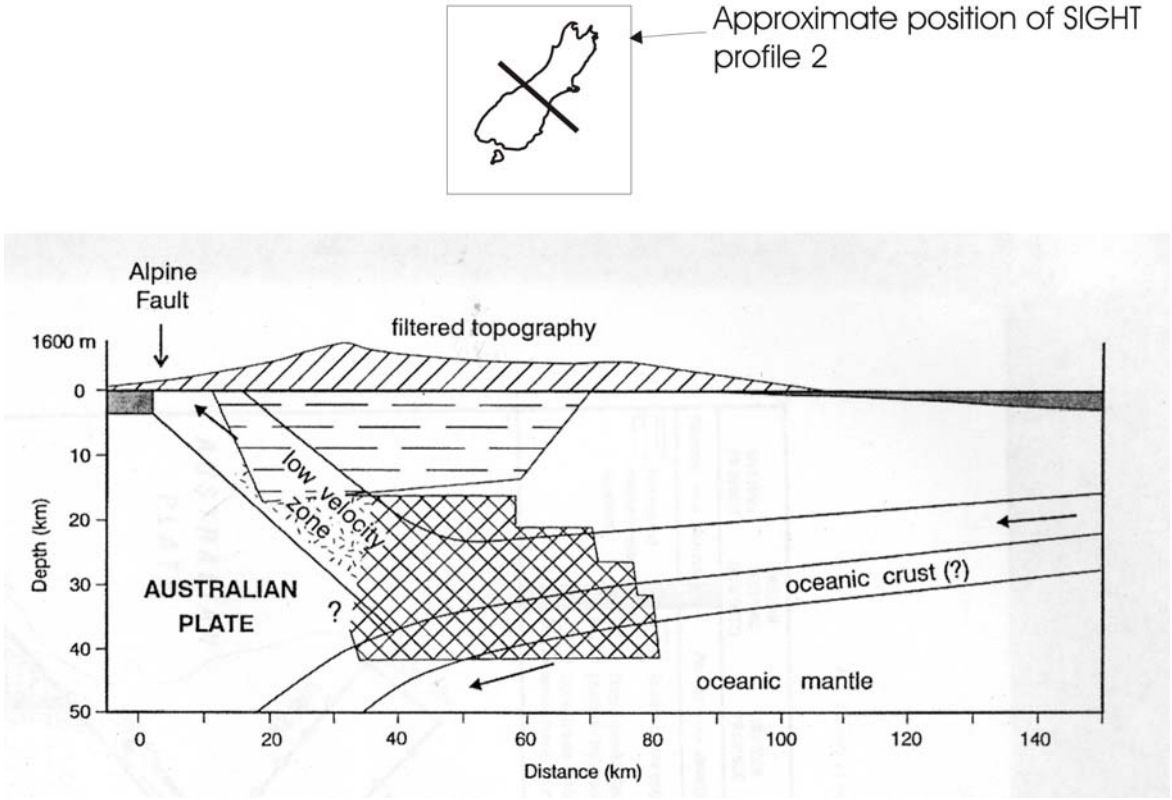

Fig.2.2 SIGHT profile number 2 illustrating a cross-section through the crust of the central South Island. Diagram from Davey *et al* (1998). Cross-hatching indicates a zone of high conductivity and the horizontal dashes indicate a high seismicity zone.

This thickness has been modified slightly by a further seismic line (SESI profile), which extended from near Christchurch to near Stewart Island, crossing the terranes of the Eastern Province and Median Batholith. The more recent SESI profile indicates a thickness of 25km in the Rakaia terrane, thickening to 32km under the Murihiku terrane (fig.2.3).

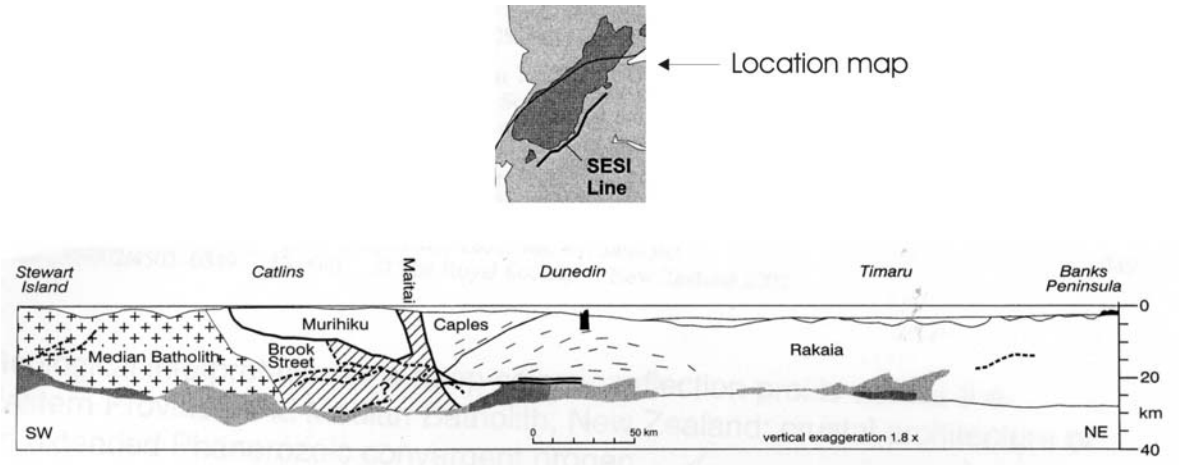

Fig.2.3 Interpretation of SESI profile (Mortimer *et al*, 2002).

Most seismic investigations in the South Island over recent years have involved the crustal structure at or below the latitude of Christchurch. Where seismic data is available to the north of Christchurch, the investigations have tended to concentrate on the Pacific-Antarctic plate boundary. However, the present day thickness of Pahau terrane appears to be similar to that of the Rakaia terrane and in the seismic profile interpretation of Eberhart-Phillips & Reyners (1997) (fig.2.4), the Pahau terrane continental crust is approximately 20km thick.

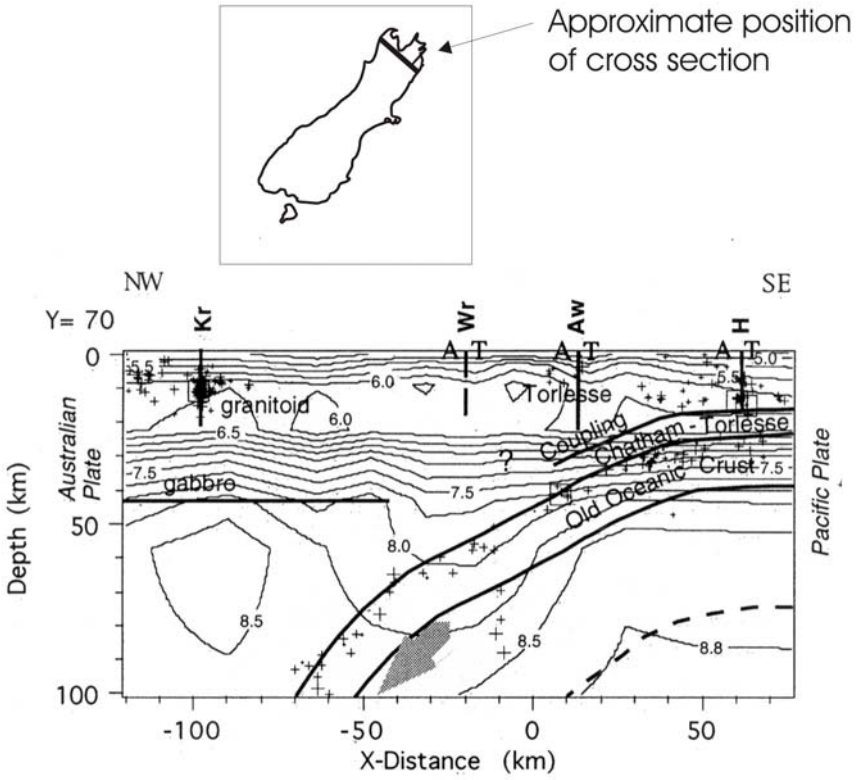

Fig.2.4 Interpretation of crustal cross section from passively-collected 3D seismic profiles (Eberhart-Phillips & Reyners, 1997). Kr: Karamea Fault, Wr: Wairau Fault, Aw: Awatere Fault, H: Hope Fault. 'A' and 'T' indicate motion away from and towards the observer respectively.

Eberhart-Phillips & Reyners (1997) note a distinct high velocity zone at shallow depth SE of the Awatere fault, which is asociated with the Tapuaenuku Igneous Complex (TIC). They also note a similar (although larger) high velocity body NW of the Awatere fault but there is no mapped igneous body in this area.

The Eastern Province terranes are not considered to have moved significantly relative to one another since the Cretaceous, evidence for which comes from the disposition of Late Cretaceous and Cenozoic sediments in the Taranaki Basin and Great South Basin (Bradshaw, 1989). There are also strong provenance links between the Pahau and Rakaia terranes, indicating that the Pahau terrane sediments were largely derived from the Rakaia terrane throughout the depositional history of the Pahau rocks (Permian to early Late Triassic) (Wandres, 2002).

2.1.5 Paleogeographic reconstruction of New Zealand prior to rifting

Numerous terrane reconstructions are found in the literature and the reconstruction displayed here (fig.2.5) is a simplified map based largely upon previously published terrane correlations and reconstructions (Bradshaw, 1989; Bradshaw *et al*, 1997; Mukasa & Dalziel, 2000; Sutherland, 1999; Veevers, 2000; Weaver *et al*, 1994; Weaver *et al*, 1996).

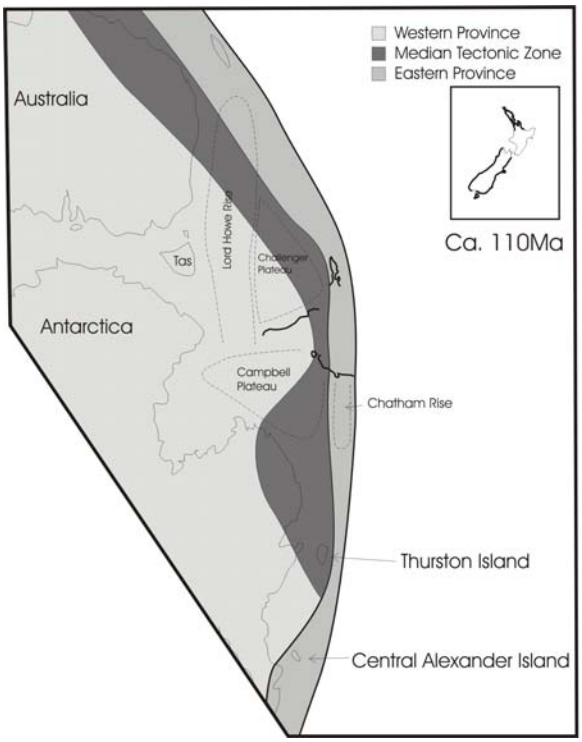

Fig. 2.5 Terrane reconstruction for the Gondwana margin at *ca* 110 Ma.

2.2 Evidence for the cessation of subduction and onset of rifting

By 118 Ma, New Zealand terrane amalgamation was complete. 118 Ma is the generally accepted age of the Separation Point Batholith which stitches the MTZ to the Western Province (Muir *et al*, 1995), however the Separation Point Batholith ages range from 119 ± 2 Ma (Gouland Granodiorite) to 111 ± 2 Ma (Muir *et al*, 1997). Equivalents of the Separation Point Batholith are found in the Eastern Fiordland Igneous Belt and are termed the Separation Point Suite (Muir *et al*, 1998). The granitoids of the Separation Point Suite in Fiordland are slightly older than their counterparts of the Separation Point Batholith in NW Nelson and the granitoid ages range from 121 Ma to 124 Ma (Muir *et al*, 1998). The Western Fiordland Orthogneiss (126 Ma) is considered to be the lower crustal equivalent of the Separation Point Suite (Muir *et al*, 1992; Muir *et al*, 1995; Muir *et al*, 1998). Collisional structures are observed in the lower crustal rocks exposed in northern Fiordland (Daczko *et al*, 2001), which are interpreted to have been caused by the collision between the MTZ and the Western Province. An MTZ-Western Province collision is also implied in the petrogenetic models of Muir *et al* (1995). However, a 'collision' is inconsistent with the Median Batholith model of Tulloch *et al* (1999) and Mortimer *et al* (1999a and b).

Between approximately 110 Ma and 95 Ma, an extensional regime developed within the New Zealand margin of Gondwana. Sedimentological evidence suggests that in the South Island, subduction of the 'Moa plate' (Sutherland & Hollis, 2001) ceased abruptly in the Motuan (105-100 Ma) at which time a major unconformity developed between heavily deformed strata and relatively undeformed strata containing the same Motuan-age fossils (Laird, 1993). The 'Motuan' corresponds to the international 'Albian' stage (Edwards *et al*, 1988). However there is evidence of substantial diachroneity between northern and southern New Zealand with respect to the cessation of subduction.

Work undertaken in the East Cape of the North Island suggests that subduction was ongoing until at least 92 Ma (Ballance, 1993; Cawood *et al*, 1999; Mazengarb & Speden, 2000). The Waipounamu erosion surface (Le Masurier & Landis, 1996), marks a period of extensive erosional levelling, which was complete by 75 Ma. Le Masurier & Landis (1996) conclude that the onset of levelling coincides with the first appearance of oceanic crust and the opening

of the Tasman Sea, at 85 Ma. They also state that the rifting and high relief present in the New Zealand area at about 100 Ma had declined greatly before the 85 Ma breakup event.

In support of continued subduction, a further terrane has been recognized in the Torlesse composite terrane of the East Cape. The 'Waioeke' terrane (Cawood *et al*, 1999; Mazengarb & Speden, 2000; Mortimer, 1995) comprises two petrofacies, the Omaio and Waioeke petrofacies. Both petrofacies display strong deformation attributed to accretion in a subduction prism environment. Recent U/Pb dating has yielded a youngest detrital zircon age of 100 Ma from the Omaio facies, with 50% of grains in the range 99 ± 2 to 133 ± 2 Ma (Cawood *et al*, 1999). The youngest detrital zircon age from a number of facies was taken to represent the maximum age of sedimentation. An evaluation of the East Cape terranes in terms of thermochronology and tectonic reconstructions was undertaken by Kamp (1999). The fission-track thermochronology indicates rapid cooling from 92-83Ma of the Omaio facies consistent with uplift and erosion which is interpreted to result from compression in a subduction environment (Kamp, 1999).

Deformational changes in the forearc strata provide more reliable evidence for the cessation of subduction than inferences made based upon uplift and erosion, or the end of calc-alkaline I-type magmatism. Processes such as uplift, extension and calc-alkaline magmatism can occur several million years following the cessation of subduction due to tectonic re-organisations, slab detachment, slab rollback, isostatic adjustments or potentially un-related processes such as the arrival of a plume head.

Large extensional half-grabens developed in the Western Province of New Zealand at *ca* 105 Ma (fig. 2.6), which formed large fault-bounded sedimentary basins (Laird, 1993). Similar trending faults are observed along the Chatham Rise, which also developed in the mid-Cretaceous although their ages are not well constrained. The Western Province grabens strike W or WNW, implying extension in a N or NE direction (Laird, 1993). The Pororari Group is found in the southern and northern Paparoa Range and was deposited into the half-grabens. The Pororari Group crops out in two extensive areas on the E and W flanks of both the southern and northern end of the Paparoa Range. In the south of the Paparoa range, the western sequence can be divided into four lithostratigraphic units (Laird, 1988), three of which can be recognised on the eastern side, with the absence of the basal unit (Laird, 1993).

The volcanic ‘Stitts Tuff’ (Bowen, 1964) occurs at the base of the Pororari Group in the northern Paparoa range (Buller Gorge). SHRIMP dating on zircon crystals extracted from the tuff has yielded crystallisation ages of 101 ± 2 Ma (2σ) and 102 ± 3 Ma (2σ) (Muir *et al*, 1997). The Stitts Tuff provides a minimum age for the onset of extension and basin formation in the northern Paparoa Range. Extension continued with syn-depositional movement along the bounding faults throughout the Pororari Group deposition (Laird, 1993).

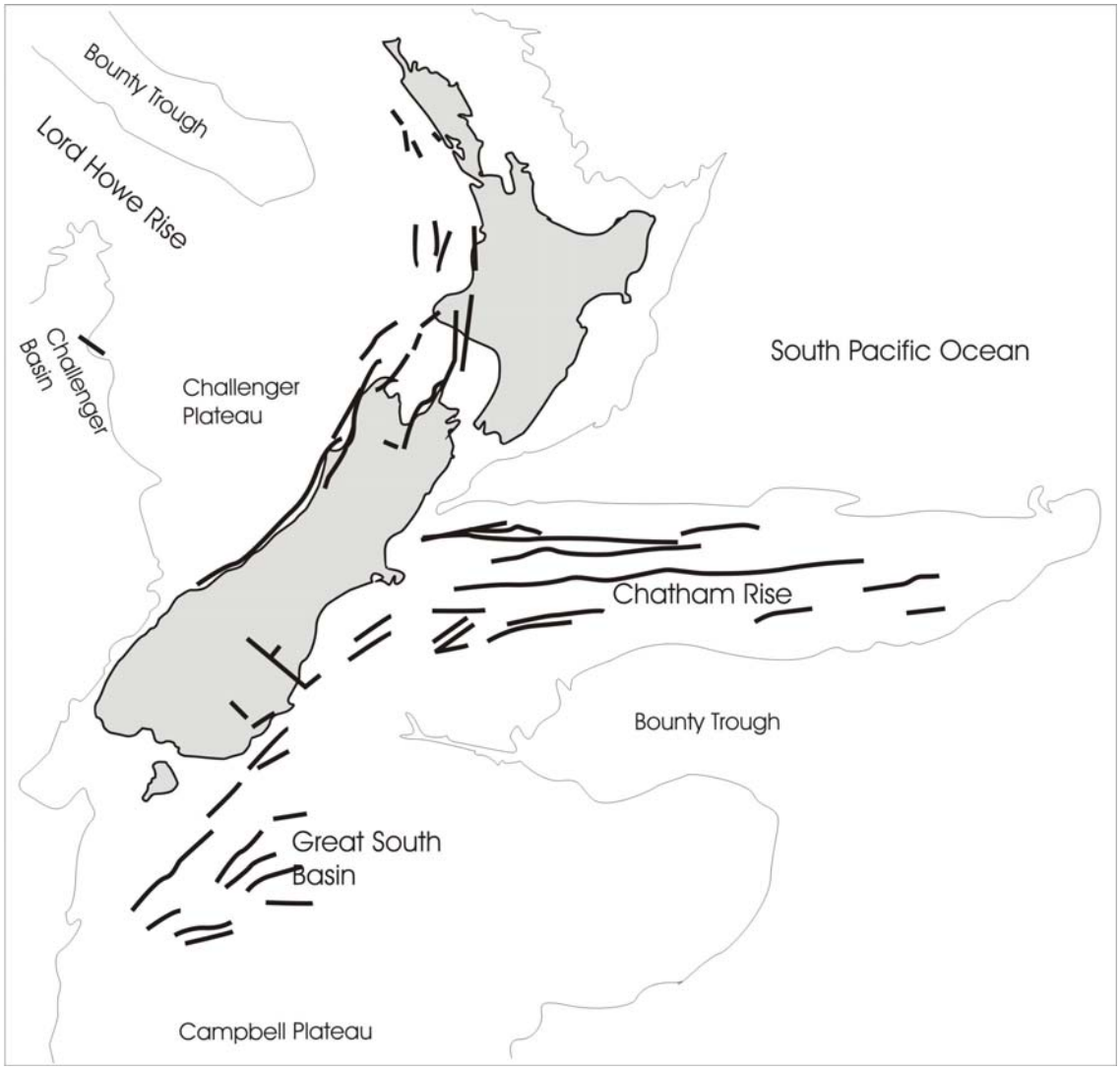

Fig. 2.6 Cretaceous age rifts in the New Zealand region. Derived from the diagram of Laird, 1993.

Another series of extensional basins, which are filled by Cenomanian (97.5 Ma) and younger deposits are found in the South Island e.g. the Great South Basin (Beggs, 1993; Cook *et al*, 1999) and southern Canterbury Basins (Field & Browne, 1989) . These slightly younger basins trend NNE-NE which is sub-parallel to the trend of the spreading axes formed during separation of New Zealand from Antarctica.

2.3 Onset of extension: igneous evidence

The 118 Ma Separation Point Batholith (fig. 2.7) is regarded as being subduction-derived, related to the underthrusting of the MTZ under the Western Province during final amalgamation, with the production of adakitic magmas (Muir *et al*, 1995). In the Buller terrane of the Western Province, granitoids were emplaced at approximately 110 Ma that retain a chemical signature inherited from Separation Point magmas (Waight *et al*, 1997; Waight *et al*, 1998b). The 114-109 Ma Hohonu Suite granitoids are interpreted to have been formed by melting of lower continental crust during the onset of an extensional tectonic regime. The Buckland granite temporally overlapped the emplacement of the last phases of the Hohonu Suite and yields a 109.6 ± 1.7 Ma emplacement age (Muir *et al*, 1994).

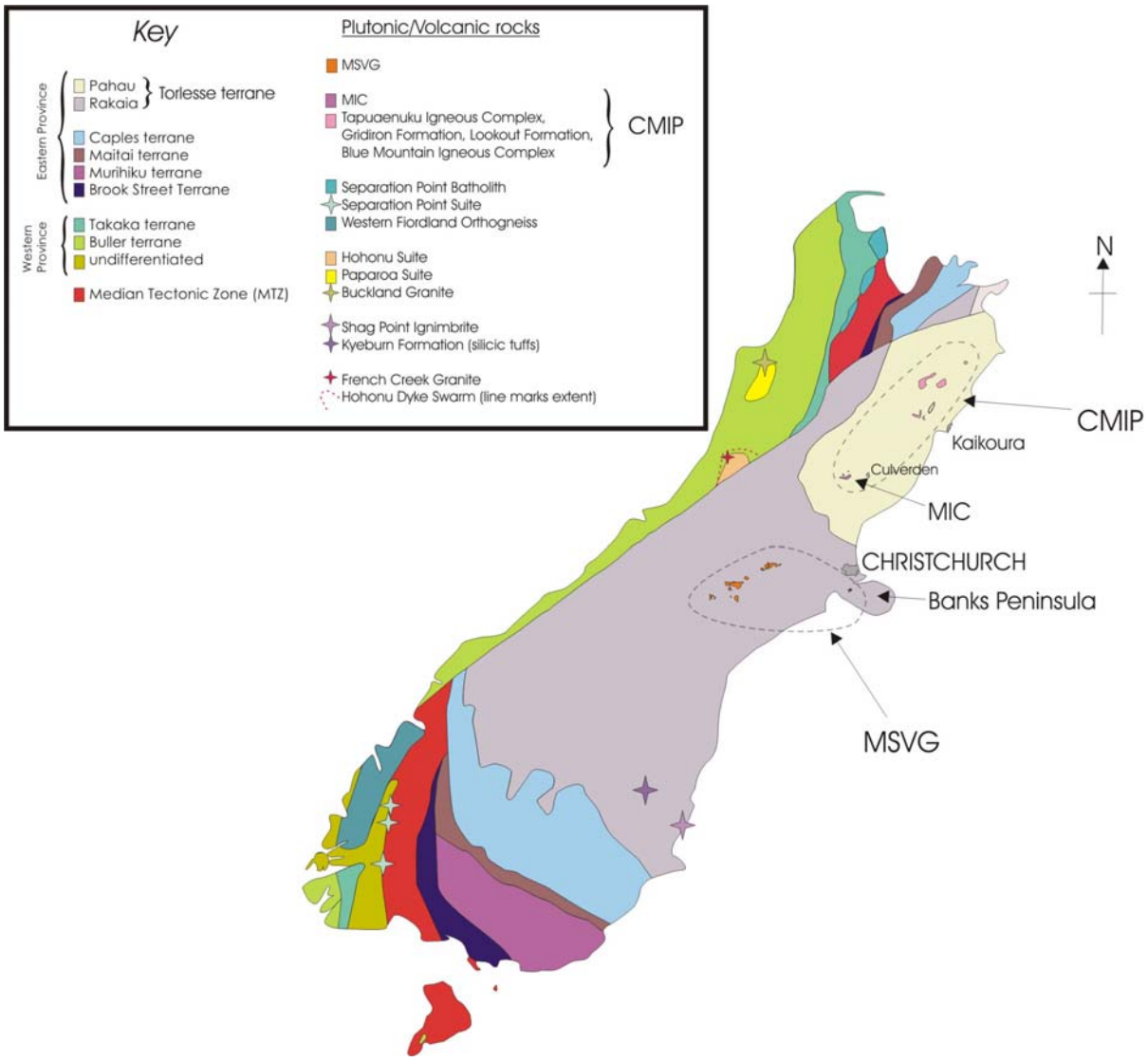

Fig. 2.7 Basement terrane map with Cretaceous intrusions and volcanics pertinent to this discussion shown.

In addition to the Stitts Tuff, evidence for mid-Cretaceous volcanism is found in other fault-related basins such as basic volcanic rocks on the Raukumara Peninsula (Mazengarb & Speden, 2000), along the eastern coast of the North Island (Moore & Speden, 1979), and in Northland (Hay, 1975). Correlatives of the Stitts Tuff may be the mid-Cretaceous Shag Point Ignimbrite in eastern Otago (Steiner *et al*, 1959) and the silicic tuffs in the Kyeburn Formation in central Otago (Adams & Raine, 1988).

The Paparoa metamorphic core complex is found SE of Westport on the West Coast of the South Island. It was rapidly unroofed during a brief interval at around 100 Ma, which continued until 90 Ma at which time slower cooling rates began (Spell *et al*, 2000). The Buckland Granite of the Paparoa Suite (mentioned previously) forms the central zone of the metamorphic core complex and has a crystallization age of 109.6 ± 1.7 Ma (Muir *et al*, 1994). The emplacement of the Buckland Granite was inferred to have occurred approximately 5 million years prior to the extension, uplift and denudation of the core complex due to the observation of post-emplacement shearing of the granite (Muir *et al*, 1994). However, Waight *et al* (1998) suggest that the emplacement of the Buckland Granite was syn-tectonic, with the unroofing leading to decompression partial melting of the lower crustal rocks.

Examples of temporally related calc-alkaline volcanism include Rangiawhia volcanics and Rangiputa Granophyre of the Mount Camel terrane (Houhora Complex) in Northland (northern tip of the North Island) (Hay, 1975; Isaac *et al*, 1994), dated at 131-94 (written communications cited in Isaac *et al* (1994)); rhyolitic samples extracted from DSDP drill site 207, leg 21 on the summit of the Lord Howe Rise, dated at 93.7 ± 1.1 Ma (McDougall & van der Lingen, 1974); and felsic volcanic pebbles and cobbles from the Tupuangi Formation (Waihere Bay Group), Chatham Islands, which are stratigraphically dated as Motuan to Teratan 105 – 87 Ma (Campbell *et al*, 1993).

The French Creek Granite (Tulloch *et al*, 1994; Waight *et al*, 1998a) is the youngest component of the Hohonu Batholith which intrudes the Greenland Group of the Buller Terrane (Western Province). It has an emplacement age of 81.7 ± 1.8 Ma (Waight *et al*, 1997) and is genetically linked to the Hohonu Dyke Swarm. This magmatism was probably generated during a second phase of extension, which occurred during mid-Campanian times

(approximately 80-84 Ma), in the southern South Island and in the west of both the North and South Islands (Laird, 1993).

The oldest oceanic magnetic anomalies are Chron 34 (84 Ma), found near the margin of the Lord Howe Rise and Tasmania (Mayes *et al*, 1990; Veevers, 2000), the oldest anomalies in the Southern Ocean are probably the same age. The 84 Ma date provides a time constraint for the onset of sea floor spreading between the Australian continent and New Zealand. The later phase of extension noted from sedimentological evidence in New Zealand is probably related to the opening of the Southern Ocean and Tasman Sea, and appearance of new oceanic crust.

2.4 Correlated igneous activity in Antarctica and Australia

2.4.1 Antarctica

Rift-related granitoid emplacement and mafic dykes and sills are found in Marie Byrd Land, Antarctica. Mafic dykes are found in Marie Byrd Land and have been dated at 107 ± 5 Ma (Spörli & Craddock, 1981; Storey *et al*, 1999; Weaver *et al*, 1992; Weaver *et al*, 1994). The intrusion of mafic dykes was followed by the emplacement of A-type granites of Edward VII Peninsula, which intrude the Swanson Formation (Western Province equivalent). The granitoids were emplaced between 95-102 Ma (Storey *et al*, 1999; Weaver *et al*, 1992).

The Fosdick Metamorphic Complex, in the Ford Ranges, was uplifted and cooled between 100 and 94 Ma (Kimbrough & Richard, 1991). The uplift and cooling event may have overlapped with the second phase of Byrd Coast Granite emplacement at 110 Ma (Adams, 1987; Weaver & Pankhurst, 1991). The uplift history of the Fosdick Metamorphic Complex shows strong similarities with the uplift history of the Paparoa Core Complex in New Zealand.

2.4.2 Australia

In Australia, the earliest magmatism ascribed to continental break-up is the Whitsunday Volcanic Province (Bryan *et al*, 1997; Bryan *et al*, 2000; Ewart *et al*, 1992; Stephens *et al*, 1995). The generation of calc-alkaline volcanics formed a magmatic belt extending some 900km with extended periods of volcanism from 132-95 Ma, with most ages falling in the range 120-105 Ma. The large quantity of volcanogenic sediment deposited into the Great Artesian, Gippsland and Otway basins, is interpreted to have been derived from the Whitsunday Volcanic Province (Bryan *et al*, 2000). The Gippsland and Otway basins lay 1500km south of the Whitsunday Volcanic Province and received $4x10^5$ km^3 of volcanogenic sediment during Aptian to Albian times. Grains have been dated by fission track geochronology as 126-103 Ma (Gleadow & Duddy, 1980).

The Whitsunday Volcanic Group has been interpreted as rift-related by Ewart *et al* (1992) and Bryan *et al* (2000) despite the volcanics having major, trace, and isotopic geochemical characteristics of subduction-derived magmas (Ewart *et al*, 1992; Stephens *et al*, 1995). Bryan *et al* (2000) ascribes the large quantities of ignimbrite as being derived from crustal partial melts and state that there is a '*geochemical connection*' between pre-breakup magmatism and younger post-breakup intraplate volcanism.

Minor volcanism and dyke emplacement in Cape Portland, NE Tasmania, has been apatite fission track dated at 98 ± 4 Ma (Gleadow & Duddy, 1980).

In eastern Australia, rapid and significant uplift accompanied the initial basin-forming and volcanic extensional phase. 1-2 km uplift of the Bathurst Batholith in New South Wales has been ascribed to the initial stage of extension which occurred at 90 ± 10 Ma (O'Sullivan *et al*, 1995). Also in New South Wales, the 6km diameter Mt. Dromedary intrusion has been dated by Rb-Sr geochronology at 98.6 ± 0.7 Ma (Smith *et al*, 1988; Williams *et al*, 1982).

Two periods of rapid cooling and denudation have been reported in the Furneaux Island, from fission track data (O'Sullivan *et al*, 2000). These events occurred in the mid-Cretaceous (94 ± 2 Ma) and in the early Tertiary (65-45 Ma). The periods of unroofing reported by O'Sullivan *et al* (2000) correlate well with the tectono-stratigraphic regime modifications termed

"Swerves of the Pacific" (Veevers, 2000). The regime changes are inferred from kinks in linear volcanic chains which occurred at 99 Ma and 43 Ma (Veevers, 2000). The change at 99 Ma is interpreted to reflect a change from head on 'Chilean-type' to oblique 'Mariana-type' subduction, and the onset of extension in eastern Australia (Veevers, 2000).

2.5 Summary

Extension-related tectonics are evident from the large sedimentary basins which formed in the New Zealand region of the Gondwana margin at *ca* 105 Ma. The Pororari basin (Laird, 1988, 1993), Bounty Trough (Carter & Carter, 1993; Davy, 1993) and Great South Basin (Beggs, 1993; Cook *et al*, 1999) are all examples of mid-Cretaceous extensional basins. The Western Province basins strike sub-parallel to the Gondwana margin, whereas the slightly younger basins (Cenomanian onwards) developed sub-parallel to the future Tasman spreading ridge.

The timing of subduction cessation remains debatable. In the North Island, north of Wairarapa, evidence suggests subduction continued until at least 92 Ma; however, the unconformity observed over much of the South Island would suggest an older date of mid-Motuan (105 - 100 Ma).

Igneous activity in New Zealand during the mid-Cretaceous is represented by the Hohonu and Separation Point Suites. These suites are dominated by granitoids displaying subduction-signatures but which are interpreted to have inherited the signatures from their sources which were enriched during extended periods of convergence. The Hohonu suite is interpreted to mark the transition from convergence to extension (Waight *et al*, 1998b).

Anorogenic, alkaline granitoids associated with extension are found in Marie Byrd Land, with the Edward VII Peninsula granites dated at 94-102 Ma (Storey *et al*, 1999; Weaver *et al*, 1992) and on the Ruppert-Hobbs coast, dated at 95-102 Ma (Weaver *et al*, 1994). The French Creek Granite is younger and broadly coincides with the first appearance of ocean crust as a result of continental drift.

In the South Island of New Zealand, the volcanics temporally associated with the transition from convergence to extension are the focus of this study.

Chapter 3:
Location of field areas and previous work

This section describes the outcrops of the two main study areas, the Mount Somers Volcanics Group (MSVG) and the Mandamus Igneous Complex (MIC). The MSVG is further subdivided because of its large geographical extent into smaller field areas as outlined in section 3.1.

3.1 Mount Somers Volcanics Group

The outcrops of the Mount Somers Volcanics Group (MSVG) studied in this thesis are listed in the table below and shown on fig.3.1.

Field area name	Locality & Sample No. prefix used
Mount Somers	MS
Gawler Downs	GD
Rangitata Gorge	RG
McQueens Valley	MV
Malvern Hills	MH

Table 3.1 MSVG field area sub-divisions and guide to prefixes.

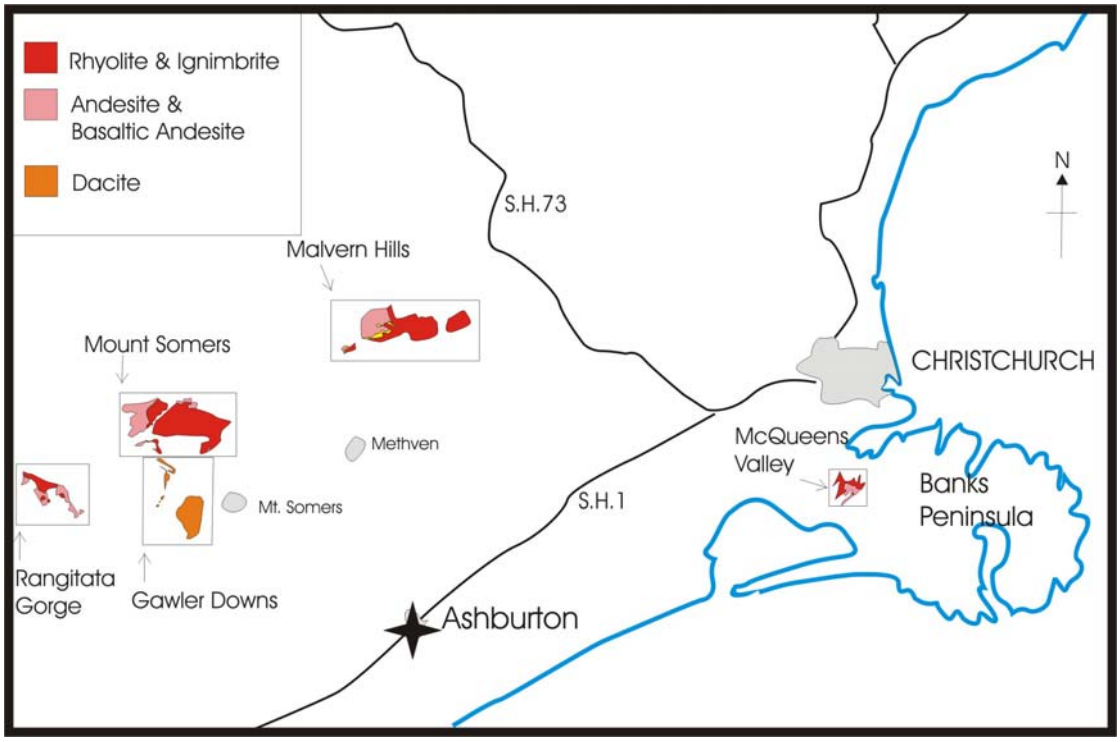

Fig. 3.1 MSVG field area locations

3.1.1 Introduction to MSVG field areas

Brief geomorphological and geological descriptions of the terrain and features of the individual areas are listed below:

3.1.1.1 Mount Somers

The Mount Somers area takes its name from the Mt. Somers township at the base of Mt. Somers (1687m) and is located 100km WSW of Christchurch (Fig. 3.1). The Mount Somers field area extends from the western edge of the Mt. Barrosa to Staveley in the east (fig. 3.2).

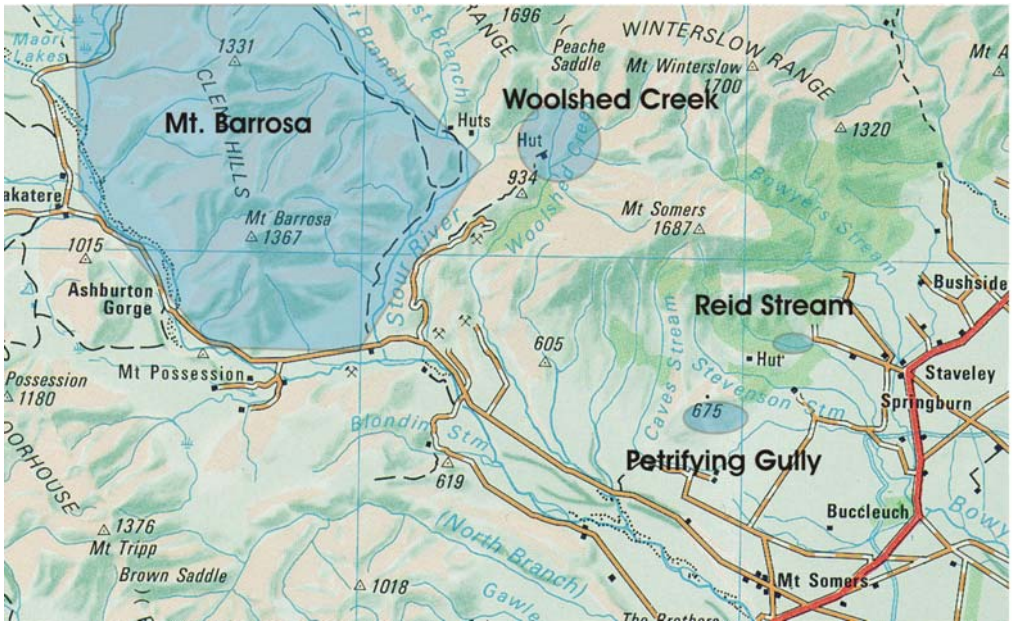

Fig 3.2 Closeup of the Mount Somers field area.

The area forms the most easterly expression of the Southern Alps at this latitude; protruding through the overlying gravel sequences of the Canterbury Plains. The terrain rises steeply some 1200m over a lateral distance of 5km, an average gradient of 1:4. The area contains the principle and largest continuous outcrop of 'Mount Somers Volcanic Group' (Cox, 1877).

The purpose of the Mount Somers study was primarily to determine a volcanic stratigraphy of the main andesite outcrops. Rhyolite and ignimbrite stratigraphy has been studied, sampled and analysed in recent years by several workers (ref. section 3.1.2). Data, maps and samples from these theses have been utilised for this study and are referenced in the text accordingly.

Mt. Barrosa

The majority of fieldwork undertaken in the Mount Somers area was in the Clent Hills, of which Mt. Barrosa (1364m) forms the summit (Fig. 3.3).

Fig. 3.3 Oblique aerial photograph of Mt. Barrosa from the SE

Mt. Barrosa contains the largest exposure of andesite in the Mount Somers Volcanic Group, and comprises andesite flows, basaltic-andesite flows, dacite blocky flows, a pitchstone horizon, rhyolitic lava flows and a rhyolite dome complex. The volcanics rest unconformably on Balmacaan Formation rocks of the Mount Taylor Group (Torlesse terrane) of probable Etalian age (mid-Triassic) (Oliver & Keene, 1990). The Clent Hills are bordered by the South Branch Ashburton River to the S and W, and by the Stour River to the E and NE. The terrain is steep, with the southwestern faces rising from the Ashburton River at average gradients of 20º with local steepening to gradients in excess of 35º. The slopes are drained by several streams with valley sides prone to scree development, particularly within the Torlesse bedrock areas (Fig.3.4).

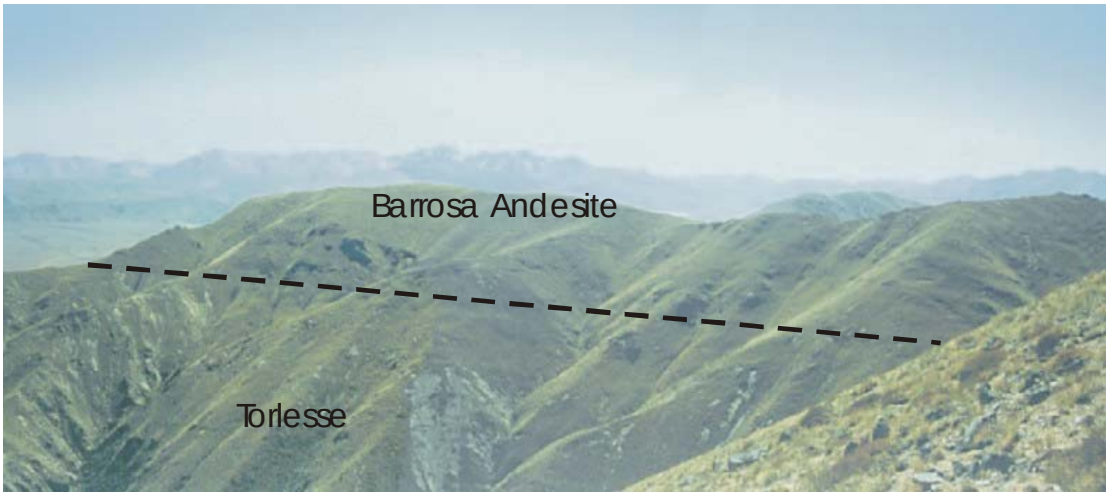

Fig. 3.4 View of northern ridge over Waterfall Stream, taken from the southeastern ridge.

The terrain to the N, S and E is somewhat easier to negotiate with only localised steep terrain and cliff sections. The vegetation is well grazed by stock with just a few patches of dense matagouri and broom in the valley bottoms. The majority of the Clent Hills is owned and stocked by Mr R. Grigg of Barrosa Station, Ashburton Gorge Road.

Petrifying Gully

Petrifying Gully is the name given to a small valley 5km NNW of Mt Somers township on the lower slopes of Mt. Somers (fig. 3.2). The area was selected because a large outcrop of andesite was reported by Oliver & Keene (1989) and Oliver (1977). The valley is heavily overgrown by native bush and access ways are made frustratingly difficult by the abundance of gorse. The most successful approach is from the southern fenced boundary; climbing the deer paddock until the native beech forest is encountered. At this point the native beech forest provides cover and conditions inhospitable to gorse enabling passage toward the stream and pond, from which the upper reaches of the gully can be accessed.

Petrifying gully is named after the petrified wood for which the gully is locally famous.

Reid Stream

The Reid Stream locality was investigated in response to a recommendation from Z. Bruce whose family owns a farm on Boyds Road, Staveley. The area is densely vegetated by native bush and access is by foot. Outcrops of pitchstone are located in the stream bed as reported by Oliver & Keene (1989).

Woolshed Creek

Woolshed Creek is a creek draining the western flanks of Mt. Somers (fig. 3.2). The area investigated in this study is in the upper reaches of Woolshed Creek. This area has been investigated thoroughly by other workers (Oliver, 1977; Richnow, 1999; Smith, 1994; Smith & Cole, 1996). For the purposes of this study, investigation of the area was reconnaissance only with minor sample collection for thin-sectioning and comparative XRF work.

The upper reaches of Woolshed Creek are most easily accessed by foot from the Woolshed Creek carpark off the Ashburton Gorge Road. The footpath is maintained by the Department of Conservation and is the start of the Mount Somers Walkway. 4-wheel drive access is possible by permission of the Department of Conservation.

Woolshed Creek flows through a steep canyon, 200m deep (fig.3.5). The footpath takes a northerly route along the western rim of the canyon.

Fig. 3.5 Woolshed Creek looking N

3.1.1.2 Gawler Downs

'Gawler Downs' is the name given to the low hills draining the northern slopes of the 'Surrey Hills', the low lying hills to the SW of Mt. Somers township (fig. 3.1 and 3.6). Some smaller areas are also included in the Gawler Downs field area and a close up of the area is shown in fig. 3.7.

Fig. 3.6 Oblique aerial photograph of the Gawler Downs (Surrey Hills) taken from the N.

The terrain is gentle, rolling, green, tussock-covered slopes with a frustrating paucity of outcrop.

Rangiatea

The land belonging to Rangiatea Station was included in the study of the Gawler Downs although this area lies some 6 km to the NW (fig.3.7). The area was investigated in order to deduce the volcanic stratigraphy of the dacites which comprise most of the area.

Access is by foot and several 4WD tracks provide easy access to ridge crests and valleys.

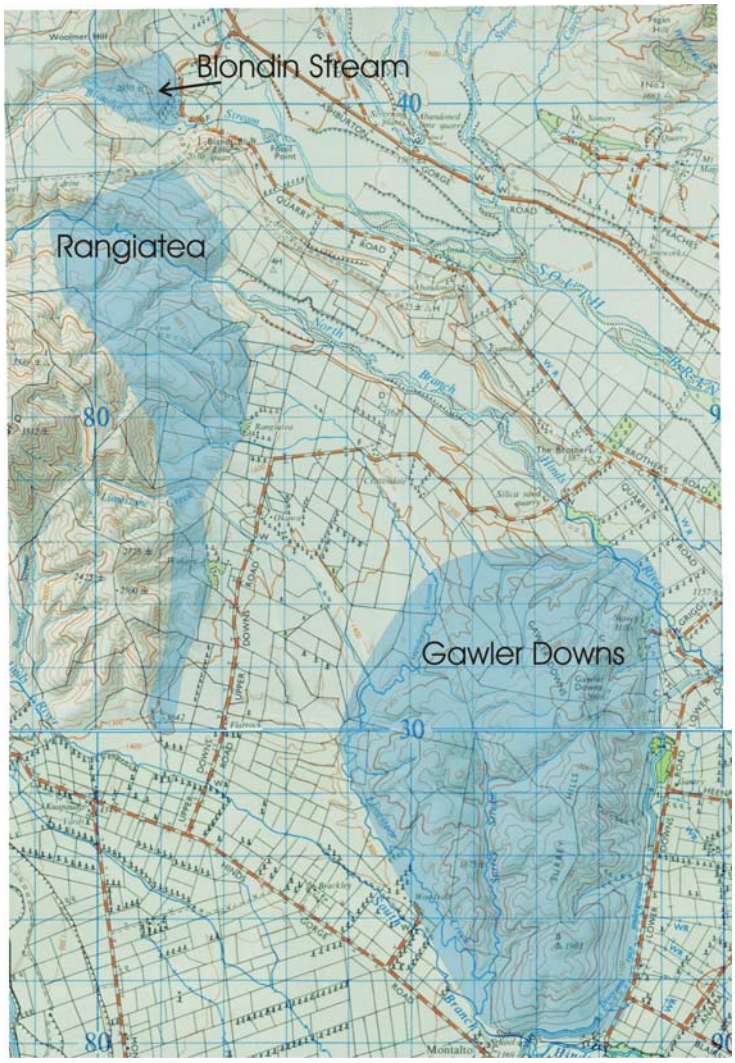

Fig. 3.7 Gawler Downs field areas overlain on topographic maps S81 and S91(DLS, 1970a, b).

Blondin Stream

This stream drains the hills behind Inverary homestead (fig. 3.7). The purpose of the fieldwork at this location was to sample the andesite and pitchstone mapped by Oliver & Keene (1989) for comparative purposes.

3.1.1.3 Rangitata Gorge

The Rangitata Gorge outcrops (fig.3.1 and 3.8) of the MSVG are a mere 13km from the closest outcrops of Mt. Barrosa, but are separated by the high Moorhouse Range and fast flowing Rangitata River which forces a detour of at least 70km. Access to the main andesite

outcrops is by foot or quad-bike as the andesites outcrop along the ridge above very steep terrain averaging a gradient of 35°.

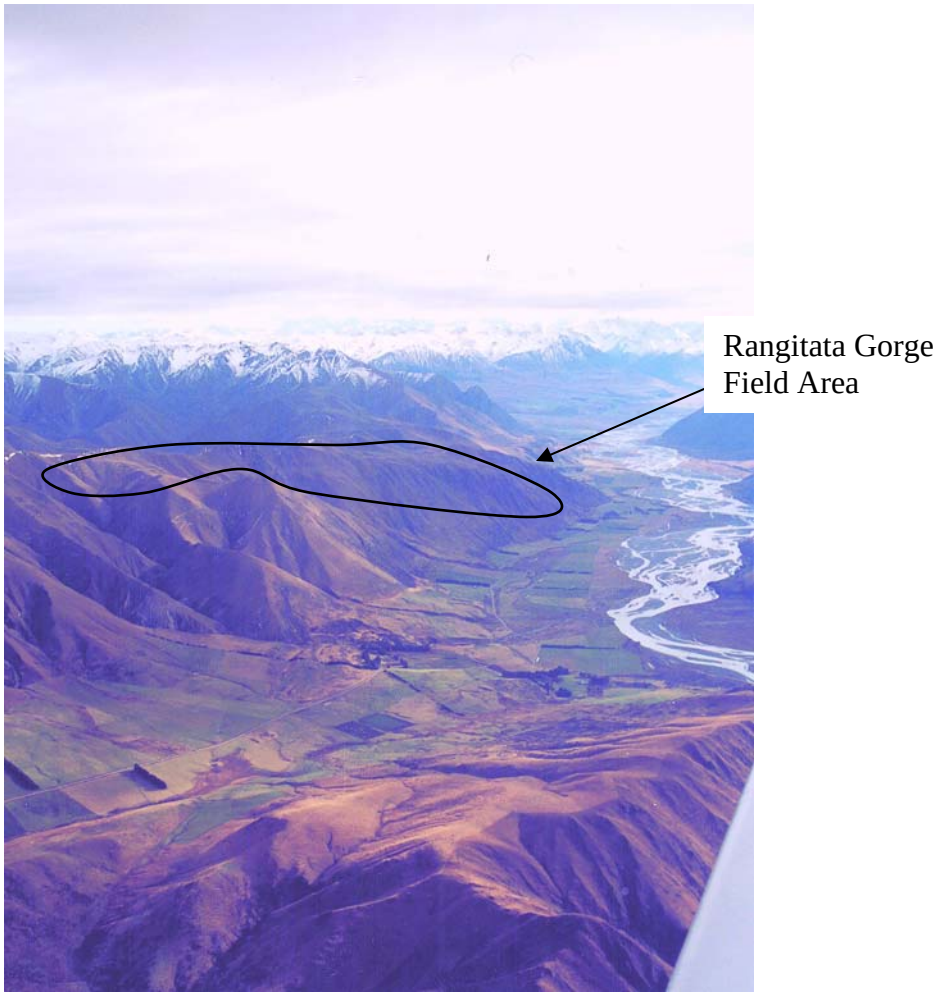

Fig. 3.8 Oblique aerial photograph of the upper Rangitata Gorge

The volcanics in the Rangitata Gorge outcrop on land belonging to Stew Point and Rata Peaks Stations. The volcanics lie unconformably on undifferentiated Torlesse bedrock (Oliver & Keene, 1990).

Generally the gradient of the terrain up the Rangitata Gorge inhibits the development of dense vegetation. Where the terrain is flatter, marshy grassland is present and generally well-grazed by stock.

3.1.1.4 McQueens Valley

Access to McQueens Valley is from the main Akaroa highway from Christchurch. The land is locally owned and access is easy and the terrain low. The MSVG volcanics here are exposed as the basement of the large Tertiary Lyttelton Volcano of Banks Peninsula (fig. 3.1).

3.1.1.5 Malvern Hills

The MSVG outcrop in the Malvern Hills from the Rakaia Gorge in an easterly direction as far as Mt. Misery (fig. 3.1). The land is divided into farm land and forestry blocks. The farm land is again divided between stations: Longspur, The Point, Birch View, Quartz Hill, Rockwood and Bryans Hill. The forestry blocks are owned by the Selwyn Plantation Board (Rockwood Forest and Pullwool Peak) and the McVicar Timber Company (Mt. Misery).

Access was achieved by negotiation with land owners and was generally easy. The terrain is easily negotiated and is well served by 4WD tracks or forestry tracks. The forested areas proved difficult to map due to burial by tree debris and dense gorse underlying the younger trees. However, the forestry and 4WD tracks provided good cuttings in places with excellent exposure of geology.

3.1.2 Previous Work on the MSVG

3.1.2.1 Mount Somers, Gawler Downs, Rangitata Gorge

The earliest reports on the geology of the Mount Somers field area are those of Haast (1862). Haast reported on 13 months of fieldwork undertaken to investigate reports of coal and auriferous deposits, as well as topographical surveying (Haast, 1862). Haast surveyed the Ashburton and Rangitata Rivers (including their tributaries, to their sources), the Malvern Hills (including the Kowai coal measures), Mount Torlesse, Thirteen Mile Bush Range, Mount Cook and the river system which forms Lake Tekapo, Pukaki and Ohou (Ohau). Of

the Mount Somers field area he noted the presence of rhyolite but was more concerned, at this time, with the potential for metalliferous deposits associated with the volcanics.
In 1872 Haast reported on the coal of the Ashburton area (Haast, 1872b). He notes the similarity between the Mt. Somers region and the Malvern Hills and likened the coal present to similar measures of New South Wales. He considered the variation in thickness of coal in the two areas to be related to a basin formed by the rhyolites in the Mt. Somers area.

Three surveys, undertaken by Haast in 1861, 1864 and 1873 are reported on in a single, short paper (Haast, 1877). He comments on the volcanics being deposited in a basin and concludes that they flowed beneath sea level. Until 1877, the majority of mapping had been undertaken by Haast. However, in 1877, Cox visited the area under the instruction of Hector to '*revise the arrangement of strata…in accordance with our later knowledge'*. Using Haast's maps and previous work, Cox remarks at the detail of the mapping and made no amendments to the map (Cox, 1877).

Cox revisited the Mt. Somers area in 1883, again under instruction, to re-examine the volcanics in order to '*fix the exact position of the quartz-porphyries* (rhyolites & ignimbrites) ….. *and associated igneous rocks'*. The reason for the re-evaluation was to obtain '*absolute proof*' of their temporal relationship to the coal-bearing strata (Cox, 1884a). In his report Cox did not contradict the earlier work which assigns an older age to the 'melaphyres' (andesites and dacites) and a younger age to the 'liparites' (rhyolites and ignimbrites) despite the 'melaphyres' clearly overlying the 'liparites' in the Malvern Hills. Instead, he proposes an endogenous growth model for both the Mt. Somers area and the Malvern Hills.

Cox provided a brief summary of the petrographic properties of the pitchstones of Mt. Somers (Cox, 1884b). The ignimbritic nature of part of the MSVG was first proposed in 1938 (Speight, 1938).

The earliest petrogenetic work on the MSVG was based on major-element ratios (Challis, 1968). Challis ascribed the Cretaceous volcanics from Mount Somers, Mandamus and inland Kaikoura as a volcanic arc.

Later work focussed on the rhyolites (Wood, 1974). The occurrence of garnet as a phenocryst phase meant that the rocks were of considerable interest. Wood noted compositional

differences between the garnets of the Mt. Misery volcanics (Malvern Hills) and the garnets of the Mount Somers area. A crustal anatexis mechanism was proposed by Wood for the generation of the rhyolites.

Oliver produced the most thorough map of the area for his PhD thesis (Oliver, 1977). The Mesozoic sedimentary rocks and their structures are reported in several papers (Oliver, 1979; Oliver *et al*, 1979; Oliver *et al*, 1982; Oliver, 1986a). The volcanic succession is also discussed in several papers (Oliver, 1980, 1984, 1986b). The thesis and papers formed the basis of the 1989 and 1990 geological maps (Oliver & Keene, 1989, 1990). In 1979, the MSVG were dated by K-Ar methods (Adams & Oliver, 1979), which provided crystallisation ages of rhyolites (88-99Ma) and andesites and dacites (87-93Ma).

Although the distribution of the various units within the MSVG had been constrained, staff and students of the University of Canterbury instigated several projects designed to investigate in more detail, the nature, origin and petrogenesis of the volcanics within the MSVG. The first project was undertaken by Barley (Barley, 1987; Barley *et al*, 1988) to establish the petrogenesis and crystallisation age of the MSVG. Barley agreed with the earlier work of Wood (1974), and concluded that the rhyolites probably formed by partial melting of quartzo-feldspathic Torlesse sediments; whereas he concluded that the andesites probably formed by fractionating and crustally contaminating a mantle parent magma. The Sr isotope work also yielded ages for the rhyolites of the MSVG at 89.3 ± 2Ma (Barley *et al*, 1988).

Kinney and Bruce undertook BSc (Hons) projects designed to map, in more detail the Mt. Alford rhyolites and Malvern Hills volcanics respectively (Bruce, 1994; Kinney, 1993). Bruce's work is described in more detail in the Malvern Hills section 3.1.2.2. Also in 1994, the extent of the ignimbrites of Mount Somers were investigated (Smith, 1994; Smith & Cole, 1996, 1997). The rhyolite domes of Mt. Somers were studied by Richnow, who also determined the distribution of the ignimbrites (Richnow, 1999).

3.1.2.2 Malvern Hills

The Malvern Hills area was first investigated by Haast in 1861 shortly after European settlement (Haast, 1862, 1863). Haast, at the time, was the Provincial Geologist for the

Province of Canterbury. Haast and Hector were the prominent geologists in the area submitting several reports to the Government of the Province of Canterbury, which, until 1876 included Westland. Haast's 1879 book (Haast, 1879) provides an excellent account of the work undertaken during the early settlement days.

On 25 November 1869 Hector submitted a report summarising the basic geological structure of the Malvern Hills (Hector, 1871). The report concentrated on the economic potential of the area, with the main emphasis on coal seam locations, grade and auriferous deposits associated with the volcanics. The report acknowledged and derived its rudiments from the earlier work of Haast (1863). He anticipated '*a source of wealth to the province*' from these deposits. Hector noted the presence of 'porphyry' (ignimbrite and rhyolite) and indicated an age older than that of the coal bearing strata. He also recognised a tabular structure in the gully behind Rockwood Station (ignimbrite) which weathers into abrupt crags and a change to pitchstone up sequence.

In July 1871, Haast submitted his preliminary report on the Malvern Hills in which he summarised the economic potential of the area (Haast, 1871a). He commented on the presence of 'quartzose porphyry, granites or granitoid porphyries, trachyte porphyries, trachyte pearlites, pitchstones, melaphyres and amygdaloids'. Of the agate geodes he suggested '*one day might form a valuable export to Europe, for the manufacture of the so-called oberstein articles…worth £30 per ton in European ports*'. He also suggested the use of porphyries (ignimbrite) as '*fine material for the erection of public buildings*'. He suggested the potential presence of 3,000,000 tons of coal which would help free New Zealand from dependency upon Australian coal.

Haast submitted the full report on 25 October 1871 (Haast, 1872a). The report is far more comprehensive, committing itself more fully to relative age determination and geological history. He comments on the presence of *Pecopteris* beds in both the Malvern and Clent Hills thereby indicating an identical age and linking them with beds of similar age in New South Wales. One significant determination was the division of the igneous rocks into two main groups: basic and acidic, the latter being reported as the younger. He referred to the basic rocks as 'melaphyres' and the acidic rocks as 'quartziferous-porphyries'. He determined that the beds are not of Tertiary age as he had previous considered but rather are associated with the melaphyres, albeit younger. He noted the presence of garnet and considered the '*principle*

centre of eruption … to have been at the head of Rockwood Creek at the base of High Peak'. He also considered all the volcanic rocks to be '*without doubt of submarine origin*'.
H.S. Cox examined and mapped the extent of the 'quartz-porphyries' (ignimbrites and rhyolites) which underlie the coal bearing strata in 1883 on the instruction of Hector (Cox, 1884a). Despite Haast reporting the name of 'rhyolite'; H.S. Cox preferred to retain Hutton's 'liparite' but resisted changing the name of the 'melaphyres'. Although agreeing with Haast (1871a) that the acidic rocks are younger than the basic rocks, he questions their submarine origin and applies a subaerial condition for their extrusion (Cox, 1884a). Although not going so far as to contradict Haast's order of extrusion, H.S. Cox does question the simplicity of the melaphyres underlying the liparites and explains the relationship by endogenous growth of the liparites. H.S. Cox explains the presence of pitchstones at Mount Somers and Malvern Hills as the rapidly chilled extremities of the quartz-porphyries (Cox, 1884b).

During this early settlement period, most geological mapping was undertaken to locate economic resources and areas of interest were continually revisited in order to further investigate the potential for exploitation. The proximity of the Malvern Hills to Christchurch made the area particularly attractive. The highest priority was the procurement of coal to release New Zealand from its dependence upon Australia. Haast, Hector and Lindop provide brief accounts of coal mining developments in the Malvern Hills (Haast, 1871a; Hector, 1871; Lindop, 1886). Ore deposits were also of economic interest and were commented on by the earliest workers (Haast, 1879; Hector, 1871). McKay in 1885 examined the cupiferous deposits in the Malvern Hills but did not advance the mapping of the volcanic units (McKay, 1886).

Between the late 1880's and the end of World War II, little progress was made and the Malvern Hills were not examined again until P.T. Cox, 39 years later, revisited the area and, with the benefit of '*newer conceptions*', made several important observations of the igneous sequence (Cox, 1926). Firstly, he renamed the 'quartz-porphyries' and 'melaphyres', as rhyolites and andesites; and secondly re-interpreted the sequence of events and determined that the rhyolites form the oldest igneous unit exposed (Cox, 1926). He examined the mineralogy of the rocks in more detail and provided 3 chemical analyses with CIPW norms. He considered that the pitchstones were successive flows of the same eruption. Given the apparent differences between the Mount Somers sequence of events and Malvern Hills sequence of events Cox postulates that a non-contemporaneous eruption of the two suites

would explain the differing age relationships. However, he then goes on to say that '*it must be considered very improbable that the eruptions of each type were not contemporaneous in both districts*'. Jobberns examined the Selwyn catchment and comments briefly on observations made of Mt Misery. He said of the rhyolites, '*obviously not a volcano of the ordinary explosive type, but probably was formed by slow accretion of a viscous lava by endogenous growth'* (Jobberns, 1926).

Two years later, in 1928, Speight published a paper which presented similar findings to P.T. Cox albeit in greater detail (Speight, 1928), with more reference to specific localities in the Malvern Hills. He also provided 5 whole-rock analyses from the area.

Oborn & Suggate produced the first 1:250 000 geological map of the area, the northern limit of which cuts the Malvern Hills to the north of the Rakaia Gorge bridge but to the south of Round Top (Oborn & Suggate, 1959). They subdivided the Malvern Hills Cretaceous volcanics into two groups and coined the names 'Round Top Volcanics' (andesite) and 'Mt. Misery Volcanics' (rhyolites). They assigned an '*? early Cretaceous*' age to the andesites and a '*? mid-Cretaceous'* age to the rhyolites; in contrast to the interpretation of P.T.Cox (1926) and Speight (1928), although they concede that the stratigraphic relation of the two are '*uncertain*'.

Gregg published Sheet 18, the bounding map that continues to the north of Sheet 21 (Gregg, 1964). This sheet contains the majority of the Malvern Hills Volcanics. The map and accompanying literature is non-committal with regard to the relationship of the two units (Round Top Andesite and Mt Misery Rhyolite).

Suggate published the 2nd edition of the Geological Map, Sheet 21, Christchurch in which he maintains the stratigraphic relationship between the rhyolites and andesites, with the latter reported as the younger of the two (Suggate, 1973).

Oliver undertook a limited amount of work in the Malvern Hills; the main emphasis of his thesis being the Mount Somers area (Oliver, 1977). However, he did re-visit the Malvern Hills again to look more closely at the nature of the rhyolites and their relationship to the andesites. Using the map of Speight (1928) he sampled the various lithologies in the area and

quotes 6 XRF analyses (Oliver, 1984). He also determined that the rhyolite is in the form of ignimbrites, domes and dykes.

McKay (1886) and Lauder (Lauder, 1953, 1962) provide limited accounts of the Malvern Hills geology whilst concentrating their efforts on the Acheron river intrusives.

More recently, Bruce (1994) completed a BSc (Hons) project in the Malvern Hills and mapped a small area in the vicinity of the Rakaia Gorge.

3.1.2.3 McQueens Valley

The McQueens Valley and Gebbies Pass outcrops of the MSVG (fig. 3.1) were first commented on by Haast, Hutton and Speight (Haast, 1879; Hutton, 1889; Speight, 1917). In 1934 Speight submitted a more thorough report on the volcanics of Gebbies Pass and McQueens Valley (Speight, 1935). In his report, he notes the similarity of the andesites and rhyolites to those of the Malvern Hills, Clent Hills and Gawler Downs. He also supports previous considerations that the rhyolite is younger than the andesites.

In 1976 Middleton assigned a Cretaceous age to the andesites, whilst assigning a Miocene age to the rhyolites (Middleton, 1976). In 1980, Price & Taylor assigned a Miocene age to the rhyolites and an Oligocene age to the McQueens Valley andesites (Price & Taylor, 1980). It was not until 1988 that Rb-Sr geochronological work determined a Cretaceous age for the McQueens valley and Gebbies pass volcanics (Barley *et al*, 1988).

The volcanics subsequently appeared on geological maps as Cretaceous in age (Sewell *et al*, 1988; Sewell *et al*, 1992).

3.1.3 Extent of the MSVG

Examples of the MSVG, as described previously, outcrop at several localities in the foothills of the Southern Alps and at the base of the Lyttelton Volcano on Banks Peninsula. The

MSVG is exposed due to the uplifting of basement in these areas. The thick sequences of Tertiary to recent cover strata of the Canterbury Plains masks the underlying basement rocks and therefore the distribution of the MSVG underneath the Canterbury Plains is inferred from drill hole data and geophysical surveys (Fig. 3.9).

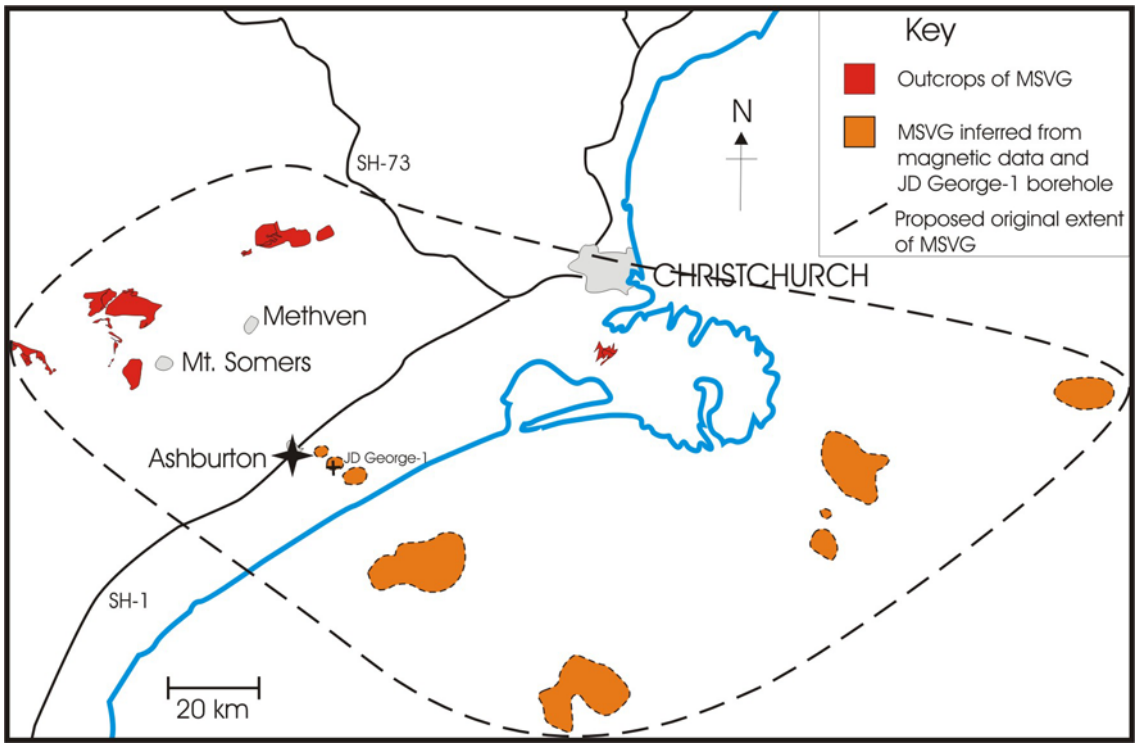

Fig.3.9 Map showing the outcrops and probable extent of the MSVG beneath the Canterbury Plains and offshore Canterbury coast. Magnetic anomalies from map 6 (Field & Browne, 1989).

The J.D.George-1 borehole near Seafield bottomed out at 1588m in andesite and minor rhyolite (Wood, 1969). The andesites of this borehole are correlated with the MSVG (Field & Browne, 1989; Wood, 1969).

Gravity, magnetic and seismic data indicate that the MSVG are probably also of regional extent under the Canterbury Plains between Mt. Somers, Geraldine and Ashburton (Field & Browne, 1989; Gavin, 2000).

Approximately 30 km^3 of MSVG is presently exposed in Canterbury. Original Cretaceous volume estimates are very difficult to establish given the uncertain location, extent and thickness of buried and offshore MSVG outcrops, however given the probable distribution of MSVG beneath the Canterbury plains and offshore Canterbury (fig.3.9), a conservative estimate of the original Cretaceous volume of MSVG is approximately 900 km^3 (based upon

an average thickness of 50m across the area). The suspected areal extent of the MSVG (fig.3.9) is approximately 18 000 km^2, which is the same as estimates for the currently active Taupo Volcanic Zone in the North Island of New Zealand (Wilson *et al*, 1995) (fig.3.10). Volume estimates for the TVZ are uncertain but are in the order of 15-20 000 km^3 (Wilson *et al*, 1995).

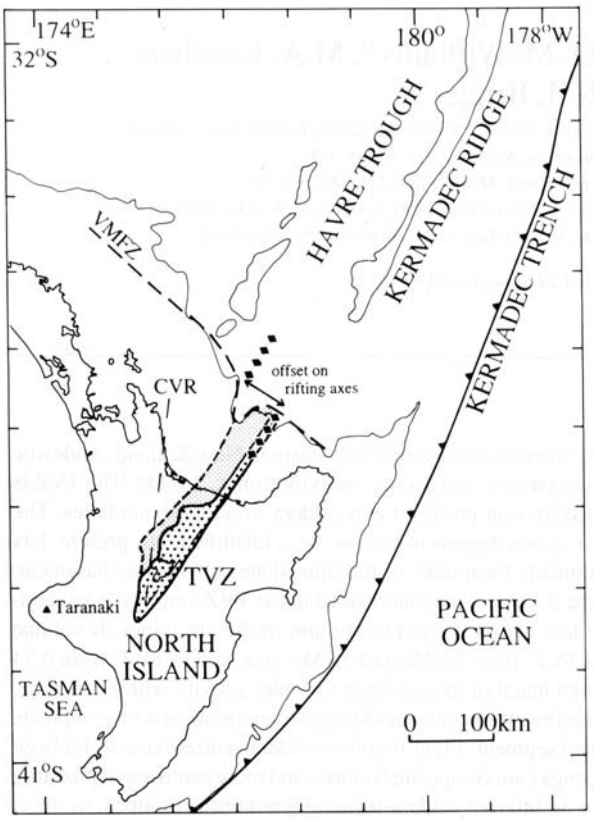

Fig.3.10 Location and extent of TVZ from Wilson *et al* (1995)

3.2 Mandamus Igneous Complex

The prefix used for outcrops of the Mandamus Igneous Complex (MIC) is 'M'. The main fieldwork for this area was undertaken in early 2001 when mapping focussed on the MIC, with particular emphasis on relative age determination of the various units from field observations. Mapping of the Tertiary succession has taken place every year for over 50 years by the students of the Geological Sciences Department, who use the area for field mapping classes.

Fieldwork was carried out on land belonging to ‘Glens of Tekoa’, ‘Island Hills’ and ‘Korari Downs’ stations. During the early phase of European colonization the area was settled by the McRae family from Scotland in 1851. The McRae family still own and run the Glens of Tekoa station in the Mandamus valley.

3.2.1 Location and physiography of the MIC field area

The MIC is located in north Canterbury in the South Island of New Zealand (fig.3.11).

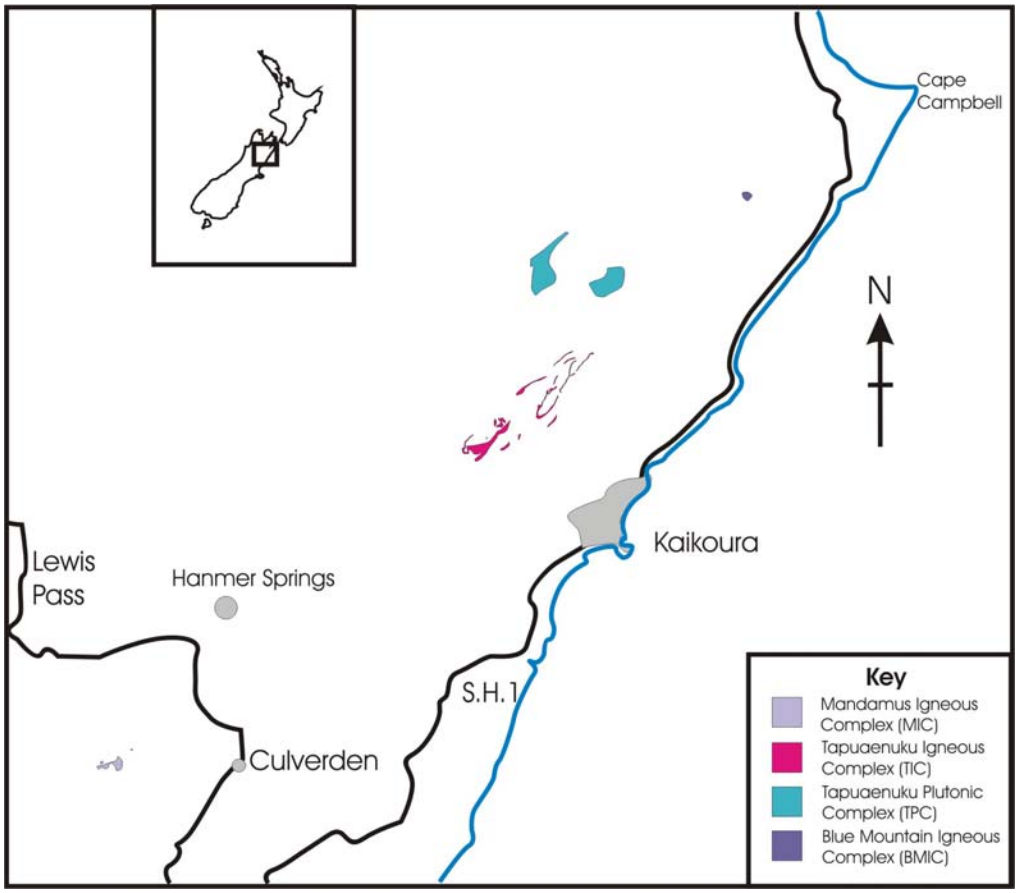

Fig.3.11 Map illustrating the location of the MIC and the other components of the Central Marlborough Igneous Province (CMIP).

The topography of the MIC field area is variable and geologically controlled. The Tertiary sediments form low lying, grass and tussock covered hills which are only locally elevated by folding which has created synclinal structures (Mould, 1992). Gradual erosion has uncovered basement geology in the Dove and Mandamus rivers. The MIC generally forms steep rugged landscapes with common shear, even cliff forming outcrops of resistant units. Some outcrops

proved to be inaccessible due to the severity of gradient, or the dense bush (broom and matagouri) cover. The MIC rises steeply to Hurunui Peak at an elevation of 937m, over 500m above the valley floors. The southern slopes descent steeply toward the Tekoa Road which marks the northern limit of the fault-controlled Culverden Basin (Armstrong, 2000; Mould, 1992).

The rivers and streams have eroded into and scoured the basement rocks allowing the detection of dykes and contacts to be easily observed.

3.2.2 Previous Work on the MIC

Following settlement in 1850, the first documented survey of the area was undertaken in 1871 (Haast, 1871b). He briefly described the Mandamus igneous material and comments on the Torlesse sediments being highly disturbed. The Coal Creek outcrop of conglomerate, he considered to be the equivalent of the igneous breccia further up the Mandamus valley. He also described the mafic dykes which cut the syenite as being linked to a later event.

Following fieldwork undertaken in 1872, Hutton described the igneous material in terms of a volcanic vent, now plugged by syenite (Hutton, 1877). He considered the volcanic agglomerate (vent breccia) to be interbedded with slates (Torlesse) but noted the absence of syenite blocks within the agglomerate (vent breccia). Hutton's interpretation of the dykes cutting the syenite in the Mandamus Gorge differed from that of Haast (1871b) in that he considered that the dykes '*may represent the original structure of the neck, having for some reason or other resisted the metamorphism that has changed the rest into syenite*'.

Mason summarised the stratigraphy of the area, following extensive mapping undertaken to produce a geological map of the Mandamus Survey District, which covered approximately 75 square miles (Mason, 1949). The map does not indicate the extensive outcrops of breccia in the hills behind Glens of Tekoa homestead and in the Mandamus river. Breccia is noted at the summit of Hurunui Peak and down the radiating ridges, but was not considered large enough in outcrop to warrant discrimination on his map (lahar deposits – this study). Whereas Hutton linked the conglomerates in Coal Creek to the breccia in the Mandamus (Hutton, 1877),

Mason assigned a lowermost Tertiary (Eocene) age to the conglomerate and did not mention the Mandamus River breccia (vent breccia – this study). The igneous suite is discussed in more detail in his 1951 paper (Mason, 1951), in which he considered all the igneous rocks to be of intrusive rather than volcanic origin. He explained the carapace of breccia as being formed '*by the shattering of the roof of the magma chamber by gas pressure in the late stages of crystallization of the syenite'*; a model adhered to by Reid (1972).

The only published geological map of the Mandamus Study area is that of Gregg (1964).

Although Sevon studied only the Tertiary stratigraphy in depth, his experience of the area, between 1961 and 1965 with the University of Canterbury Second Year students, enabled him to suggest that '*detailed mapping and petrology of these rocks will reveal a more complex history of intrusion than is reported by Mason'* (Sevon, 1969).

Such an investigation, as suggested by Sevon was undertaken by Reid in 1971, who, at the time, was a Masters student at the Victoria University of Wellington (Reid, 1972). Reid produced the first map of the igneous material and coined the term 'Mandamus Igneous Complex'. Reid envisaged three main phases of activity; a volcanic phase, extruding trachytes; an intrusive phase, with the intrusives (syenite, gabbro) reaching high levels under the volcanic carapace; and a late stage brecciation event as a consequence of volatile release which '*drilled a vent (diatreme) up through the Mandamus Complex and probably reached the surface as a violent explosive eruption'*. The breccias and agglomerate he interpreted as filling a vent and thus having sub-vertical contacts with the intrusives (Reid, 1972). Reid did not indicate further outcrops of breccia in the Mandamus River or behind Glens of Tekoa homestead.

Coincidentally, also in 1971, Tulloch undertook an undergraduate project whilst a student at the University of Canterbury. The thesis was unobtainable from the author, however the findings of the research were published in 1991 (Tulloch, 1991). The map drawn by Tulloch (1991) more closely resembles the map determined during the course of fieldwork for this thesis (Chapter 5). In contrast to Reid (1972), Tulloch maps the lithic lapilli tuffs ('lahar deposits', this thesis) as surface deposits overlying the rest of the complex. Tulloch also notes the presence of breccia in the stream outcrops further north up the Mandamus river. The 'melanocratic trachyte' (mafic lavas – this study), which is encountered near the summit of

Hurunui Peak is interpreted by Tulloch to be a vent deposit, having near vertical contacts with the syenites (*cf*. this thesis, Chpt. 5). The paper provides a good overview of the petrographic characteristics of the various units forming the MIC and K-Ar data yielded an emplacement age of 97 ± 3 Ma to 96 ± 2 Ma for the plutonic rocks and a 93 Ma age for the trachyte.

Rb-Sr dating yielded an age of 97.0 ± 0.5 Ma (Weaver & Pankhurst, 1991), using both volcanic and plutonic samples. The Sr isotope work also yielded an initial $^{87}Sr/^{86}Sr$ ratio of 0.70342 ± 0.00002.

Work involving the tectonics and stratigraphy of the surrounding area are numerous (Armstrong, 2000; Field & Browne, 1989; Mould, 1992; Powers, 1962; Speight, 1918). The reader is referred to Armstrong (2000) for a full overview of previous work on the Culverden Basin.

Chapter 4:
Volcanology and temporal evolution of the Mount Somers Volcanic Group (MSVG)

This section describes the results from the fieldwork component of this thesis.

4.1 Mt. Barrosa

The units determined during the course of mapping at Mt. Barrosa are shown in table 4.1 and the map can be found at fig. 4.1. The mapping focussed on the differentiation of the intermediate lava flows and determination of flow directions, source areas, and overall evolution of the complex.

Six units have been established for Mt. Barrosa, named B-I through to B-VI. The andesitic and dacitic lavas (units B-I to B-IV) are described in section 4.1.1, and the rhyolitic lavas (units B-V and B-VI) are described in section 4.1.2.

This thesis – for Mt. Barrosa	Oliver & Keene (1989)
B-I	Barrosa Andesite
B-II	Barrosa Andesite
B-III	Barrosa Andesite
B-IV	Barrosa Andesite
B-V	Somers Rhyolite (Pitchstone)
B-VI	Somers Rhyolite

Table 4.1 List of units mapped at Mt. Barrosa and their equivalents as mapped by Oliver and Keene (1989).

INSERT GEOLOGICAL MAP OF MT. BARROSA HERE (Figure 4.1)

The nomenclature used here (i.e. B-I to B-VI) is applicable **only** to the outcrops observed at Mt. Barrosa. Subsequent descriptions involving re-mapping of sequences at other exposures of MSVG will have nomenclature specific to them, and will be outlined at the beginning of each section as appropriate. Where several indicators of flow direction (e.g. disposition of the rubble/slab interface, orientation of amygdales and joint orientation) correlate, a strike and dip measurement is indicated on the geological maps.

4.1.1 Andesitic to Dacitic Sequence

Mt Barrosa is principally composed of andesite lava flows with subordinate basaltic-andesites and dacites, which unconformably overlie Balmacaan Formation rocks belonging to the Mount Taylor Group of the Torlesse terrane. Fig.4.2 illustrates the units determined during the course of geological mapping.

The intermediate lava flows on Mt Barrosa are sufficiently well exposed to enable the determination of a volcanic stratigraphy (fig.4.1 and 4.2). From field evidence, geochemistry and textural characteristics, the intermediate lava sequence can be subdivided into four units, B-I, B-II, B-III and B-IV. A summary of their stratigraphic relationships is given in fig. 4.2.

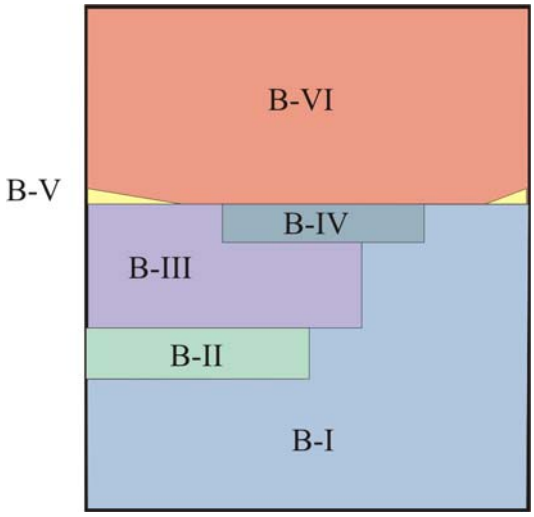

Fig. 4.2 Simplified stratigraphy of volcanic units on Mt. Barrosa, e.g. B-IV is observed to overlie B-III and B-I and is overlain by B-VI. B-II does not immediately underlie B-IV but is stratigraphically below it.

The textural characteristics of the lavas in each of the four units are summarised in table 4.2. The diagnostic properties of each unit are highlighted in red.

	B-I	B-II	B-III	B-IV
Flow Thickness	Generally >10m, although range is 4-30m.	Generally >10m	**0.5-10m**	Undetermined, at least 10m
Flow Features	Abundance of scoriaceous horizons with some well developed columnar jointing. **Flows tend to be laterally continuous**	**Predominance of very well developed columnar jointing.** Upper flows contain large rounded tennis-ball shape geodes.	**Thin, laterally discontinuous flows**	**Blocky flows are dominant.**
Colour and texture of Groundmass	**Generally mid-grey with white flecks** some v.dark and splintery, commonly **holocrystalline**	Dark grey/black predominantly **hypocrystalline**	Absence of glassy flows, **groundmass commonly displays mauve tinge.**	Pale to mid-grey sometimes splintery
Size of Phenocrysts	**Generally very fine <2mm, observed as flecks in groundmass**	<2.5mm	**Large glomerocrysts generally 2.5 - 7mm** with fine phenocrysts in groundmass	≤2mm
Presence of Glomerocrysts	Yes – equant and acicular	Yes – equant and acicular	**Large, up to 1cm**	**Yes**
Xenoliths	Present	Present in abundance	Absent or rare	**Abundant**
General Flow Direction	East-southeast	North-east	East	East
Photo-micrograph of typical texture			 ← **1cm** →	
Geochemical classification	Andesite	Andesite	Basaltic-andesite	Dacite

Table 4.2. Table describing the main characteristics of units I-IV

The definition of the four units is based upon field observations, petrography and XRF geochemistry. B-I is the lowermost unit and is chemically and petrographically similar to B-II. The distinction between these two units is based upon flow direction and lava morphology. B-III volcanism overlies both B-I and B-II units and has been used as a correlation marker. B-IV lavas are morphologically and chemically distinct from the older

three units and are restricted to the SE of the Barrosa field area. A small area of dacite (B-IV) is also found at locality MS/127 (GR J36/6729 2898). The exact stratigraphic relationship of this outcrop to the adjacent outcrops is uncertain, however it is most likely that this outcrop represents the onset of B-IV volcanism in the northern area of Mt. Barrosa, and is therefore included in the data set.

It is possible to trace individual flows of units B-I and B-II up to a maximum distance of 500m. B-III flows are distinctive but thin and can therefore only be traced laterally for short distances. The following characteristics are typical of those used in the field for mapping and correlation purposes:

- Flow thickness
- Presence/absence of columnar jointing (& width of joints)
- Flow direction/dip
- Groundmass colour
- Groundmass size and texture e.g. glassy, splintery
- Presence/absence and size of phenocrysts or glomerocrysts

The field correlations were checked using XRF analysis and petrographic examination of specimens. It was not possible to determine the entire succession of B-I and B-II volcanic piles because some flows were not exposed. In some cases minor flows could not be followed at all. The trends established in this study should therefore be regarded as representative of the stratigraphy rather than a complete stratigraphic cross-section of Mt. Barrosa.

It should be stressed that the sequence is only a part of what was undoubtedly a larger volcanic pile and an unknown quantity of material has either been removed or is buried by recent glacial outwash deposits. Therefore the sequence exposed in Mt. Barrosa may only represent a small proportion of a larger volcano and thus a complete geochemical evolution is impossible to establish.

Banded agates in the Barrosa field area have yielded post-eruption tectonic tilting measurements of between 8 ºE, 10 º E and 16 º NNW. The deformation is therefore not uniform and is not considered severe enough to warrant any re-interpretation of general flow

directions since in most instances the flow directions are in an easterly direction and dip at angles significantly greater than 10º. Reconstruction of dip direction would not affect the direction of flow, merely lessen it. Evaluation of tectonic tilting follows the methods of Oliver (1977) and utilises banded agates (fig.4.3). The assumption made is that the bands in the agates represent paleo-horizontal surfaces.

Fig.4.3 Banded agate used for post-eruption tectonic tilt measurements

4.1.1.1 B-I: Andesite

Barrosa I, or B-I is the name given to the monotonous sequence of andesitic lava flows which form the base of Mt Barrosa, and upon which the sequences B-II, B-III and B-IV rest. The upper boundary of B-I is delineated by the onset of markedly differing lava chemistry to the east (B-III), and a sequence of chemically similar, albeit morphologically distinct lavas to the north (B-II) (fig. 4.1).

The earliest phase of activity preserved on Mt. Barrosa is located adjacent to the Ashburton Gorge Road at the southern tip of the Clent Hills. At this location andesite flows overlie rocks of the Torlesse terrane (Balmacaan Formation). The flow dips are variable but are generally to the SSE at angles up to 40 º. The flows are heavily fractured and are relatively thin (<10m). These flows form the base of a large pile of andesitic flows (B-I), which are approximately 400m thick. The earliest lavas probably exploited a paleotopographic depression such as a valley in the Torlesse bedrock which would account for their anomalous

strike and dip directions and their relationship to the underlying basement (Fig 4.1). Detailed mapping of the area has revealed more Torlesse rocks to the east of Mount Possession point which probably represents the other side to the paleo-depression.

The flows assigned to B-I are not continuously exposed, however individual flows can be traced laterally and identified in adjacent valleys.

B-I outcrops tend to display incomplete sections through each flow, with the massive internal zones of lava flows most likely to form outcrops. The upper and lower rubble zones are softer and more easily eroded and are commonly vegetated. The flows form rugged, steep terrane and abundant cliff sections. Their thickness' vary between 4 and 30 metres with an average thickness of approximately 10m. Amygdales are common and tend to be concentrated in the lower and upper rubble zones although smaller amygdales are also frequently observed in the internal massive zone.

From observation of individual complete lava flows the following cross-section can be drawn:

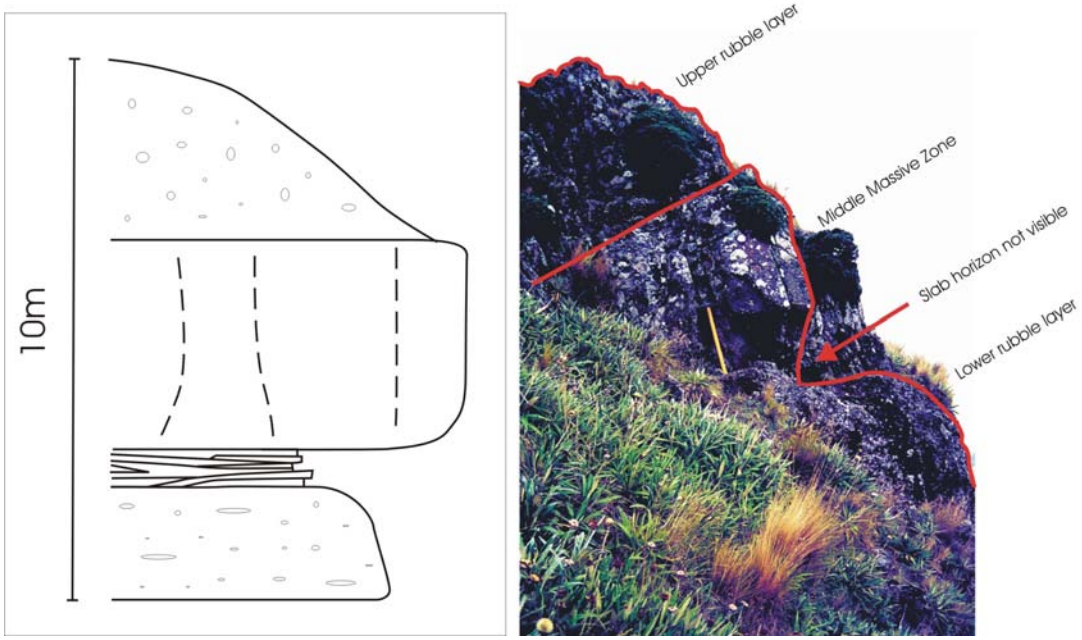

Fig.4.4 cross-section and photograph illustrating the typical appearance of B-I lava flows in the field.

The above sketch is idealised, and often multiple repetitions of massive zones within rubble zones were observed, with massive zones being thin and lens shaped.

Flows are typically ‘aa’, delineated by a narrow rubbly amygdaloidal zone at the base which is commonly black but can also be red, overlain by a sheared slab horizon beneath the massive central zone. The shearing at the base of the flow probably formed as a result of ‘rafting’ of the central massive zone after it had solidified (Johnson, 1970). This sequence is capped by a thicker rubbly amygdaloidal zone, normally at least the thickness of the basal rubbly amygdaloidal zone, and usually red. The amygdales at the base of the flows tend to be more heavily compressed and distorted. Where several flows are observed, a red horizon is commonly present between flows which probably represents a paleo-erosion surface or thin ash layer. Some minor flows are almost entirely rubble with few localised lens-shaped massive zones.

Columnar jointing is observed in many flows, particularly those which contain central massive zones in excess of 2m in thickness. Joints usually have 4, 5 and rarely 6 sides (Fig.4.5). Where present, joints are observed to lie perpendicular to the dip of the flow. This is an expected observations since columns develop perpendicular to cooling surfaces (Scrope, 1825).

Fig. 4.5 Columnar joints in cross-section

4.1.1.2 B-II: Andesite

B-II lavas display many properties akin to B-I. The lavas of B-II have been assigned to a different unit because they are morphologically distinct. The age relationships between the upper flows of B-I and the flows of B-II cannot be established. However, the B-II flows are clearly younger than a large portion of B-I flows as shown in Fig. 4.2.

B-II consists of at least 6 flows. The lower two flows are morphologically distinct from the upper, thinner flows. The upper flows of B-II resemble B-I flows, and are stratigraphically equivalent to the upper flows of B-I. The flows are only exposed in a northerly direction from the summit of Mt. Barrosa (Fig. 4.1). B-II flows overlie both Torlesse bedrock and B-I flows (fig. 4.1). The onset of Group B-II volcanism is marked by a thick sequence of impressive, columnar jointed, glassy andesite flows (fig.4.6).

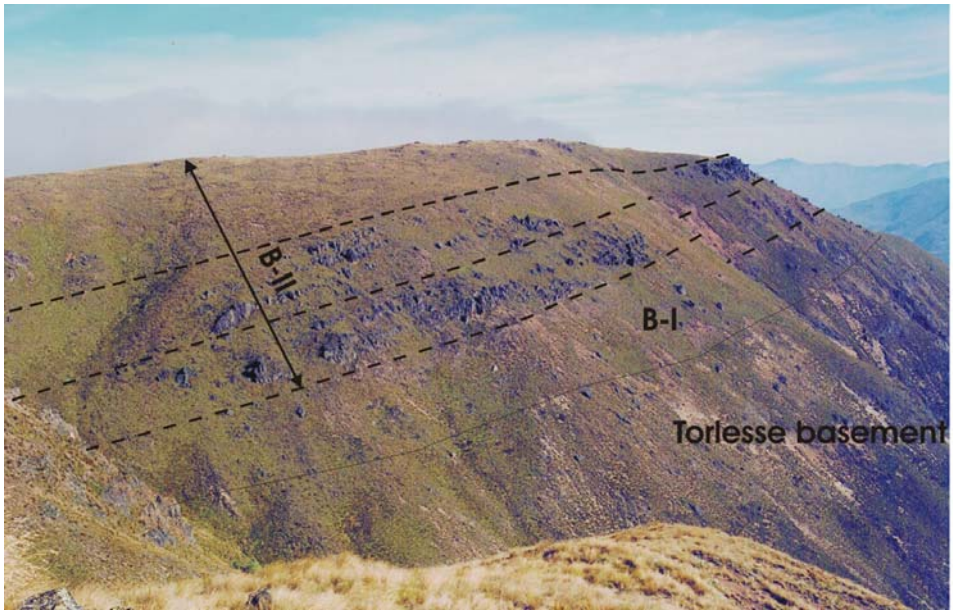

Fig.4.6 Columnarly jointed group B-II flows overlying group B-I and Torlesse basement

Oliver (1977) commented on one of these outcrops (fig. 4.7) and considered it to be a dyke. The main mass of the lower B-II outcrops are clearly not dykes as they are conformable to the stratigraphy and display upper and lower rubble zones.

Fig.4.7 Photograph of columnar joints at MS/94 GR: J36/6943 3296. Note the yellow-handled hammer in the middle-distance for scale.

That this outcrop is a dyke cannot be ruled out, but the presence of such well developed columnar joints in itself is not diagnostic. As illustrated previously, columnar jointing is not unusual in the flows of Mt. Barrosa. Rather, I consider this to be a broken up outcrop of the central massive zone of a thick flow unit throughout which the distribution and quality of columnar jointing is unevenly developed.

As shown on the geological map of Mt. Barrosa (fig. 4.1), the contact between B-II and the Torlesse bedrock is seen to approximately parallel the topographic contours to the north until it is terminated by the Barrosa Fault (fig. 4.8).

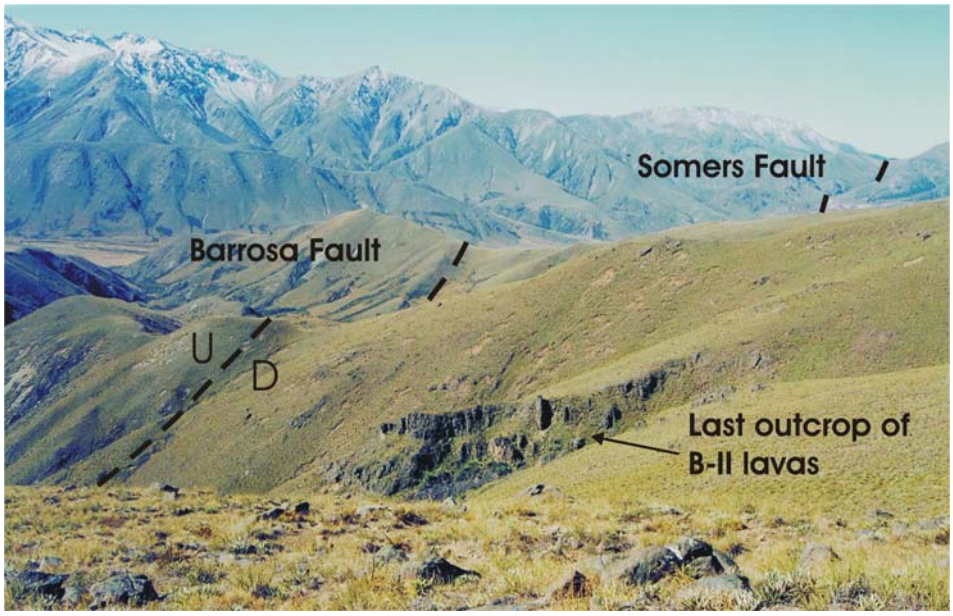

Fig.4.8 Final outcrop of B-II lavas before being terminated by the Barrosa Fault

Although B-II is dominated by its thick columnar flows, B-III does not appear until at least 40m of thinner flows. It is these overlying flows which resemble B-I flows. They are generally thinner and comprise rubble, slab and massive zones as described previously for B-I flows. These overlying thinner flows on the whole are more amygdaloidal, with the massive zones containing unusually large geodes up to tennis ball size.

4.1.1.3 B-III: Basaltic-andesite

The flows of B-III are widespread and are chemically, petrographically and morphologically distinct. B-III flows are of variable thickness but are generally thin with many flow units only measuring between 60 and 120cm thick (fig. 4.9). They are also laterally discontinuous (fig. 4.10).

Fig.4.9 Outcrop displaying the typically thin B-III flows. Note the yellow hammer for scale

B-III lavas overlie both B-I and B-II, and are widely distributed (fig.4.1). The maximum thickness of a B-III flow is a 30m thick flow occurring at MS/147 (GR J36/6816 2895), in which the central massive zone is 15m thick. This is an unusual flow for the B-III group and is the only flow of this thickness. The flow has 5m of basal rubble layer, 15m of central massive zone and 10m of upper rubble zone.

Fig.4.10 Photograph showing the lateral discontinuity of B-III flows.

B-III flows generally dip in an easterly direction at variable angles of up to 35º. The dip angles gradually increase from W to E. The flows are characteristically alternating bands of rubble and massive zones on a fine scale (generally <50cm). Identifying flows is simple, but their narrow width means they cannot be followed laterally for more than a few metres. No flows (except MS/147) could be correlated across slopes which indicates that they are narrow both in thickness and in width of flow. The more mafic nature of these lavas suggests that they were hotter and less viscous with flows travelling relatively rapidly in thin tongues.

Amygdales are generally confined to the upper and lower rubble zones where they are present in abundance. At locality MS/49 (J36/6831 6925), tubular amygdale 'pipes' are observed (fig.4.11). These probably represent gas escape structures rising through a flow. The lack of distortion of the pipes suggests that the flow was stationary but still molten, facilitating gas escape. The fact that pockets of air were permitted to travel in a vertical fashion to the surface also suggests that the lavas were still relatively hot and soft. The inclination of the pipes (10° E) provides another method for measuring post-eruption deformation; assuming the pipes represent vertical gas escape. Amygdales are more prevalent and less distorted in the overlying rubble layers, often resembling golf-balls.

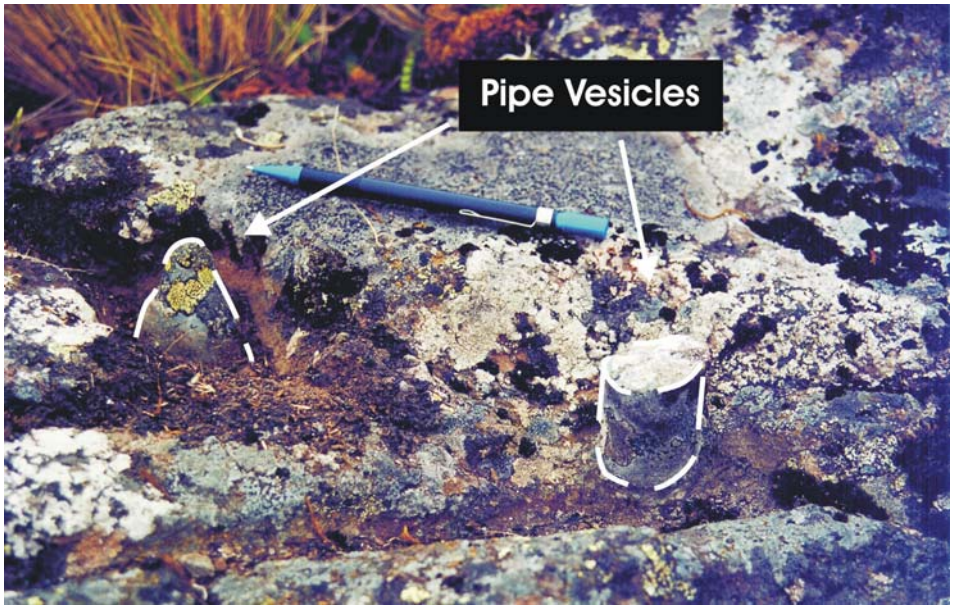

Fig.4.11 Pipe Vesicles in group B-III lavas

The flag zone and lower rubble zone described in section 4.1.1.1 (fig. 4.4) are generally absent from B-III flows. Commonly only the massive and upper rubble zones are present. The general absence of flag zones is probably the result of thinner, more mobile flows, the

movement of which is not facilitated by shearing underneath a solid, or partially solidified central massive zone. The thinner, less viscous flow model is supported by geochemical evidence, which indicates lower SiO_2 contents and higher MgO contents, therefore hotter and less viscous flows. The presence or absence of a lower rubble zone is dependent upon the thickness of flow. Where the flow is thick, the lower rubble zone is present. The majority of B-III flows, however, are thin and the lower rubble zone is therefore absent.

Columnar jointing is occasionally present in the thicker flows >10m, but on the whole is rare because such thick flows are uncommon.

4.1.1.4 B-IV: Dacite

B-IV lavas are generally restricted to the east of Mt. Barrosa, although an isolated outcrop of B-IV lava does occur towards the north of the mapped area as shown on the map (fig.4.1). B-IV lavas clearly overlie B-III lavas and are morphologically and geochemically distinct. The lavas of B-IV plot as dacite on the total alkali versus silica diagram (Le Maitre *et al*, 1989).

Fig.4.12 Blocky flow of B-IV lavas. Hammer for scale.

The lowest flows of B-IV are thin, and resemble the B-III flows, however the main flows of B-IV are easily recognisable because they are morphologically distinct from the other flows on Mt. Barrosa. The flows are noticeably blocky as shown on fig. 4.12.

The block sizes range from <1cm to 80cm diameter. The blocky flow model is supported by the lava geochemistry. Higher silica contents correlates with higher apparent viscosity. On the whole, the flows are at least 20m thick. Precise measurements of strike and dip are unobtainable due to the general lack of flow foliation in the outcrops. However from a distance, apparent strike and dips can be obtained (fig.4.13). The distribution of the flows of B-IV provide a structure contour which is consistent with an easterly dip.

Fig. 4.13 Flows of B-IV

Amygdales and vesicles are common in the blocks, and where foliation is observed, the amygdales appear to be elongated parallel to foliation, indicating relatively late-stage shearing. Quartz-veining throughout the outcrops is also a common feature of these flows.

4.1.2 Rhyolitic Sequence

Overlying units I-IV, are the rhyolitic volcanics. The rhyolitic sequence of Mt. Barrosa is divided into two units B-V and B-VI. The rhyolites in the vicinity of Woolshed Creek (section 3.1.1.1) and forming the main mass of Mt. Somers have been examined in this study

and are interpreted to be continuous with the rhyolites of Mt. Barrosa and no geomorphic or geochemical differences are observed.

4.1.2.1 B-V: Pitchstone

B-V is clearly younger than B-IV (dacite). Although a contact is not seen, the propogation of structure contours suggests that B-V pitchstone is conformable with B-IV dacites.

Unit B-V rests unconformably on B-III flows to the east of the area (fig.4.1), where B-IV flows are absent. The presence of B-V pitchstone on Mt. Barrosa is usually indicated by float because the rock is susceptible to erosion.

B-V reaches a maximum thickness of 50m (true thickness) and is conformable with the dips of the over and under-lying sequences. From structure contours, the pitchstones have an apparent dip of <60 º to the east (fig.4.14).

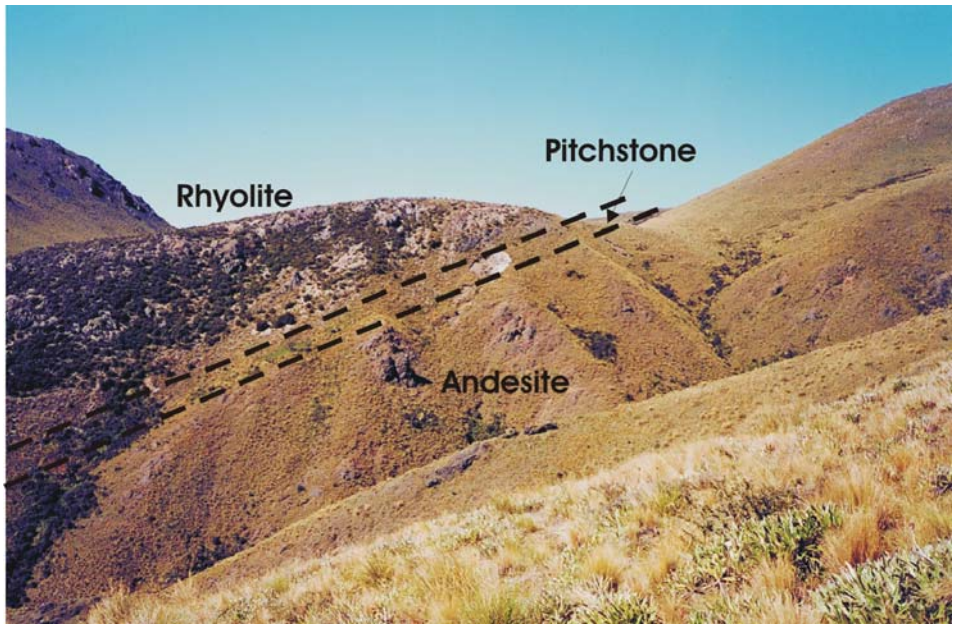

Fig.4.14 Contact observed between the andesite (B-I), pitchstone (B-V) and rhyolite (B-VI)

Outcrops of B-V are discontinuous and it is inferred to pinch out (figs. 4.1 and 4.2). The pitchstone does not contain shattered phenocrysts or eutaxitic texture which would be

expected if the pitchstone had an ignimbrite origin. Flow banding is commonly observed in thin section (ref. Appendix 2).

The irregularity of the occurrence of the sandwiched pitchstones on Mt. Barrosa suggests that the pitchstones were generated by lava flows erupted prior to the widespread and voluminous rhyolitic volcanism (unit B-VI) and ignimbritic volcanism observed on the summit flanks of Mount Barrosa (described by Richnow, 1999; Smith, 1994; Smith *et al*, 1997).

4.1.2.2 B-VI: Rhyolite

The rhyolites of Mt. Barrosa are petrologically and geochemically indistinguishable from the rhyolites of Woolshed Creek and the main mass of Mt. Somers which have been investigated in detail by previous workers (Barley, 1987; Oliver, 1977; Oliver & Keene, 1989, 1990; Richnow, 1999; Smith, 1994; Smith & Cole, 1996, 1997; Wood, 1974).

Fig.4.15 Photograph of onion skin jointing observed in the rhyolites adjacent to the Stour River. Note purple rucksack at base of outcrop for scale.

The rhyolite outcrops that immediately overlie pitchstone do not show clear columnar jointing and appear to be conformable on top of the pitchstone. These rhyolites are therefore considered to be flows. However, the rhyolites become increasingly columnarly jointed towards the east of Mt. Barrosa and are considered to have formed by endogenous growth in

the form of domes (fig.4.15). The rhyolites that outcrop either side of the Stour River have morphology and columnar jointing typical of that reported by Richnow (1999) for the rhyolites of Mt. Somers.

4.1.3 Faulting

As shown on the geological map (fig.4.1), Mt. Barrosa is dissected by an ENE to WSW trending fault, which juxtaposes the MSVG against the sedimentary rocks of the Balmacaan Formation (Torlesse). Oliver (1980) reported baking of Torlesse rocks abutting the fault which would indicate that the fault was initially syn-volcanic. The fault is near vertical and terminates the lavas of the MSVG on Mt. Barrosa, the trace of the fault is shown on fig.4.16.

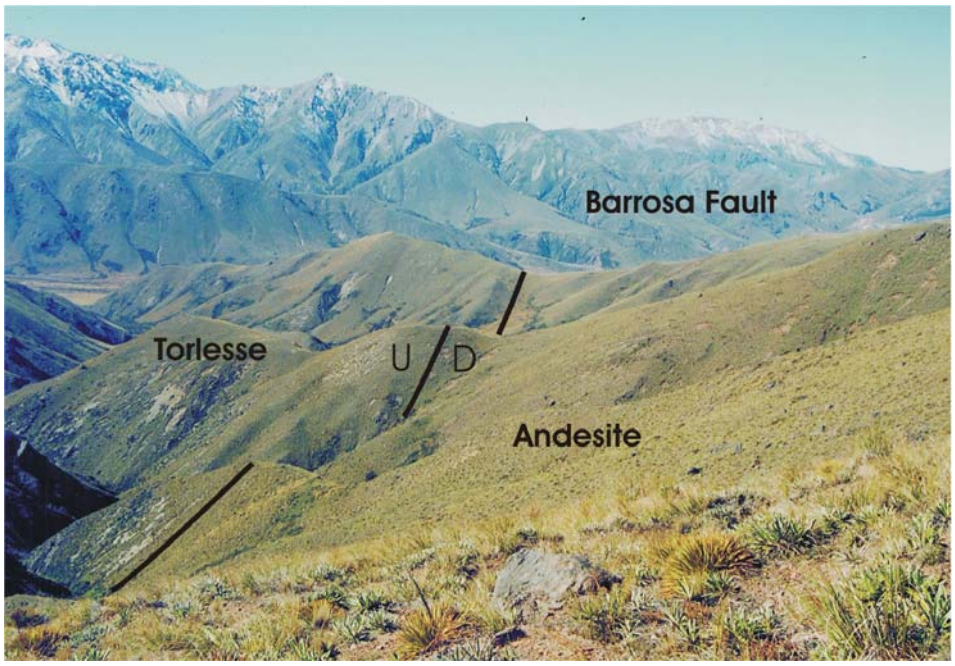

Fig.4.16 Photograph indicating the position of the Barrosa Fault in the Clent Hills

A syn-volcanic fault is also inferred at Mt Somers (Smith, 1994), where a series of probable normal faults juxtapose rhyolite against 'Woolshed Creek Ignimbrite' (Smith & Cole, 1996). The rhyolite fines against the contact in places, indicating a chilled margin, and rhyolite dykes appear to have exploited the fault plane (fig.4.17).

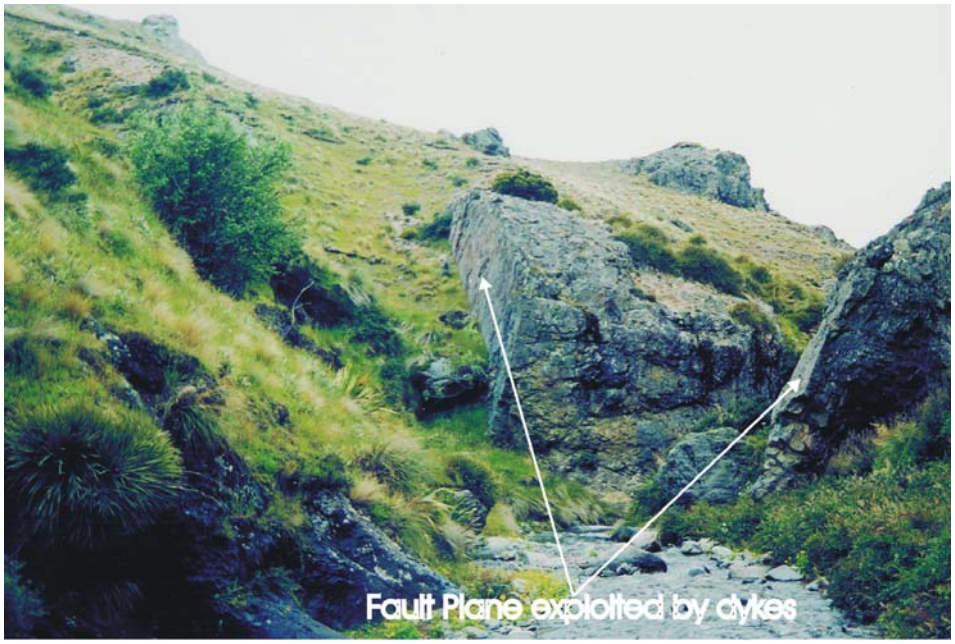

Fig.4.17 Fault exploited by rhyolite dykes in Woolshed Creek. Rhyolites are juxtaposed against ignimbrite and andesite.

4.2 Gawler Downs

Dacite is the dominant rock type in the Gawler Downs field area, which includes the Surrey Hills, Rangiatea and Blondin Stream areas (section 3.1.1.2). The quality and size of sparse outcrop made stratigraphic mapping difficult.

Fig. 4.18 illustrates the geological map of Oliver & Keene (1989), which has been modified during the course of mapping for this project.

The rock types encountered in the Gawler Downs field area are summarised in table 4.3.

This thesis – for Gawler Downs	**Oliver & Keene (1989)**
Dacite	Hinds River Dacite
Andesite	Barrosa Andesite
Rhyolite	Somers Rhyolite
Tuff	Surrey Hills Tuff
Pitchstone	Somers Rhyolite (pitchstone)

Table 4.3 Summary of rock types mapped in the Gawler Downs field area and their equivalent as mapped by Oliver & Keene (1989).

GD map fig 4.18

4.2.1 Volcanic Succession

4.2.1.1 Dacite

The dacites are dominated by heavily weathered, often rubbly and amygdaloidal flows. Where the flows are massive and fresh they tend to broken into large boulders which are not in-situ, although they probably represent the geology immediately beneath them. Taking strike and dip readings was therefore very difficult.

Occasionally, igneous foliation enabled strike and dip measurements to be recorded, although such measurements must be treated with caution since foliation does not necessarily always develop parallel to the flow direction. Basal and upper rubble zones in relation to central massive zones provided another method of determining flow orientation. Flow banding was also used to indicate the general flow orientation. Occasionally columnar jointing is observed.

The strike of the dacite flows varies between 015 and 300 º, which is a wide range but 75% of the flows measured fall between 220 and 300 º, with dips between SE and SW. This correlates with a source in the direction of Mt. Barrosa, which lies to the NW of the dacite outcrops. Furthermore, the most northerly outcrops of dacites occur less than 1km from the most southerly expression of andesite, in Blondin Stream. Although dacite is probably buried beneath alluvium, it still outcrops only 3km from the most southerly outcrops of the main mass of andesite at Mt. Barrosa. Despite there being no actual contact between the dacites and andesites, the field evidence strongly suggests that dacites overlie andesites. The dacites of the Gawler Downs may be the equivalent of the group B-IV dacites from Mt. Barrosa. As shown in Chapter 7, their chemistries are very similar.

The general attitude of the dacite flows suggest that they post-date andesite volcanism, although their relationship to most units is poorly constrained due to lack of exposed contacts.

4.2.1.2 Andesite

Within the Gawler Downs, one outcrop of andesite occurs at locality GD/4 (K36/7840 1383, Sample GD-2). This outcrop is small and no strike and dip measurements could be obtained. The andesite is either an andesite erupted during the main dacite phase, or an intrusion.

A small outcrop of andesite also occurs in Blondin Stream at GD/40 (K36/7139 2492), near the Inverary homestead. The flow units appear to be less than 2m thick and are flaggy and rubbly and highly vesicular and/or amygdaloidal. Where banded agates are seen, they are horizontal with apparently no post-eruption deformation.

4.2.1.3 Rhyolite

One outcrop of rhyolite occurs at loc GD/16 (K36/7816 1581). Rhyolite has not previously been found on the Gawler Downs and indicates that rhyolite was erupted in this area but has probably been largely removed by erosion leaving a base of dacite.

Petrographically, the rhyolite contains the same phenocryst assemblage as the rhyolites described for Mt. Barrosa, however with the absence of biotite and garnet as phenocryst phases. The rock is heavily altered and fractured.

4.2.1.4 Tuff

The tuff is an attractive deposit of pale peppermint green and pink laminated fine siltstone (fig.4.19) and was probably the earliest phase of MSVG eruptives (Oliver & Keene, 1989). The tuff is commonly silicified and is found in the largest quantities in the Gawler Downs. The most extensive outcrops of tuff are found alongside the access track to the microwave station behind Surrey Hills homestead at GR K36/7877 1693.

The tuffs contain angular crystal fragments and evidence of devitrified fiammé. The mineral assemblage consists of: plagioclase, sanidine, quartz, biotite, garnet and opaques (ilmenite) which indicates a relationship between the tuff and the overlying volcanic units.

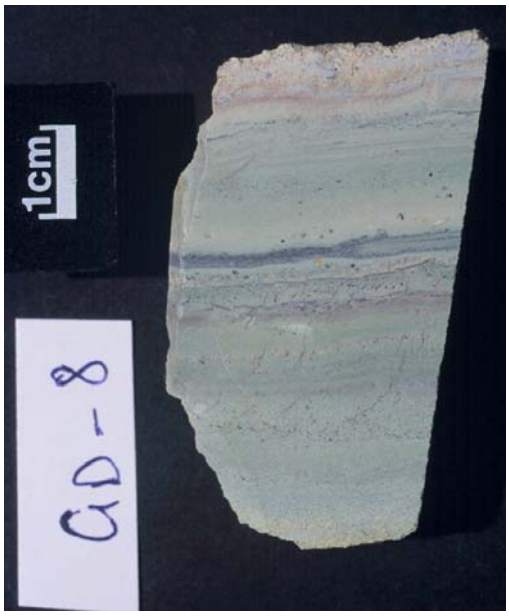

Fig.4.19 Gawler Downs Tuff (GD-8)

The whole-rock chemistry of the tuffs is of dacitic composition and the mineral assemblage and texture of the tuff is consistent with a pyroclastic deposit which has settled through water (Oliver, 1977). Biotite crystals are up to 0.7mm long indicating limited re-working.

4.2.1.5 Pitchstone

In Blondin Stream, a large outcrop of pitchstone occurs (fig.4.20), which is composed entirely of pitchstone and resembles a thick, blocky lava flow front. Its stratigraphic relationship to the andesite and rhyolite is uncertain but its close proximity to both andesite and rhyolite is consistent with the stratigraphic position of the pitchstone at Mt. Barrosa (B-V) where pitchstone is found between andesite and rhyolite.

The pitchstone is seen to be banded in thin section with colourless glassy groundmass with perlitic cracks. The rock is porphyritic with 13% phenocryst content. Phenocryst phases present are quartz, plagioclase, biotite and garnet.

fig. 4.20 photograph of the rubbly pitchstone flow, Blondin Stream (note hammer for scale)

4.2.2 Post-volcanic stratigraphy and faulting

The MSVG of the Gawler Downs are bounded to the east by a N-S trending fault, which juxtaposes the dacites of the Gawler Downs against gravels of the Windwhistle Formation. To the north of the area Hororata outwash gravels are seen to immediately overlie the dacite.

Sedimentary rocks of the Otiake Group are distributed throughout the area and in addition to those mapped by Oliver & Keene (1989); further outcrops of Homebush sandstone (Carlson *et al*, 1980) are distributed over the hills to the NW of Rangiatea (e.g. GD/36, K36/7235 2320).

4.3 Malvern Hills

The volcanics of the Malvern Hills consist of at least 6 phases of volcanic activity. The Malvern Hills comprise: andesite, pitchstone, rhyolite and ignimbrite with a noteable absence of dacite. The succession of volcanics is different from that observed at all other outcrops of MSVG because the uppermost unit of the Malvern Hills is andesite rather than rhyolite (fig.4.22).

4.3.1 Pre-Volcanic Stratigraphy

The volcanics of the Malvern Hills rest upon Torlesse bedrock, of the Balfour Series (Triassic), which is mantled by a veneer of Torlesse-dominated fresh-water conglomerates and minor coal horizons, known as the Wakaepa plant beds (Gregg, 1964).

Fig. 4.21 Wakaepa Plant Beds, ruler length 15cm.

INSERT GEOLOGICAL MAP (FIG. 4.22)

Although in the text accompanying the map of Gregg (1964), the volcanics are said to 'unconformably overlie the Wakaepa Plant Beds'; on the geological map they are mapped overlying lower Torlesse units. Although not present on the map of Gregg (1964), a thin layer of conglomerate, blue-silts and fine organic lenses is found at locality MH/128 (GR L35/1056 4843) immediately overlying Torlesse bedrock with no intervening volcanics (fig.4.21). This unit is interpreted to be a previously un-mapped occurrence of the Wakaepa plant beds.

4.3.2 Volcanic Stratigraphy

The lithologies mapped in the Malvern Hills are summarised in table 4.4.

This thesis – for Malvern Hills	Other workers' nomenclature
Iron Bridge Rhyolite	Mt. Misery Volcanics (Gregg, 1964) Iron Bridge Rhyolite (Bruce, 1994)
Rockwood Ignimbrite	Mt. Misery Volcanics (Gregg, 1964) Ignimbrite (Bruce, 1994)
Glassy Ignimbrite (lower)	Pitchstone (Bruce, 1994)
Glassy Ignimbrite (upper)	White pyroclastics (Bruce, 1994)
Round Top Andesite	Round Top Andesite (Gregg, 1964) Round Top Andesite (Bruce, 1994)

Table 4.4 Nomenclature for the Malvern Hills from previous workers.

4.3.2.1 Iron Bridge Rhyolite

The oldest unit is rhyolite, named Iron Bridge Rhyolite of Bruce (1994). The rhyolite occurs at predominantly low levels, and in the Rakaia Gorge is weathered by the river water action, but provides sturdy support to the legs of the Iron Bridge, hence the name. The rhyolite is commonly altered to a reddy-pink colour, due to the mobilisation and oxidation of iron. Its chemistry is that of high silica rhyolite, with silica contents of 75-76%. The high silica concentrations may have been enhanced by secondary removal of other major-elements during alteration.

Flow banding is common and displays convoluted flow folding in places (fig.4.23). The rhyolite reaches a maximum elevation of 600m which is fairly constant, which may indicate a plateau of rhyolitic material. The flow banding is typically oriented at angles up to 50º to the NNW, indicating a source to the SSE. The disparity between an apparent plateau morphology and steep dip angles to flow banding indicates that the rhyolite was probably eroded prior to the emplacement of the overlying ignimbrite.

Fig.4.23 Flow banding in the 'Iron Bridge Rhyolite'.

The rhyolites of Mt. Misery and those to the SW of Pullwool Peak show the large scale morphology more consistent with rhyolite domes than ignimbrite deposits, and are therefore grouped with the Iron Bridge Rhyolites (fig. 4.22). No eutaxitic texture was observed at these locations, nor the characteristic hard cragg-forming morphology of the ignimbrite units.

The Iron Bridge Rhyolite is porphyritic in a cryptocrystalline, felsitic, devitrified groundmass which locally coarsens. Flow banding is observed in thin section by variations in colour and

alignment of biotite phenocrysts. The phenocryst phases are: quartz, plagioclase (oligoclase – andesine), alkali-feldspar (sanidine), garnet, biotite, opaques (ilmenite). Minerals which are visible but present only in trace amounts are orthopyroxene, zircon, apatite and titanite.

4.3.2.2 Pitchstone dykes

Immediately overlying the rhyolite at MH/8 (GR K35/0153 4264) is a pitchstone. Angular, broken phenocrysts of variable size are common. Flow banding is visible, depicted by subtle changes in glass colouration from colourless to pale brown. Just 200m further upstream, another outcrop of pitchstone is present just above the water's edge (MH/17). The 10m wide outcrop mapped originally by Bruce (1994) shows abrupt contact with ignimbrite on either side, bentonitic alteration along margins with well developed joint sets perpendicular to unit margins. Petrographically the pitchstone units are remarkably similar, both being highly porphyritic with both rounded and shattered phenocrysts of plagioclase, quartz, biotite and garnet.

Both these outcrops of pitchstone are considered to be dykes, which possibly fed the stratigraphically higher Glassy Ignimbrite (described later in this section).

A concentration of pitchstone is also seen above Birch View (MH-24, MH/49, K35/0691 4531) to the south side of the walkway. Although only found in the bank of the track, pitchstone is intolerant to weathering and therefore it is assumed that the pitchstone float in this locality represents the sub-surface geology. An outcrop of pitchstone at this locality is complementary to that in the Rakaia Gorge since this locality is also the inferred boundary between ignimbrite and rhyolite. Again, this pitchstone is remarkably similar to both the pitchstone at MH/8 (MH-5) and that at MH/17 (MH-12).

The pitchstones referred to as pitchstone 'dykes' here are MH-5, MH-12 and MH-24. The pitchstones are porphyritic in a pale grey, transparent glass, which contains abundant perlitic cracks. Flow banding is obvious and is depicted by varying colour glass lenses, commonly surrounding phenocrysts. Biotite crystals are aligned parallel to flow banding. Lenses of devitrified glass are seen, commonly surrounding phenocrysts. Microlites, where present, often form rims around phenocrysts. Spherulite growth is observed in some sections.

4.3.2.3 Rockwood Ignimbrite

In the Rakaia Gorge the contact between ignimbrite and rhyolite is not clearly marked, however it is suspected that the pitchstone dyke (MH/8) exploits the contact along the true left bank. Along the true right bank, Quaternary gravels are offset against lithic-rich ignimbrite and the reverse fault shown in fig.4.37 may exploit the ignimbrite/rhyolite boundary.

The lithic-rich nature of the ignimbrite abutting the fault may indicate close proximity to the base of the ignimbrite (fig.4.24). Between the Rakaia Gorge and the K35/07 northerly gridline, the ignimbrite unit maintains a constant thickness. To the east of the northerly gridline 07, the ignimbrite thickens considerably and this area is likely to represent a paleotopographic low or basin into which the ignimbrite ponded. The bluffs at K35/077 464 show a break, or weak plateau in the ignimbrite along which the bluffs have been weathered. This horizon may represents a break in deposition.

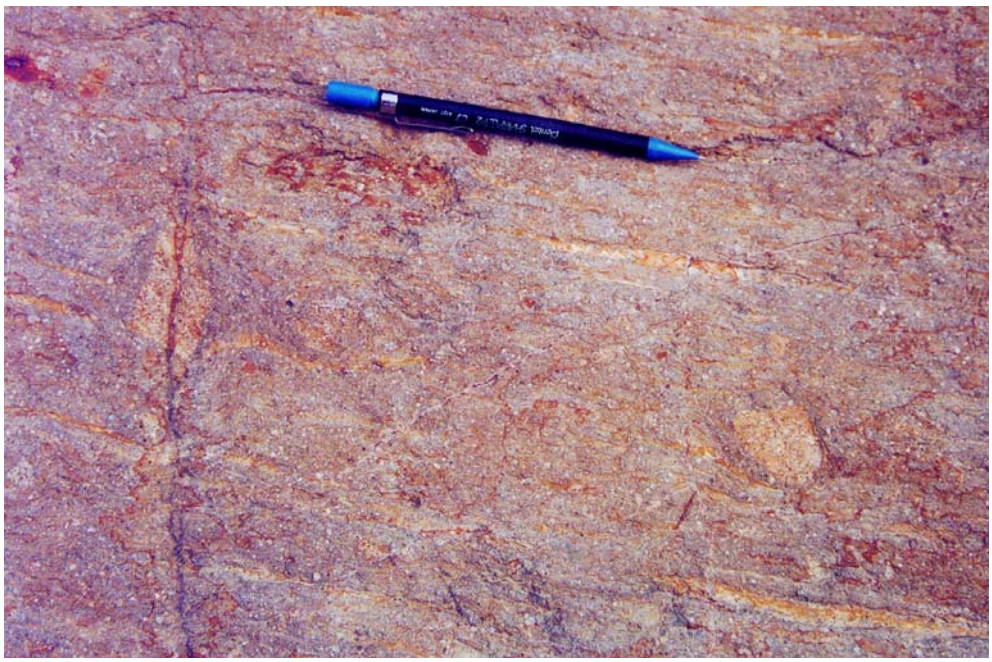

Fig.4.24 Close up of the lithic rich nature of the Rockwood Ignimbrite in the Rakaia Gorge.

The ignimbrites are composed of several flow units since individual outcrops vary in regard to size and composition of clasts, degree of induration, development of eutaxitic texture, degree of flattening of clasts and size and concentration of crystals. The ignimbrites generally display a clear slabby, bluff forming outcrop pattern and a clear eutaxitic texture is often evident in hand specimen fig.4.25.

Fig.4.25 Eutaxitic texture in MH-17

At locality MH/83 (L35/1082 4685), at the base of Rockwood Forest, the ignimbrite is very lithic rich. Lithics reach a maximum observed size of 18 cm (long axis) (fig.4.26). The garnet content of this ignimbrite is also high (2%).

Fig. 4.26 large lithic in the Rockwood Ignimbrite (locality MH/83)

Further evidence for multiple flow units is the presence of andesite at locality MH/80 (L35/1040 4711). Initially mapped by Gregg (1964) before planting by Selwyn Plantation Board in 1985, the andesite has the discontinuous morphology of lava, but could also be an intrusive feeder dyke for the overlying andesitic lavas. Ignimbrite activity may have been interrupted by sporadic and short-lived andesitic episodes. 20m further up the forestry track

from MH/80, the ignimbrite appears to be glassy, and is therefore probably the fused base of the overlying flow. This observation would support the hypothesis that the andesite at MH/80 is actually a lava flow rather than a dyke.

The contact between the Rockwood Ignimbrite and Torlesse sandstone follows the High Peak Road, which runs in a westerly direction approximately 2km north of Pullwool Peak. The Torlesse bedrock along the road is of fine to medium quartzo-feldspathic sandstone, which contains well sorted, angular fragments with minor muscovite and chlorite alteration. The contact appears to strike and dip at 270/55º S (fig.4.27). This probably represents one abutment of the paleotopographic basin where the ignimbrite ponded. The strike and dip of the abutment is consistent with the hypothesis that this paleotopographic slope may be the footwall of a Cretaceous, pre- or syn-volcanic normal fault. This equates to the faulting that Oliver (1977) suggested was syn-eruptional in the Clent Hills and Mt. Somers.

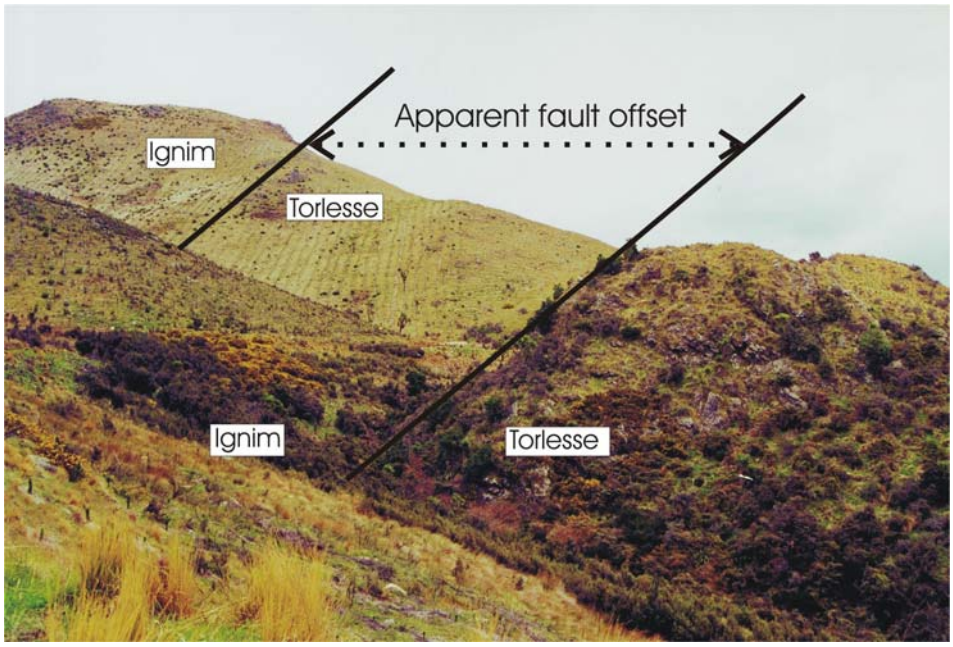

Fig. 4.27 Slope of contact between Torlesse basement and Rockwood Ignimbrite and offset of contact due to inferred normal fault.

The contact between the ignimbrite and Torlesse basement at locality MH/107 and MH/110 is displaced 100m horizontally, NE-SW (fig.4.27). This is inferred to be the position of a normal fault, dipping in an easterly direction, and marked by the position of the valley running from L35/126 478 to just west of Loc. MH/107 (L35/1293 4838). The western valley side of which may represent the footwall of the normal fault.

The foliation in the ignimbrite is pronounced but highly variable in direction. This may be due to tectonic disturbances or slumping of the ignimbrites toward the centre of the basin.

A small, localised outcrop of debris/mud flow material is found at locality MH/118 (L35/1904 4745), formed predominantly from fresh ignimbrite clasts and small charcoal fragments (fig.4.28). The outcrop is lithified, however its age is uncertain.

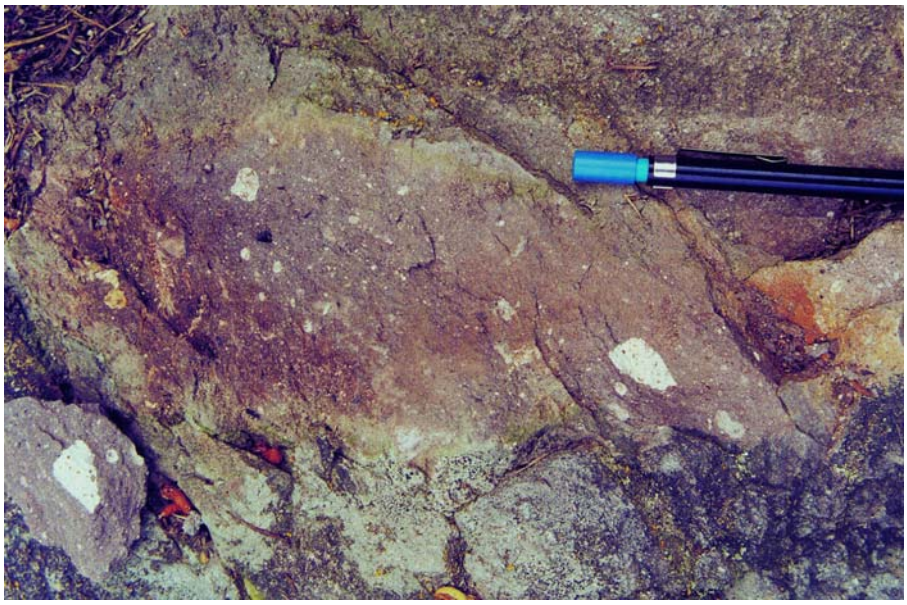

Fig.4.28 Mud/debris flow deposit.

The Rockwood Ignimbrite is generally highly porphyritic with up to 24% phenocryst content (average 15%). The ignimbrite characteristically has a holocrystalline, cryptocrystalline felsitic groundmass containing abundant crystals and crystal fragments often enclosed by devitrified or vitric fiammé, defining a clear eutaxitic texture.

Abundant lithics are found in the ignimbrite and are commonly recrystallised quartzose lithics. Some lithics are metasedimentary containing quartz, feldspar, biotite and colourless spinel and some lithics contain garnet. Some quartz crystal-pairs may actually be xenocryts due to their adjoining 120º faces.

4.3.2.4 Glassy Ignimbrite (lower)

The Glassy Ignimbrite refers to the welded pyroclastic deposit which conformably overlies the Rockwood Ignimbrite west of Rockwood Forest. The Glassy Ignimbrite can be sub-divided further into two units: upper and lower.

The lower Glassy Ignimbrite is fresh and resembles the pitchstone dykes on fresh surface. The upper Glassy Ignimbrite is the devitrified equivalent of the lower Glassy Ignimbrite.

The glassy nature of the deposit is interpreted to be primary due to fusing upon deposition.

The maximum true thickness of the Glassy Ignimbrite is approximately 30m, although it is variable and is not observed in some areas. It is usually easily located in the field by black, sandy float along tracks and cuttings. The pitchstone is commonly spheroidally weathered, as observed at locality MH/63 (GR K35/0719 4667)(Fig.4.29) and reduced to a fine brown sand. However, 100m further up the track from MH/63, the Glassy Ignimbrite displays columns at least 3m high (fig.4.30).

Fig.4.29 Spheroidally weathered Glassy Ignimbrite

Fig.4.30 Massively jointed Glassy Ignimbrite

The well developed eutaxitic texture in thin section suggests that the Glassy Ignimbrite is of pyroclastic origin rather than a lava flow. In outcrop, the eutaxitic texture is more evident on weathered surfaces than fresh (fig. 4.31).

Fig.4.31 Photograph showing eutaxitic texture on a weathered surface of the lower Glassy Ignimbrite

In thin section, different colour glass lenses, obsidian fragments and shattered phenocrysts are present which provide compelling evidence for a pyroclastic origin. The pitchstone dykes described previously may be feeder dykes for the Glassy Ignimbrite. The Glassy Ignimbrite commonly has a banded appearance, which may be the result of rheomorphic processes operating once the ignimbrite had erupted and welded.

The glassy ignimbrite commonly consists of brown, crystal-shard rich fiammé, interfingered with colourless fiammé containing a paucity of shards or phenocrysts. Where fine scale mingling of brown and colourless glass exists, the crystal shards are dispersed evenly.

4.3.2.5 Glassy Ignimbrite (upper)

The upper Glassy Ignimbrite overlies the lower Glassy Ignimbrite as the name implies, it is very similar, both petrographically and geochemically to the lower Glassy Ignimbrite, with variations due to the devitrified and slightly altered nature of the upper Glassy Ignimbrite relative to the lower Glassy Ignimbrite (ref. section 7.2.4). The only petrographical difference between the upper and lower Glassy Ignimbrite is the nature of the groundmass. The groundmass of the upper Glassy Ignimbrite is cryptocrystalline rather than hyaline and is characteristically a pale spearmint colour on fresh surfaces.

The contact between upper and lower Glassy Ignimbrite is not sharp, along the transition zone the rock is partially devitrified and appears brown and spearmint green in hand specimen.

4.3.2.6 Round Top Andesite

The Round Top Andesite conformably overlies the Glassy Ignimbrite and extends from the Rakaia River in a NE direction as far as the saddle to the SW of High Peak. The Round Top Andesites consist of basaltic-andesite and andesite in a volcanic pile, locally at least 200m thick. Individual flows are laterally discontinuous and range in thickness from 4 to >10m. Flows are commonly heavily amygdaloidal and the area is well known for its large agate geodes. Flow banding in some flows is common, as shown in the smooth surface of a basaltic-andesite in the Rakaia River bank fig.4.32.

Andesite also occurs as a spatially restricted lava flow at loc MH/80 (L35/1040 4711), and an andesite dyke occurs near the Birch View homestead at loc MH/51 (K35/0738 4516).

Fig.4.32 Flow banding in the Round Top Andesite. (Length of hammer visible is approx. 50cm)

The Round Top Andesite is highly porphyritic with phenocryst contents generally approximately 20%. The groundmass of the andesites is generally hypocrystalline and flow banding is sometimes depicted by varying devitrification of the groundmass (see Appendix 2 for petrographic summary).

4.3.2.7 Rhyolite fissure dyke

A linear series of pinnacles along the ridge running generally easterly from High Peak between K35/087 458 and K35/095 460, represent a rhyolite fissure dyke similar to that described by Oliver & Keene (1989) for 'The Pinnacles' at Mt. Somers. The outcrops are pinnacle shaped (fig.4.33) and can be clearly seen from the Windwhistle Road leading to the Rakaia Gorge Bridge. The linear outcrop pattern, brecciated appearance of the rhyolite in closeup (fig.4.34), and the lack of eutaxitic texture leads to the interpretation that the outcrops represent a relatively narrow rhyolite fissure dyke, emplaced following or during the eruption of the ignimbrites.

Fig.4.33 Large rhyolite fissure dyke which defines the ridge in an easterly direction from High Peak.

Fig.4.34 Close up of rhyolite dyke, note purple rucksack and hammer at base of outcrop for scale.

The rhyolite fissure exploited the normal fault plane, which may have been active during the eruption of the rhyolites and ignimbrites. The discovery of a rhyolite fissure in the Malvern Hills supports the theory of Oliver & Keene (1989) for the origin of 'The Pinnacles' at Mt. Somers (fig.4.35). Smith (1994) disputed the origin of 'The Pinnacles' at Mt. Somers, and suggested an origin as a hydrothermally welded crush zone due to their proximity to the fault.

This report would agree with the original interpretation of Oliver & Keene for 'The Pinnacles' at Mt. Somers as originating through the extrusion of viscous rhyolitic magma, which may have provided a source for future ignimbrite eruptions. The faults of both the Malvern Hills and Mt. Somers are spatially associated with the rhyolite fissures, which suggests that syn-volcanic faulting was associated with the large volumes of erupted material.

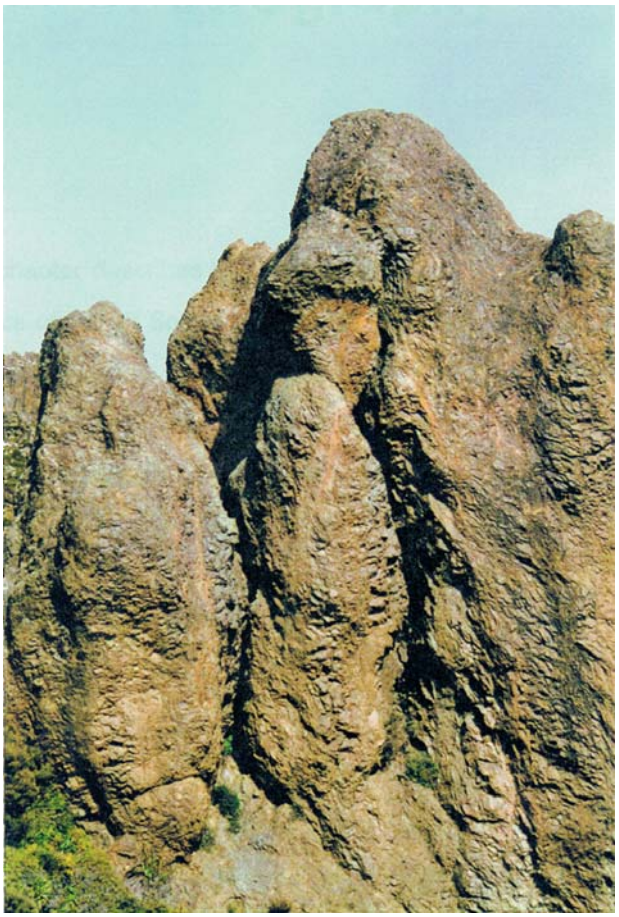

Fig.4.35 Photograph of the Mt. Somers 'Pinnacles' (from Smith, 1994 p78)

In thin section the rhyolite fissure dykes are strongly porphyritic with phenocryst contents of at least 20%. The phenocrysts are generally large and unbroken - evidence of their non-pyroclastic origin.

4.3.2.8 Tertiary dykes

Basaltic and micro-gabbro dykes have been found in the area and these are probably related to the Tertiary volcanic activity responsible for the Harper Hills volcanics found near Coalgate, east of the Malvern Hills. These dykes are marked on the map in red (fig.4.22).

4.3.3 Post-Volcanic Stratigraphy

The sediment cover immediately overlying the volcanic succession is composed of late Cretaceous sediments which are dominated by rhyolite/ignimbrite, matrix-supported conglomerate, interbedded with coal measures of Monro Conglomerate, the basal member of the Eyre Group (Andrews *et al*, 1987). This initial cover is exposed at locality MH/114 (GR L35/1895 4810), beside the Mt. Misery forestry track in the vicinity of Monro Stream (fig.4.36).

Fig.4.36 Monro conglomerate and coal measures, MH/114.

Conformably overlying the Monro Conglomerate are the voluminous sediments of the Broken River Formation, a thick sedimentary sequence which reaches a maximum thickness of 200m in the Whitecliffs area (Andrews *et al*, 1987). Sediments of the Broken River Formation bevel the volcanics of the Malvern Hills and consist of pale, soft, quartzose fine to medium sand.

Small, localised outcrops of pale pinkish and cream marble are exposed at locality MH/126 (GR L35/1070 4915), these marbles correspond to those described by Speight (1928), which mentions a quarry in the vicinity of High Peak Saddle. These small outcrops of marble may be correlated with the Amuri Limestone, not previously described from this area.

Several phases of glacial activity have deposited a large amount of outwash gravel in the Rakaia Gorge (Gregg, 1964; Soons, 1964; Soons & Gullentops, 1972; Soons & Burrows, 1978; Suggate, 1973). The dating of the glacial outwash sequences in the Rakaia Gorge has proved problematic due to a lack of datable material, however movement along the Longspur fault (fig 4.37) at loc MH/10 (GR K35/0088 4256) has occurred within the last 70 000 years (Elvy, 1999).

Fig.4.37 Fault on true right bank of Rakaia River, glacial deposits to the left and ignimbrite to the right. Yellow sledge hammer is aligned along the fault plane.

4.3.4 Faulting

Two faults are named in this thesis, the Longspur and Rakaia Gorge faults. The Longspur fault is the name given to the long WSW-ENE trending high angle fault which cuts through the volcanic sequence. The Rakaia Gorge fault may be connected to the Longspur fault (as

shown on the geological map, fig. 4.22) and is a high angle reverse fault that displaces ignimbrite against Quaternary deposits in the Rakaia Gorge.

The Longspur fault is orientated in a similar direction to several range front faults studied by Elvy (1999) (fig.4.38). Previously noted by Bruce (1994), the position of the Longspur fault was adjusted in this study. The Longspur fault strikes in a W-E direction through the hills (fig. 4.22) and is inferred to pass through Phillips Saddle and is linked to the fault inferred by Gregg (1964).

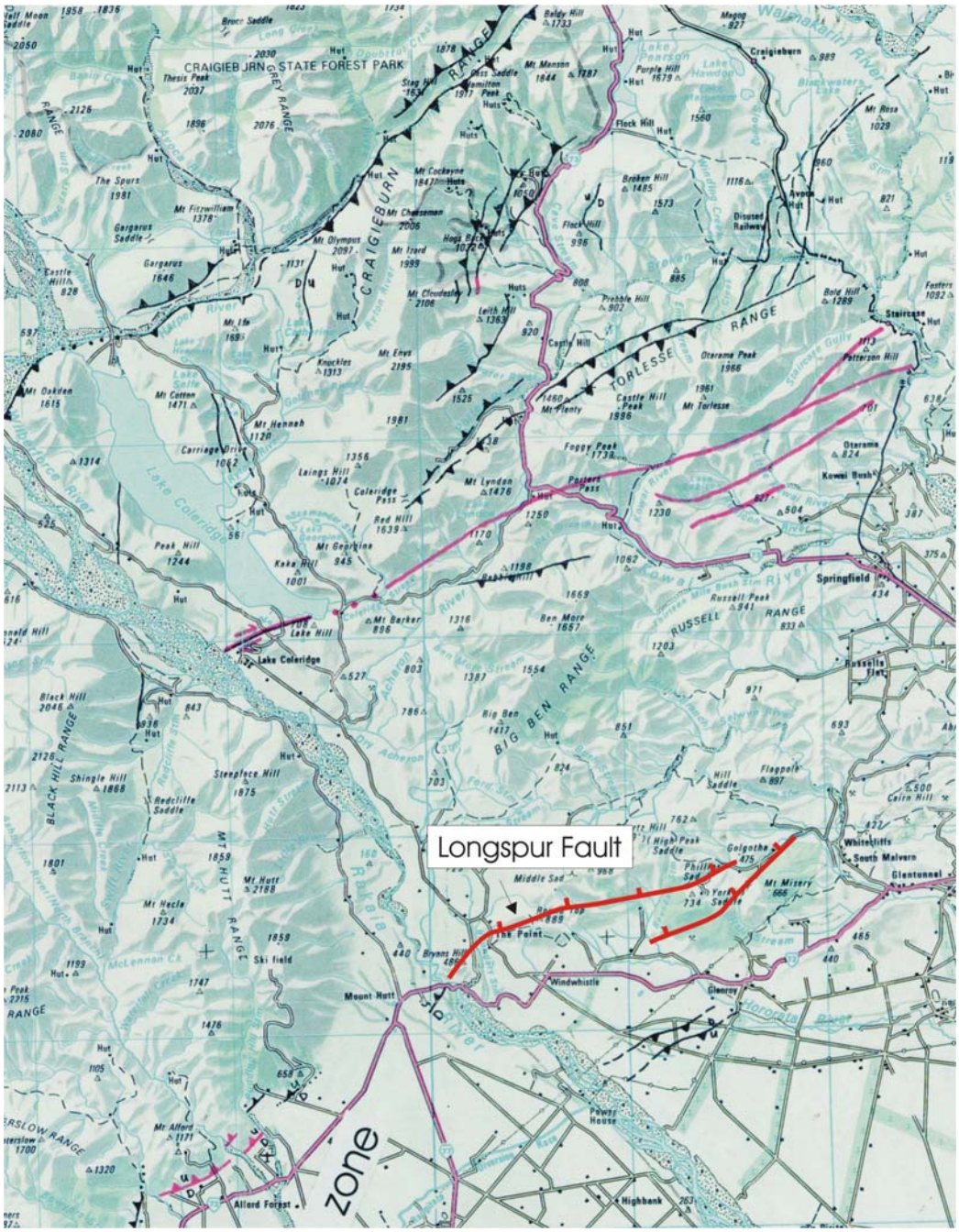

Fig. 4.38 The relationship between the Longspur fault (red), the fault inferred to run along the flanks of Mt. Misery (red), and the faults indicated by Elvy (1999) (pink/black) for the Rakaia River region.

The linkage of the Longspur and Rakaia Gorge faults requires a SW kink in the strike of the fault towards the gorge. An alternative possibility is that the Rakaia Gorge fault is offset from the Longspur fault by another fault striking in a NW-SE direction with a strike-slip component serving to offset the two faults. Another possibility is that the Rakaia Gorge fault is a splay of the main fault. The Rakaia Gorge fault trace is consistent with the orientation of a major scarp observed in the ignimbrite bluffs.

The displacement of the Rakaia Gorge fault in the gorge is clearly reverse, juxtaposing the Cretaceous ignimbrite unit against Quaternary glacio-fluvial sequences. The strike and dip of the fault plane is 003/41°W. No slickensides were visible, therefore displacement vectors could not be established. The Longspur fault, which dissects the mapped area is either a high angle reverse or normal fault. The orientation of the fault plane is difficult to establish, however from structure contours, although very irregular, it appears as though the main fault is actually a high angle normal fault *cf.* the displacement of the Rakaia Gorge fault.

The fault through the main volcanic sequences has probably not been active recently, because no fault trace is visible on aerial photographs.

Another fault is inferred to run down the western edge of Mt. Misery and abut the southern limit of the ignimbrites in Pullwool Peak. The main evidence for this fault is from the abrupt change in topography and the preferential erosion of the softer, post-volcanic sediments, leading to lower gradient topographic elevation.

A small fault displaces the Torlesse-Rockwood Ignimbrite contact to the NW of Pullwool Peak. The displacement along the fault is difficult to establish, however the result is to offset the inferred bounding Cretaceous fault scarp in a NE-SW direction. This displacement can be generated by either dip-slip or strike-slip movement due to the dipping nature of the contact (fig.4.27).

4.4 McQueen's Valley, Banks Peninsula

The McQueen's Valley field area is small when compared to the other areas, and is composed of andesites, rhyolites, pitchstones and ignimbrites, which are partially covered by Tertiary volcanics, mainly of trachytic composition. The reader is referred to Fig.4.39, based on the earlier work of Sewell *et al* (1988).

Stratigraphic relationships are difficult to ascertain, and no contacts can be seen in the area.

4.4.1 Rhyolite & Ignimbrite

Rhyolite outcrops are generally dome-like in outcrop pattern and have cavernous weathering and are generally unsuitable for detailed geochemical analysis. The presence of garnet and absence of smoky quartz in the MSVG rhyolites distinguishes them from the rhyolites of the Lyttelton volcano (Tertiary).

Ignimbrite units are also distributed throughout the area and are concentrated at the head of McQueen's Valley, beside the recently cut forestry track (fig.4.39b). An ignimbritic origin is inferred from the presence of devitrified fiammé and abundance of crystal fragments in the groundmass.

4.4.2 Andesites

The distribution of andesites as marked on the map of Sewell *et al* (1988) has been amended based on XRF geochemistry of the intermediate lava flows (chpt.7), which indicates that the majority of lavas are trachytic, with higher Nb contents than any of the andesites of the MSVG. A sample from these lavas has yielded an age of 11.59 ± 0.08 Ma (Chapter 6) and therefore these trachytic lavas are interpreted to be part of the Tertiary Lyttleton Volcanic Group.

MSVG andesites are found in McQueens valley but are of limited extent (fig.4.39).

MV maps fig 4.39

Petrographically, the andesites of McQueens valley resemble those of unit B-III of Mt. Barrosa with clear, large glomerocrysts comprising up to 30% of the rock. The glomerocrysts are large and measure up to 1cm diameter. The groundmass is generally hypocrystalline with fine microlites of plagioclase and opaques in a brown glass. Phenocryst phases present include plagioclase, orthopyroxene (with pigeonite pseudomorphs and overgrowths) and pigeonite primary phenocryst phases. The opaque phase is probably ilmenite.

4.4.3 Pitchstone

An outcrop of pitchstone is present at locality MV/11 (M36/8141 2250). Macroscopically, the pitchstone does not appear to contain garnet, and no garnet is seen in thin section, however, the low Nb content of the pitchstone suggests that it is Cretaceous in age, rather than Tertiary.

The pitchstone shows clear flow banding (fig.4.40) and probably represents a pitchstone flow, related to the nearby rhyolitic outcrops.

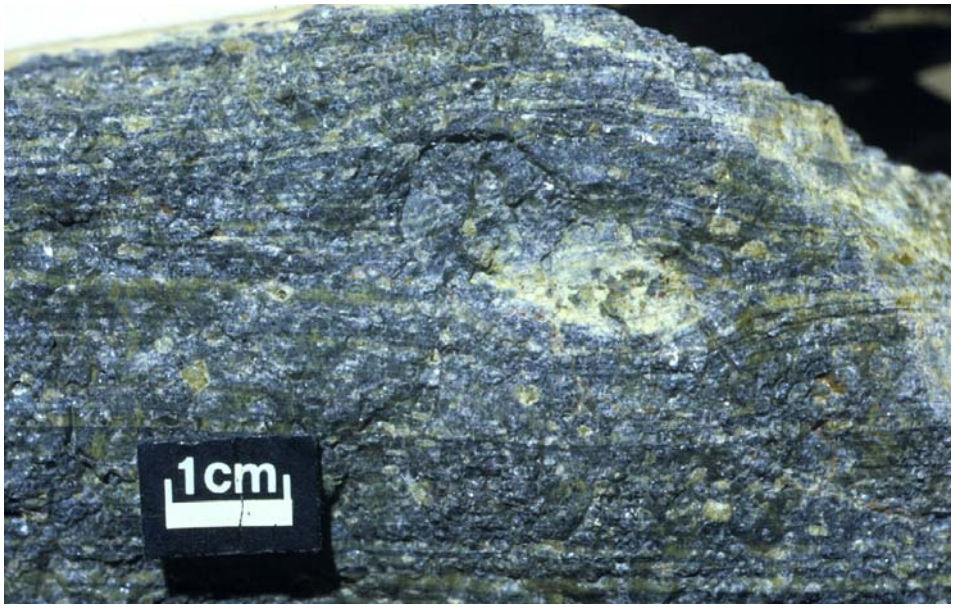

Fig.4.40 Flow banding in the pitchstone found at locality MV/11

4.5 Rangitata Gorge

On the map of Oliver & Keene (1990), the Rangitata Gorge volcanics appear to be fairly simple. However, as shown on fig. 4.42, the intermediate lavas range in composition from basaltic-andesite to trachyte and dacite (TAS classification). The relationship between the intermediate volcanics and the rhyolites is uncertain since the contacts are obscured by surface wash and glacial deposits. Where the relationship can be inferred (e.g. from topography), the rhyolites overlie the intermediate lava sequence (fig.4.41). It is likely that the andesites are the oldest members of the exposure in the Rangitata Gorge, which would be consistent with the relationship described previously for most other members of the MSVG, with the exception of the Malvern Hills.

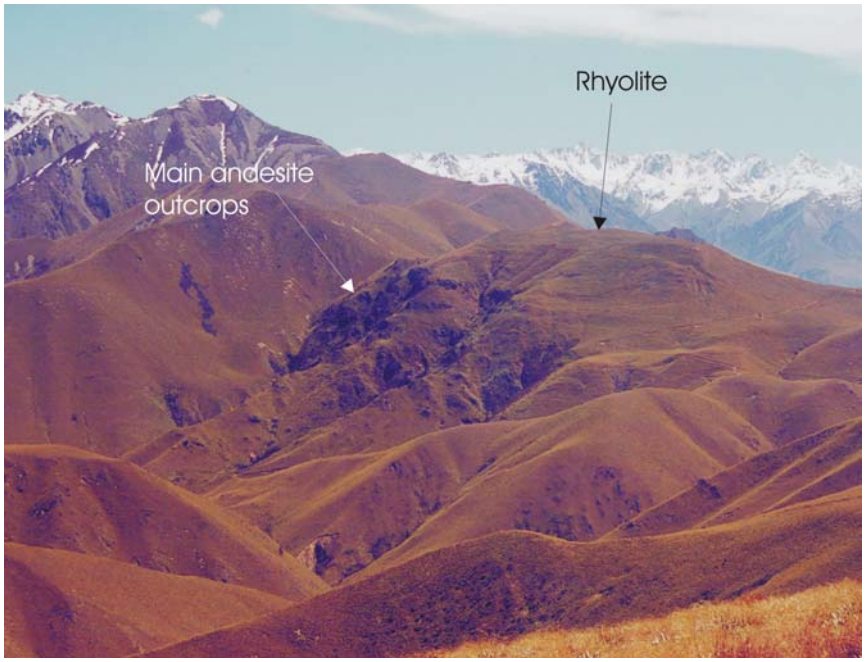

Fig.4.41 Major outcrop of andesite flows, the rounded hill is capped by rhyolite which is therefore inferred to be younger.

4.5.1 Pre-Volcanic stratigraphy

The Rangitata Gorge volcanics unconformably overlie undifferentiated Torlesse rocks (Oliver & Keene, 1990).

The Hewson Formation (Oliver, 1986c), is a pre-volcanic conglomerate which is found near the confluence of Quartz Creek and Hewson River (fig.4.42).

The conglomerate is composed entirely of Torlesse cobbles and is therefore interpreted to have been deposited prior to the onset of MSVG magmatism, although no contacts are seen. The unit is thin and outcrops over a small area.

Fig.4.42 Hewson Formation: conglomerate dominated by Torlesse sandstone clasts.

4.5.2 Volcanic Stratigraphy

The volcanics can be divided into two groups: ‘rhyolite flows’ and ‘intermediate lava flows’. The relationship between the terminology used in this section and that of Oliver & Keene (1990) is shown in table 4.5.

This thesis – for Rangitata Gorge	**Oliver & Keene (1990)**
Intermediate lava flows: Basaltic andesite, andesite, trachyte and dacite	Stew Point Andesite
Rhyolite flows	Rata Peaks Rhyolite

Table 4.5 Summary of rock types mapped in the Rangitata field area and their equivalent as mapped by Oliver & Keene (1990).

RG map – fig 4.43

4.5.2.1 Intermediate lava flows

As shown on fig.4.43, the intermediate lava flows range in composition between basaltic-andesite to dacite and trachyte (based on TAS classification). Although the main part of the bluffs shown in fig.4.41 were inaccessible, at the base of the bluffs are basaltic-andesite flows. An overall stratigraphy for the Rangitata Gorge intermediate flows cannot be established due to the discontinuous nature of the outcrops.

The intermediate flows contain the same phenocryst phases: plagioclase feldspar, orthopyroxene, clinopyroxene (pigeonite), Fe-oxide (ilmenite). The higher silica contents of the dacites is explained as a result of the greater abundance of sedimentary xenoliths in these rocks.

The intermediate flows are commonly amygdaloidal with banded agates often depicting shear/flow direction. Generally the bands were observed only in two dimensions (fig.4.44), although where measured, post-eruption deformation appears to be <10º W or SW.

Fig.4.44 Banded agates in the intermediate lavas of the Rangitata Gorge, note hand lens for scale.

The flows of the Rangitata Gorge are of variable thickness from 2m to >20m. Commonly only the massive flow interiors are visible as outcrop, with the lower and upper rubble zones masked by vegetation or forming small scree slopes.

4.5.2.2 Rhyolite Flows

The rhyolite is generally observed to form flow morphologies rather than dome-shapes, and flows are commonly columnar jointed (fig.4.45).

Fig.4.45 Columnar jointed rhyolite flow, note hammer for scale.

The rhyolites are commonly weathered to a pinky colour due to iron mobilisation. The lavas are porphyritic with phenocryst contents of approximately 15%.

Chapter 5:

Volcanology and temporal evolution of the Mandamus Igneous Complex (MIC)

5.1 Introduction

The geological features mapped during the course of this study are presented in fig.5.6 and the corresponding cross-section in fig.5.7. Each component of the MIC is described in detail in section 5.2.

5.1.1 Basement Geology

The basement lithology of the Mandamus field area is quartzo-feldspathic interbedded sandstones and mudstones of the Pahau subterrane (Torlesse terrane) (Gregg, 1964; MacKinnon, 1983). Recent work has suggested that the Pahau type section in the Pahau River to the north of the Mandamus Field area is dominated by marine fan-delta deposits with sedimentation due to fluvial activity (Orlowski, 2001). The depositional age of the Pahau terrane is considered to be Early Jurassic to Cretaceous (MacKinnon, 1983).

5.1.2 Relationship between the MIC and the Torlesse basement

The MIC is spatially constrained by Torlesse bedrock to the W and E, and by 2 bounding faults to the N and S, the Island Hills and Waitohi Downs Faults respectively (Mould, 1992) (figs.5.6 and 5.7). Section 5.1.3 deals with the structural elements of the area.

The contact between Torlesse and MIC along its eastern margin is not linear and clearly defined, rather it is irregular and indistinct with alternating outcrops of hornfelsed Torlesse, trachyte and microsyenite. The NE contact runs in a SE direction towards the ridge, which

runs ENE from Hurunui Peak. The Torlesse outcrops are generally hornfelsed. The irregular nature of the contact and presence of hornfelsed Torlesse indicates that the contact between the syenite and Torlesse in this location is intrusive.

The western contact of the MIC with the Torlesse basement is defined along a narrow bulldozed fence track. The contact is abrupt but preceded by numerous microsyenite and trachyte dykes. Approaching the contact, the Torlesse becomes increasingly hornfelsed and is a purply-grey colour on fresh surface. The actual contact between the Torlesse and syenite is exposed at locality M/204 (M33/7305 2478) (fig.5.1).

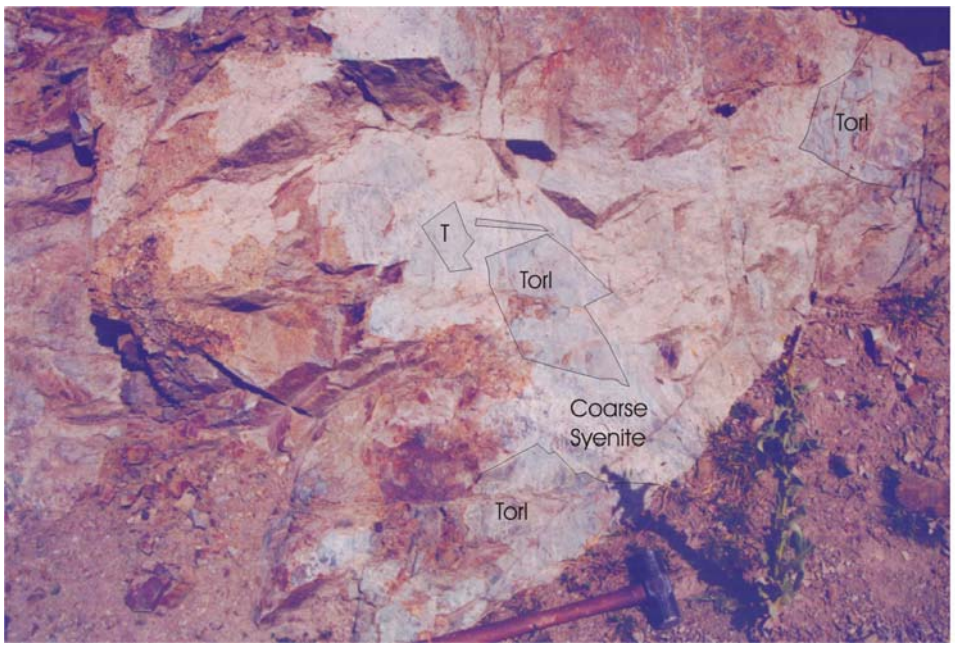

Fig.5.1 Angular baked blocks of Torlesse within the syenite at the Torlesse-Syenite contact.

The contact shows angular clasts of Torlesse sandstone surrounded by syenite, and fig.5.1 illustrates the relationship between the Torlesse blocks and syenite. The very narrow zone of fining of syenite and the heavily baked nature of the Torlesse country rock indicates that the intrusion process was slow, thereby allowing for the temperature of the country rock to be raised considerably. The high temperature of the country rock would result in a very narrow, or absent ‘chilled margin’ to the syenite. At the Torlesse-syenite contact, the Torlesse blocks have been baked but show no indication of melting.

5.1.3 Structural elements of the MIC field area

The MIC field area is situated in the NW corner of the fault-bounded Culverden Basin (fig.5.2). The MIC is bound to the south, by the Waitohi Downs Fault, which is one of the largest bounding faults of the Culverden Basin (Armstrong, 2000; Mould, 1992), and the Island Hills Fault to the north (fig 5.6).

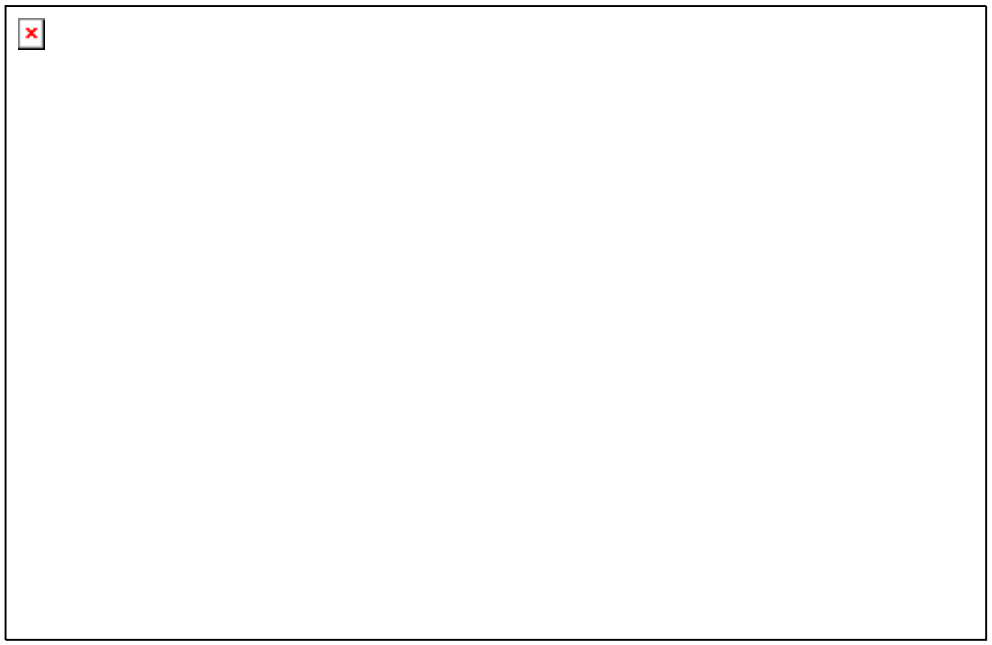

Fig.5.2 Landsat image of the Culverden Basin, adapted from Mould (1992)

5.1.3.1 Waitohi Downs Fault

The Waitohi Downs Fault (fig.5.6) runs, along its length north of the Hurunui River, sub-parallel to a N-S lineament, which may be a structurally weak zone in the Torlesse bedrock (fig.5.2). Mould (1992) suggests that the N-S trending lineaments may have been exploited both by the Waitohi Downs Fault and the MIC. South of the Hurunui River, the Waitohi Downs Fault strikes obliquely to the range front lineations bounding the western edge of the Culverden Basin.

The Waitohi Downs Fault is a NW dipping reverse fault where the MIC has been upthrown relative to the Tertiary succession exposed at Flaxdown Quarry.

5.1.3.2 Island Hills Fault

The Island Hills Fault dips in a SE direction (fig.5.3), deforming the Tertiary sedimentary sequence to the NW (fig. 5.8). The displacement is reverse and the fault is responsible for a 50m wide zone of shearing in the Mandamus River. In the wide shear zone, syenite is juxtaposed against trachyte, and thin slivers of Tertiary greensand are also noted. It is likely, as shown on the cross-section, that several splays are present within the vicinity of the main shear zone. The possible splays are described below (section 5.1.3.3). Where the Island Hills Fault juxtaposes syenite and lahar deposits against unbaked Torlesse bedrock, the fault plane can be seen more clearly.

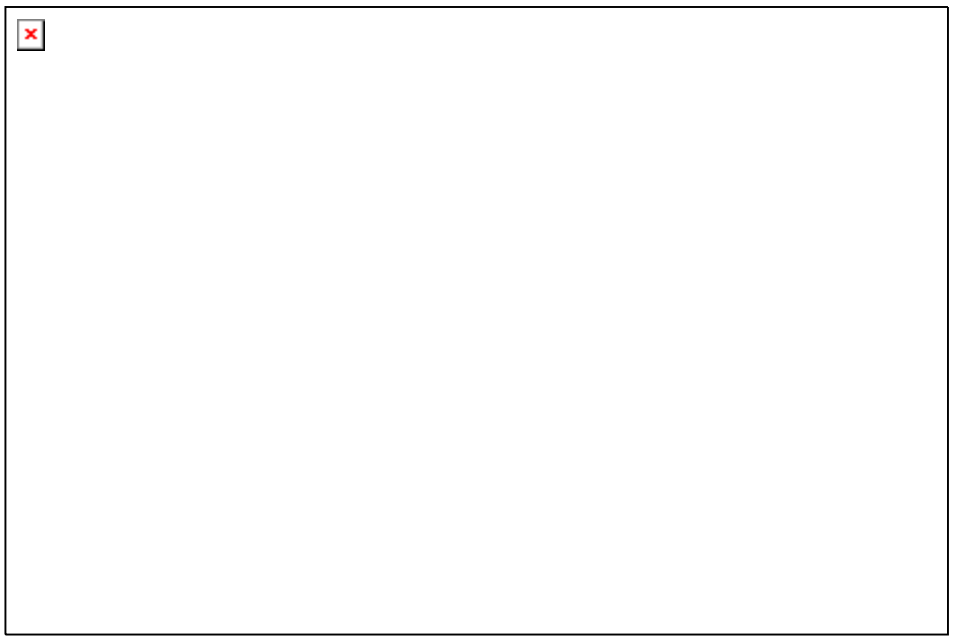

Fig. 5.3 Island Hills Fault plane

5.1.3.3 Island Hills Fault-Splays and local landslides

A broad shear zone is present where the Mandamus River intersects the Island Hills Fault. Localised fault splays are inferred due to disruption of Tertiary greensand and sharp topographic features. One fault splay is mapped to explain the deep valley that runs sub-parallel to the Island Hills Fault as shown on the geological map (fig.5.6 and 5.8). This deep valley also runs along the intrusive contact between the trachyte and syenite. The intrusive contact may have provided a weak lineament along which a fault propagated.

Another splay is inferred in the greensand at locality M/176 (M33/7358 2561). Locally developed concretions are orientated parallel to the shear zone and probably developed along a depositional horizon (fig. 5.4). Some concretions are cut by the shear zone indicating an older age.

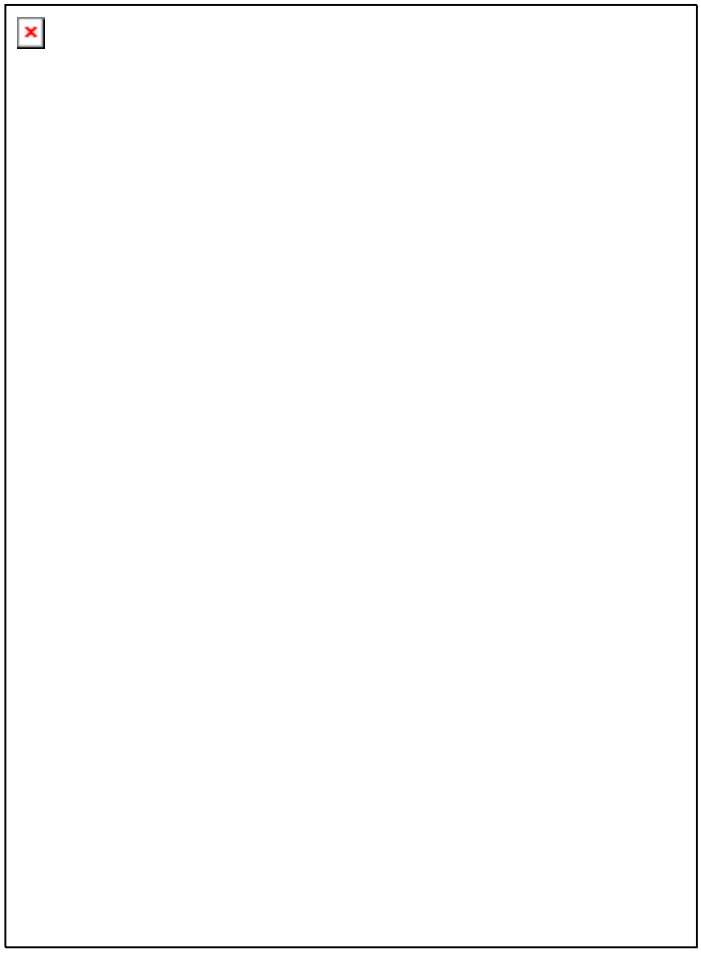

Fig.5.4 Shearing in the greensand resulting from a splay of the main Island Hills Fault

Two major landslides are seen in the area and marked on the geological map (fig.5.6). The debris from the landslide in the vacinity of the Mandamus River masks the contact with the syenite (fig.5.5). The landslide in the Mandamus Gorge was probably initiated by undercutting by the Mandamus River. The friable nature of the syenite and steep gradient of the terrain in the area of the landslide to the east of the mapped area, probably led to the failure.

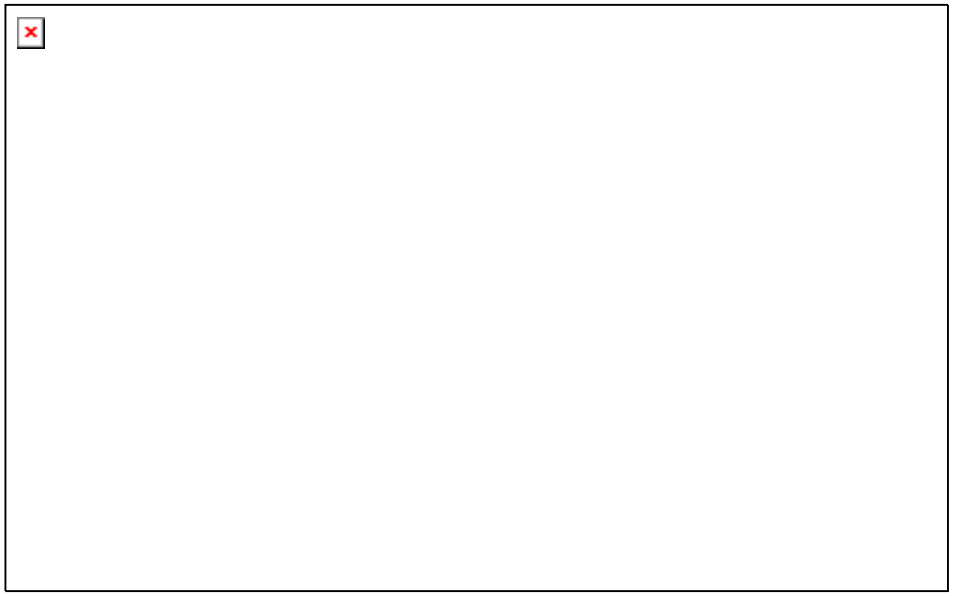

Fig.5.5 Landslide obscuring the Torlesse-syenite contact above the Mandamus River

5.2 Mandamus Igneous Complex

The igneous geology in the Mandamus field area is dominated by a syenite plutonic complex with a carapace of trachytic and mafic lava flows and lahar deposits, which have been subsequently cut by alkaline mafic and intermediate dykes. The sequence of events is complicated by cross-cutting dykes which indicate repeated ‘pulses’ of activity.

Insert map here – fig 5.6

Insert cross-section here – fig. 5.7

The earliest phase of activity was the eruption of lava flows of predominantly trachytic composition. These lavas are present in the field area and form a carapace over the syenite intrusion. The contact between the syenite and trachyte (lavas) is intrusive, as observed in the Mandamus River (locality M/181 GR: M33/7380 2531). The syenite is chilled against the trachyte suggesting that the syenite intrudes the lava pile. Abundant micro-syenite dykes intrude the trachyte, and the contact between syenite and trachyte is often irregular. The contact extending down a stream to the west of Hurunui Peak is inferred to have been subsequently exploited by a fault. The fault is implied from the topography and is probably a splay of the Island Hills Fault (fig. 5.8).

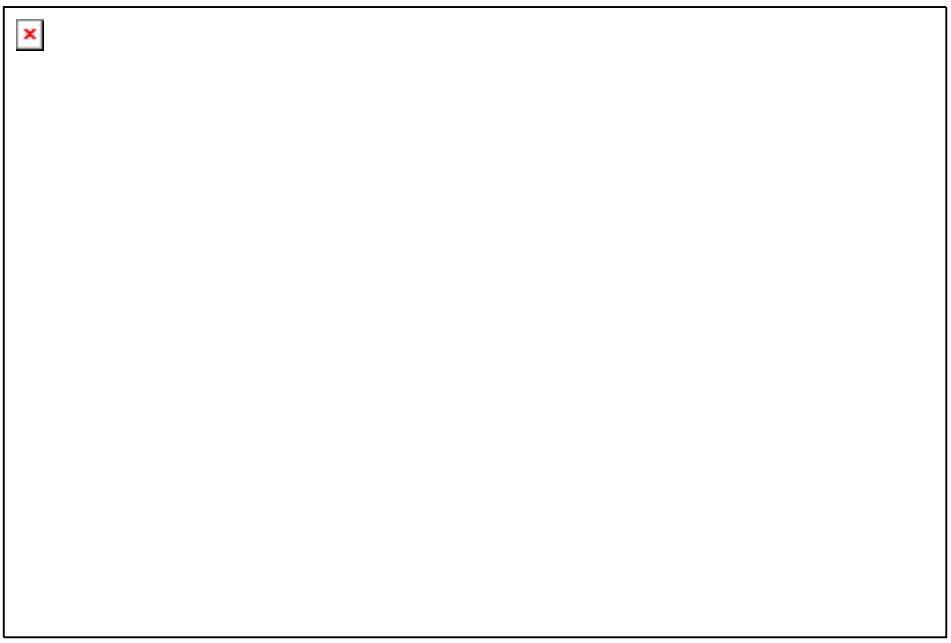

Fig.5.8 Photograph showing the major structural elements of the Mandamus field area

The hard, water-worn exposure of breccia in the Mandamus River is not observed to be physically connected to the rest of the MIC and is surrounded by Torlesse bedrock. The breccia is near circular in outcrop pattern, which would also be consistent with an origin as a vent breccia. The notable absence of syenite clasts suggests that the deposit may pre-date the emplacement of the syenite pluton. Petrographically, the river breccia contains crystal fragments in the groundmass, indicating a primary rather than re-worked origin. The breccia found in the Mandamus River is interpreted to be a filled vent related to the eruption of the lava flows. Trachyte dykes are observed to occur in close proximity with the vent breccia's contact with the neighbouring Torlesse basement.

The major pluton is compositionally varied and can be divided into syenite, syenodiorite and alkali microgabbro (fig.5.6). The gabbro found in Hut Creek may represent the primitive end member of the gabbro-syenite suite.

The syenite and trachyte form clasts in the widely distributed lahar deposits. The lahars were deposited following the uncapping of the syenite pluton and the clasts appear to be locally derived. For example, the lahar deposits which overlie syenite contain an abundance of syenite clasts, together with trachyte. Whereas the lahar deposits, which rest upon the trachyte, are overwhelmingly composed of trachyte clasts.

The final phase of activity in the MIC was the intrusion of dykes (mainly trachytic) into the overlying lahar deposits and therefore the underlying units as well. Such late stage magmatism indicates that magmatism was of low volume but long-lived in order to allow for the unroofing of the large intrusive bodies.

Each unit of the MIC is described in more detail below.

5.2.1 Trachyte Lavas

The trachytic lavas are shown in brown on the map (fig.5.6). They form a carapace over the syenite intrusion and are concentrated adjacent to the Island Hills Fault. The trachytes are generally pale grey in colour and commonly heavily hydrothermally altered, especially in close proximity to the Island Hills Fault. A thin sliver of trachyte is found to the west of the Mandamus River, forming a slice between the Island Hills Fault and the fault splay which runs along the contact between the syenite and the trachyte. Localised outcrops of trachyte are also found dispersed over the syenite.

The contact between the trachyte and the Tertiary succession (M/175 M33/73642549) in the Mandamus River does not appear to be faulted, rather a steeply inclined termination of trachyte. The contact between the trachyte and Waipara Greensand Formation is not seen. The most northerly outcrop of trachyte in the Mandamus is not sheared, and occurs 10m upstream from the onset of the heavily sheared zone. The steeply inclined surface may represent an up-tilted erosion surface, upon which the Tertiary sediments were deposited.

5.2.2 Mafic Lavas

The volcanics near the summit of Hurunui Peak are highly porphyritic to aphyric and are very dark in colour (*cf.* the trachyte lavas). These volcanics are more mafic and generally mildly Si-undersaturated in composition compared with the trachyte lava flows, and range from basalt to tephri-phonolite. The outcrop pattern along the summit ridge of Hurunui Peak, coupled with the near horizontal contact with the syenite suggests that the rocks are lava flows rather than dykes or vent fill (*cf.* Tulloch, 1991). These darker lavas are also cut by micro-syenite dykes and probably form part of the same volcanic carapace as the trachyte lavas.

The presence of the mafic lavas along the ridge lines suggests that the harder shell of the lavas at these points had protected the underlying syenite from erosion. The mafic lavas are generally less altered than their trachytic counterparts, which is probably a function of their lower alkali feldspar contents (which are particularly susceptible to alteration).

5.2.3 Syenite

Syenite is the most voluminous rock type in the MIC and intrudes both the lava carapace and the Torlesse basement. The syenite is generally very coarsely crystalline and heavily altered.

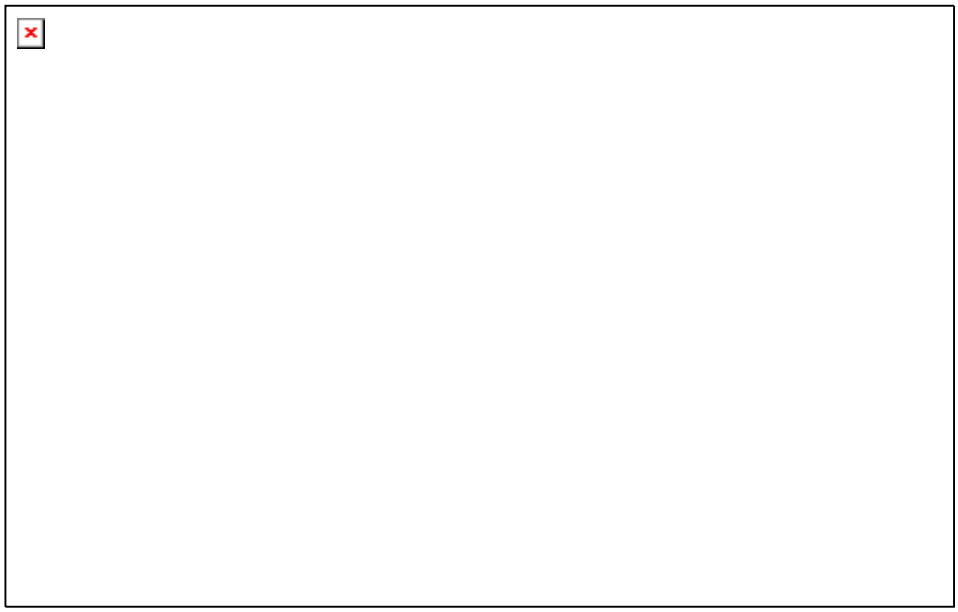

Fig.5.9 Large outcrop of syenite with an abundance of cross cutting trachyte dykes. Note single sheep for scale.

At locality M/97 (M33/7642 2607) the syenite becomes locally pegmatitic with crystals of alkali-feldspar reaching 1.2cm long. This outcrop is in close proximity to the trachyte-syenite contact at M/95 (M33/7634 2605) and probably represents the top of the intrusion, subsequently unroofed by erosion. Several trachytic dykes cut the syenite at this locality.

Close to the summit on the northern flanks of Hurunui Peak at locality M/95 (M33/7634 2605) the contact between syenite and trachyte is observed. The trachyte is hydrothermally altered and the contact is obscured by fracturing and alteration, but the syenite is seen to fine markedly over a 10cm margin adjacent to the volcanic trachyte. The narrow width of chilled margin suggests that the trachyte was heated prior to final contact. No evidence of trachyte consumption by stoping was observed at this locality.

The best exposures of the contacts between the syenite and lahar deposits are in the narrow valley running to the NW of Hurunui Peak. This valley is interpreted to cut into the chilled micro-syenite roof of the syenite intrusion, which is capped by lahar deposits. Although microsyenite is observed to cut through the lahar deposits, the lahar deposits contain syenite clasts and therefore post-date the main syenite pluton emplacement event.

The contacts between syenite and syenodiorite, and between syenite and alkali micro-gabbro are not seen. Detailed petrographic analysis by Reid (1972) led to the conclusion that the syenite intrudes (and is therefore younger) than the syenodiorite.

5.2.4 Syenodiorite

Syenodiorite is observed to form a small peak to the west of Hurunui Peak and continues down to the contact with the Waitohi Downs Fault. The rock is noticeably different from the syenite due to its slight colour difference and freshness. The syenodiorite is black and white, whereas the syenite tends to be creamy white and black. The syenodiorite is less altered than the syenite.

The contact between the syenite and syenodiorite is not visible in the field but can be well constrained.

The syenodiorite was also subjected to the late stage dyke emplacement, and trachyte dykes are observed at locality M/155 (M33/7506 2510) and M/172 (M33/7496 2506). No lahar deposits were found to overlie the syenodiorite.

5.2.5 Alkali Microgabbro

The alkali microgabbro outcrops in the NE of the mapped area and is exposed along a small farm track and is distinguished from the surrounding syenite by its finer texture and pinkish colouration. The microgabbro is also cut by minor dykes, as shown on the map (fig.5.6).

5.2.6 Hut Gabbro

The Hut Gabbro outcrops in a small tributary of the Dove River called Hut Creek. The creek cuts a narrow valley through gravels to expose the bedrock of Torlesse and eventually gabbro, approximately 2km from the confluence with the Dove River.

The contact between the Hut Gabbro and Torlesse bedrock is heavily eroded and vegetation covered. However, the Torlesse close to the contact appears hornfelsed and is heavily fractured immediately adjacent to the contact, indicating an intrusive relationship.

The gabbro is isolated from the main plutonic complex, however its close proximity to the complex is not considered to be coincidental and it is interpreted to be petrogenetically linked to the rest of the MIC. Its composition is likely to be closely representative of the parent magma.

The gabbro is cut by a dyke 55cm wide. The dyke is of basaltic-trachyandesite composition.

5.2.7 Lahar deposits

The lahar deposits outcrop in several places over the area mapped (fig.5.6). The breccias are highly variable in terms of spatial extent, clast composition, sorting and welding (fig.5.10).

Several localised breccia outcrops contain locally derived clasts which are not seen in other breccia outcrops. This can be interpreted in one of two ways; either the breccias were formed at different times when different lithologies were available, or the breccias are a local phenomena sourced from the immediate vicinity. In either case this observation would preclude a vent-fill genesis as suggested by Reid (1972). Rather, a surface deposit is envisaged, such as a lahar deposit. Stratification is seen at loc M/106 (M33/7609 2667) and M/108 (M33/7582 2652), where the 'beds' are seen to dip to the west. At locality M/108 the outcrop appears to be matrix supported.

Fig.5.10 Typical lahar deposit

The breccias differ in their degree of sorting, predominant clast size and clast:matrix ratios. At M/83 (M33/7688 2666), the breccia appears to be clast supported with little or no matrix interstitially. Grading was not observed during this study, however Tulloch (1991) does describe grading. Predominant clast size can vary dramatically between outcrops. For example, at M/92 (M33/7656 2610), a breccia is observed to contain large clasts up to 40cm diameter of porphyritic trachyte and syenite whereas at M/93 (M33/7671 2597), just the other side of a ridge, the clasts are <5cm.

The presence of a heavily porphyritic trachyte dyke intruding the breccia at M/113 (M33/7611 2614) (fig.5.11) indicates that the breccia was not the last phase of volcanic activity and that the complex was subjected to a relatively long-lived period of activity.

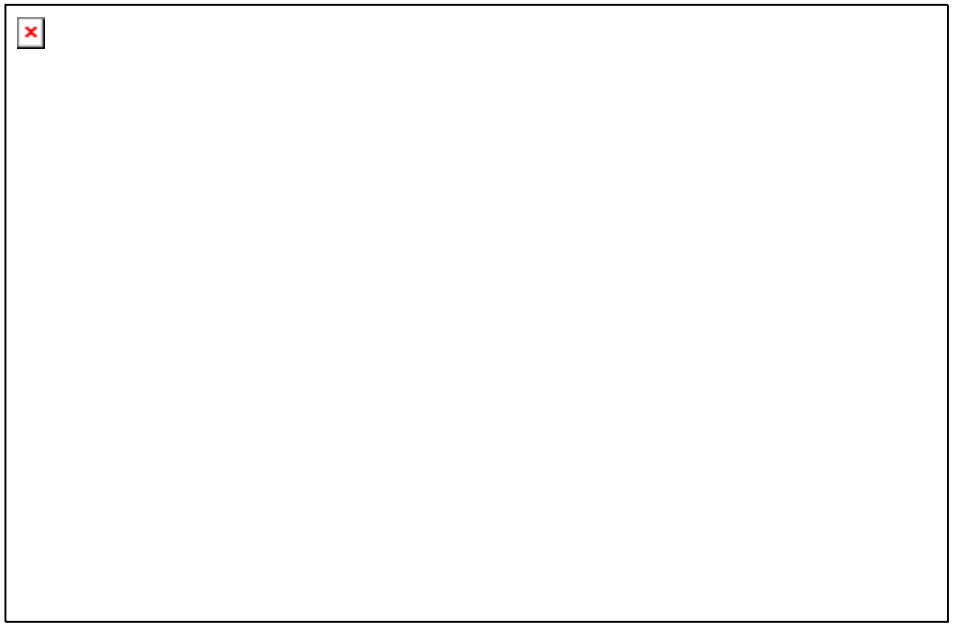

Fig.5.11 Trachyte dyke intruding the lahar deposit. Note hammer in foreground for scale

5.2.8 Vent Breccia

The term ‘vent breccia’ is used to describe the outcrop of volcanic breccia which can be found in the Mandamus River and the slopes of the hill behind Glens of Tekoa homestead.

The sub-circular outcrop pattern supports the hypothesis that this breccia represents a plug of material infilling the former conduit of a volcano. The presence of crystal fragments in the groundmass and the lack of any sedimentary structures would preclude significant reworking. The breccia contains a variety of clast types with a predominance of trachyte clasts. Torlesse clasts are also found in the breccia. There is a notable absence of syenite clasts in the breccia which would indicate that the breccia may have been formed prior to the emplacement of the syenite, or, that the conduit did not pass through syenite on its route to the surface. The latter seems unlikely since the syenite clearly forms a large part of the MIC. It is possible that the vent breccia fills a vent from which some of the early lavas were extruded, prior to the emplacement of the syenite.

Trachyte dykes are found in the Torlesse country rock within a few metres of the breccia which would be consistent with the vent breccia hypothesis.

5.2.9 Dykes cutting Torlesse

Atleast 54 dykes outcrop in the Dove River between Island Hills homestead and the confluence of Hut Creek with the Dove River (figs.5.6 and 5.12). The strike direction of dykes is predominantly within 45º of the strike of the river. This may be a factor of 'noticeability', whereby dykes which cut the river banks at near-perpendicular angles are more likely to be noted than dykes which cut obliquely (<45º) to the strike direction of the river. Tulloch (1991) differentiated between dykes intruding Torlesse and dykes intruding the igneous complex but with limited numbers of 36 dykes in the Torlesse and 18 dykes in the igneous complex. Tulloch's (1991) rose diagram suggests that the dykes '*define an apparent radial pattern*', however it is unclear whether the dykes are radial or random with respect to the igneous complex.

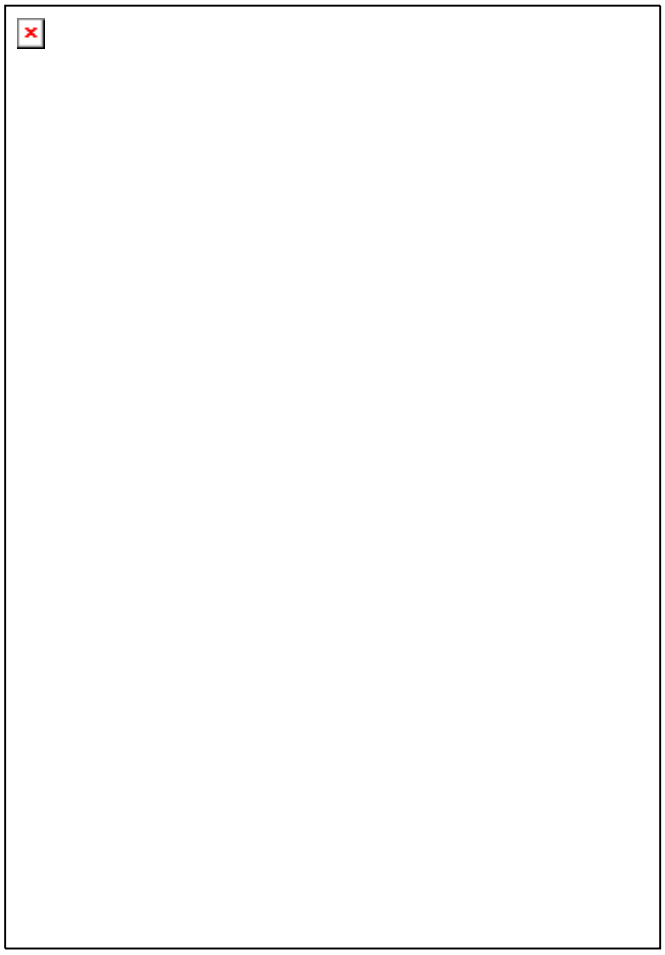

Fig. 5.12 Trachyte dyke intruding Pahau Torlesse rocks

Reid (1972) sampled 163 dykes and drew a rose diagram illustrating their orientation. Unfortunately this did not differentiate between those intruding Torlesse and those intruding

the igneous complex. If inferences are to be made about possible emplacement mechanisms and the presence, or not, of radial dyke patterns then this information is pertinent. Reid's diagram (1972, fig.66) showed a predominance for NNW and ENE orientation and from his geological map, the dykes appear to be orientated in both a radial and concentric manner, consistent with the emplacement of an igneous centre. It must also be noted that individual dykes are seen to vary considerably in orientation within a few metres, such as at M/9 (M33/7851 2864), and often pinch out within the outcrop indicating the lateral discontinuity of such minor intrusions. The dykes intruding the Torlesse increase in abundance with proximity to the MIC.

The dykes vary considerably in terms of geochemical composition, mineralogy, texture and width. The dykes, however, are consistently alkaline and range from tephrite to trachyte in composition. Some dykes have acted as foci for re-intrusion of magma. At loc M/10 (M33/7872 2866), an orange weathered trachyte dyke is cut by a trachy-basalt dyke (fig.5.13).

Fig.5.13 Trachy-basalt dyke intruding trachyte dyke, Dover River

At loc M/14 (M33/7836 2863) a net-vein complex (Hall, 1996) is observed illustrating magma mingling between magmas of different compositions (based on appearance only), with one chilled against the other (fig.5.14).

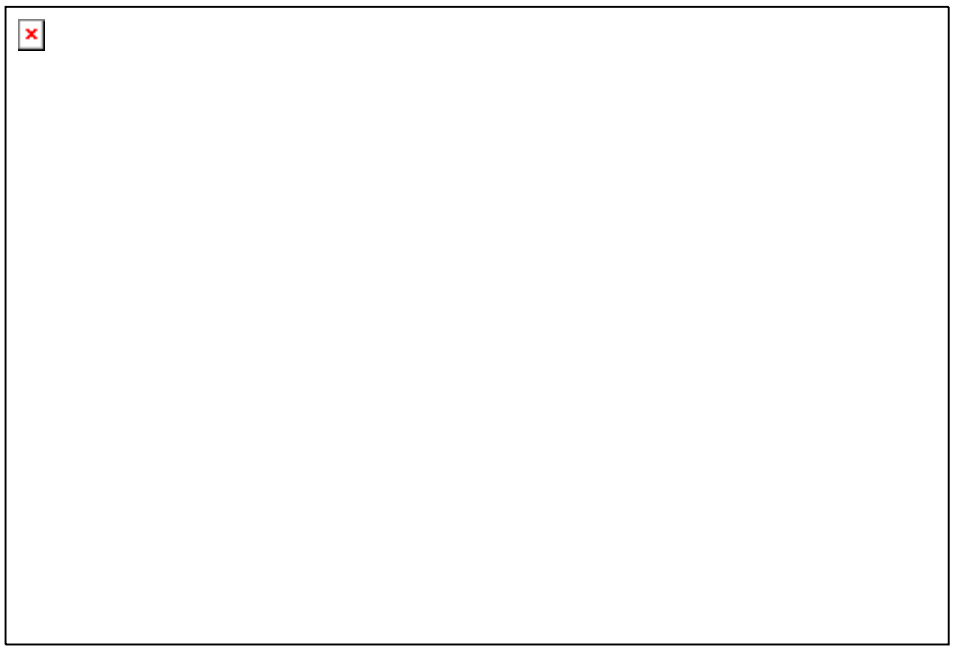

Fig.5.14 Net-veining of porphyritic and aphyric trachyte

The contacts between Torlesse country rock and the dyke material are variably discordant and individual dykes are commonly seen to pass from horizontal to vertical attitude as they cut through the Torlesse basement.

5.2.10 Dykes cutting the MIC

The inter-relationship of each phase of igneous activity is quite complex as described briefly in the opening paragraphs of section 5.2. Relative age determinations are usually permissible by analysis of cross-cutting relationships. However, in the MIC repeated pulses of trachyte and syenite intrusion are observed. For instance, micro-syenite dykes are seen to intrude trachyte (GR's: M33: 7756 2740, 7708 2631, 7557 2589, 7551 2558). Micro-syenite also intrudes breccia (M/87, M33/7667 2665) and the coarse syenite pluton at M/205 (M33/7305 2475).

In turn, trachyte and basaltic-trachyandesite dykes are seen to intrude syenite (M/33 7725 2697), syeno-diorite (M33/ 7506 2510), breccia (e.g. M/33 7634 2639), trachytic volcanics (M/33 7555 2596) and Hut Gabbro (M33/7878 2865).

In addition, one outcrop of tephriphonolite can be found at loc M/227 (M33/7723 2605), and is inferred to cut syenite, although actual contacts are masked by vegetation.

The syenite is commonly cut by trachytic and trachybasalt dykes (fig. 5.15). In the Mandamus River an exposure of syenite contains disseminated dyke material, which consists of small blebs of dark material (fig. 5.16). Many of these minor intrusions are irregularly shaped and appear to have been emplaced whilst the syenite was still relatively ductile.

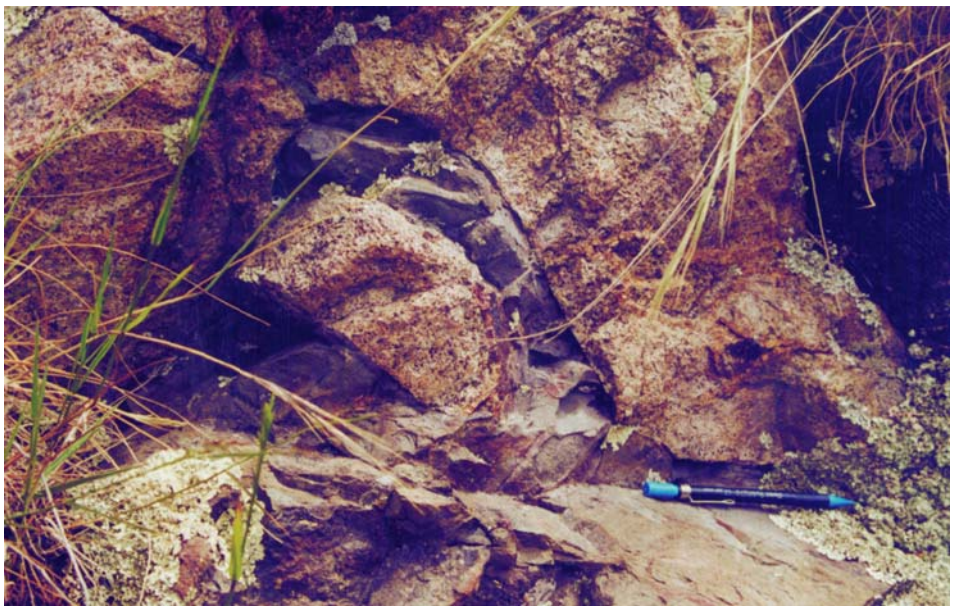

Fig.5.15 Trachybasalt dyke intruding syenite

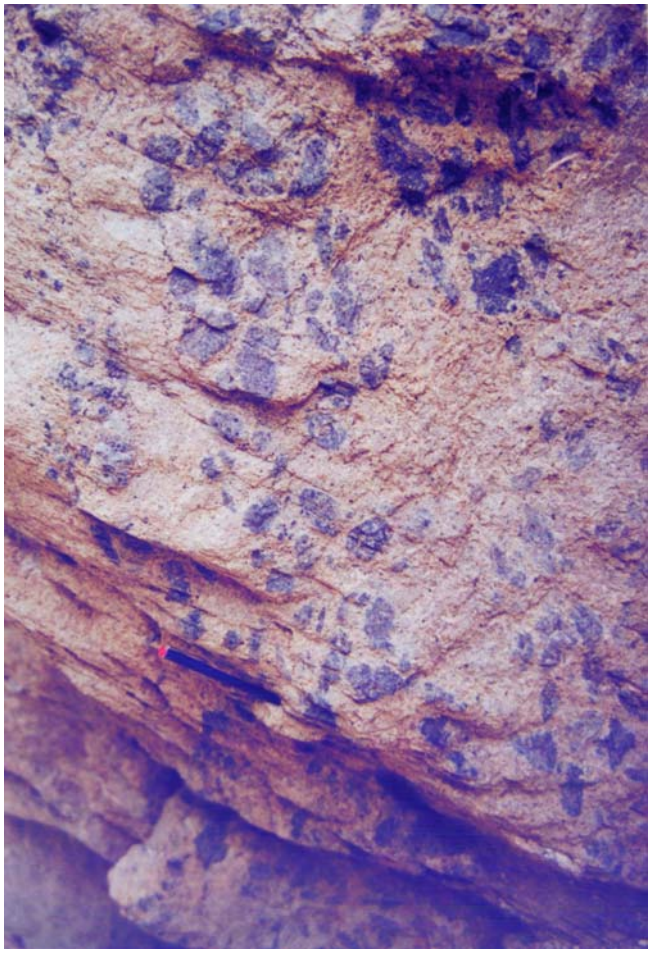

Fig.5.16 Disseminated dyke material in syenite. Note pen for scale.

5.3 Post-volcanic geology

The post-volcanic sediments of the Mandamus field area form a transgressive sequence illustrating the sedimentation accompanying relative sea level rise.

The earliest post-volcanic sediments are observed in Coal Creek (M33/728252). The earliest post-volcanic lithology belongs to the Eyre Group (Andrews *et al*, 1987) and is a MIC-clast dominated conglomerate of the Broken River Formation (Haumurian age: 80-66.5 Ma), which unconformably overlies heavily fractured Torlesse rocks. The conglomerate is associated with discontinuous lenses of coal up to 0.6m thick. The formation exposed in coal creek represents a fluvial-derived conglomerate and delta top coal deposits which form the base of a transgressive sequence.

The shallow marine Waipara Greensand Formation (also of the Eyre Group) follows, with 40m being exposed in Coal Creek and substantial amounts around the base of the Tekoa syncline. The formation is interpreted to have been deposited slowly in shallow marine conditions (Brown & Field, 1985). The Waipara Greensand is assigned a late Teurian to Waipawan age (Paleocene, 62-55.5Ma).

The Waipara Greensand is capped by the Tekoa Formation which is a local formation of the Cookson Volcanics Group (Brown & Field, 1985). The Tekoa Formation (Tekoa Tuff) (Andrews, 1963) is a submarine basaltic tuff with abundant small bombs and lapilli with localised lenses of limestone. Brown & Field (1985) re-named the 'Tekoa Tuff' the 'Tekoa Formation', and re-assigned the tuff as a localised member of the Cookson Volcanics Group rather than a member of the otherwise non-volcanogenic Omihi Formation. The Tekoa Formation is Duntroonian (late Oligocene: 28-24 Ma) in age.

Flaxdown Limestone (Andrews, 1963) of the Omihi Formation (Motunau Group) overlies the Tekoa Formation and at its base shows considerable reworking of the preceding volcanogenic sediments. The type section is found up the slope of the syncline opposite the Glens of Tekoa homestead. The Flaxdown Limestone is Duntroonian to Waitakian (28-22Ma) in age.

Chapter 6:

Geochronology of the MSVG and MIC

6.1 Introduction

Three zircon separates from rhyolite samples of the MSVG were dated using the Sensitive High Resolution Ion Micro-Probe SHRIMP II mass spectrometer at ANU, Canberra. In addition, twenty four single crystal and matrix separates from both the MSVG and MIC were analysed using a 25W Spectra Physics argon ion laser and a MAP 216 series mass spectrometer by Dr. P. van den Bogaard at GEOMAR Research Institute, Kiel, Germany.

For a full description of analytical techniques and data sets refer to Appendix 6.

Previously published geochronological data for the MSVG and MIC can be found below in table 6.1.

Technique	Age (Ma)	Reference
Rb-Sr	89.3 ± 2 Ma (rhyolite, Mt. Somers - MSVG) 80.9 ± 1.9 Ma (rhyolite, Gebbies Pass - MSVG)	Barley *et al* (1988)
K-Ar	88-99 Ma (rhyolite - MSVG) 87-93 Ma (andesite & dacite - MSVG)	Adams (1979)
Rb-Sr	97.5 ± 0.5 Ma (whole-rock and mineral separates for the MIC)	Weaver and Pankhurst (1991)

Table 6.1 Summary of previously published ages for the MSVG and MIC

6.2 SHRIMP data

The SHRIMP results are summarised in table 6.2 below:

Sample No.	Rock type	Age (Ma)	Error ($2\sigma_m$)
MH-8	Ignimbrite	97.0	1.5
MV-19	Ignimbrite	98.0	1.2
MS-226	Rhyolite	97.6	1.2

Table 6.2: Summary of SHRIMP data for the MSVG

The data from each sample are discussed in sections 6.2.1 to 6.2.3.

6.2.1 MH-8 (Ignimbrite – Malvern Hills)

The zircons analysed from sample MH-8 showed a distinct cluster of ages very close to concordia on fig.6.1, corresponding to a crystallisation age of 97 Ma ± 1.5 Ma.

Fig.6.1 Tera-Wasserburg concordia diagram for sample MH-8.

Some crystals, which appeared to be well shaped, yielded ages of 131, 158, 225 and 226 Ma indicating that the zircons did not crystallise from the MSVG melt but were inherited from previous magmatic episodes (fig. 6.2). Therefore, in the calculation of the age of the MSVG, only 10 of 15 analyses were used. However, the reproducibility of the 10 samples was very good (MSWD=1.08), resulting in a small error (± 1.5 Ma, $2\sigma_m$). Common Pb is low in all samples ($f206$ <1%).

Fig. 6.2 Cumulative probability versus age of zircon crystals analysed with histogram depicting the number of crystals of each age range analysed.

6.2.2 MV-19 (Ignimbrite – McQueens Valley)

Sample MV-19 yielded an age of 98.0 ± 1.2Ma ($2\sigma_m$) with a good fit to concordia on the Tera-Wasserburg diagram (fig.6.3). All 13 crystals analysed yielded consistent $^{207}Pb/^{206}Pb$ / $^{238}U/^{206}Pb$ ratios with a MSWD of 1.44. No inherited zircons were analysed.

Fig.6.3 Tera-Wasserburg concordia diagram for sample MV-19

Fig.6.4 Cumulative probability versus age of zircon crystals analysed.

6.2.3 MS-226 (Rhyolite – Mt. Barrosa)

Sample MS-226 shows a cluster close to concordia (fig.6.5), yielding an age of 97.6 ± 1.2Ma ($2\sigma_m$).

In the calculation of the age, 11 of 15 crystals analysed were used, with a MSWD of 1.28. Two samples yielded ages of 375 and 382 Ma which indicates their crystallisation from a previous magmatic episode (fig. 6.6). Common Pb is low (<1%).

Fig.6.5 Tera-Wasserburg concordia diagram for sample MS-226

Fig.6.6 Cumulative probability versus age of zircon crystals analysed with histogram depicting the number of crystals of each age range analysed.

6.2.4 Inheritance

The robust chemical and physical characteristics of zircons means that they are able to be recycled through many episodes of magmatic and surface processes. Inherited zircons are often easily recognised with the use of cathodoluminescence (CL) images.

The MSVG rhyolites showed some evidence of inherited zircons (see fig.6.2). The ages of the inherited zircons are almost entirely consistent with incorporation of Rakaia terrane sedimentary rocks (fig. 6.7). The only exceptions being the younger inherited zircons which yielded ages of 131 and 158 Ma in sample MH-8, which can be explained by the incorporation of younger sediments. The Torlesse basement in the vicinity of the Malvern Hills is undifferentiated and may contain slightly younger age sediments (and therefore younger zircons) than those shown in figure 6.7 for the Rakaia terrane. Alternatively, the younger zircon ages may have resulted from analysing the boundary between the core and rim of a crystal, thereby 'averaging' the age.

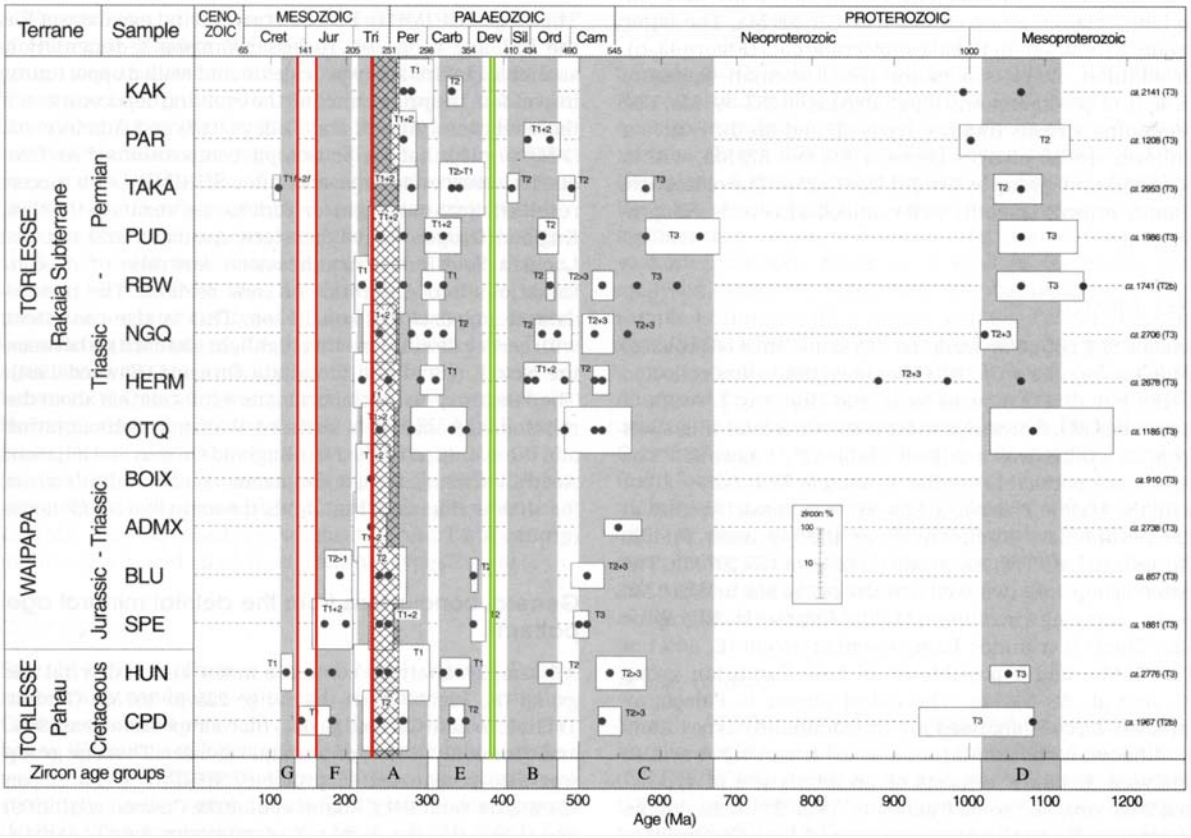

Fig. 6.7 Diagram illustrating the ages of inherited zircons in sample MS-226 (green) and MH-8 (red) overlain onto a diagram illustrating the ages of detrital zircons from the Torlesse and Waipapa basement terranes (Pickard *et al*, 2000). The black dots indicate the ages of zircon crystals extracted from each of the terranes listed on the left hand side of the diagram. The red and green lines can be used to see which terranes the inherited zircons are likely to have been derived from.

6.3 ^{40}Ar-^{39}Ar Data

The ^{40}Ar-^{39}Ar results with MSWD <3 are summarised in table 6.3 below. A full list of data can be found in Appendix 6.

	Sample No.	Crystal	Age (Ma)	Error ($2\sigma_m$)	MSWD
MSVG	MS-146	Feldspar	90.7	1.6	2.31
	MS-29	Feldspar	93.4	0.8	0.60
	MS-36	Feldspar	92.3	1.6	0.86
	MS-40	Feldspar	93.4	1.2	0.82
	MS-68	Feldspar	88.4	1.4	2.34
	MS-96	Feldspar	92.7	1.8	0.45
	MH-29	Feldspar	93.6	0.8	2.04
	MH-7	Biotite	94.2	0.8	1.66
	MV-11	Feldspar	91.0	2.6	0.87
	RG-11	Feldspar	95.7	1.8	0.77
	RG-2	Feldspar	94.1	2.2	1.96
MIC	M-12	Biotite	95.1	0.8	1.47
	M-66	Biotite	94.0	1.4	2.71
	M-77	Feldspar	90.0	2.4	2.86
	M-9	Biotite	94.8	0.6	0.72
	MV-4	K-feldspar	11.59	0.08	0.49

Table 6.3 Summary table of ^{40}Ar-^{39}Ar results for MSVG and MIC samples, together with one trachyte sample from McQueens Valley (MV-4).

The data shown in table 6.3 are plotted on fig. 6.8 for comparitive purposes (excluding sample MV-4). At MSWD <3, the ages obtained for the MSVG range from 95.7 ± 1.8 Ma to 88.4 ± 1.4 Ma, and the ages obtained for the MIC range from 95.1 ± 0.8 Ma to 90.0 ± 2.4 Ma.

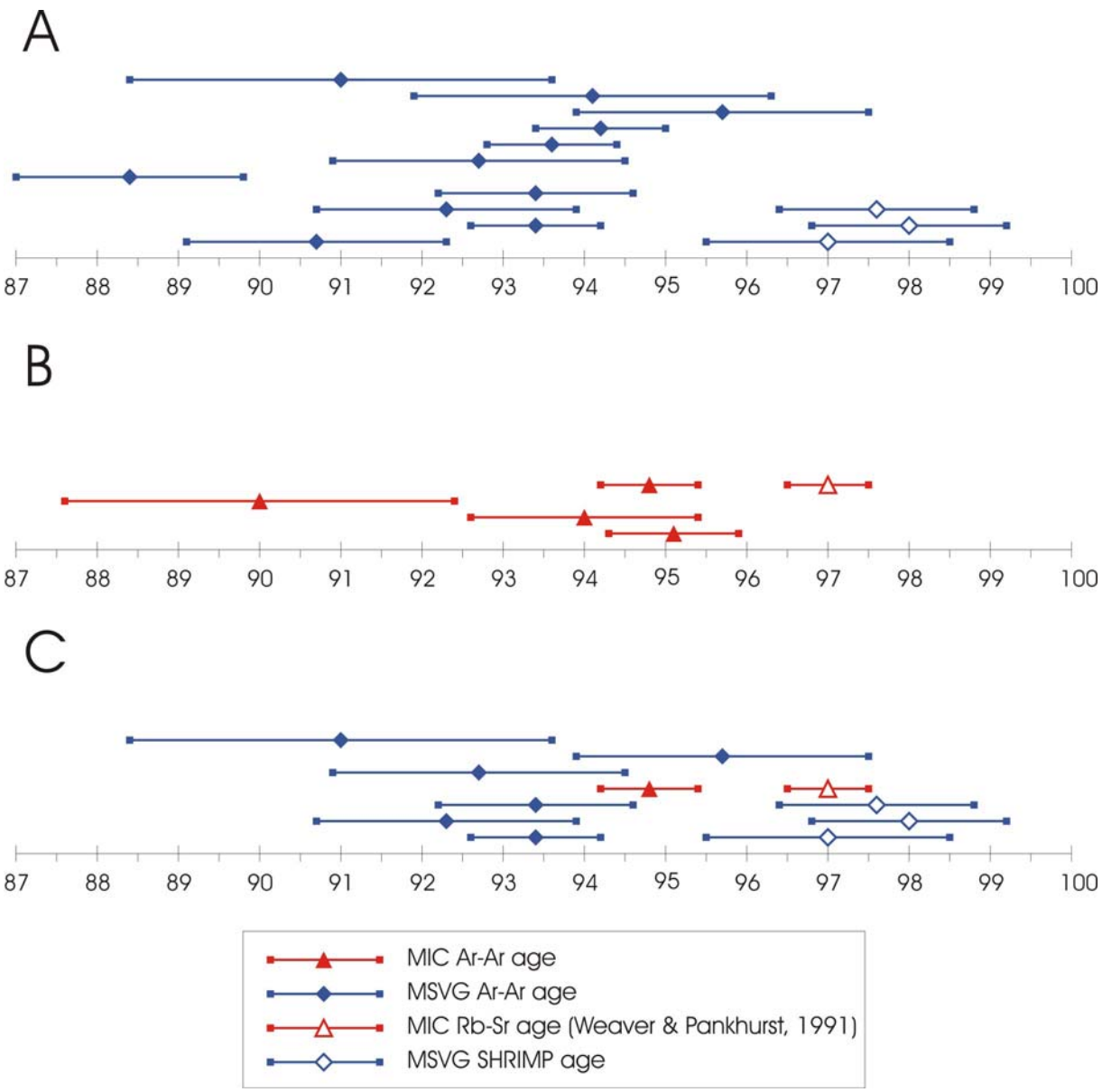

Fig. 6.8 Diagram comparing the Ar-Ar data with the SHRIMP and Rb-Sr data (with error bars indicated) for the MSVG and MIC. 'A' compares the MSVG Ar-Ar (MSWD < 3) data with the SHRIMP data for the MSVG; 'B' compares the MIC Ar-Ar (MSWD < 3) with the Rb-Sr data for the MIC; 'C' compares the most precise (MSWD <1) Ar-Ar data for both the MSVG and MIC with the SHRIMP and Rb-Sr data. The systematic difference in age between the Ar-Ar and the other techniques (SHRIMP and Rb-Sr) is clearly shown in 'C'. The Ar-Ar data, although systematically yielding slightly younger ages, indicate that the MSVG and MIC activity was broadly coeval.

The Mt. Barrosa samples (those with MS- prefix), range from 88.4 to 93.4 Ma. The stratigraphy of Mt. Barrosa is outlined in Chapter 4. The samples dated by the Ar-Ar method were chosen according to their stratigraphic position. The lavas of B-I should be the oldest, and the lavas of B-IV the youngest. The Ar-Ar ages in relation to the stratigraphy are shown in table 6.4.

	Sample Number	Age (Ma)	Error (2 sigma)
B-I	MS-40	93.4	1.2
B-II	MS-68	88.4	1.4
	MS-146	90.7	1.6
B-III	MS-36	92.3	1.6
	MS-96	92.7	1.8
B-IV	MS-29	93.4	0.8

Table 6.4 Mt. Barrosa samples organised according to unit number, based upon the stratigraphy described in Chapter 4.

The ages of the samples listed in table 6.4 overlap within error of each other. The ages given are inconsistent with the stratigraphy, furthermore a 5 Ma age span for the Mt. Barrosa stratigraphy is considered to be extremely unlikely. The spread of ages to younger values as shown on table 6.3 and fig. 6.8 may be due to differential Ar loss from the feldspar crystals. The age of the biotite crystal analysed from the MSVG (94.2 ± 0.8 Ma) is considered to be the preferred minimum age, which is consistent with the feldspar samples dated at >94 Ma. Averaging of these samples yields an age of 94.5 ± 3 Ma for the MSVG (weighted average).

Similarly, the biotite single crystal analyses for the MIC cluster around 94.5 Ma, however the one date determined from feldspar crystals gives an age of 90.0 Ma. Therefore the biotite ages are considered to yield the most reliable ages. Averaging of the three biotite ages gives an age of 94.2 ± 1.7 Ma for the MIC (weighted average).

Despite the apparent discrepency in ages between the SHRIMP and Rb-Sr, and the Ar-Ar data, the Ar-Ar data does indicate that the MSVG and MIC magmatism was broadly contemporaneous, albeit yielding a slightly younger age for both suites.

6.4 Discussion

The SHRIMP ages summarised in table 6.2 are, within error, the same from the three widely separated areas. Although the crystals were targeted based upon their pristine crystal shape and apparent lack of inherited cores on cathodoluminescence photographs, some grains yielded older ages, consistent with inheritance of basement rocks.

The ages yielded by the SHRIMP geochronology are within error of the Rb-Sr age of Weaver & Pankhurst (1991) suggesting that the magmatism of the MIC was contemporaneous with the magmatism of the MSVG. The ages determined by Ar-Ar geochronology also indicate that the MSVG activity was coeval with the MIC activity (fig. 6.8).

The Ar-Ar data show systematically younger ages than the SHRIMP and Rb-Sr geochronology (fig. 6.8). Of particular note, sample MH-8 (SHRIMP dated) yielded an age of 97 ± 1.5 Ma, whereas sample MH-7 (Ar-Ar, biotite) yielded an age of 94.2 ± 0.8 Ma. These two samples were taken from the same outcrop, approximately 0.4m apart. The systematic variance in ages (approx. 3 Ma) between U-Pb and Ar-Ar ages is similar to that described for the Ferrar Province, Antarctica (Riley & Knight, 2001), and may be due to differences in the decay constants available for the K-Ar system (Min *et al*, 2000), or uncertainty surrounding the age of standards used (Villeneuve *et al*, 2000).

The SHRIMP ages determined in 2001 are cited throughout the rest of this thesis as the Ar-Ar data were received at a late stage.

Chapter 7:

Geochemistry and Petrogenesis of the MSVG

Major and trace element concentrations were determined using the Philips PW2400 XRF at the University of Canterbury. Additional trace element and REE data were acquired at the Institute of Geological Research at the Christian Albrechts University, Kiel, Germany. Radiogenic isotope chemical preparation and analyses were undertaken at GEOMAR Research Institute in Kiel, Germany, using a Finnigan MAT 262 mass spectrometer. Stable isotope analyses were carried out in conjunction with IGNS, Lower Hutt, New Zealand.

For a full description of techniques used and data tables, refer to Appendices 3, 4, 5, 7 and 8. For a petrographic summary for each unit, refer to Appendix 2.

The mineralogy of the MSVG will be discussed first, followed by a discussion on each area of the MSVG in terms of bulk composition of volcanic units. The major element variations of the MSVG will be discussed as a whole. Trace element and REE characteristics of the MSVG will be discussed according to lava type rather than area.

7.1 Mineralogy

7.1.1 Basaltic-andesites

As described in the petrographic summary in Appendix 2, the basaltic-andesites of the MSVG are characterised by the anhydrous equilibrium assemblage of plagioclase-orthopyroxene-ilmenite. The absence of clinopyroxene exsolution laminae in the orthopyroxene phenocrysts suggests that orthopyroxene is a primary phenocryst phase rather than inverted pigeonite. The size of the plagioclase and orthopyroxene phenocrysts (generally 1-4mm) would suggest that cooling was initially slow resulting in the rapid growth of large crystals. Large glomerocrysts (measuring up to 1cm diameter) of plagioclase and orthopyroxene are noted from the basaltic-andesite lavas, which are interpreted to have been plucked from the magma chamber and conduit walls. The plagioclase crystals (An_{60-45}) generally retain their euhedral to subhedral

shape, whereas the orthopyroxene crystals are subhedral to anhedral due to late stage resorption. Although orthopyroxene-plagioclase-ilmenite comprises the main phenocryst phases, the groundmass is composed of orthopyroxene-plagioclase-pigeonite-ilmenite.

Orthopyroxene can crystallise without olivine at high pressures and low H_2O contents (e.g. >10kbar and approx 1300 ºC for H_2O content of 2% for high Mg contents of 10% [Nicholls, 1973 #216]. The stability field of orthopyroxene narrows at higher H_2O contents as does the crystallisation temperature. As temperature and pressure fall, clinopyroxene joins orthopyroxene. The more evolved nature of the basaltic-andesite from the MSVG compared with the experimental P-T conditions determined by Nicholls & Lorenz [Nicholls, 1973 #216] for high Mg tholeiites from Germany suggests slightly lower P-T conditions for the crystallisation of orthopyroxene and a low H_2O content inferred from the absence of olivine. The resorption of orthopyroxene and to a lesser extent plagioclase suggests that the phenocryst assemblage became out of equilibrium with the melt. The groundmass assemblage, which contains clinopyroxene (pigeonite) indicates that the groundmass crystallised rapidly at lower pressure and temperature. The crystallisation of pigeonite is consistent with a decreasing Mg/Fe ratio at increasing levels of differentiation, coupled with crystallisation at lower pressures, thus preferentially crystallising clinopyroxene in preference to orthopyroxene.

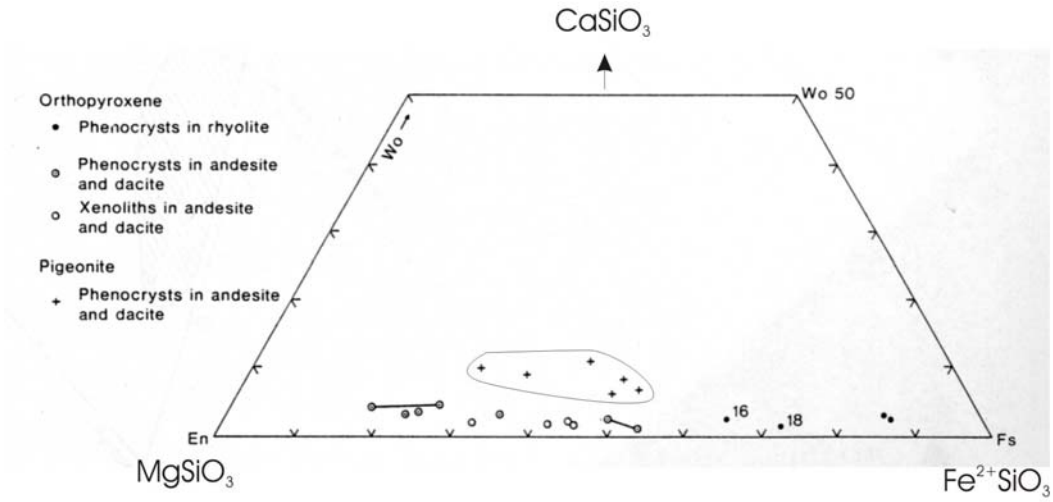

Fig. 7.1 Combined ortho- and clino-pyroxene ternary diagram illustrating the composition of orthopyroxene and pigeonite crystals (outlined) in andesite and dacite. Diagram adapted from Barley (1987)

Subsequent rapid eruption and chilling of the lavas prevented the pigeonite overgrowths from reverting to orthopyroxene by slow cooling.

The high pressure phenocryst assemblage suggests that contamination took place at depth. Petrographic examination of xenoliths in the lavas of the MSVG by Barley (1987) indicated a granulite facies mineral assemblage in the xenoliths which is consistent with their incorporation near the base of the crust at high pressures. Xenoliths are not an important constituent of the basaltic-andesites, when compared with the andesites and dacites of the MSVG.

7.1.2 Andesites

The andesites contain the same phenocryst assemblage as the basaltic-andesite with plagioclase-orthopyroxene-ilmenite, although the phenocrysts are appreciably smaller (<2mm) than those of the basaltic-andesites. Orthopyroxene phenocrysts are commonly subhedral-anhedral and rimmed by small pigeonite crystals, orthopyroxene is also seen to be completely pseudomorphed by pigeonite in some samples. Petrographic examination suggests that the orthopyroxene crystals (and plagioclase crystals to a lesser extent) were resorped prior to the crystallisation of the pigeonite. The observed petrographic relationship between orthopyroxene and pigeonite, where pigeonite is clearly seen to form reactionary overgrowths surrounding orthopyroxene appears to be contradictory to the typical scenario, in which pigeonite inverts to orthopyroxene at low pressure [Hess, 1941 #215;Deer, 1978 #212;Brown, 1972 #150]. Pigeonite rims around orthopyroxene are not common but examples have been reported from the Taupo Volcanic Zone [Froude, 1985 #213]; Soufrière volcano, St. Vincent [Lewis, 1967 #147]; Weiselberg, Germany [Nakumara, 1970 #214]. The replacement of orthopyroxene during later stages of crystallisation is due to the reaction hypersthene + liquid ↔ pigeonite [Nakumara, 1970 #148]. Pigeonite replaces orthopyroxene as the low Ca phase as the Fe/Mg ratio increases due to fractionation. The transition to clinopyroxene and continued absence of olivine is due to low H_2O contents and a reduction in P-T conditions.

The abundance of clinopyroxene (pigeonite) in the groundmass and as overgrowths and pseudomorphs of orthopyroxene, coupled with the change in plagioclase composition (An_{55-40}) indicates that the andesite phenocryst assemblage and subsequent crystallisation took place from increasingly evolved magmas. The xenolith content of the andesites is substantially

higher than that observed in the basaltic-andesites and indicates increased levels of contamination and interaction with continental crust.

7.1.3 Dacites

The dacites of the MSVG contain the phenocryst assemblage: plagioclase-orthopyroxene-magnetite. The phenocryst phases are similar in size (<2.5mm) to the andesite phenocrysts. Pigeonite forms overgrowths and pseudomorphs of orthopyroxene and the prior resorption of orthopyroxene indicates the pigeonite crystallisation occurred at a later stage; pigeonite is also found in the groundmass with magnetite and plagioclase. Plagioclase crystals show normal zoning and are generally An_{25-45}, which is more albite rich than the andesite and basaltic-andesite. Xenoliths are commonly observed in the dacites and are more abundant than in the andesites. Xenoliths occasionally contain garnet crystals and xenocrysts of garnet can be occasionally observed.

7.1.4 Rhyolites

Petrographic evidence suggests that the MSVG phenocryst assemblage quartz-garnet-plagioclase-(±orthopyroxene)-(±biotite) formed in equilibrium (see Appendix 2 for summary petrographic descriptions). This is due to the commonly observed intergrowths between the above phenocryst phases.

Garnet is a relatively uncommon phenocryst phase in igneous rocks but has been described from I, M and S type rhyolites from western Europe, Japan, New Zealand, Australia, Caribbean and Antarctica e.g. [Clemens, 1984 #269;Harangi, 1999 #267;Harangi, 2001 #217;Reymer, 1983 #266;Thirlwall, 1983 #268;Kano, 1976 #373;Barley, 1987 #8;Davidson, 1989 #374;Hamer, 1982 #375]. The presence of garnet is usually ascribed to the interaction of crustal material with the parental magma resulting in Al-enriched melts. The P-T conditions and relative proportions of Fe, Mg, Mn and Ca determine the garnet compositions.

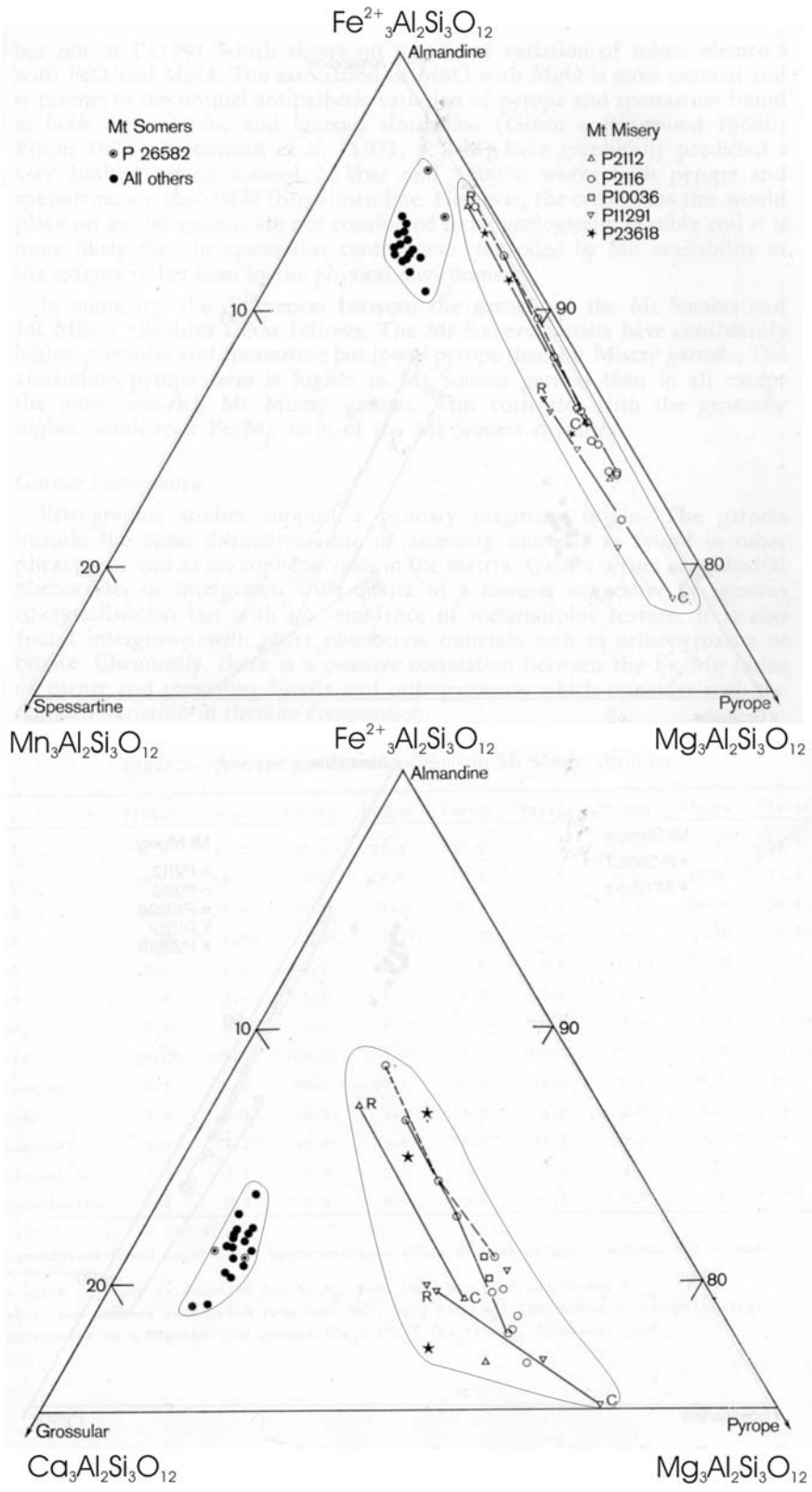

Fig. 7.2 Analyses of magmatic garnets from Mt. Somers and Malvern Hills – diagrams adapted from Wood (1974). C=core, R=rim.

The majority of the garnets in the Mount Somers and Malvern Hills areas appear to be primary magmatic phenocrysts due to the absence of typical metamorphic textures; the

inclusion of accessory minerals such as zircon, apatite and ilmenite; the intergrowth with other phenocryst phases; and a correlation between the Fe/Mg ratios of garnet and the coexisting ferro-magnesian phases biotite and orthopyroxene as noted by Wood (1974). Wood (1974) also noted the presence of xenocrystic garnets which are associated with metamorphosed xenoliths. Such xenocrysts commonly have thick reaction rims and are clearly distinct from the commonly subhedral magmatic garnets which generally have either absent, or very thin reaction rims. The xenocryst garnets are easily identified in thin section and are rare compared with the magmatic garnets. The xenocryst garnets were not analysed for δO^{18} during the course of this research.

Extensive micro-probe analyses of the co-existing phenocryst phases were undertaken by Wood (1974) and later by Barley (1987). The garnets of Mt. Somers are unzoned and are compositionally predominantly almandine (approx. 76-80%) with lesser pyrope, spessartine and grossular [Wood, 1974 #125]. The garnets from Mt. Somers ('Type A' garnets of Barley, 1987) are compositionally distinct from those garnets analysed from the Malvern Hills (Mt. Misery of Wood, 1974). The Malvern Hills' garnets are termed 'Type B' by Barley, 1987. The Malvern Hills garnets generally show strong zonation from pyrope rich cores to rims richer in almandine (fig.7.2), i.e. increasing Fe/Mg ratio. Wood considered both the cores and rims to be of magmatic origin, however Barley proposed that the cores may also be xenocrystic. In thin section, the garnets of the Malvern Hills contain inclusions of apatite, zircon and ilmenite, therefore similar to the inclusions of the Mt. Somers garnets, and the compositional zonation is gradational (as depicted by fig.7.2). Therefore it is considered unlikely that the cores of the Malvern Hills garnets (Type B) are xenocrystic, but rather that the changing compositional variation shown by the Malvern Hills garnets is due to changing magma composition and P-T conditions. Wood (1974) concluded that the lack of zoning in the Mt. Somers garnets was due to their formation under stable physical conditions, whereas the substitution of almandine for pyrope in the Malvern Hills garnets indicates rapidly falling temperatures.

Recent work by Harangi *et al* (2001) has suggested a link between the CaO and oxygen isotope composition of igneous garnets with the mode of formation of the host magmas. Based upon the northern Pannonian Basin garnet-bearing volcanics and literature surveys, Harangi *et al* (2001) concluded that S-type volcanic rocks tend to host CaO poor garnets (CaO <4 wt%), whereas I or M-type volcanic rocks contain garnets with higher CaO concentrations

(CaO >4wt%) [Harangi, 2001 #217]. The $\delta^{18}O$ values for magmatic garnets from the Pannonian Basin ranged from 6.1-7.3‰ whereas composite garnets (with xenocryst cores) had $\delta^{18}O$ values in excess of 8‰.

The CaO contents of MSVG garnets are listed in table 7.1, together with the one ^{18}O value determined during the course of this research. Samples from the Rangitata Gorge and Banks Peninsula field areas were not analysed during the course of this study due to the heavily altered nature of the rhyolites

Sample origin	Rock type	Author	CaO content	$\delta^{18}O$ (‰)
Mt. Somers	Rhyolite	Wood (1974)	5.8	
"	"	"	5.4	
"	"	"	5.5	
"	"	"	5.7	
"	"	"	5.1	
"	"	"	5.1	
"	"	"	5.1	
"	"	"	5.2	
"	"	"	5.1	
Malvern Hills	Rhyolite	Wood (1974)	3.3-2.9	
"	"	"	2.8-2.5	
"	"	"	3.3-2.6	
"	"	"	2.1-3.3	
"	"	"	3.8-2.8	
Mt. Somers	Rhyolite	Barley (1987)	5.02	
"	"	"	4.98	
Malvern Hills	Rhyolite	Barley (1987)	2.46	
"	"	"	1.91	
Malvern Hills	Rhyolite	This project		8.7-8.9

Table 7.1 CaO content in garnets analysed by Wood (1974) and Barley (1987) from the Malvern Hills and Mt. Somers.

The rhyolites of the Mt. Somers area were ascribed to deep level crustal melting by both Wood (1974) and Barley (1987). Two of the Malvern Hills analyses reported by Barley (1987) were used in support of the low CaO – 'S' type petrogenetic relationship by Harangi *et al* (2001), however the data published by both Wood (1974) and Barley (1987) for the Mt. Somers garnets do not support such an 'S' type relationship with CaO (based on the criteria of Harangi *et al*, 2001). The classification of Harangi (2001) based upon CaO concentration suggests that the Malvern Hills magmas were subjected to greater degrees of mixing with a crustal end-member than the Mt. Somers rhyolites. This is in direct contrast to the radiogenic isotope data produced during the course of this research (section 7.7), which indicates that the Malvern Hills magmas were contaminated to lesser degrees than the rest of the MSVG.

The grossular (and therefore CaO) content of magmas is influenced not only by magma composition but also heavily influenced by the pressure of crystallisation. High grossular contents of primary igneous garnets have been ascribed to extremely high pressure conditions which commonly exceed 10 kbar [Gilbert, 1989 #273;Green, 1968 #272], which has also been used as an indication of a mantle origin e.g. [Day, 1992 #271]. However, high grossular contents (7-17.5%) of the Pyrenees have been attributed to high pressure melting of a sedimentary source at the base of the continental crust [Gilbert, 1989 #273]. Therefore the grossular content has a useful application in terms of pressure estimates but petrogenetic implications are dependent upon reasonable estimates of the crustal thickness. The MSVG garnets have relatively high grossular contents for igneous garnets (Mt. Somers = 13.8-15.9 and Malvern Hills = 6.3-10.4, data from Wood, 1974) which correspond to the high pressure environments implied in the geobarometry [Wood, 1974 #125;Barley, 1987 #8]. The lower grossular content of the Malvern Hills' garnets may be due to the crystallisation of the phenocryst assemblage at slightly lower pressures or at higher H_2O contents [Green, 1992 #274] since the bulk CaO content of the rocks are generally the same as those for the rest of the MSVG. It is therefore considered that the CaO content alone is an insufficient means by which to differentiate between S, I or M type petrogeneses.

The Malvern Hills' garnets are variably zoned. The garnet compositions decrease in CaO, MgO, and Al_2O_3, and increase in FeO and MnO from core to rim [Wood, 1974 #125]. The decrease in CaO and MgO is expected at increasing degrees of differentiation and has been described in garnets by Green & Ringwood (1968) and du Bray (1988). Increasing FeO contents of garnets have been observed as melts become more silicic [Clemens, 1984 #269], the FeO content in the crystallising garnet will increase as the MgO is preferentially taken up by orthopyroxene. The decreasing MnO content of the Malvern Hills requires more careful consideration as Mn contents are generally observed to increase towards the rims of garnet phenocrysts [du Brey, 1988 #275;Green, 1968 #272;Miller, 1981 #276]. This inverse zonation may be due to the crystallisation of magnetite which is dominant over garnet as the Mn-phase.

Wood (1974) and Barley (1987) both calculated P-T conditions for the formation of the MSVG rhyolites, based upon micro-probe data for the phenocryst phases. As shown in table 7.2, Wood ascribed the variation in phenocryst assemblage (presence or absence of biotite and

orthopyroxene) to relatively subtle adjustments in temperature, water vapour pressure and water content.

	Wood (1974)	Barley (1987)	This project
Total Pressure	10-15 kbar	7 kbar	
Temperature (ºC)	Garnet rhy 1000-1050 Garnet-biotite rhy 900-950 Gnt-opx (±biot) 900-1000	> 850	764 – based on oxygen isotope data
Water Content	Garnet rhy 2% Garnet-biotite rhy 4% Gnt-opx-(±biot) >5%	<3.5 %	
Water vapour pressure	Garnet rhy 500 bar Garnet-biotite rhy 1 Kbar Gnt-opx-(±biot) 1.5-2.5 Kbar		

Table 7.2 Geothermobarometric constraints as determined by Wood (1974) and Barley (1987). Also included is the temperature calculated from oxygen isotope data in this project.

The P-T conditions of Barley (1987) are in general agreement with those of Wood (1974), however a lower pressure of crystallisation is inferred for the phenocryst assemblage. The discrepancy between the temperature calculation of Barley (1987) and those of Wood (1974) is due to the application of more recent experimental data [Clemens, 1981 #270] by Barley (1987) concerning the temperature stability field of orthopyroxene. More recent geothermobarometric investigations of garnet-orthopyroxene-plagioclase-quartz assemblages from granulites implies temperature ranges of 690-860ºC and pressure ranges of 5-10 kbar [Lal, 1993 #277]; which supports the findings of Barley (1987).

The temperature dependence of stable isotope fractionation allows the application of stable isotopes to geothermometric calculations. Stable isotopes are largely unaffected by pressure changes (with the exception of hydrogen isotopes) and therefore the temperature calculations are applicable irrespective of geobarometric constraints. The temperature of 764ºC calculated in this study is based upon the oxygen isotope analyses of garnet and quartz mineral separates in sample MH-12. The geothermometry calculations are given in Appendix 7. The disparity between the ^{18}O geothermometric results and the conventional geothermometric results reported by Barley (1987) may be due to the zonation observed in the quartz crystals (fig.7.34). The cores of the crystals may have crystallised under different temperature

conditions to the rim and therefore the 'averaged' ^{18}O values reflect the average magmatic values over the course of quartz crystallisation.

7.2 Major Element Geochemistry

The MSVG is a suite of sub-alkaline, medium to high K volcanic rocks which vary in composition from basaltic andesite (54.5% - MH-11) to high silica (78.13% - MH-66) rhyolite and ignimbrite (fig 7.3). The main exposures of MSVG all display similar geochemical characteristics.

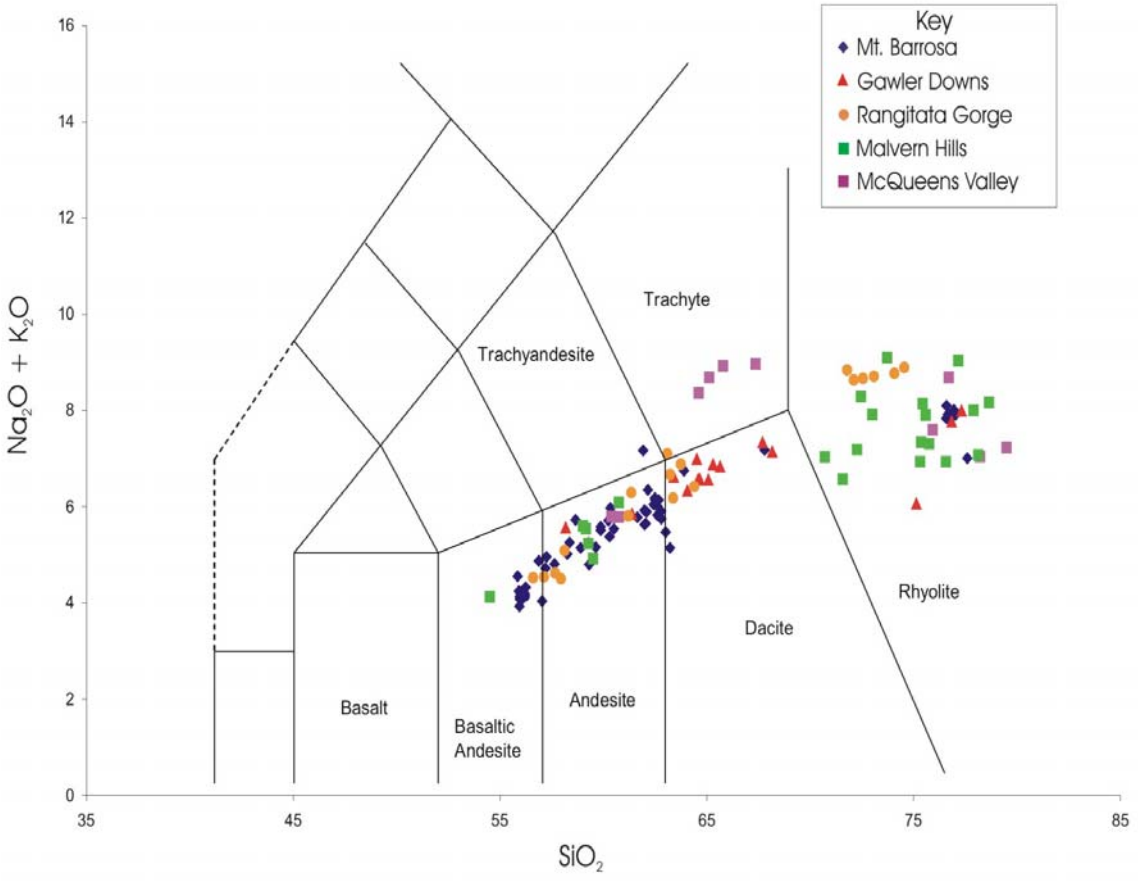

Fig.7.3 Total Alkali-Silica (TAS) diagram for the MSVG [Le Maitre, 1989 #63].

7.2.1 Mt. Barrosa

Mount Barrosa represents the most voluminous sequence of andesitic volcanism in the MSVG. The mountain and surrounding area were thoroughly mapped and systematically sampled to provide a comprehensive geochemical stratigraphy. The volcanic sequence is subdivided into units based on lava morphology (Chapter 4) and geochemistry. B-I being the lowermost and therefore earliest part of the exposed sequence and B-VI being the uppermost and therefore youngest part of the sequence. The sequence described is complete from the unconformable boundary with the Torlesse basement through to the onset of rhyolite domes, flows and ignimbrites.

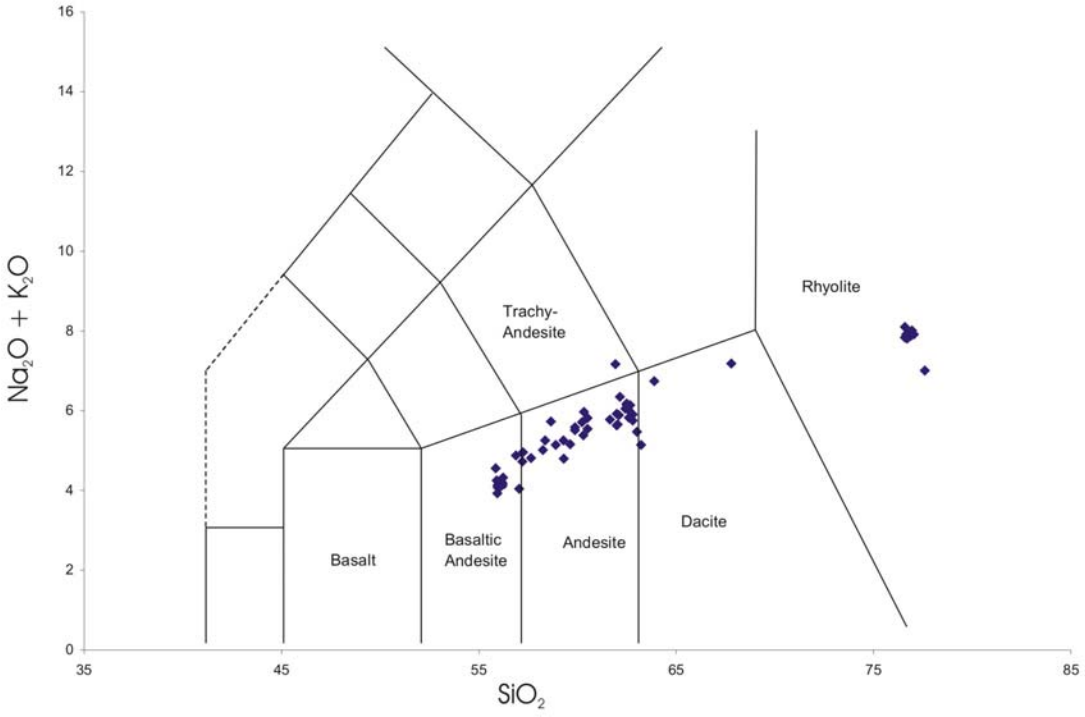

Fig.7.4 TAS diagram for Mt. Barrosa

As described in Chapter 4, the exposure on Mt. Barrosa was such that a volcanic stratigraphy could be established. Unit B-I is the oldest series of flows exposed on Mt. Barrosa and is overlain by both B-II and B-III. To the east of Mt. Barrosa, unit B-II is absent and B-III immediately overlies B-I. The relationship between B-I and B-II is unclear. B-II lavas are clearly younger than most of the B-I lavas, however because the relationship is uncertain, two geochemical stratigraphic cross-sections can be drawn, sequences A and B. The sample localities and routes are displayed in Fig. 7.5. Sequence A samples units B-I, B-III and B-IV. Sequence B incorporates all the units, however only a small portion of B-I.

INSERT SEQUENCE SAMPLING ROUTES HERE – FIG. 7.5

Fig 7.6 illustrates the up-sequence variation in SiO_2 contents. The SiO_2 concentration of unit B-I generally decreases up-sequence. The andesites of B-I give way to the basaltic-andesite flows of B-III in sequence A as the SiO_2 content decreases. In sequence B, the SiO_2 content is generally fairly constant up-sequence, but the transition to the overlying B-III is sharper than that observed in sequence A. In both sequences there is a sharp compositional change from B-III flows (basaltic andesites) to the dacites of B-IV.

Although not shown on fig.7.6, the largest compositional gap occurs between the B-IV dacites and the onset of rhyolitic volcanism and the emplacement of Group V pitchstones. The Group V pitchstones rest unconformably on units B-II and B-III lavas to the east of the area, which suggests that significant erosion of the volcanic pile took place before the eruption of the Group V pitchstones. This implies an extended period of quiescence, during which extreme fractionation and/or contamination could have occurred.

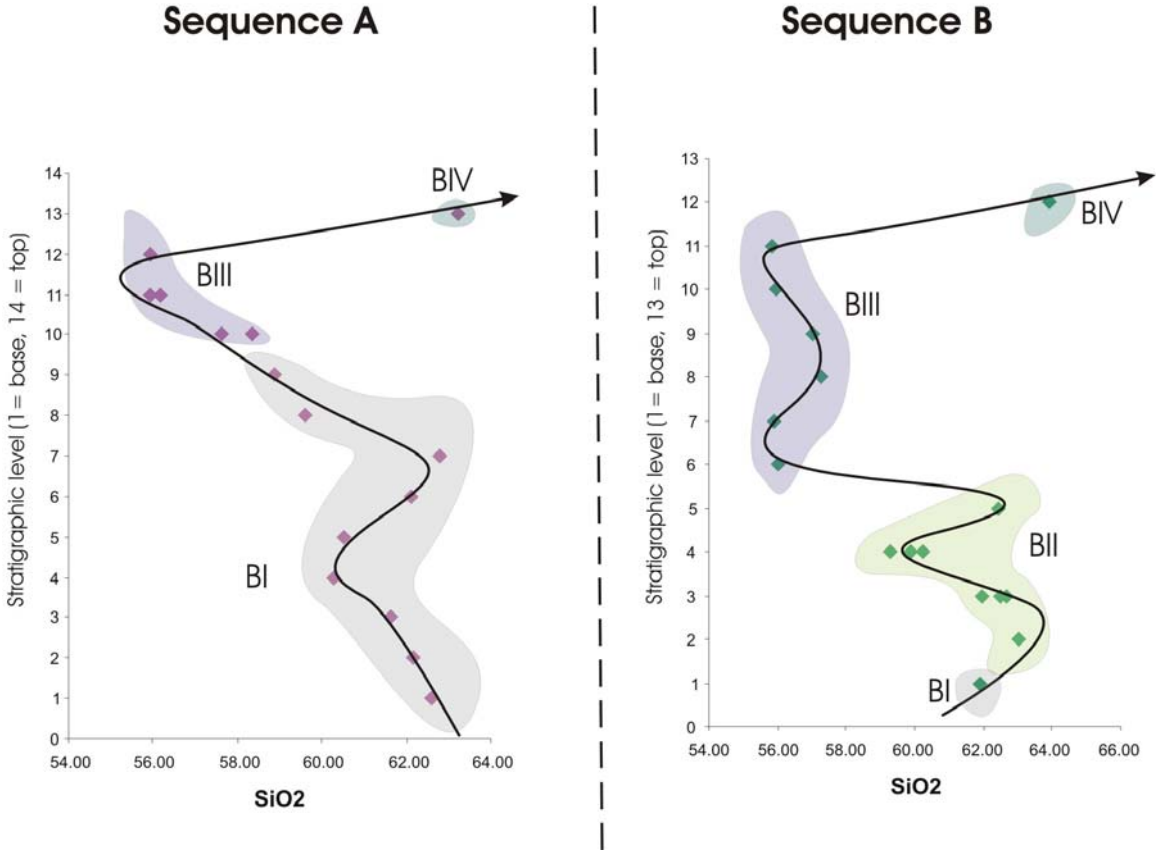

Fig.7.6 Diagram showing the up-sequence variation of SiO_2 for sequences A and B

The sequence of major element versus stratigraphic level plots on figs 7.7 and 7.8 indicates the corresponding evolutionary trends of MgO, Cr, Sr and Rb up-sequence.

Fig 7.7 Variations of MgO and Cr with stratigraphic level

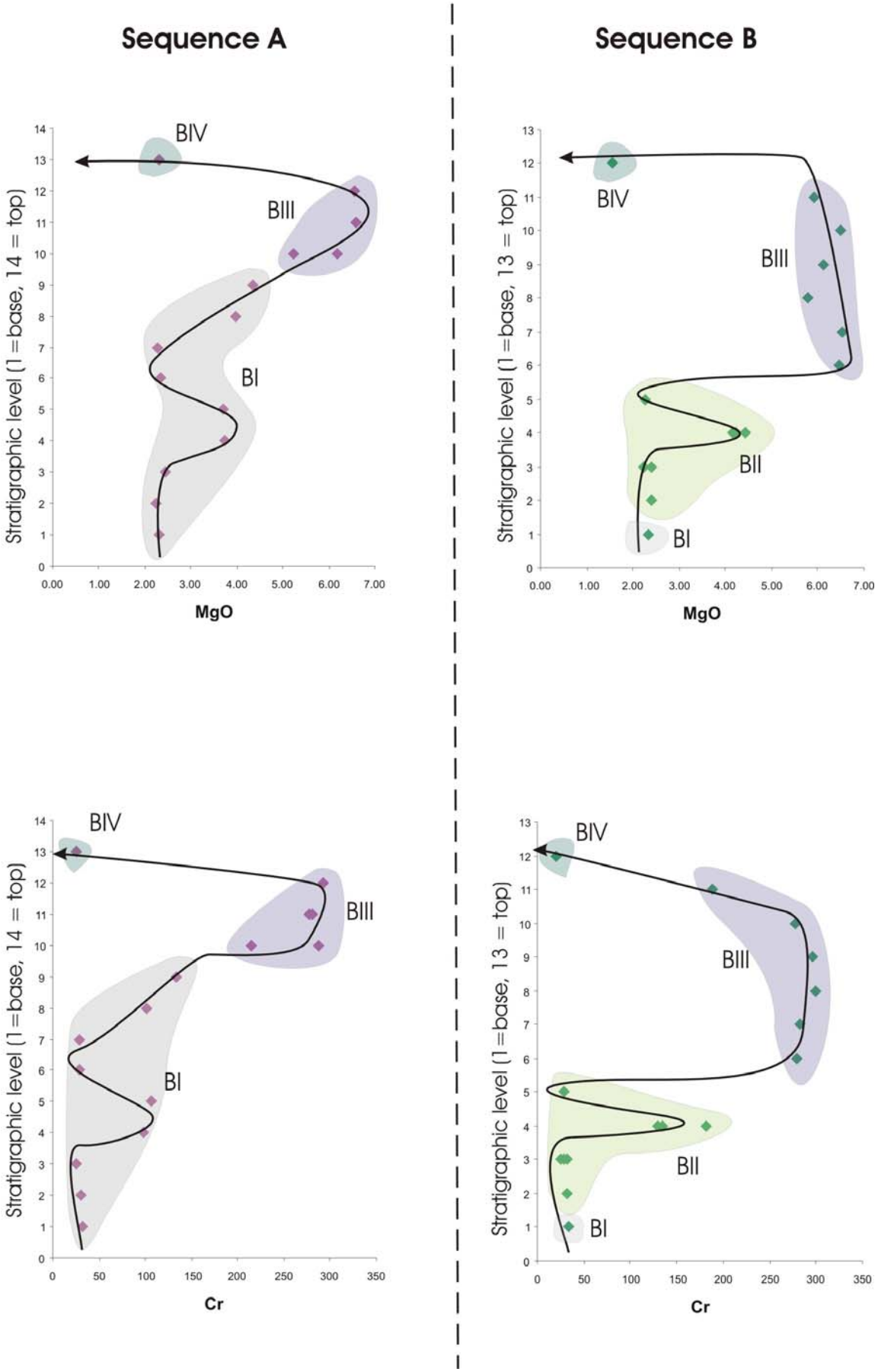

Fig 7.8 Variations of Sr and Rb with stratigraphic level

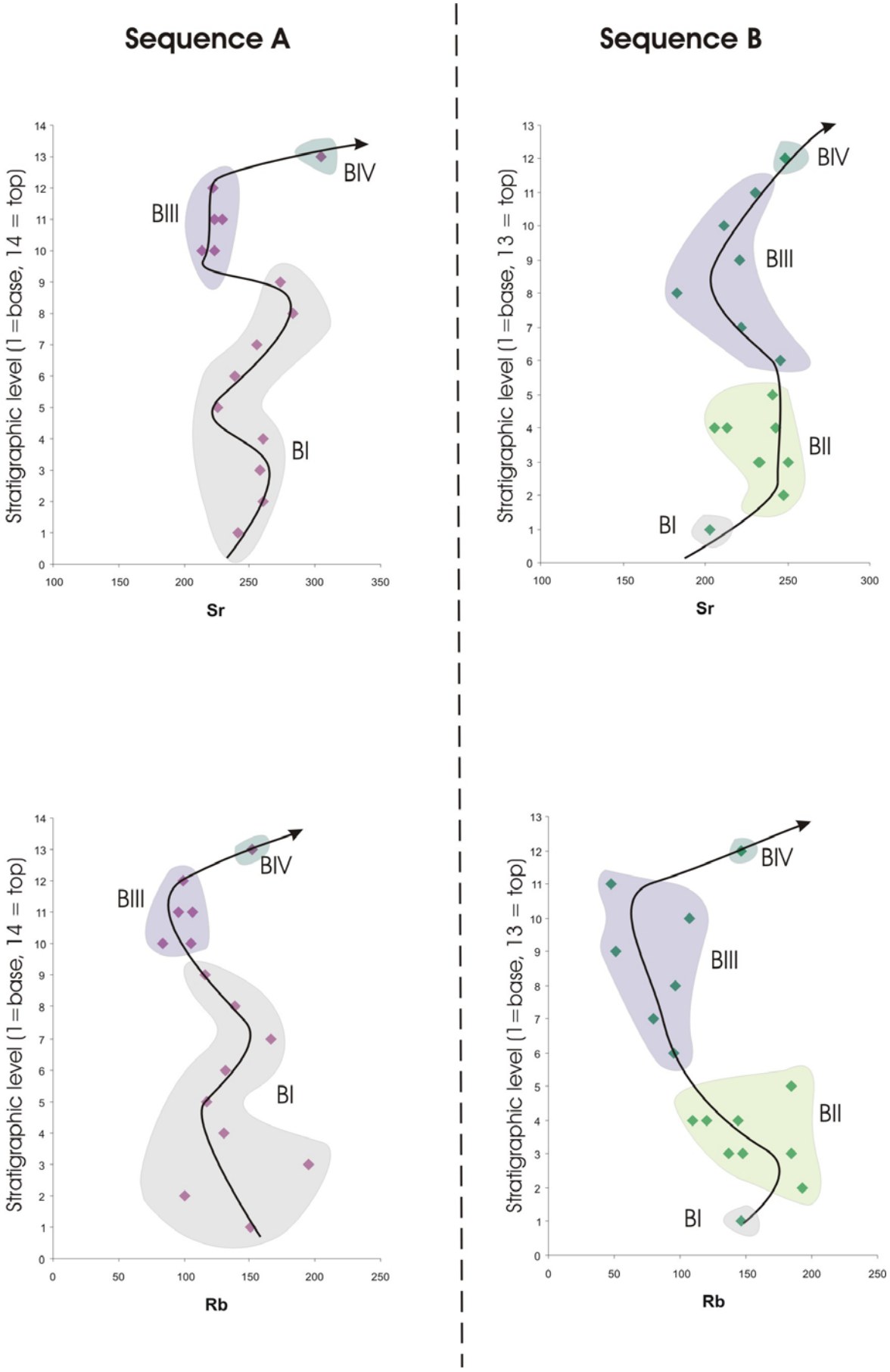

The general evolutionary trends of the andesites to basaltic-andesites would support a common origin hypothesis and gradual tapping of a single zoned magma chamber. However minor compositional shifts within the andesites (B-I and B-II) and basaltic andesites (B-III) (figs. 7.7 and 7.8), suggest that the evolution may be more complex, and may involve periodic re-charge and/or varying degrees of contamination between eruptive events. The abrupt change to dacitic compositions indicates a change in magmatic regime which can either be explained by increased levels of contamination and/or fractionation; or the magmas may have been sourced from a different reservoir.

7.2.2 Gawler Downs

The Gawler Downs display a range of lava chemistry similar to other outcrops of MSVG (fig.7.9). The dacites display less scatter on the TAS diagram than the dacites of Mt. Barrosa. However, no basaltic andesites are found in the Gawler Downs.

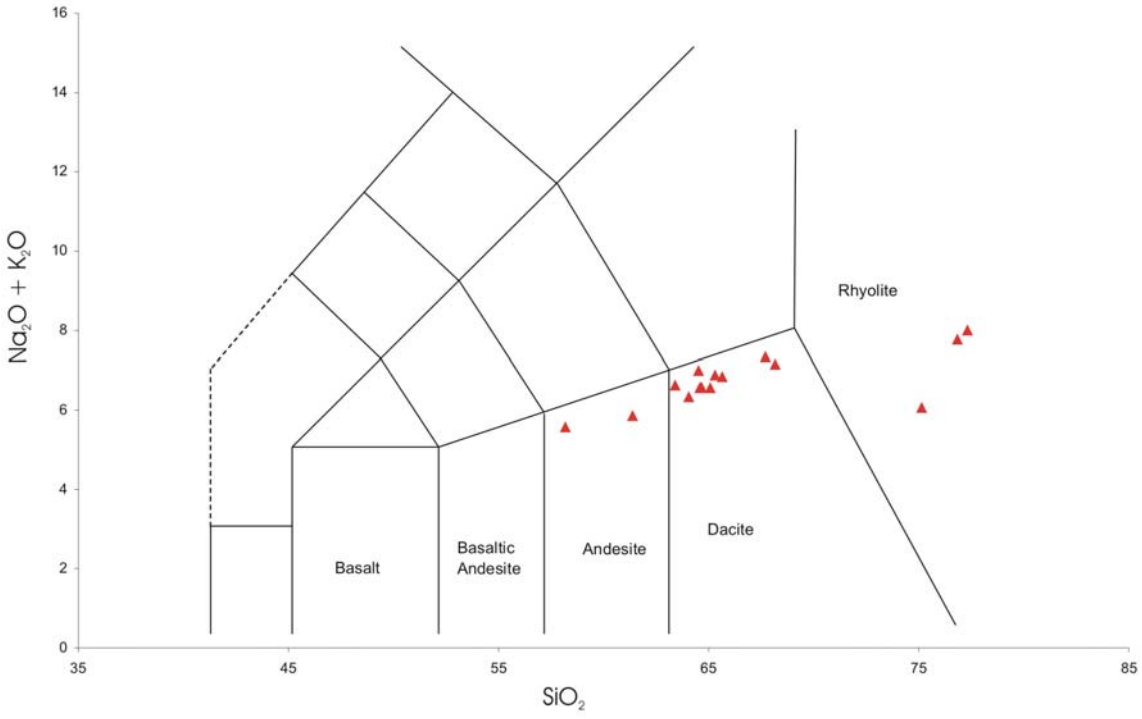

Fig.7.9 TAS diagram showing the compositional variation within the Gawler Downs area.

The presence of abundant crustal xenoliths in the dacites of the Gawler Downs suggests that crustal assimilation was a major process operating to modify the compositions of the magmas, however these xenoliths were too small to be extracted for separate analysis.

7.2.3 Rangitata Gorge

The Rangitata Gorge rocks display the same broad compositional spectrum as seen in the Mt. Barrosa and Gawler Downs areas, from basaltic andesite through to rhyolite (Fig 7.10). The exposure in the Rangitata Gorge area was not sufficient to enable systematic up-sequence sampling.

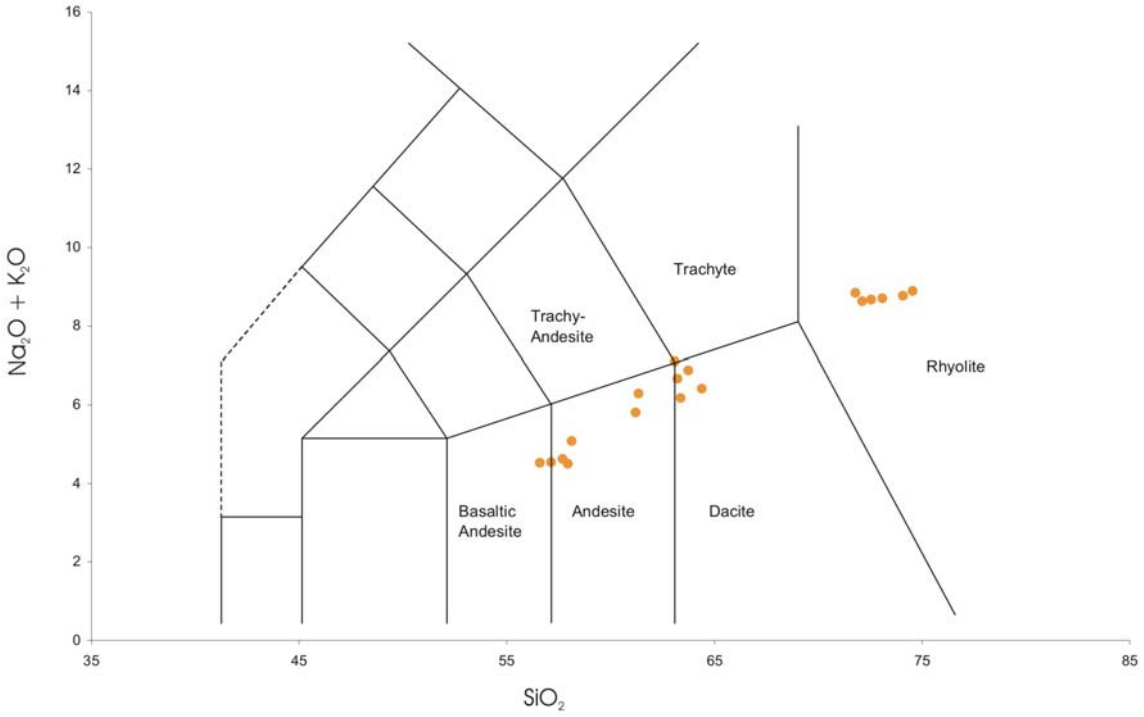

Fig.7.10 TAS diagram illustrating the compositional variation of the lavas in the Rangitata Gorge field area.

The stratigraphic relationship between the rhyolite and andesite in the Rangitata Gorge is uncertain (Chapter 4). The absence of good stratigraphic controls precludes the plotting of stratigraphic level versus geochemical variation.

7.2.4 Malvern Hills

The Malvern Hills comprise a succession of volcanic rocks which differ in appearance and stratigraphic relationships from the main mass of MSVG at Mt. Barrosa, Gawler Downs and Rangitata Gorge. For a description of the units, refer to Chapter 4. However, the major element geochemistry and array of compositions on the TAS diagram below (fig.7.11) are similar to those forming the rest of the MSVG.

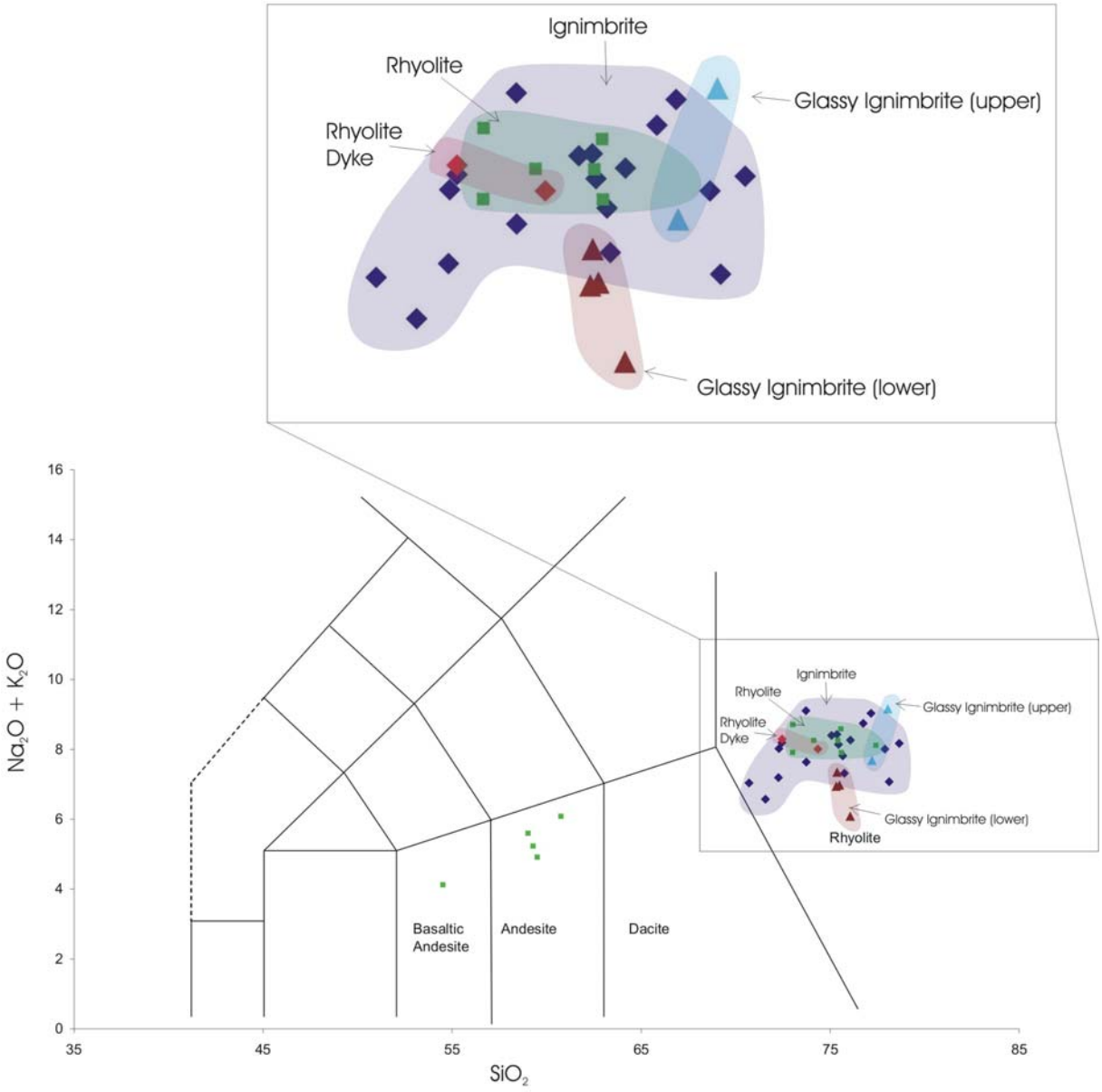

Fig.7.11 TAS diagram showing the compositional variation within the Malvern Hills field area.

The cluster of data points in the rhyolite field are subdivided into the units described in Chapter 4. It is clear from fig 7.11 that there is substantial overlap between fields. The rhyolitic units display a considerable range in total alkali and silica values. This is probably a function of variable phenocryst concentrations and degree of alteration. Only the Glassy Ignimbrite (lower) can be considered to be fresh. Some of the ignimbrites show evidence of considerable alteration.

The main difference between the Malvern Hills and the rest of the MSVG is that the andesites are the youngest members of the sequence and there is no overlying rhyolite *c.f.* all other areas of the MSVG. There is a large compositional gap between the older rhyolites and ignimbrites, and the younger andesites and basaltic andesite, and a notable absence of dacite.

7.2.5 McQueens Valley

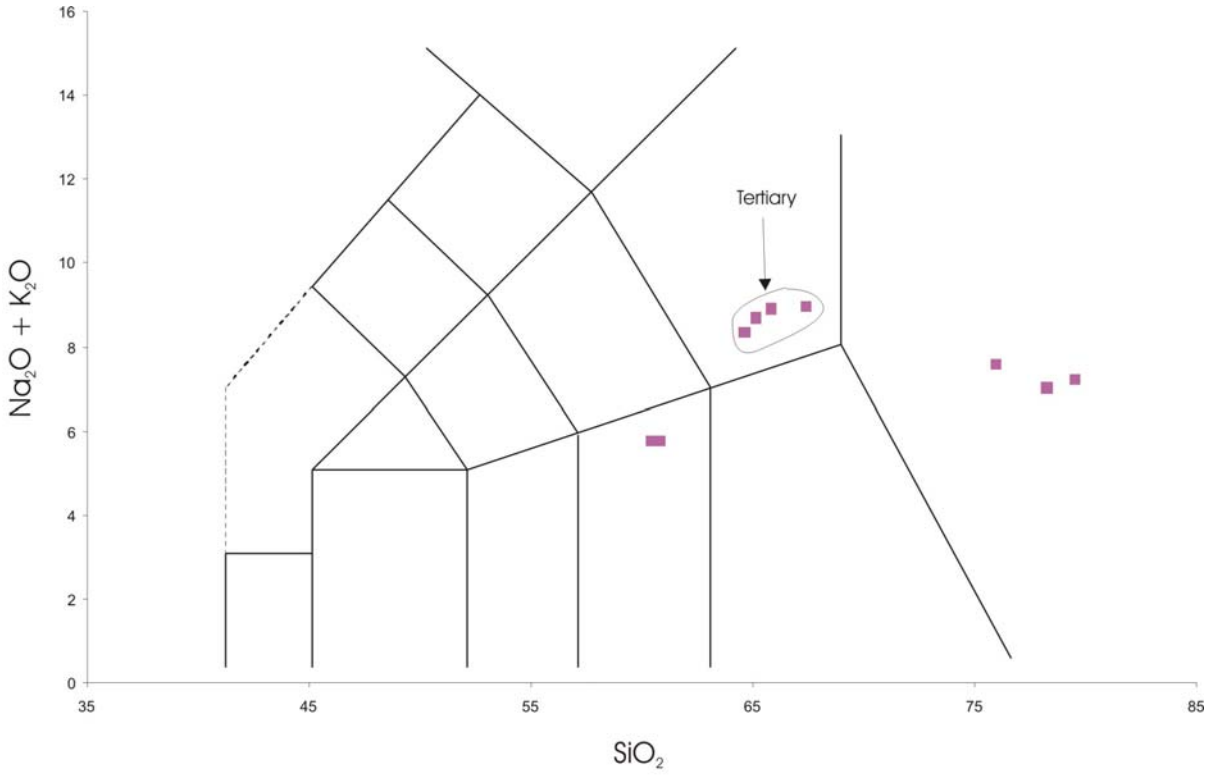

Fig.7.12 TAS diagram showing the chemical variation in samples from McQueens Valley

McQueens Valley shows a generally bimodal distribution of andesite and rhyolite with a notable absence of dacite. The area in which the trachytes outcrop is mapped as Cretaceous in age on the geological map of Sewell *et al* (1988), however the trachytes are of Tertiary age

(Chapter 6) and are mapped accordingly in this study (Chapter 4). The Tertiary volcanics have distinctively high Nb contents (fig. 7.13).

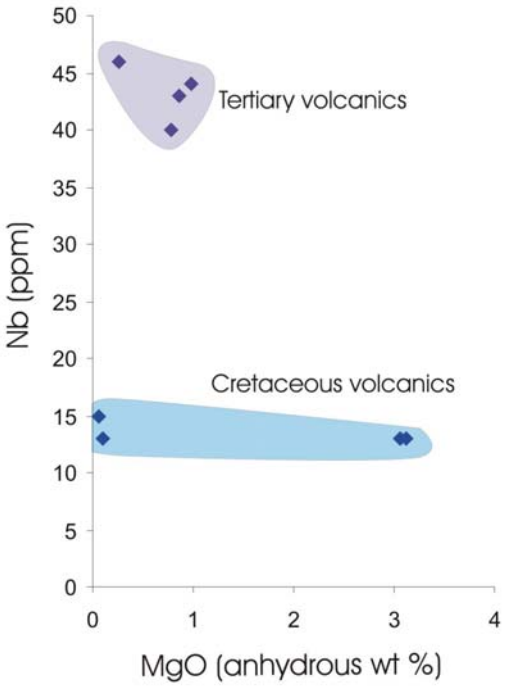

Fig. 7.13 MgO versus Nb for the McQueens Valley

7.2.6 Major Element variation of the MSVG

Trends on Harker diagrams can be used to establish a possible common evolutionary history and can elucidate processes operating during the development of an igneous suite. For instance, trends can be used to model fractional crystallisation processes where microprobe analyses of phenocryst phases are needed to model the effect of 'removal' of elements from the system as crystal phases. However, partial melting can resemble the role of fractional crystallisation and therefore genetic implications are difficult to establish. Crustal contamination or 'assimilation', and magma mixing can also govern trends on Harker Diagrams.

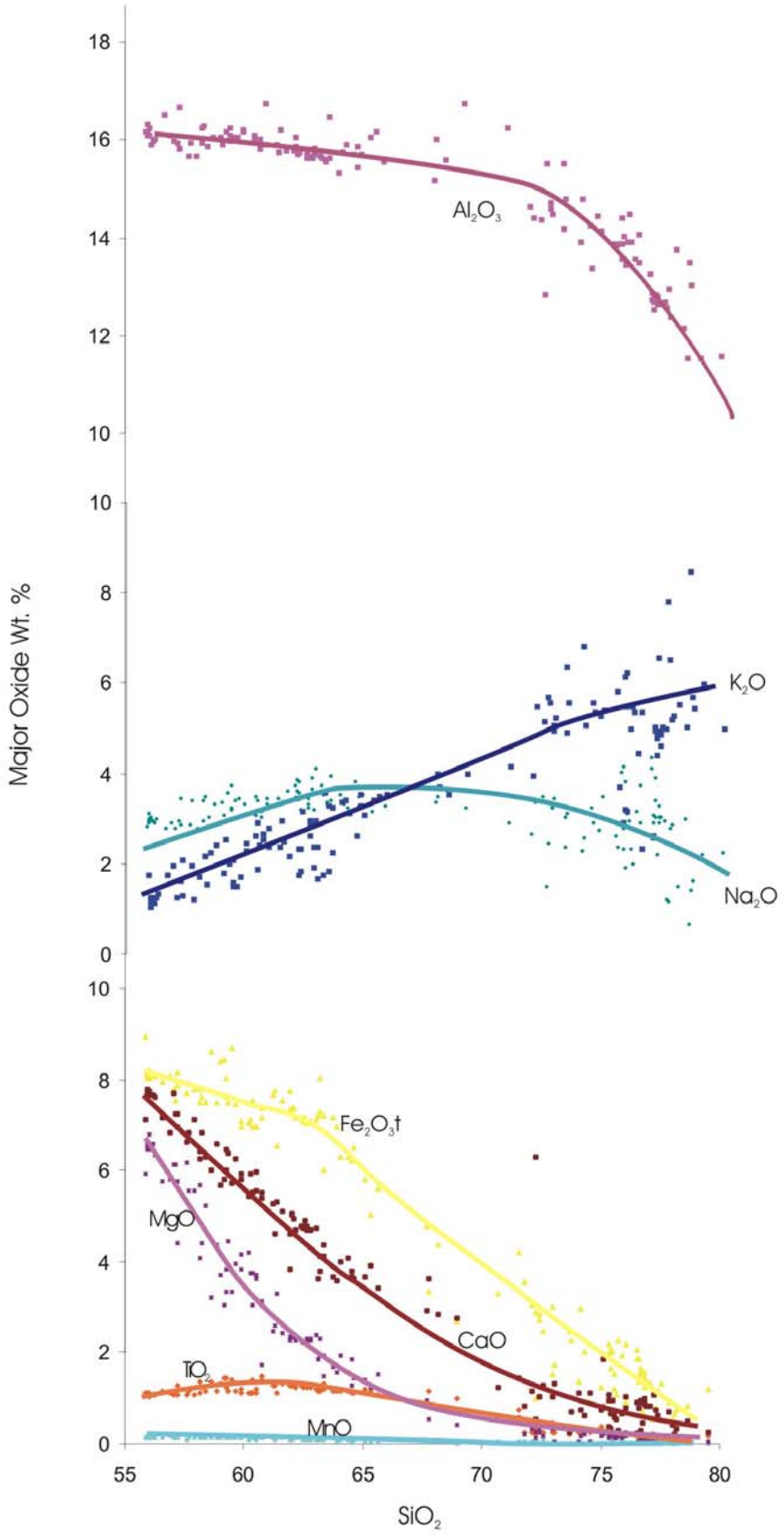

Fig.7.14 Major Element versus SiO_2 diagram for the MSVG (Harker Diagram)

The major oxides versus SiO_2 plots for the MSVG display considerable scatter; this is most likely to be the result of variable phenocryst contents, crustal xenolith contents and degree of alteration. However, despite the scatter, trends can be clearly observed which are consistent with the removal of fractionating phenocryst phases.

FeO, MgO and CaO display strong negative correlations with SiO_2, mainly as a result of orthopyroxene, pigeonite and Ca-rich plagioclase fractionation. TiO_2 and MnO show slight negative correlation with SiO_2. K_2O displays a positive correlation with SiO_2, due to its general incompatibility until K_2O-rich phenocryst phases start to crystallise such as K feldspars and biotite in the rhyolites. Na_2O increases at first but then decreases due to the incoming Na-rich phases such as plagioclase feldspar. Al_2O_3 shows an inflection at about 70% SiO_2 from where it starts to decrease markedly with increasing SiO_2 concentration owing to feldspar fractionation.

Harker diagrams can typically be used to illustrate the onset of different fractionating mineral phases, however in the diagram of the MSVG the earliest phenocryst phases may not be seen because of the lack of basaltic samples in the MSVG.

Although clear and consistent trends are present on the Harker diagrams, their interpretation is not a simple matter. The trends could be produced by fractional crystallisation, partial melting or mixing between separate magma chambers.

7.3 Trace Element Geochemistry

All members of the MSVG will be considered together in this section due to the compositional similarity (previous section) and their contemporaneity (ref. Chapter 6). Each compositional group will be considered in turn before a discussion of the overall trends.

7.3.1 Basaltic Andesites

The trace element signatures of the basaltic andesites are represented in Fig. 7.15. The data are normalised to N-MORB values [Hofmann, 1988 #179]. Also plotted on the graph is the average of the analysed samples of Rakaia subterrane, through which the MSVG were erupted.

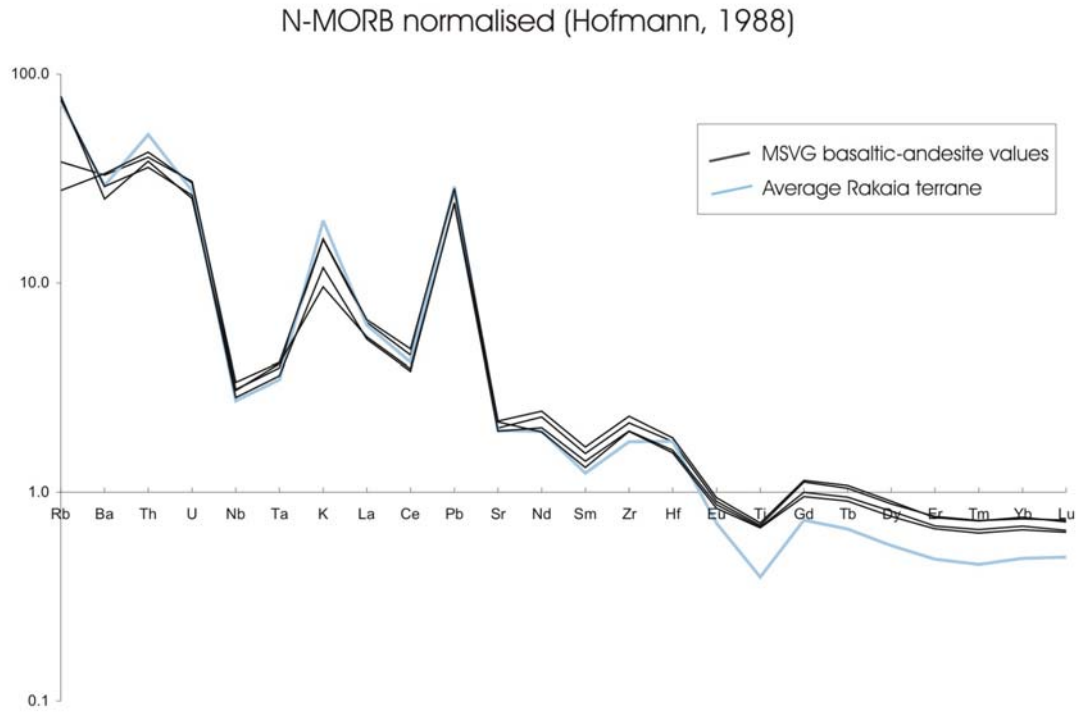

Fig.7.15 Spider diagram displaying the typical 'spiky' subduction signature of the basaltic-andesites of the MSVG. Data is normalised to N-MORB values [Hofmann, 1988 #179].

The spider diagram displays an irregular 'spiky' pattern. Such a pattern with Nb and Ta troughs coupled with a Pb peak is typical of magmas derived from subduction processes. The production of calc-alkaline magmas along destructive plate margins generally involves partial melting in the source region as a result of the dehydration of a subducting slab. The 'source region' may be N-MORB of the subducted slab, enriched asthenospheric mantle wedge, or subcontinental lithosphere. The added complication associated with subduction along continental margins, is the extent of contamination by continental crust, either in the crust or in the source region by melting of subducting sediments.

Contamination can take place in the zone of partial melting as a result of input from subducted oceanic sediments, or at various levels in the continental crust. The dehydration of a downgoing slab releases volatiles into the overlying mantle wedge or sub-continental lithosphere, which stimulates partial melting by lowering the mineral solidi. The addition of volatiles sourced from the down-going slab result in melts preferentially enriched in the incompatible mobile elements, the large ion lithophile elements (LILE). The rare earth elements (REE) and high field strength elements (HFSE) are generally considered to be compatible and therefore immobile, however at high degrees of partial melting the REE are incompatible. The light REE (LREE) are generally more incompatible than the heavy REE (HREE) and therefore more sensitive to partial melting processes and may be concentrated into partial melts. The mobility of the LILE results in their addition, by metasomatism, to the mantle wedge and their incompatibility results in their enrichment in subsequent partial melts. HFSE are compatible and therefore are not concentrated into partial melts or transported from the slab by fluid phases. The REE are only concentrated into melts through high degrees of partial melting, LREE are generally enriched to higher degrees than HREE due to their lower compatibility. Subduction related calc-alkaline magmas are therefore characterised by very high LILE/HFSE, high LILE/REE ratios, and by moderately high LREE/HFSE ratios [Pearce, 1982 #183].

Such elevated ratios are present for the MSVG. The basaltic andesites are enriched in Rb, Ba, Th and U relative to Nb and Ta and the LREE. They also show a pronounced peak at Pb. The MSVG basaltic andesites show high LILE/HFSE and LREE/HFSE ratios (Ba_N/Nb_N = 8.2 - 10.6 and La_N/Nb_N = 1.8 and 2.1 (data normalised to N-MORB of Hofmann, 1988)).

The similarity of the trace-element signature of the basaltic-andesites to that of the Rakaia terrane is not only in the fluid-mobile LILE which include Rb, Ba, K and Sr, but also the HFSE Nb and Ta (fig. 7.15). The large positive Pb peak suggests the involvement of continental crust, although this input need not necessarily be large, just 2% of sediment input is likely to provide half the Pb in a MORB/mantle wedge – sediment mixture [Hawkesworth, 1982 #184].

Unfortunately, any interpretation based on chemical similarity between the Rakaia terrane and the MSVG must be treated with caution because the Rakaia terrane is itself derived from a continental magmatic arc of granodioritic bulk composition [Roser, 1999 #185]. Sediments

derived from a calc-alkaline, continental arc would reflect the chemistry of the original arc. The problem is discussed further with the aid of isotopic data in section 7.7. The similarity between the sediments of the Rakaia sub-terrane and those subducting at present-day magmatic arcs is shown on fig.7.16.

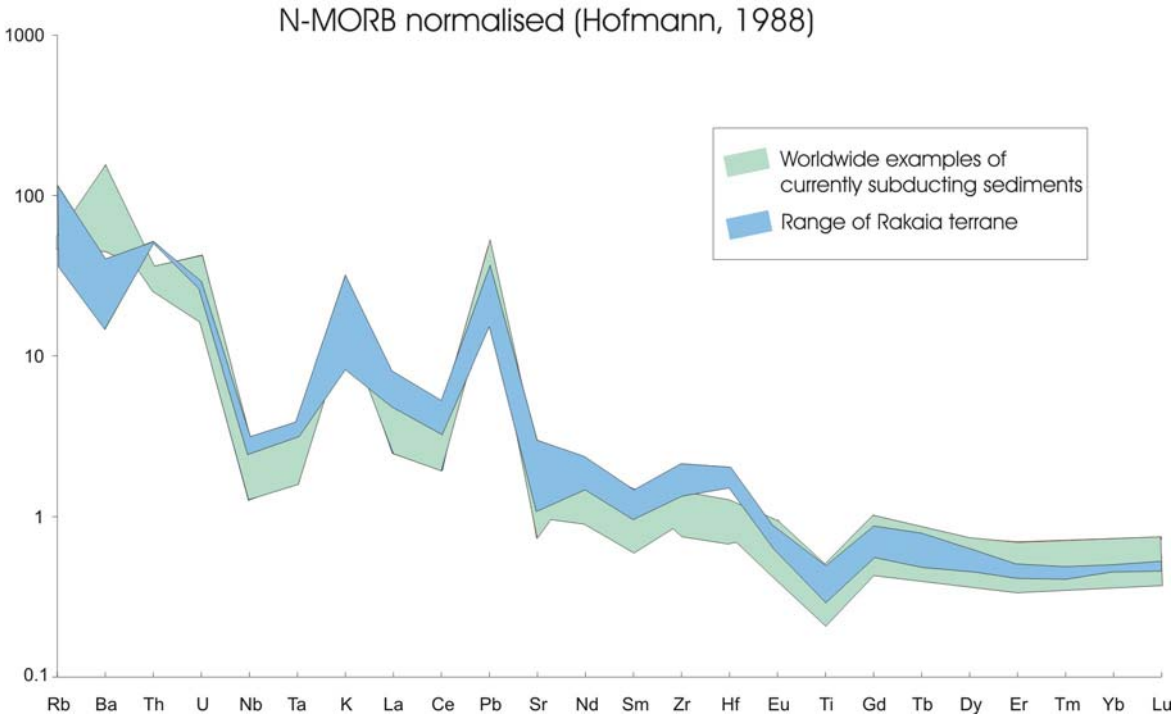

Fig.7.16 Spiderdiagram illustrating the similarity between the average Rakaia terrane samples and data for Aleutians, Cascadia, Kurile and South Sandwich trenches [Plank, 1998 #180].

The basaltic andesites begin to diverge from the sediment pattern in fig.7.15 at Nd and the degree of divergence increases slightly towards the right, in the more compatible REE. The magmas are depleted in Ti and the HREE with respect to N-MORB, but are intermediate between the sediment samples and N-MORB. Since the HREE are compatible relative to the LREE, their values would be expected to be suppressed in mantle wedge partial melts. The REE patterns of the basaltic andesites are most readily explained by normal-mantle partial melting processes.

Partial melting of a mantle wedge is required to elevate the HFSE Nb, Ta, Zr, Hf, Y, P, Yb, V & Sc above MORB values [Tatsumi, 1986 #187]. The addition of subducted sediment or assimilation of crust would provide a source for the LILEs, Pb, U, Th and La. The relative contribution of subducted sediment versus crustal contamination in early formed melts can be tested through the use of combined O-Sr isotope analysis, however modelling of the MSVG is

likely to yield ambiguous results due to the absence of primitive basaltic magmas in the MSVG. Therefore early source contamination in the magmas of the MSVG is unlikely to be represented on O-Sr mixing curves [James, 1981 #177].

The nature of the subducting sediments is unlikely to be Rakaia terrane because evidence suggests that the Pahau terrane was present between the Rakaia terrane and the proposed subduction zone (Chapter 2). Nevertheless, the sediments accumulating in the trench may be chemically similar to the Rakaia terrane since much of the Pahau terrane is considered to be recycled from the Rakaia terrane [Wandres, 2002 #340], and, as indicated on fig.7.16, the Rakaia terrane is similar to sediments subducting around the globe at the present day.

7.3.2 Andesites and Dacites

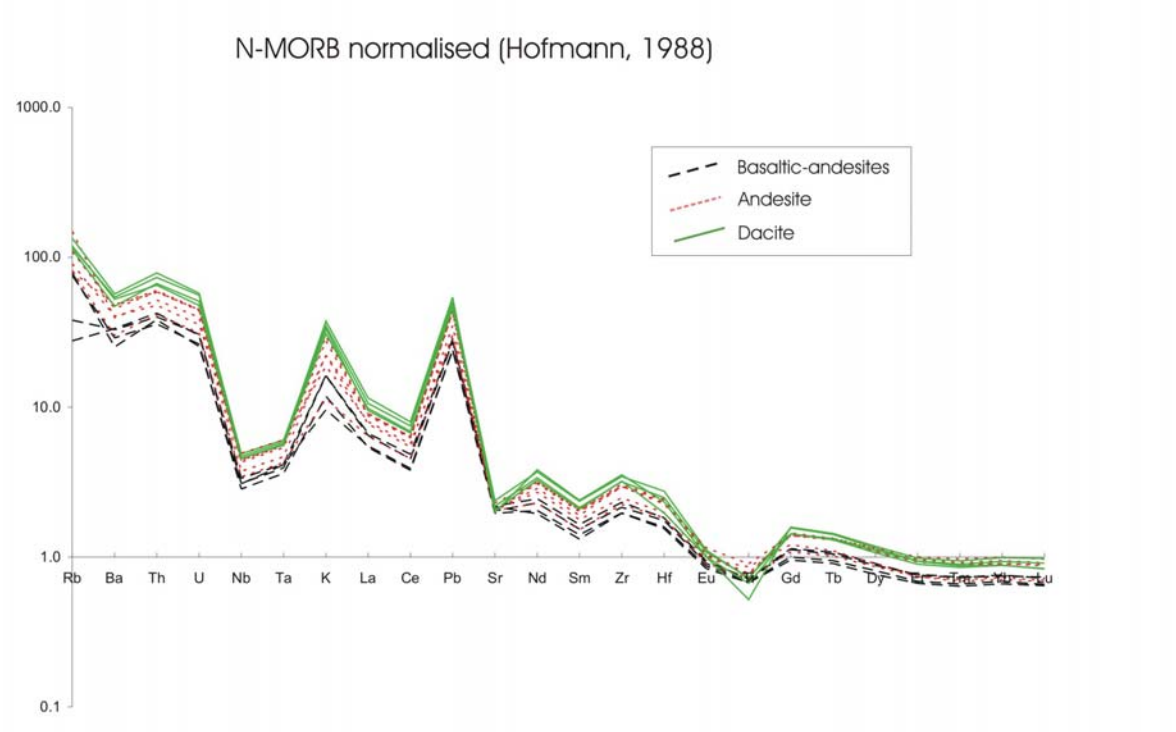

Fig.7.17 Spiderdiagram indicating the transition from basaltic-andesite, through to andesite and dacite.

The andesites and dacites are most likely to be modified derivatives of the basaltic-andesites. They display higher concentrations of all elements except Sr, Eu and Ti. This is consistent with fractional crystallisation processes which are acting to elevate all the values of the incompatible trace elements relative to the parent magma. The constancy of the Sr values and

the generation of a slight negative Eu anomaly are consistent with the continuing crystallisation of plagioclase feldspar. The reduction in Ti is probably linked to the crystallisation of ilmenite as the mafic oxide phase in these rocks. Simultaneous assimilation of crustal partial melts would also serve to elevate the incompatible elements. This process is undoubtedly relevant during the production of andesite and dacite lavas since abundant granulite-facies xenoliths are seen in these rocks [Barley, 1987 #8].

7.3.3 Rhyolites

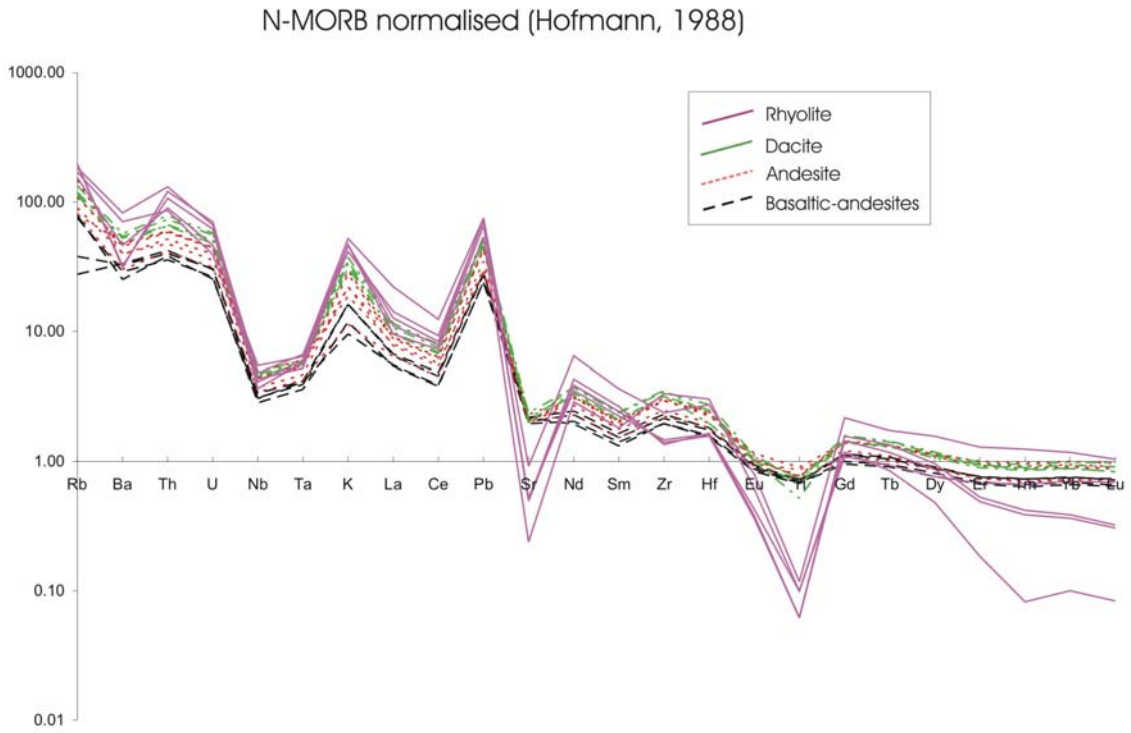

Fig.7.18 Spiderdiagram showing the rhyolite end-member compositional relationship to the andesites and dacites of the MSVG.

The rhyolites show elevated values for most of the incompatible elements, with the exception of Ba which shows depletion for some samples; probably as a result of Ba exchanging for K in the K-bearing phases such as K-feldspar and biotite. Sr is also strongly depleted due to feldspar fractionation, as is Ti due to magnetite fractionation.

The strong variation in HREE concentrations is discussed in the following section.

7.4 Rare Earth Element (REE) Data

The rare earth element plots are all normalised to C1 chondrite values [Boynton, 1984 #182]. The REE data are presented in Appendix 4 and were obtained using an upgraded VG Plasmaquad PQ1 Inductively Coupled Plasma-Mass Spectrometer (ICP-MS) at the Geological Institute, Christian Albrechts University of Kiel, Germany [Garbe-Schönberg, 1993 #206]. The normalisation of REE data relative to chondrite follows the general convention and allows for ease of comparison with published data.

The REE patterns in the following diagrams show very small but consistent positive Pr anomalies and negative Ho anomalies which are interpreted to be due to systematic analytical bias rather than petrogenetic factors. They are also noted in the magmas of the MIC (Chapter 8).

7.4.1 Basaltic Andesites

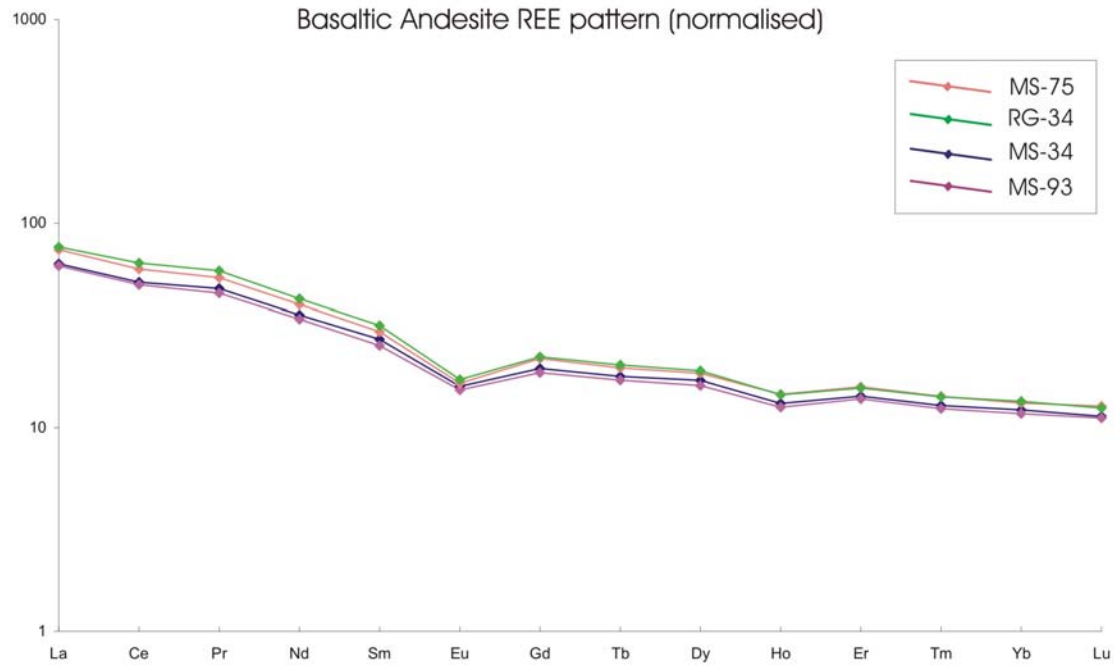

Fig.7.19 REE pattern for basaltic-andesites

The basaltic-andesites of the MSVG show strong fractionation of light to heavy rare earth elements with La_N/Lu_N ratios for Mt. Barrosa of 5.54 - 5.82 and the ratio for a Rangitata Gorge sample RG-34 of 7.13. The most fractionated samples (highest La_N/Lu_N) display the strongest negative Eu anomaly (fig.7.20).

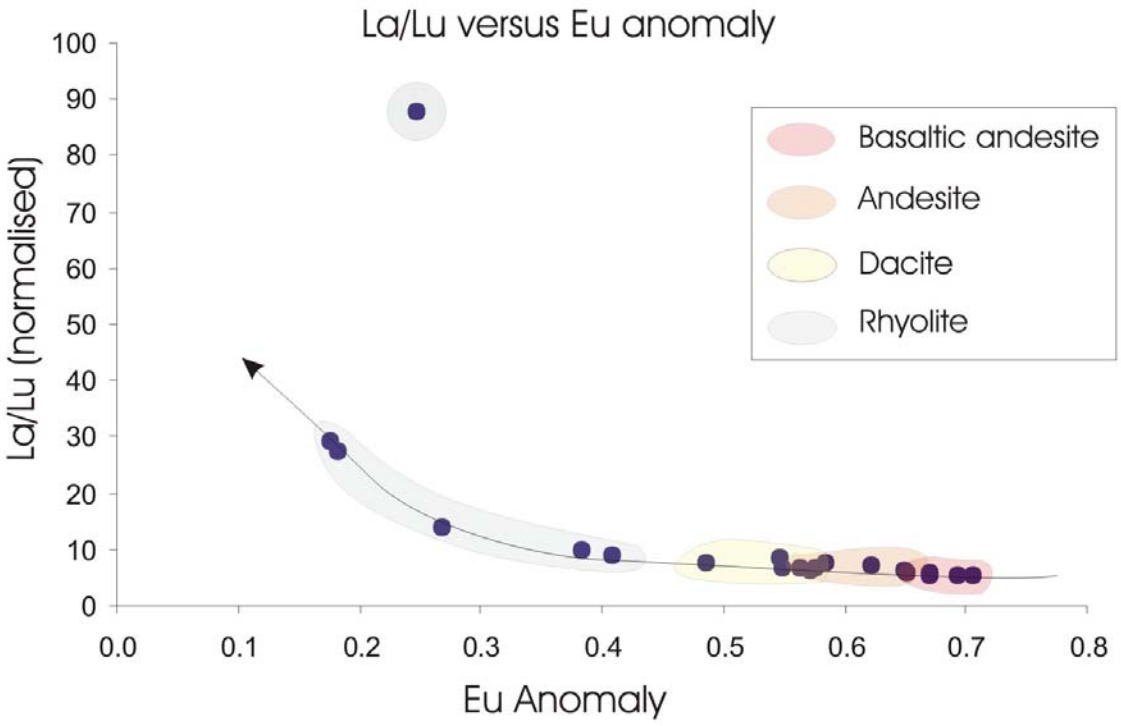

Fig.7.20 La/Lu versus Eu anomaly. The outlier represents sample MH-8 which has very low concentrations of HREE as shown by fig. 7.25.

All the basaltic andesites analysed display a negative Eu anomaly of value 0.71 - 0.65 (Eu anomaly is calculated by dividing the normalised Eu value by the square root of the product of normalised Sm and Gd (Taylor, 1985 #181)). The data for the basaltic andesites of the MSVG show little variation, indicating a uniform source and petrogenetic process.

There is a strong correlation between SiO_2 content and the magnitude of the Eu anomaly up to a SiO_2 content of 76.5% (anhydrous). High SiO_2 samples display the strongest negative Eu anomaly (values >1 = positive Eu anomaly, values <1 = negative Eu anomaly), ref. fig 7.21. This is consistent with plagioclase fractionation in all samples, and in the case of the andesites, demonstrating that plagioclase fractionation is controlling Eu partition rather than orthopyroxene (also present in andesites).

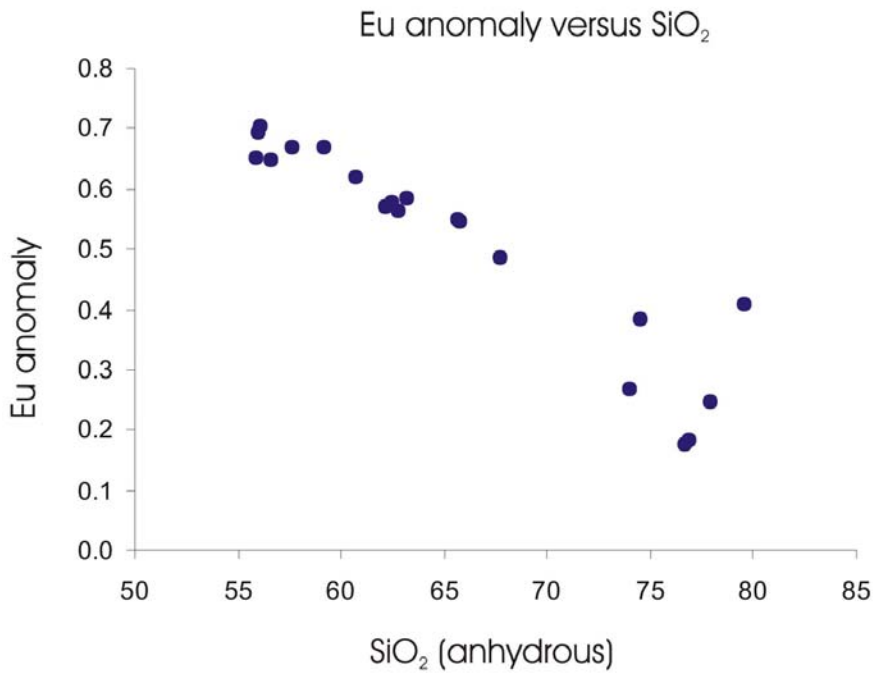

Fig.7.21 Europium anomaly variations with silica content.

7.4.2 Andesites

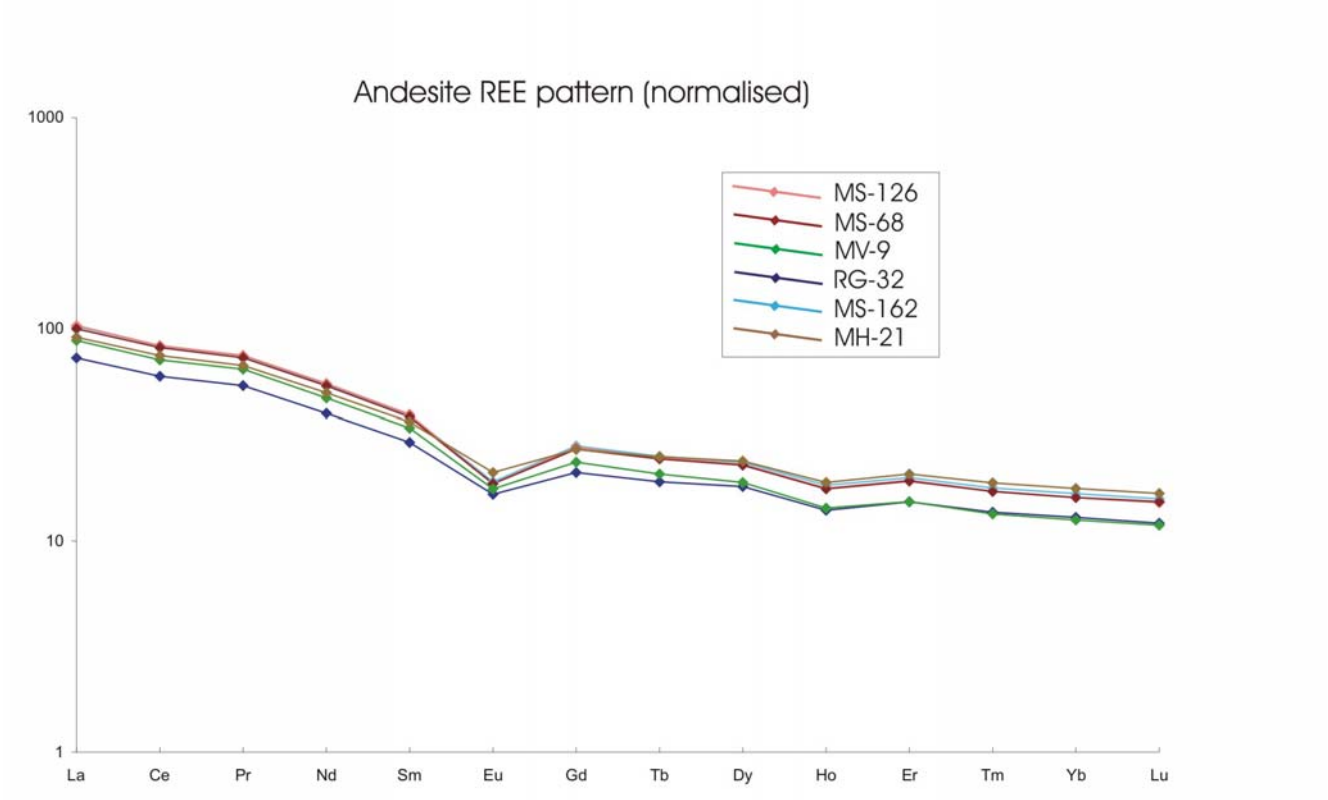

Fig.7.22 REE diagram for MSVG andesites

The andesites of the MSVG display the same patterns as the basaltic andesites but on the whole contain higher concentrations of all the REE. La_N/Lu_N ratios are slightly higher ranging from 6.02 - 7.43. Regional variability is more pronounced in the andesites with the Malvern Hills and McQueen's Valley samples (MH-21 and MV-9 respectively) plotting lower than the Rangitata Gorge (RG-32) and Barrosa samples (MS-68, 126 and 162). This variability is probably the result of the Malvern Hills and McQueen's Valley samples being slightly more primitive (lower SiO_2, higher Mg#).

The Eu anomalies are more pronounced in the andesites than the basaltic-andesites and range from 0.67 - 0.56. Again, the Rangitata Gorge and Malvern Hills samples show the smallest anomalies, consistent with their more primitive character.

7.4.3 Dacites

The dacites are strikingly consistent across the MSVG illustrating again, a consistent petrogenetic process operating over a large area. The dacites show marginally higher concentrations of light and middle-REEs (excluding Eu), with the most marked differences in the lightest-REE: La-Pr. The elevated LREE concentrations are apparently related to the SiO_2 contents (fig.7.23).

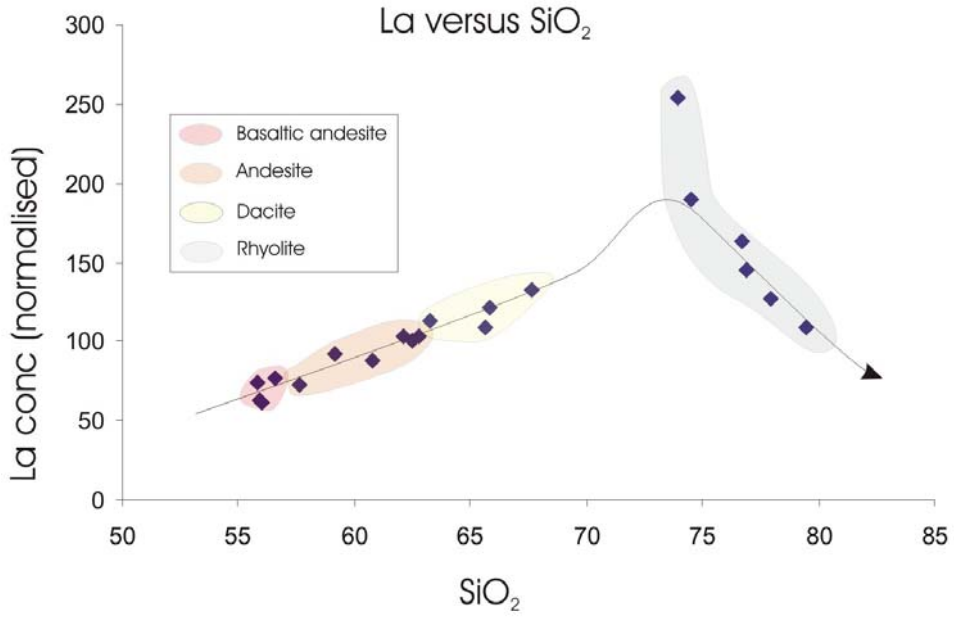

Fig.7.23 La versus SiO_2

The dacites are strongly fractionated with La_N/Lu_N ratios between 6.91 and 8.31. The Eu anomalies are again more pronounced ranging from 0.58 - 0.49. The highest value, again corresponding to the lowest SiO_2 sample (fig.7.21).

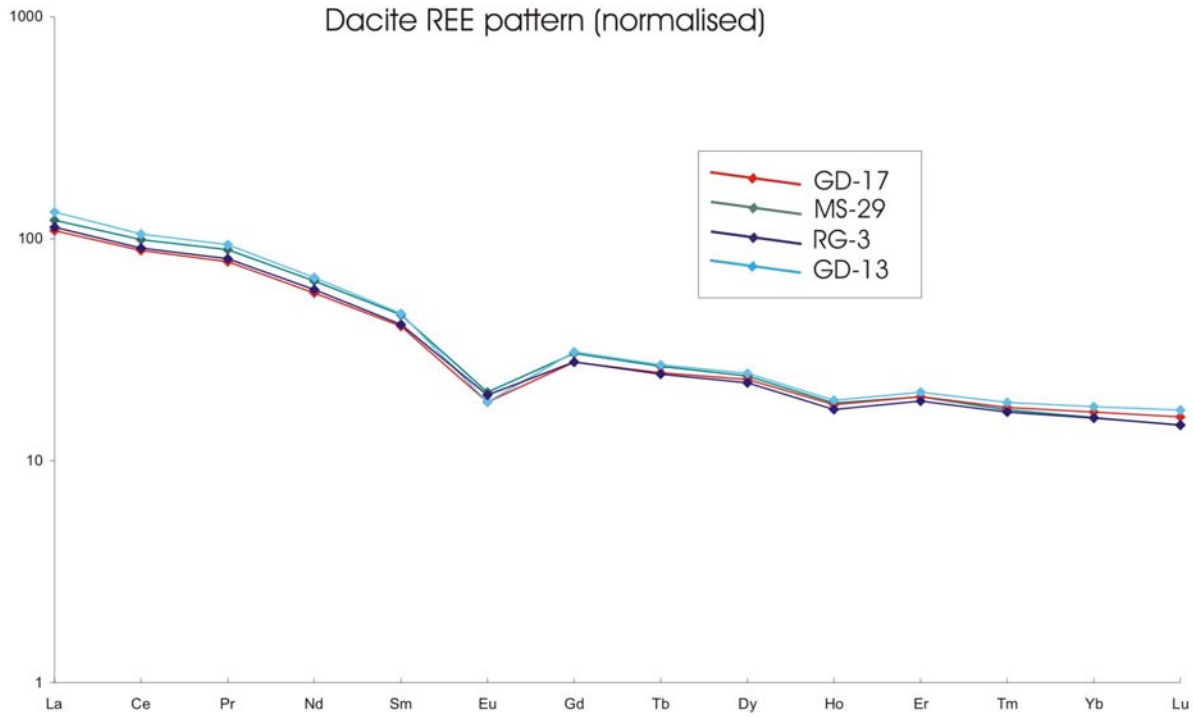

Fig.7.24 REE pattern for the Dacite lavas of the MSVG

7.4.4 Rhyolites

The rhyolites show the greatest variability within the MSVG. La_N/Lu_N ratios generally range from 9.14 - 29.14 with an outlier (MH-8) of 87.93, which is due to the anomalously low value of HREE in this sample. The rhyolites contain higher concentrations of LREEs although there is some overlap with the dacites.

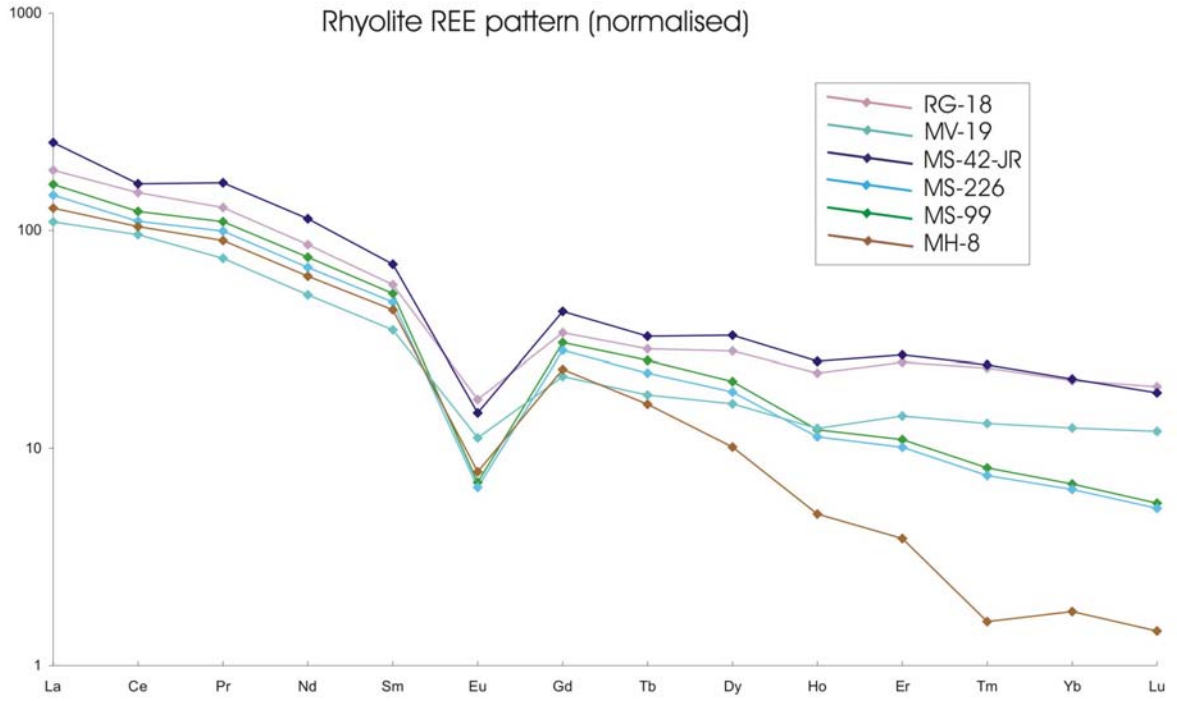

Fig.7.25 Rhyolite REE pattern

One of the most interesting features is that the LREE content decreases with increasing silica content. This is the reverse of the trend for the andesites and dacites, where the samples with higher concentrations of SiO_2 corresponded to the samples which were the most enriched in the LREE. This contrasting relationship is depicted clearly in fig. 7.23. The La depletion in the rhyolites is likely to be the result of the crystallisation of biotite, allanite (lanthanide-rich epidote) and monazite. Partition co-efficients of allanite reach over 2000 in rhyolite [Mahood, 1983 #189]. Allanite is present as a minor accessory phase in the rhyolites of the MSVG as noted by Wood (1974) and Barley (1987). Monazite is present in the MSVG rhyolites and was separated with zircon during SHRIMP preparation.

Ba contents also decrease sharply with increasing SiO_2 contents in the rhyolites and are probably due to the crystallisation of sanidine, and to a lesser extent biotite (fig. 7.26).

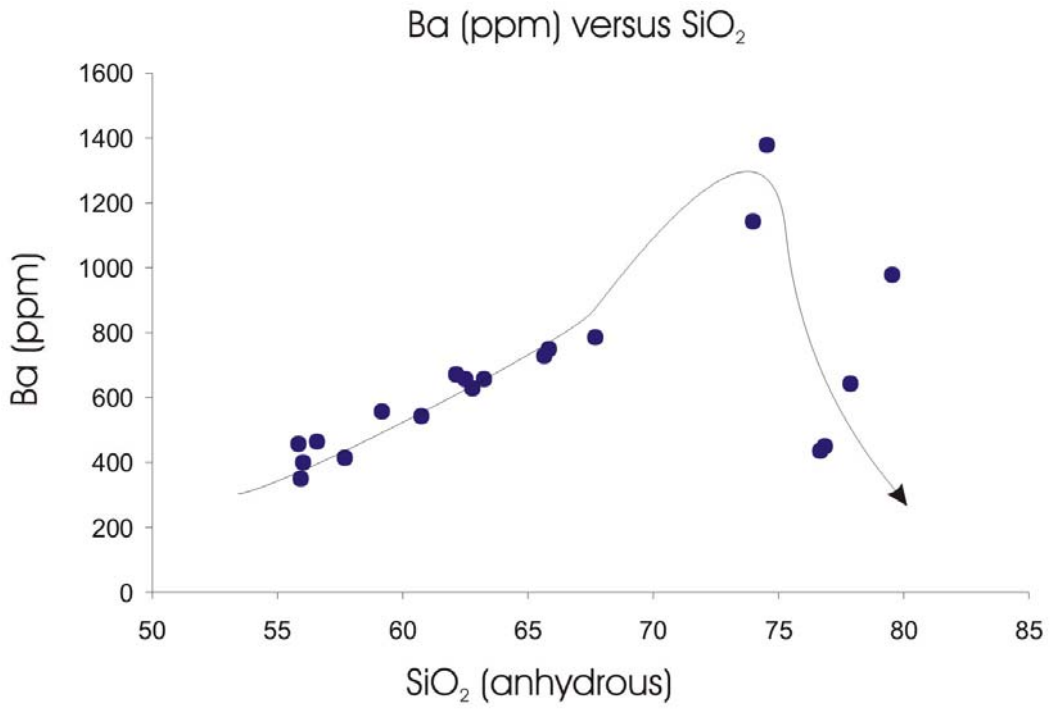

Fig.7.26 Ba concentration versus SiO_2

The rhyolites show variable negative Eu anomalies from 0.43 - 0.18, stronger than those recorded in any of the other suites (a value <1 is negative and the closer the value to 0, the stronger the anomaly). Again, the size of the Eu anomaly is related to the degree of fractionation of REE pattern (Fig. 7.20). The dominant controls over the size of the Eu anomaly in the rhyolitic melts of the MSVG are the feldspars. The continued fractionation of plagioclase and alkali-feldspar would continue to deplete the melt in Eu and thereby strengthen the negative Eu anomaly.

The scatter of Eu anomaly with SiO_2 content at rhyolitic compositions (fig. 7.21) is probably due to the interplay between the feldspars (increasing the strength of the Eu anomaly) and garnet (which decreases the size of the anomaly).

The rhyolites of the MSVG are extremely variable in their HREE compositions. The partitioning of the HREE is apparently unrelated to SiO_2 content (fig. 7.27). The affinity of the HREE for zircon in siliceous melts [Mahood, 1983 #189;Nash, 1985 #188] and the relationship between Zr and Gd/Lu ratios (fig. 7.28), leads to the conclusion that the depletion in HREE is related to the crystallisation of zircon. Apatite may also be responsible but to a lesser extent than zircon.

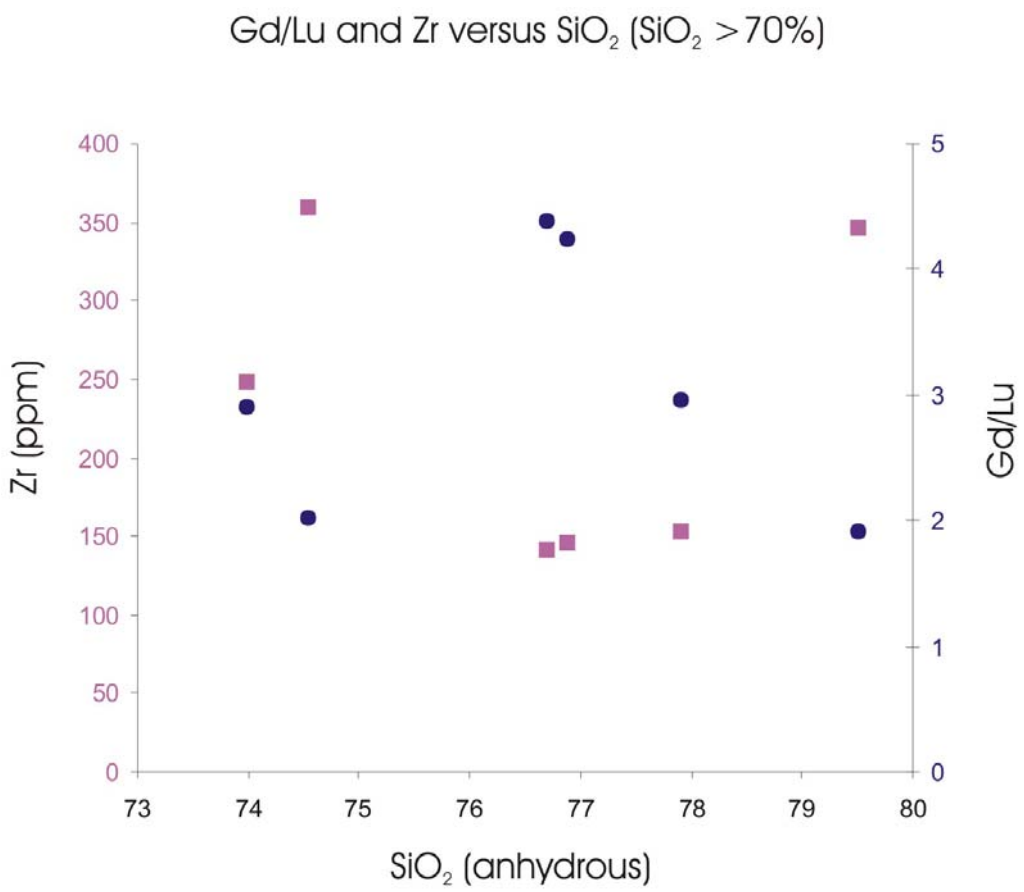

Fig.7.27 Gd/Lu and Zr versus SiO_2

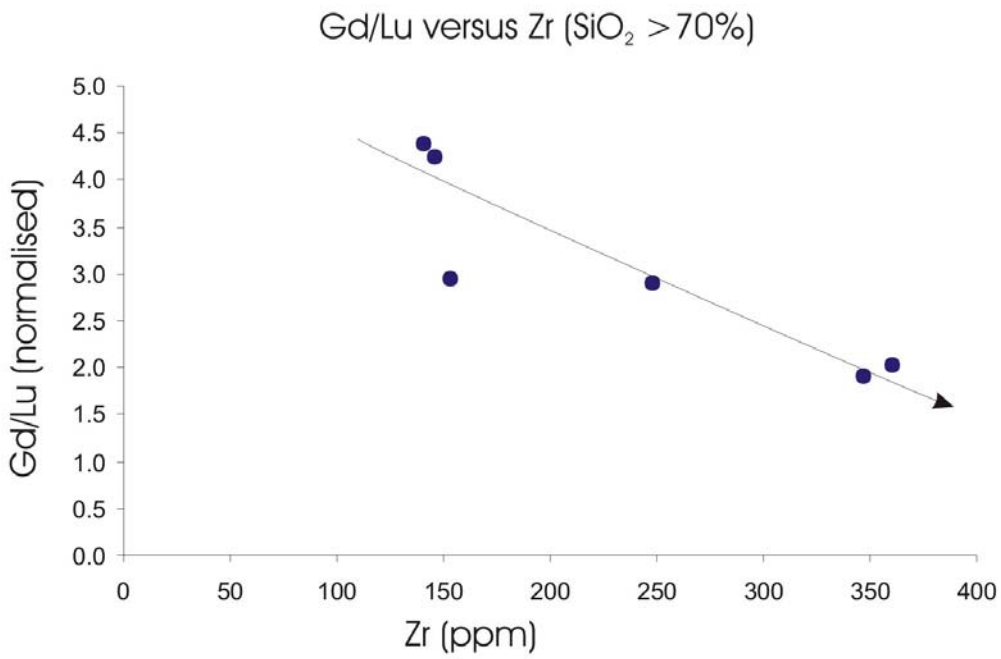

Fig.7.28 Gd/Lu versus Zr for rhyolites with >70% SiO_2

The crystallisation of zircon appears to be unrelated to SiO_2 content (fig.7.27). However a clear relationship exists between zircon (+apatite) formation and the strength of the Eu anomaly and Gd/Lu ratio (fig. 7.29).

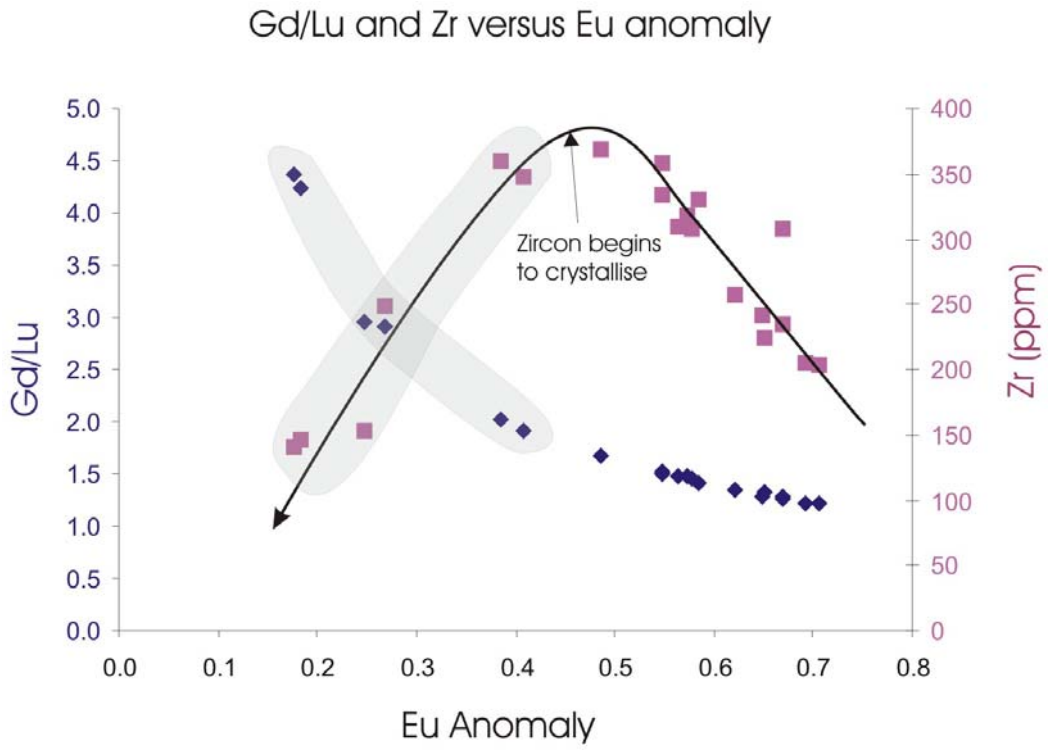

Fig.7.29 Gd/Lu and Zr versus Eu anomaly (rhyolites shaded grey)

From fig. 7.29, the onset of zircon crystallisation can be seen to occur with the formation of rhyolite melts and results in a depletion of Zr and relative increase in Gd/Lu ratio.

The LREE fractionate with increasing SiO_2 contents (fig. 7.23), whereas the HREE fractionate independently of the SiO_2 content (fig. 7.27) but fractionate with respect to Eu anomaly (fig. 7.29). Therefore zircon (+ apatite) crystallisation is related to the phases which control the partitioning of Eu (feldspars and garnet).

7.5 Assimilation – fractional crystallisation modelling

The presence of xenoliths in the lavas of the MSVG suggests that assimilation occurred concurrently with crystallisation and therefore the following models have been produced based upon the AFC equation [DePaolo, 1981 #264]. The three samples of Rakaia terrane analysed by ICP-MS for trace-element data are averaged to provide an assimilant end member 'C_A' in the equations of DePaolo (1981).

Modelling indicated that the trends of the trace-element variation diagrams cannot be produced by constant values of 'r' (ratio of assimilation rate to crystallisation rate in AFC). The best fit to the MSVG data was produced when the value of 'r' increased with increasing degrees of differentiation and the 'r' values are labelled beside the corresponding model points on the diagrams. The bulk partition coefficients used for different rock types of the MSVG are identified on the AFC diagrams by their rock name (e.g. basaltic-andesite model points use the basaltic-andesite bulk partition coefficients as calculated in Appendix 8). The bulk partition coefficients and crystallising phase proportions used in modelling are found in Appendix 8.

The model points on the diagrams are plotted at 0.05 increments of 'F' (proportion of melt remaining), the first point at 0.95 and the last point generally 0.5 (or 50% crystallisation of the parent magma).

In order for each diagram to be consistent, the degree of 'F' at which the bulk partition co-efficient shifts from one magma type to another e.g. from basaltic-andesite to andesite remains the same for all diagrams. At F=0.85 the andesite bulk partition co-efficient is introduced. At F=70, the dacite bulk partition co-efficient is introduced and at F=0.50, the rhyolite bulk partition co-efficient is introduced. Likewise, the ratio of rate of assimilation to crystallisation 'r' remains the same at given 'F' values for each model. At F=0.95 to 0.80 r=0.4; at F=0.75 to 0.70 r=0.5; at F=0.65 to 0.60, r=0.6; at F=0.55, r=0.7 and at F=0.50, r=0.8.

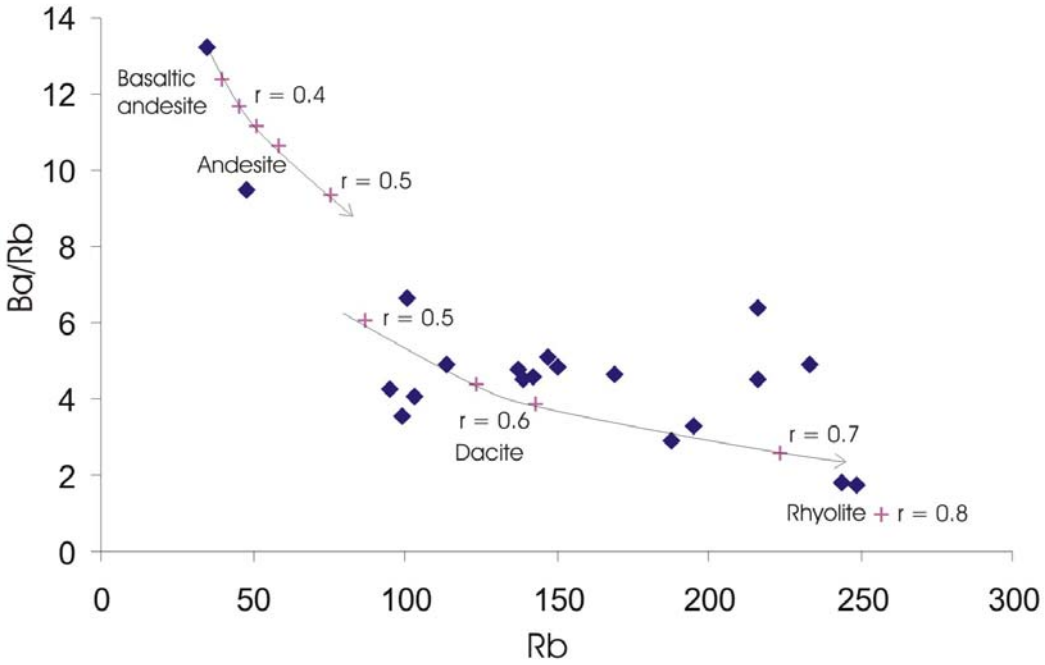

Fig. 7.30 AFC trends for Ba/Rb v Rb for the MSVG. MSVG samples are blue diamonds and the model points are pink crosses.

On a plot of Ba/Rb versus Rb, the modelled trend broadly follows the trend produced by the MSVG samples. The model requires the increasing degrees of assimilation as represented by 'r' in order to produce a good correlation. The rhyolitic end-members are variable in composition. This is interpreted to represent the varying phenocryst populations from one sample to another, whereas the model is based upon the average modal proportions (ref. Appendix 8 for proportions used in modelling). The abundance of biotite in the rhyolites has a significant effect upon the Ba/Rb ratio and the samples displaced to higher Ba/Rb ratios contain a higher proportion of biotite. The contrasting concentration of Rb in the parental magma and assimilant means that Rb provides a good means of identifying and modelling AFC processes.

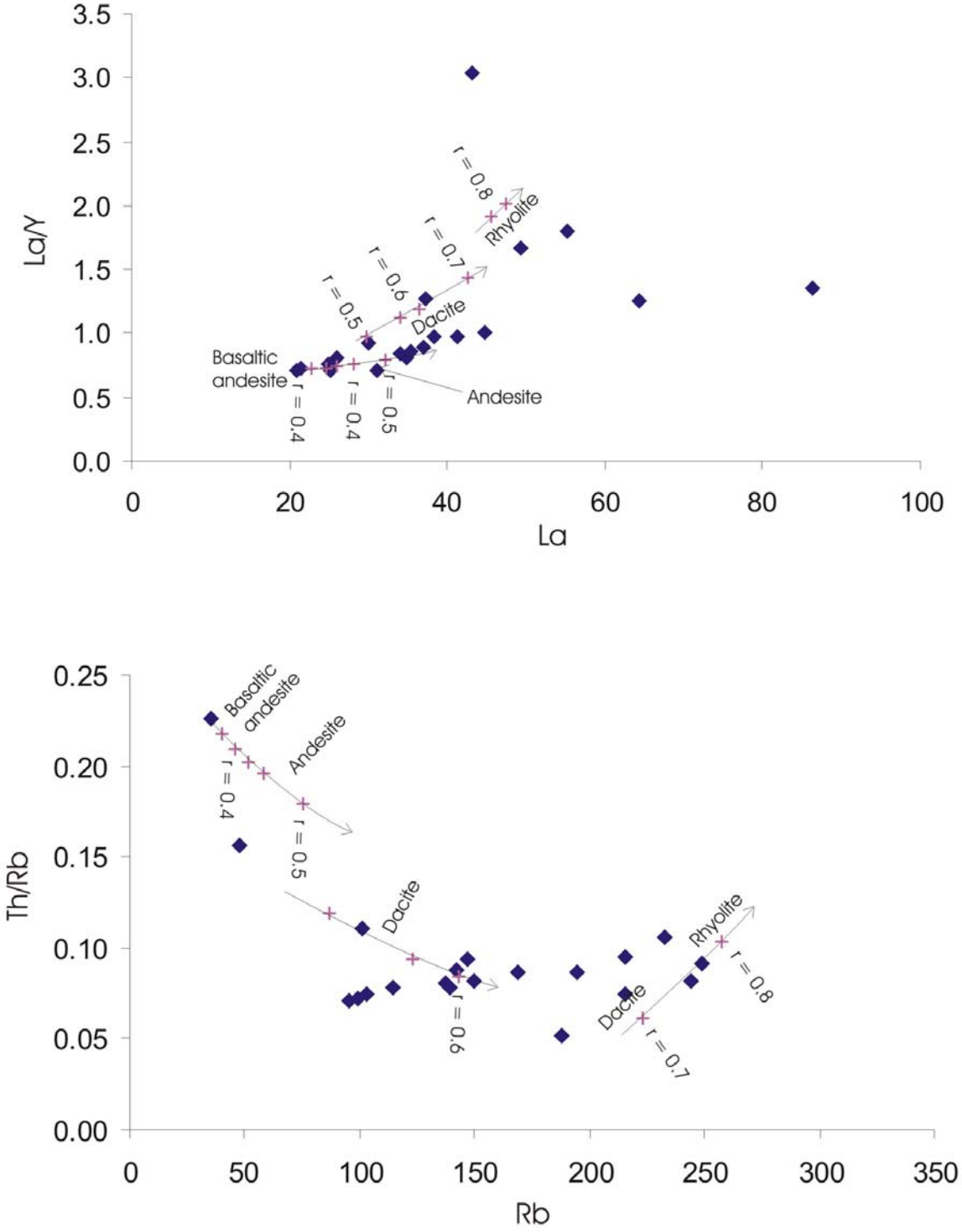

Fig.7.31 AFC trends for La/Y versus La and Th/Rb versus Rb for samples from the MSVG. AFC points are pink crosses and MSVG samples are blue triangles.

The La/Y versus La diagram shows a good correlation between the modelled values for andesites, dacite and rhyolites and the MSVG samples. The trend for the basaltic-andesites and andesites appears to deviate from the fractional crystallisation trend for the dacites and

appears to be a continuation of the lower ‘r’ trend. This apparent deviation would indicate that the majority of andesite samples are consistent with fractional crystallisation with lower degrees of ‘r’, i.e. assimilation played a smaller role in their petrogenesis. The rhyolites of the MSVG show significant scatter which is related to the relative proportions of garnet and accessory minerals such as apatite, zircon and allanite.

On the Th/Rb v Rb diagram, the basaltic andesites do not show a good correlation with the observed MSVG data. This probably results from the uncertainty of Th partition co-efficients applicable during the crystallisation of basaltic andesites. The rest of the MSVG samples do show a good similarity to the modelled trend.

Although the modelled trends do not provide a perfect AFC scenario, the MSVG trends have been approximated by using a sensible set of modelling parameters. In order to produce the AFC curves drawn in figs 7.30 and 7.31, the rate of assimilation must increase during fractionation from basaltic-andesite through to dacite and rhyolite. Modelling of the evolved compositions is somewhat hampered by the dependence upon many incompatible trace-elements to be taken up into late stage accessory phases, which produces scatter in the plots.

Assimilation of large quantities of country rock is indicated by the AFC modelling. Such high degrees of assimilation are difficult to achieve. The heat required to melt and assimilate country rock is usually provided by the latent heat of the minerals crystallizing from the melt. Assimilation would have the effect of speeding up the crystallisation process and thereby inhibiting further assimilation. Large scale partial melting of lower crust has previously been attributed to decompression as a result of extension e.g. [Pankhurst, 2000 #279], anomalously high temperature asthenosphere e.g. [Pankhurst, 1995 #280;Ewart, 1998 #281] or a combination where hot asthenosphere rises due to lithospheric extension e.g.[Harangi, 2001 #217]. Therefore mixing with partial-melts of continental crust, enhanced by the application of an external heat source or by decompression melting is implied.

7.6 Stable Oxygen Isotope Geochemistry

$\delta^{18}O$ analyses were carried out on selected garnet, quartz and whole-rock samples from the MSVG. Analyses were carried out in conjunction with Dr Kevin Faure, IGNS, Lower Hutt. The analytical techniques employed are described at Appendix 7.

The crystals analysed were taken from pitchstones of the Malvern Hills, Mount Somers and Gawler Downs field areas. The glassy and unaltered nature of the pitchstones implies little or no hydrothermal alteration and therefore elevation of ^{18}O due to hydrothermal alteration [King, 1997 #169] is considered negligible.

7.6.1 Principles of stable oxygen isotope geochemistry

Oxygen isotope values are typically stated in per mil values (‰) derived from the following equation:

$$\delta^{18}O = \frac{^{18}O/^{16}O\ (\text{sample}) - {}^{18}O/^{16}O\ (\text{standard})}{^{18}O/^{16}O\ (\text{standard})} \times 1000$$

Variation in $\delta^{18}O$ is caused by mass based, temperature-dependent isotopic fractionations. ^{18}O is a stable isotope and therefore its abundance is not affected by radioactive decay.

The ^{18}O fractionation factors between liquid and solid at relatively high temperatures in magmatic melts are small [Hoefs, 1997 #166]. Therefore, it is reasonable to say that the concentration of ^{18}O in the sum of the crystallised minerals broadly represents the ^{18}O concentration of the magmatic water present in the melt, and by analysing the $\delta^{18}O$ value of constituent oxygen-bearing minerals, the $\delta^{18}O$ of the melt can be calculated. The $\delta^{18}O$ value of the original magma can be calculated from $\delta^{18}O$ values determined from quartz crystals. The $\delta^{18}O$ value of quartz in a granitoid is dependent upon the isotope fractionation between

quartz and the melt (Δquartz-magma), the cooling rate (which is reflected in the grain size) and the temperature of closure of the quartz to oxygen diffusion [Giletti, 1986 #256]. To correct for 'closure' effects, the $\Delta_{quartz\text{-}magma}$ for quartz porphyries and rhyolites is assumed to be +1‰ [Taylor, 1986 #170].

Basic lavas are very uniform in $\delta^{18}O$ (fig 7.32), with values ranging from 5.3‰ to 6.5‰ for MORB (Mid-Atlantic Ridge and East Pacific Rise) [Kyser, 1986 #171]. Oceanic Island Basalts (OIBs) and Continental Basalts are very similar and have a larger range of values from 4.8‰ to greater than 8‰. OIBs, although showing the same overall range of $\delta^{18}O$ values, tend to be concentrated at the lower end of the range [Kyser, 1986 #171]. There appears to be no measurable $\delta^{18}O$ variation between the MORB reservoir and the primordial mantle [Taylor, 1986 #170]. The uniformity of the MORB reservoir with respect to ^{18}O appears to extend back, at least as far as the Cretaceous [Gregory, 1981 #172].

Fig.7.32 Diagram showing the range of $\delta^{18}O$ values for basic lavas, from Kyser (1986).

The high temperature nature of the MSVG pitchstones from which the MSVG samples were taken would be expected to prevent any sub-solidus oxygen isotope exchange. Therefore, the values from the phenocrysts can be used to calculate magmatic values at the time of formation.

During fractional crystallisation, the $\delta^{18}O$ values of magmas from closed-system fractionation will increase as the system evolves. This is because SiO_2 rich minerals (of which quartz is the

highest ^{18}O mineral) preferentially concentrate ^{18}O [Taylor, 1967 #176]. However, at high temperatures (>900˚C) the rhyolite end member is only expected to contain <1‰ more $\delta^{18}O$ than the basaltic end member [Taylor, 1986 #170;Matsuhisa, 1979 #173]. Therefore, closed-system fractional crystallisation has only a small effect on $\delta^{18}O$ values.

Taylor & Sheppard (1986) assert that '*Any igneous rock series in which the oxygen isotope variations are larger than 1 per mil, other processes in addition to crystal fractionation should be strongly suspected as being involved'.*

The concept of S- and I-type granites was first introduced by Chappell & White in 1974 [Chappell, 1974 #249]. The model is based on the derivation of granitoids from melting of sedimentary and igneous source rocks respectively.

It has been demonstrated that oxygen isotopes provide a good means of discerning between S- and I-type granites [O'Neil, 1977 #254;O'Neil, 1977 #255]. S-type granites from the New England and Berridale Batholiths of Australia have $\delta^{18}O$ values greater than 10‰ whereas I-type granites from the same batholiths generally have values less than 10‰ [O'Neil, 1977 #255]. More recently it has been found that oxygen isotope analyses of quartz separates provide a better indication of the oxygen isotope ratio of the initial magma than whole-rock analyses [Harris, 1997 #257], due to post-magmatic changes in $^{18}O/^{16}O$ ratio which can affect whole-rocks.

7.6.2 $\delta^{18}O$ Data

Sample Number	Mineral	$\delta^{18}O$ ‰ VSMOW	Average $\delta^{18}O$ (‰)	Replication difference
GD-28 (pitchstone)	Quartz	10.7, 10.6	10.7	± 0.05
MS-99 (pitchstone)	Quartz	9.9, 10.6	10.3	± 0.35
MH-12 (pitchstone)	Quartz Garnet	11.4, 11.5 8.7, 8.9	11.5 8.8	± 0.05 ± 0.1
RG-4 Rakaia terrane	Whole-rock	10.0, 9.4, 9.3	9.6	± 0.4
M-65a Rakaia terrane	Whole-rock	9.6, 9.6	9.6	Nil
MS-37 Rakaia terrane	Whole-rock	9.7, 9.6	9.7	± 0.05
M-80 Pahau terrane	Whole-rock	2.9, 2.9, 3.0	2.9	± 0.1

Table 7.3 $\delta^{18}O$ data from MSVG samples.

7.6.3 $\delta^{18}O$ data discussion

The $\delta^{18}O$ values of quartz from the MSVG have values greater than 10‰. Based on the $\Delta_{quartz\text{-}magma}$ of 1‰, the $\delta^{18}O_{magma}$ value is greater than 11‰, indicating that the MSVG rhyolitic melts, from which the quartz crystallised have been significantly influenced by continental crust. The magma values are greater than those of the Rakaia terrane samples analysed, which would imply that the assimilant had higher $\delta^{18}O$ values than the Rakaia terrane. This is problematic because modelling of radiogenic isotopes indicates that high degrees of assimilation of rocks similar in composition to the Rakaia terrane took place (section 7.7).

Two hypotheses are presented to explain the $\delta^{18}O$ values derived from the MSVG:

7.6.3.1 Model 1

The high $\delta^{18}O$ values of quartz from the MSVG can be reconciled with the radiogenic isotope data if the crystals are not entirely of magmatic origin. If the cores of the quartz crystals are detrital, with magmatic overgrowths, the analyses would average the two values. This would require a core with $\delta^{18}O$ value greater than 10‰ and a rim with $\delta^{18}O$ value less than 10‰.

Detrital quartz grains analysed from siltstones and sandstones from the greywacke terranes of the North Island have systematically higher $\delta^{18}O$ values than their respective 'whole-rock' values [Woldemichael, 1999 #235](fig 7.33). For example, a greywacke of whole-rock $\delta^{18}O$ concentration of 9‰ might be expected to have quartz $\delta^{18}O$ concentration of >15‰.

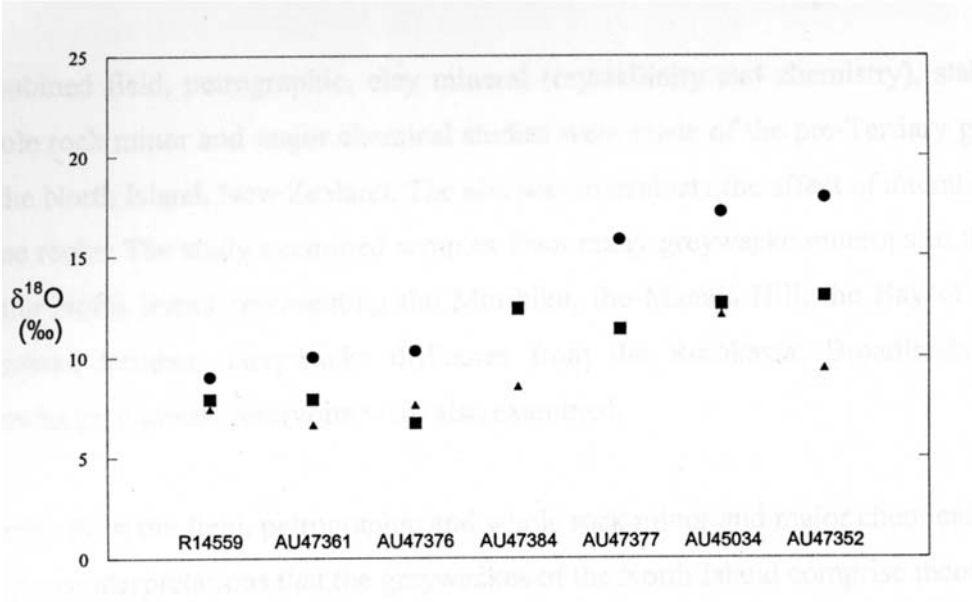

Fig.7.33 Relationship between quartz (circles), feldspar (triangles) and whole-rock (squares) data for selected samples from pre-Tertiary greywacke rocks from the North Island, New Zealand. Diagram is reproduced from Figure 7.4 of Woldemichael (1999).

The average Rakaia terrane sediment value is 9.6‰ (based on 7 analyses from 3 samples, see table 7.3). Averaging of the Rakaia terrane whole-rock results can only be done if grain size is assumed to have a negligible affect on the $\delta^{18}O$ value. This was shown to be the case for the North Island Torlesse terrane [Woldemichael, 1999 #235], and can therefore be considered to be appropriate for the South Island Torlesse terranes. The quartz grains derived from the Rakaia terrane (whole-rock = 9.6‰) would be expected to have $\delta^{18}O$ values in excess of 12‰.

The average quartz values derived from the rhyolites of the MSVG is 10.8 ‰ (based on 3 analyses, see table 7.3).

Based on this model, the quartz phenocrysts would be expected to have inherited cores of value ≥ 12 ‰ with overgrowths of < 9.6 ‰. This would provide a melt composition lower than that of the Rakaia terrane, whilst resulting in a single quartz crystal with a $\delta^{18}O$ value greater than that of the Rakaia terrane.

Selected rhyolite and ignimbrite samples from the MSVG were examined using a scanning electron microscope (SEM) at the University of Canterbury, to look for inherited crystal cores. No evidence of rounded detrital cores were found in any of the quartz crystals examined from 3 rock samples. Interestingly, the crystals did show distinct zoning (fig.7.34), however since the $\delta^{18}O$ value of the melt would be expected to increase as the system evolves through AFC processes, the inner zones would be expected to have lower $\delta^{18}O$ values than the rims.

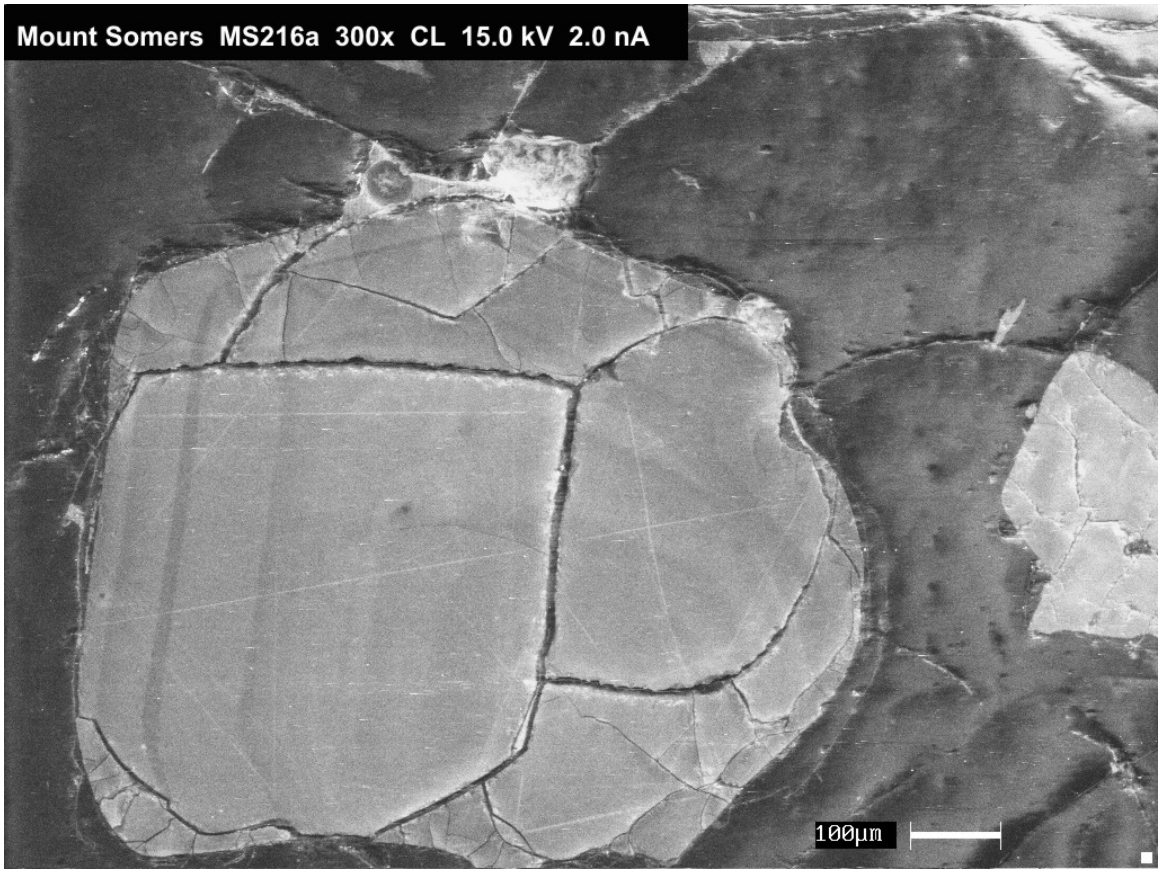

Fig.7.34 Zoned quartz crystal from the pitchstone MS-216a.

The CL images strongly indicate that inherited quartz grains are not present in the quartz phenocrysts of the MSVG rhyolites and ignimbrites, therefore Model 1 can be discounted.

7.6.3.2 Model 2

The high $\delta^{18}O$ values of the quartz grains analysed (10.8‰) indicates a $\delta^{18}O_{magma}$ value of approximately 11.8‰. An assimilant with similar Sr and Nd radiogenic isotope characteristics to the Rakaia terrane, but with $\delta^{18}O$ values in excess of 12‰ is implied.

There are limited data available on the Eastern Province terranes of New Zealand, however the Pahau terrane can be eliminated as a likely contaminant due to its very low $\delta^{18}O$ value (2.9‰). The elimination of the Pahau as a significant contaminant is also supported by Sr and Nd radiogenic isotopic compositions. However, sample MH-8 does appear to have experienced some interaction with rocks containing Pahau age zircons (section 6.2.4).

Considerable scatter of $\delta^{18}O$ values have been determined for 128 samples from North Island accretionary terranes, with values ranging from 6.5 to 16.8 [Woldemichael, 1999 #235]. No additional data were available from the South Island Eastern Province terranes but a more detailed $\delta^{18}O$ investigation of the Eastern Province terranes is necessary to provide a robust data set from which implications of likely contaminants can be made.

7.6.4 $\delta^{18}O$ Conclusions

Model 1 can be eliminated as a possible cause of the unexpectedly high $\delta^{18}O$ values due to the absence of any evidence of inherited cores in the quartz phenocrysts. The data is more consistent with Model 2, and suggests that the assimilant had a higher $\delta^{18}O$ concentration than the three Rakaia terrane samples analysed. It is possible that an assimilant with similar radiogenic isotope systematics but higher $\delta^{18}O$ value may be present in the lower crust of the Rakaia terrane. The Rakaia terrane may be heterogeneous with respect to $\delta^{18}O$ and further analyses may yield a broader range of compositions, as has been found in the North Island terranes. Ideally further work involving the in-situ $\delta^{18}O$ measurement of the quartz zones and

a greater $\delta^{18}O$ reconnaissance of the Torlesse terrane would be required, however this is clearly outside the scope and budget of this thesis.

7.7 Radiogenic Isotope Geochemistry

The importance of radiogenic isotopes in petrogenetic studies is due to the fact that they are largely unaffected by the chemical fractionation processes through which a magma passes as it evolves. All samples for this study were analysed for Sr, Nd and Pb isotopic compositions using the Finnigan MAT 262 Thermal Ionisation Mass Spectrometer (TIMS) at GEOMAR Research Institute, Kiel, Germany. See Appendix 5 for a full description of methods employed.

7.7.1 Principles of radiogenic isotope geochemistry

7.7.1.1 Lead Isotopes

There are 4 isotopes of lead: ^{204}Pb, ^{206}Pb, ^{207}Pb and ^{208}Pb. ^{204}Pb is stable and is therefore used as a reference isotope. The other lead isotopes are derived by radiogenic decay as follows:

$^{238}U \rightarrow {}^{234}U \rightarrow \mathbf{^{206}Pb}$
$^{235}U \rightarrow \mathbf{^{207}Pb}$
$^{232}Th \rightarrow \mathbf{^{208}Pb}$

The ratio $^{238}U/^{204}Pb$ is known as μ and high values of μ (high-μ, or 'HIMU') are typically associated with enriched mantle plumes. The parental ^{238}U in such 'enriched' mantle plumes may be derived from the recycling of subducted slabs and associated sediments into the lower mantle during subduction [Chase, 1981 #205;Hofmann, 1982 #204].

As with the Nd-Sm and Rb-Sr systems, the isotopic composition of Pb at the time of formation of the Earth should be the same as that in meteorites. Since 3 out of the 4 lead isotopes are radiogenic, their abundances will have changed since the formation of the Earth.

The isotope ratios of co-genetic suites of igneous rocks should define straight lines (isochrons) in plots of $^{206}Pb/^{204}Pb$ versus $^{207}Pb/^{204}Pb$ (or $^{208}Pb/^{204}Pb$). However, Pb-Pb diagrams may also reflect mixing of leads of different isotopic composition and must therefore be treated with caution.

U and Th are both preferentially concentrated in silicate melts compared with Pb, and consequently the U/Pb and Th/Pb ratios of crustal rocks are higher than those of the mantle. The concentration of U and Th in upper crustal rocks results in the upper and lower crusts having distinctly different Pb isotope characteristics. Therefore, Pb isotopes provide powerful constraints for the interaction of mantle-derived melts with crustal material and may also be used to constrain the nature of the crustal contaminant in continental volcanic suites.

Pb is particularly sensitive to crustal contamination and only 1-2% of sediment is needed to significantly affect the Pb isotope composition of the rock [Armstrong, 1971 #195;Kay, 1978 #219;Davidson, 1996 #186]. Therefore Pb is particularly useful in the study of enriched mantle, but is not particularly useful in the study of magmas heavily contaminated by continental crust.

7.7.1.2 Strontium Isotopes

^{87}Rb decays to the stable isotope ^{87}Sr, with the release of a β-particle. The amount of ^{87}Sr in a mineral or rock containing Rb increases continuously as a function of time. The decay of ^{87}Rb to ^{87}Sr, with a known half-life, provides a useful geochronological tool. The reference isotope ^{86}Sr is not produced by radioactive decay, and is therefore considered a constant. The 'initial ratio' of $^{87}Sr/^{86}Sr$ is the $^{87}Sr/^{86}Sr$ ratio at time=0 and is the $^{87}Sr/^{86}Sr$ ratio of the magma from which the rocks crystallised. It is the initial $^{87}Sr/^{86}Sr$ ratio which is particularly useful in petrogenetic studies. The initial $^{87}Sr/^{86}Sr$ ratio is dependent upon the rubidium/strontium enrichment or depletion processes which operated prior to the magma generation.

The rocks of the continental crust are enriched in Rb, and have higher Rb/Sr ratios than the rocks of the upper mantle. Therefore, melts derived from the continental crust can be expected to have high initial ratios. Typical initial ratios are listed below for oceanic island basalts (OIB) and continental crust [Faure, 1972 #196].

OIB $^{87}Sr/^{86}Sr_i$ = 0.7037 (average)

Continental crust $^{87}Sr/^{86}Sr_i$ = 0.719

When rocks undergo fractional crystallisation in a closed system, all the resulting rocks should have the same initial $^{87}Sr/^{86}Sr$ ratio regardless of their chemical composition. They form a 'linear array' or an 'isochron', which intersects the y axis ($^{87}Sr/^{86}Sr$) at time=0 ($^{87}Rb/^{86}Sr=0$). The presence of a 'linear array' on a $^{87}Sr/^{86}Sr$ versus $^{87}Rb/^{86}Sr$ plot, together with geological evidence for co-magmatic origin is very strong evidence for a suite of igneous rocks being sourced from a single closed-system magma chamber.

Where the initial $^{87}Sr/^{86}Sr$ ratio varies within rocks from the same group, it can be assumed that the rocks were derived from parental magmas with different Sr histories. The variance can be used to indicate the role of magma mixing or crustal contamination as the magmas evolve. The elevation of initial $^{87}Sr/^{86}Sr$ ratios indicates the involvement of a contaminant of high initial $^{87}Sr/^{86}Sr$, normally crustal or subducted-sediment contamination. A correlation between increased silica content and increased initial $^{87}Sr/^{86}Sr$ ratios is a good indication of the involvement of continental crust as a contaminant. Mixing curves can be drawn to model the involvement of crustal material of known $^{87}Sr/^{86}Sr$ (at the time of formation of the igneous material) and likely parental magmas [Langmuir, 1978 #192].

7.7.1.3 Neodymium Isotopes

^{143}Nd is derived from the radioactive decay of ^{147}Sm with the release of an α-particle. The half life ($T_{½}$) of ^{143}Nd is 1.06 x 10^{11} years. It is the change in abundance of ^{143}Nd relative to the other Nd isotopes that is of interest to Earth scientists.

$^{147}Sm/^{143}Nd$ ratio is sensitive to certain geologic processes and insensitive to others in a manner that is complementary to the other nuclide pairs (^{87}Rb – ^{86}Sr, ^{235}U – ^{207}Pb, ^{238}U – ^{206}Pb & ^{232}Th – ^{208}Pb). The chemical properties of Sm and Nd makes them useful elements as they magnify the effects of some processes which would otherwise be undetectable using the other nuclide pairs.

Crustal rocks are enriched in Sm, Nd, Rb, Sr, U, Th relative to chondrites. The behaviour of the REE differ with respect to their ionic radii (which decreases regularly with increasing atomic number). The abundance of light REE in naturally occurring rocks varies greatly, compared with the heavy REE, which show limited variability. Nd is lighter than Sm, and therefore Nd shows greater variability. The Sm/Nd ratio of a rock can therefore by used to reflect the overall pattern of the REE.

A low Sm/Nd ratio is indicative of LREE enrichment
A high Sm/Nd ratio is indicative of LREE depletion

Continental crust is generally enriched in the light REE relative to heavy REE. Therefore rocks which show a low Sm/Nd ratio, can be inferred to have had continental crust involved in their petrogenesis.

Sm and Nd are chemically very similar. It is this similarity which results in minor fractionation, with Sm/Nd ratios of 0.1-0.5 [DePaolo, 1988 #193]. This is important because other nuclide pairs, e.g. in the U-Th-Pb system, or the Rb-Sr system, the strong chemical differences between the parent and daughter elements result in large fractionation effects. Isotopic variations in Nd and Sm are very slight compared with Rb-Sr and U-Th-Pb, but are still very important, because they are less mobile than Rb-Sr or U-Th-Pb, and are therefore generally undisturbed by near-surface processes.

It is unclear how mobile REE are during metamorphism and hydrothermal activity but it is likely that '*Sm-Nd isotopes are less vulnerable to disturbance during mild metamorphism than are Rb-Sr isotopes*' [DePaolo, 1988 #193].

Sm and Nd values are normalised to ^{144}Nd and ^{154}Sm respectively to give 'isotopic ratios'. One point of interest is that ^{144}Nd is itself radioactive so any ratio can be tainted by the decay of ^{144}Nd. This is considered negligible because the T½ is 4.5×10^{9} years, therefore since the formation of the solar system the abundance of ^{144}Nd has only decreased by 0.00015% [DePaolo, 1988 #193].

The variation of the ratio $^{143}Nd/^{144}Nd$ is quite minor (3-4 decimal places) in igneous systems and therefore a representation in terms of the deviation from a 'standard' value is useful. The

standard value commonly used is the CHondrite Uniform Reservoir (CHUR) [DePaolo, 1976 #194]. The amount of deviation is known as $\varepsilon_{Nd.}$ If the value is negative, the rock is said to be 'enriched' relative to CHUR and a positive value is said to be 'depleted' relative to CHUR. If $\varepsilon_{Nd}(T_x) = 0$ The rock is considered to be derived from a reservoir that had Sm/Nd ratio the same as CHUR during the time between the age of the earth T_0 and $T_{x.}$

From a rock of known age (any geochronological evidence), the initial Sm/Nd ratio can be calculated.

Mantle-derived magmas with a certain $^{143}Nd/^{144}Nd$ ratio, can assimilate crustal material with a different ratio of $^{143}Nd/^{144}Nd$ which results in igneous rocks of intermediate isotopic compositions. The incorporation of crust lowers the ε_{Nd} values. This may not be discernable with Sr isotopes alone because the contaminant may have similar $^{87}Sr/^{86}Sr$ ratios to the parental magma.

'Intraplate', 'OIB', or 'mantle-plume' related magmatism tend to display large ranges of ε_{Nd} values. This is due to the association of such enriched-magmas with crustal re-cycling [Weaver, 1991 #197].

Suites formed by fractional crystallisation alone will have consistent ε_{Nd} values whereas those formed by crustal contamination/assimilation/mixing will show a variety of ε_{Nd} values. Combined fractional crystallisation and contamination can be modelled using an ε_{Nd} or $^{143}Nd/^{144}Nd$ versus $^{87}Sr/^{86}Sr$ diagram.

7.7.2 Isotopic Data

A limited number of sedimentary rock samples from the Rakaia and Pahau Torlesse terranes were analysed alongside the volcanic samples to constrain a possible mixing end member in modelling. The data for the Torlesse samples are supplemented by unpublished data from Wandres (2002).

Crustal contamination as a modification of radiogenic isotope data may be tested by plotting the $^{87}Sr/^{86}Sr_i$ values against SiO_2; a positive correlation indicating the effects of crustal contamination. Fractional crystallisation alone would have the effect of raising SiO_2 contents as the magmas evolve but the initial Sr ratio should remain unchanged. A fractional crystallisation array would lie parallel to the x-axis on such a graph.

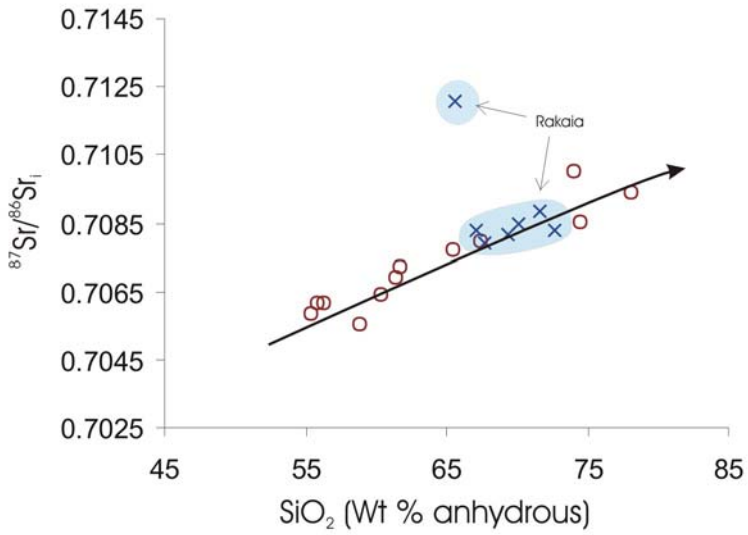

Fig.7.35 Initial Strontium versus SiO_2 content of MSVG lavas. Rakaia terrane samples are re-calculated to 97.5Ma.

The samples from the MSVG clearly indicate a positive correlation between increasing SiO_2 composition and $^{87}Sr/^{86}Sr_i$ ratio (fig.7.35). This strongly indicates that the lavas were contaminated by material with higher initial strontium ratios. The field of analysed Rakaia samples includes data from Wandres (2002) and provides a plausible contaminant by which to increase the the initial Sr ratio. The outlier is a mudstone from the Rakaia terrane. The elevation of SiO_2 beyond values recorded from the Rakaia terrane, requires either fractionation or partial melting of the Rakaia terrane.

The same trend is observed in fig.7.36, where the initial Nd isotopic composition decreases systematically with increasing SiO_2 composition. The interesting point to note from fig.7.36 is that the trend lies above the general field of Rakaia terrane. Certainly in the case of the Malvern Hills samples, the two filled circles lie on a trend which is similar to the general MSVG trend, however from fig.7.36 the contaminant would be interpreted to have significantly higher bulk Nd composition.

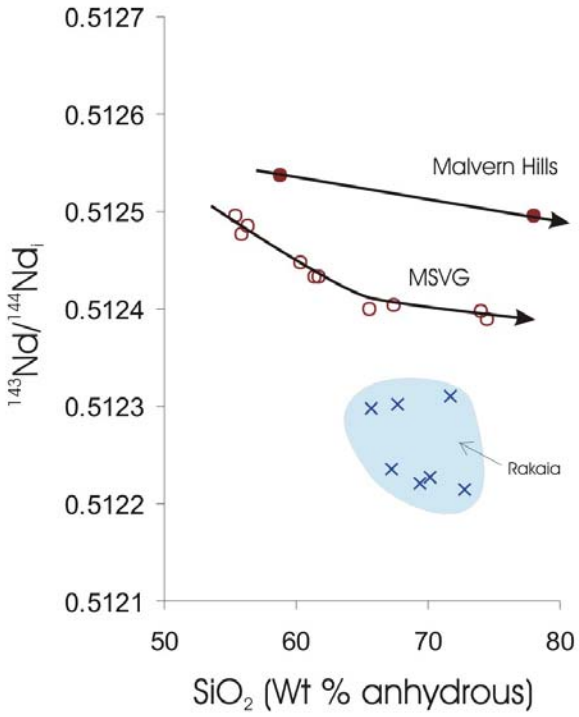

Fig.7.36 Initial Nd isotope values versus SiO_2 composition for the Malvern Hills and MSVG samples. Rakaia terrane samples are re-calculated to 97.5 Ma.

The trend of the MSVG on fig.7.36, appears to flatten out towards the higher silica contents. A flat trend would indicate that the drive in increased silica contents is as a result of fractional crystallisation and not increased contamination. From fig.7.36, the MSVG trend is consistent with combined contamination by partial melts of Rakaia terrane, coupled with fractionation up to a silica content of approximately 67%, followed by crystal fractionation processes which served to elevate the silica contents without a further significant decrease in Nd composition.

The Malvern Hills trend is inconsistent with contamination with the Rakaia terrane, as the trend lies well above the field for the analysed Rakaia terrane sediments. A contaminant with a higher Nd ratio is inferred as a mixing component. It must, however, be conceded that the

Malvern Hills 'trend' on the Nd versus SiO_2 plot is derived only from two data points and it is possible that the Rakaia terrane may have been incorporated in minor amounts followed by extensive fractionation, this is considered to be unlikely.

The Sr and Nd versus SiO_2 diagrams clearly show that contamination played a large role in the petrogenesis of the MSVG magmas. With the use of combined Nd and Sr isotopic data, parental and contaminant compositions can be modelled to explain the evolutionary trends (figs.7.37, 7.38 and 7.39).

The use of combined Nd and Sr isotopes gives a clearer indication of the role and composition of the parent and contaminant end-members.

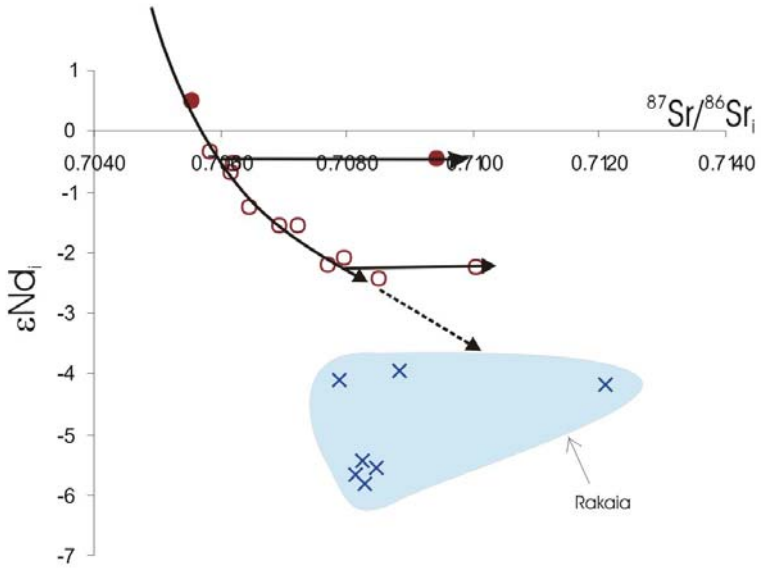

Fig.7.37 Initial εNd versus initial strontium for samples from the Malvern Hills and MSVG. Filled circles indicate Malvern Hills samples.

The arrows on Fig.7.37 indicate the deviation from the general trend of two rhyolite samples. The two outliers have elevated initial Sr contents but maintain the same εNd values. This can be explained in terms of two separate mixing end-members as shown in fig. 7.38, or artificial enhancement of Sr by hydrothermal alteration (fig. 7.39).

Simple two-component mixing can be modelled using a general mixing equation [Langmuir, 1978 #192]. The parameters used and the results of the modelling used in this project are presented in figs. 7.38 and 7.39.

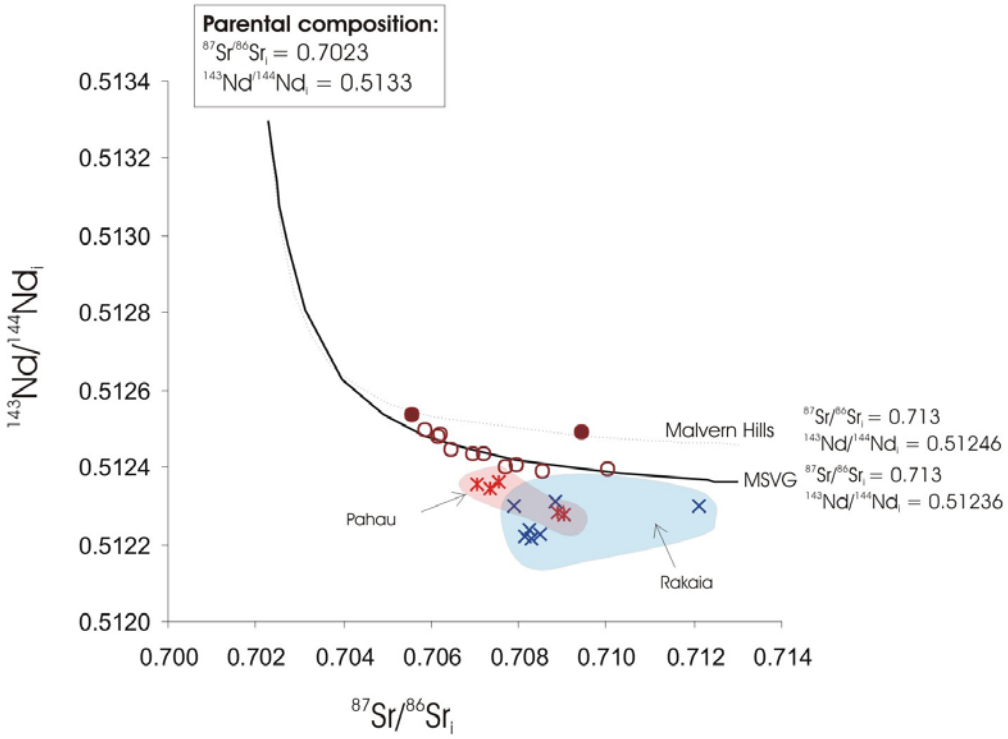

Fig.7.38 Model:1: $^{143}Nd/^{144}Nd_i$ versus $^{87}Sr/^{86}Sr_i$ for the samples from the MSVG. Malvern Hills curvature is based on Sr/Nd ratio of 0.7 and the curvature of the main MSVG trend is based on Sr/Nd ratio of 1.1. Filled circles represent Malvern Hills samples.

In model 1 (fig.7.38), which includes the two outliers identified in fig.7.37, the MSVG samples are clearly seen to trend down towards the field of the Rakaia terrane. The Nd values are, on the whole, slightly higher than those for the Rakaia terrane as is shown by the end member mixing composition for the main MSVG trend. This cannot be explained in terms of simple contamination by Rakaia terrane. Extrapolation of the trend of the graph towards parental compositions requires a parental magma composition of $^{87}Sr/^{86}Sr_i = 0.7023$ and $^{143}Nd/^{144}Nd_i = 0.5133$. The isotope ratio of the proposed parental magma is consistent with a derivation from spinel peridotite, based on the range of isotopic compositions of spinel peridotite [Hawkesworth, 1990 #199;Dickin, 1995 #200]. This is consistent with the partial melting of mantle wedge peridotite.

This model requires two separate end-member sediment mixing components to account for the two apparent mixing curves.

An alternative model would require one mixing end-member with the deviation of the two rhyolite outliners explained by hydrothermal alteration which elevates the initial Sr composition from the main trend (fig.7.39).

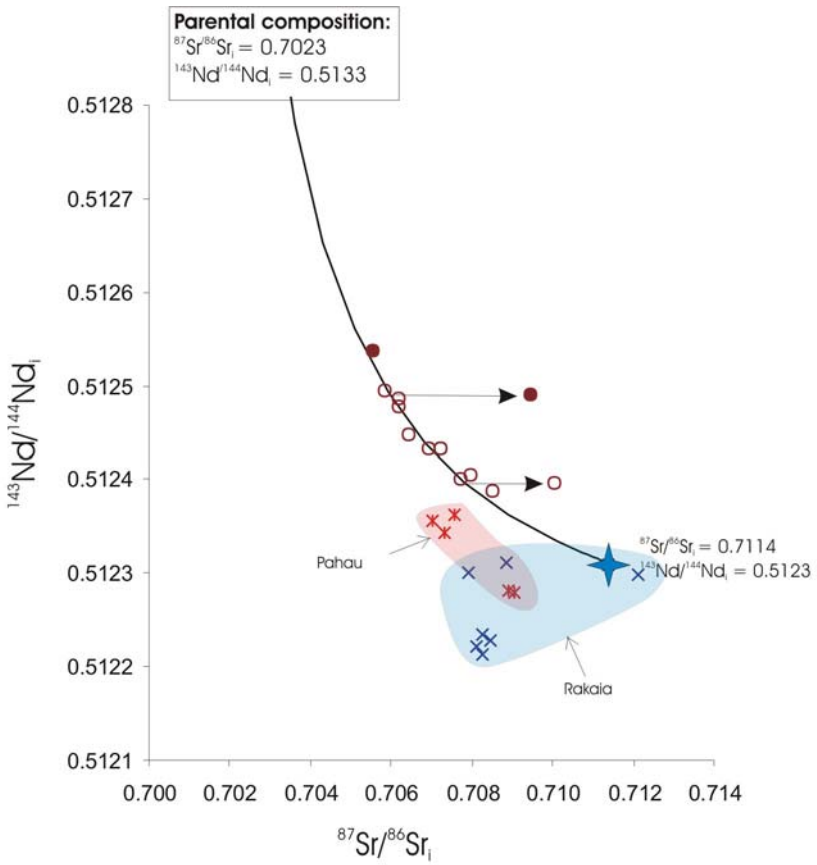

Fig.7.39 Model 2: initial Nd versus initial Sr isotope diagram illustrating the elevation of $^{87}Sr/^{86}Sr$ for the MH (filled circles) and MS (open circles) rhyolites due to hydrothermal alteration.

The mixing end-member does not plot in the centre of the Rakaia terrane field, however it does plot within the field which is a more satisfactory mixing component than the two end-member compositions required in fig.7.38. The high Sr sample plotted in fig. 7.38 and 7.39 is a mudstone. Given the heterogeneous nature of the Torlesse, which contains a substantial amount of mudstone, the bulk Rakaia terrane isotopic composition would be expected to fall between the fine sandstone samples and the mudstone. The proportion of mudstone to sandstone in the assimilant is unknown but the end-member modelled in fig. 7.39 is an acceptable composition. By extrapolating the two rhyolite outliers back to the main trend, their position down the mixing line implies that fractional crystallisation (elevating the SiO_2), played a more important role in the petrogenesis of the Malvern Hills samples than with the rest of the MSVG samples.

A supporting factor for model 2 (fig.7.39) would be that another rhyolite sample (MS-99), which is a pitchstone, plots at the end of the main trend, closest to the Rakaia end-member. Obviously fresh samples were of paramount importance in this study, however in order to attain a good cross-section of lithologies, both pitchstone and ignimbrite were analysed for the MSVG. Model 2 would suggest that the ignimbrites have been subjected to alteration which has preferentially enriched the initial Sr values, whereas the fresh pitchstones such as MS-99 are unaltered.

The mobility of the LILE such as Rb and Sr means that they are susceptible to hydrothermal alteration. The outlying samples in fig.7.39 are interpreted to have elevated initial Sr values resulting from the removal of Rb during hydrothermal alteration.

Pb isotopes are of limited use when substantial degrees of crustal contamination have taken place. Fig.7.40 illustrates the Pb isotopic variation of the MSVG samples. Also plotted on Fig. 7.40 are the three Pb isotope values from the analysed Rakaia terrane rock samples; the Rakaia terrane samples are re-calculated to an age of 97.5Ma. Sample RG-4, which is the coarsest Rakaia terrane sample, extends the field to high values of $^{206}Pb/^{204}Pb_i$. The MSVG samples form a linear trending field which extends towards the field of analysed Rakaia terrane. All the samples are more radiogenic than MORB with respect to $^{207}Pb/^{204}Pb$, which has $^{207}Pb/^{204}Pb$ ratios of approximately 15.3 to 15.6. This indicates that the MSVG magmas experienced crustal interaction during their formation and evolution.

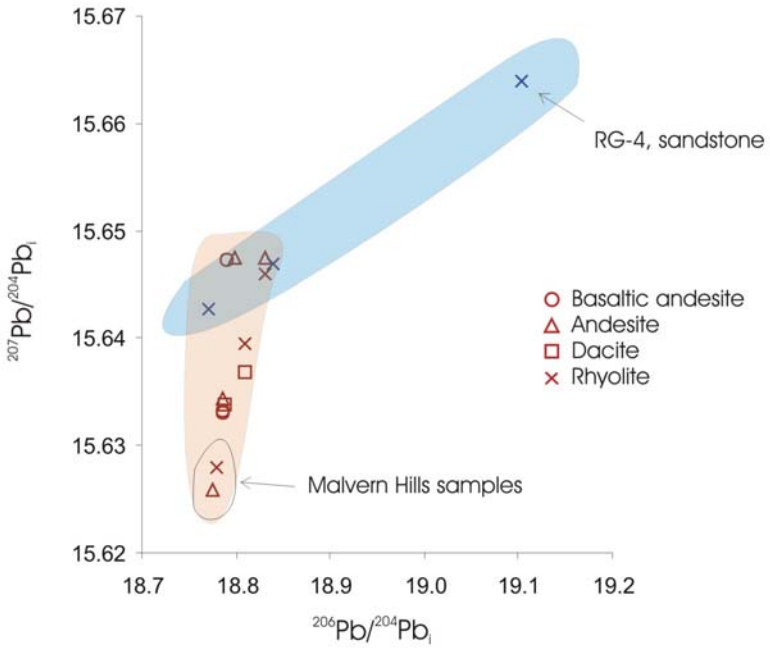

Fig. 7.40 Initial $^{207}Pb/^{204}Pb$ versus initial $^{206}Pb/^{204}Pb$ ratio for samples from the MSVG. All samples, including Rakaia terrane samples were re-calculated to 97.5Ma.

The MSVG samples are highly variable in terms of $^{207}Pb/^{204}Pb$ ratio, which varies from 15.626 to 15.647. The Malvern Hills samples have the lowest $^{207}Pb/^{204}Pb$ ratios which supports the interpretation that the Malvern Hills magmas were contaminated to lower degrees than the rest of the MSVG. There is a great deal of overlap and the most evolved samples (highest SiO_2) do not have the highest Pb ratios. Limited information can be drawn from fig 7.40 without further Pb isotopic analysis of the Rakaia terrane. It is likely that the field for Rakaia terrane is considerably larger than that displayed in fig. 7.40.

7.8 Conclusions

- The MSVG was derived from partial melting of a subduction-modified mantle wedge of probable spinel peridotite composition.

- The andesites, dacites and rhyolites evolved from the basaltic-andesites through assimilation fractional crystallisation (AFC) processes (*cf* Barley, 1987 and Wood, 1974). The modelled assimilant has trace element characteristics of the Rakaia

terrane. AFC modelling indicates that the rate of assimilation increased as the magmas evolved, generating dacites and eventually rhyolites. The Nd radiogenic isotope data indicates that the rhyolites retain an isotopic link with the basaltic-andesites.

- In the Malvern Hills, assimilation of Rakaia crust played a lesser role than in the other areas of the MSVG, and crystal fractionation imparted a stronger influence on the petrogenetic path from basaltic-andesite to rhyolite.

- The nature of the contaminant remains un-resolved, however an end-member similar in composition to the Rakaia terrane surface samples analysed, but with potentially different oxygen isotope characteristics is implied. The oxygen isotope data suggests that the assimilant was probably more enriched in O^{18} than the three analysed surface samples of Rakaia terrane.

- Equilibrium phenocryst assemblages and geobarometry data (Wood, 1974 and Barley, 1987) shows that the early phenocryst phases of the MSVG magmas crystallised at significant depth, probably at or near the crust-mantle transition zone.

- The rapid rise of the rhyolite magmas (which precluded significant resorption of the high-pressure phenocryst assemblage) from the lower crust, was probably tectonically controlled. The anhydrous nature of the rhyolites would have facilitated the transport of these magmas to low crustal levels. The volatile content of the rhyolitic magmas was probably the determining factor in whether rhyolite or ignimbrite was erupted. The andesites and dacites show evidence of P-T re-equilibration as they rose through the crust.

Chapter 8:

Geochemistry and Petrogenesis of the MIC

8.1 Introduction

The major and trace element geochemistry was obtained using the Philips 2400 XRF at the University of Canterbury. Additional trace element and rare earth element data were acquired at the Institute of Geological Research at the Christian Albrechts University, Kiel, Germany. Radiogenic isotope chemical preparation and analyses were undertaken at GEOMAR Research Institute in Kiel, Germany; using a Finnigan MAT 262 mass spectrometer.

For a full description of techniques used, and tables of data refer to Appendices 3, 4 and 5.

8.2 Mineralogy

The MIC is composed of a variety of plutonic, hypabyssal and volcanic rocks which have evolved through predominantly crystal fractionation processes to end-members which are both silica (over)saturated and silica-undersaturated (refer Appendix 2 for petrographic summaries).

The silica (over) saturated rocks of the MIC range from basalt-trachybasalt-basaltic trachyandesite-trachyandesite-trachyte and their plutonic equivalents. The mineral assemblage progresses from augite-olivine-plagioclase-magnetite; to plagioclase-augite-magnetite with minor brown amphibole and biotite; to plag-alkali feldspar-augite-magnetite with minor brown amphibole and biotite; and finally to alkali feldspar-± quartz-biotite-brown amphibole-magnetite.

The mildly silica undersaturated rocks of the MIC range from tephrite-phonotephrite-tephriphonolite, but do not extend to phonolite compositions. The mineral assemblage is alkali feldspar-plagioclase-amphibole (brown hornblende and arfvedsonite)-biotite-epidote

(late stage deuteric phase)-magnetite; to alkali feldspar-amphibole-clinopyroxene (aegirine and augite)-plagioclase-magnetite-(± nepheline). The silica undersaturated sequence contains a higher proportion of hydrous minerals (amphibole and biotite), which are also high K/Na phases.

The plutonic rocks crystallised at low pressures. This is clearly evident from their intrusive contacts with the volcanic carapace and the development of pegmatite zones towards the top of the intrusions (Chapter 5).

8.3 Major Element Geochemistry

The MIC comprises a suite of alkaline, intrusive and volcanic rocks which display a wide range in bulk composition from picro-basalts to tephri-phonolites, syenites and trachytes (fig 8.1).

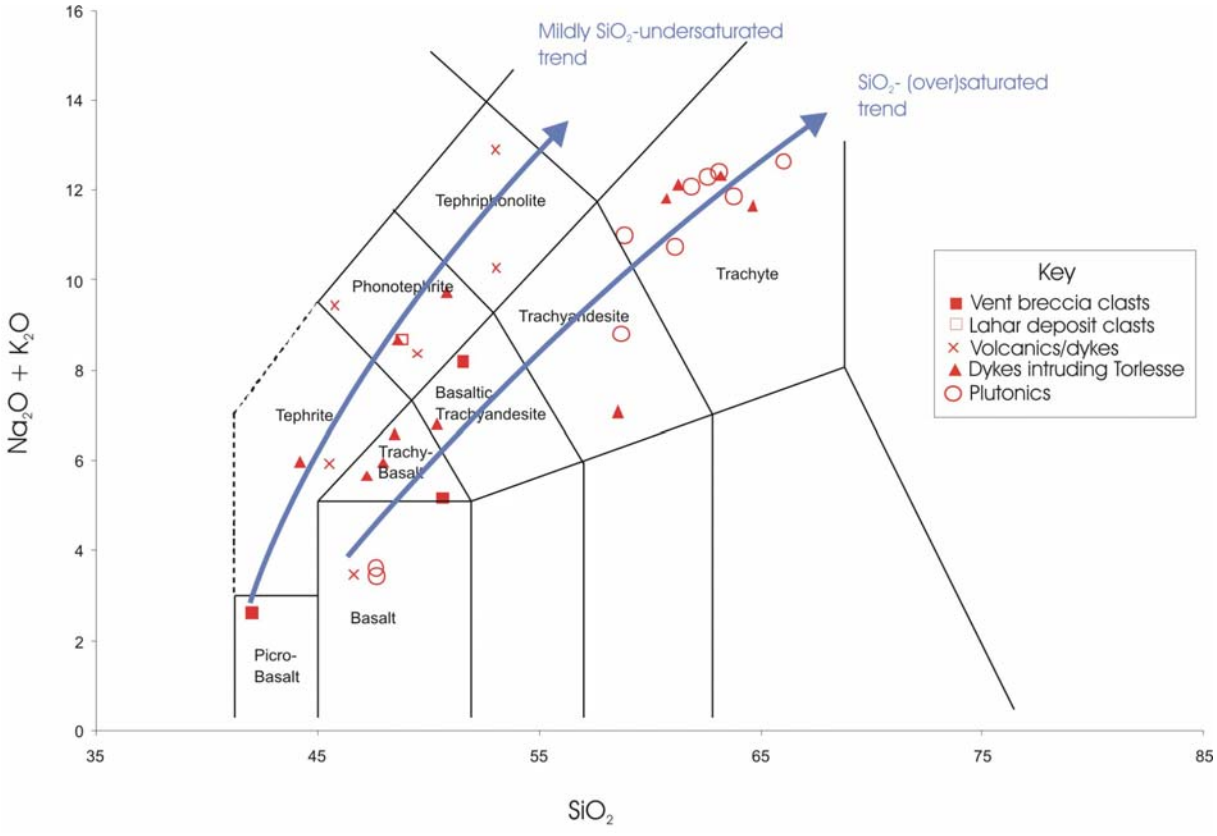

Fig.8.1 Total Alkali-Silica (TAS) diagram showing the data from the MIC (Le Maitre *et al.*, 1989).

The TAS diagram shows fine-grained volcanic nomenclature, however the open circles are the plutonic equivalents. Each component of the MIC (e.g. lahar clasts, plutonics, lava flows) show a progressive trend to higher alkali and SiO_2 contents. The increase in alkali content is due to the general incompatibility of these elements in the early stages of fractionation.

The TAS diagram in fig. 8.1 shows two distinct trends originating from mafic compositions that probably had a range in the degree of silica under-saturation. The slightly silica under-saturated trend extends to tephriphonolite compositions and the silica (over)saturated trend extends to trachyte and quartz-bearing syenite. The under-saturated trend is probably due to lower degrees of partial melting, the melt fractions from which fractionated separately from the more saturated higher degree melts thereby producing two fractionation trends on the AFC diagram (fig.8.1). The silica under-saturated rocks are generally of small volume and manifest as dykes intruding both the Torlesse basement and syenite, and form the main mass of the 'Mafic lavas' and 'Alkali Microgabbro' (ref. Chapter 5). The age relationships between the mildly under-saturated and (over)saturated trends are relatively complex. The under-saturated units are observed to both intrude syenite (tephriphonolite dyke intruding syenite at GR M33/7723 2605) and to be intruded by syenite (Mafic lavas intruded by micro-syenite veins at GR M33/7551 2558).

The plutonic rocks shown in fig. 8.1 are all silica-saturated or oversaturated and the syenites often have small quantities of quartz (ref. Appendix 2 for petrographic summaries). The scatter in the trend in fig.8.1 is a result of differing crystallising phases, variable degrees of crustal contamination and alteration. The heavily altered trachyte lava flows were not analysed for major or trace elemental analysis which is why there appears to be no volcanics of trachytic composition in the data set.

For the purposes of trace-element plotting the TAS diagram can be sub-divided into three fields. Field one can be described as the 'mafic' components: gabbro, basalt, tephrite and trachy-basalt; field two can be described as the 'intermediate' components: basaltic-trachyandesite, phono-tephrite, tephri-phonolite, trachy-andesite and diorite; and field three can be described as 'evolved': trachyte and syenite (fig.8.2).

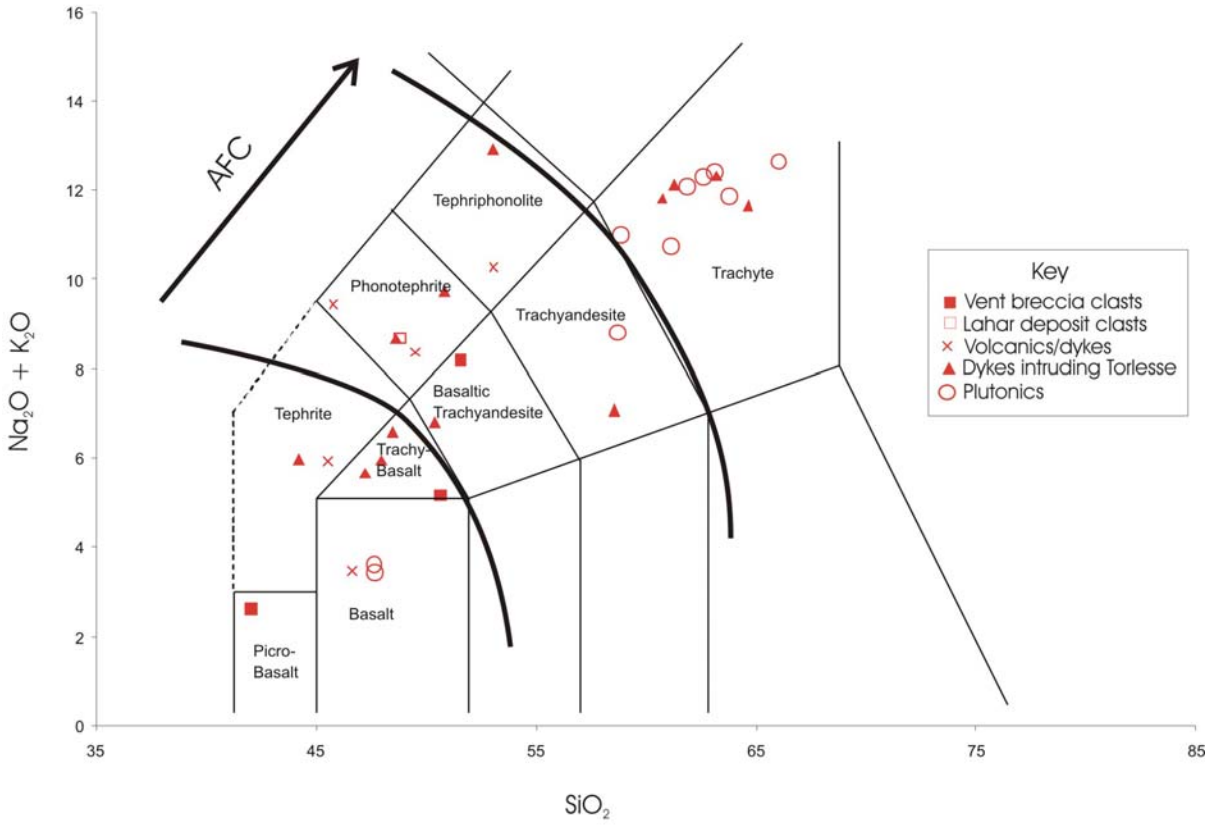

Fig.8.2 Modification of the TAS diagram to show the subdivision of the MIC for the ease of trace-element plotting and interpretation.

The major element variation with increasing SiO_2 content is shown in fig.8.3.

Al_2O_3 and Na_2O increase initially to SiO_2 concentrations of approximately 50-55%, as they are incompatible during the early stages of fractionation. After the 50-55% threshold, they both show a steady decline due to depletion by crystallising plagioclase (labradorite-andesine). The under-saturated trend is similar, but the concentrations of Al_2O_3 and Na_2O are slightly higher. Fe_2O_3t and MgO decline due to the early crystallisation of olivine and clinopyroxene in the less evolved samples (lower SiO_2). The Fe_2O_3t trend is similar for both the saturated and under-saturated samples. The MgO and CaO trends for the under-saturated samples are parallel, and the SiO_2 undersaturated trend is displaced to lower SiO_2 concentrations.

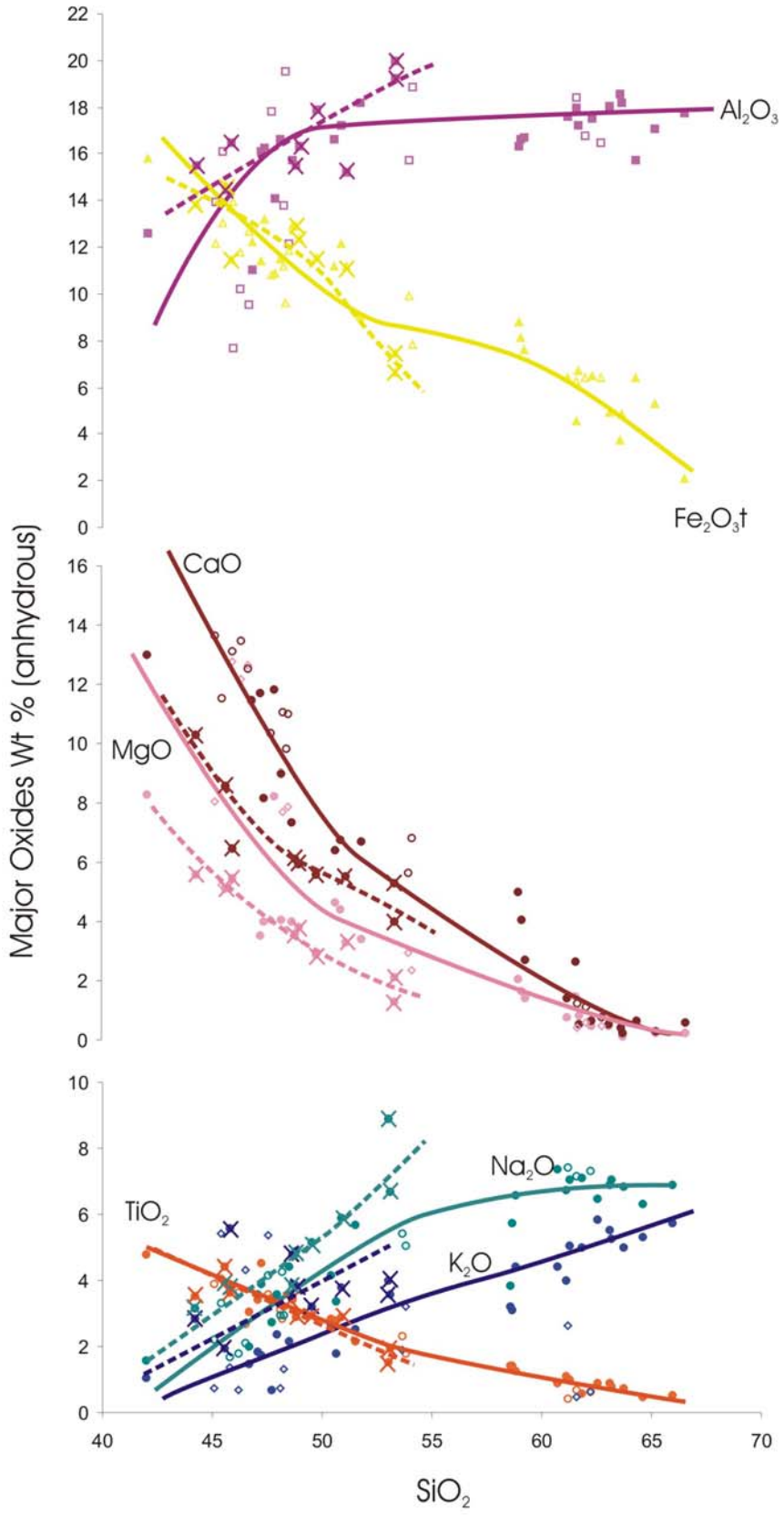

Fig.8.3 Compound Harker diagram showing the major element variation in the MIC. Hollow symbols represent unpublished data of S.Weaver, they are coloured to represent the same element as the data from this study. Crosses indicate samples from the SiO_2-undersaturated sequence shown in fig. 8.1. Solid lines show the trend of SiO_2-(over)saturated sequence and dashed lines show the trend of the SiO_2-undersaturated sequence.

MgO and CaO decline due to the incorporation of MgO into olivine and CaO into Ca-clinopyroxene and Ca-rich plagioclase. TiO_2 is continuously depleted due to the crystallisation of Fe-Ti oxides such as titano-magnetite. K_2O shows a gradual increase toward the more evolved samples, indicating its general incompatibility. The concentrations of K_2O in the under-saturated trend are higher due to the incompatibility of K_2O and its preferential concentration during partial melting.

8.4 Trace Element Geochemistry

Seven samples from the MIC were analysed for 26 trace elements and REE by ICP-MS. All samples are displayed on one spider diagram, normalised to primitive mantle (Hofmann, 1988). The SiO_2 under-saturated samples (M-40, M-84 and M-86) are included in the diagram below because they show similar trends to their SiO_2 (over) saturated counterparts (approximately M-66, M-78 and M-12 respectively). The variation is due to the separate fractionation paths followed by the two sequences (fig. 8.1).

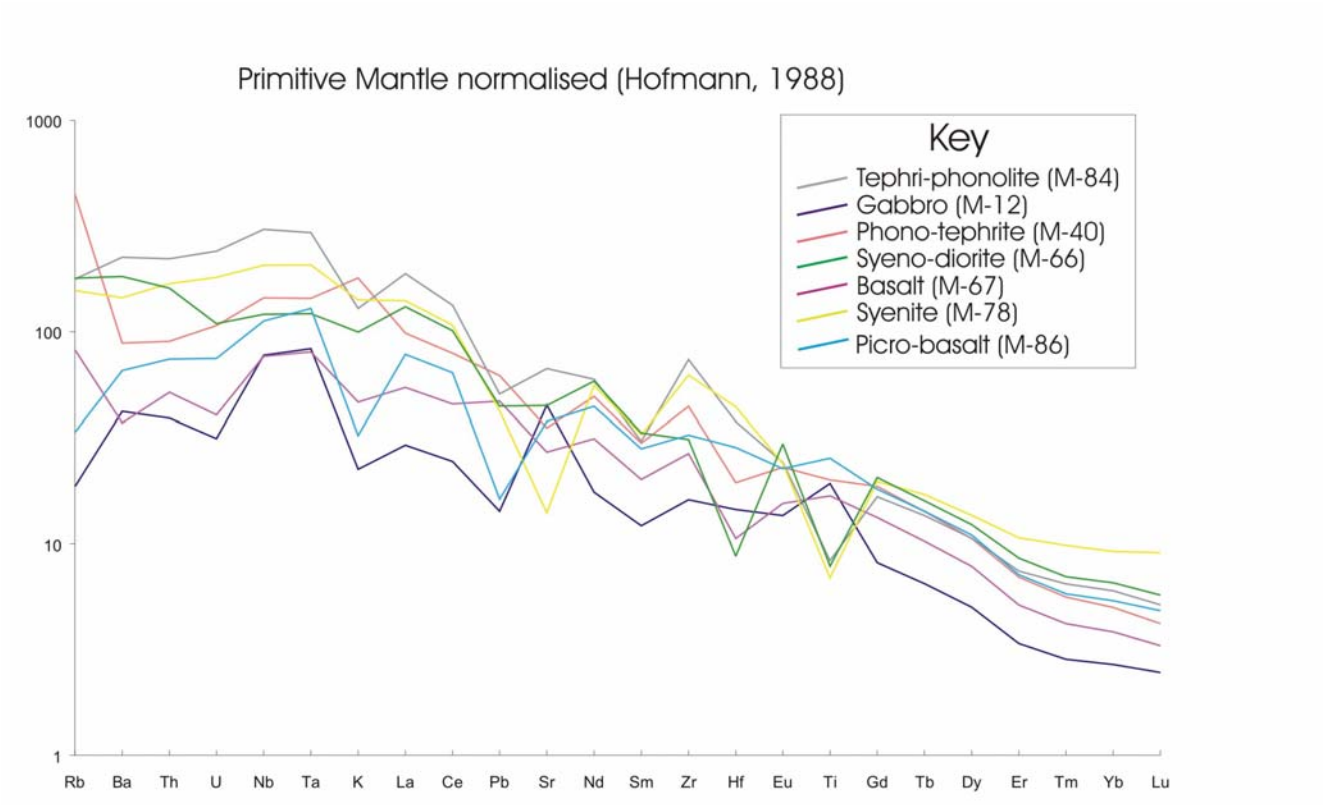

Fig.8.4 Multi-element diagram normalised to primitive mantle (Hofmann, 1988).

The spider diagram displays a range of trace element patterns but with a notable absence of the typical 'spiky' subduction signature exhibited by the MSVG. Instead, the samples show strong enrichment in the highly incompatible elements and light REE, with a trough, or flat pattern at Pb.

The limited data available from the MIC is supplemented by unpublished data provided by S.Weaver. The supplementary data was measured using XRF and NAA. To aid interpretation, the spiderdiagram is re-plotted in fig.8.5 and shaded according to the subdivision described for fig.8.2.

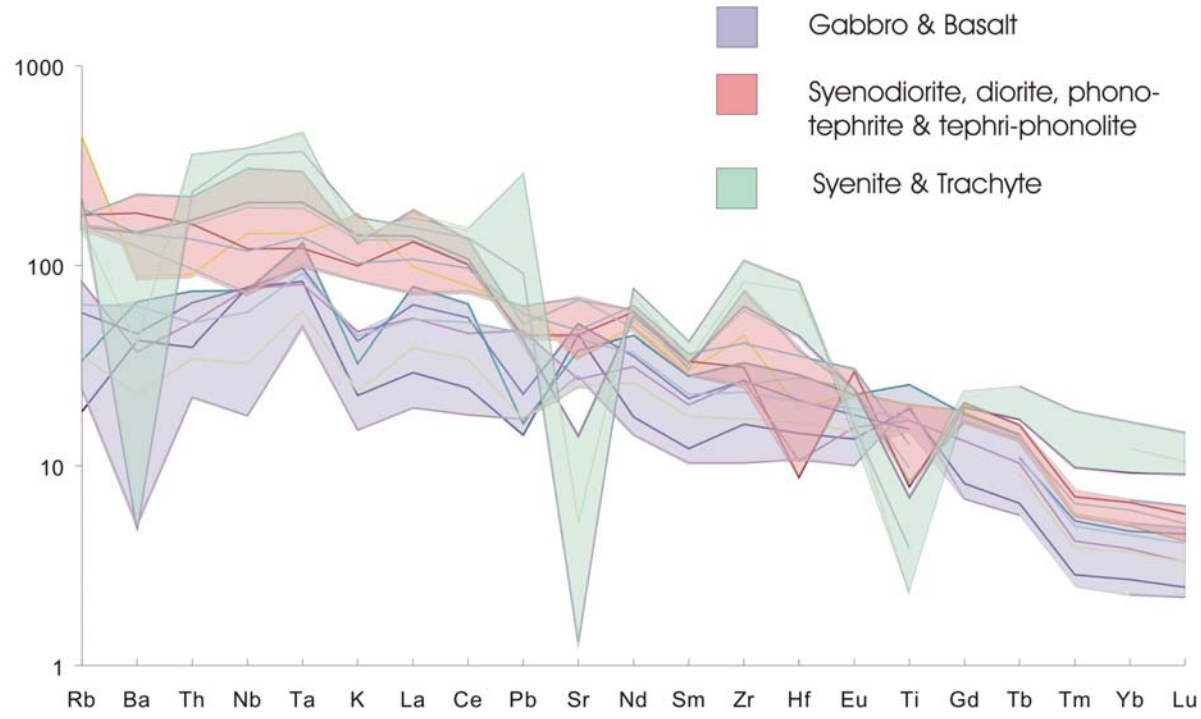

Fig.8.5 Spiderdiagram incorporating unpublished data from S.Weaver.

The MIC samples have La/Nb ratios of 0.38-1.09 with an average of 0.69. This ratio is significantly lower than the La/Nb ratio of subduction derived magmas or MORB. It is more akin to the HIMU end-member composition of La/Nb=0.66 – 0.77 (Weaver, 1991).

All samples from the MIC are highly enriched in incompatible elements relative to primitive mantle. The mafic rocks (gabbro and basalts) show the lowest concentrations of trace elements with peaks at Nb, Ta, Zr, Ti and the LREE. The intermediate rocks (syenodiorite, diorite, phonotephrite and tephriphonolite) show a general elevation in all elements, however

strong variation is observed between the HFSE: Nb, Ta, Zr, Hf and Ti concentrations. The more evolved samples (syenite and trachyte) show highly irregular trace element patterns with strong enrichment in Th, Ta, Nb, Zr and Hf, coupled with extreme depletion in Sr and Ti. Ba is moderately to strongly depleted relative to the mafic and intermediate samples. The REE are generally elevated although the lightest REE show similar values to those of the intermediate samples. Pb is highly enriched in one sample.

Sample M-84 (tephriphonolite) from the SiO_2-undersaturated trend (fig. 8.1) forms the upper limit of the intermediate group shaded on fig. 8.5 from Rb to Ce. This is consistent with the rock being formed through fractional crystallisation from a parent magma containing higher concentrations of incompatible elements and lower SiO_2 contents than its SiO_2 saturated counterpart. This relationship is consistent with the SiO_2-undersaturated parent magma being the product of lower degrees of partial melting.

The elevation of incompatible elements and REE is consistent with fractional crystallisation processes in which the incompatible elements are concentrated into the most evolved samples. The clear depletion of Sr and Ba is consistent with plagioclase feldspar fractionation (Long, 1978) (fig.8.6) and the gradual depletion in Ti is related to the continual crystallisation of Fe-Ti oxide phases such as titano-magnetite (as shown from the TiO_2 variance on fig.8.3).

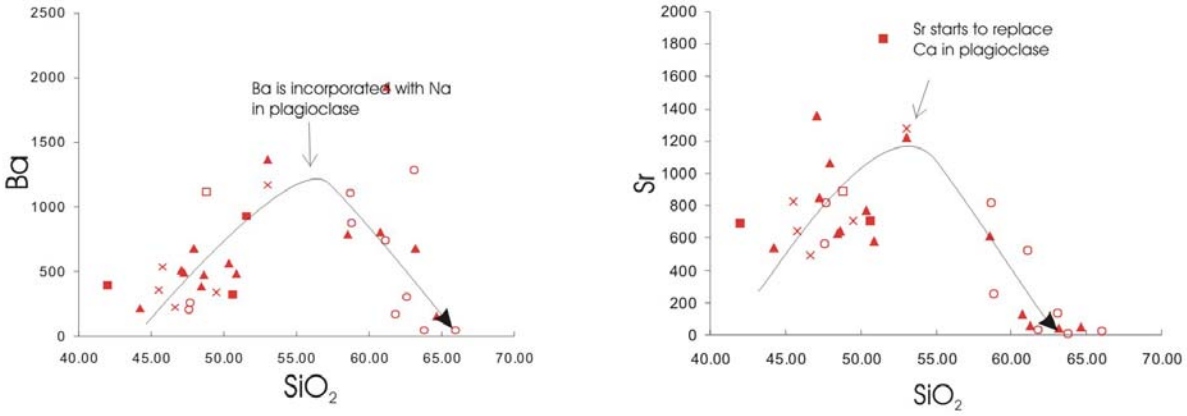

Fig.8.6 Ba and Sr variation with SiO_2 content in MIC samples. The symbols are the same as those used in fig.8.1.

On bivariate plots of incompatible elements (fig.8.7), a good correlation is generally noted and therefore the ratios of incompatible elements are relatively constant. The SiO_2-undersaturated samples (M-84, M-86 and M-40) fall on the same trend as the SiO_2-saturated

samples, which indicates that the incompatible element ratios of the source region of the two trends was the same. Variation in incompatible-element concentrations between points of the same SiO_2-saturation (whilst maintaining a constant ratio), are due to fractional crystallisation processes.

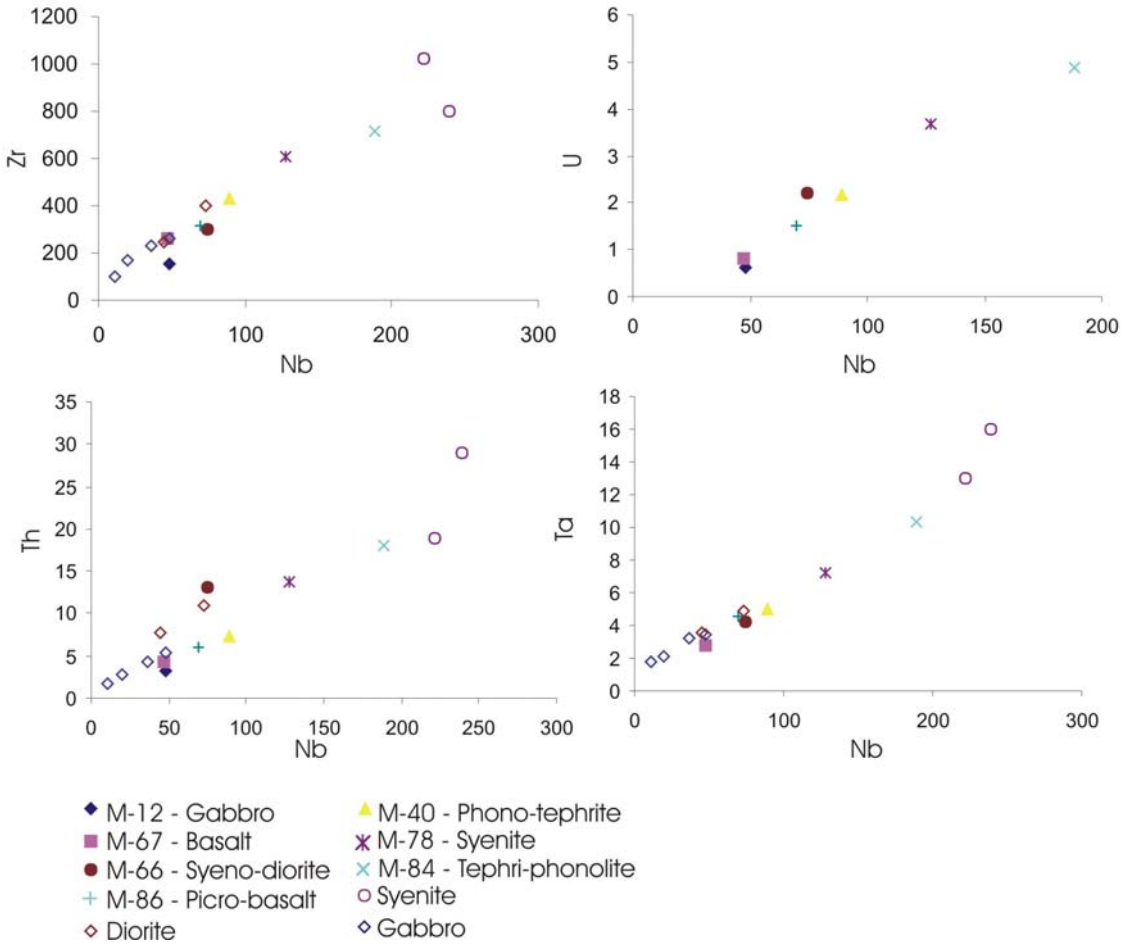

Fig.8.7 Bivariate plots of incompatible trace elements for the MIC. Open symbols represent unpublished data provided by S.Weaver.

Fig 8.8 compares the MIC with the generally accepted composition of N-MORB, E-MORB, OIB and St. Helena HIMU mantle reservoirs. The very high concentration of incompatible elements displayed by the MIC is similar to those of oceanic island basalts (OIB) and St. Helena HIMU.

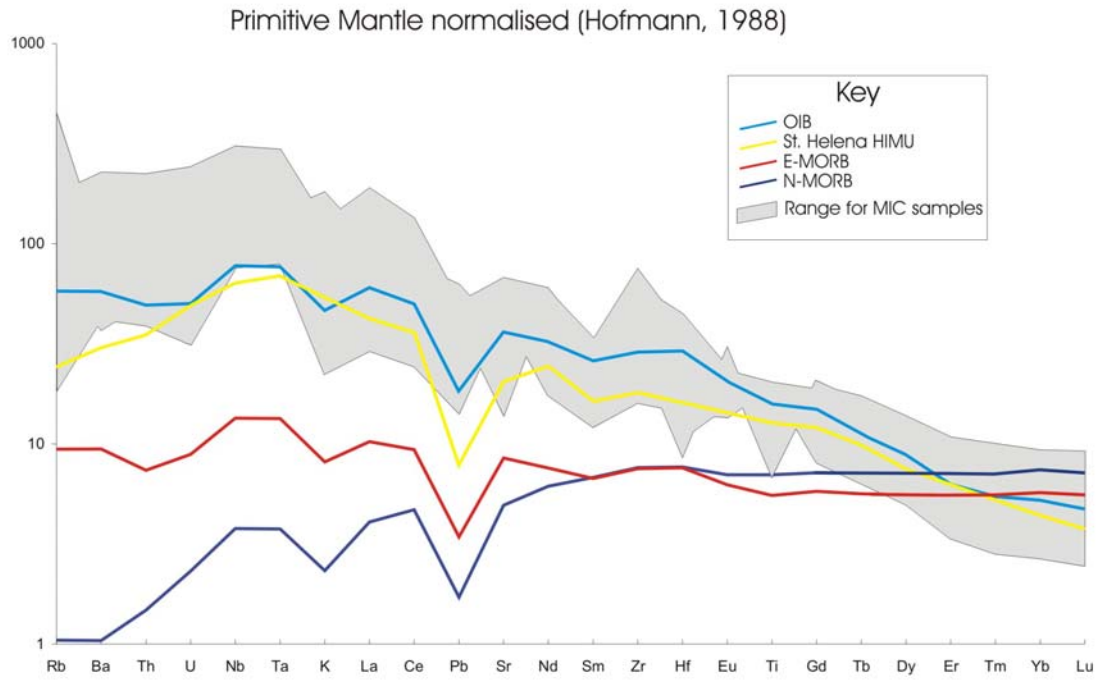

Fig.8.8 Multi-element diagram showing the range of values for the MIC samples compared with N-MORB, E-MORB, OIB (Sun & McDonough, 1989)and St. Helena HIMU (Chaffey *et al.*, 1989).

Using the Ti/Y versus Nb/Y tectonic discrimination diagram (Pearce, 1982), the basalt and gabbro samples (as subdivided in fig.8.2) from the MIC fall clearly within the field for 'Within Plate Basalts' (fig.8.9). The intermediate and evolved samples such as syenodiorite and syenite are excluded since the tectonic discrimination diagram is only appropriate for samples of basaltic composition.

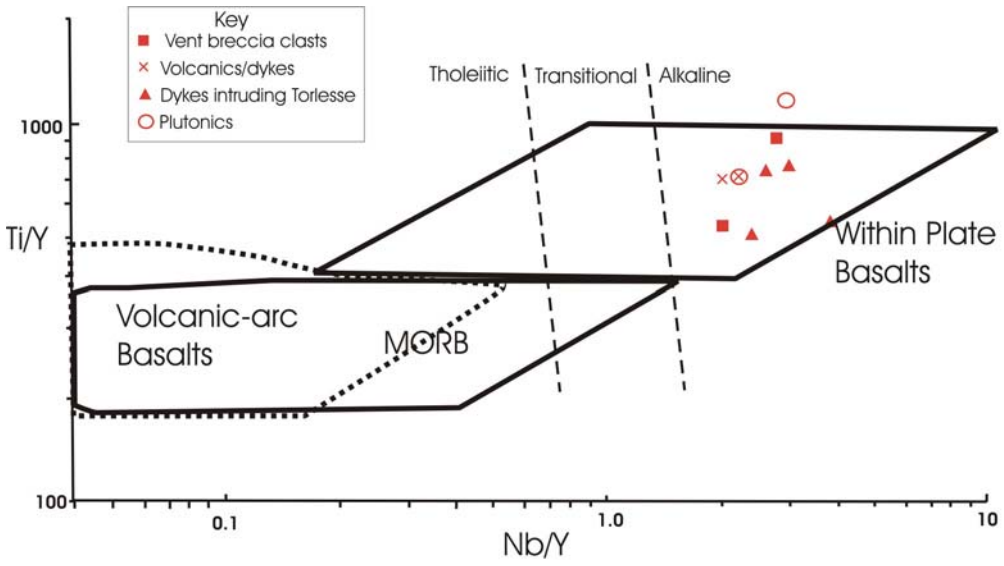

Fig.8.9 Ti/Y versus Nb/Y for MIC basaltic samples. Diagram adapted from Pearce (1982).

Given the within-plate, OIB characteristics of the MIC, it is reasonable to try to establish a parental source magma based upon the end members of oceanic island basalts (OIB). The typical enrichment of OIB in incompatible elements, especially the HFSE, has led to the subdivision of OIBs into EMI, EMII and HIMU end-members based upon the ratios of incompatible elements (Hart, 1988; Weaver, 1991). Fig.8.10 illustrates one such variation diagram upon which the three end-members can be plotted.

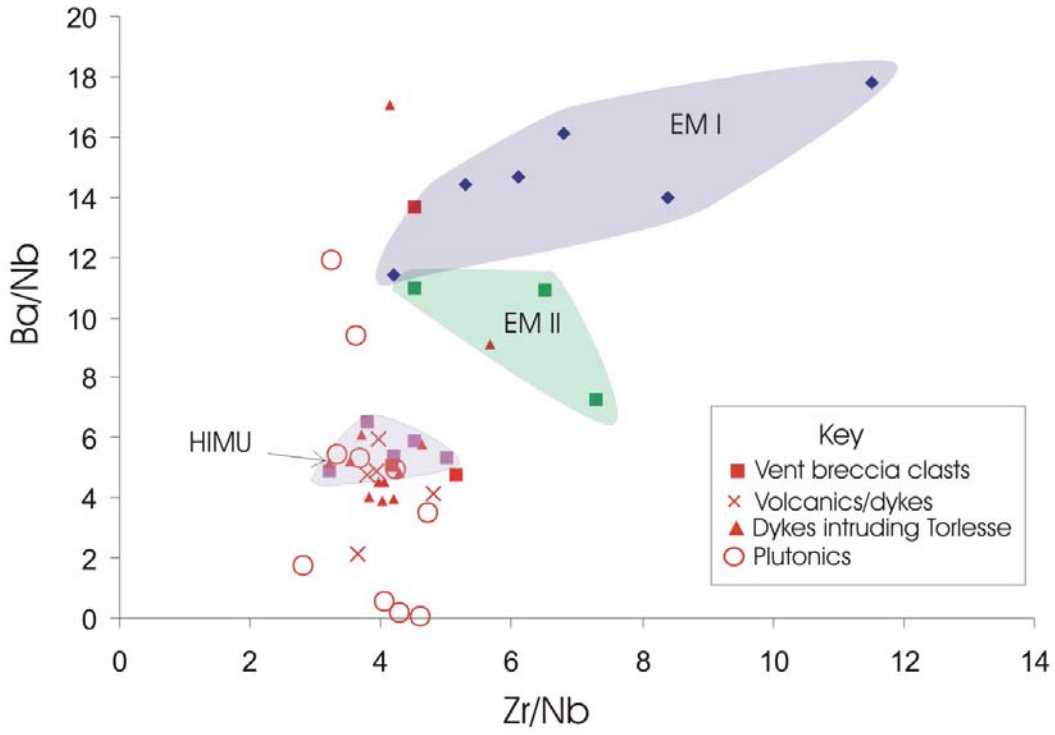

Fig.8.10 Ba/Nb versus Zr/Nb plot indicating the fields of EM I, EM II and HIMU oceanic island basalt groups. Data plotted for the fields is derived from Weaver (1991) and references therein (Weaver, 1991). MIC samples are plotted as small red triangles.

The MIC samples show a range of Ba/Nb ratios with a predominant cluster close to the field of HIMU. Elevation to higher Ba/Nb ratios is due to high concentrations of plagioclase feldspar in the intermediate plutonics and volcanics (e.g. syenodiorite and trachyandesite). The vent breccia clast which falls inside the EM-I field is a foid-bearing monzonite with a high proportion of plagioclase feldspar.

The samples which plot below the values in the HIMU field are generally the more evolved rocks e.g. syenite, trachyte and tephri-phonolites. The decrease in Ba with associated levels of SiO_2 is clearly depicted in fig.8.6. The incompatibility of Nb results in its enrichment at

greater degrees of differentiation compounding the decreased Ba/Nb ratios at high levels of differentiation.

Figure 8.10 is therefore most appropriately used for fine-grained mafic rocks. When only the fine grained mafic rocks (as shown in fig.8.2) are displayed on the same diagram (fig.8.11) the samples are clearly seen to fit within or close to the field of HIMU.

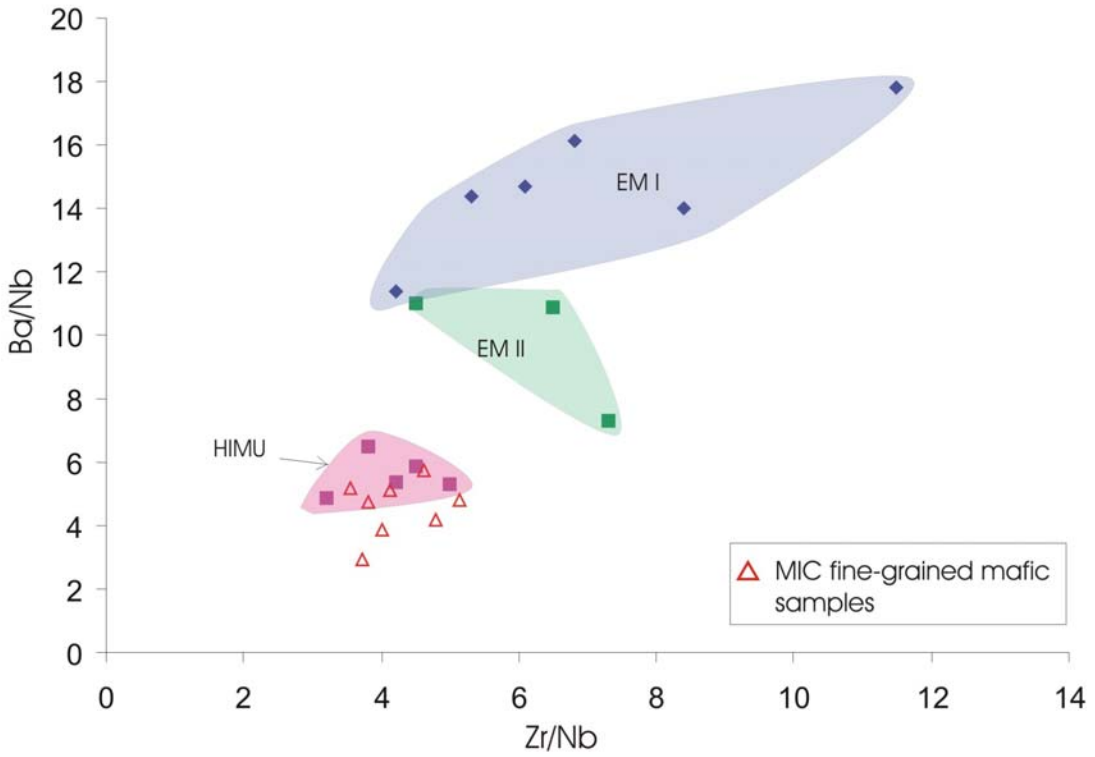

Fig.8.11 Ba/Nb versus Zr/Nb for fine-grained mafic samples from the MIC. Fields and data points for EM I, EM II and HIMU are from Weaver (1991).

8.5 Rare Earth Element (REE) Data

For data tables refer to Appendix 4.

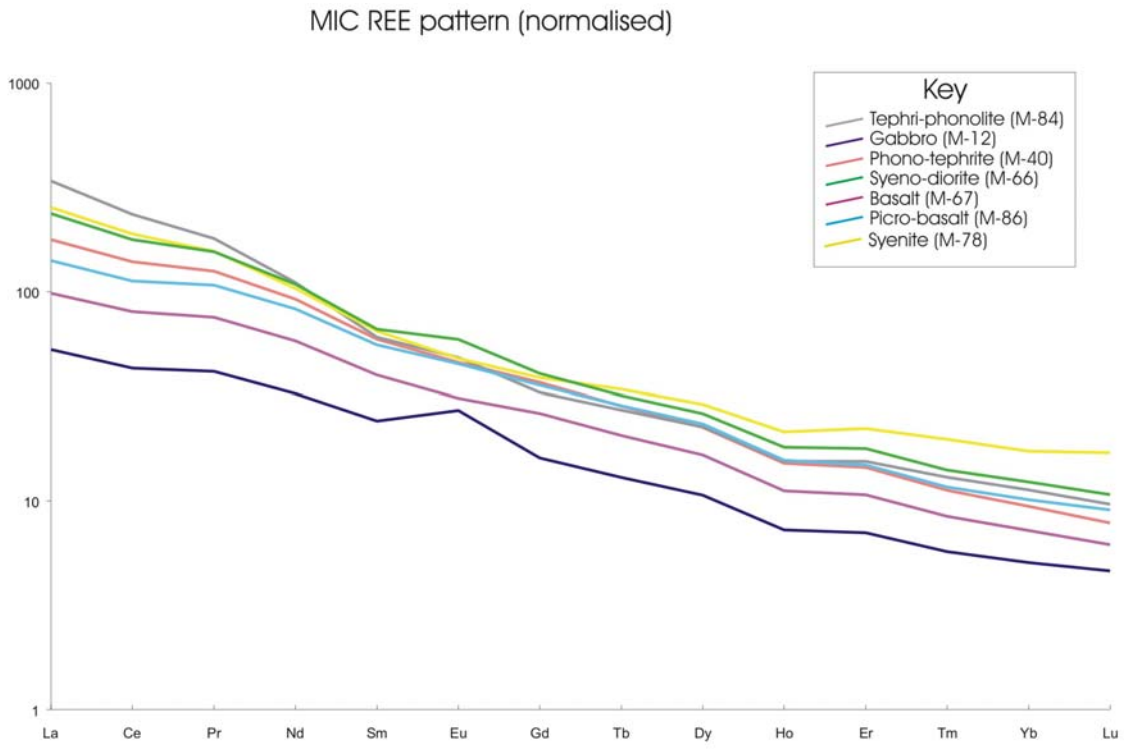

Fig.8.12 REE patterns for samples from the MIC, data normalised to chondrite values of Boynton (1984).

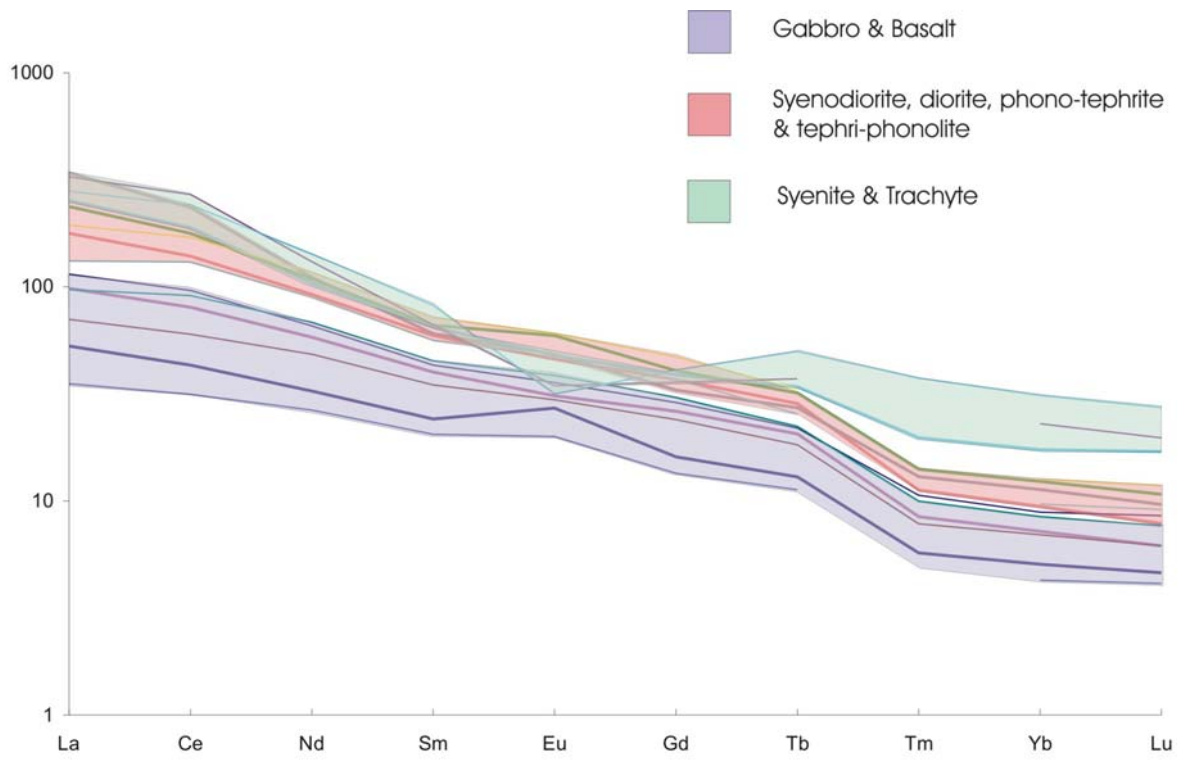

Fig.8.13 REE pattern for the MIC plus additional unpublished data from S.Weaver. Values normalised to chondrite value of Boynton (1984).

The MIC display LREE enriched patterns (fig.8.12), with La_N/Lu_N ranging from 11.45 to 35.25 (Average=19.70). As shown in fig.8.14, the concentration of LREE (represented by La) increases with increasing degree of differentiation (increasing SiO_2 content). The plutonic samples (and basalt) show a good positive correlation with SiO_2. The under-saturated samples (M-40, M-84 and M-86) also show a positive correlation with SiO_2, however are generally displaced to lower SiO_2 and higher La levels. La forms a good correlation with Lu up to the field for the evolved samples (syenite and trachyte), where the trend plateaus. Lu concentrations continue to increase, whereas La concentrations plateau. This is a result of the compatibility of La at high levels of differentiation and the incorporation of the LREE into lanthanide epidote (allanite) and monazite.

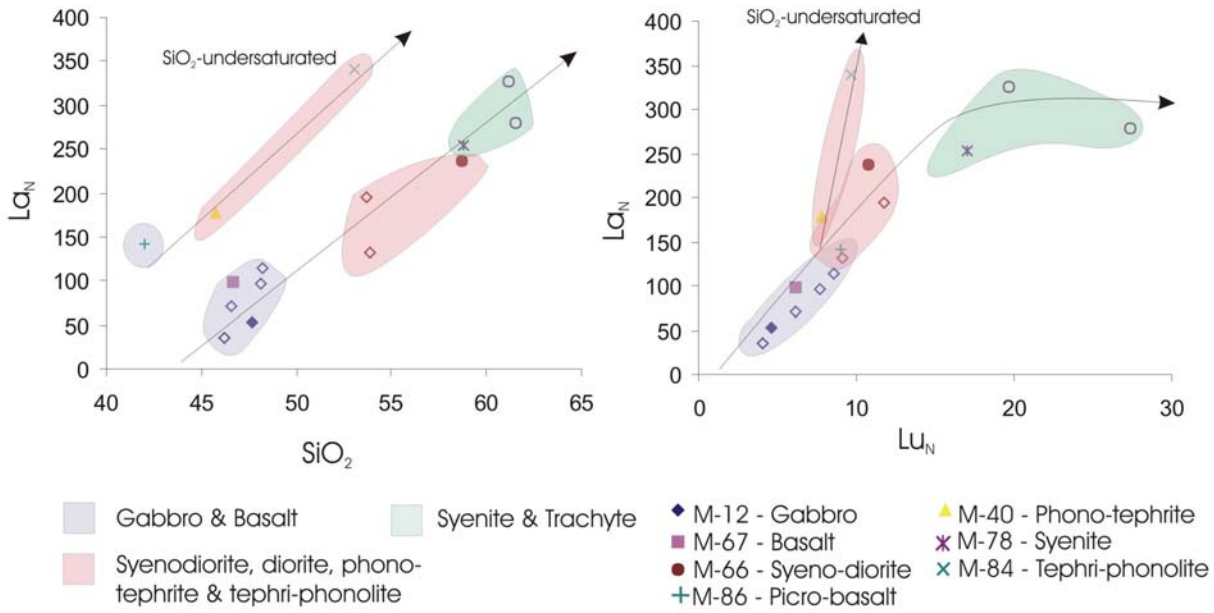

Fig.8.14 La versus SiO_2 and La versus Lu for the MIC samples. Additional unpublished samples were provided by S.Weaver and are represented by open symbols. The main trend shows the SiO_2-(over)saturated samples, whereas the separate trends involve samples M-40 and M-84 which are SiO_2-undersaturated.

There is a slight positive Eu anomaly shown by some of the mafic (gabbro and basalt) samples. The presence of a positive Eu anomaly in gabbros such as M-12 (shown in figs 8.12 and 8.13) is due to the accumulation of plagioclase which forms interstitially between large olivine and augite crystals in these samples. The middle REE concentrations are elevated in the intermediate (syenodiorite, diorite etc.) samples relative to the mafic samples, and a slight positive Eu anomaly is also noted in some samples, particularly the plutonic samples such as M-66 (see fig.8.12), which is plagioclase rich. It must be noted that Gd was only measured for the MIC samples and one of the unpublished data points, therefore the flat trends may

result from interpolation. The evolved samples show a pronounced decrease in the middle REE, and some samples have negative Eu anomalies, this is interpreted to reflect the depletion of Eu during fractional crystallisation. There is a broad correspondence between the value and strength of the Eu anomaly with degree of differentiation, as shown in fig.8.13 from positive to weakly positive to flat to generally negative, however there is a great deal of variation between samples, which is largely dependent upon whether the rock is cumulate or volcanic and whether plagioclase is a dominant crystal phase.

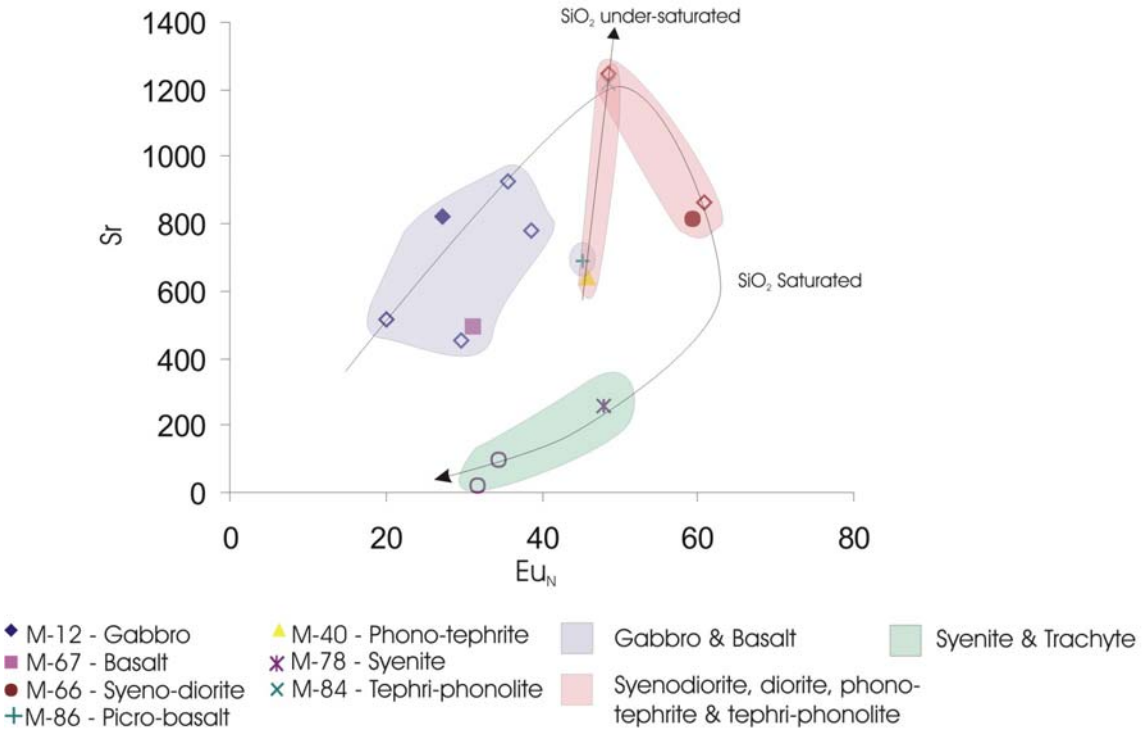

Fig. 8.15 Sr versus Eu (normalised) for MIC samples. Open symbols represent additional data provided by S.Weaver.

The main control on the Eu anomaly is the amount of feldspar being removed from the system by crystal fractionation. The relationship between Sr and Eu, resulting from plagioclase crystallisation in the SiO_2-saturated rocks is shown in fig.8.15. Sr initially increases due to its incompatibility up to SiO_2 contents of 53-54% (fig.8.6). The Eu content also increases due to the incompatibility of Eu in melts of basaltic composition. Sr values fall as it substitutes for Ca in the plagioclase crystal lattice and is depleted from subsequent melts. Eu decreases as it becomes compatible with plagioclase and strongly depleted when the availability of Sr is low. The SiO_2-undersaturated trend is formed from 3 points and is therefore difficult to interpret. Sample M-84 has an SiO_2 content of 52% and the apparent elevation in figure 8.15 may be due to the general incompatibility of Sr at low SiO_2 contents (e.g. fig. 8.6).

8.6 Radiogenic Isotope Geochemistry

The MIC samples were analysed for Sr, Nd and Pb isotopic compositions using the Finnigan MAT 262 Thermal Ionisation Mass Spectrometer (TIMS) at GEOMAR Research Institute, Kiel, Germany. See Appendix 5 for a full description of methods employed and for data tables. Background information on the principles of radiogenic isotope geochemistry can be found in Chapter 7.

A limited number of sedimentary rock samples from the Rakaia and Pahau Torlesse terranes were analysed in addition to the MIC samples to constrain a possible mixing end member in modelling. The data for the Torlesse samples are supplemented by unpublished data from Wandres (2002).

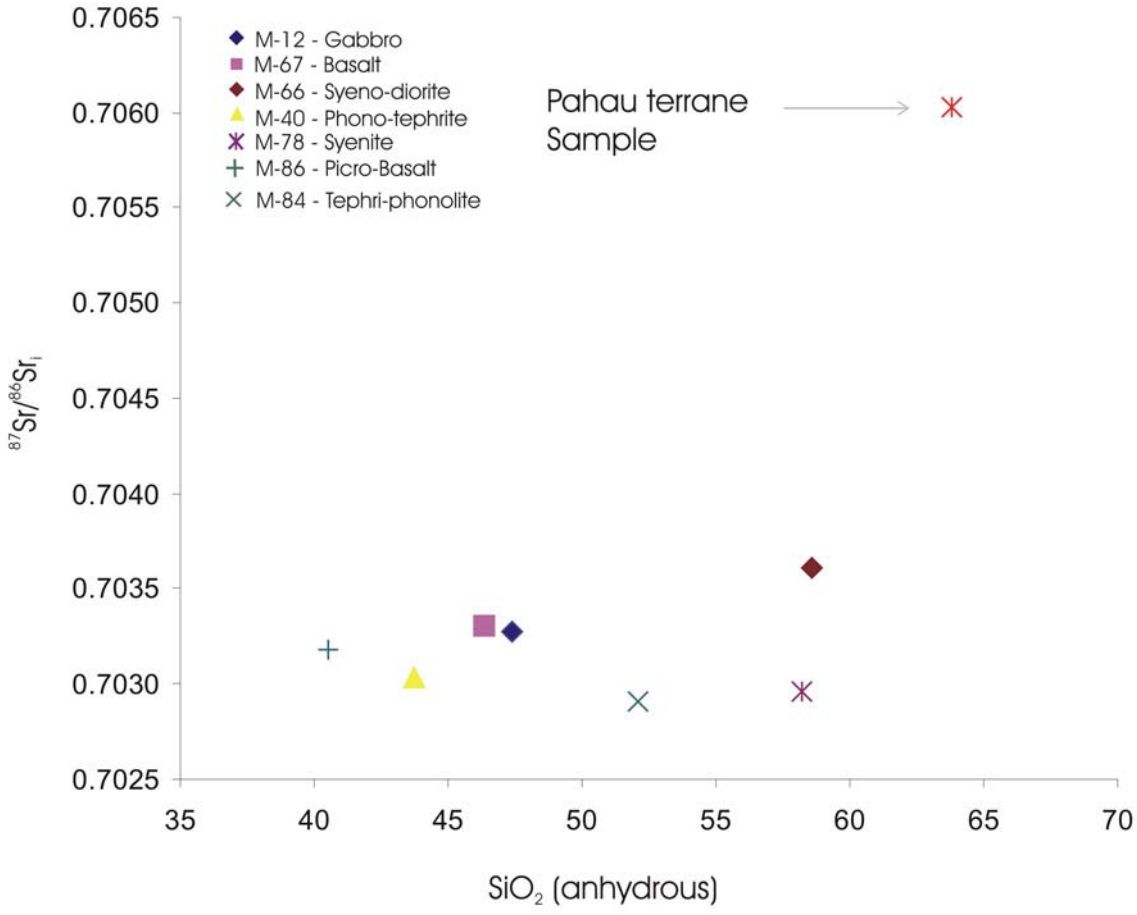

Fig.8.16 Initial Strontium versus SiO_2 content of MIC samples. Rakaia and Pahau samples re-calculated to 97.5Ma.

The samples from the MIC maintain a low initial strontium ratio, within the range 0.7029 to 0.7036. The samples display differing degrees of interaction with more radiogenic Sr. A positive correlation between increasing SiO_2 content (increased level of differentiation) and initial Sr ratio can be interpreted as mixing between the parental magma and a crustal component. The diagram in fig. 8.16 shows two trends, one which is clearly seen to increase with SiO_2 content and another trend which is flat and more readily explained by simple crystal fractionation processes. The under- and (over) SiO_2-saturated sequences are indiscernable on the Sr versus SiO_2 diagram (and the Nd versus SiO_2 diagram, fig. 8.17) indicating that the source of each sequence was the same and that major and trace element variations are due to differing degrees of partial melting. The error on the data in fig.8.16 is found in the data table in Appendix 5, it was not plotted because the error bars are smaller than the sample symbols in the figure and therefore make the diagram more difficult to read.

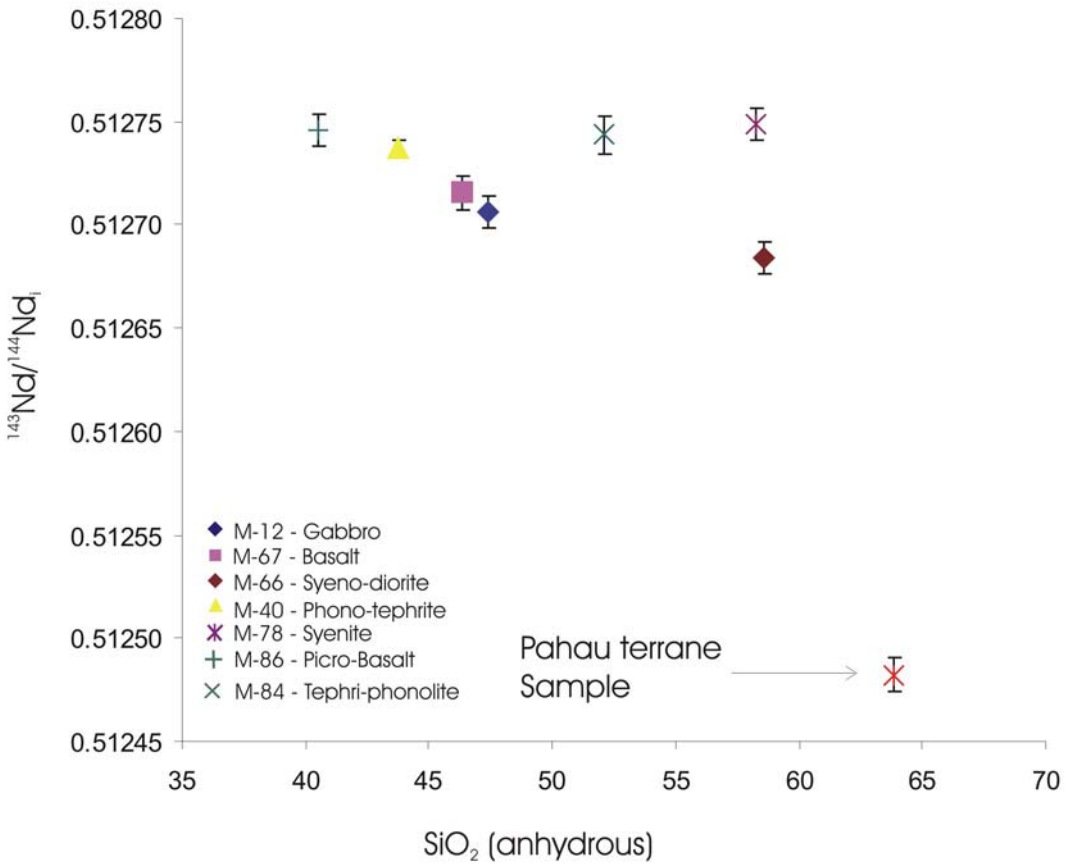

Fig.8.17 Initial $^{143}Nd/^{144}Nd$ versusSiO_2 content for the MIC samples. Pahau and Rakaia samples re-calculated to 97.5Ma.

The Sr versus SiO_2 trends are mirrored in fig.8.17, which illustrates the variation in initial Nd isotopic composition with degree of fractionation (increasing SiO_2). The same samples which showed crustal interaction in fig.8.16 show the same interaction in fig.8.17, with ratios decreasing towards the analysed Pahau terrane value. Samples M-84 and M-78 again do not show the same interaction and appear to have evolved through crystal fractionation alone, without the influence of crustal material.

The decrease in $^{143}Nd/^{144}Nd_i$ ratio and increase in $^{87}Sr/^{86}Sr_i$ can be observed more clearly on Nd-Sr plots (fig.8.18).

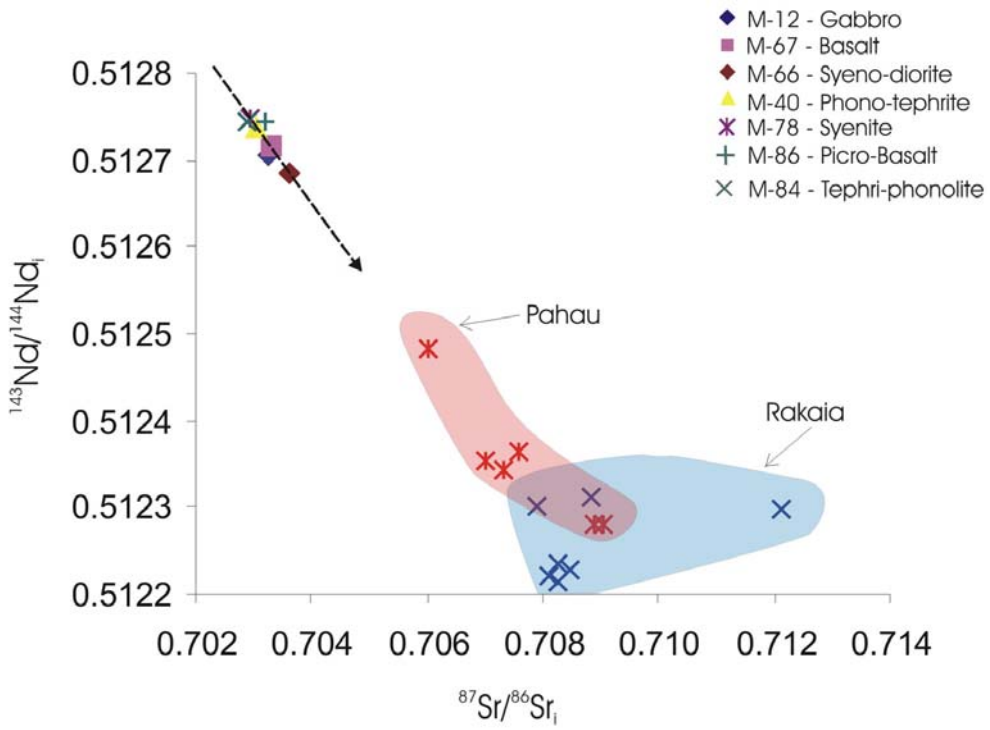

Fig.8.18 Initial $^{143}Nd/^{144}Nd$ versus initial $^{87}Sr/^{86}Sr$ for the MIC. Supplementary data points for the Pahau and Rakaia fields was provided by A.Wandres. The errors are not shown in this diagram because they are smaller than the sample symbols.

Figure 8.18 shows the correlation between the increase in $^{87}Sr/^{86}Sr_i$ coupled with the decrease in $^{143}Nd/^{144}Nd_i$. The samples from the MIC form a tight cluster with a distinct downward trend which is orientated towards the field of the Pahau samples, which indicates that although the contamination is minimal, it is detected by the combined use of Nd and Sr isotopes, the amount of contamination is quantitively modelled in fig.8.21.

The trend of the MIC samples may conceivably be interpreted as variations within the mantle source area since the samples are parallel to the mantle array (DePaolo, 1979). However, the

correlation between Nd and Sr with SiO_2 in some samples argues strongly in favour of a common parental magma composition which has been modified during fractionation. Those samples which do not show the correlation with SiO_2 have very similar initial Sr and Nd ratios.

The sensitivity of Pb isotopes (relative to Sr and Nd isotopes) to contamination by continental crust makes them useful tools in determining mixing end-members. However, only very small quantities of Pb contamination are needed to swamp the isotopic signature of the magmas. Therefore on a plot of initial Nd and Sr versus initial Pb values (fig.8.19), the sensitivity of Pb to contamination compared with the sensitivity of Nd and Sr means that the Pb values would approach those of the contaminant with much lower degrees of contamination. The two mixing lines drawn in fig.8.19 clearly trend towards the potential contaminant (Pahau terrane).

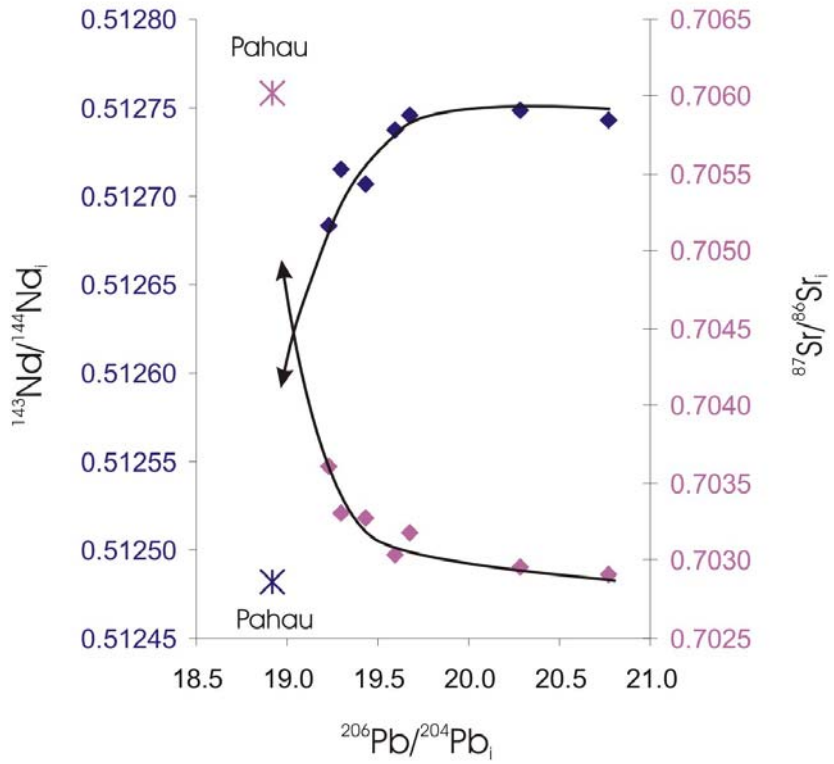

Fig.8.19 initial Nd and Sr versus initial Pb data for the MIC, showing the one analysed sample from the Pahau terrane. The Pb and Sr error bars are smaller than the symbols plotted and the Nd error bars were not plotted because they are very small and add unnecessary clutter.

On the Pb-Pb plot (fig.8.20), the MIC samples point clearly towards the Pahau composition, indicating that the isotopic variation within the MIC is a result of crust-magma mixing.

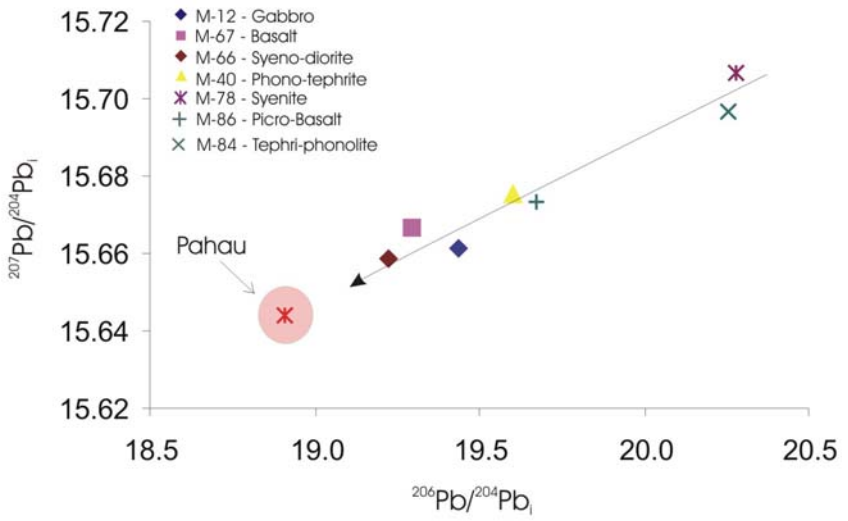

Fig.8.20 Initial $^{207}Pb/^{206}Pb$ versus initial $^{206}Pb/^{204}Pb$ for the MIC samples illustrating the extrapolation of the mixing trend towards Pahau terrane values.

To evaluate the amount of Pahau terrane material that would be required to contaminate the Sr and Nd compositions to their observed values, a simple two-component mixing equation can be used to superimpose a mixing curve on the Nd-Sr diagram (fig.8.21).

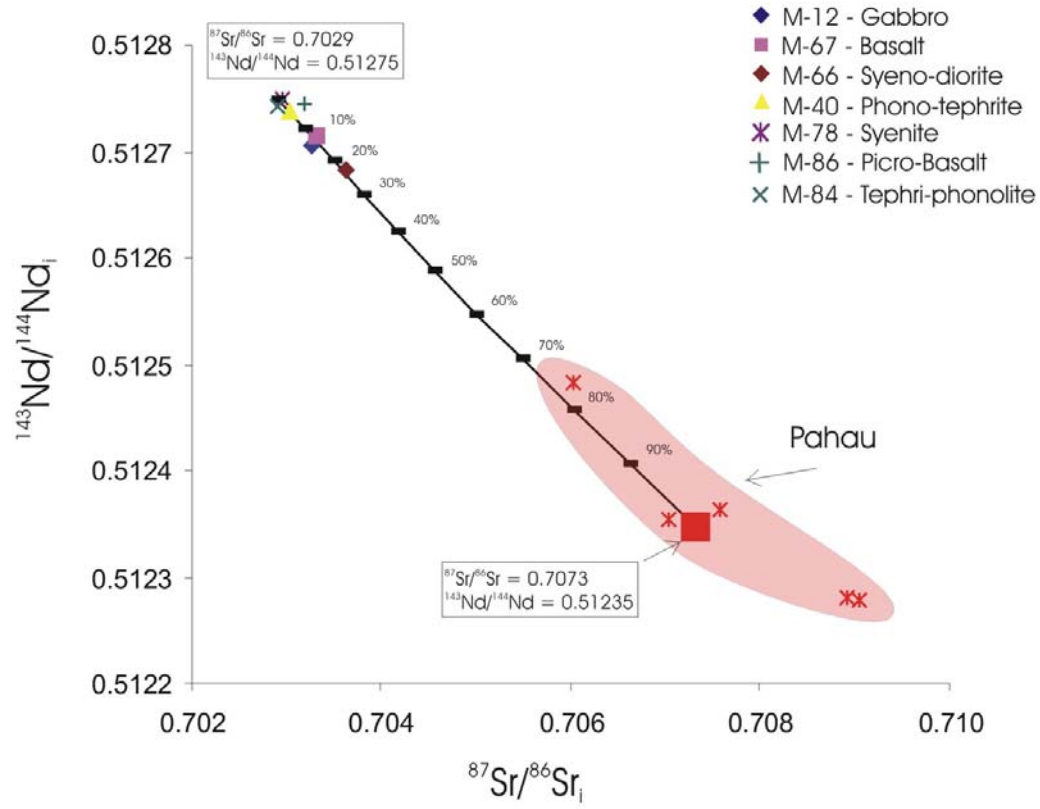

Fig.8.21 Two-component Sr-Nd mixing model for the MIC. The one data point for the Pahau terrane from this study is supplemented with data from Wandres (2002).

From the Nd-Sr diagram in fig.8.21, the amount of material incorporated into the melts which formed the MIC ranges from 0 to 20%. Sample M-66 requires over 20% assimilation. The line on the graph is straight because the Sr/Nd ratio of the initial OIB composition and the Sr/Nd ratio of the analysed Pahau terrane sample (M-80) are approximately the same.

The samples from the MIC form a broad field which lies close to the field for HIMU on radiogenic isotope plots e.g. fig.8.22. The MIC field shown on fig.8.22 deviates somewhat from the HIMU field.

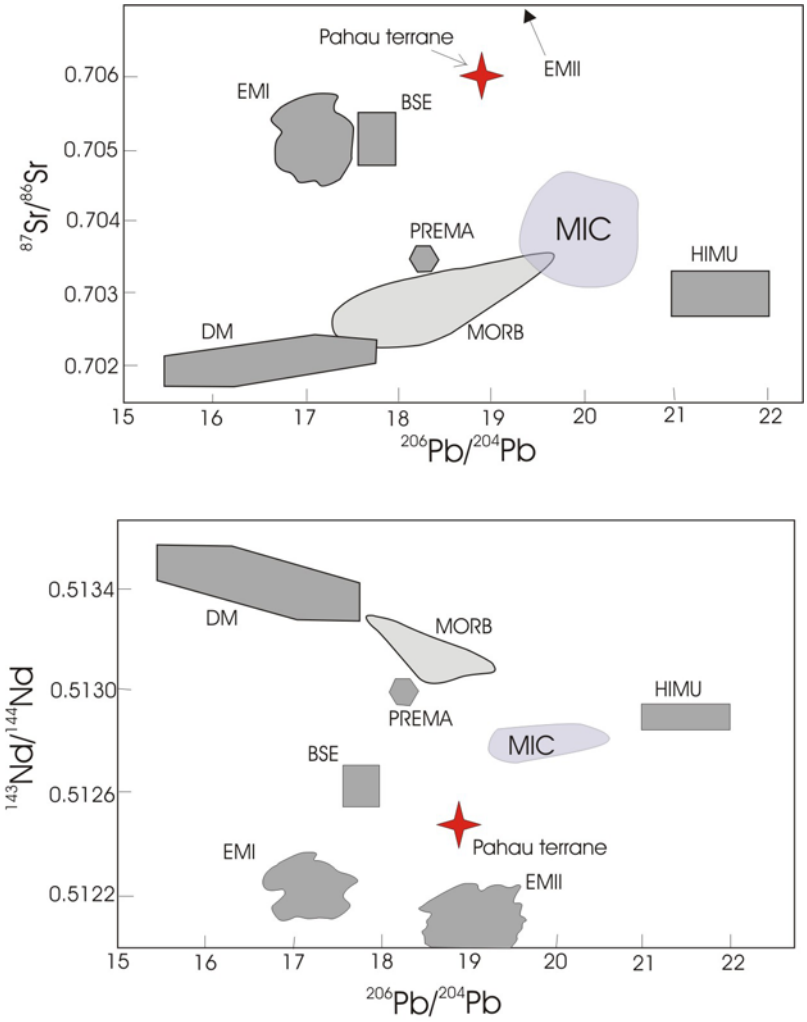

Fig.8.22 Measured Sr and Nd versus $^{206}Pb/^{204}Pb$ for samples from the MIC, overlain on the original diagram of Rollinson (Rollinson, 1993). Fields for the various mantle components are derived from Zindler & Hart (Zindler & Hart, 1986). End-member compositions are: DM, Depleted Mantle; MORB, Mid Ocean Ridge Basalt; PREMA, PREvalent MAntle composition; HIMU, high $^{238}U/^{204}Pb$ mantle; BSE, Bulk Silicate Earth; EMI and EMII, Enriched Mantle.

The position of the MIC field indicates that the parent magma, although similar in composition to HIMU, also contained an EMI component. The spatial extent of the MIC field is probably due to the subsequent interaction with the Pahau terrane.

HIMU (high μ) relates to the μ value ($^{238}U/^{204}Pb$), and is calculated largely upon the actual concentration of U/Pb (ppm values). When the μ value is plotted against MgO content, there is considerable scatter in the data (fig 8.23). HIMU rocks are generally considered to be those with $^{206}Pb/^{204}Pb$ ratios greater than 20.5 (Hart, 1988).

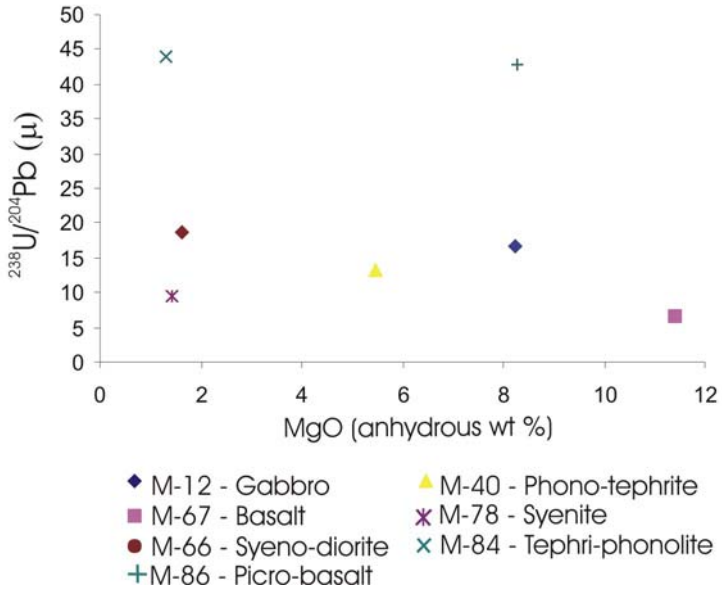

Fig.8.23 Diagram showing the variation in μ-values with MgO content.

Contamination with crustal material of the Pahau terrane (e.g. sample M-80), would not be expected to reduce the HIMU value because the U/Pb ratio of M-80 is itself very high. The most primitive samples as shown on the Sr-Nd isotope diagram shown in fig.8.21 have very high-μ values. As shown on U versus MgO diagram (fig.8.24), the samples which contain the highest concentrations of U also have the highest μ ratios (samples M-84 and M-86). However sample M-78 also has primitive Sr and Nd ratios but has a relatively low μ ratio. Under oxidising conditions, U becomes highly mobile which may explain the decrease in μ values. Removal of U as a result of hydrothermal alteration in some samples provides an explanation for the reduced μ values.

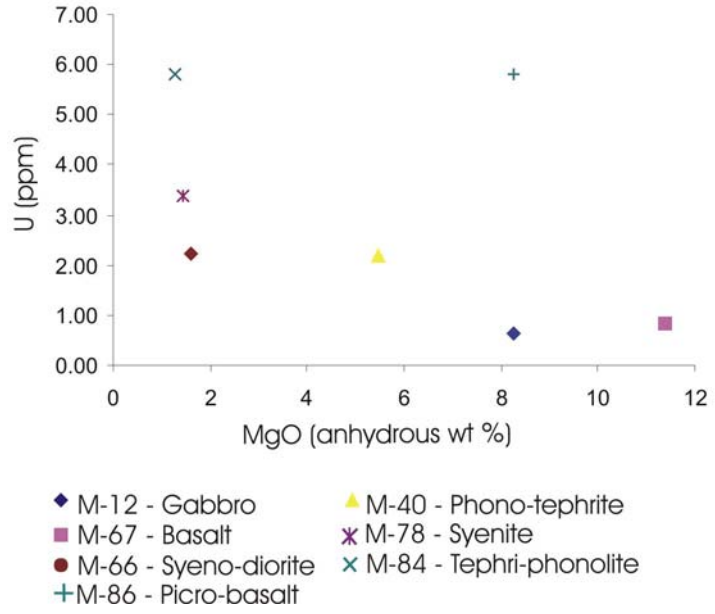

Fig.8.24 U versus MgO for samples from the MIC, note the higher values of M-84 and M-86.

Sample M-84 is from a very fresh, almost glassy dyke and sample M-86 is a fresh clast which was collected from the vent breccia. These samples are therefore interpreted to have their original U/Pb ratios and their μ values can be considered primary.

8.7 Discussion

Alkaline magmas displaying extreme enrichment in the incompatible elements Ba, Th, U, Nb, Ta, and the LREE can be described as 'enriched' magmas relative to 'normal' upper mantle 'depleted' trace-element signatures. The upper mantle is continuously subjected to partial melting processes both in mantle wedge environments and in the genesis of mid-ocean ridge basalts (MORB). Strong enrichment in the incompatible elements, with particular peaks at Nb and Ta are typical characteristics of a distinct set of volcanic rocks termed 'oceanic island basalts' (OIB).

Magmas generated at mid-ocean ridges are enriched relative to mantle peridotite, but do not show the extreme enrichment that is displayed by typical OIB. Magmas generated as a consequence of subduction are also enriched relative to mantle-peridotite and are highly enriched relative to MORB, due to the enhancement of partial melting by metasomatism.

However, magmas generated in a subduction environment display very distinctive trace-element signatures resulting from the enrichment of LILEs and LREEs relative to HFSE by fluids derived from the subducting slab (ref. Chapter 7). Partial melts of mantle wedges are usually depleted in Nb and Ta relative to the other incompatible elements and it is generally considered that the HFSE are retained in the down-going slab due to their high charge and low ionic potentials which make them highly insoluble in the fluids derived from the down-going slab.

It is the release of LILEs from the subducting slab, and to a lesser extent the release of LREEs which provide a residual slab with low LILE/HFSE and LREE/HFSE ratios. Many authors have ascribed the formation of OIBs with the recycling of 'fossil slabs' in the deep mantle (Chase, 1981; Hofmann & White, 1982; Kamber & Collerson, 2000).

The key conclusions regarding the geochemistry and petrogenesis of the MIC are as follows:

- The MIC was derived from an enriched-mantle source with trace-element and isotopic composition similar to the HIMU end-member. Some samples have been subjected to hydrothermal removal of U, which has affected the μ-value of the resulting volcanics.

- The MIC rocks show both silica undersaturated and (over)-saturated trends. The two trends were produced from the same source through differing degrees of partial melting (under SiO_2 saturated trend through lower degrees of partial melting) and evolved along different fractional-crystallisation paths.

- Most of the MIC samples display varying degrees of crustal assimilation, up to a maximum of 25%, but generally less than 10%. The modelled assimilant had an isotopic composition similar to the Pahau terrane. Generally the later stage units of the MIC (syenite and tephri-phonolite dyke) show the least interaction with the Pahau terrane.

- The parent magma had isotopic characteristics intermediary between the HIMU and EMI mantle end-member compositions.

- The magmas crystallised at low pressures. This is clearly evident because the plutonic complex rises to high levels and intrudes the volcanic carapace (Chapter 5). The abundance of pegmatite zones within the main syenite intrusion is also consistent with the percolation of late stage hydrous fluids.

The MIC illustrates a rapid and short lived pulse of magmatism in this area, which rose rapidly through the continental crust, possibly aided by extensional tectonics, with little interaction with the crust. The units of the MIC were progressively emplaced but re-charge and repetition of various units illustrates that the sequence of events is not straight forward.

8.8 Relationship between the MIC and temporally related volcanics/intrusives in the South Island

Temporally and geochemically related volcanics have been described from other areas of the South Island, which were termed the Central Marlborough Igneous Province (CMIP) (Grapes, 1972). The volcanics and intrusives temporally related to the MIC are listed in table 8.1.

Name of component	Description	References
Blue Mountain Igneous Complex	Ring complex consisting of 800m of ultramafic and gabbroic rocks intruded by ring dykes of gabbro and lamprophyre	(Grapes, 1972, 1975)
Tapuaenuku Igneous Complex (TIC)	A series of plutonic rocks (Tapuaenuku Plutonic Complex) with associated dykes	(Baker, 1990; Baker *et al.*, 1994; Nicol, 1977)
Lookout Formation	Alkaline volcanics which are geochemically very similar to the dykes of the TIC. The lavas overlie conglomerate and coal measures of Ngaterian age.	(Challis, 1960, 1966; Grapes *et al.*, 1992; Warner, 1990)
Gridiron Formation	Alkaline volcanic rocks, similar to the Lookout Volcanics, interbedded with both fresh water and marine sediments.	(Challis & Reay, 1993; Reay, 1980; Suggate, 1958; Warner, 1990)
Other minor exposures	Small gabbroic intrusions and dykes in the Marlborough area.	(Mason, 1958; Nicol, 1977)

Table 8.1 Volcanics and Intrusives of Marlborough, temporally and geochemically related to the MIC. Based on the original compilation by Baker *et al* (1994).

The similarity between the volcanic and plutonic rocks listed in table 8.1 and the MIC is striking, and the MIC was included in the CMIP of Grapes (1972).

A summary of the published ages (and unpublished) for each member of the CMIP is reproduced in table 8.2 (from the original compilation of Baker *et al*, 1994).

Igneous Suite	Notes	Age (Ma)	Dating technique	References
Tapuaenuku Plutonic Complex	Kaersutite from pegmatite Plutonic rocks Zircon Titanite	101.2 ± 1.4 90 ± 8 93 ± 10 103 ± 11	K-Ar Rb-Sr Fission track Fission track	(Nicol, 1977) } } (Baker, 1990) }
Radial dyke swarm	21 basanite and trachybasalt dykes, Awatere Valley Trachybasalt dyke, Aorangi Ranges	59.8 ± 1.1 to 100.0 ± 1.4 98.9 ± 3.2	K-Ar K-Ar	(Grapes *et al.*, 1992) (George, 1988)
Lookout Volcanics	6 trachybasalt flows, Awatere Valley	90.3 ± 1.6 to 99.9 ± 0.7	K-Ar	Nicol (unpublished but quoted in Baker *et al*, 1994)
Gridiron Volcanics	Trachybasalt flows, Clarence Valley	94.6 ± 1.3 to 97.6 ± 1.6	K-Ar	(Reay, 1993)
Mandamus Igneous Complex	Plutonic and volcanic rocks plus mineral separates	97.0 ± 0.5	Rb-Sr	(Weaver & Pankhurst, 1991)

Table 8.2 Table of ages for the mid-Cretaceous Marlborough volcanics/plutonics

The ages of the CMIP suites as listed in table 8.2 show considerable spread, which may be a function of the different geochronological techniques employed. K-Ar age dating is particularly susceptible to error due to the gaseous nature of the daughter product (Ar) from the radioactive decay of K. When Ar is lost from the mineral in which it was first incorporated, it is not taken up by co-existing mineral phases, unlike in the Rb-Sr system. Therefore the K-Ar system is particularly susceptible to Ar loss during thermal events. Whole-rock K-Ar ages have, therefore been treated with caution in recent years and whole-rock ages should be considered minimum ages.

Gross averaging of the maximum ages in table 8.2 (excluding MIC age) provides a mean age of 98 Ma. The mean age of 98 Ma is extremely close to the 97 Ma age derived from Rb-Sr geochronology (Weaver & Pankhurst, 1991).

The CMIP consists of several major occurrences of plutonic, volcanic and related dyke swarms which vary in composition from ultramafic cumulate plutonic rocks to quartz syenite

and volcanic equivalents. The Tapuaenuku Igneous Complex (TIC of Nicol, 1977) evolved from a trachy-basalt parent magma (Baker, 1990) with fractional crystallisation producing both silica undersaturated and oversaturated lineages similar to those observed in the MIC. The variable volatile content and silica content were the dominant controls on phenocryst assemblage, as in the MIC.

Detailed geochemical analysis on the TIC has been carried out by Baker (1990) and Baker *et al* (1994) and selected trace-elements are plotted for comparison with the MIC (fig.8.25 and 8.26).

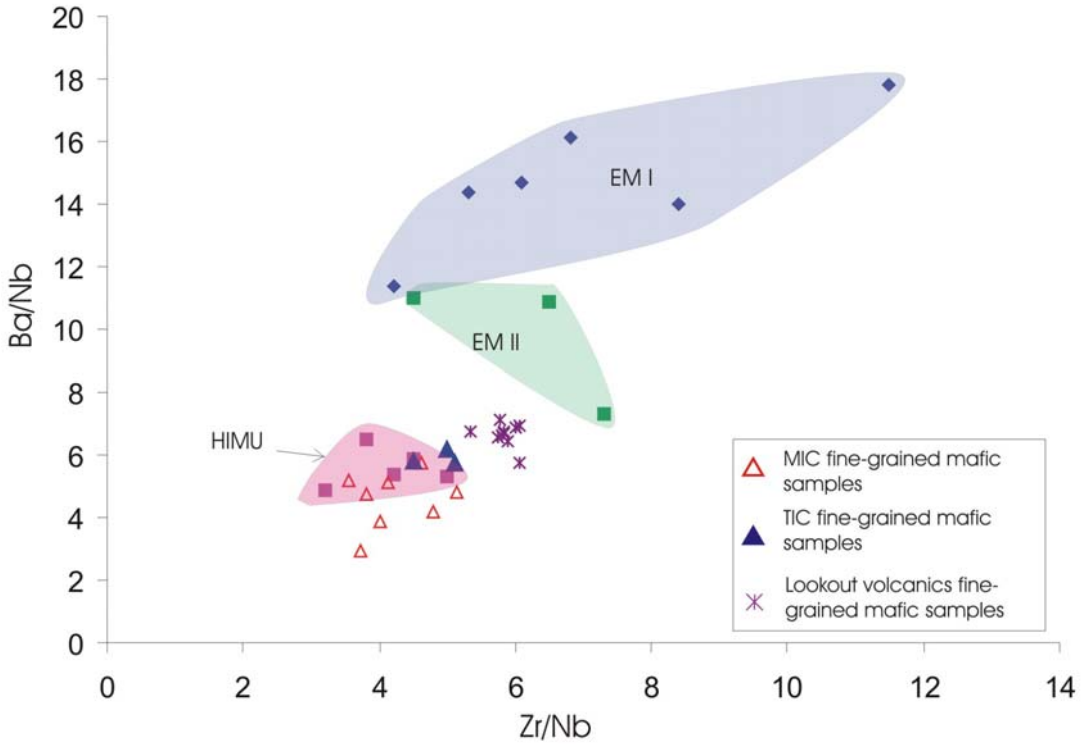

Fig.8.25 Ba/Nb versus Zr/Nb for both MIC and TIC samples. Only fine-grained mafic samples were plotted due to the variability in Ba/Nb ratio at high levels of differentiation. TIC data from Baker (1994).

The TIC samples plot within the field for HIMU on the Ba/Nb versus Zr/Nb diagram (fig.8.25), illustrating the affinity with the HIMU mantle end-member for both the MIC and TIC. The Gridiron volcanics analysed by Warner (1990) have Zr/Nb ratios between 4.3 and 4.8, however the extremely high Ba enrichment in the Gridiron volcanics results in a Ba/Nb ratio of 16 to 47. The data from the Gridiron Volcanics were therefore not plotted in fig.8.25. Warner (1990) ascribed the high Ba contents to source heterogeneity, possibly resulting from the previous extraction of strongly alkaline magmas.

The TIC and MIC show similar trace-element patterns on the spiderdiagram in fig.8.26. The range of data is narrow because cumulate rocks and evolved samples were excluded from the data set. The data plotted are for the mafic fine-grained samples such as dykes and lava flows from the MIC, TIC, Gridiron Volcanics and Lookout Volcanics.

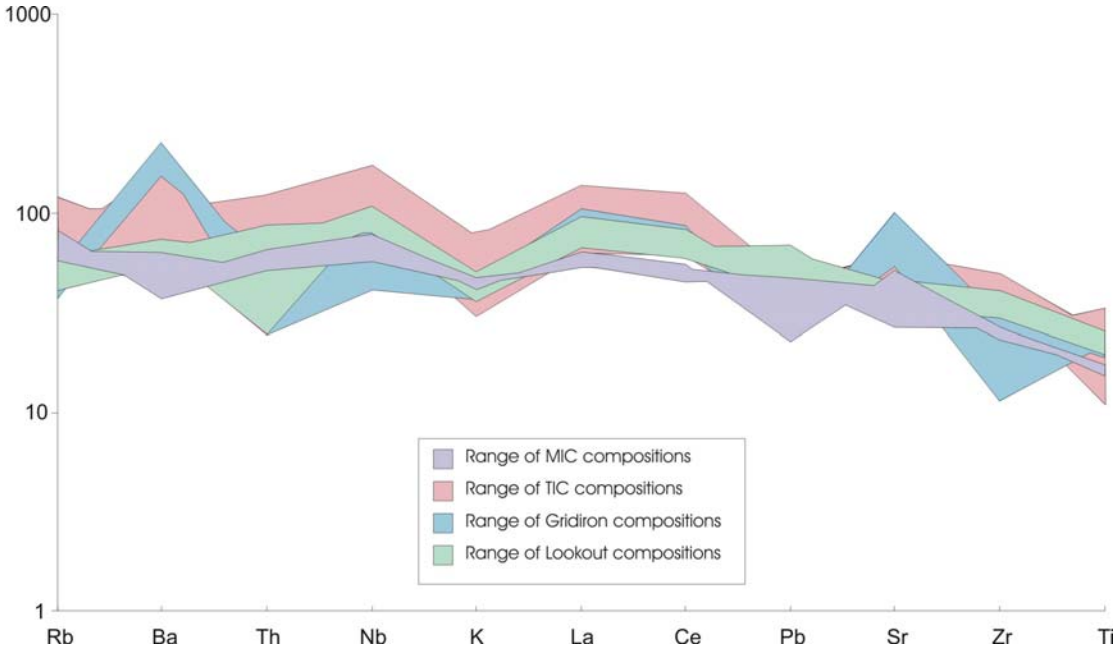

Fig.8.26 Spiderdiagram illustrating the similarity in trace-element ranges of the MIC, TIC, Gridiron volcanics and the Lookout volcanics. Data plotted are from fine grained mafic samples only, no cumulate or evolved samples are plotted. Data normalised to primitive mantle of Hofmann (1988). TIC data from Baker *et al* (1994); Gridiron and Lookout volcanics data from Warner (1990).

Isotopic studies have indicated that the TIC was derived from a HIMU OIB mantle source based upon Sr-Nd-Pb data and trace element ratios (Baker *et al*, 1994). Sr isotope analysis of the Lookout Volcanics indicates an initial Sr isotope ratio similar to the TIC and MIC (table.8.3) (Warner, 1990).

From table 8.3, it is clear that there is significant overlap between the TIC, MIC and Lookout Volcanics in terms of Sr isotopic composition. As discussed in Chapter 7, the elevation to higher $^{87}Sr/^{86}Sr_i$ ratios is a function of crustal contamination. The TIC may comprise material, less radiogenic in Sr and Nd. The age used for the re-calculation of εNd and $^{206}Pb/^{204}Pb$ for the TIC samples is 95 Ma rather than 97.5 Ma and is taken from the published data of Baker *et al* (1994). The absence of measured isotope ratios and U, Pb, Sm, Nd trace element concentrations in Baker *et al* (1994) precluded the re-calculation of the Nd and Pb

isotope ratios to 97.5 Ma. However, the 2.5 Ma disparity would have a negligible effect on the isotopic data at the given precision.

Name (age for re-calculation)	$^{87}Sr/^{86}Sr$ (initial)	ε Nd	$^{206}Pb/^{204}Pb$ (initial)
Lookout volcanics (97.5)	0.7028-31	n/d	n/d
TIC (97.5)	0.7028-34	+3.5 to +5 (at 95Ma)	20.1 (at 95Ma)
MIC (97.5 Ma)	0.7029-36	+2.3 to +3.6	19.2 – 20.3

Table 8.3. Initial Sr, ε Nd and 206Pb/204Pb for the TIC and MIC and Lookout volcanics (based on data included in Baker *et al*, 1994; Baker, 1990 and Warner, 1990).

The data in table 8.3 plots close to the field of HIMU (fig 8.27), and probably extends to the lower ε Nd and higher $^{87}Sr/^{86}Sr_i$ shown due to mixing with Pahau terrane sediments.

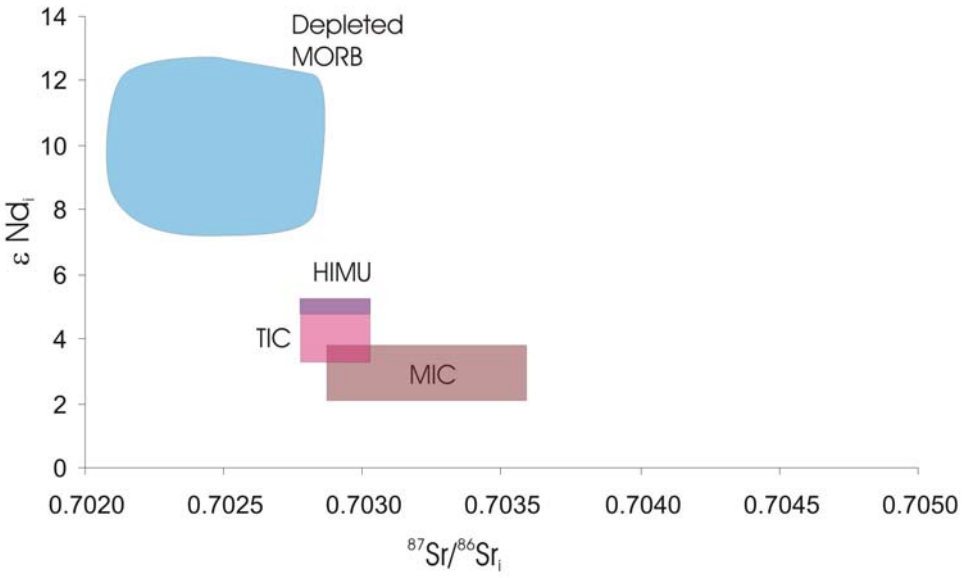

Fig.8.27 ε Nd_i versus $^{87}Sr/^{86}Sr_i$ for the MIC and TIC. Also plotted are restricted fields for depleted MORB and HIMU (Sun & McDonough, 1989; Weaver, 1991).

Given the similarity in geochemistry between the various members of the CMIP and their similar ages, there appears to be little doubt that they are part of the same tectonomagmatic event.

The MIC and related CMIP record a period of OIB style magmatism, contaminated to variable degrees with the continental crust, which occurred through the Pahau terrane of New Zealand. The OIB magmatism was essentially coeval with the MSVG magmatism in the Rakaia terrane.

Chapter 9:

Tectono-magmatic models for the formation of the MSVG and MIC

9.1 Introduction

The models presented here must satisfy the parameters given in the following section, take into account other New Zealand, Marie Byrd Land and Australian geological constraints, and must consider previously published models for the formation, amalgamation and magmatic evolution of the Gondwana margin from the Early Cretaceous.

The following discussions incorporate summaries of the main tectonic and magmatic features that were described in greater detail in chapter 2.

9.2 Parameters to be satisfied and outline of models

Listed below are the key conclusions drawn from the research undertaken, together with relevant published data. Each of the following points must be accommodated in a satisfactory model:

1. The MSVG is restricted to the Rakaia terrane, whereas the MIC is restricted to the Pahau terrane.

2. The MSVG is the only calc-alkaline magmatism to be erupted through the Rakaia terrane and its correlatives along the Gondwana margin, after an extended period of convergence.

3. The MSVG magmatism was coeval with MIC magmatism, as shown by both the Ar-Ar and SHRIMP/Rb-Sr geochronology (Chapter 6). SHRIMP dating of the

MSVG yields a crystallisation age of 97.5 ± 1.5 Ma, which is within error of the MIC magmatism, dated at 97.0 ± 0.5 Ma (Weaver & Pankhurst, 1991). These ages are also consistent with, and overlap the broad range of ages published for the CMIP.

4. The MSVG was a product of melting of subduction-modified mantle wedge, coupled with contamination by Rakaia terrane in the lower crust and fractional crystallisation.

5. The MIC magmatism shows trace-element and isotopic characteristics typical of OIB magmas. These characteristics are also noted from the Lookout and Gridiron volcanics of Marlborough (Warner, 1990), and the TIC (Baker, 1990; Baker *et al*, 1994).

6. Petrogenetic modelling of the MIC and MSVG requires different parental magma compositions derived from different mantle reservoirs.

7. The eruption of the MSVG was associated with extensional faulting.

8. The onset of MSVG and MIC volcanism/magmatism appears to have been rapid and of short-lived duration, with SHRIMP dated samples having a narrow range of ages for the MSVG and crystal and whole-rock samples from the MIC producing a good single Rb-Sr isochron.

9. Following the MIC and MSVG magmatism and the onset of sea-floor spreading in the Southern Ocean and Tasman Sea, New Zealand underwent a long period of subsidence and marine transgression/progression.

There are two models which are considered to be feasible for the generation of the MSVG and MIC magmatism. Each model involves the ascent of enriched 'HIMU' asthenosphere to account for the broadly distributed OIB-type magmatism which was closely associated with the break-up of New Zealand from Antarctica. A short summary of each model follows and detailed descriptions can be found in section 9.4.

Model 1: Slab detachment and localised upwelling of enriched asthenospheric mantle

Following the cessation of subduction at the Gondwana margin in the Motuan Stage (105 – 100 Ma), the previously subducting slab detached, triggering the decompression melting of the mantle wedge beneath the Rakaia terrane and the upwelling of asthenosphere into the slab window beneath the Pahau terrane.

This model proposes a localised rise of 'passive' asthenosphere which was of widespread availability under the Gondwana continental margin in the mid-Cretaceous and is broadly analogous to the 'fossil-plume' models of Panter *et al* (2000); Hart *et al* (1997) and Rocholl *et al* (1995).

Model 2: Large-scale mantle plume

A single wide diameter plume, centred underneath Marie Byrd Land provided a heat source to generate the calc-alkaline magmas from beneath the Rakaia terrane, and directly sourced the CMIP.

This model is broadly consistent with the plume-enhanced break-up models of Weaver *et al* (1994) and Storey *et al* (1999), who concluded that a large diameter mantle plume defined the locus of rifting of the New Zealand block from Gondwana.

9.3 Structural and petrological considerations from Marie Byrd Land, Antarctica and Australia

The following text summarises the precursory tectonic and magmatic events to the MSVG and MIC magmatism, which have been described in greater detail in Chapter 2. Episodes which have a bearing on the mid-Cretaceous evolution of the Eastern Province are the magmatic history of the MTZ (Median Batholith) and the uplift and extension of the Western Province and their counterparts in Antarctica and Australia.

9.3.1 Convergent magmatism

I-type magmatism in the MTZ was prolonged and lasted from 247-131 Ma with a pronounced gap from 190 to 160 Ma (Kimbrough *et al*, 1994; Muir *et al*, 1998). I-type magmatism in Marie Byrd Land ranges from 320 to 110 Ma in the west (Ruppert and Hobbs coast) and continued until 94 ± 3 Ma in the east (Kohler Range and Pine Island Bay). The younger, although similar duration I-type magmatism in Marie Byrd Land may illustrate the diachronous nature of subduction from west to east along the Gondwana margin (Mukasa & Dalziel, 2000; Weaver *et al*, 1994; Weaver *et al*, 1997). Correlatives of the MTZ have also been described in Australia and the similarity between the Middle Triassic I-type plutons in Australia with the MTZ have been discussed by Mortimer *et al* (1999 a & b).

The trench location for the subduction-related magmatism in the MTZ and Marie Byrd Land is by no means resolved. Muir *et al* (1995) and Waight *et al* (1998b) ascribe the formation of the MTZ magmas to the subduction of oceanic crust outboard of the Murihiku terrane but inboard of the Eastern Province terranes (figs. 9.1 and 9.2). These models require another subducting slab at the margin, outboard of the Pahau terrane to explain the deformation in these outermost Torlesse accretionary prisms.

A complicating factor is the relationship between the MTZ and the Western Province. Whether or not the MTZ collided with the Western Province to produce the Separation Point Batholith has been a matter of recent debate. Muir *et al* (1995) proposed a model whereby the Separation Point magmas formed by the melting of MTZ arc-rocks in response to the partial under-thrusting of the MTZ beneath the Western Province (fig. 9.1). This is supported by lower crustal rocks exposed in northern Fiordland (Daczko *et al*, 2001). However, Mortimer *et al* (1999a and b) suggest that the MTZ did not forcibly collide with the Western Province, and suggest that the MTZ was an autochthonous terrane. They cite the emplacement of the Separation Point magmas along the contact between the MTZ and Western Province in support of their autochthonous model and suggest that the Median Tectonic Zone be named the Median Batholith. However, the models of Mortimer *et al* (1999a and b) do not provide an explanation for the formation of the Separation Point Suite. Muir *et al* (1995) ascribe the adakitic nature of the Separation Point Batholith to the under-thrusting of a portion of the Median Tectonic Zone underneath the Western Province. This, as shown in the models of

Muir *et al* (1995), requires an additional subducting slab underneath the Western Province (fig.9.1).

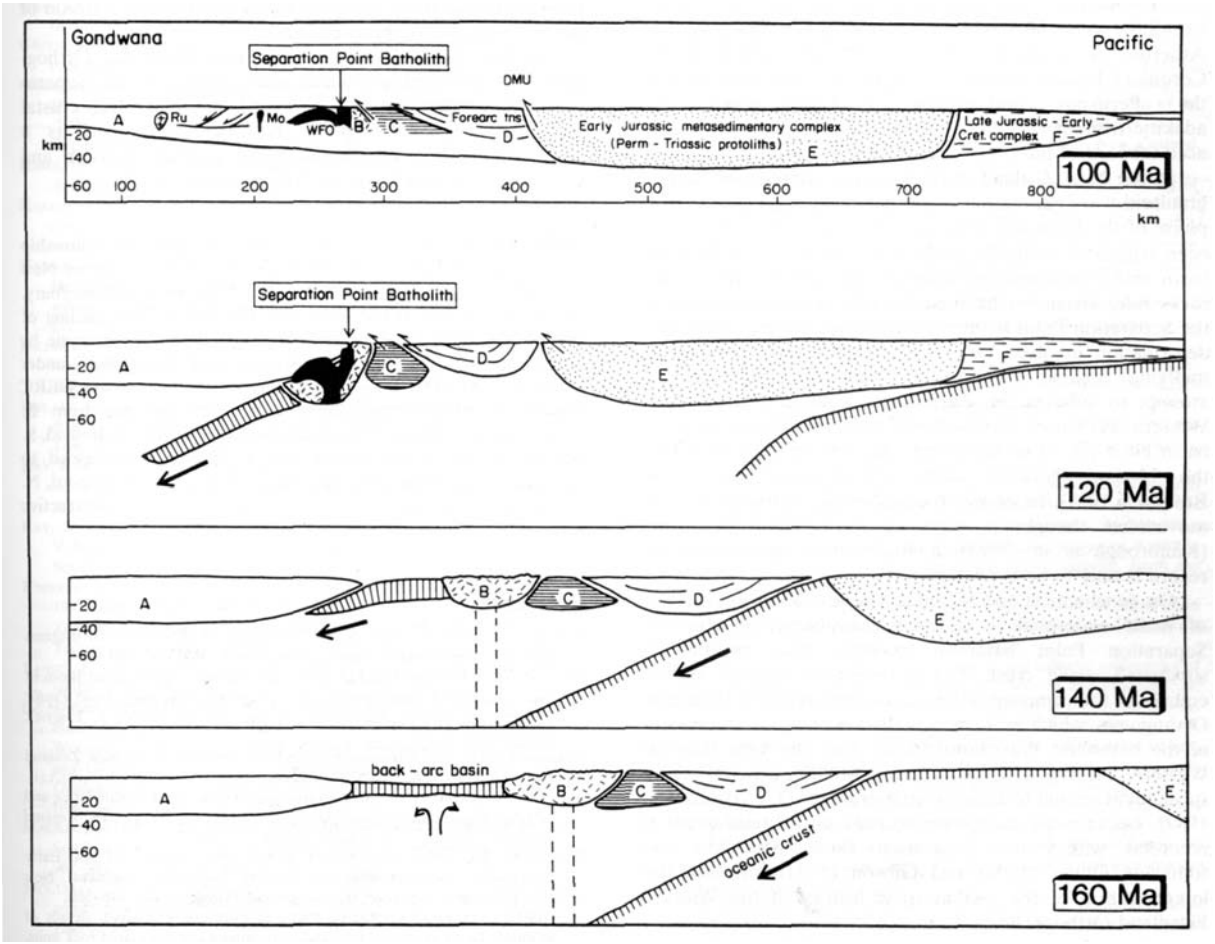

Fig.9.1 Diagram of Muir *et al* (1995) for the formation of the Separation Point Suite. A: Western Province, B: Median Tectonic Zone, C: Brook Street terrane, D: Maitai terrane, E: Haast Schist, F: Torlesse terrane.

The MTZ in New Zealand is significantly narrower than its counterparts in Australia and Antarctica, which may be related to the partial under-thrusting of the MTZ. The elongate nature of the Separation Point Batholith and its counterparts along the suture of the Western Province and Median Batholith may imply a strike-slip component in the mechanism of emplacement and melt generation.

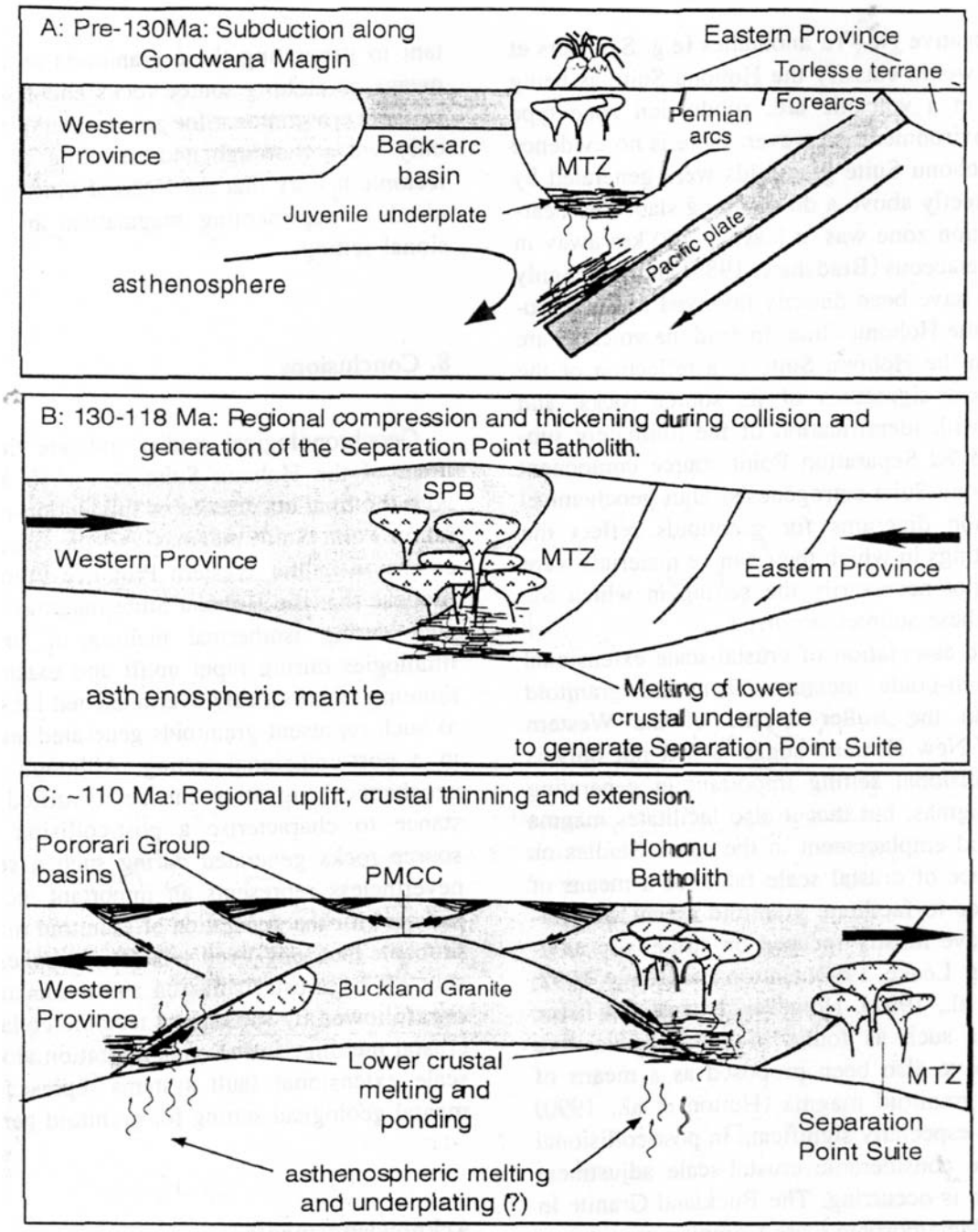

Fig.9.2 Model of Waight *et al* (1998b) for the formation of MTZ, Separation Point Suite and Western Province extension, uplift and granitoid emplacement.

The presence of a subduction zone at the Gondwana margin, outboard of the Pahau terrane is strongly indicated by sedimentological evidence. Given the striking sedimentological evidence for convergence and deformation at the margin, the lack of calc-alkaline subduction derived magmas in the Rakaia terrane is puzzling. It is conceivable that the latter stages of Median Batholith intrusives are related to subduction at the Gondwana margin, however a

great distance (>600km) and therefore very shallow subducting slab would be required to account for such a large trench-arc gap (fig.9.3).

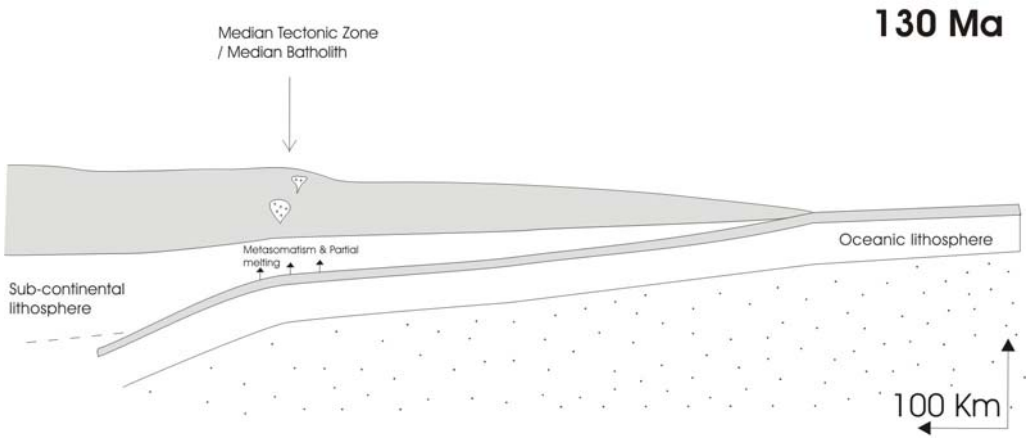

Fig.9.3 Model illustrating the necessarily shallow subducting slab for the formation of the Median Tectonic Zone magmatism.

A shallow subduction model would imply the fortuitous emplacement of latest subduction-derived magmatism in the MTZ, the location of which coincided with the products of long-lived subduction illustrated by the MTZ. This would imply that in order to maintain the site of subduction-derived magmatism, the angle of the subducting slab would have to shallow considerably to allow for the widening forearc between the early Triassic to the early Cretaceous. The subduction of oceanic crust outboard of the Pahau terrane and shallow subduction resulting in magmatism in the Median Batholith would, however, account for the lack of subduction-related magmatism in the Rakaia terrane.

Flat subduction provides an alternative mechanism for the formation of the Separation Point Batholith, which has geochemical characteristics similar to adakites. Adakites related to the flattening of subducting slabs have been described for southern Equador (Beate *et al*, 2001), with flattening due to the subduction of the more buoyant Inca Plateau. However shallow subduction is one of only 7 models proposed for the formation of adakites (Defant & Kepezhinskas, 2001).

The cause of flat slab subduction is far from resolved. Recent research has indicated that the subduction of thicker oceanic plateaux may account for a shift to shallow subduction (van Huhen *et al*, 2002), however the maximum flat slab extent in this scenario is approx. 300 km (van Huhen *et al*, 2002). In the case of the MTZ, unless an oceanic plateau was subducted, of

which there is no present-day indication, this does not account for the necessarily shallow dip of the slab as indicated in fig.9.3. Furthermore, the arc-trench gap (>600km) is far in excess of the 300 km maximum suggested for van Hunen *et al* (2002) for this process. Van Hunen *et al* (2002) propose that flat-slab segments up to 500 km long may be explained by overthrusting of the overriding plate to explain the long flat-slab segments below Peru and Central Chile. The 'Plume-modified orogeny' model (Murphy *et al*, 1998), suggests that the rise of a mantle plume beneath a subducting slab may lead to shallowing of the slab, cessation of subduction-related magmatism and uplift of the overlying continental crust. The same process has been suggested for the Mesozoic Gondwanide fold belt of South America, southern Africa and Antarctica (Dalziel *et al*, 2000). However, the shallowing of a pre-existing > 600km slab to produce a flat slab is untenable. Furthermore, the magmatism was long-lived in the MTZ without a significant landward migration of volcanism, as would be expected from a shallowing slab angle. The presence of an extremely shallow slab beneath the Eastern Province would be expected to have produced significant uplift and deformation of the overlying terranes e.g. the Laramide orogeny of the North American Cordillera (Bump, 2001; Murphy, 2001). A shallow subduction model also poses problems regarding the timing and origin of a metasomatised mantle wedge beneath the Rakaia terrane, which is required to produce the MSVG magmas.

The shallow-slab mechanism for the formation of the MTZ is therefore considered to be unlikely and the models which propose more than one subduction zone e.g. Muir *et al* (1995) and Waight *et al* (1998b) are preferred as the precursory tectonic conditions prior to the MSVG and MIC magmatism.

9.3.2 Uplift, extension and the end of subduction

Extension-related magmas were produced in the Western Province as a result of significant uplift and extension which resulted in the unroofing of metamorphic core complexes and formation of deep sedimentary basins. The uplift and extension was initiated at approximately 110 Ma with the emplacement of granitoids of the Hohonu Suite (Waight *et al*, 1998b) (fig. 9.2). Uplift was closely followed by extension and the deposition of the Pororari Group into the resultant half-grabens. The age of sedimentation of the Pororari Group is

constrained by the Stitts Tuff, which is found near the base of the Group and has yielded ages of 101 ± 2 Ma (2σ) and 102 ± 3 Ma (2σ) (Muir *et al*, 1997). The grabens strike W or WNW, implying extension in a N or NE direction (Laird, 1993). The WNW strike is essentially parallel to the trend of the Cretaceous spreading axes in the Tasman Sea (Tulloch *et al*, 1991).

In Marie Byrd Land a clear transition is noted from I-type (124-108 Ma) to A-type intrusions (102-95 Ma) and mafic dyke emplacement (110-95 Ma) which are interpreted to represent the change in tectonic regimes from a subduction influence to an extensional regime (Weaver *et al*, 1996). The area of Marie Byrd Land described by Weaver *et al* (1996) affected by A-type intrusions and mafic dykes was adjacent to, and corresponds with the MTZ and Western Province of New Zealand (fig.9.4).

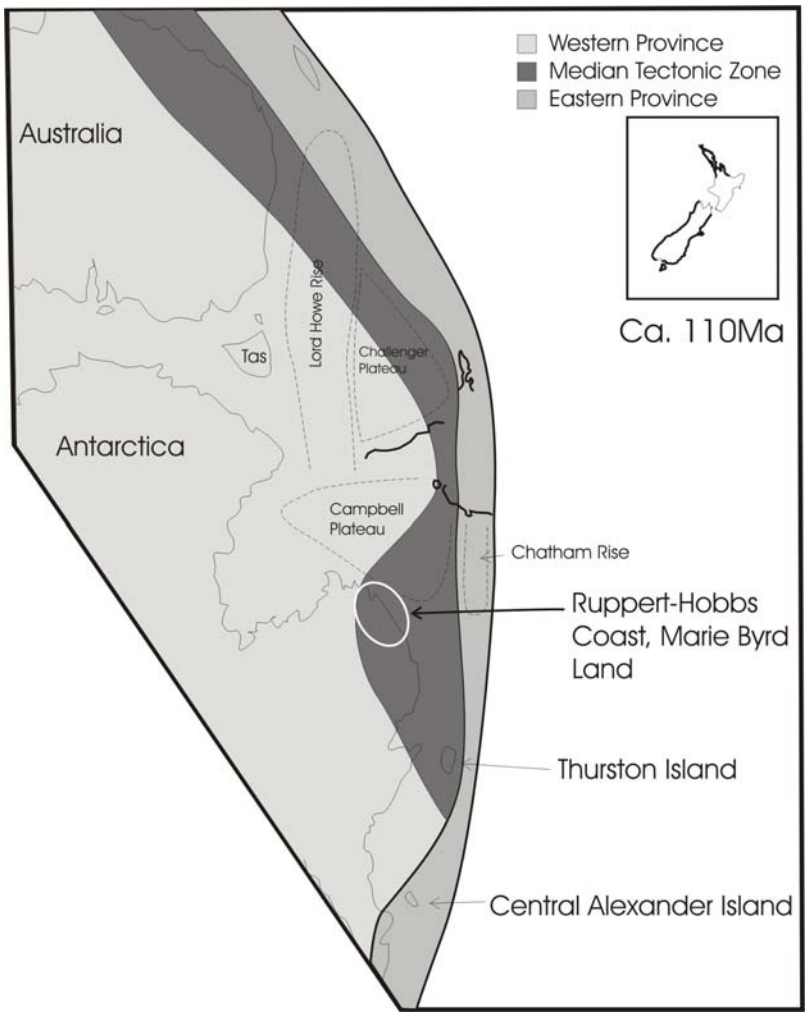

Fig.9.4 Gondwana margin reconstruction illustrating the area of the Marie Byrd Land coast affected by rift-related magmatism.

A major angular unconformity is noted in Marlborough between the heavily deformed Pahau terrane and overlying relatively mildly deformed marine sediments (Laird, 1993). The unconformity marks the change in tectonic regime from convergent margin to extension and is Motuan in age (105-100 Ma) (Laird, 1992, 1993). This change in tectonic regime has been attributed to the arrival of a spreading ridge and subsequent cessation of subduction (Bradshaw, 1989); and also by the process of 'slab capture' due to the close arrival and stalling of a spreading ridge (Luyendyk, 1995). The overlying, relatively undeformed, mainly gravity flow marine sediments were deposited into extensional half-grabens. These deposits measure up to 2000m in thickness (Laird, 1992).

The cessation of subduction, as indicated in the sedimentary record of Marlborough occurred 5 Ma after the 'post-collisional' magmatism began in the Western Province e.g. Hohonu Suite, 110Ma (Waight *et al*, 1998b). Therefore, the uplift events recorded in the Western Province may not be directly related to the cessation of subduction at the Gondwana margin. If the magmatism in the Western Province was a result of the cessation of subduction then this poses the question of why the uplift and extension-related magmatism was concentrated in the Western Province rather than closer to the margin. It is possible that the uplift, extension and magmatism in the Western Province is not directly related to the tectonic activity at the margin, and may be related to the processes immediately underlying the region.

If, as concluded by Waight *et al* (1998b) and Muir *et al* (1995), the MTZ collided with the Western Province prior to 118 Ma (age of stitching Separation Point Batholith), then subducting oceanic lithosphere is indicated beneath the Western Province at this time (figs. 9.1 and 9.2).

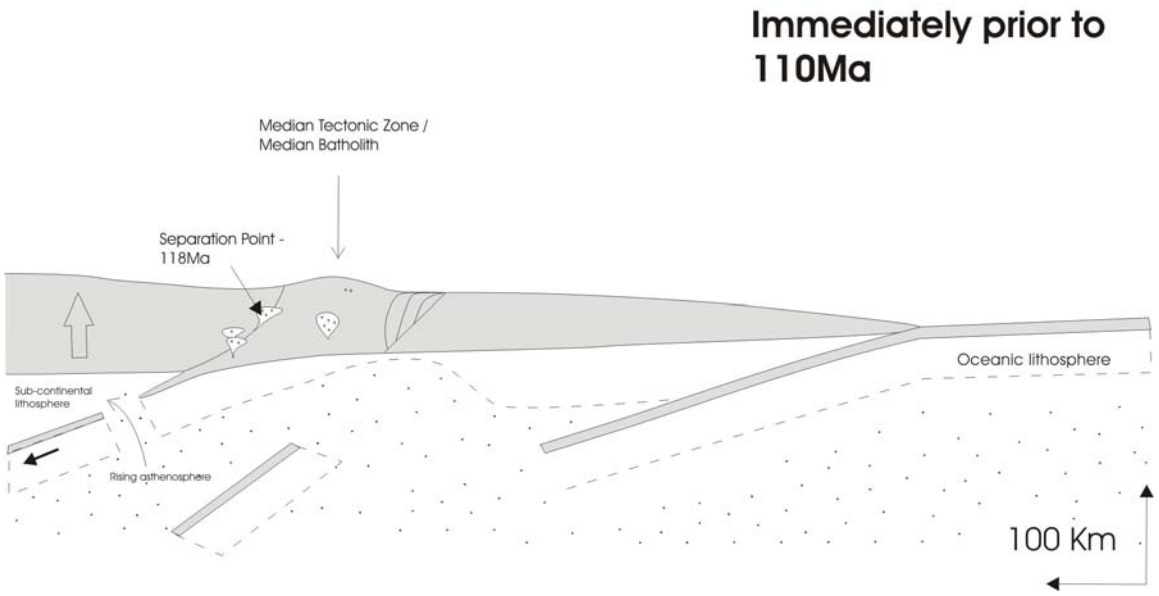

Fig.9.5 Multiple subduction zone model for the formation of the Separation Point Suite involving three subduction zones. Detachment of the MTZ/Western Province subducting lithosphere resulting in uplift of the Western Province.

Melting of the MTZ underplate is concluded by Muir *et al* (1995) for the generation of Separation Point Batholith melts. The onset of melting is thought to have occurred rapidly following a period of strong deformation of MTZ rocks (Kimbrough *et al*, 1993; Muir *et al*, 1995). The detachment of the previously subducting oceanic crust which was subducting beneath the Western Province may have promoted the decompression melting of the MTZ underplate to produce the Separation Point Batholith (fig. 9.5). Slab detachment is indicated in the diagram of Muir *et al*, 1995 (fig.9.1), but is highlighted in fig. 9.5.

Extensional tectonics associated with uplift following the cessation of subduction is used as one of the diagnostic features of slab detachment following continental collision by Davies & von Blanckenburg (1995). Uplift as a consequence of slab detachment and continental collision in the central Alps resulted in the uplift of 13 km of metamorphic and magmatic units within 6 Ma, and deposition of large volumes of sediments into basins generated as a consequence of the uplift and extension (Carrapa & DiGiulio, 2001). The rapid uplift and extensional tectonics of southern Spain are also attributed to slab detachment (Zeck, 1995). Therefore it is proposed that the production of the Separation Point magmas may have been enhanced by the detachment of the subducting slab, and slab detachment may have been responsible for the rapid uplift and extension which resulted in the deposition of the Pororari Group.

Half-graben development was not confined to the Western Province, and major extensional basins formed in the S and SE of the South Island. The Great South Basin and southern Canterbury Basins, which are filled by Cenomanian (97.5 Ma) and younger sediments, strike NNE-NE which is sub-parallel to the trend of the spreading axes formed during the separation of New Zealand from Antarctica. These rift-related basins are broadly contemporaneous with the onset of MSVG and MIC magmatism and are younger than the first rift-related basins on the West Coast of the South Island. The mid-Cretaceous fault systems striking E-W, which flank the southern edge of the Chatham Rise may have been originally parallel to the WNW striking West Coast faults. Since the strike of the Chatham Rise is considered by most authors to be parallel to the Gondwana margin, the mid-Cretaceous Western Province basins and the Bounty Trough probably developed sub-parallel to the paleo-Gondwana margin. In contrast, the slightly younger (Cenomanian onwards) basins, e.g. the Great South Basin, developed in a NE-SW direction, parallel to the trend of later Cretaceous spreading between New Zealand and Antarctica.

9.4 Models for the formation of the MSVG and MIC

9.4.1 Model 1 – Slab detachment and localised upwelling of enriched asthenospheric mantle

In this model, the rapid onset of magmatism (both MSVG and MIC) is triggered by the detachment of the subducting slab following the cessation of subduction due to the arrival of the Hikurangi Plateau and spreading ridge and subsequent slab capture (Luyendyk, 1995). The opening of the slab window allowed enriched asthenospheric mantle to rise up through the slab window. The asthenospheric mantle reached sufficiently shallow levels beneath the Pahau terrane to partially melt, producing the alkaline magmatism of the CMIP. The thickened lithosphere of the Rakaia terrane and the presence of a metasomatised mantle wedge precluded the production of alkaline magmatism, however the decompression associated with the slab detachment promoted partial melting of the mantle wedge to produce the calc-alkaline volcanics of the MSVG. Partial melting was enhanced by the juxtaposition of relatively cold mantle wedge lithospheric mantle with hot asthenosphere.

9.4.1.1 Model 1: description

Following the cessation of subduction in the Motuan Stage (105-100 Ma), significant subsidence occurred in Marlborough, which is implied by the thick marine sediments, which can be locally demonstrated to be related to active extension and half-graben development (Laird, 1992). These thick marine sediments pre-date the emplacement/eruption of the CMIP. In other areas the age relationship between half-graben formation and sediment deposition are uncertain, however it is likely that the subsidence was accompanied by half-graben development. The age of the mid-Cretaceous faults of the Chatham Rise, which contain Ngaterian Stage sediments cannot be demonstrated to be syn-depositional, however their orientation is parallel to the paleo-Gondwana margin. This post-subduction subsidence may be explained by the pre-detachment extension initiated as the Gondwana margin was 'captured' by the divergent Pacific plate. In the model of Luyendyk (1995), slab capture occurred with the Hikurangi Plateau adjacent to the Gondwana margin (fig.9.6).

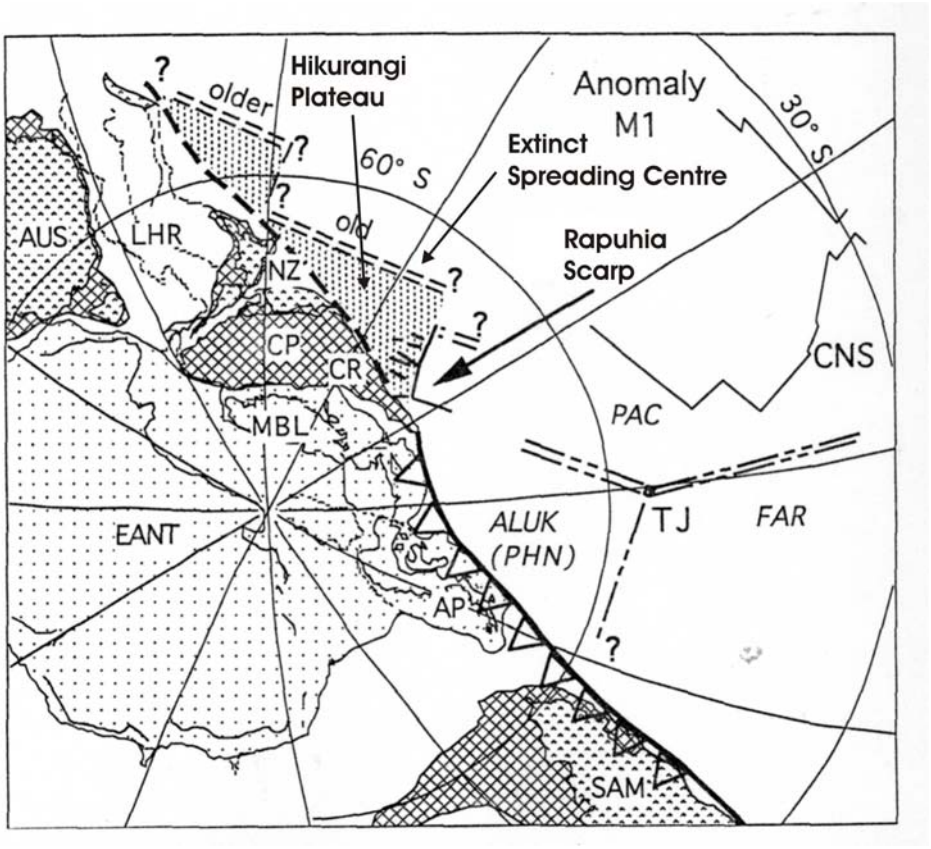

Fig.9.6 Annoted reconstruction illustrating the identified failed spreading centre and the Rapuhia Scarp paleo-transform at 100 Ma (Luyendyk, 1995). CP: Campbell Plateau, CR: Chatham Rise, NZ: New Zealand, LHR: Lord Howe Rise, TJ: Triple Junction.

The cessation of subduction and detachment of the subducting slab can occur as a result of the attempted or achieved subduction of a spreading ridge which has been indicated, amongst others, in Costa Rica (Abratis & Wörner, 2001), Chile (Rogers & Saunders, 1989), northern Baja California (Dickinson & Snyder, 1979; Hole *et al*, 1991; Rogers *et al*, 1985) and the Antarctic Peninsula (Hole, 1988, 1990). A spreading ridge may reach the trench but be too buoyant to subduct, or may stall offshore as described for southern Baja California (Hole *et al*, 1991) and parts of the East Pacific Rise (EPR) - western North America interaction, specifically the approach and stall of the Monterey plate on the eastern side of the EPR (Nicholson *et al*, 1994).

There are thermal and therefore age constraints on whether or not oceanic crust can be subducted, which are dependent upon cooling by interaction with seawater (Severinghaus & Atwater, 1990). The presence of ridges which stall and fail before they reach a subduction zone suggest that young, hot slabs resist subduction due to their lack of negative buoyancy (Severinghaus & Atwater, 1990). The 'capture' of young slabs due to the failure of a ridge, either at the continental margin or stalling offshore, results in the two, originally spreading plates, becoming one and the previously subducting plate and slab taking on the motion of the plate that captures it, i.e. the overriding plate (Nicholson *et al*, 1994).

The initial subsidence which occurred immediately following the cessation of subduction along the New Zealand sector of the Gondwana margin may be due to the gradual opening of a slab window in response to the tensional stress exerted by the divergent Pacific plate (fig.9.7), rather than an abrupt detachment. Full detachment and opening of the slab 'gap' is not indicated until the emplacement and eruption of the CMIP. Therefore a 2 to 7 Ma time period is implied for the gradual extension and subsidence of the margin prior to final detachment and rapid uplift which accompanied the magmatism. A 7 Ma time delay is comparable to other slab-detachment related volcanism (Alexander Island: 18 to 48 Ma (Hole, 1988); eastern Europe: 12 Ma (Nemcok *et al*, 1998); Scotland and Ireland: at least 5 Ma with a pronounced peak of activity after 20 Ma (Atherton & Ghani, 2002)).

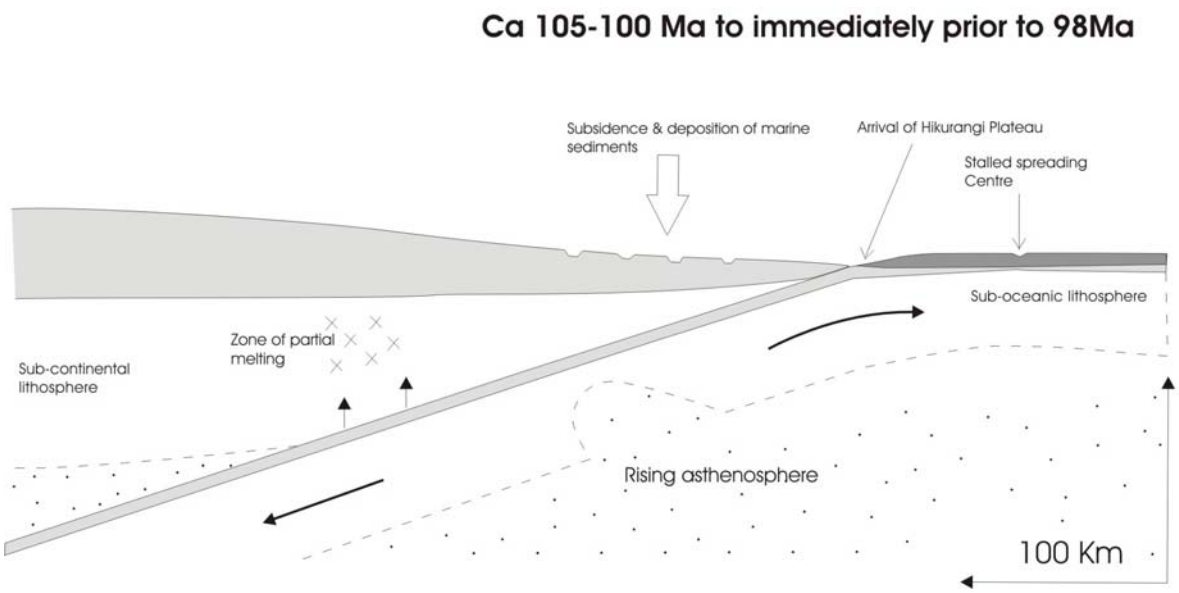

Fig.9.7 Subsidence in Marlborough immediately prior to the detachment of the slab resulting in the deposition of relatively undeformed marine sediments which are up to 2000 m thick (Laird, 1992).

Another unconformity is noted in Marlborough which separates the mildly deformed half graben marine deposits from a sequence of overlying non-marine to shallow marine siliciclastic sediments (Laird, 1992). The tectonic event was Ngaterian (100-94 Ma) and more specifically probably lower Cenomanian in age (*ca.* 97.5 Ma) (Laird, 1992). The non-marine and shallow marine sediments indicate a possible relative sea level drop of approximately 500m (Laird, pers comm). The non-marine sediments are interbedded with lava flows and pyroclastic deposits which are correlated with the Central Marlborough Igneous Province (CMIP) (Warner, 1990). The lower Cenomanian tectonic event appears to be a relatively localised phenomenon, described as local 'updoming' by Laird (Laird & Bradshaw, 2002), and which is closely associated with the emplacement and eruption of magmas of the CMIP. This 'doming' may be a localised effect due to the emplacement of plutons and magmas to shallow levels in the crust.

Deposition of sediments in the Rakaia terrane from 105 Ma to the onset of MSVG volcanism was terrestrial, and minor quantities of Torlesse sandstone-dominated conglomerates are found immediately underlying the MSVG (Hewson Formation). Petrified wood and tree trunks indicate that the Mt. Somers area was vegetated prior to the eruption of the MSVG.

The generation of calc-alkaline magmas as a result of slab detachment occurs as a consequence of the juxtaposition of hot asthenosphere against thickened lithospheric mantle of the overriding plate leading to the melting of the metasomatised wedge and the production

of calc-alkaline melts (Aldanmaz *et al*, 2000; Davies & von Blanckenburg, 1995; Nemcok *et al*, 1998). If the asthenosphere continues to thermally erode the base of the overriding lithospheric mantle, it may reach sufficiently high enough levels to partially melt, and a transition from calc-alkaline to transitional to alkali-basalt magmas are produced (Aldanmaz *et al*, 2000; Coulon *et al*, 2002). Calc-alkaline volcanism can be produced both by the heat influx of upwelling asthenospheric mantle or by adiabatic decompression resulting from lithospheric extension or uplift (e.g. Aldanmaz *et al,* 2000; Nemcok *et al*, 1998).

No transitional or alkali-basaltic magmas were produced during the mid-Cretaceous in the Rakaia terrane and therefore the thermal erosion of the base of the lithospheric mantle beneath the Rakaia terrane is interpreted to have been too short-lived for a transition to alkaline melts to occur.

The MIC (and other members of the CMIP) were sourced directly from the upwelling asthenosphere (fig. 9.8). The formation of alkaline magmas following slab detachment is ascribed to decompression melting of asthenospheric mantle as it rises up into and through the 'gap' or 'window' in the slab. Asthenospheric mantle will probably not melt unless it rises to depths shallower than 50 km or is volatile rich (Davies & von Blanckenburg, 1995). Therefore melting of asthenosphere is dependent upon the depth of slab detachment. The rate of subduction has a strong effect on the depth of slab detachment, with slower subduction velocities (e.g. 1cm/yr) promoting detachment at depths of 50 to 120 km. At faster velocities, detachment occurs at deeper levels (Davies & von Blanckenburg, 1995). Therefore relatively young, hot slabs tend to detach at shallower levels (50 - 120 km).

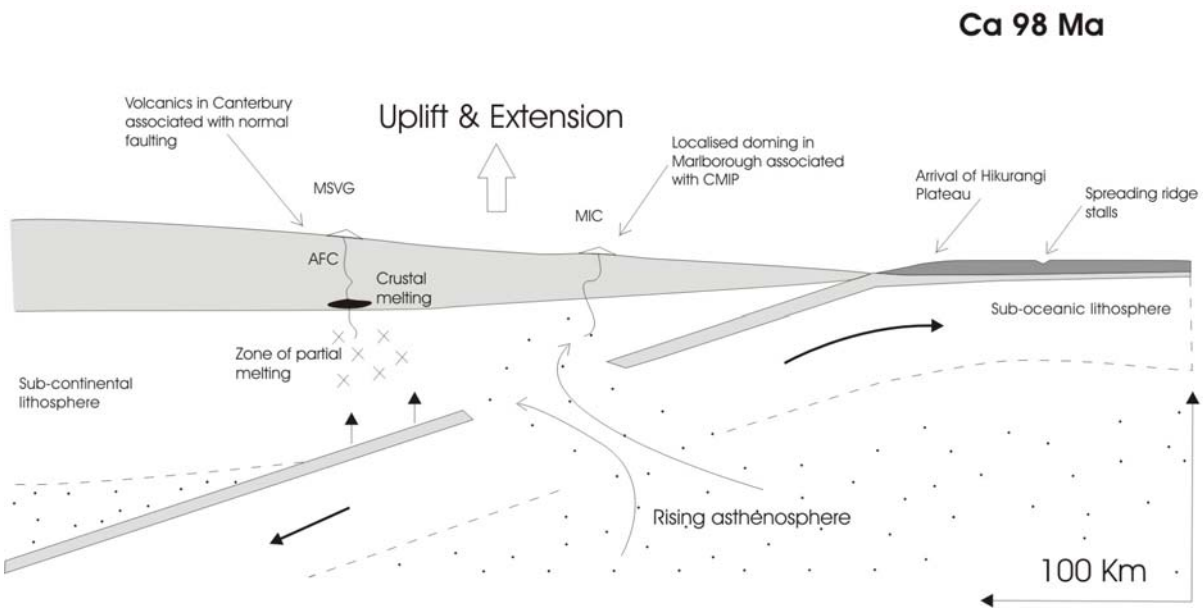

Fig.9.8 Slab detachment at *ca.* 98 Ma resulting in the localised uplift in Marlborough associated with MIC and other CMIP magmatism. MSVG magmas produced as a result of partial melting of the sub-continental lithosphere as a consequence of the pressure-release. Partial melting to produce the calc-alkaline magmatism may have been enhanced by the juxtaposition of lithospheric mantle wedge and hot asthenosphere.

The nature of the volcanism produced as a result of slab detachment is largely dependent upon the nature of asthenosphere underlying the overriding plate. Small degrees of partial melting have been implicated to account for the alkaline nature of most post-subduction magmas, however the enriched nature of some magmas generated as a consequence of slab detachment are indistinguishable from OIB-type magmas generated as a result of mantle plume activity (Hole *et al*, 1991). The MIC (and other members of the CMIP) have characteristics indistinguishable from OIB and have HIMU signatures. These characteristics are shared by slab detachment related volcanics in Algeria (based upon trace element evidence) (Coulon *et al*, 2002). In Algeria, the HIMU signature is considered to be derived from the upwelling (due to slab detachment) of a large (2500 x 4000 km) asthenospheric 'sheet' which underlies the base of the lithosphere from the eastern Atlantic Ocean, central Europe, western Mediterranean and North Africa (Carminati *et al*, 1998; Hoernle *et al*, 1995) (fig. 9.9). The scale of the western European asthenospheric 'sheet' is twice that proposed for plume heads from the lower mantle (Griffiths & Campbell, 1990; White & McKenzie, 1989).

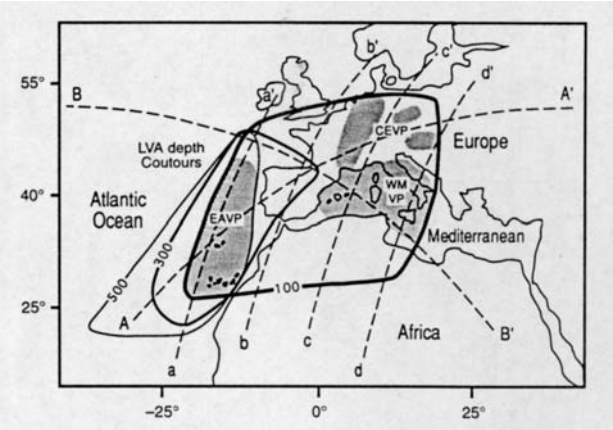

Fig.9.9 Extent of asthenospheric 'sheet' underlying central and western Europe and north Africa (Hoernle *et al*, 1995).

The asthenosphere 'sheet' described above is in contrast to the discrete 'mantle plumes' described and tomographically imaged for the Mediterranean region e.g. (Granet *et al*, 1995; Wilson & Bianchini, 1999).

A HIMU signature is also observed from post-subduction, slab detachment-related volcanics in Costa Rica. The source of lavas in Costa Rica is interpreted to be from the nearby Galapagos plume (Abratis & Wörner, 2001) (fig. 9.10).

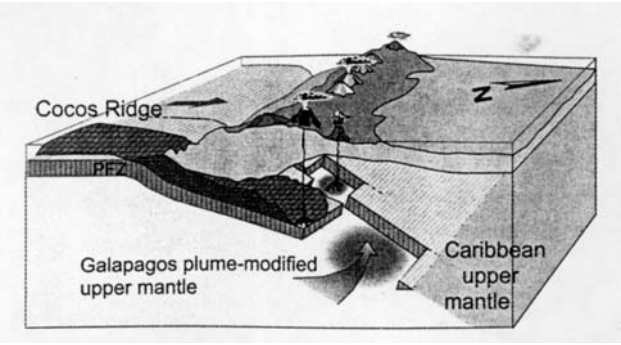

Fig.9.10 of slab windows beneath Costa Rica (from Abratis & Wörner, 2001).

The enriched asthenosphere responsible for the CMIP volcanism/plutonism in this model may be the same source responsible for the widespread occurrence of HIMU magmatism of similar age in Marie Byrd Land (Storey *et al*, 1999). The geochemically similar southeastern Australia magmatism (Smith *et al*, 1988; Williams *et al*, 1982), Tasmanian dykes and intrusions (Gleadow & Duddy, 1980), Balleny plume (Lanyon *et al*, 1993), Late Cretaceous magmatism in the Chatham and Antipodes Islands (Panter *et al*, 1997) and perhaps the Hikurangi Plateau may also have been derived from the same widespread source.

A large 'weak' or 'fossil' plume fixed beneath the Gondwana lithosphere has been proposed to explain the Cenozoic alkaline volcanism asociated with the West Antarctic Rift System (WARS) (Hart *et al*, 1997; Rocholl *et al*, 1995). The 'fossilized' plume was elaborated on by Panter *et al* (2000) who suggest that in addition to the 'fossil plume', a modest Cretaceous plume (600-800 km) underplated a pre-existing metasomatised layer within the Gondwanaland lithosphere at around 100 Ma, resulting in localised true HIMU magmatism in Marie Byrd Land. The pre-existing metasomatised layer is proposed to have been enriched during the Jurassic Bouvet plume (~ 200 Ma) (Panter *et al*, 2000). The variable value of $^{206}Pb/^{204}Pb$ (true HIMU $\geq$ 20.5) from approximately 19.5 to 20.7 can be divided into lower-μ (<20.5) and HIMU ($\geq$ 20.5) for all 'plume-derived' dykes, volcanics and intrusives from the former Gondwana borderland regions (Panter *et al*, 2000). Such a large area (>3 x 10^6 km^2) of the lower-μ component requires a plume head in excess of 2000 km (as decribed by Weaver *et al*, 1994). Panter *et al* (2000) conclude that underplating by a HIMU mantle plume (of smaller diameter than that proposed by Weaver *et al* (1994)), preceded the rifting of New Zealand and Antarctica, however the '*rifting caused adiabatic decompression melting of the fossil plume and overlying plume-modified lithosphere'*.

The widespread enrichment of asthenosphere and metasomatism of the overlying lithosphere due to a previous plume event (the Jurassic Bouvet plume) as suggested by Panter *et al* (2000) provides a more satisfactory explanation for the widespread and long-lived occurrence of Gondwana break-up and post-break up HIMU magmatism (including the MIC). The additional impact of a more modest Cretaceous plume (Panter *et al,* 2000) provides a satisfactory explanation for the higher-MU signature in the mafic dykes of Marie Byrd Land (Storey *et al,* 1999).

The SHRIMP ages from the Malvern Hills, Mount Somers and McQueens Valley areas indicate a maximum duration of rhyolitic magmatism of 3.7 Ma (Chapter 6). Gross averaging of available geochronological data for the CMIP (using maximum K-Ar ages) yields an age of 98 Ma. The sediments which confine some of the CMIP lavas and pyroclastic deposits range from lower Cenomanian (97.5 Ma) to uppermost Ngaterian (New Zealand stage 100 Ma to 94 Ma) (Laird, 1992). It therefore appears as though both the MSVG and MIC magmatism were relatively short-lived. Similar short duration slab-detachment related volcanism is documented from Costa Rica: 3.8 Ma (Abratis & Wörner, 2001), Algeria: 3.2 Ma (Coulon *et al*, 2002) and Croatia: 3.1 Ma (Nemcok *et al*, 1998).

The short-lived nature of the MSVG and MIC is likely to be a function of the thermodynamic properties of the underlying asthenosphere, as well as the rate of extension as a result of slab capture by the Pacific plate. The initial thermal contrast upon slab detachment facilitates the rapid upwelling of asthenosphere, however this cannot be long-lived if the asthenosphere rises in a passive response to rifting. Where asthenosphere rises in the form of a plume head, the continuous supply of heat promotes the long-lived buoyant nature of plumes. This is not the case where asthenosphere wells up in a passive response to rifting, unless the rifting is also long-lived e.g. at spreading centres. Another consideration is the strain induced into the continental crust. If the strain due to detachment is rapidly dispersed inland, asthenosphere may not rise to sufficiently shallow levels to cause any major uplift or magmatism.

This model is consistent with a subduction zone at the Gondwana margin leading to the deformation of the Pahau terrane rocks until 105-100 Ma. This model argues against a previously shallow subduction zone for the formation of the MTZ (e.g. fig 9.3) because this would have led to a stripping of the sub-continental lithosphere and limited opportunity for a metasomatised mantle wedge to develop.

9.4.1.2 Problems with model 1

- If the sub-continental lithosphere beneath the Rakaia terrane was being modified by the addition of fluids from the subducting slab prior to 98 Ma, why were calc-alkaline magmas not generated in the Eastern Province terranes prior to 98 Ma?

The absence of calc-alkaline magmas in the overlying Rakaia terrane prior to 98 Ma implies that either the conditions required for partial melting of the mantle wedge were not met, or that magmas formed but did not penetrate the relatively thick continental crust. It is unknown whether granitoids are found at deep levels in the crust, but there is no evidence of this in the form of xenoliths within the MSVG rocks.

9.4.2 Model 2 – Large-scale mantle plume

Model 2 suggests a single plume, of wide diameter (2000 km, Weaver *et al* (1994)), may have provided the mechanism for, or arrived shortly after the uplift and extension in the Western Province, provided a heat source for the generation of calc-alkaline magmas under the Rakaia terrane, and directly sourced the CMIP (including the MIC). This model is broadly consistent with the plume-enhanced break-up models of Weaver *et al* (1994) and Storey *et al* (1999), who concluded that a large diameter mantle plume defined the locus of rifting of the New Zealand block from Gondwana.

9.4.2.1 Model 2: Description

Accretion and subduction were long-lived processes operating along the Gondwana margin. Modification of the mantle wedge underneath the Eastern Province continued until the cessation of subduction approximately 105 - 100Ma.

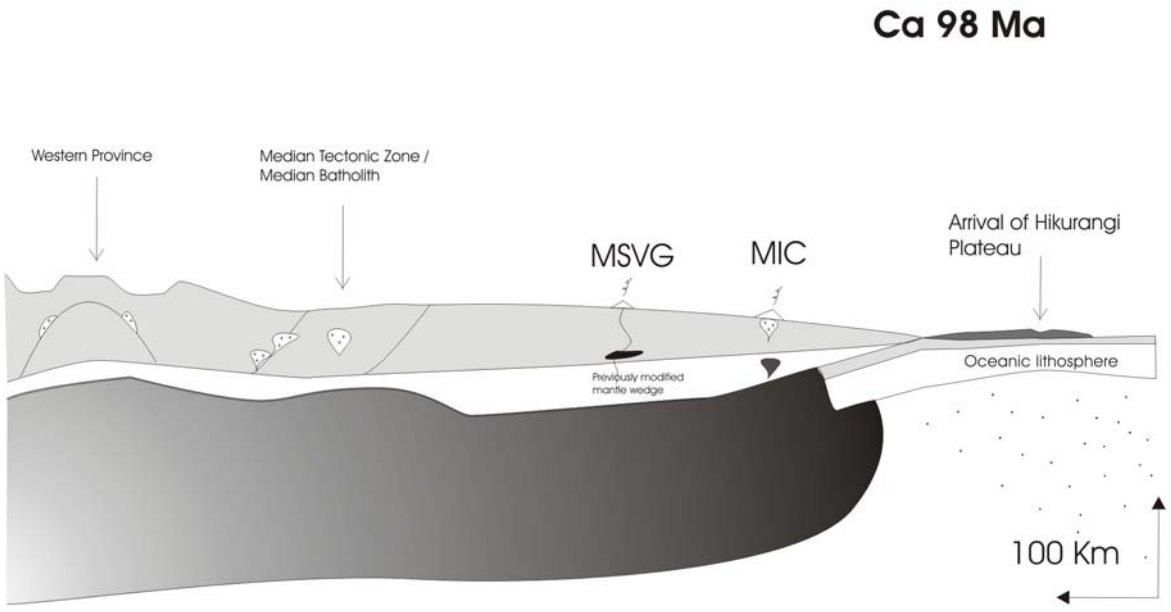

Fig 9.11 Plume impact led to uplift and extension in the Western Province and the melting of subduction-modified mantle wedge under the Rakaia terrane, whilst a small batch of plume material was sourced from the plume head under the Pahau terrane. Western Province section modified from Waight *et al* (1998b)

The extensional regime initiated in the Western Province was aided by or caused by the impingment of a plume head, centred under western Marie Byrd Land. The impinging plume

provided a mechanism to produce the uplift and extension which resulted in the large Cretaceous grabens and sedimentary basins (9.11).

The plume provided the heat source and uplift necessary for the partial melting of the modified former mantle wedge beneath the Rakaia terrane of the Eastern Province. The plume did not encounter modified mantle beneath the Pahau terrane and was able to source small volcanic centres within the Pahau terrane (i.e. MIC and other members of the CMIP). The same plume, as suggested by Weaver *et al* (1994), may also be responsible for the present-day volcanism at Mt. Erebus in Antarctica (fig. 9.12).

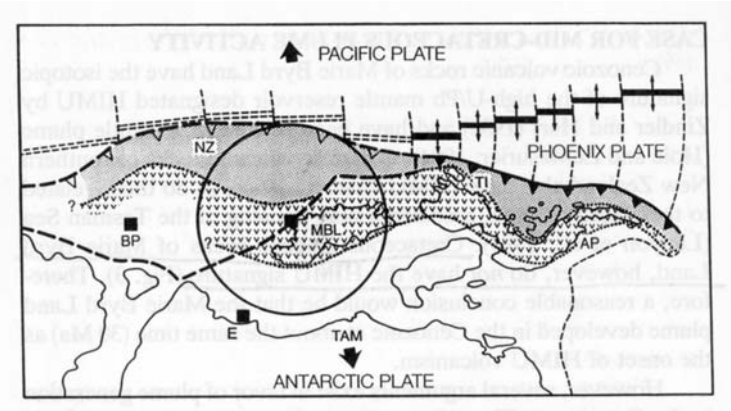

Fig.9.12 From Weaver *et al* (1994).

There are a number of timing problems associated with the plume model. The transition from compression to extension in the Western Province was initiated at *ca.* 110 Ma (Waight *et al*,1998b). If this was as a result of the impact of a plume head, which would broadly correspond to the emplacement of mafic dykes of HIMU affinity in Marie Byrd Land (Storey *et al*, 1999), there are considerations as to the cessation of subduction at the Gondwana margin, which, based on sedimentological evidence occurred 105 -100 Ma. Therefore, subduction continued for approximately 5-10 Ma following the initial impact of the plume under western Marie Byrd Land. The presence of a plume is indicated by the CMIP at *ca* 98 Ma. Therefore diachroneity and a margin-ward migration or spreading of a plume head is implied to account for the younger age of the CMIP. An alternative explanation is that the plume did not impinge on the base of the continent until *ca.* 98 Ma, in which case the uplift of the Western Province cannot be attributed to the arrival of a plume-head. This is difficult to achieve if the magmatic activity (e.g. mafic HIMU dykes: 110 to 95 Ma) in western Marie Byrd Land are related to the same plume as the CMIP magmatism.

Another important consideration is the position and age of the Hikurangi Plateau. Storey *et al* (1999) suggest that the Hikurangi Plateau may be the result of excess melt production at a spreading centre caused by the close proximity of a plume head. If this is the case, the Hikurangi Plateau must be of very similar age to the CMIP and MSVG. This would thereby preclude the arrival of the Hikurangi Plateau as a mechanism for the cessation of subduction since this occurred some 2-7 Ma earlier. The Hikurangi Plateau must therefore either be unrelated to the Marie Byrd Land plume (*cf* Storey *et al*, 1999), or was sourced from the same plume and therefore cannot be implicated in the cessation of subduction (*cf* Luyendyk, 1995). The arrival of the Hikurangi Plateau as a mechanism for the cessation of subduction is incompatible with the same plume producing the CMIP magmatism.

It is possible that the Hikurangi Plateau was sourced from a different plume. Further research and dating of the Hikurangi Plateau is required in order to fully explore the possible role that the plateau played in the break-up story.

9.4.2.2 Problems with model 2

- No mid-Cretaceous HIMU magmatism is associated with the large extensional basins in the Western Province.

The absence of A-type granites and mafic dykes of a similar age to those found along the Ruppert-Hobbs coast of Marie Byrd Land in the Western Province of New Zealand is interesting. As drawn on the diagram of Weaver *et al* (1994) (fig. 9.12), the Western Province of New Zealand may have been too far from the plume head to have been affected by the HIMU magmatism. If the Western Province was within the influence of the plume, it is possible that the plume head did not reach sufficient levels to partially melt to produce alkaline magmatism.

- The MIC and other members of the CMIP are of limited geographical extent and of short-lived duration, inconsistent with a large scale plume-head incursion.

The CMIP magmatism in Marlborough has a preserved extent of 200 km^3 (Baker *et al*, 1994). The MIC is considerably smaller and has a preserved extent of 3 km^3. Although the combined extent is by no means small, it does not fit the criteria for ancient mantle plumes which are *'characterised by massive flows that can be correlated over large distances… and lava floods over a large equidimensional area that is typically 2000 to 2500 km across'* (Campbell, 2001). The association of plutonic with volcanic rocks and the shallow nature of the intrusives indicates that only a limited amount of material is likely to have been removed and that the CMIP is unlikely to have had proportions akin to igneous provinces ascribed to the impact of a mantle plume e.g. Karoo province 2.5 x 10^6 km^3, Ferrar province 0.5 x 10^6 km^3 or the Chon Aike silicic province 1.7 x 10^6 km^3 (Storey & Kyle, 1997) and references therein.

- There is no OIB signature inherited by the MSVG and no OIB-signatured dykes of mid-Cretaceous age have been identified in the MSVG or Rakaia terrane.

Where a plume rises beneath modified lithospheric mantle, the first products are likely to be partial melts of the overlying lithospheric mantle and/or melts of the continental crust which may be accompanied by or followed by basaltic magmatism and volcanism. Calc-alkaline magmatism in the MSVG may have been produced by anomalously hot asthenosphere, but this does not provide a distinction between Model 1 and Model 2. What is clear is the absence of any OIB affinity dykes in the Rakaia terrane. It is likely that the MSVG did not directly interact with a plume; this may be because the plume head did not reach sufficiently shallow levels to melt, or that magmatism was of such short-lived duration that the thermal erosion of the mantle lithosphere did not give way to transitional and eventually alkaline melts as observed in Algeria and Turkey (Aldanmaz *et al*, 2000; Coulon *et al*, 2002).

- HIMU OIB magmas are restricted to the Pahau terrane.

The absence of mid-Cretaceous HIMU dykes or intrusives in any of the other Eastern Province terranes may be due to the thickness of the lithosphere during the mid-Cretaceous.

The Pahau terrane, being the outboard terrane is likely to have been thinner than the inboard terranes. The subsidence of the Pahau terrane and deposition of 2000m of marine sediments suggests thinning of the Pahau terrane prior to the emplacement and eruption of the CMIP. The relatively small degrees of contamination of the MIC magmas by continental crust is consistent with the Pahau terrane being thinner than the Rakaia terrane in the mid-Cretaceous, and probably also thinner than the other Eastern Province terranes.

9.5 Discussion

Evidence that subduction was taking place along the Gondwana margin is largely from the deformation of the sediments in the Rakaia and Pahau terranes. As described in Chapter 2, the cessation of subduction is indicated by an unconformity which separates heavily deformed, accretionary wedge sediments and relatively undeformed overlying sediments of slightly younger age. This change in deformation is marked by a major angular unconformity that divides Motuan age deposits (105-100 Ma).

The lack of a volcanic arc in the Rakaia terrane as a consequence of prolonged subduction until the end of subduction (105 – 100 Ma) implies that either a subducting slab was not deep enough to dehydrate, or that melts were not permitted to ascend through the crust. The suggestion that the Median Batholith may be the arc associated with the accretionary wedge deformation of the Pahau terrane requires a very flat slab underneath the Eastern Province terranes. This would provide an explanation for the lack of arc-related magmatism in the Rakaia terrane. However, the presence of a shallow slab beneath the Eastern Province of the Gondwana margin would have caused extensive deformation, uplift and erosion of the sub-lithospheric mantle. Erosion of the sub-lithospheric mantle due to stripping by a shallow slab leads to timing problems related to the metasomatism of the mantle wedge which eventually sourced the MSVG. The shallow slab model also creates problems regarding the formation of the Separation Point Suite and Hohonu Suite which would require an alternative mechanism for their generation than those suggested by Muir *et al* (1995) and Waight *et al* (1998b). Additionally, the MTZ-trench distance (>600 km) far exceeds the maximum length of flat-slab subduction as proposed by van Huhen *et al* (2002). Therefore the models proposed by Muir *et al*, 1995 and Waight *et al,* 1998b are favoured, in which more than one subduction

zone was responsible for the MTZ and deformation of the Rakaia and Pahau accretionary prisms.

Given the documented common association of OIB magmatism with slab detachment, closely following the cessation of subduction, the possibility that a similar scenario exists to explain the occurrence of the MIC and MSVG must be taken seriously. The occurrence of HIMU magmatism in the Pahau terrane suggests that the asthenospheric source was enriched relative to normal 'depleted' asthenospheric partial melts such as those produced at ocean spreading centres (N-MORB). The presence of HIMU-OIB is commonly associated with mantle plumes which elevate enriched lower mantle magma into the upper mantle e.g. (Weaver *et al*, 1987). However, a similarly enriched asthenospheric domain has been mapped geochemically and tomographically under western Europe, which is not considered to be a typical 'plume', but rather a 'sheet-shaped' enriched mantle upwelling (Carminati *et al*, 1998; Hoernle *et al*, 1995). Alternatively, a 'fossil plume' residing beneath the lithosphere has been implicated for the origin of the Cretaceous and Cenozoic alkaline magmatism found in the Marie Byrd Land and the West Antarctic Rift System respectively (Hart *et al*, 1997; Panter *et al*, 2000; Rocholl *et al*, 1995).

Weaver *et al* (1994) and Storey *et al* (1999) conclude that rifting between New Zealand and Antarctica occurred under the influence of a mantle plume, the impact of which was coincident with rifting. However the effects of a single mid-Cretaceous plume underlying Marie Byrd Land would have had to have been very widespread and extend from the Australian and Tasmanian margin, to the Chatham Islands and the area studied in this thesis, the Mandamus Igneous Complex and correlated activity. The Hikurangi Plateau is also suggested to have formed as a consequence of the same plume (Storey *et al*, 1999). In this case the plume would be expected to have a diameter of at least 2000 km (fig.9.12) (Weaver *et al*, 1994). However, the temporally and geochemically related magmatism in Australia (the *ca.* 99 Ma Mt. Dromedary alkalic complex in New South Wales (Williams *et al*, 1982)), and the Hikurangi Plateau (age unknown) (Mortimer & Parkinson, 1996) would have been outside the influence of such a plume, although Storey *et al* (1999) suggest that the plateau may have formed as a consequence of excess melt production caused by the influence of the mid-Cretaceous plume.

The Hikurangi Plateau is an ideal candidate to have formed directly from the influence of an impinging plume head. If the Hikurangi Plateau was formed in close proximity to the Gondwana margin it is conceivable that the same plume head may have been propagated into the Gondwana continent. Given the model of Luyendyk (1995), which indicates that the Hikurangi Plateau was docked alongside the Gondwana margin with a spreading centre to the other side, the Hikurangi Plateau must be older than the cessation of subduction at the Gondwana margin, and therefore a similar, if not the same age as the Ontong Java and Manihiki Plateaux which formed between 115 and 130 Ma e.g.(Mahoney & Spencer, 1991; Mahoney *et al*, 1993). Mortimer & Parkinson (1996) correlate the Hikurangi Plateau with the Ontong Java and Manihiki Plateaux and suggest that the Hikurangi Plateau is therefore no older than 125 Ma.

A large scale enriched asthenospheric anomaly, akin to the 'fossil plume' component of Rocholl *et al*, 1995; Hart *et al,* 1997 and Panter *et al,* (2000) (Model 1) is favoured due to the large number of small–scale plumes that would otherwise be required to account for the mid-Cretaceous magmatism associated with the break-up of the Pacific margin of Gondwana. As described for Model 2, a large single plume is difficult to reconcile with the sedimentological evidence for the cessation of subduction, uplift in the Western Province, magmatism in Marie Byrd Land and the possible affinity with the Hikurangi Plateau, which is alongside the Chatham Rise and is implied in the models of Luyendyk (1995) to have interacted with the Gondwana margin prior to slab capture. The 'fossil plume' of Hart *et al* (1997), Panter *et al* (2000), and Rocholl *et al* (1995) provides a good explanation for the widely dispersed, relatively low volume magmatism that is associated with extensional tectonics, without invoking the ascent of several small, or a single large-diameter plume head. A mantle plume-head underlying Marie Byrd Land at the time of break-up as described by Weaver *et al* (1994) provides a good mechanism for controlling the position of rifting between New Zealand and Antarctica, and the extensive A-type magmatism observed in Marie Byrd Land. However, the extension of such a plume underneath the Western Province, MTZ and Eastern Province as indicated in Fig. 9.12 is considered to be unlikely given the disparity between the sedimentological evidence from different regions of New Zealand, and the lack of large-scale plume-related magmatism similar to that observed in Marie Byrd Land. A smaller diameter plume, initiated in the mid-Cretaceous, as described by Panter *et al* (2000), measuring 600-800 km would explain the large volume HIMU magmatism in Marie-Byrd Land, but the mobilisation of a 'fossil plume' reservoir is implied to account for the smaller volume post-

subduction magmatism which produced the MIC and CMIP. The 'fossil plume component' may also have sourced the Late Cretaceous HIMU magmatism from the Antipodes and Chatham Islands (Panter *et al*, 1997) and the Tertiary intraplate volcanism in the South Island of New Zealand (Weaver & Smith, 1989), the origin of which remains unresolved.

In summary, the 'fossil plume' of Panter *et al* (2000) is considered to provide the most satisfactory explanation for the widespread and long-lived OIB-affinity magmas which intruded the Gondwana margin during the Mid to Late Cretaceous. The fossil plume was tapped periodically as a consequence of extension due to a series of (micro-)plate collisions and slab capture processes which occurred in rapid succession prior to the onset of the final rifting phase which culminated in the separation of New Zealand from Antarctica and Australia. The MIC and MSVG magmatism was an effect of the slab-detachment process following the arrival of the Hikurangi Plateau and failure of the associated spreading ridge. The capture by the Pacific Plate is considered to be the dominant control on continental separation rather than the impact of a large mantle plume.

9.6 Conclusions

- The arrival of the Hikurangi Plateau and consequential stalling of the Pacific spreading ridge was the driving force behind the rifting of New Zealand from Antarctica and Australia rather than the impact of a mantle plume under western Marie Byrd Land.

- The geographical restriction of the MSVG to the Rakaia terrane is a function of its proximity to the margin and its position above a modified mantle wedge. In contrast, the restriction of the MIC to the Pahau terrane is a function of its position above the resulting slab window as a consequence of slab detachment.

- The CMIP was able to sample enriched asthenospheric mantle because a slab window had opened following the arrival of the Hikurangi Plateau. The thinner nature of the Pahau terrane facilitated the relatively uninhibited rise of magmas, which show low degrees of contamination relative to the MSVG.

- The MSVG was sourced from a different parent magma and did not sample the same enriched asthenospheric mantle as the MIC. The MSVG was produced from the previously modified mantle wedge through adiabatic decompression melting due to slab detachment, and was aided by the thermal contrast with the adjacent asthenospheric mantle which had risen through the slab window.

- The extensional regime which facilitated the eruption of the MSVG was triggered by the detachment of the subducting slab and the capture of the Gondwana margin by the divergent Pacific Plate.

- The short-lived nature of the MSVG and MIC magmatism is due to the passive nature of asthenospheric upwelling as a consequence of slab-detachment.

- The CMIP is unlikely to have been sourced from the same plume as the Marie Byrd Land magmatism and is more likely to have sampled previously enriched asthenospheric mantle, which may have been enriched in the Jurassic as suggested by Panter *et al*, 2000.

Chapter 10:

Summary of Main Conclusions

This thesis presents the first combined study of the MSVG and MIC (part of the CMIP) and their significance in relation to the mid-Cretaceous rifting of New Zealand from Antarctica and Australia. The main conclusions of the study are as follows:

- The MSVG was a relatively extensive volcanic field with an aerial extent of at least 18,000 km^2 which is comparable to the presently active Taupo Volcanic Zone in the North Island of New Zealand.

- The eruptives of the MSVG can be demonstrated to be associated with normal faulting in a subaerial environment, and rhyolitic dykes are seen to exploit the active faults in both the Mount Somers and Malvern Hills field areas.

- The MSVG was sourced from separate centres within the Rakaia terrane of the South Island. The products of the volcanism are consistent at each major outcrop of the MSVG and the sequence is usually andesite-rhyolite-ignimbrite, however in the Malvern Hills, the sequence is rhyolite-ignimbrite-andesite. At Mt. Barrosa a stratigraphy has been established which indicates that the earliest exposed product of volcanism was andesite, which was followed by basaltic-andesite and dacite lavas. The dacitic phase was followed by pitchstone flows, rhyolite flows, rhyolite domes and eventually ignimbrite.

- The geochemistry of the MSVG indicates that the magmas formed by partial melting of a subduction-modified mantle wedge. The melts evolved from the basaltic-andesites to the rhyolites through assimilation fractional crystallisation (AFC) processes. AFC modelling requires the rate of assimilation to increase as the magmas evolved. Radiogenic isotope modelling shows that the rhyolites retain an isotopic link with the basaltic-andesites and that the assimilant has isotopic compositions similar to those of the Rakaia terrane.

- Radiogenic isotope modelling strongly suggests that the magmas of the Malvern Hills were contaminated by Rakaia terrane to lesser degrees than the other outcrops of the MSVG.

- The MIC is part of the larger CMIP and erupted both silica saturated and mildly under-saturated lavas, which were subsequently intruded by high level plutons of syenite, syenodiorite and alkali gabbro. The plutonic complex, volcanic carapace and lahar deposits were subsequently intruded by dykes of similar composition to the trachytic and mafic lavas.

- All units of the MIC were derived from the same enriched mantle source, similar to the HIMU end-member. The MIC samples analysed show varying degrees of crustal assimilation up to a maximum of 25%, but generally less than 10%. The modelled assimilant had an isotopic composition similar to the Pahau terrane samples analysed. The latter stages of the MIC (syenite and tephri-phonolite dyke) show the least contamination, which would suggest that they were emplaced along pre-existing pathways.

- The MSVG yielded SHRIMP crystallisation ages of 97 ± 1.5 Ma to 98 ± 1.2 Ma which are within error of the Rb-Sr age of 97 ± 0.5 for the MIC (Weaver & Pankhurst, 1991). The Ar-Ar ages confirm the coeval nature of the MSVG and MIC magmatism, however they are systematically younger than the Rb-Sr and SHRIMP ages. The Ar-Ar age of the MSVG can be considered to be 94.5 ± 3 Ma and the age of the MIC to be 94.2 ± 1.7 Ma. The deviation of the Ar-Ar from the SHRIMP and Rb-Sr is likely to be function of the 3 different radiogenic systems used, and could be the result of decay constant uncertainty, or uncertainty surrounding the age of standards used.

- The tectonic trigger responsible for the simultaneous onset of MIC and MSVG magmatism was the detachment of the subducting slab following the arrival of the Hikurangi Plateau and subsequent stalling of the associated spreading ridge. The slab window, which opened once slab detachment had occurred, allowed enriched asthenospheric mantle to rise and melt through decompression to source the MIC. The

same decompression and juxtaposition of asthenospheric mantle resulted in the partial melting of the mantle wedge underlying the Rakaia terrane to source the MSVG.

- The restriction of the MIC (and CMIP) to the Pahau terrane, and the MSVG to the Rakaia terrane is a function of their paleo-geographical position relative to the trench at the Gondwana margin. The Pahau terrane was the most outboard terrane in the mid-Cretaceous and was not underlain by a modified mantle wedge. During slab detachment, the Pahau terrane was exposed to upwelling asthenospheric mantle, whereas the Rakaia terrane had an intervening mantle wedge from which the MSVG magmas were sourced.

- MSVG and MIC were short-lived because they were erupted/emplaced in a passive response to tectonic re-organisations which involved the transfer of plate boundary forces from the failed Pacific spreading centre to the Gondwana margin.

References

Abratis, M. and Wörner, G., 2001. Ridge collision, slab-window formation, and the flux of Pacific asthenosphere into the Caribbean realm, *Geology, 29*, 127-130.

Adams, C.J.D. and Oliver, P.J., 1979. Potassium-argon dating of Mount Somers Volcanics, South Island, New Zealand: Limitations in dating Mesozoic volcanic rocks., *New Zealand Journal of Geology and Geophysics, 22*, 455-463.

Adams, C.J.D., 1987. Geochronology of granite terranes in the Ford Ranges, Marie Byrd Land, Antarctica, *New Zealand Journal of Geology and Geophysics, 30*, 51-72.

Adams, C.J.D. and Raine, J.I., 1988. Age of Cretaceous silicic volcanism at Kyeburn, central Otago, and Palmerston, eastern Otago, South Island, New Zealand., *New Zealand Journal of Geology and Geophysics, 31*, 471-475.

Aldanmaz, E., Pearce, J.A., Thirlwall, M.F. and Mitchell, J.G., 2000. Petrogenetic evolution of late Cenozoic, post-collision volcanism in western Anatolia, Turkey, *Journal of Volcanology and Geothermal Research, 102*, 67-95.

Andrews, P.B., 1963. Stratigraphic nomenclature of the Omihi and Waikari Formations, North Canterbury, *New Zealand Journal of Geology and Geophysics, 6*, 228-256.

Andrews, P.B., Field, B.D., Browne, G.H. and McLennan, J.M., 1987. Lithostratigraphic Nomenclature for the Upper Cretaceous and Tertiary sequence of Central Canterbury, *Technical Report New Zealand Geological Survey, Record 24*.

Armstrong, M.J., 2000. Geomorphological and Geophysical Investigation of the effects of Active Tectonic Deformation on the Hydrogeology of the North Culverden Basin, North Canterbury, PhD thesis, Canterbury University, Christchurch.

Armstrong, R.L., 1971. Isotopic and chemical constraints on models of magma genesis in volcanic arcs, *Earth and Planetary Science Letters, 12*, 137-142.

Arth, J.G., 1976. Behaviour of trace elements during magmatic processes - a summary of theoretical models and their applications, *Journal of Results of the U.S. Geological Survey, 4*, 41-47.

Atherton, M.P. and Ghani, A.A., 2002. Slab breakoff: a model for Caledonian, Late Granite syn-collisional magmatism in the orthotectonic (metamorphic) zone of Scotland and Donegal, Ireland, *Lithos, 62*, 65-85.

Baker, J.A., 1990. Geology of the western margin of the Tapuaenuku Plutonic Complex, Marlborough, New Zealand, MSc thesis, Victoria, Wellington.

Baker, J.A., Gamble, J.A. and Graham, I.J., 1994. The age, geology and geochemistry of the Tapuaenuku Igneous Complex, Marlborough, New Zealand, *New Zealand Journal of Geology and Geophysics, 37*, 249-268.

Ballance, P.F., 1993. The Paleo-Pacific, Post-Subduction, Passive Margin Thermal Relaxation Sequence (Late Cretaceous - Paleogene) of the Drifting New Zealand Continent., in *South Pacific Sedimentary Basins (Sedimentary Basins of the World 2)*, edited by P.F. Ballance, pp. 93-110, Elsevier Science Publishers, B.V., Amsterdam.

Barley, M.E., 1987. Origin and evolution of mid-Cretaceous, garnet-bearing, intermediate and silicic volcanics from Canterbury, New Zealand, *Journal of Volcanology and Geothermal Research, 32*, 247-267.

Barley, M.E., Weaver, S.D. and de Laeter, J.R., 1988. Strontium isotope composition and geochronology of intermediate-silicic volcanics, Mt Somers and Banks Peninsula, New Zealand, *New Zealand Journal of Geology and Geophysics, 31*, 197-206.

Beate, B., Monzier, M., Spikings, R., Cotten, J., Silva, J., Bourdon, E. and Eissen, J., 2001. Mio-Pliocene adakite generation related to flat subduction in southern Ecuador: the Quimsacocha volcanic center, *Earth and Planetary Science Letters, 192*, 561-570.

Begg, J.D. and Johnston, M.R., 2000. Geology of the Wellington area., 1:250 000, Institute of Geological and Nuclear Sciences Limited, Lower Hutt

Beggs, J.M., 1993. Depositional and Tectonic History of the Great South Basin, in *South Pacific Sedimentary Basins (Sedimentary Basins of the World 2)*, edited by P.F. Ballance, pp. 365-373, Elsevier Science Publishers B.V., Amsterdam.

Bottinga, Y. and Javoy, M., 1975. Oxygen isotope partitioning among the minerals in igneous and metamorphic rocks, *Reviews of Geophysics and Space Physics, 13*, 401-418.

Bowen, F.E., 1964. Sheet 15: Buller, 1:250 000, Department of Scientific and Industrial Research, Wellington

Boynton, W.V., 1984. Geochemistry of the rare earth elements: meteorite studies, in *Rare earth element geochemistry*, edited by P. Henderson, pp. 63-114, Elsevier.

Bradshaw, J.D., 1989. Cretaceous geotectonic patterns in the New Zealand Region, *Tectonics, 8*, 803-820.

Bradshaw, J.D., 1993. A review of the Median Tectonic Zone: terrane boundaries and terrane amalgamation near the Median Tectonic Line, *New Zealand Journal of Geology and Geophysics, 36*, 117-125.

Bradshaw, J.D., Pankhurst, R.J., Weaver, S.D., Storey, B.C., Muir, R.J. and Ireland, T.R., 1996. The Mesozoic continental margin: Carboniferous-Mesozoic arc terranes in West Antarctica, New Zealand and Australia., in *Mesozoic Geology of the Eastern Australia Plate Conference*, vol. Extended Abstracts: 43, pp. 114-123, Geological Society of Australia Inc.

Bradshaw, J.D., Pankhurst, R.J., Weaver, S.D., Storey, B.C., Muir, R.J. and Ireland, T.R., 1997. New Zealand Superterranes Recognized in Marie Byrd Land and Thurston Island, in *The Antarctic Region: Geological Evolution and Processes*, pp. 429-436.

Brown, G.H. and Field, B.D., 1985. The lithostratigraphy of late Cretaceous to early Pleistocene rocks of northern Canterbury, New Zealand, New Zealand Geological Survey Record 6,

Brown, G.M., 1972. Pigeonitic pyroxenes: A review, *Memoir of the Geological Society of America, 132*, 523-534.

Bruce, Z., 1994. Petrology and volcanology of the Rakaia Gorge and Mt. Misery volcanics, BSc (Hons) thesis, University of Canterbury, Christchurch.

Bryan, S.E., Constantine, A.E., Stephens, C.J., Ewart, A., Schön, R.W. and Parianos, J., 1997. Early Cretaceous volcano-sedimentary successions along the eastern Australian Continental margin; implications for the break-up of eastern Gondwana, *Earth and Planetary Science Letters, 153*, 85-102.

Bryan, S.E., Ewart, A., Stephens, C.J., Parianos, J. and Downes, P.J., 2000. The Whitsunday Volcanic Province, Central Queensland, Australia: lithological and stratigraphic investigations of a silicic-dominated large igneous province., *Journal of Volcanology and Geothermal Research, 99*, 55-78.

Bump, A.P., 2001. Three-dimensional Laramide deformation of the Colorado Plateau; competing influences of the Sevier thrust belt and the flat Farallon slab, *Abstracts with Programs - Geological Society of America, 33*, 326-327.

Campbell, H.J., Andrews, P.B., Beu, A.G., Maxwell, P.A., Edwards, A.R., Laird, M.G., Hornibrook, d., Mildenhall, D.C., Watters, W.A., Buckeridge, J.S., Lee, D.E., Strong, C.P., Wilson, G.J. and Hayward, B.W., 1993. *Cretaceous-Cenozoic Geology and Biostratigraphy of the Chatham Islands, New Zealand*, Institute of Nuclear and Geological Sciences Monograph **2**, Lower Hutt.

Campbell, H.J. and Grant-Mackie, J.A., 2000. The marine Triassic of Australasian and its interregional correlation, in *Developments in Palaeontology and Stratigraphy*, vol. 18, edited by H. Yin, *et al.*, Elsevier, Amsterdam.

Campbell, I.H., 2001. Identification of ancient mantle plumes, in *Mantle plumes: Their Identification Through Time, Geological Society of America Special Paper 352*, edited by R.E. Ernst and K.L. Buchan, pp. 5-21, Geological Society of America, Boulder.

Carlson, J.R., Grant-Mackie, J.A. and Rodgers, K.A., 1980. Stratigraphy and sedimentology of the Coalgate area, Canterbury, New Zealand, *New Zealand Journal of Geology and Geophysics, 23*, 79-92.

Carminati, E., Wortel, M.J.R., Spakman, W. and Sabadini, R., 1998. The role of slab detachment processes in the opening of the western-central Mediterranean basins: some geological and geophysical evidence, *Earth and Planetary Science Letters, 160*, 651-665.

Carrapa, B. and DiGiulio, A., 2001. The sedimentary record of the exhumation of a granitic intrusion into a collisional setting: the lower Gonfolite Group, Southern Alps, Italy, *Sedimentary Geology, 139*, 217-228.

Carter, L. and Carter, R.M., 1993. Sedimentary Evolution of the Bounty Trough, in *South Pacific Sedimentary Basins (Sedimentary Basins of the World 2)*, edited by P.F. Ballance, Elsevier Science Publishers, B.V., Amsterdam.

Cawood, P.A., Nemchin, A.A., Leverenz, A., Saeed, A. and Ballance, P.F., 1999. U/Pb dating of detrital zircons; implications for the provenance record of Gondwana margin terranes, *Geological Society of America Bulletin, 111*, 1107-1119.

Chaffey, D.J., Cliff, R.A. and Wilson, B.M., 1989. Characterization of the St Helena magma source, in *Magmatism in the Ocean Basins, Geological Society, London: Special Publication No.42*, edited by A.D. Saunders and M.J. Norry, Geological Society of London.

Challis, G.A., 1960. The structure and petrology of the Mt Lookout area, Awatere Valley., MSc thesis, Victoria, Wellington.

Challis, G.A., 1966. Cretaceous stratigraphy and structure of the Mt Lookout area, Awatere Valley, *Transactions of the Royal Society of New Zealand, 4*, 119-137.

Challis, G.A., 1968. The K_2O:Na_2O ratios of ancient volcanic arcs in New Zealand, *New Zealand Journal of Geology and Geophysics, 11*, 200-211.

Challis, G.A. and Reay, M.B., 1993. Hypabyssal intrusives of the Gridiron Volcanics, in *Geology of the Middle Clarence Valley*, pp. 71-72, Institute of Geological and Nuclear Sciences, Lower Hutt.

Chappell, B.W. and White, A.J., 1974. Two contrasting granite types, *Pacific Geology, 8*, 173-174.

Chase, C., 1981. Oceanic island Pb: two-stage histories and mantle evolution, *Earth and Planetary Science Letters, 52*, 277-284.

Clayton, R.N. and Mayeda, T.K., 1963. The use of bromine pentafluoride in the extraction of oxygen from oxides and silicates for isotopic analysis, *Geochimica et Cosmochimica Acta, 27*, 43-52.

Clemens, J.D. and Wall, V.J., 1981. Crystallization and origin of some peraluminous (S-type granitic magmas, *Canadian Mineralogist, 19*, 111-132.

Clemens, J.D. and Wall, V.J., 1984. Origin and evolution of a peraluminous silicic ignimbrite suite: the Violet Town Volcanics, *Contributions to Mineralogy and Petrology, 88*, 354-371.

Cook, R.A., Gregg, R.C. and Bennett, D.J., 1999. New thinking on the petroleum prospectivity of deep Mesozoic sediments in New Zealand basins, in *Australian Petroleum Production & Exploration Association conference.*, vol. 39, *APPEA Journal*, pp. 386-398, Australian Petroleum Production and Exploration Association, Canberra, Australia.

Coulon, C., Megartsi, M., Fourcade, S., Maury, R.C., Bellon, H., Louni-Hacini, A., Cotten, J., Coutelle, A. and Hermitte, D., 2002. Post-collisional transition from calc-alkaline to alkaline volcanism during the Neogene in Oranie (Algeria): magmatic expression of a slab breakoff, *Lithos, 62*, 87-110.

Cox, H.S., 1877. Report on the Geology of the Mt. Somers district, *Report on Geological Explorations during 1876-77, 10*, 1-10.

Cox, H.S., 1884a. On Mount Somers and Malvern Hills district, *Report on Geological Explorations during 1883-84, 16*, 22-43.

Cox, H.S., 1884b. On the relations of the quartz-porphyries and pitchstones of Mount Somers and Malvern Hills, *Report on Geological Explorations during 1883-84, 16*, 107-109.

Cox, P.T., 1926. Geology of the Rakaia Gorge District, *Transactions of the New Zealand Institute, 56*, 91-111.

Crampton, J., Mumme, T., Raine, I., Roncaglia, L., Schioler, P., Strong, P., Turner, G. and Wilson, G., 2000. Revision of the Piripauan and Haumurian local stages and correlation of the Santonian - Maastrichtian (Late Cretaceous) in New Zealand, *New Zealand Journal of Geology and Geophysics, 43*, 309-333.

Cumming, G.L. and Richards, J.R., 1975. Ore lead isotope ratios in continuously changing earth, *Earth and Planetary Science Letters, 28*, 155-171.

Daczko, N.R., Klepeis, K.A. and Clarke, G.L., 2001. Evidence of Early Cretaceous collisional-style orogenesis in northern Fiordland, New Zealand and its effects on the evolution of the lower crust, *Journal of Structural Geology, 23*, 693-713.

Dalziel, I.W.D., Lawver, L.A. and Murphy, J.B., 2000. Plumes, orogenesis, and supercontinental fragmentation, *Earth and Planetary Science Letters, 178*, 1-11.

Davey, F.J., Henyey, T., Holbrook, W.S., Okaya, D., Stern, T., Melhuish, A., Henrys, S., Anderson, H., Eberhart-Phillips, D., McEvilly, T., Uhrhammer, R., Wu, F., Jiracek, G.R., Wannamaker, P.E., Caldwell, G. and Christensen, N., 1998. Preliminary results from a geophysical study across a modern, continent-continent collisional plate boundary - the Southern Alps, New Zealand, *Tectonophysics, 288*, 221-235.

Davidson, J.P., 1996. Deciphering Mantle and Crustal Signatures in Subduction Zone Magmatism, in *Subduction Top to Bottom*, vol. 96, *Geophysical Monograph*, edited by G.E. Rebout, *et al.*, pp. 251-262, American Geophysical Union.

Davies, J.H. and von Blanckenburg, F., 1995. Slab breakoff: A model of lithosphere detachment and its test in the magmatism and deformation of collisional orogens, *Earth and Planetary Science Letters, 129*, 85-102.

Davy, B., 1993. The Bounty Trough - Basement Structure Influences on Sedimentary Basin Evaluation, in *South Pacific Sedimentary Basins (Sedimentary Basins of the World 2)*, edited by P.F. Ballance, pp. 69-92, Elsevier Science Publishers B.V., Amsterdam.

Day, R.A., Green, T.H. and Smith, I.E.M., 1992. The origin and significance of Garnet Phenocrysts and Garnet-Bearing Xenoliths in Miocene Calc-alkaline Volcanics from Northland, New Zealand, *Journal of Petrology, 33*, 125-161.

Deer, W.A., Howie, R.A. and Zussman, J., 1978. *Single-Chain Silicates*, Longman.

Defant, M.J. and Kepezhinskas, P., 2001. Evidence suggests slab melting in arc magmas, *EOS, Transactions, American Geophysical Union, 82*, 65-69.

DePaolo, D.J. and Wasserburg, G.J., 1976. Nd isotopic variations and petrogenetic models, *Geophysics Research Letters, 3*, 743 - 746.

DePaolo, D.J., 1979. Petrogenetic mixing models and Nd-Sr isotopic patterns, *Geochimica et Cosmochimica Acta, 43*, 615-627.

DePaolo, D.J., 1981. Trace element and isotopic effects of combined wallrock assimilation and fractional crystallisation, *Earth and Planetary Science Letters, 53*, 189-202.
DePaolo, D.J., 1988. *Neodymium Isotope Geochemistry, An Introduction*, Springer-Verlag.
Dickin, A.P., 1995. *Radiogenic Isotope Geology*, Cambridge University Press, Cambridge.
Dickinson, W.R. and Snyder, W.S., 1979. Geometry of subducted slabs related to the San Andreas transform, *Journal of Geology, 87*, 609-627.
DLS, 1970a. S81: Mt Somers, 1:63,360, E.C.Keating, Government Printer, Wellington
DLS, 1970b. S91: Mt. Peel, 1:63,360, E.C.Keating, Government Printer, Wellington
Dostal, J., Dupuy, C., Carron, J.P., Le Guen de Kerneizon, M. and Maury, R.C., 1983. Partition coefficients of trace elements: application to volcanic rocks of St Vincent, West Indies, *Geochimica et Cosmochimica Acta, 47*, 525-533.
duBrey, E.A., 1988. Garnet compositions and their use as indicators of peraluminous granitoid petrogenesis - southeastern Arabian Shield, *Contributions to Mineralogy and Petrology, 100*, 205-212.
Duffield, W.A. and Dalrymple, G.B., 1990. The Taylor Creek Rhyolite of New Mexico, a rapidly emplaced field of lava domes and flows, *Bulletin of Volcanology, 52*, 475-487.
Eberhart-Phillips, D. and Reyners, M., 1997. Continental subduction and three-dimensional crustal structure: the northern South Island, New Zealand, *Journal of Geophysical Research, 102*, 11843 - 11861.
Edwards, A.R., Hornibrook, d., Raine, J.I., Scott, G.H., Stevens, G.R., Strong, C.P. and Wilson, G.J., 1988. A New Zealand Cretaceous-Cenozoic geological time scale, *New Zealand Geological Survey Record, 35*, 135-149.
Elvy, J.M., 1999. Tectonic Geomorphology and Paleoseismic Investigations, Mount Hutt District, Canterbury, MSc thesis, University of Canterbury, Christchurch.
Ewart, A., Schon, R.W. and Chappell, B.W., 1992. The Cretaceous volcanic-plutonic province of the central Queensland (Australia) coast - a rift related calc-alkaline province, *Transactions of the Royal Society of Edinburgh: Earth Sciences, 83*, 327-345.
Ewart, A., Milner, S.C., Armstrong, R.A. and Duncan, A.R., 1998. Etenedeka Volcanism of the Goboboseb Mountains and Messum Igneous Complex, Namibia. Part II: Voluminous Quartz Latite Volcanism of the Awahab Magma System, *Journal of Petrology, 39*, 227-253.
Faure, G. and Powell, J.L., 1972. *Strontium Isotope Geology*, Springer-Verlag.
Field, B.D. and Browne, G.H., 1989. Cretaceous and Cenozoic sedimentary basins and geological evolution of the Canterbury Region, South Island, New Zealand, in *New Zealand Geological Survey Basin Studies 2*, New Zeland Geological Survey, Lower Hutt.
Froude, D.O. and Cole, J.W., 1985. Petrography, mineralogy and chemistry of Titiraupenga volcano, North Island, New Zealand, *New Zealand Journal of Geology and Geophysics, 28*, 487-496.
Fujimaki, H., Tatsumoto, M. and Aoki, K., 1984. Partition coefficients of Hf, Zr and REE between phenocrysts and groundmasses, *Proceedings of the 14th Lunar and Planetary Science Conference. Journal of Geophysical Research, 89*.
Garbe-Schönberg, D.C., 1993. Simultaneous determination of thirty seven trace elements in twenty-eight international rock standards by ICP-MS, *Geostandards Newsletters, 17*, 81-97.
Gavin, B.P., 2000. Geophysical investigation of the nature of bedrock in South Canterbury, New Zealand, BSc (Hons) thesis, University of Canterbury, Christchurch.
George, A.D., 1988. Accretionary prism rocks of the Torlesse Terrane Western Aorangi Range - Cape Palliser, New Zealand, PhD thesis, Victoria, Wellington.
Gilbert, J.S. and Rogers, N.W., 1989. The significance of garnet in the Permo-Carboniferous volcanic rocks of the Pyrenees, *Journal of the Geological Society of London, 146*, 477-490.
Giletti, B.J., 1986. Diffusion effects on oxygen isotope temperatures of slowly cooled igneous and metamorphic rocks, *Earth and Planetary Science Letters, 77*, 218-228.
Gill, J.B., 1981. *Orogenic andesites and plate tectonics*, Springer, Berlin.
Gleadow, A.J.W. and Duddy, I.R., 1980. Early Cretaceous volcanism and the early break-up history of southeastern Australia: Evidence from fission track dating of volcaniclastic sediments, *Fifth International Gondwana Symposium, Wellington*, 295-300.
Granet, M., Wilson, M. and Achauer, U., 1995. Imaging a mantle plume beneath the French Massif Central, *Earth and Planetary Science Letters, 136*, 281-296.
Grapes, R.H., 1972. Petrology of the Blue Mountain Igneous Complex, Marlborough, PhD thesis, Victoria, Wellington.
Grapes, R.H., 1975. Petrology of the Blue Mountain Igneous Complex, Marlborough, New Zealand, *Journal of Petrology, 16*, 371-428.
Grapes, R.H., Lamb, S.H. and Adams, C.J., 1992. K-Ar ages of basanitic dikes, Awatere Valley, Marlborough, New Zealand, *New Zealand Journal of Geology and Geophysics, 35*, 415-419.

Green, T.H. and Ringwood, A.E., 1968. Origin of the garnet phenocrysts in calc-alkaline rocks, *Contributions to Mineralogy and Petrology, 18*, 163-1174.
Green, T.H., Sie, S.H., Ryan, C.G. and Cousens, D.R., 1989. Proton microprobe determined partitioning of Nb, Ta, Zr, Sr and Y between garnet, clinopyroxene and basaltic magma at high pressure and temperature, *Chemical Geology, 74*, 201-216.
Green, T.H., 1992. Experimental phase equilibrium studies of garnet-bearing I-type volcanics and high-level intrusives from Northland, New Zealand, *Transactions of the Royal Society of Edinburgh: Earth Sciences, 83*, 429-438.
Gregg, D.R., 1964. Sheet 18: Hurunui, 1:250 000, Department of Scientific and Industrial Research, Wellington
Gregory, R.T. and Taylor, H.P.J., 1981. An oxygen isotope profile in a section of Cretaceous oceanic crust, Samail ophiolite, Oman: Evidence for d18O buffering of the oceans by deep (>5 km) seawater-hydrothermal circulation at mid-ocean ridges, *Journal of Geophysical Research, 86*, 2737-2755.
Griffiths, R.W. and Campbell, I.H., 1990. Stirring and structure in mantle starting plumes, *Earth and Planetary Science Letters, 99*, 66-78.
Gruenewaldt, G.v., 1970. On the phase-change orthopyroxene-pigeonite and the resulting textures in the main and upper zones of the Bushveld Complex in the eastern Transvaal, *The Geological Society of South Africa, Special Publication, 1*.
Haast, J.v., 1862. Notes on the Geology of the province of Canterbury, New Zealand, in *New Zealand Government Gazette*, Province of Canterbury,
Haast, J.v., 1863. Reports of the Provincial Geologist on the coal measures and lignitiferous beds of the River Kowai, tributary of the River Waimakariri, in *New Zealand Government Gazette*, Province of Canterbury,
Haast, J.v., 1871a. Preliminary report on the Malvern Hills, Canterbury, *Report on Geological Explorations during 1870-71, 6*, 135-146.
Haast, J.v., 1871b. On the Geology of the Amuri District, in the Provinces of Nelson and Marlborough, *Report on Geological Explorations during 1870-71, 6*, 25-46.
Haast, J.v., 1872a. Report on the Geology of the Malvern Hills, Canterbury, *Report on Geological Explorations during 1871-72, 7*, 1-85.
Haast, J.v., 1872b. Report on the Coal Deposits of the Ashburton District, *Report on Geological Explorations during 1871-72, 7*, 141-146.
Haast, J.v., 1877. Geology of the Clent Hills and Mt. Somers Districts, *Report on Geological Explorations during 1873-74, 8*, 1-19.
Haast, J.v., 1879. *Geology of the provinces of Canterbury and Westland, New Zealand*, Times Office, Christchurch.
Hall, A., 1996. *Igneous Petrology*, Longman.
Harangi, S.Z., 1999. Geochemistry and petrogenesis of the volcanic rocks from Csódi Hill (Dunabogdány, Visegrád Mts., Hungary), *Topographia Mineralogica Hungaria, 6*, 59-85.
Harangi, S.Z., Downes, H., Kósa, L., Szabó, C.S., Thirlwall, M.F., Mason, P.R.D. and Mattey, D., 2001. Almandine Garnet in Calc-alkaline Volcanic Rocks of the Northern Pannonian Basin (Eastern-Central Europe): Geochemistry, Petrogenesis and Geodynamic Implications, *Journal of Petrology, 42*, 1813-1843.
Harris, C., Faure, K., Diamond, R.E. and Scheepers, R., 1997. Oxygen and hydrogen isotope geochemistry of S- and I-type granitoids; the Cape Granite Suite, South Africa, *Chemical Geology, 143*, 95-114.
Hart, S.R., 1988. Heterogeneous mantle domains: Signatures, genesis and mixing chronologies, *Earth and Planetary Science Letters, 90*, 273-296.
Hart, S.R., Blusztajn, J., LeMasurier, W.E. and Rex, D.C., 1997. Hobbs Coast Cenozoic volcanism: Implications for the West Antarctic rift system, *Chemical Geology, 139*, 223-248.
Hawkesworth, C.J., 1982. Isotope characteristics of magmas erupted along destructive plate margins, in *Andesites: orogenic andesites and related rocks*, edited by R.S. Thorpe, pp. 549 - 571, John Wiley & Sons.
Hawkesworth, C.J., Kempton, P.D., Rogers, N.W., Ellam, R.M. and van Calsteren, P.W.C., 1990. Continental mantle lithosphere, and shallow level enrichment processes in the Earth's mantle, *Earth and Planetary Science Letters, 96*, 256-268.
Hay, R.F., 1975. Sheet N7 Doubtless Bay, 1:63 360, DSIR, Wellington
Hector, J., 1871. On the Geological Structure of the Malvern Hills, *Report on Geological Explorations during 1870-71, 6*, 46-55.
Henderson, P., 1982. *Inorganic geochemistry*, Pergamon, Oxford.
Hess, H.H., 1941. Pyroxenes of common mafic magmas, *American Mineralogist, 26*, 515-535.
Hoefs, J., 1997. *Stable Isotope Geochemistry*, Springer.

Hoernle, K., Zhang, Y. and Graham, D., 1995. Seismic and geochemical evidence for large-scale mantle upwelling beneath the eastern Atlantic and western and central Europe, *Nature, 374*, 34-38.

Hoernle, K.A. and Tilton, G.R., 1991. Sr-Nd-Pb isotope data for Fuerteventura (Canary Islands) basal complex and subaerial volcanics: applications to magma genesis and evolution, *Schweizerische Mineralogische und Petrographische Mitteilungen, 71*, 3-18.

Hofmann, A.W. and White, W.M., 1982. Mantle plumes from ancient oceanic crust, *Earth and Planetary Science Letters, 57*, 421-436.

Hofmann, A.W., 1988. Chemical differentiation of the Earth: the relationship between mantle, continental crust, and oceanic crust, *Earth and Planetary Science Letters, 90*, 297-314.

Hole, M.J., 1988. Post-subduction alkaline volcanism along the Antarctic Peninsula, *Journal of the Geological Society of London, 145*, 185-988.

Hole, M.J., 1990. Geochemical evolution of Pliocene-Recent post-subduction alkalic basalts from Seal Nunataks, Antarctic Peninsula, *Journal of Volcanology and Geothermal Research, 40*, 149-167.

Hole, M.J., Rogers, G., Saunders, A.D. and Storey, M., 1991. Relation between alkalic volcanism and slab-window formation, *Geology, 19*, 657-660.

Hutton, F.W., 1877. Report on the Geology of the north-east portion of the South Island, from Cook Straits to the Rakaia, *Report on Geological Explorations during 1873-74*, 27-58.

Hutton, F.W., 1889. The Eruptive Rocks of New Zealand, *Journal of the Royal Society of New South Wales, 23*, 102-156.

Irving, A.J. and Frey, F.A., 1978. Distribution of trace elements between garnet megacrysts and host volcanic liquids of kimberlitic to rhyolitic composition, *Geochimica et Cosmochimica Acta, 42*, 771-787.

Isaac, M.J., Herzer, R.H., Brook, F.J. and Hayward, B.W., 1994. *Cretaceous and Cenozoic sedimentary basins of Northland, New Zealand*, Institute of Geological and Nuclear Sciences Monograph **8**.

James, D.E., 1981. The combined use of oxygen and radiogenic isotopes as indicators of crustal contamination, *Annual Review of Earth and Planetary Sciences, 9*, 311-344.

Jobberns, G., 1926. Geology of Cordy's Flat, Malvern Hills, Canterbury, *Transactions of the New Zealand Institute, 56*, 214-225.

Johnson, A.M., 1970. *Physical processes in geology*, Freeman, Cooper, San Francisco.

Kamber, B.S. and Collerson, K.D., 2000. Role of "hidden" deeply subducted slabs in mantle depletion, *Chemical Geology, 166*, 241-254.

Kamp, P.J.J., 1999. Tracking crustal processes by FT thermochronology in a forearc high (Hikurangi margin, New Zealand) involving Cretaceous subduction termination and mid-Cenozoic subduction initiation, *Tectonophysics, 307*, 313-343.

Kay, R.W., Sun, S.S. and Lee-Hu, C.N., 1978. Pb and Sr isotopes in volcanic rocks from the Aleutian Islands and Pribilof Islands, Alaska, *Geochimica et Cosmochimica Acta, 42*, 263-273.

Kimbrough, D.L. and Richard, S.M., 1991. Geochronology of Basement Rocks in the Fosdick mountain region of west Antarctica and correlation with Cretaceous extensional terranes of southern New Zealand, *6th Internation Symposium on Antarctic Earth Sciences*, 313-316.

Kimbrough, D.L., Tulloch, A.J., Geary, E., Coombs, D.S. and Landis, C.A., 1993. Isotopic ages from the Nelson region of the South Island, New Zealand; Crustal structure and definition of the Median Tectonic Zone, *Tectonophysics, 225*, 433-448.

Kimbrough, D.L., Tulloch, A.J., Coombs, D.S., Landis, C.A., Johnston, M.R. and Mattinson, J.M., 1994. Uranium-lead zircon ages from the Median Tectonic Zone, South Island, New Zealand, *New Zealand Journal of Geology and Geophysics, 37*, 393-419.

King, E., Tucker Barrie, C. and Valley, J.W., 1997. Hydrothermal alteration of oxygen isotope ratios in quartz phenocrysts, Kidd Creek mine, Ontario: Magmatic values are preserved in zircon, *Geology, 25*, 1079-1082.

Kinney, R., 1993. Structure and petrology of the Mount Alford rhyolites and associated deposits., BSc (Hons) thesis, University of Canterbury, Christchurch.

Kyser, K.T., 1986. Chapter 5: Stable isotope variations in the mantle, in *Stable Isotopes in high temperature geological processes*, vol. 16, *Reviews in Mineralogy*, edited by J.W. Valley, *et al.*, pp. 141-164, BookCrafters, Inc., Chelsea, Michigan.

Laird, M.G., 1988. Sheet 37: Punakaiki, 1:63,360, Department of Scientific and Industrial Research, Wellington

Laird, M.G., 1992. Cretaceous Stratigraphy and Evolution of the Marlborough Segment of the East Coast Region, in *New Zealand Oil Exploration Conference Proceedings*, Crown Minerals Operations Group, Energy Resources Division.

Laird, M.G., 1993. Cretaceous Continental Rifts: New Zealand Region, in *South Pacific Sedimentary Basins (Sedimentary Basins of the World, 2)*, edited by P.F. Ballance, pp. 37-49, Elsevier, Amsterdam.

Laird, M.G. and Bradshaw, J.D., 2002. The break-up of a long-term relationship: The Cretaceous separation of New Zealand from Gondwana, in *Gondwana 11: Correlations and Connections, Programme and Abstracts*, Christchurch, New Zealand,

Lal, R.K., 1993. Internally consistent recalibrations of mineral equilibria for geothermobarometry involving garnet-orthopyroxene-plagioclase-quartz assemblages and their application to the South Indian granulites, *Journal of Metamorphic Geology, 11*, 855-866.

Landis, C.A., Kimbrough, D.L., Cawood, P.A. and Pillai, D.D.L., 1984. Newly recognised Mesozoic granite-bearing conglomerate; implications for structure, stratigraphy and geological history of the Productus Creek region, Southland, in *Geological Society of New Zealand annual conference 1984; programme and abstracts.*, vol. 31a, *Geological Society of New Zealand Miscellaneous Publication*, edited by Howorth and Russell, Geological Society of New Zealand, Christchurch, New Zealand.

Langmuir, C.H., Vocke, R.D., Hanson, G.N. and Hart, S.R., 1978. A General Mixing Equation with Applications to Icelandic Basalts, *Earth and Planetary Science Letters, 37*, 380-392.

Lanphere, M.A. and Dalrymple, G.B., 2000. First principles calibration of 38Ar tracers; implications for the ages of 40Ar/39Ar fluence monitors, U.S.Geological Survey Professional Paper P1621,

Lanyon, R., Varne, R. and Crawford, A.J., 1993. Tasmanian Tertiary basalts, the Balleny plume, and opening of the Tasman Sea (southwest Pacific Ocean), *Geology, 21*, 555-558.

Lauder, W.R., 1953. The geology of the Acheron Outlier, MSc thesis, University of Otago, Dunedin, New Zealand.

Lauder, W.R., 1962. Teschenites from Acheron River, Mid-Canterbury, New Zealand, with notes on the Geology of the Surrounding Country, *Transactions of the Royal Society of New Zealand: Geology, 1*, 109-127.

Le Maitre, R.W., Bateman, P., Dudek, A., Keller, J., Lemeyre Le Bas, M.J., Sabine, P.A., Schmid, R., Sorensen, H., Streckeisen, A., Woolley, A.R. and Zanettin, B., 1989. *A classification of igneous rocks and glossary of terms*, Blackwell, Oxford.

Le Masurier, W.E. and Landis, C.A., 1996. Mantle-plume activity recorded by low-relief erosion surfaces in West Antarctica and New Zealand, *Geological Society of America Bulletin, 108*, 1450-1466.

Leverenz, A., 2000. Trench-sedimentation versus accreted submarine fan - an approach to regional-scale facies analysis in a Mesozoic accretionary complex: "Torlesse" terrane, northeastern North Island, New Zealand, *Sedimentary Geology, 132*, 125-160.

Lewis, J.F. and White, E.W., 1967. Pyroxene relations in basalts and basaltic andesites from the Soufriere volcano, St. Vincent, West Indies, *Transactions of the American Geophysical Union, 48*, 227.

Lillie, A.R. and Brothers, R.N., 1970. The geology of New Caledonia, *New Zealand Journal of Geology and Geophysics, 13*, 145-183.

Lindop, A.B., 1886. On the coal mines in the Malvern District, *Report on Geological Explorations during 1885, 18*, 15-20.

LINZ, 1984. M36 Lincoln, 1: 50 000, Land Information New Zealand, Wellington

LINZ, 1989. M33 Waikari, 1:50 000, Government Printer, Wellington

LINZ, 1991. J36 Mount Harper, 1: 50 000, Land Information New Zealand, Wellington

LINZ, 1998. K35 Coleridge, 1: 50 000, Land Information New Zealand, Wellington

Long, P.E., 1978. Experimental determination of partition coefficients for Rb, Sr and Ba between alkali feldspar and silicate liquid, *Geochimica et Cosmochimica Acta, 42*, 833-846.

Luyendyk, B.P., 1995. Hypothesis for Cretaceous rifting of east Gondwana caused by subducted slab capture, *Geology, 233*, 373-376.

MacKinnon, T.C., 1983. Origin of the Torlesse terane and coeval rocks, South Island, New Zealand, *Geological Society of America Bulletin, 94*, 967-985.

Mahoney, J.J. and Spencer, K.J., 1991. Isotopic evidence for the origin of the Manihiki and Ontong Java oceanic plateaus, *Earth and Planetary Science Letters, 104*, 196-210.

Mahoney, J.J., Storey, M., Duncan, R.A., Spencer, K.J. and Pringle, M., 1993. Geochemistry and age of the Ontong Java Plateau, in *The Mesozoic Pacific: Geology, Tectonics and Volcanism, Geophysical Monograph Series 77*, edited by M.S. Pringle, *et al.*, AGU, Washington, D.C.

Mahood, G. and Hildreth, W., 1983. Large partition coefficients for trace elements in high-silica rhyolites, *Geochimica et Cosmochimica Acta, 47*, 11-30.

Mason, B., 1949. The geology of Mandamus-Pahau District, North Canterbury, *Transactions of the Royal Society of New Zealand, 77*, 403-428.

Mason, B., 1951. The Syenite and Associated Rocks of the Mandamus-Pahau Area, North Canterbury, New Zealand, *Transactions of the Royal Society of New Zealand, 79*, 261-275.

Mason, B.H., 1958. The intrusive rocks of the Kaikoura Mountains, *Transactions of the Royal Society of New Zealand, 85*.

Matsuhisa, Y., 1979. Oxygen isotopic compositions of volcanic rocks from the East Japan island arcs and their bearing on petrogenesis, *Journal of Volcanology and Geothermal Research, 5*, 271-296.
Mayes, C.L., Lawver, L.A. and Sandwell, D.T., 1990. Tectonic History and New Isochron Chart of the South Pacific, *Journal of Geophysical Research, 95*, 8543-8567.
Mazengarb, C. and Speden, I.G., 2000. Geology of the Raukumara area, 1:250 000, Institute of Geological & Nuclear Sciences Limited, Lower Hutt
McDougall, I. and van der Lingen, G.J., 1974. Age of rhyolites of the Lord Howe Rise and the evolution of the southwest Pacific Ocean, *Earth and Planetary Science Letters, 21*, 117-126.
McKay, A., 1886. On the cupriferous Diabasic rocks of the Malvern Hills, Selwyn County, *Report on Geological Explorations during 1885, 17*, 6-8.
Middleton, L., 1976. Geochemistry & Petrography of Gebbies Rhyolite & McQueens Andesite (Banks Peninsula), BSc (Hons) thesis, University of Canterbury, Christchurch.
Miller, C.F. and Stoddard, E.F., 1981. The role of manganese in the paragenesis of magmatic garnet: an example from the Old Woman-Piute range, California, *Journal of Geology, 89*, 233-246.
Min, K., Mundil, R., Renne, P.R. and Ludwig, K.R., 2000. A test for systematic errors in 40Ar/39Ar geochronology through comparison with U/Pb analysis of a 1.1-Ga rhyolite, *Geochimica et Cosmochimica Acta, 64*, 73-98.
Moore, P.R. and Speden, I.G., 1979. Stratigraphy, structure, and inferred environments of deposition of the early Cretaceous sequence, eastern Wairarapa, New Zealand, *New Zealand Journal of Geology and Geophysics, 22*, 417-434.
Mortimer, N., 1995. Origin of the Torlesse Terrane and coeval rocks, North Island, New Zealand, *International Geology Review, 36*, 891-910.
Mortimer, N. and Parkinson, D., 1996. Hikurangi Plateau: a Cretaceous large igneous province in the southwest Pacific Ocean, *Journal of Geophysical Research, 101*, 687-696.
Mortimer, N., Gans, P., Calvert, A. and Walker, N., 1999a. Geology and thermochronometry of the east edge of the Median Batholith (Median Tectonic Zone): a new perspective on Permian to Cretaceous crustal growth of New Zealand, *The Island Arc, 8*, 404-425.
Mortimer, N., Tulloch, A.J., Spark, R.N., Walker, N.W., Ladley, E., Allibone, A. and Kimbrough, D.L., 1999b. Overview of the Median Batholith, New Zealand:a new interpretation of the geology of the Median Tectonic Zone and adjacent rocks, *Journal of African Earth Sciences, 29*, 257-268.
Mortimer, N., Davey, F.J., Melhuish, A., Yu, J. and Godfrey, N.J., 2002. Geological interpretation of a deep seismic reflection profile across the Eastern Province and Median Batholith, New Zealand: Crustal architecture of an extended Phanerozoic convergent orogen, *New Zealand Journal of Geology and Geophysics, 45*, 349-363.
Mould, R.J., 1992. Structure and kinematics of late Cenozoic deformation along the western margin of the Culverden Basin, North Canterbury, New Zealand, MSc thesis, Canterbury, Christchurch.
Muir, R.J., Weaver, S.D. and Bradshaw, J.D., 1992. The Separation Point Batholith: Early Cretaceous subduction-related magmatism in New Zealand, *Geological Society of New Zealand Miscellaneous Publication, 63a*, 109.
Muir, R.J., Ireland, T.R., Weaver, S.D. and Bradshaw, J.D., 1994. Ion microprobe U-Pb zircon geochronology of granitic magmatism in the Western Province of the South Island, New Zealand, *Chemical Geology, 113*, 117-189.
Muir, R.J., Weaver, S.D., Bradshaw, J.D., Eby, G.N. and Evans, J.A., 1995. The Cretaceous Separation Point Batholith, New Zealand; granitoid magmas formed by melting of mafic lithosphere, *Journal of the Geological Society of London, 152*, 689-701.
Muir, R.J., Ireland, T.R., Weaver, S.D., Bradshaw, J.D., Waight, T.E., Jongens, R. and Eby, G.N., 1997. SHRIMP U-Pb geochronology of Cretaceous magmatism in northwest Nelson-Westland, South Island, New Zealand, *New Zealand Journal of Geology and Geophysics, 40*, 453-463.
Muir, R.J., Ireland, T.R., Weaver, S.D., Bradshaw, J.D., Evans, J.A., Eby, G.N. and Shelley, D., 1998. Geochronology and geochemistry of a Mesozoic magmatic arc system, Fiordland, New Zealand, *Journal of the Geological Society of London, 155*, 1037-1053.
Mukasa, S.B. and Dalziel, I.W.D., 2000. Marie Byrd Land, West Antarctica; evolution of Gondwana's Pacific margin constrained by zircon U-Pb geochronology and feldspar common-Pb isotopic compositions, *Geological Society of America Bulletin, 112*, 611-627.
Murphy, J.B., Oppliger, G.L., Brimhall, G.H. and Hynes, A., 1998. Plume-modified orogeny; an example from the western United States, *Geology, 26*, 731-734.
Murphy, J.B., 2001. Flat slab subduction in the geological record: consideration of modern analogues, *Abstracts with Programs - Geological Society of America, 33*, 208.
Nakumara, Y. and Kushiro, I., 1970a. Compositional Relations of Coexisting Orthopyroxene, Pigeonite and Augite in a Tholeiitic Andesite from Hakone Volcano, *Contributions to Mineralogy and Petrology, 26*.

Nakumara, Y. and Kushiro, I., 1970b. Equilibrium relations of hypersthene, pigeonite and augite in crystallizing magmas; microprobe study of a pigeonite andesite from Weiselberg, Germany., *American Mineralogist, 55*, 1999-2015.

Nash, W.P. and Crecraft, H.R., 1985. Partition coefficients for trace elements in silicic magmas, *Geochimica et Cosmochimica Acta, 49*.

Nemcok, M., Pospisil, L., Lexa, J. and Donelick, R.A., 1998. Tertiary subduction and slab break-off model of the Carpathian-Pannonian region, *Tectonophysics, 295*, 307-340.

Nicholls, I.A. and Lorenz, V., 1973. Origin and crystallisation history of Permian tholeiites from the Saar-Nahe Trough, SW Germany, *Contributions to Mineralogy and Petrology, 40*, 327-344.

Nicholson, C., Sorlien, C.C., Atwater, T., Crowell, J.C. and Luyendyk, B.P., 1994. Microplate capture, rotation of the western Transverse Ranges, and initiation of the San Andreas transform as a low angle fault system, *Geology, 21*, 491-495.

Nicol, E.R., 1977. Igneous Petrology of Clarence and Awatere Valley, Marlborough, PhD thesis, Victoria, Wellington.

Norrish, K. and Hutton, J.T., 1969. An accurate X-ray spectrograph method for the analysis of a wide range of geological samples, *Geochimica et Cosmochimica Acta, 33*, 431-453.

Oborn, L.E. and Suggate, R.P., 1959. Sheet 21: Christchurch, 1:250 000, Department of Scientific and Industrial Research, Wellington

Oliver, P.J., 1977. The Mesozoic Geology of the Mt Somers Area, Canterbury, including Geochemical and Palaeomagnetic Studies of the Cretaceous calc-alkaline Mt Somers Volcanics, PhD thesis, University of Canterbury, Christchurch, New Zealand.

Oliver, P.J., 1979. Structure and tectonic history of the Mesozoic rocks of the foothills of the Southern Alps in mid-Canterbury, in *Origin of the Southern Alps*, vol. 18, edited by R.I. Walcott and M.M. Cresswell, pp. 105-111, The Royal Society of New Zealand Bulletin.

Oliver, P.J., Mumme, T.C., Grindley, G.W. and Vella, P., 1979. Palaeomagnetism of the Upper Cretaceous Mount Somers Volcanics, Canterbury, New Zealand, *New Zealand Journal of Geology and Geophysics, 22*, 199-212.

Oliver, P.J., 1980. Cretaceous Volcanism in Canterbury, in *Geological Society of New Zealand Annual Conference Abstracts 76*, Christchurch,

Oliver, P.J., Campbell, J.D. and Speden, I.G., 1982. The stratigraphy of the Torlesse rocks of the Mt Somers area (S81) mid-Canterbury, *Journal of the Royal Society of New Zealand, 12*, 243-271.

Oliver, P.J., 1984. The mid-Cretaceous Volcanic Rocks of Rakaia Gorge and Malvern Hills area, Canterbury, *New Zealand Geological Survey Record, 3*, 86-91.

Oliver, P.J., 1986a. Hewson Formation, *New Zealand Geological Survey Record, 14*, 7-9.

Oliver, P.J., 1986b. Mount Somers Volcanics, *New Zealand Geological Survey Record, 14*, 9.

Oliver, P.J., 1986c. Hewson Formation *In:* Lithostratigraphy of Cretaceous and Tertiary sediments, southern Canterbury, *New Zealand Geological Survey Record, 14*, 55.

Oliver, P.J. and Keene, H.W., 1989. Sheet K36 AC and part Sheet K35: Mount Somers, 1:50 000, Department of Scientific and Industrial Research, Wellington

Oliver, P.J. and Keene, H.W., 1990. Sheet J36 BD and part sheet J35: Clearwater, 1:50 000, Department of Scientific and Industrial Research, Wellington

O'Neil, J.R. and Chappell, B.W., 1977. Oxygen and hydrogen isotope relations in the Berridale batholith, *Journal of the Geological Society of London, 133*, 559-571.

O'Neil, J.R., Shaw, S.E. and Flood, R.H., 1977. Oxygen and Hydrogen Isotope Compositions as Indcators of Granite Genesis in the New England Batholith, Australia, *Contributions to Mineralogy and Petrology, 62*, 313-328.

Orlowski, R.J., 2001. A sedimentological profile of the Pahau terrane type locality, MSc thesis, University of Canterbury, Christchurch.

O'Sullivan, P.B., Kohn, B.P., Foster, D.A. and Gleadow, A.J.W., 1995. Fission track data from the Bathurst Batholith: Evidence for rapid mid-Cretaceous uplift and erosion within the eastern highlands of Australia, *Australian Journal of Earth Sciences, 42*, 597-607.

O'Sullivan, P.B., Mitchell, M.M., O'Sullivan, A.J., Kohn, B.P. and Gleadow, A.J.W., 2000. Thermotectonic history of the Bassian Rise, Australia; implications for the breakup of eastern Gondwana along Australia's southeastern margins, *Earth and Planetary Science Letters, 182*, 31-47.

Pankhurst, R.J., Millar, I.L., Grunow, A.M. and Storey, B.C., 1993. The pre-Cenozoic magmatic history of the Thurston Island crustal block, West Antarctica, *Journal of Geophysical Research, 98*, 11835-11849.

Pankhurst, R.J. and Rapela, C.R., 1995. Production of Jurassic rhyolite by anatexis of the lower crust of Patagonia, *Earth and Planetary Science Letters, 134*, 23-36.

Pankhurst, R.J., Weaver, S.D., Bradshaw, J.D., Storey, B.C. and Ireland, T.R., 1998. Geochronology and geochemistry of pre-Jurassic superterranes in Marie Byrd Land, Antarctica, *Journal of Geophysical Research, 103*, 2529-2547.

Pankhurst, R.J., Riley, T.R., Fanning, C.M. and Kelley, S.P., 2000. Episodic Silicic Volcanism in Patagonia and the Antarctic Peninsula: Chronology of Magmatism Associated with the Break-up of Gondwana, *Journal of Petrology, 41*, 605-625.

Panter, K.S., Blusztajn, J., Hart, S. and Kyle, P.R., 1997. Late Cretaceous-Neogene basalts from Chatham Island: implications for HIMU mantle beneath continental borderlands of the southwest Pacific., in *7th Annual V.M. Goldschmidt Conference*, vol. LPI Contribution 921, pp. 156,

Panter, K.S., Hart, S.R., Kyle, P.R., Blusztanjn, J. and Wilch, T., 2000. Geochemistry of Late Cenozoic basalts from the Crary Mountains: characterization of mantle sources in Marie Byrd Land, Antarctica, *Chemical Geology, 165*, 215-241.

Pearce, J.A. and Norry, M.J., 1979. Petrogenetic implications of Ti, Zr, Y and Nb variations in volcanic rocks, *Contributions to Mineralogy and Petrology, 69*, 33-47.

Pearce, J.A., 1982. Trace element characteristics of lavas from destructive plate boundaries, in *Andesites: Orogenic andesites and related rocks*, edited by R.S. Thorpe, pp. 525-548, John Wiley & Sons.

Philpotts, J.A. and Schnetzler, C.C., 1970. Phenocryst-matrix partition coefficients for K, Rb, Sr and Ba with applications to anorthosite and basalt genesis, *Geochimica et Cosmochimica Acta, 34*, 307-322.

Pickard, A.L., Adams, C.J. and Barley, M.E., 2000. Australian provenance for Upper Permian to Cretaceous rocks forming accretionary complexes on the New Zealand sector of the Gondwanaland margin, *Australian Journal of Earth Sciences, 47*, 987-1007.

Plank, T. and Langmuir, C.H., 1998. The chemical composition of subducting sediment and its consequences for the crust and mantle, *Chemical Geology, 145*, 325-394.

Powers, W.E., 1962. Terraces of the Hurunui River, New Zealand, *New Zealand Journal of Geology and Geophysics, 5*, 114-129.

Price, R.C. and Taylor, S.R., 1980. Petrology and Geochemistry of the Banks Peninsula Volcanoes, South Island, New Zealand, *Contributions to Mineralogy and Petrology, 72*, 1-18.

Reay, M.B., 1980. Cretaceous and Tertiary stratigraphy of part of the Middle Clarence Valley, Marlborough, MSc thesis, Canterbury, Christchurch.

Reay, M.B., 1993. *Geology of the Middle Clarence Valley. Scale 1:50 000*, Institute of Geological and Nuclear Sciences, Lower Hutt.

Reid, D.L., 1972. A Petrological Study of the Mandamus Igneous Complex, North Canterbury, MSc thesis, Victoria University of Wellington, Wellington, New Zealand.

Reymer, A.P.S., 1983. Occurrence of Garnet-bearing Rhyolite in Sinai, *Israel Journal of Earth-Sciences, 32*, 117-121.

Richnow, J., 1999. Eruptional and post-eruptional processes in rhyolite domes, PhD thesis, University of Canterbury, Christchurch, New Zealand.

Riley, T.R. and Knight, K.B., 2001. Review: Age of pre-break-up Gondwana magmatism, *Antarctic Science, 13*, 99-110.

Rocholl, A., Stein, M., Molzahan, M., Hart, S.R. and Wörner, G., 1995. Geochemical evolution of rift magmas by progressive tapping of a stratified mantle source beneath the Ross Sea rift, Northern Victoria Land, Antarctica, *Earth and Planetary Science Letters, 131*, 207-224.

Rogers, G., Saunders, A.D., Terrell, D.J., Verma, S.P. and Marriner, G.F., 1985. Geochemistry of Holocene volcanic rocks associated with ridge subduction in Baja California, Mexico, *Nature, 315*, 389-392.

Rogers, G. and Saunders, A.D., 1989. Magnesian andesites from Mexico, Chile and the Aleutian Islands: Implications for magmatism associated with ridge-trench collisions, in *Boninites and related rocks*, edited by A.J. Crawford, pp. 416-445, Unwin Hyman, London.

Rollinson, H., 1993. *Using geochemical data: evaluation, presentation, interpretation*, Longman Group, UK.

Roser, B.P. and Korsch, R.J., 1999. Geochemical characterization, evolution and source of a Mesozoic accretionary wedge: the Torlesse terrane, New Zealand, *Geological Magazine, 136*, 493-512.

Sambridge, M.S. and Compston, W., 1994. Mixture modeling of multi-component data sets with application to ion-probe zircon ages, *Earth and Planetary Science Letters, 128*, 373-390.

Schock, H.H., 1979. Distribution of rare-earth and other trace elements in magnetites, *Chemical Geology, 26*, 119-133.

Scrope, G.P., 1825. *Considerations on Volcanos, the Probable Causes of Their Phenomena, the Laws Which Determine Their March, the Disposition of Their Products, and Their Connexion with the Present State and Past History of the Globe; Leading to the Establishment of a New Theory of the Earth*, W. Phillips, London.

Severinghaus, J. and Atwater, T.M., 1990. Cenozoic geometry and thermal state of the subducting slabs beneath North America, in *Basin and Range extensional tectonics near the latittude of Las Vegas: Geological Society of America Memoir*, vol. 176, edited by B.P. Wernicke, pp. 1-22,

Sevon, W.D., 1969. Stratigraphy and sedimentology of the Tertiary rocks of the Mandamus-Dove River area, North Canterbury, *New Zealand Journal of Geology and Geophysics, 12*, 283-309.

Sewell, R.J., Weaver, S.D. and Thiele, B.W., 1988. Sheet M36 BD: Lyttelton, 1:50 000, Department of Scientific and Industrial Research, Wellington

Sewell, R.J., Weaver, S.D. and Reay, M.B., 1992. Geology of Banks Peninsula, 1:100 000, Institute of Geological & Nuclear Sciences, Lower Hutt

Sharp, Z.D., 1990. Laser-based microanalytical method for the in situ determination of oxygen isotope ratios of silicates and oxides., *Geochimica et Cosmochimica Acta, 54*, 1353 - 1357.

Smith, I.E.M., White, A.J.R., Chappell, B.W. and Eggleton, R.A., 1988. Fractionation in a zoned monzonite pluton: Mount Dromedary, southeastern Australia, *Geological Magazine, 125*, 273-284.

Smith, T.R., 1994. The Somers Ignimbrite and related volcanics; Mt. Somers, Mid-Canterbury, New Zealand, MSc thesis, University of Canterbury, Christchurch, New Zealand.

Smith, T.R. and Cole, J.W., 1996. Mt. Somers Volcanic Group, mid-Canterbury, New Zealand: Stratigraphic and petrological variation, *New Zealand Journal of Geology and Geophysics, 39*, 445-460.

Smith, T.R. and Cole, J.W., 1997. Somers Ignimbrite Formation; Cretaceous high-grade ignimbrites from South Island, New Zealand, *Journal of Volcanology and Geothermal Research, 75*, 39-57.

Soons, J.M., 1964. Ice-marginal drainage channels in the Rakaia valley, *New Zealand Geographer, 20*, 153-164.

Soons, J.M. and Gullentops, M., 1972. Glacial advances in the Rakaia valley, New Zealand, *New Zealand Journal of Geology and Geophysics, 16*, 425-438.

Soons, J.M. and Burrows, C.J., 1978. Dates for Otiran deposits, including plant microfossils and macrofossils fromthe Rakaia valley, *New Zealand Journal of Geology and Geophysics, 21*, 607-615.

Speight, R., 1917. Geology of Banks Peninsula, *Transactions of the New Zealand Institute, 49*, 365-392.

Speight, R., 1918. Structural and glacial features of the Hurunui Valley, *Transactions of the New Zealand Institute, 50*, 93-105.

Speight, R., 1928. The Geology of the Malvern Hills, *New Zealand Department of Scientific and Industrial Research Geological Memoir, 1*.

Speight, R., 1935. The Geology of Gebbies Pass, Banks Peninsula, *Transactions and Proceedings of the Royal Society of New Zealand, 65*, 305-328.

Speight, R., 1938. The Geology of the Mount Somers District, *New Zealand Departmentof Scientific and Industrial Reserach Memoir, 1*.

Spell, T.L., McDougall, I. and Tulloch, A.J., 2000. Thermochronologic constraints on the breakup of the Pacific Gondwana margin: The Paparoa metamorphic core complex, South Island, New Zealand, *Tectonics, 19*, 433-453.

Spörli, K.B. and Craddock, D., 1981. Geology of the Rupert Coast, Marie Byrd Land, Antarctica, in *Gondwana V*, edited by M.M. Cresswell and P. Vella, pp. 243-250,

Steiner, A., Brown, D.A. and White, A.J.R., 1959. Occurrence of ignimbrite in the Shag Valley, north-east Otago, *New Zealand Journal of Geology and Geophysics, 2*, 380-384.

Stephens, C.J., Ewart, A., Bryan, S.E. and Schön, R.W., 1995. Rift-related large-volume silicic volcanism associated with lower Cretaceous continental breakup, eastern Australia, in *IUGG XXI General Assembly*, vol. A443, Boulder,

Storey, B.C. and Kyle, P.R., 1997. An active mantle mechanism for Gondwana breakup, *South African Journal of Geology, 100*, 283-290.

Storey, B.C., Leat, P.T., Weaver, S.D., Pankhurst, R.J., Bradshaw, J.D. and Kelley, S., 1999. Mantle Plumes and Antarctica-New Zealand rifting: evidence from mid-Cretaceous mafic dykes, *Journal of the Geological Society of London, 156*, 659-671.

Suggate, R.P., 1958. The geology of the Clarence Valley from Gore Stream to Bluff Hill, *Transactions of the Royal Society of New Zealand, 85*, 397-408.

Suggate, R.P., 1973. Sheet 21: Christchurch, 1:250 000, Department of Scientific and Industrial Research, Wellington

Sun, S.S. and McDonough, W.F., 1989. Chemical and isotopic systematics of oceanic basalts: implications for mantle composition and processes, in *Magmatism in the Ocean Basins, Geological Society, London: Special Publication No.42*, edited by A.D. Saunders and M.J. Norry, Geological Society of London.

Sutherland, R., 1999. Basement geology and tectonic development of the greater New Zealand region: an interpretation from regional magmetic data, *Tectonophysics, 308*, 341-362.

Sutherland, R. and Hollis, C., 2001. Cretaceous demise of the Moa plate and strike-slip motion at the Gondwana margin, *Geology, 29*, 279-282.

Tatsumi, Y., Hamilton, D.L. and Nesbitt, R.W., 1986. Chemical characteristics of fluid phase released from a subducted lithosphere and the origin of arc magmas: evidence from high-pressure experiments and natural rocks., *Journal of Volcanology and Geothermal Research, 29*, 293-309.

Taylor, H.P., 1967. Oxygen isotope studies of hydrothermal mineral deposits, in *Geochemistry of hydrothermal ore deposits*, Rinehart and Winston, New York.

Taylor, H.P.J. and Sheppard, S.M.F., 1986. Chapter 8: Igneous Rocks: I. Processes of isotopic fractionation and isotope systematics, in *Stable Isotopes in high temperature geological processes*, vol. 16, *Reviews in Mineralogy*, edited by J.W. Valley, *et al.*, pp. 227-271, BookCrafters, Inc., Chelsea, Michigan.

Taylor, S.R. and McLennan, S.M., 1985. *The continental crust: its composition and evolution*, Blackwell, Oxford.

Tera, F. and Wasserburg, G.J., 1972. U-Th-Pb analyses of soil from the Sea of Fertility, *Earth and Planetary Science Letters, 13*, 457-466.

Terralink, 1997. L35 Waimakariri, 1: 50 000, Land Information New Zealand, Wellington

Terralink, 1998. K36 Methven, 1: 50 000, Land Information New Zealand, Wellington

Thirlwall, M.F. and Fitton, J.G., 1983. Sm-Nd garnet age for the Ordovician Borrowdale Volcanic Group, English Lake District, *Journal of the Geological Society of London, 140*, 511-518.

Todt, W., Cliff, R.A., Hanser, A. and Hofmann, A.W., 1996. Evaluation of a ^{202}Pb-^{205}Pb double spike for high precision lead isotope analyses, in *Earth Processes: Reading the Isotopic Code*, vol. 5, *Geophysical Monograph*, edited by A. Basu and S. Hart, AGU, Washington D.C.

Tranter, T.H., 1991. Accretion and subduction processes along the Pacific margin of Gondwana, central Alexander Island, in *Geological Evolution of Antarctica; proceedings of the Fifth International Symposium on Antarctic Earth Sciences*, Cambridge University Press.

Tulloch, A.J., 1991. Alkaline plutonic and volcanic rocks of the late Cretaceous Mandamus Igneous Complex, North Canterbury, *New Zealand Geological Survey Record, 43*, 15-23.

Tulloch, A.J., Kimbrough, D.L. and Wood, R.A., 1991. Carboniferous granite basement dredged from a site on the southwest margin of the Challenger Plateau, Tasman Sea, *New Zealand Journal of Geology and Geophysics, 34*, 121-126.

Tulloch, A.J., Kimbrough, D.L. and Waight, T.E., 1994. The French Creek Granite, North Westland, New Zealand - Late Creatceous A-type plutonism on the Tasman passive margin, in *Evolution of the Tasman Sea Basin: Proceedings of the Tasman Sea Conference*, edited by G.J. van der Lingen, *et al.*, A.A.Balkema, Rotterdam, Christchurch, New Zealand,

Tulloch, A.J., Kimbrough, D.L., Landis, C.A., Mortimer, N. and Johnston, M.R., 1999. Relationships between the Brook Street Terrane and Median Tectonic Zone (Median Batholith); evidence from Jurassic conglomerates, *New Zealand Journal of Geology and Geophysics, 42*, 279-293.

van Huhen, J., van den Berg, A.P. and Vlaar, N.J., 2002. On the role of subducting oceanic plateaus in the development of shallow flat subduction, *Tectonophysics, 352*, 317-333.

Veevers, J., 2000. Change of tectonostratigraphic regime in the Australian Plate during the 99Ma (Mid-Cretaceous) and 43Ma (Mid-Eocene) swerves of the Pacific, *Geology, 28*, 47-50.

Villeneuve, M., Sandeman, H.A. and Davis, W.J., 2000. A method for intercalibration of U-Th-Pb and 40Ar-39Ar ages in the Phanerozoic, *Geochimica et Cosmochimica Acta, 64*, 4017-4030.

Waight, T.E., Weaver, S.D., Ireland, T.R., Maas, R., Muir, R.J. and Shelley, D., 1997. Field characteristics and geochronology of the Hohonu Batholith, North Westland, New Zealand, *New Zealand Journal of Geology and Geophysics, 40*, 1-17.

Waight, T.E., Weaver, S.D., Maas, R. and Eby, G.N., 1998a. French Creek Granite and Hohonu Dyke Swarm, South Island, New Zealand: Late Cretaceous alkaline magmatism and the opening of the Tasman Sea, *Australian Journal of Earth Sciences, 45*, 823-835.

Waight, T.E., Weaver, S.D. and Muir, R.J., 1998b. Mid-Cretaceous granitic magmatism during the transition from subduction to extension in southern New Zealand: a chemical and tectonic synthesis, *Lithos, 45*, 469-482.

Wandres, A.M.C., 2002. Provenance study of the Torlesse Terranes - Implications for the origin of the Continental Crust of Eastern New Zealand, PhD thesis, University of Canterbury, Christchurch.

Warner, T.L., 1990. The extrusive igneous rocks of the Marlborough region and their geological significance, MSc thesis, University of Canterbury, Christchurch.

Weaver, B.L., Wood, D.A., Tarney, J. and Joron, J.L., 1987. Geochemistry of ocean island basalts from the South Atlantic: Ascension, Bouvet, St. Helena, Gough and Tristan de Cunha, in *Alkaline Igneous Rocks*, vol. 30, *Geological Society of London Special Publication*, edited by J.G. Fitton and B.G.J. Upton, pp. 253-267, The Geological Society.

Weaver, B.L., 1991. The origin of ocean island basalt end-member compositions: trace element and isotopic constraints, *Earth and Planetary Science Letters, 104*, 381-397.

Weaver, S.D. and Smith, I.E.M., 1989. New Zealand intraplate volcanism, in *Intraplate volcanism in eastern Australia and New Zealand*, edited by R.W. Johnson, *et al.*, Cambridge University Press.

Weaver, S.D. and Pankhurst, R.J., 1991. A precise Rb-Sr age for the Mandamus Igneous Complex, North Canterbury, and regional tectonic implications, *New Zealand Journal of Geology and Geophysics, 34*, 341-345.

Weaver, S.D., Adams, C.J., Pankhurst, R.J. and Gibson, I.J., 1992. Granites of Edward VII Peninsula, Marie Byrd Land: anorogenic magmatism related to Antarctic-New Zealand rifting, *Transactions of the Royal Society of Edinburgh: Earth Sciences, 83*, 281-290.

Weaver, S.D., Storey, B.C., Pankhurst, R.J., Mukasa, S.B., DiVenere, V.J. and Bradshaw, J.D., 1994. Antarctica-New Zealand rifting and Marie Byrd Land lithospheric magmatism linked to ridge subduction and mantle plume activity, *Geology, 22*, 811-814.

Weaver, S.D., Bradshaw, J.D., Pankhurst, R.J., Muir, R.J., Storey, B.C., Waight, T.E. and Ireland, T.R., 1996. Cretaceous Magmatism, make-up and break-up of the SW Pacific Gondwana Margin, in *Mesozoic Geology of the Eastern Australian Plate*, vol. 43, pp. 548-556, Geological Society of Australia, Extended Abstracts,

Weaver, S.D., Bradshaw, J.D. and Muir, R.J., 1997. Mesozoic magmatic and tectonic events in New Zealand Gondwanic terranes, in *Terrane dynamics 97; international conference on Terrane geology; abstracts of papers presented*, edited by J.D. Bradshaw and S.D. Weaver, pp. 161-164,

White, R.S. and McKenzie, D.J., 1989. Magmatism at rift zones; the generation of volcanic continental margins and flood basalts, *Journal of Geophysical Research, 94*, 7685-7729.

Williams, I.S., Tetley, N.W., Compston, W. and McDougall, I., 1982. A comparison of K-Ar and Rb-Sr ages of rapidly cooled igneous rocks ; two points in the Palaeozoic time scale re-evaluated, *Journal of the Geological Society of London, 139*, 557-568.

Wilson, C.J.N., Houghton, B.F., McWilliams, M.O., Lanphere, M.A., Weaver, S.D. and Briggs, R.M., 1995. Volcanic and structural evolutino of Taupo Volcanic Zone New Zealand: a review, *Journal of Volcanology and Geothermal Research, 68*, 1-28.

Wilson, M. and Bianchini, G., 1999. Tertiary-Quaternary magmatism within the Mediterranean and surrounding regions, in *The Mediterranean Basins: Tertiary Extension within the Alpine Orogen*, vol. 156, *Geological Society Special Publication*, edited by B. Durand, *et al.*, The Geological Society, Cambridge.

Woldemichael, S., 1999. Low grade metamorphism and hydrothermal alteration in the basement greywacke terranes of the northern and central North Island, New Zealand: reconnaissance study., PhD thesis, University of Auckland, Auckland.

Wood, B.L., 1969. J.D.George-1: New Zealand Petroleum Co. Ltd Report., *Unpublished openfile Petroleum Report, 527*.

Wood, C.P., 1974. Petrogenesis of garnet-bearing rhyolites from Canterbury, New Zealand, *New Zealand Journal of Geology and Geophysics, 17*, 759-787.

Zeck, H.P., 1995. Betic-Rif orogeny: subduction of Mesozoic Tethys lithosphere under eastward drifting Iberia, slab detachment shortly before 22 Ma, and subsequent uplift and extensional tectonics, *Tectonophysics, 254*, 1-16.

Zindler, A. and Hart, S., 1986. Chemical geodynamics, *Annual Review of Earth and Planetary Sciences, 14*, 493-571.

Appendix 1: Catalogue of rock samples and their analytical treatment

This appendix lists all samples collected from both the MSVG and MIC field areas. Listed below is a guide to the various symbols and abbreviations used in the table.

A1.1 Key to Symbols and Abbreviations

A1.1.1 Specimen Number

Refers to the field number applied to each specimen. The prefixes indicate which field area the specimen was collected from and these are listed below:

MS- Mount Somers and Mount Barrosa
MV- McQueens Valley and Gebbies Pass, Banks Peninsula
GD- Gawler Downs
MH- Malvern Hills
RG- Rangitata Gorge
M- Mandamus River

Where the sample numbers are given a letter suffix, this indicates that a number of samples were collected from the immediate vicinity or outcrop, and appeared to display differing properties. The absence of MS-81 from the catalogue is intentional due to a numbering error whilst mapping.

A1.1.2 Locality Grid Reference

Eight figure grid references are provided for optimum accuracy in most cases which serves to narrow the locality position to a $100m^2$ area rather than $1000m^2$ in the case of six figure grid references. Six figure references are provided for localities where the fourth and eighth digit

is a zero. Each grid reference is prefixed by a map reference e.g. K36/ for ease of relocation by future workers. The Map series' used is the Land Information 260 1:50 000 scale. For example, K36/ corresponds to : 'Topographic Map 260 K36 METHVEN'. A full list of maps used during the field mapping component of this thesis is listed below:

K36 METHVEN
J36 MOUNT HARPER
M36 LINCOLN
K35 COLERIDGE
L35 WAIMAKARIRI
M33 WAIKARI

A1.1.3 Brief Notes

The 'brief notes' column indicates the locality number from which a sample was taken. For example MS-1 was collected from locality MS/2. Locality numbers are differentiated from sample numbers by the presence of a back-slash rather than a hyphen. Sample locality numbers, in most cases, do not correlate with sample numbers because samples were not collected from every locality.

A1.1.4 Unit codes

The 'unit' column of the catalogue provides a basic indication of the rock type at the locality. The abbreviations used in the catalogue are explained below.

And	Andesite	**Trach**	Trachyte
Rhy	Rhyolite	**Brecc**	Breccia
Ignim	Ignimbrite	**Sye**	Syenite
B-I, B-IV etc.	Barrosa units B-I to B-IV	**U-GI**	Upper Glassy Ignimbrite
Torl	Torlesse supergroup units	**Tuff**	Tuff
Pitch	Pitchstone	**m-Sy**	microSyenite
Dac	Dacite	**B-and**	Basaltic andesite
Gabb	Gabbro	**m-Gab**	microGabbro

P-Tep	/Phonotephrite	**Teph**	Tephrite
T-and	/Trachyandesite	**T-bas**	Trachybasalt
B-T-a	/Basaltic Trachyandesite	**P-bas**	Picrobasalt
F-Mz	/foid-bearing Monzonite	**Sy-Di**	Syenodiorite
T-Pho	Tephriphonolite		

A1.2 Rock Catalogue

The following pages provide information about each rock specimen collected during the course of this research.

Specimen Number	Locality GR*	Brief Notes	Unit	Thin Section	Notes	XRF No.	Ar-Ar	SHRIMP ANU No.	ICP-MS	Sr-Nd-Pb	O^{18}
Woolshed Creek											
MS-1	K36/752 331	MS/2									
MS-2	K36/7535 3320	MS/4									
MS-3	K36/748 327	MS/5	And	•							
MS-4	K36/7470 3285	MS/6	And	•							
MS-5	K36/7470 3285	MS/6									
MS-6	K36/7498 3280	MS/7	And	•							
MS-7	K36/7510 3265	MS/8									
MS-8	K36/7498 3310	MS/9									
MS-9	K36/7501 3313	MS/10	Rhy	•	Rhyolite Breccia						
MS-10	K36/7501 3313	MS/10									
MS-11	K36/7497 3228	MS/12	Rhy	•							
MS-12a	K36/7530 3265	MS/17	Ignim	•							
MS-12b	K36/7530 3265	MS/17	Ignim	•							
MS-13	K36/7543 3260	MS/19									
MS-14	K36/7501 3313	MS/10									
MS-15	K36/7505 3313	MS/20	Ignim	•							
MS-16a	K36/7530 3326	MS/23		•							
MS-16b	K36/7530 3326	MS/23		•							
MS-17a	K36/7556 3315	MS/25		•							
MS-17b	K36/7556 3315	MS/25		•							
MS-18	K36/7500 3319	MS/26		•							
MS-19	K36/7480 3370	MS/27									
MS-20	K36/7448 3367	MS/28		•							
MS-21	K36/7422 3352	MS/29									
MS-22	K36/7419 3360	MS/30		•							
MS-23	K36/7391 3355	MS/31		•							
MS-24	K36/7430 3340	MS/34	And	•							
Barrosa											
MS-25	J36/6913 2925	MS/35	And			33235					
MS-26	J36/6913 2925	MS/36									
MS-27	J36/6909 2922	MS/37	B-IV	•		32433					
MS-28	J36/6910 2919	MS/38									

Specimen Number	Locality GR*	Brief Notes	Unit	Thin Section	Notes	XRF No.	Ar-Ar	SHRIMP ANU No.	ICP-MS	Sr-Nd-Pb	O^{18}
MS-29	J36/6905 2925	MS/39	B-IV	•		33236	•		•	•	
MS-30	J36/6906 2927	MS/40									
MS-31	J36/6895 2930	MS/42									
MS-32	J36/6875 2923	MS/43									
MS-33	J36/6846 2923	MS/46									
MS-34	J36/6831 2925	MS/49	B-III	•		32865			•	•	
MS-35	J36/6831 2925	MS/49									
MS-36	J36/6831 2925	MS/49	B-III	•		33237	•				
MS-37	J36/6798 2810	MS/50	Torl	•		33238			•	•	•
MS-38	J36/6795 2815	MS/51	B-I								
MS-39	J36/6792 2825	MS/52									
MS-40	J36/6788 2835	MS/53	B-I			33239	•				
MS-41	J36/6784 2838	MS/54									
MS-42	J36/6769 2864	MS/56									
MS-43	J36/6773 2888	MS/59									
MS-44	J36/6767 2890	MS/60									
MS-45	J36/6768 2905	MS/62									
MS-46	J36/6761 2902	MS/63	B-I	•		32440					
MS-47	J36/6747 2911	MS/65									
MS-48	J36/6753 2917	MS/66									
MS-49	J36/6756 2922	MS/67									
MS-50	J36/6665 2840	MS/68	Torl			33240					
MS-51	J36/6692 2836	MS/69									
MS-52	J36/6710 2840	MS/70									
MS-53	J36/6729 2837	MS/72									
MS-54	J36/6725 2825	MS/73	B-I	•		32439					
MS-55	J36/6738 2845	MS/75	B-I	•							
MS-56	J36/6745 2849	MS/76									
MS-57	J36/6763 2847	MS/77	B-I	•							
MS-58	J36/6740 2869	MS/80									
MS-59	J36/6738 2864	MS/81									
MS-60	J36/6714 2859	MS/83									
MS-61	J36/6710 2853	MS/84									
MS-62	J36/6585 2920	MS/85	Torl			33241					
MS-63	J36/6635 2980	MS/86	Torl								

Specimen Number	Locality GR*	Brief Notes	Unit	Thin Section	Notes	XRF No.	Ar-Ar	SHRIMP ANU No.	ICP-MS	Sr-Nd-Pb	O^{18}
MS-64	J36/6647 2985	MS/87	Torl								
MS-65a	J36/6655 3000	MS/89	Torl			33242			•	•	•
MS-65b	J36/6665 3009	MS/90	Torl	•	Breccia						
MS-66	J36/6684 3027	MS/92									
MS-67	J36/6667 3031	MS/93									
MS-68	J36/6693 3030	MS/94	B-II	•		32434	•		•	•	
MS-69	J36/6708 3025	MS/95	B-II								
MS-70	J36/6708 3065	MS/96	B-II	•							
MS-71	J36/6738 3105	MS/98	B-IV	•		32866					
MS-72	J36/6740 3113	MS/99	And	•							
MS-73	J36/6735 3116	MS/100	And	•		32867					
MS-74	J36/6748 3123	MS/101									
MS-75	J36/6757 3126	MS/102	B-III	•		32441			•	•	
MS-76	J36/6727 3148	MS/103	And			32891					
MS-77	J36/6684 3156	MS/104	B-II	•		32435					
MS-78	J36/6617 3146	MS/105	B-II	•							
MS-79	J36/6570 3137	MS/106	B-II	•							
MS-80	J36/6782 2767	MS/107									
MS-82	J36/6774 2792	MS/108	B-I	•		32868					
MS-83	J36/6771 2798	MS/110									
MS-84	J36/6773 2801	MS/111									
MS-85	J36/6767 2810	MS/113	B-I	•		32869					
MS-86	J36/6779 2806	MS/114									
MS-87	J36/6763 2812	MS/115	B-I	•		32870					
MS-88	J36/6765 2822	MS/116									
MS-89	J36/6734 2827	MS/119									
MS-90	J36/6746 2796	MS/121									
MS-91	J36/6972 3335	MS/126									
MS-92	J36/6932 3333	MS/127	B-IV	•		32871					
MS-93	J36/6938 3297	MS/128	B-III	•		32442			•		
MS-94	J36/6943 3296	MS/129									
MS-95	J36/6949 3269	MS/131									
MS-96	J36/6914 3222	MS/133	B-III			33243	•				
MS-97	J36/6860 3193	MS/136									

Specimen Number	Locality GR*	Brief Notes	Unit	Thin Section	Notes	XRF No.	Ar-Ar	SHRIMP ANU No.	ICP-MS	Sr-Nd-Pb	O^{18}
MS-98	J36/6849 3184	MS/137									
MS-99	J36/6962 3192	MS/139	Pitch	•		32436			•	•	•
MS-100	J36/6994 3267	MS/141									
MS-101a	J36/6805 2846	MS/142									
MS-101b	J36/6805 2846	MS/142									
MS-102a	J36/6815 2880	MS/143									
MS-102b	J36/6815 2880	MS/143									
MS-103	J36/6822 2878	MS/144									
MS-104	J36/6827 2915	MS/145									
MS-105	J36/6823 2920	MS/146	B-III			32872					
MS-106a	J36/6816 2895	MS/147	B-III								
MS-106b	J36/6816 2895	MS/147	B-III	•		32443					
MS-106c	J36/6816 2895	MS/147	B-III								
MS-107	J36/6800 2897	MS/148									
MS-108	J36/6793 2897	MS/149									
MS-109	J36/6795 2891	MS/150									
MS-110	J36/6794 2888	MS/151									
MS-111	J36/6783 2892	MS/152									
MS-112	J36/6805 2910	MS/153									
MS-113	J36/6797 2926	MS/154									
MS-114	J36/6831 2878	MS/155									
MS-115	J36/6831 2861	MS/156									
MS-116	J36/6818 2825	MS/157	Torl								
MS-117a	J36/6900 2891	MS/158	B-III	•							
MS-117b	J36/6900 2891	MS/158	B-III	•							
MS-117c	J36/6900 2891	MS/158	B-III								
MS-118	J36/6870 2895	MS/159	B-III			33244					
MS-119a	J36/6868 2895	MS/160									
MS-119b	J36/6868 2895	MS/160									
MS-120	J36/6869 2905	MS/161									
MS-121	J36/6881 2870	MS/162									
MS-122	J36/6875 2871	MS/163									
MS-123	J36/6895 2868	MS/164									
MS-124	J36/6676 2845	MS/165									
MS-125	J36/6679 2850	MS/166									

Specimen Number	Locality GR*	Brief Notes	Unit	Thin Section	Notes	XRF No.	Ar-Ar	SHRIMP ANU No.	ICP-MS	Sr-Nd-Pb	O^{18}
MS-126	J36/6700 2847	MS/167	And			33245	•		•	•	
MS-127	J36/6729 2898	MS/168									
MS-128	J36/6705 2890	MS/169									
MS-129	J36/6688 2895	MS/170									
MS-130	J36/6674 2891	MS/171									
MS-131	J36/6669 2881	MS/173									
MS-132	J36/6665 2883	MS/174									
MS-133	J36/6654 2897	MS/175		•							
MS-134	J36/6710 2986	MS/177	B-I			32873					
MS-135	J36/6703 3006	MS/178									
MS-136a	J36/6704 3014	MS/179	B-II	•							
MS-136b	J36/6704 3014	MS/179									
MS-137	J36/6729 2990	MS/180	B-II	•		32874					
MS-138	J36/6728 2933	MS/181	B-I			32875					
MS-139	J36/6710 2923	MS/182									
MS-140	J36/6703 2869	MS/183	B-I	•		32444					
MS-141	J36/6466 3177	MS/185	Torl			33246					
MS-142	J36/6458 3179	MS/186	Torl								
MS-143	J36/6529 3160	MS/188	B-II	•							
MS-144	J36/6558 3186	MS/189	B-II	•							
MS-145	J36/6559 3163	MS/190	B-II	•							
MS-146	J36/6591 3165	MS/191	B-II			33247	•				
MS-147	J36/6597 3182	MS/192									
MS-148	J36/6600 3193	MS/193	B-II	•							
MS-149	J36/6637 3193	MS/194									
MS-150	J36/6682 3204	MS/195									
MS-151	J36/6680 3217	MS/196	B-II								
MS-152	J36/6666 3222	MS/197	B-II	•							
MS-153	J36/6635 3217	MS/198	B-II	•							
MS-154	J36/6596 3220	MS/199	Torl								
MS-155	J36/6574 3211	MS/200									
MS-156	J36/6689 2748	MS/201									
MS-157	J36/6696 2766	MS/202									
MS-158	J36/6716 2788	MS/204									

Specimen Number	Locality GR*	Brief Notes	Unit	Thin Section	Notes	XRF No.	Ar-Ar	SHRIMP ANU No.	ICP-MS	Sr-Nd-Pb	O^{18}
MS-159	J36/6701 2785	MS/205									
MS-160	J36/6702 2740	MS/206									
MS-161	J36/6712 2736	MS/207									
MS-162	J36/6738 2729	MS/208	B-I	•		32437			•		
MS-163	J36/6744 2720	MS/209									
MS-164	J36/6726 2713	MS/210									
MS-165	J36/6707 2720	MS/211	B-I	•		32445	•				
MS-166	J36/6700 2729	MS/212									
MS-167	J36/6723 3250	MS/213		•	Breccia						
MS-168	J36/6707 3220	MS/214	B-II								
MS-169	J36/6692 3215	MS/215	B-II		Massive andesite						
MS-170	J36/6728 3171	MS/216				32876					
MS-171	J36/6735 3160	MS/217	And		10m Thick flow						
MS-172	J36/6770 3170	MS/218									
MS-173	J36/6766 3187	MS/219									
MS-174	J36/6759 3190	MS/220	B-III	•							
MS-175	J36/6760 3210	MS/221									
MS-176	J36/6768 3237	MS/222									
MS-177	J36/6798 3190	MS/223									
MS-178	J36/6811 3165	MS/224	B-III	•							
MS-179	J36/6841 3185	MS/225									
MS-180	J36/6841 3195	MS/226									
MS-181	J36/6831 3203	MS/227									
MS-182	J36/6819 3248	MS/228									
MS-183	J36/6832 3257	MS/229	B-II	•		32446					
MS-184	J36/6960 2999	MS/230	B-II			32877					
MS-185	J36/6947 3021	MS/231									
MS-186	J36/6929 3042	MS/232									
MS-187	J36/6943 3117	MS/233									
MS-188	J36/6933 3137	MS/234	B-II	•							
MS-189	J36/6922 3140	MS/235	B-II	•		32878					
MS-190	J36/6889 3144	MS/236									
MS-191	J36/6858 3128	MS/237	B-III	•		32438					
MS-192	J36/6830 3115	MS/238	B-III			32879					
MS-193	J36/6872 3114	MS/239	B-III			32880					

Specimen Number	Locality GR*	Brief Notes	Unit	Thin Section	Notes	XRF No.	Ar-Ar	SHRIMP ANU No.	ICP-MS	Sr-Nd-Pb	O^{18}
MS-194	J36/6905 3108	MS/242	B-III	•		32447					
MS-195	J36/6914 3094	MS/243									
MS-196	J36/6895 3053	MS/244									
MS-197	J36/6939 3013	MS/245									
MS-198	J36/6745 2994	MS/246	B-II	•		32448					
MS-199	J36/6755 3006	MS/247									
MS-200	J36/6759 3014	MS/248									
MS-201	J36/6766 3019	MS/249									
MS-202	J36/6786 3015	MS/250									
MS-203	J36/6803 3013	MS/251		•							
MS-204	J36/6798 3049	MS/252									
MS-205	J36/6767 3053	MS/253	B-II	•		32881					
MS-206	J36/6857 3048	MS/255	B-I	•		32882					
MS-207	J36/6833 2994	MS/257									
MS-208	J36/6807 2945	MS/258	B-III			32883					
MS-209	J36/6837 2932	MS/259	B-III			32884					
MS-210	J36/6895 2949	MS/262									
MS-211	J36/6729 2594	MS/264		•							
MS-212	J36/6788 2635	MS/265	B-III	•		32506					
MS-213	J36/6844 2655	MS/266	And	•		32507					
MS-214	J36/6875 2665	MS/267		•							
MS-215	K36/7923 2574	MS/268	And	•	Petrified Gully	32508					
MS-216a	K36/7923 2574	MS/268	Pitch	•	Petrified Gully						
MS-216b	K36/7923 2574	MS/268	Pitch	•	Petrified Gully	32509					
MS-217	J36/7035 2936	MS/269	And	•	Barrosa Nobble	32510					
MS-218	J36/7042 2933	MS/270	Rhy	•	Barrosa Nobble	32511					
MS-219	K36/8145 2775	MS/271	Rhy	•		32885					
MS-220	K36/7265 3270	MS/272	Rhy	•		32886					
MS-221	K36/7195 3323	MS/276	Rhy	•		32887					
MS-222	K36/7139 3316	MS/277	Rhy	•		32888					
MS-223	K36/7136 3288	MS/278	Rhy	•		32889					
MS-224	K36/7180 3240	MS/279	Rhy								
MS-225	K36/7203 3178	MS/280	Rhy								
MS-226	K36/7183 3120	MS/281	Rhy	•		32890		118	•		

Specimen Number	Locality GR*	Brief Notes	Unit	Thin Section	Notes	XRF No.	Ar-Ar	SHRIMP ANU01-	ICP-MS	Sr-Nd-Pb	O^{18}
McQueens Valley, Banks Peninsula											
MV-1	M36/817 222	MV/1	Rhy								
MV-2	M36/8115 2217	MV/4									
MV-3	M36/8103 2228	MV/6		•							
MV-4	M36/811 226	MV/7	Trach	•	Tertiary	32449	•				
MV-5	M36/811 226	MV/7	Trach	•	Tertiary	32450					
MV-6	M36/8107 2286	MV/8		•							
MV-7	M36/8140 2265	MV/10	Trach	•	Tertiary	32451					
MV-8	M36/8141 2250	MV/11	Pitch	•		32452					
MV-9	M36/8204 2185	MV/12	And	•		32518			•	•	
MV-10	M36/8208 2166	MV/13									
MV-11	M36/8206 2160	MV/14	And	•		32519	•				
MV-12	M36/8183 2149	MV/16	Trach	•	Tertiary	32520					
MV-13	M36/8143 2106	MV/18	Rhy	•	Tertiary	32521					
MV-14	M36/8123 2096	MV/19		•							
MV-15	M36/8202 2259	MV/20									
MV-16	M36/8207 2294	MV/21									
MV-17	M36/8201 2231	MV/22	Ignim	•		32522					
MV-18	M36/7899 2299	MV/23									
MV-19	M36/7979 2316	MV/24	Ignim	•		32792		115	•		
Gawler Downs											
GD-1	K36/7815 1368	GD/01									
GD-2	K36/7840 1383	GD/04	And	•		32523	•				
GD-3	K36/7822 1342	GD/05	Dac	•							
GD-4	K36/7766 1438	GD/07	Dac	•		32524					
GD-5	K36/765 145	GD/08	Dac								
GD-6	K36/7657 1412	GD/10	Dac	•		32525					
GD-7	K36/7702 1260	GD/12	Dac	•							
GD-8	K36/7877 1693	GD/13		•							
GD-9	K36/7871 1674	GD/15	Dac	•							
GD-10	K36/7816 1581	GD/16	Rhy	•		32790					
GD-11	K36/7795 1610	GD/17	Dac								
GD-12	K36/7798 1682	GD/18	Dac	•							

Specimen Number	Locality GR*	Brief Notes	Unit	Thin Section	Notes	XRF No.	Ar-Ar	SHRIMP ANU01-	ICP-MS	Sr-Nd-Pb	O^{18}
GD-13	K36/7794 1702	GD/20	Dac	•		32526			•		
GD-14	K36/7849 1728	GD/22	Dac	•							
GD-15	K36/7862 1760	GD/23	Tuff	•		32527					
GD-16	K36/7221 2091	GD/24	Dac	•	Segregation vesicles	32528					
GD-17	K36/7175 2140	GD/26	Dac	•		32529			•	•	
GD-18	K36/7156 2189	GD/27	Torl			33251					
GD-19	K36/7097 2252	GD/28	Dac	•		32530					
GD-20	K36/7222 2248	GD/31	Dac	•		32531					
GD-21	K36/7188 2400	GD/33	Dac	•		32532					
GD-22	K36/7207 2365	GD/34	Dac	•		33252	•				
GD-23	K36/7216 2330	GD/35	Dac								
GD-24	K36/7235 2320	GD/36	Torl	•							
GD-25	K36/7258 2333	GD/38	Dac								
GD-26	K36/7151 2485	GD/39	And	•	Blondin Stream Andesite	32533					
GD-27	K36/7139 2492	GD/40	And		Blondin Stream Andesite						
GD-28	K36/7139 2511	GD/41	Pitch	•		32534					•
GD-29	K36/7157 2543	GD/42	Rhy	•	Blondin Stream	32535					
GD-30	K36/7242 1797	GD/43	Dac	•		32791					
GD-31	K36/7230 1770	GD/44	Tuff	•							
GD-32	K36/7217 1739	GD/47	Dac	•							
Malvern Hills											
MH-1	K35/0038 4326	MH/2	Basalt	•	Dyke	32512					
MH-2	K35/0071 4278	MH/4	Ignim	•							
MH-3	K35/010 428	MH/5	Ignim	•		32513					
MH-4	K35/0154 4270	MH/7	Rhy	•							
MH-5	K35/0153 4264	MH/8	Pitch	•	Dyke	32514					
MH-6	K35/0136 4244	MH/9	Rhy	•		32515					
MH-7	K35/0088 4256	MH/10	Ignim	•		32516	•				
MH-8	K35/0088 4256	MH/10	Ignim	•		32517		117	•	•	
MH-9	K35/0031 4326	MH/13	And								
MH-10	K35/0028 4322	MH/14	And	•							
MH-11	K35/0021 4309	MH/16	B-and	•		32793					
MH-12	K35/0149 4265	MH/17	Pitch	•	Dyke	32794	•				•

Specimen Number	Locality GR*	Brief Notes	Unit	Thin Section	Notes	XRF No.	Ar-Ar	SHRIMP ANU01-	ICP-MS	Sr-Nd-Pb	O^{18}
MH-13	K35/0571 4476	MH/21	Pitch	•		32795					
MH-14	K35/0566 4532	MH/26	And	•		32796					
MH-15	K35/0560? 4547	MH/29	And	•	Black amygs	32797					
MH-16	K35/0582 4504	MH/31	U-GI	•		32798					
MH-17	K35/0602 4471	MH/33	Ignim	•		32799					
MH-18	K35/0701 4581	MH/36	And	•							
MH-19	K35/0697 4619	MH/38	And	•							
MH-20	K35/0672 4634	MH/39	And	•	Black amygs	32800					
MH-21	K35/0651 4690	MH/42	And	•		32801			•	•	
MH-22	K35/0684 4669	MH/43	Ignim	•		32802					
MH-23	K35/0692 4692	MH/45	Ignim	•							
MH-24	K35/0691 4531	MH/49	Pitch	•							
MH-25	K35/0738 4516	MH/51	And dyke	•							
MH-26	K35/0977 4588	MH/56	Ignim	•		32803					
MH-27	K35/0796 4559	MH/60	Ignim	•							
MH-28	K35/0780 4579	MH/61	U-GI	•		32804	•				
MH-29	K35/0719 4667	MH/63	Pitch	•		32805					
MH-30	K35/0719 4667	MH/63	Pitch	•		32806					
MH-31	K35/0792 4745	MH/75	And	•	Qz bearing						
MH-32	K35/1011 4693	MH/76	Ignim	•		32807					
MH-33	K35/0943 4742	MH/77	Ignim	•		32808					
MH-34	K35/0946 4774	MH/78	Rhy dyke	•		32809					
MH-35	L35/1040 4711	MH/80	And	•	Qz bearing						
MH-36	L35/1052 4730	MH/82	And			32810					
MH-37	L35/1082 4685	MH/83	Ignim	•	Large lithic clasts						
MH-38	L35/1108 4575	MH/84	Si sand								
MH-39	L35/1125 4501	MH/87	Rhy	•		32811					
MH-40	L35/1319 4601	MH/91	Ignim	•		32812					
MH-41	L35/1330 4663	MH/93	Ignim	•							
MH-42	L35/1207 4629	MH/96	Ignim	•		32814					
MH-43	L35/1249 4660	MH/97	Ignim								
MH-44	L35/1181 4651	MH/99	Coal		+ Silica sand						

Specimen Number	Locality GR*	Brief Notes	Unit	Thin Section	Notes	XRF No.	Ar-Ar	SHRIMP ANU01-	ICP-MS	Sr-Nd-Pb	O^{18}
MH-45	L35/1385 4725	MH/101	m-gab	•	Dyke?	32815					
MH-46	L35/1372 4827	MH/105	Torl	•		32816					
MH-47	L35/1365 4824	MH/106	Ignim	•		32817					
MH-48	L35/1249 4818	MH/109	Ignim	•							
MH-49	L35/1840 4897	MH/112	Ignim	•		32818					
MH-50	L35/1742 4775	MH/115	Rhy	•		32819					
MH-51	L35/1904 4745	MH/118	Lahar	•							
MH-52	L35/1917 4691	MH/119	Rhy								
MH-53	K35/0040 4245	MH/120	Ignim		Bell Rock						
MH-54	K35/0591 4405	MH/121	Rhy	•		32820					
MH-55	K35/0157 4248	MH/122	Rhy	•		32821					
MH-56	K35/0135 4232	MH/123	Rhy	•		32822					
MH-57	L35/1101 4980	MH/125	Torlesse	•							
MH-58	L35/1070 4915	MH/126	Marble	•							
MH-59	L35/1076 4840	MH/129	Basalt	•	Dyke	32823					
MH-60	L35/1099 4842	MH/131	Ignim			32824					
MH-61	L35/1035 4829	MH/134	Ignim	•		32825					
MH-62	K35/0892 4771	MH/136	Rhy	•	Fissure dyke	32826					
MH-63	K35/0857 4778	MH/137	Ignim	•		32827					
MH-64	K35/0756 4795	MH/140	And								
MH-65	K35/0786 4855	MH/141	Ignim	•		32828					
MH-66	K35/0610 4804	MH/144	Ignim	•		32829					
MH-67	K35/0693 4721	MH/147	And								
MH-68	K35/0616 4721	MH/148	And								
MH-69	K35/0591 4737	MH/149	And	•		32830					
MH-70	K35/0541 4751	MH/151	Ignim			32831					
MH-71	K35/0544 4745	MH/152	Pitch	•		32832					
MH-72	K35/0558 4870	MH/154	Ignim								
MH-73	K35/0440 4695	MH/155	Ignim								
MH-74	K35/0496 4707	MH/156	U-GI	•	Not in-situ						
MH-75	K35/0501 4703	MH/157	Pitch	•							
MH-76	K35/0532 4693	MH/159	And	•							

Specimen Number	Locality GR*	Brief Notes	Unit	Thin Section	Notes	XRF No.	Ar-Ar	SHRIMP ANU01-	ICP-MS	Sr-Nd-Pb	O^{18}
Rangitata Gorge											
RG-1	J36/5909 1479	RG/1	And								
RG-2	J36/5894 1445	RG/3	And		Black amygs	33248	•				
RG-3	J36/5882 1447	RG/4	Dac	•		32771			•		
RG-4	J36/5885 1440	RG/5	Torl	•		33249			•	•	•
RG-5	J36/5839 1454	RG/11	Dac	•	Large no of xenos	32772					
RG-6	J36/5797 1498	RG/14	And								
RG-7	J36/5788 1502	RG/15	And	•		32773					
RG-8	J36/5761 1562	RG/17	And								
RG-9	J36/5820 1575	RG/20	And		Base of flow						
RG-10	J36/5721 1791	RG/21	And		Black amygs	32774					
RG-11	J36/5689 1815	RG/22	And		7m thick flow	33250	•				
RG-12	J36/5689 1815	RG/22	And								
RG-13	J36/5584 1901	RG/23	Trach	•		32775					
RG-14	J36/5579 1905	RG/24	Dac	•		32776					
RG-15	J36/5551 1902	RG/25	Rhy								
RG-16	J36/5519 1883	RG/27	Rhy	•		32777					
RG-17	J36/5497 1872	RG/28	Rhy								
RG-18	J36/5316 1952	RG/29	Rhy	•		32778			•		
RG-19	J36/5293 1994	RG/30	Rhy								
RG-20	J36/5272 2000	RG/31	Rhy								
RG-21	J36/5249 2005	RG/33	Rhy	•		32779					
RG-22	J36/5146 2073	RG/35	Rhy								
RG-23	J36/5088 2063	RG/36	Rhy								
RG-24	J36/5036 2066	RG/37	Rhy								
RG-25	J36/5066 2003	RG/38	Rhy	•		32780					
RG-26	J36/5057 1980	RG/40									
RG-27	J36/5056 1934	RG/41									
RG-28	J36/5256 1760	RG/43	And		Black amygs						
RG-29	J36/5272 1797	RG/45	And		Black amygs						
RG-30	J36/5266 1820	RG/46	Dac	•		32781					
RG-31	J36/5238 1874	RG/47									
RG-32	J36/5424 1600	RG/48	And	•		32782			•		
RG-33	J36/5386 1565	RG/49	Torl	•	Clast from breccia	32783					

Specimen Number	Locality GR*	Brief Notes	Unit	Thin Section	Notes	XRF No.	Ar-Ar	SHRIMP ANU01-	ICP-MS	Sr-Nd-Pb	O^{18}
RG-34	J36/5366 1595	RG/50	B-and	•		32784			•	•	
RG-35	J36/5365 1627	RG/51									
RG-36	J36/5354 1662	RG/53	Rhy								
RG-37	J36/5339 1737	RG/55	And	•		32785					
RG-38	J36/5470 1649	RG/57	Rhy			32786					
RG-39	J36/5551 1883	RG/58	Rhy	•		32787					
Mandamus											
M-1	M33/7765 2785	M/1			Dark blue-grey dyke int. torl						
M-2	M33/7780 2807	M/3	T-and	•	Dyke int. torl	32833					
M-3	M33/7800 2828	M/6	T-bas	•	Dyke int. torl	32834					
M-4	M33/7851 2864	M/9			Dyke int. Torl						
M-5	M33/7872 2866	M/10			Orange wthrd dyke int. torl						
M-6	M33/7872 2866	M/10	T-bas	•	Black dyke int. dyke (M-5)	32835					
M-7	M33/7872 2866	M/10									
M-8	M33/7878 2865	M/11	B-T-a	•	Dyke int. Gabbro	32836					
M-9	M33/7878 2865	M/11	Gabb			33253	•				
M-10	M33/7878 2865	M/11									
M-11	M33/7878 2865	M/11	Gabb								
M-12	M33/7895 2872	M/12	Gabb	•	Petrographically – Ol Gabb	32837	•		•	•	
M-13	M33/7836 2863	M/14	Trach		Dyke int. torl						
M-14	M33/7836 2863	M/14	Trach		Dyke int. torl						
M-15	M33/7757 2776	M/15			Dyke int. torl						
M-16	M33/7750 2780	M/17	Trach	•	Creamy coloured dyke int. torl	32838					
M-17	M33/7600 2760	M/21			Black dyke int. torl						
M-18	M33/7600 2760	M/21			Dark grey dyke int. torl						
M-19	M33/7620 2697	M/24									
M-20	M33/7654 2718	M/27	Torl								
M-21	M33/7662 2757	M/28	Brecc								
M-22	M33/7732 2746	M/33	Torl			33254					
M-23	M33/7751 2779	M/35	Sye	•		32839	•				
M-24	M33/7756 2740	M/36	Trach		Trach cut by stringers of m-sy						
M-25	M33/7758 2736	M/37			Sy/trach contact - ?dyke						
M-26	M33/7775 2746	M/39									

Specimen Number	Locality GR*	Brief Notes	Unit	Thin Section	Notes	XRF No.	Ar-Ar	SHRIMP ANU01-	ICP-MS	Sr-Nd-Pb	O^{18}
M-27	M33/7771 2741	M/40	Trach								
M-28	M33/7762 2664	M/44	Trach		Amygdaloidal (calcite)						
M-29	M33/7736 2673	M/46	Sye								
M-30	M33/7732 2670	M/47	Sye								
M-31	M33/7725 2702	M/49		•							
M-32	M33/7380 2674	M/55	T-bas	•	Dyke cont. px	32840					
M-33	M33/7377 2672	M/56			Dyke cont. calcite amygs						
M-34	M33/7681 2723	M/67	Torl								
M-35	M33/7711 2715	M/68	Sye	•		32841					
M-36	M33/7706 2701	M/69									
M-37	M33/7718 2705	M/70	Teph	•		32842					
M-38	M33/7714 2684	M/72	Sye								
M-39	M33/7711 2636	M/75									
M-40	M33/7708 2631	M/76	P-Teph	•	Volcs cut by M-Sy stringers	32843			•	•	
M-41	M33/7676 2631	M/79	Sye	•		32844					
M-42	M33/7691 2654	M/80		•	Dyke int. sye	32845					
M-43	M33/7698 2664	M/81	Trach	•	Dyke int. sye	32846					
M-44	M33/7688 2666	M/83									
M-45	M33/7683 2672	M/84	Trach		Dyke int. breccia						
M-46	M33/7667 2665	M/87	Brecc		Cont. M-Sy dyklet						
M-47	M33/7642 2607	M/97			Dyke int. Sye						
M-48	M33/7642 2607	M/97			Dyke (porph) int. Sye						
M-49	M33/7634 2639	M/99	Trach	•	Sill int. breccia	32847					
M-50	M33/7613 2652	M/103	Sye	•		32848					
M-51	M33/7608 2660	M/104									
M-52	M33/7582 2652	M/108									
M-53	M33/7611 2614	M/113									
M-54	M33/7601 2603	M/118	Trach		Heavily porph ?dyke int. sye						
M-55	M33/7562 2647	M/123									
M-56	M33/7575 2632	M/124	Trach		Dark, aphyric ?dyke						
M-57	M33/7575 2613	M/128	Brecc								
M-58	M33/7555 2596	M/134	Trach								
M-59	M33/7555 2596	M/134	P-Teph	•	Stringer dyke (dark)	32849					
M-60	M33/7564 2593	M/137	Trach	•	Dyke int. m/sy	32850					

Specimen Number	Locality GR*	Brief Notes	Unit	Thin Section	Notes	XRF No.	Ar-Ar	SHRIMP ANU01-	ICP-MS	Sr-Nd-Pb	O^{18}
M-61	M33/7564 2577	M/141	Sye	•		32851					
M-62	M33/7564 2577	M/141	P-Tep	•	Black, aphyric dyke int. Sye	32852					
M-63	M33/7462 2548	M/148									
M-64	M33/7483 2533	M/152	Sye	•		32853					
M-65	M33/7506 2510	M/155			Dyke int. dior -same as M-63?						
M-66	M33/7506 2510	M/155	Sy-Di	•		32854	•		•	•	
M-67	M33/7521 2525	M/156	Basalt	•	Melanocratic	32855			•	•	
M-68	M33/7570 2563	M/163	P-Tep	•	Aphyric & melanocratic	32856					
M-69	M33/7625 2584	M/169	Brecc								
M-70	M33/7496 2506	M/172			Dyke int. Dior						
M-71	M33/7470 2504	M/173	Torl			33255					
M-72	M33/7368 2544	M/178			Sheared ?mafic material						
M-73	M33/7368 2544	M/178	Trach								
M-74	M33/7381 2537	M/180			Green sandy dyke int shr zn						
M-75	M33/7380 2531	M/181	m-Sy		Adjacent to contact						
M-76	M33/7380 2531	M/181	Trach		Adjacent to contact						
M-77	M33/7382 2513	M/183	Teph	•	Dark grey dyke int. Syenite	32857	•				
M-78	M33/7379 2497	M/184	Sye	•		32858			•	•	
M-79	M33/7351 2521	M/193			Mafic, same as M-72?						
M-80	M33/7307 2436	M/200	Torl			33256			•	•	•
M-81	M33/7302 2458	M/206	Torl								
M-82	M33/7293 2447	M/202	m-Sy		Dyke int. torl						
M-83	M33/7756 2661	M/226	T-Pho	•	Mafic lavas	32859					
M-84	M33/7723 2605	M/227	T-Pho	•	Blue-grey ?dyke	32860			•	•	
M-85	M33/7696 2479	M/236	Sye								
M-86	M33/7348 2607	M/237	P-bas		Vent breccia	32861			•	•	
M-87	M33/7348 2607	M/237	B-T-a		Vent breccia	32862					
M-88	M33/7348 2607	M/237	T-bas		Vent breccia	32863					
M-89	M33/7743 2707	M/51	F-Mz		Clast from lahar deposit	32864					
M-90	M33/7748 2708	M/238	Sye								

Appendix 2: Petrographic summaries of thin sections

This appendix provides a summary of the key petrographic features of each major rock type within the MSVG and MIC.

A2.1 MSVG

A2.1.1 Mt. Barrosa

A2.1.1.1 B-I Andesite

The B-I andesites are porphyritic, with hypo- or more commonly holocrystalline groundmasses. Phenocryst phases present are plagioclase feldspar, orthopyroxene, clinopyroxene and opaques, probably ilmenite.

The plagioclase (An_{35-64}) is generally subhedral or euhedral, commonly embayed and displaying differing levels of alteration. The size of plagioclase crystals varies but generally lies in the range 1-3mm. Plagioclase phenocrysts form 7-21% of the rock, with an average of 13.5% (N=12). The phenocryst plagioclase crystals are generally low aspect ratio, whereas the groundmass crystals are typically much higher aspect ratio crystals, indicating more rapid cooling.

Orthopyroxene is the second most common phenocryst phase but only forms 1-7% of the rock (average = 3.3%, N=12). Orthopyroxene crystals are commonly subhedral to anhedral displaying common overgrowths of clinopyroxene (pigeonite) (e.g. fig. A2.6), occasionally being completely pseudomorphed by clinopyroxene. Orthopyroxene crystals measure between <0.7 – 2.9mm, although are normally <2mm long.

Clinopyroxene (pigeonite) is not present as a primary phenocryst phase. It is predominantly associated with orthopyroxene and forms fine aggregate overgrowths and rarely complete pseudomorphs of orthopyroxene. It is therefore a minor phenocryst phase and forms

generally <1% of the rock. Where identifiable, the clinopyroxene is pigeonite. The co-existence of pigeonite and orthopyroxene has been discussed by a number of authors (e.g. Brown, 1972; Gruenewaldt, 1970; Lewis & White, 1967; Nakumara & Kushiro, 1970). Pigeonite usually inverts to orthopyroxene but in the case of the Barrosa andesites, the orthopyroxene is a primary phase and the transition to pigeonite is a considered to be due to crystallisation at lower P-T conditions and increased Fe/Mg ratio. Pigeonite is also observed to forms microlites in the groundmass.

Other minor phenocryst phases include ilmenite and magnetite, which can form up to 2% of the rock and are also abundant in the groundmass; quartz and spinel are commonly associated with xenoliths.

The presence of xenoliths in the andesites of Mt. Barrosa has been described in detail by Barley (1987). In the lavas of B-I, the xenoliths form a maximum of 4% by surface area of the slides examined. The xenoliths are commonly monominerallic and composed entirely of quartz. Some xenoliths contain quartz, feldspar, orthopyroxene, mafic phases and spinel. The maximum size of xenoliths observed in the samples examined is 2-3mm although the most common size is <1mm. Clusters composed entirely of small subhedral plagioclase crystals (fig.A2.1) were initially interpreted by Oliver (1977) to be recrystallised quartzo-feldspathic sedimentary xenoliths; however Smith & Cole (1996) re-interpreted these monominerallic clusters to be cognate magmatic xenoliths.

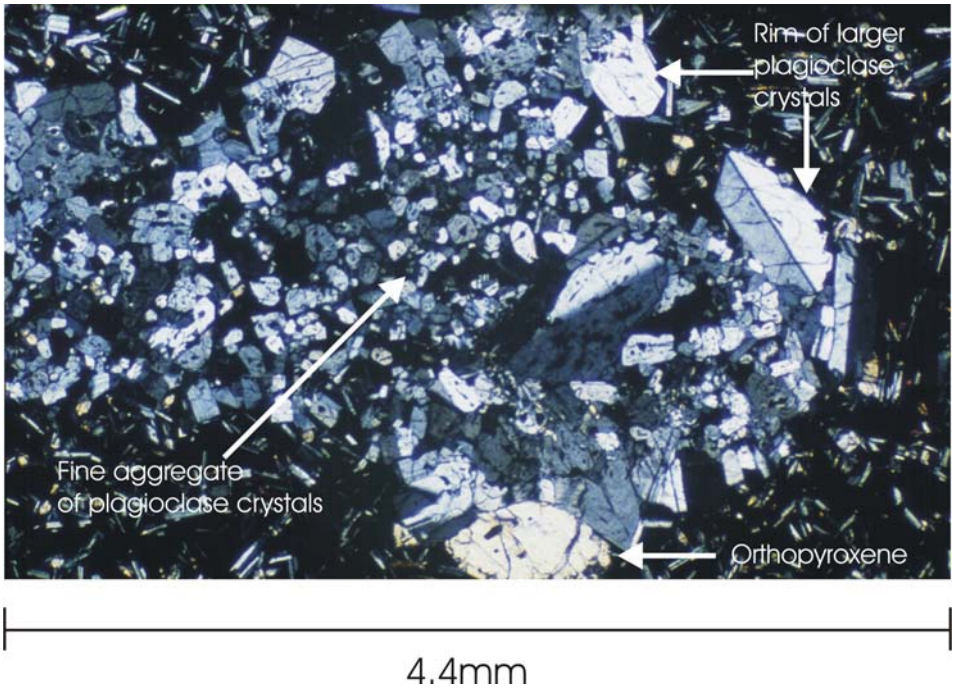

Fig.A2.1 Example of cognate magmatic xenolith under crossed-polarised light. The magmatic xenolith has a core of plagioclase feldspar which is surrounded by a coarser rim of plagioclase and orthopyroxene crystals.

Glomerocrysts are relatively common and are generally of three types: equant, acicular and monominerallic (plagioclase) aggregates. Equant glomerocrysts commonly consist of intergrown plagioclase and orthopyroxene (see fig.A2.2), whereas acicular glomerocrysts, although they too consist of plagioclase and orthopyroxene, the crystals present are of much higher aspect ratio (fig.A2.3). Equant glomerocrysts measure up to 5mm diameter whereas the acicular glomerocrysts measure up to 11mm in diameter. The equant and acicular glomerocrysts commonly have interstitial groundmass which is texturally and optically different to that of the host rock, indicating an origin as cognate magmatic xenoliths. Equant glomerocrysts are more common than the acicular glomerocrysts but both types can occur in a single sample. The monominerallic aggregates of plagioclase feldspar can be variable sizes but are commonly <2mm diameter.

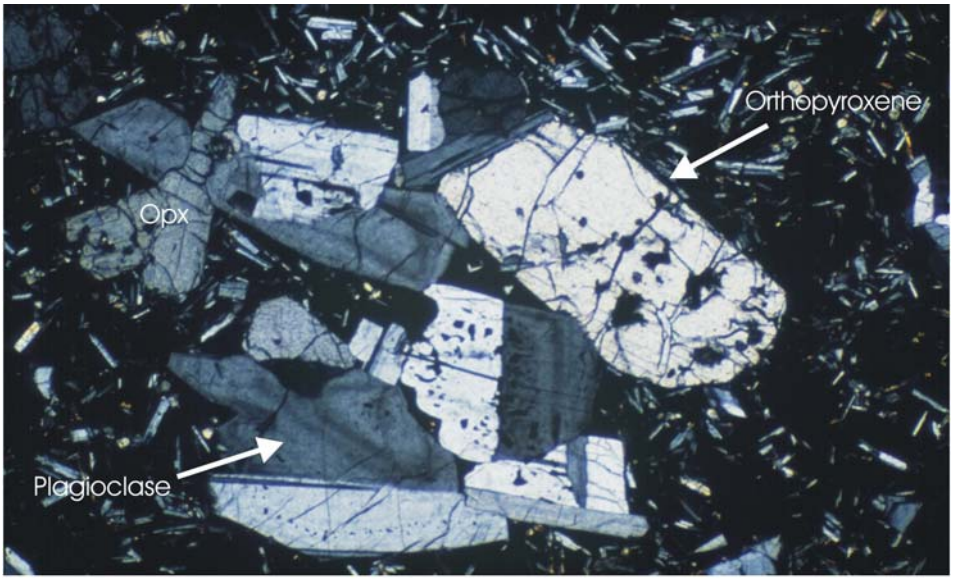

A2.2 Photomicrograph of equant glomerocryst taken under crossed-polarised light. The crystals of the equant glomerocrysts are generally sub-euhedral, interlocking and are composed of orthopyroxene and plagioclase crystals.

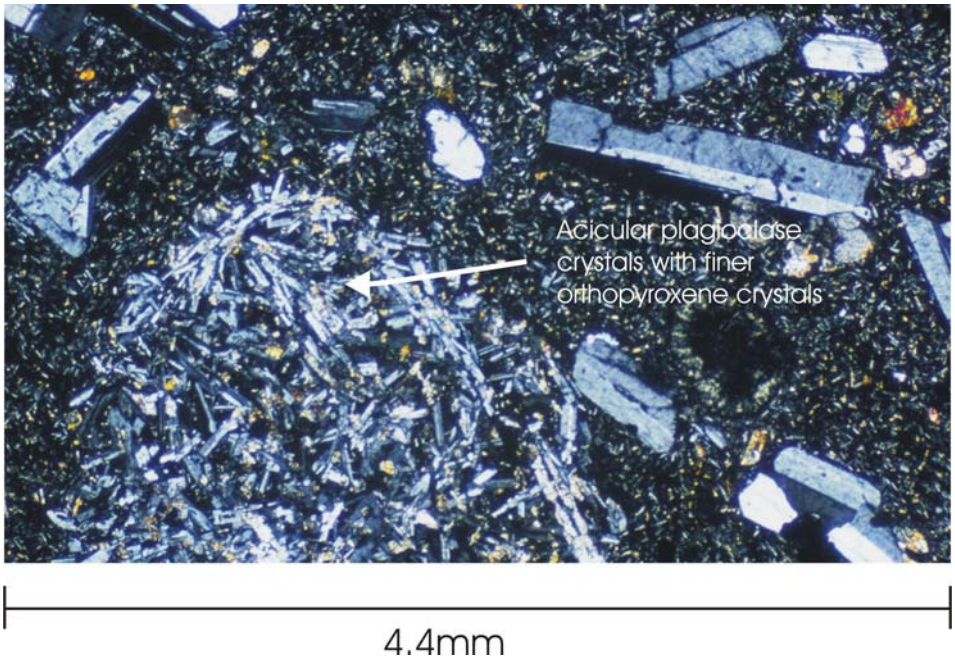

A2.3 Photomicrograph of an acicular glomerocryst containing high aspect ratio plagioclase crystals and small orthopyroxene crystals in crossed-polarised light. The crystals in the acicular glomerocryst are very fine compared with the larger plagioclase crystals distributed throughout the groundmass.

A2.1.1.2 B-II Andesite

The lavas of B-II are strongly porphyritic (ave. 18%), with hypocrystalline groundmasses of pale pinky to pale brown glass with microlites of plagioclase feldspar, pyroxene (ortho- and clino- pyroxenes) and opaques.

Phenocryst phases are plagioclase feldspar ($An_{>50}$), orthopyroxene, clinopyroxene (pigeonite) and opaques (ilmenite with rare magnetite). Quartz and spinel are present associated with xenoliths, which can reach considerable size in these lavas.

Plagioclase feldspar phenocrysts are commonly euhedral or subhedral measuring up to 3mm in length and are tabular. Poikilitic inclusion of ortho- and clino- pyroxene is observed. Normal zoning is common and resorption leading to pronounced embayments is also commonly noted. Plagioclase feldspar phenocrysts comprise an average of 12% of the rock (N=16).

Orthopyroxene is grey in PPL and is weakly pleochroic in some samples. Melt inclusions are common and overgrowths of cpx are almost ubiquitous. Oscillitory and sector zoning is observed in some crystals. The orthopyroxene phenocrysts rarely exceed 2mm length and are generally subhedral. The crystals comprise, on an average of 16 samples, 2.3% of the rock.

Clinopyroxene is present as secondary replacement aggregates of orthopyroxene and also as primary phenocrysts. Primary phenocrysts rarely exceed 1.8mm in length and are often overgrown by the secondary replacement clinopyroxene (pigeonite). The clinopyroxene, primary or secondary forms subhedral – anhedral crystals. Secondary clinopyroxene, where measured, is pigeonite and commonly forms aggregates of small crystals surrounding orthopyroxene and in some instances pseudomorphs orthopyroxene. Clinopyroxene is a minor phenocryst phase and forms 1-2% of the rock.

The opaque mineral phase is predominantly ilmenite with subordinate magnetite observed in some slides. The ilmenite is commonly elongate and rarely exceeds 1.5mm in length. Although also present in the groundmass, the ilmenite phenocrysts account for 1% of the rock in most slides.

Quartz, although not a true phenocryst is present as single crystals (xenocrysts), inferred to be derived from the break-down of quartz xenoliths observed in most slides.

The lavas of B-II commonly contain glomerocrysts, both equant and acicular, measuring up to 3mm diameter. Where both types of glomerocrysts are observed, the interstitial groundmass associated with each type of glomerocryst is a different colour and/or texture to that of the lava.

Xenoliths are often large, up to 14mm long and are composed of quartz, feldspar, pyroxene, with spinel and associated opaque phases.

A2.1.1.3 B-III Basaltic Andesite

The lavas of B-III are characteristically glomeroporphyritic, in some slides, phenocrysts are only observed in glomerocrysts. The groundmass is commonly holocrystalline, although some samples have hypocrystalline groundmass with brown glass and microlites of plagioclase and pyroxene.

The rocks contain 9.3% phenocrysts on an average of 7 samples described. This is considerably lower than either group B-I or B-II. Phenocryst phases present are plagioclase feldspar, orthopyroxene, clinopyroxene and opaques (ilmenite). In some samples only plagioclase feldspar and orthopyroxene are described.

Plagioclase feldspar is euhedral to subhedral and rarely exceeds 5mm length. Melt inclusion and normal zoning is common with poikilitic inclusion of orthopyroxene commonly observed. Embayments are observed in some slides. Plagioclase is the dominant phenocryst phase and forms 6.6% of the rock (N=10).

Orthopyroxene crystals are generally 1-5mm long, although commonly <3mm, and are pale pinky brown to grey in PPL. Orthopyroxene crystals are commonly overgrown by fine aggregates of clinopyroxene crystals. Orthopyroxene generally forms <4% of the rock.

Clinopyroxene is a minor phase (<1%) and forms both primary and secondary phenocrysts <1mm diameter. Secondary clinopyroxene forms fine overgrowths surrounding much larger orthopyroxene phenocrysts. Rarely, clinopyroxene forms complete pseudomorphs of orthopyroxene.

Opaque phase is dominantly ilmenite which rarely exceeds 1mm length and forms only 1-2% of the rock.

The lavas of B-III are characteristically dominated by the presence of large glomerocrysts, measuring up to 1cm diameter which are both equant and acicular, although predominantly equant. Flow banding is sometimes seen, but flow alignment of phenocrysts is commonly observed.

Xenoliths are observed and generally measure <5mm. The xenoliths are comprised of quartz, feldspar and pyroxene crystals, with larger crystals developed at their margin.

A2.1.1.4 B-IV Dacite

The lavas of group-IV are strongly porphyritic, with approximately 24% phenocryst content. The groundmass is commonly hyaline or devitrified. Xenoliths are abundant and are feldspathic, often with green spinel. The phenocryst phases present are plagioclase feldspar, orthopyroxene, clinopyroxene, opaques and quartz which is inferred to be derived from the xenoliths.

Plagioclase feldspar is the most abundant phenocryst phase and constitutes 14% of the rock. It forms small (<2mm) crystals which are commonly skeletal or embayed.

Orthopyroxene forms 5% of the rock and is generally subhedral with common embayments and minor clinopyroxene overgrowths.

Clinopyroxene is not present as a primary phenocryst phase but forms small crystal overgrowths around orthopyroxene phenocrysts and constitutes 2% of the rock.

The opaque crystals are ilmenite and are present in similar abundance to the rocks of groups I-III (2-3%).

The rocks contain significant proportion of xenoliths which are generally small <2mm, and are either monominerallic quartz xenoliths or comprised of feldspar with green spinel crystals.

Amygdales are common in the rocks of group IV.

A2.1.1.5 B-V Pitchstone

The pitchstones of Mt. Barrosa contain approximately 10% phenocrysts by surface area. The groundmass is hypocrystalline with colourless glass displaying perlitic cracks and microlites of feldspar and quartz, together with small crystal fragments. Flow banding is evident from the alternating presence and absence of fine microlites in the glass (fig. A2.4). Phenocryst phases in order of abundance are quartz, plagioclase ($An_{>10\%}$), alkali feldspar (sanidine), biotite and garnet.

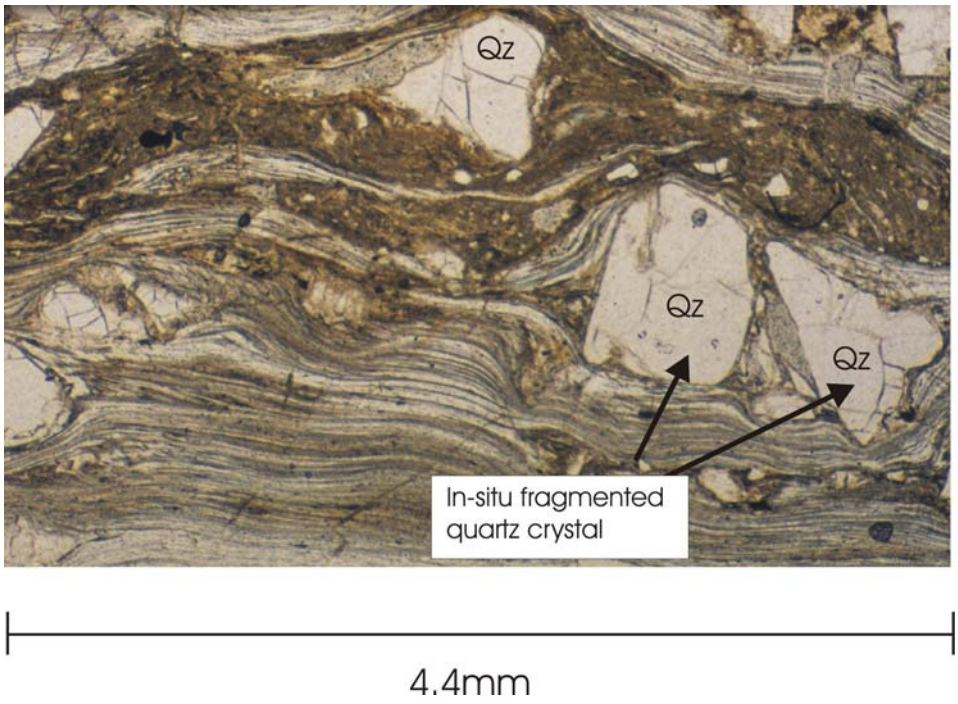

Fig.A2.4 Photomicrograph taken in plane polarised light illustrating the flow banding and in-situ compaction shattering of quartz phenocrysts.

Quartz is the most abundant phenocryst phase and crystals are often euhedral to subhedral, with curvaceous cracks. The maximum size of quartz crystals is 1mm. The quartz crystals contain fine glass inclusions and embayments.

Sodic plagioclase is the most dominant feldspar phase in the pitchstones and constitutes approximately 2-3% of the rock. The plagioclase crystals are commonly subhedral and display normal concentric zonation.

Sanidine crystals are present, but their proportions are inferred, because differentiating between un-twinned sanidine from quartz is difficult in thin section. Generally the sanidine crystals are the same size as the quartz crystals and sometimes larger, up to 3mm diameter. The shape of larger crystals is often subhedral to anhedral with common embayments and fractures.

Biotite is often euhedral or subhedral, up to 1mm long and displays strong pleochroism between straw to dark brown. Biotite is a useful indicator of preferred orientation in the pitchstones.

Garnet and orthopyroxene are present in small quantities in the Barrosa pitchstone (<1%). Where present they are <0.3mm diameter and subhedral.

A2.1.1.6 B-VI Rhyolite

The rhyolites of Mt. Barrosa are porphyritic with cryptocrystalline, felsitic groundmasses which locally coarsen. Phenocryst content is consistently approximately 20% and phases present as phenocrysts are: quartz, alkali-feldspar, plagioclase and garnet, with trace amounts of zircon.

The quartz crystals are generally <1.8mm and are subhedral to anhedral, often rounded, and heavily fractured. Embayments are common in larger crystals.

Alkali feldspar is sanidine but is commonly untwinned which makes discerning between sanidine and quartz difficult in many cases. Crystals are <3.5mm and are commonly

corroded, with orange alteration along fractures. Alkali feldspar constitutes about 6% of the rhyolite.

Plagioclase forms approximately 3% of the rhyolites and is oligoclase (maximum). Generally subhedral or anhedral and <3mm. Commonly in the rhyolite, the plagioclase is only associated with equant glomerocrysts.

Garnet is present in minor quantities, rarely exceeding 1%. Individual crystals are up to 2mm diameter and commonly enclose quartz, zircon and magnetite. The crystals are euhedral to subhedral and are commonly fractured. Oxidation of garnets has occurred in many rhyolites, and often the garnets are completely removed.

A2.1.2 Gawler Downs

A2.1.2.1 GD Dacite

The dacites of the Gawler Downs contain plagioclase, orthopyroxene, garnet, clinopyroxene, opaques (ilmenite & magnetite), alkali feldspar (sanidine) and quartz (as xenocryst phase). Some Rangiatea samples contain, in addition, biotite and amphibole (hornblende). The rocks are porphyritic with phenocryst contents of 12 to 19% with an average of 14.2% (N=14). The dacites commonly have a hypocrystalline groundmass with microlites of plagioclase and orthopyroxene. Glomerocrysts are abundant and equant, measuring up to 5mm diameter. Acicular glomerocrysts are also observed but do not occur in the same abundance as the equant glomerocrysts. Some glomerocrysts have interstitial glass of different colour from that of the rock, indicating that they were crystallised from a melt of differing chemistry.

Xenoliths are commonly observed and measure up to 4mm diameter with associated green spinel and opaques. Preferred orientation is clearly displayed in many sections.

Plagioclase is found in all the dacites and is the most abundant phenocryst phase, comprising on average 6.9% of the rock (N=15). Plagioclase commonly contains inclusions of zircon and orthopyroxene. The crystals are generally subhedral and rarely exceed 3mm length, are concentrically zoned, sometimes with resorped cores and embayments.

Orthopyroxene is generally of poor quality and is subhedral to anhedral. It is commonly associated with glomerocrysts and is often overgrown by clinopyroxene, sometimes to the extent of being completely pseudomorphed by clinopyroxene. Differing degrees of pleochroism are observed from pale green to straw colours. Orthopyroxene comprises approximately 3% of the dacite.

Alkali feldspar is present in almost all samples of dacite and, where twinning is visible, indicates sanidine. The crystals rarely exceed 1mm length and are euhedral to subhedral in crystal shape. Some resorption is present and some crystals appear to be broken. Alkali feldspar makes up approximately 1.8% of the dacite (N=13).

Other minor phenocryst phases are clinopyroxene (which forms overgrowths surrounding orthopyroxene), garnet (which is present in small quantities but generally forms large crystals ≤ 2.5mm diameter), amphibole (pleochroic and late stage development) and opaques (which are ilmenite and magnetite). Haematite is also present in the groundmass of some samples.

A2.1.2.2 GD Andesite

The andesites of the Gawler Downs are glomeroporphyritic and contain phenocrysts of plagioclase, minor alkali feldspar (sanidine), orthopyroxene and clinopyroxene. Phenocrysts comprise 18% of the andesites. The andesites contain xenoliths, one of which reaches 2.5mm x 0.7mm, purple spinel has crystallised in association with the xenoliths. Glomerocrysts are both equant and acicular and consist of plagioclase and orthopyroxene. Clinopyroxene occurs as overgrowths around orthopyroxene cores. The phenocrysts are heavily resorped and embayments are common.

A2.1.2.3 Blondin Pitchstone

The quartz crystals are subhedral to anhedral with extensive embayments. The crystals are commonly fractured and broken but most are fairly rounded and intact. Quartz constitutes 8% of the rock. The plagioclase is generally associated with glomerocrysts and is subhedral to

anhedral in shape. The plagioclase is oligoclase and is a minor phase, comprising just 2% of the rock. Biotite crystals are generally euhedral and strongly pleochroic from pale to dark brown and measuring up to 1mm in length. Biotite forms 2% of the rock. The biotites crystals are preferentially aligned indicating sense of flow direction. Garnet is observed in thin section but is very rare.

A2.1.3 Malvern Hills

A2.1.3.1 Iron Bridge Rhyolite

The Iron Bridge Rhyolite of the Malvern Hills is porphyritic in a cryptocrystalline, felsitic, devitrified groundmass which locally coarsens. Flow banding is observed in thin section by variations in colour and alignment of biotite phenocrysts. The phenocryst phases are: quartz, plagioclase (anorthoclase – andesine), alkali-feldspar (sanidine), garnet, biotite, opaques (ilmenite). Minerals which are visible but present only in trace amounts are orthopyroxene, zircon, apatite and titanite.

Quartz is generally the most predominant with the exception of MH-50 (L35/1742 4775), which has a paucity of quartz and an abundance of alkali feldspar. The crystals are generally subhedral and show hexagonal or square cross sections. Crystal sizes are generally <3mm with larger crystals commonly fractured or displaying internal cracks. Rounded and embayed quartz crystals are also common. Quartz phenocrysts comprise 8% of the rhyolite (average N=7). Quartz is observed to intergrow with feldspar.

Plagioclase is not a common constituent of the Iron Bridge Rhyolite and is not seen in every slide examined. Generally it constitutes <3% of the rock and where present is extensively corroded.

The alkali feldspar, where determinable is sanidine and forms subhedral to anhedral phenocrysts which are commonly embayed or sieved. Crystals measure <3mm and in heavily altered samples only ghosts remain. With the exception of sample MH-50, alkali feldspar constitutes 5% of the rhyolite.

Garnet is ubiquitous but present in small quantities with subhedral, anhedral or fragmented crystals. It generally forms only 1% of the rock with crystals measuring a maximum of 1.9mm. Inclusions of zircon, quartz, titanite and opaque crystal phases are common.

Biotite is rarely fresh, mostly oxidised and heavily altered. Where fresh, the biotite is pleochroic pale green to dark brown. Biotite is a useful indicator of preferred orientation. Biotite is not present in all slides, however it may be confused with opaque minerals due to oxidation. It is only present in small quantities <1% of the rock.

The opaque phases are probably ilmenite due to the acicular or pseudohexagonal nature of the crystals.

A2.1.3.2 Pitchstone dykes

The rocks are highly porphyritic with phenocryst contents from 15 to 22%. Phenocrysts are commonly cracked and displaced, although in thin section, fragments are separated by interstitial glass or alteration but have not be transported indicating that fragmentation occurred in-situ.

Phenocryst phases present are quartz, alkali feldspar (sanidine), plagioclase (oligoclase), garnet, biotite, orthopyroxene, opaques (ilmenite) with trace amounts of zircon, titanite and unidentified micaceous (? celadonite) alteration.

Quartz forms subhedral to anhedral phenocrysts <2mm diameter with internal cracks and embayments common. Shards of quartz are commonly seen in the groundmass.
Quartz constitutes 8.7% of the rock (N=3).

Alkali feldspar forms large crystals, commonly exceeding 3mm length and are usually subhedral with pervasive alteration along cracks. Embayments and evidence of resorption is common. Where twinning is seen it is simple indicating sanidine. The rocks contain variable proportions of alkali feldspar ranging from 2.5% to 8%. The difficulty in discerning between alkali feldspar and quartz may be a factor in the differing percentages.

Garnet is ubiquitous and forms subhedral to euhedral large crystals up to 2mm diameter, although fragments are also seen in the groundmass. Inclusion of zircon, feldspar, opaques and quartz is common. Although obvious in thin section, garnet forms only 1% of the rock.

Biotite is commonly fresh and euhedral although oxidised crystals are observed in some sections. Although small (<1mm), the crystals are often tabular and low aspect ratio. Pleochroism is common between brown and dark brown. Biotite clearly shows preferred orientation consistent with the orientation of bands. Biotite forms <1% of the rock.

Orthopyroxene is present in trace amounts and often only 1-2 crystals are seen in each slide. Pleochroism is clear from straw to pale green and crystals are <0.8mm long, commonly resorped with associated opaques.

The opaque mineral phase is considered to be ilmenite due to the elongate or pseudohexagonal morphology of the mineral. It is often associated with zircon and is present only in trace amounts.

Zircon is a trace phase, commonly associated with garnet and other mafic phases, the crystals are very small «0.1mm.

Lithic fragments are observed to be generally un-recrystallised indicating late stage incorporation.

A2.1.3.3 Rockwood Ignimbrite

The phenocryst phases are quartz, alkali feldspar (sanidine), garnet, opaques (ilmenite), plagioclase (oligoclase-andesine), biotite, with trace amounts of zircon and orthopyroxene.

The quartz phenocrysts are often anhedral and shattered with seriate shards. The appearance of fine cracks is common but not as pervasive as those observed in the pitchstone dykes. The crystals do not normally exceed 2mm diameter and are commonly resorped and embayed. Quartz is often intergrown with alkali-feldspar, garnet and rarely biotite (fig. A2.5). Quartz is the most abundant phenocryst phase and is present in concentrations of up to 18% of the rock,

although the average is 7%. Occasionally quartz phenocrysts display undulose extinction indicating straining.

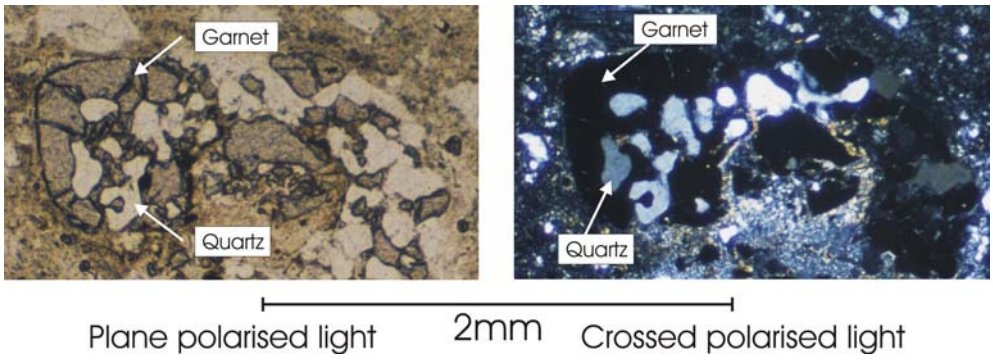

Fig.A2.5 Intergrown quartz and garnet in thin section.

Alkali feldspar forms crystals up to 2.5mm and is commonly untwined. Where twinning is present it indicates the phase to be sanidine. The crystals are heavily resorped to the point of being skeletal. The alkali feldspar crystals are commonly subhedral or fragmented shards and comprise approximately 3.5% of the rocks. Inclusion of glass and biotite, and intergrowth with quartz is observed in some slides.

Garnet is present in all slides and is generally anhedral fragments measuring <2mm although occasional larger crystals are seen. The intergrowth with quartz and inclusion of zircon, quartz, opaques, plagioclase and rarely hornblende indicates the co-existence of garnet with the other phases (fig. A2.5). Garnet crystals commonly have fine biotite and opaque crystals associated with them, which may indicate an iron rich nature.

Biotite is present in all slides and is generally fresh and <1.6mm long although commonly euhedral. Where fresh pleochroism is from pale to dark brown and rarely reddy brown. In some slides the biotite is almost completely altered and oxidised and appears opaque. Broken and angular fragments do occur and the concentration of biotite does not exceed 2% in any of the slides examined.

The opaque present is generally pseudohexagonal and is associated with the mafic phases. The opaque is probably ilmenite, although it is only present in minor quantities, generally <1%.

Plagioclase is another minor phase and does not constitute more than 5% of the rock and in some slides is not encountered at all. Where present it is commonly heavily altered (sericite), embayed and resorped. The maximum extinction angle measured was An_{47}, although on average the measurements were approximately An_{30}. Plagioclase crystals are commonly small <2mm.

Trace phases include orthopyroxene, zircon and apatite.

A2.1.3.4 Glassy Ignimbrite (lower)

The phenocryst phases are quartz, alkali feldspar, plagioclase (typically oligoclase, An_{25}), biotite and garnet with trace quantities of orthopyroxene and zircon.

The brown glass fiammé typically contain 10% quartz, whereas the clear fiammé only tend to contain approximately 3%.

A2.1.3.5 Glassy Ignimbrite (upper)

Petrographically the Glassy Ignimbrite is porphyritic with approximately 18% phenocryst content. The phenocrysts are commonly shattered with a propensity of angular crystal shards in the groundmass. Evidence of post-deformation compaction or shearing, is the fragmentation but not dispersal of phenocrysts, with fragments separated from the main mass by fine intervening tuff or devitrified glass. The groundmass is predominantly cryptocrystalline and occasionally vitric. Eutaxitic texture is clear in some slides (e.g. MH-28), where differing degrees of devitrification of fiammé have occurred.

The phenocryst phases present are: quartz, alkali feldspar, plagioclase feldspar, biotite, garnet, opaques. Quartz is the most predominant phase constituting approximately 10% of the rock. The quartz crystals are commonly shattered into shards and where intact contain fine fractures. The crystals rarely exceed 2mm diameter and are commonly embayed. Inclusions of zircon in quartz are observed in several sections.

Alkali feldspar is sanidine although simple twinning is only rarely observed. Crystals are subhedral to anhedral and are heavily resorped. Fragments of alkali feldspar litter the

groundmass together with other crystal fragments. Crystals of alkali feldspar are usually < 2.2mm. Alkali feldspar constitutes only a small (2%) percentage of the rock.

Plagioclase feldspar is found to be a maximum of An_{45} (andesine) and crystals are small (<1.2mm) and subhedral. Plagioclase is a minor phase, constituting only 2% of the total rock.

Biotite is commonly fresh and pleochroic up to 1.2mm long. In some sections it appears to be oxidised. Biotite crystals are commonly euhedral or subhedral and are not generally shattered although evidence of post-depositional compaction is seen.

Garnet is seen to enclose opaques and zircon occasionally with quartz overgrowths. Crystals can be relatively large (<2mm) and can form up to 1.5% of the rock.

Minor phases include the opaques (ilmenite), zircon and apatite.

A2.1.3.6 Round Top Andesite

The Round Top Andesite is highly porphyritic with phenocryst contents generally approximately 20%. The groundmass of the andesites is generally hypocrystalline and flow banding is sometimes depicted by varying devitrification of the groundmass. Glomerocrysts are common and are both equant and acicular, some crystals in the acicular glomerocrysts are 9mm long. Xenoliths are generally recrystallised quartz and feldspar, but are not very common and where present are generally small.

The Round Top Andesites contain plagioclase feldspar (andesine – bytownite) and orthopyroxene as phenocryst phases. Orthopyroxene commonly displays rims of clinopyroxene (pigeonite). Pigeonite is also a constituent phase of the groundmass. Pigeonite commonly overgrows orthopyroxene and is clearly a later phase.

Plagioclase feldspar is the most abundant phenocryst (15% of rock) with compositions up to $An_{35\text{-}78}$. High aspect ratio crystals are common and up to 3mm long. Concentric zoning and dove-tails are common. Resorption is also commonly observed in plagioclase crystals.

Orthopyroxene is associated with plagioclase crystals in glomerocrysts but also forms independent phenocrysts. Commonly seriate textured, subhedral to anhedral, and measuring up to 1.8mm. Orthopyroxene crystals show pleochroism from grey to brown and crystals are often resorped. Orthopyroxene crystals are often rimmed by clinopyroxene (pigeonite). Orthopyroxene forms approximately 3% of the andesites.

Clinopyroxene generally forms as overgrowths around opx but also nucleate on plagioclase crystals and form primary phenocrysts. The crystals are generally very small (<0.5mm) and only constitute 1% of the andesites.

Minor phases present in the andesites include opaques (ilmenite) and apatite.

A2.1.3.7 Rhyolite Fissure dyke

In thin section the rhyolite fissure dykes are strongly porphyritic with phenocryst contents of at least 20%. The phenocrysts are generally large and unbroken - evidence of their non-pyroclastic origin. Phenocryst phases are quartz, alkali feldspar (sanidine), plagioclase feldspar ($An_{>48}$ – Andesine-Labradorite), garnet and opaques (ilmenite). The groundmass is felsitic and cryptocrystalline.

Quartz crystals are generally subhedral to euhedral, intergrown with garnet in some sections and <2.5mm size. Crystals are not fragmented, however internal fractures are commonly visible. Quartz constitutes 4-8% of the rhyolite.

Alkali feldspar is the most dominant phenocryst phase although twinning is not commonly visible. The crystal shape and larger size and the appearance of occasional simple twinning (sanidine) enables determination of alkali feldspar from quartz. Phenocrysts of alkali feldspar are large (<4mm) and generally subhedral. Alteration is common, especially in the larger crystals. Graphic intergrowth with quartz is seen in one slide. The alkali feldspar constitutes between 6 and 10% of the rock.

Plagioclase feldspar, based on extinction angle, is at least An_{48} (andesine), although when taken as a minima, the composition probably extends into labradorite. This is high compared

with the rhyolites of Mt. Barrosa. Plagioclase is a minor constituent forming approximately 2-3% of the rock and the crystals tend to be very highly corroded and measure <2mm.

The minor phenocryst phases are garnet and ilmenite, forming <1% of the rock. Garnet is observed to intergrow with quartz in MH-34.

A2.1.4 McQueens Valley

A2.1.4.1 Ignimbrite

The ignimbrites of McQueens valley are porphyritic with a phenocryst content of 5-7%. The phenocrysts are set in a felsitic and cryptocrystalline groundmass. Eutaxitic texture is depicted by fiammé which are more coarsely crystalline. The phenocrysts are generally subhedral to anhedral and are commonly shattered and distributed throughout the groundmass. The phenocryst phases are sanidine (4%), Quartz (2%) and trace amounts of biotite which measure <0.05mm length. Sanidine crystals are generally subhedral and measure ≤ 1.3mm. Quartz crystals are rounded or shattered and generally measure <1mm, although quartz fragments are distributed throughout the groundmass. Garnet was not observed in thin section, however small oxidation spots which may represent oxidised garnet are common in the rhyolitic/ignimbritic rocks of McQueens Valley.

A2.1.4.2 Andesite

Petrographically, the andesites of McQueens valley resemble those of group B-III of Mt. Barrosa with clear, large glomerocrysts comprising up to 30% of the rock. The glomerocrysts are large and measure up to 1cm diameter. The groundmass is generally hypocrystalline with fine microlites of plagioclase and opaques in a brown glass.

Phenocryst phases present include plagioclase, orthopyroxene (with pigeonite pseudomorphs and overgrowths fig. A2.6) and pigeonite primary phenocryst phases. The opaque phase is probably ilmenite.

Plagioclase crystals are generally euhedral or subhedral and up to 4mm long, they are high andesine ($An_{>47}$), and therefore probably extend into labradorite. Commonly forming a major constituent of the glomerocrysts, plagioclase is also present as microlites in the groundmass.

Orthopyroxene is present as a major phenocryst phase but has commonly been overgrown or pseudomorphed by pigeonite. It is differentiated from pigeonite by its straight extinction and lower interference colours. The crystals measure up to 2mm long and are low aspect ratio, subhedral to anhedral crystal shapes. Orthopyroxene forms approximately 4% of the rock.

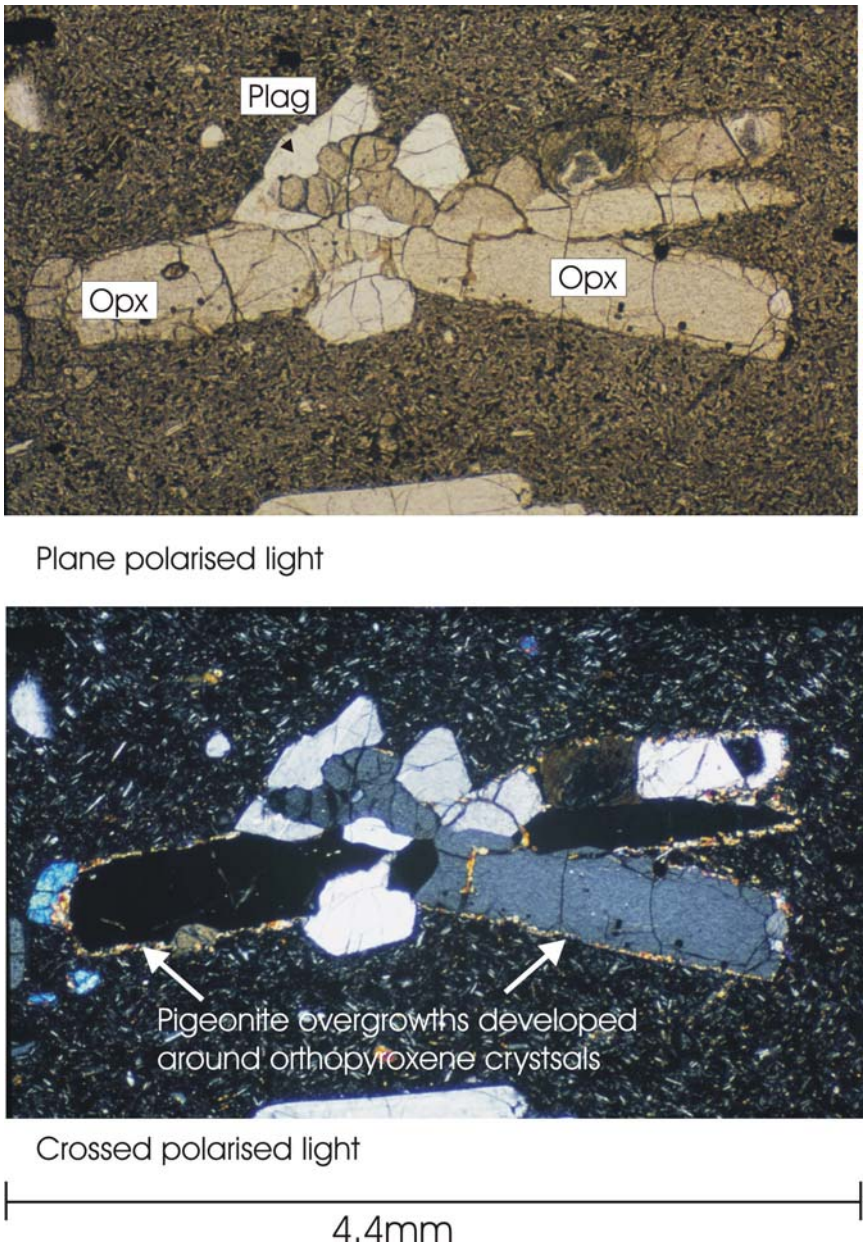

A2.6 Plane and crossed-polarised light photomicrographs showing orthopyroxene phenocrysts with pigeonite overgrowths in an equant glomerocryst.

Pigeonite is more abundant than orthopyroxene and commonly replaces orthopyroxene in the glomerocrysts. Pigeonite as the clinopyroxene phenocryst phase is determined based on its biaxial positive, low 2V (where observed) and lamellar twinning. Primary pigeonite phenocrysts are also present but are generally smaller than the pigeonite pseudomorphs. The

crystals generally take the shape of the original orthopyroxene crystals and are therefore subhedral to anhedral, measuring up to 4.5mm. Pigeonite is slightly more abundant than orthopyroxene and constitutes up to 5% of the rock.

The opaque phase dominantly forms hexagonal crystals but elongate crystals are also present which probably indicates ilmenite. The opaque phase is generally associated with the pyroxene crystals and measures up to 0.7mm. The opaque phenocryst phase constitutes only 1% of the rock, but is also present in abundance in the groundmass.

A2.1.4.3 Pitchstone

The pitchstone in McQueens Valley is porphyritic with a 3% phenocryst content, which consist predominantly of sanidine with plagioclase ($An_{\sim 25}$) and minor quartz. The phenocrysts are generally aligned parallel to flow banding (fig.A2.7) and measure ≤ 1mm.

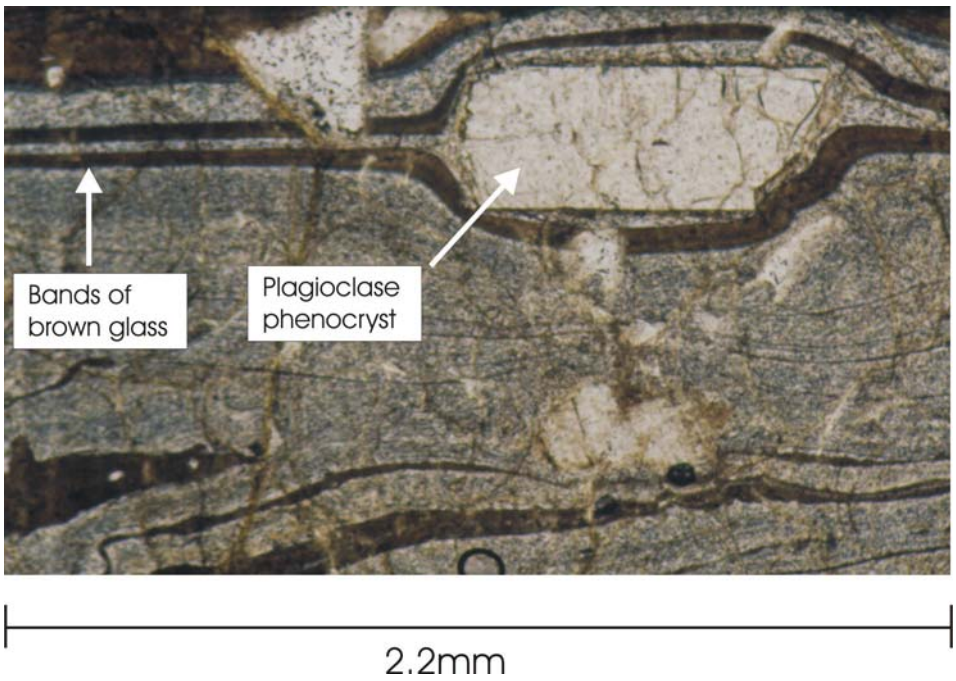

Fig.A2.7 Plane polarised light photomicrograph illustrating the intricate flow banding observed in the McQueens Valley pitchstone. The brown glass bands are shown to fold around the plagioclase phenocryst. The phenocrysts are generally aligned parallel to flow banding.

A2.1.5 Rangitata Gorge

A2.1.5.1 Intermediate flows

The plagioclase feldspar compositions are consistent throughout the rock types at $An_{>65}$ (labradorite). The andesites and basaltic-andesites have a lower phenocryst content (ave = 17%) than the dacites (ave = 24%), and commonly have a hypocrystalline rather than holocrystalline groundmass (c.f. the dacites). The dacite flows also tend to be more highly altered. The presence of both acicular and equant glomerocrysts is found throughout the range of compositions.

A2.1.5.2 Rhyolite flows

Alkali feldspar (sanidine) forms approximately 7% of the rock and is more abundant than plagioclase ($An_{>27}$, Oligoclase), which forms approximately 5% of the flows. An interesting observation is the general lack of quartz phenocrysts. Quartz is only observed to form up to 2% of the rocks and where present is fractured, anhedral and commonly embayed. Garnet is commonly only preserved inside feldspar crystals and is generally anhedral forming <1% of the rock. Zircon is abundant relative to the rhyolites of the other MSVG field areas and forms high aspect ratio crystals ≤ 0.6mm long and constitutes up to 1% of the rock. The opaque phase is probably magnetite as the crystals are commonly square shaped although some elongate crystals are seen.

A2.2 MIC

A petrographic summary of each rock type identified in Chapter 8 is described below:

A2.2.1 Picro-Basalt

One picro-basalt was found in the MIC. It occurs as a clast in the vent breccia and was selected for sampling due to its unusual appearance and relatively large pyroxene crystals in hand specimen.

The picro-basalt sample is strongly porphyritic with a holocrystalline groundmass containing microlites of abundant opqs, feldspar (plagioclase) and pyroxene. The phenocryst content is high (24%) and the primary phenocryst phases are clinopyroxene (augite), olivine and opaques. The most abundant phase (12%) is pinky clinopyroxene (augite), which measures ≤3mm, the crystals are subhedral-anhedral and are heavily fractured. Olivine constitutes 10% of the rock and is euhedral to subhedral, ≤3mm and is commonly replaced by chlorite and calcite. The opaque mineral (2%) is irregularly shapped, commonly skeletal or square and measures <0.1mm.

A2.2.2 Tephrite

Two tephrite samples were collected from the MIC. They are very similar in chemical composition but are petrographically different.

The tephrite that intrudes Torlesse basement (M-37) is almost aphyric with very small quantities of plagioclase phenocrysts (<1%) measuring <2mm, set in a holocrystalline groundmass composed of fine opaques (some with very high aspect ratio and dendritic), alkali-feldspars, brown amphibole and weakly pleochroic olivine (pale yellow to colourless indicating high Fe content).

The tephrite that intrudes syenite (M-77) is a fine grained hypabyssal dyke which consists predominantly of alkali-feldspar (40%) (which is generally heavily altered and ≤ 0.7mm), plagioclase (15%), brown hornblende (4%) (strongly pleochroic ≤ 0.3mm, commonly forms in association with the calcite), arfvedsonite (3%) (strongly pleochroic pale-dark green, ≤ 1.2mm long, subhedral), biotite (1%) (pleochroic pale cream to greeny brown, ≤ 0.2mm), epidote (1%) (mildly pleochroic, colourless to pale yellow, late-stage and often enclosed by calcite), opaques (2%) (square) and calcite (2%) (very large, irregular areas which enclose euhedral crystals of epidote and arfvedsonite). The calcite does not appear to be amygdales because of their irregular contact with the surrounding crystals and the inclusion of crystals. They are probably late stage deuteric crystals. The mineral proportions don't sum to 100% because some areas of the slide were indeterminable with intense calcite replacement.

A2.2.3 Phonotephrite

Four phonotephrites were collected from the MIC, two dykes intruding Torlesse basement, and two dykes intruding the igneous complex. The phonotephrites are predominantly aphyric or very weakly porphyritic with holocrystalline, often cryptocrystalline groundmasses. Where phenocrysts are observed, they are alkali-feldspar (≤1%) and a pseudohexagonal opaque phase. Groundmasses are microcrystalline or cryptocrystalline and composed of high aspect ratio feldspar and opaque microlites. In one sample, the phenocryst phases are pseudomorphed by calcite with the exception of minor quanitites of nepheline (<1%), but their shapes suggest that the primary phenocryst phases were amphibole and feldspar.

A2.2.4 Foid-bearing monzonite

The foid-bearing monzonite is the plutonic equivalent to the phonotephrites and was extracted from a lahar deposit.

The rock is plutonic with a predominance of plagioclase (40%) and alkali feldspar (30%) with biotite (5%), opaques (4%) and minor quantity of nepheline (<1%). The crystal contents do not sum to 100% because 20% of the rock is heavily altered but may be aegirine augite (green) and/or brown amphibole.

A2.2.5 Tephriphonolite

The tephri-phonolites come from closely spaced outcrops (M/226 and M/227). One tephri-phonolite is associated with the mafic lavas and the other from an outcrop which is interpreted to be a dyke, intruding the syenite.

The tephriphonolite associated with the mafic lavas (M-83) is strongly porphyritic with a phenocryst content of 28%. The phenocrysts are set in a holocrystalline, cryptocrystalline groundmass which is grey in crossed polarised light indicating a high proportion of feldspars in the groundmass. The phenocryst phases are alkali feldspar (10%), plagioclase (15%), clinopyroxene (1%), a pseudohexagonal opaque phase (2%) and nepheline (1%). The phenocrysts are pseudomorphed by calcite, which has also filled cavities in the rock.

The tephriphonolite dyke (M-84) shows no indication of calcite replacement. The rock contains a lower phenocryst content than M-83 and contains 2-3% phenocrysts. The groundmass is holocrystalline with abundant opaques and dark grey interstices, which are cryptocrystalline, possibly feldspathoids but are not identifiable. There is a moderately well developed preferred orientation of phenocrysts. Xenoliths of syenite and trachyte are present in the rock indicating contamination of the magma by interaction with these pre-existing rock types. The phenocrysts are alkali feldspar (1.5%), Plagioclase (tr), brown amphibole (1%), opaques (<1%) and a few green clinopyroxene (aegirine) crystals (<1). The alkali feldspar is subhedral commonly with irregular terminations and often show clear simple twinning, generally measuring ≤ 2mm. Some of the small, untwinned crystals may be nepheline but this could not be confirmed. Plagioclase is commonly corroded and crystals are rare measuring ≤ 0.8mm. The dominant mafic mineral is amphibole and is variable shades of brown (hornblende), commonly strongly pleochroic and crystals are commonly euhedral and measuring up to 1.2mm. Aegirine augite is also present but is rare compared with the amphibole phase. Where identified aegirine is associated with small opaque crystals.

A2.2.6 Basalt

One basalt sample was collected from the MIC (M-67) and came from the mafic lavas. The rock is strongly porphyritic (37%) with large phenocrysts of augite (20%), plagioclase (5%) and olivine (completely altered to bowlingite). The groundmass is holocrystalline, very fine grained with abundant square opaque crystals, clinopyroxene and fine plagioclase microlites.

The clinopyroxene is a pinky colour in thin section (augite) and commonly twinned. The augite forms large euhedral-subhedral crystals ≤ 7mm diameter. The plagioclase phenocrysts are high aspect ratio ≤ 6mm long and are An_{40-56} in composition. Olivine is completely removed by alteration and pseudomorphed by green bowlingite. The original olivine crystals were subhedral and ≤ 5mm diameter.

A2.2.7 Gabbro

The gabbro is composed of plagioclase (48%), clinopyroxene – augite (30%), olivine (10%), opaques (7%), biotite (3%) and brown amphibole - kaersutite (2%). The plagioclase forms in the interstices between the other mineral phases and was probably the last phase to crystallise, it has a composition of An_{40-60}. The clinopyroxene is commonly zoned with colourless cores and deeper mauve rims, indicating progressively higher Ti-content. Olivine is anhedral and commonly encloses opaque minerals. The crystals show bowlingite alteration along cracks and at margins.

A2.2.8 Trachybasalt

Four samples of trachybasalt were collected from the MIC, three from dykes intruding Torlesse basement and one from the vent breccia. The trachybasalts are porphyritic with phenocryst contents of generally 5-7%. The phenocryst phases are plagioclase, clinopyroxene (augite) with minor olivine and opaques. The groundmasses are holocrystalline, very fine grained consisting of alkali feldspar, plagioclase, opaques, hornblende and calcified clinopyroxene and olivine pseudomorphs. Trachytic texture is commonly well developed.

Plagioclase crystals are subhedral, ≤ 3mm and are An_{54-75} in composition. Plagioclase phenocrysts constitute 2-3% of the rock. Augite is commonly altered and occasionally completely pseudomorphed by calcite. The augite phenocrysts or pseudomorphs are commonly euhedral and measure up to 3.4mm diameter and the phenocrysts constitute ~3% of the rock. Olivine is rarely preserved and is more commonly heavily altered. Original crystals were euhedral and rarely exceed 1%.

A2.2.9 Basaltic-trachyandesite

Two samples of basaltic-trachyandesite were collected from the MIC. One from a dyke intruding the Torlesse basement and one from the vent breccia.

The sample from a dyke (M-8) is weakly porphyritic with plagioclase, alkali-feldspar, olivine, clinopyroxene and opaque phenocrysts in a holocrystalline groundmass consisting of feldspar

and opaque microlites with cryptocrystalline groundmass interstitially. Plagioclase is the most abundant phenocryst constituting approximately 1% of the rock. The crystals are subhedral, high aspect ratio and are ≤ 1.5mm long. The plagioclase crystals show a strong preferred orientation. Minor phenocryst phases are alkali feldspar (which form subhedral, high aspect ratio simply twinned crystals ≤ 1.2mm long), olivine (which are pseudomorphed by serpentine, maximum size 1mm), opaques (square and clustered around clinopyroxene) and clinopyroxene (which is commonly very heavily altered, measuring ≤ 1.5mm).

The sample from the vent breccia (M-87) is more heavily porphyritic with 11% phenocryst content in a holocrystalline very fine-grained groundmass consisting of opaques, feldspar and clinopyroxene microlites. The main phenocryst phases are: plagioclase (3%), amphibole (4%), clinopyroxene (2%) and opaques (2%). Plagioclase crystals are subhedral showing some corrosion and extensive embayments. Crystals are generally subhedral and measure ≤ 3.2mm. The amphibole is brown and strongly pleochroic (kaersutite?). The crystals are subhedral to euhedral and are often completely altered to serpentine and opaque phases. Clinopyroxene is a pinky colour (augite) and commonly encloses opaque crystals. The clinopyroxene phenocrysts are subhedral and do not exceed 1mm diameter. The opaque phase is square and pseudohexagonal, measuring <0.2mm.

A2.2.10 Trachy-andesite

One trachy-andesite sample was collected from the MIC (M-2) and comes from a dyke intruding the Torlesse basement. The rock is strongly porphyritic with a phenocryst content of 19%. The phenocryst phases are alkali feldspar (8%), plagioclase feldspar (7%), clinopyroxene (2%) and quartz (<1%). The alkali feldspars show clear simple twinning and measure ≤ 6mm. The crystals are euhedral-subhedral and show severe calcitic alteration. Plagioclase is also heavily altered and the euhedral-subhedral crystals measure ≤ 2.3mm. Clinopyroxene is completely altered to calcite and serpentine. Oxidised opaque minerals form poikilitic inclusions within the clinopyroxene pseudomorphs/crystals. Quartz is a minor phase and occurs interstitially in the groundmass.

A2.2.11 Syenodiorite

The syenodiorite is composed of alkali-feldspar (50%), plagioclase (35%), amphibole (7%), quartz (4%), with minor amounts of biotite (<1%), Apatite (tr), opaques (2%) and zircon (tr). The alkali-feldspar is the dominant phase and the crystals generally measure <5mm. Plagioclase (An_{30-40}) is generally fresher than the alkali-feldspar and the crystals are of similar size. Both feldspar phases are generally heavily altered. The amphibole is strongly pleochroic straw-brown (hornblende) and commonly encloses apatite crystals. The amphibole is commonly altered to chlorite around the edges and rarely contains small clinopyroxene (augite) crystals.

A2.2.12 Trachyte

Four trachyte dykes were collected from dykes intruding the Torlesse basement. The trachyte lavas were too heavily altered for geochemical analysis but they are petrographically similar to the trachyte dykes described here. The trachytes are porphyritic with phenocrysts comprising 6-12% of the rocks. The phenocrysts are set in a fine grained holocrystalline groundmass often displaying strong trachytic texture. Individual feldspar laths in the groundmasses are up to 0.6mm long. Opaque phases are also abundant in the groundmasses but are generally heavily oxidised. Abundant pleochroic small brown amphibole crystals are also present in the groundmass. The phenocrysts are: alkali feldspar (6-8%), quartz (0-2%) and opaques (1%). The alkali-feldspar phenocrysts are of variable size but are commonly 6-8mm long and subhedral to euhedral. The alkali-feldspars are generally highly altered. Quartz is not always present but in M-16 it forms anhedral crystals within the groundmass. The crystallisation of quartz was probably coeval with the crystallisation of the groundmass since the rims of the quartz crystals (in M-16) are seen to intergrow with the groundmass feldspars and preserve the trachytic texture.

A2.2.13 Syenite

Syenite is one of the most voluminous rock types in the MIC. Several samples were analysed and described in thin section. The major mineral phases in the syenites are alkali-feldspar, plagioclase, amphibole (both brown and green) with minor quantities of biotite, clinopyroxene

(aegirine), opaques, apatite, zircon, titanite and in some samples quartz. Alkali feldspar is the dominant phase, commonly constituting at least 65% of the rock. Plagioclase is less abundant (generally <20%), followed by amphibole (~6%). The opaque minerals are commonly clustered around amphibole. The alkali feldspars show coarse perthitic unmixing of Na-feldspar (albite) from the host K-feldspar. Amphibole is generally pleochroic straw-brown (hornblende) and commonly <1mm diameter. Minor amounts of blue-green amphibole are observed (generally <1%) which are probably the Na-amphibole Arfvedsonite. Clinopyroxene is not a major crystal phase but commonly forms 2-3% and is pleochroic pale brown to bottle green (aegirine). The alkali-feldspar crystals form the framework of the rock with the ferro-magnesian phases forming in the interstices.

A2.2.14 Vent Breccia

The vent breccia contains clasts of dominantly trachyte and Torlesse sandstone and mudstone, however the breccia also contains clasts of more mafic composition e.g. picro-basalt and basaltic-trachyandesite. The clast sizes varied from outcrop to outcrop but were generally less than 10cm. The matrix/groundmass contains finer clasts and fragments and can also be seen to contain unbroken phenocrysts (fig.A2.8) indicating that the breccia has not been significantly reworked. A primary vent breccia origin is implied for this deposit.

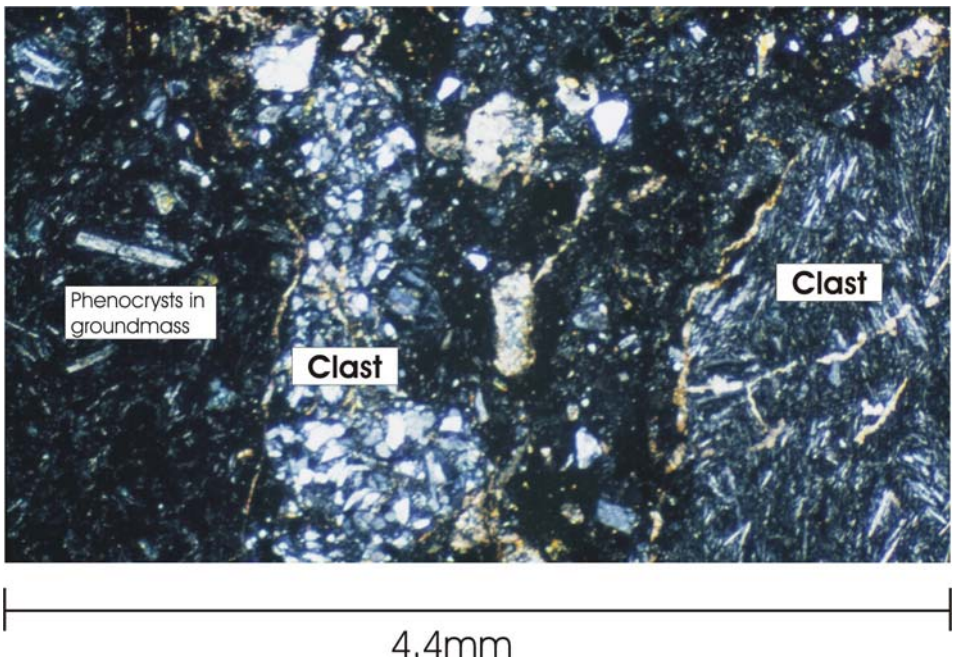

Fig.A2.8 Vent Breccia thin section under crossed-polars indicating the phenocryst content of the groundmass and therefore the primary nature of the deposit.

Appendix 3: XRF analytical procedures and data set

Sample preparation was undertaken in the geochemistry lab at the University of Canterbury. Analyses were performed on a Philips PW-2400 X-ray Fluorescence spectrometer operated by Stephen Brown at the University of Canterbury following the general technique of Norrish & Hutton (1969). International reference standards were used to calibrate the XRF.

A3.1 Sample preparation

A3.1.1 Major Element Analysis

Each sample was crushed and fresh fragments milled in a tungsten carbide ring mill. 1.3g of finely ground rock powder was dried overnight before being mixed with 6.98g of lithium tetraborate flux in platinum crucibles, which reduces the melting point of the powder. After mixing, 3 micro-spatulas of ammonium nitrate (oxidant) were added to each sample crucible to raise the oxidation state of the Iron to Fe_2O_3 (XRF cannot determine between different oxidation states). After mixing, 3 drops of 10% ammonium iodide solution were added to each sample crucible to act as mould release agents.

The crucibles were placed in a furnace at 1030ºC and agitated for 15 minutes. After 15 minutes the crucibles were removed and allowed to cool to balance-room temperature with crucible lid on to prevent loss of material when the glass cracked. When the crucibles were at room temperature they were weighed and their weights recorded to calculate Loss On Ignition (LOI).

After re-weighing the crucibles were returned to the furnace for 10 minutes to re-melt the mix. At the same time as returning the crucibles to the furnace, the platinum moulds were also placed inside the furnace to heat. After 10 minutes the molten sample mixtures were poured into their respective mould and rapidly cooled over a cool air flow. The glass beads

were turned out and labelled on the non-analytical surface before being placed in an un-used plastic sachet.

The crucibles and moulds were cleaned in an ultra-sound bath before being placed in a hot citric acid bath. If residual glass remained on any of the surfaces of the crucibles, discarded flux beads were re-melted inside the crucible, cooled and the cleaning process repeated.

Major Element chemistry was determined using a rhodium tube set at 50KV/46 mA.

A3.1.2 Trace-Element analysis

12g of finely ground rock powder was placed into a clean glass beaker. 16-20 drops of 7% Mowiol solution were added to the beaker and mixed to bind the powder together. The mixture was poured into a pellet die which was compacted by using a compressed air pump. 4000psi was used to compact the mix. The pellet was removed from the die and dried overnight at 60ºC. Once dried, the pellets were labelled along their edges and placed in clean, un-used plastic sachets and stored in a dessicated box to await analysis.

The trace element chemistry was determined with a rhodium tube set at 60 KV/46 mA. Some trace elements are quoted as a “less than” value indicating that their abundances are below the detection limit of the spectrometer.

A3.2 Data Set

Please see the following pages for the complete data set from the MSVG and MIC.

The data presented are as analysed, with LOI reported, but were re-calculated LOI free before plotting on diagrams.

Mount Somers Samples

Field No.	**MS-25**	**MS-27**	**MS-29**	**MS-34**	**MS-36**	**MS-37**	**MS-40**	**MS-46**	**MS-50**
UOC Sample No.	33235A	32433A	33236A	32865A	33237A	33238A	33239A	32440A	33240A
SiO_2	56.79	61.58	67.41	55.34	55.67	65.62	61.53	59.28	68.06
TiO_2	1.25	1.11	1.15	1.09	1.08	0.75	1.28	1.15	0.59
Al_2O_3	16.56	15.2	15.92	16.16	16.14	16.23	15.69	15.97	15.29
FeO_t	8.11	7.83	3.32	8.05	7.97	5.31	7.30	7.4	4.33
MnO	0.12	0.11	0.04	0.12	0.14	0.08	0.11	0.11	0.06
MgO	4.36	2.25	0.53	6.50	6.44	1.86	2.34	3.94	1.61
CaO	7.18	3.99	3.61	7.60	7.65	1.35	5.04	6.21	2.59
Na_2O	3.43	3.22	3.45	2.88	3.00	2.78	3.79	3.42	3.95
K_2O	1.26	1.79	3.69	1.01	1.20	3.20	1.82	1.71	1.76
P_2O_5	0.23	0.33	0.31	0.18	0.18	0.19	0.28	0.23	0.15
LOI	1.05	3.06	0.85	1.14	0.90	3.00	1.31	0.94	2.02
Total	100.34	100.47	100.28	100.07	100.37	100.37	100.49	100.36	100.41
V	119	57	62	144	132	108	76	96	91
Cr	87	25	18	293	285	59	26	101	42
Ni	27	8	7	117	113	20	15	34	16
Zn	87	93	98	77	75	86	90	79	64
Zr	231	338	358	205	204	183	316	248	191
Nb	12	15	17	10	10	11	15	14	9
Ba	373	546	753	350	365	544	654	528	390
La	30	46	52	18	20	25	52	24	35
Ce	57	115	97	52	52	55	79	64	57
Nd	46	48	58	36	31	34	63	31	49
Ga	20	22	24	18	19	20	21	20	17
Pb	14	22	24	15	12	20	23	16	19
Rb	95	152	147	99	93	146	168	139	76
Sr	248	304	269	222	219	126	288	283	400
Th	14	15	22	10	15	17	19	10	15
Y	34	46	45	30	31	24	44	35	24

Field No.	**MS-54**	**MS-62**	**MS-65a**	**MS-68**	**MS-71**	**MS-73**	**MS-75**	**MS-76**	**MS-77**
UOC Sample No.	32439A	33241A	33242A	32434A	32866A	32867A	32441A	32891A	32435A
SiO_2	61.31	63.96	67.67	61.36	61.84	59.50	55.77	60.49	60.99
TiO_2	1.27	0.73	0.64	1.21	1.19	1.12	1.12	1.20	1.25
Al_2O_3	15.5	16.62	14.92	15.36	15.38	16.12	16.14	15.83	15.8
FeO_t	7.27	5.35	4.35	6.94	6.99	6.93	8.9	6.96	7.17
MnO	0.11	0.06	0.06	0.1	0.10	0.11	0.14	0.10	0.1
MgO	2.33	1.93	1.64	2.19	2.36	4.15	5.91	3.63	2.35
CaO	4.86	1.91	3.24	4.69	4.65	5.76	7.12	5.98	4.92
Na_2O	3.54	2.26	3.52	3.18	3.66	3.05	2.83	3.01	3.81
K_2O	2.28	4.26	2.12	2.89	1.71	2.43	1.72	2.53	1.73
P_2O_5	0.27	0.23	0.17	0.27	0.27	0.22	0.21	0.25	0.27
LOI	1.52	2.85	2.08	2.22	1.82	0.75	0.51	0.5	2.07
Total	100.26	100.16	100.41	100.41	99.97	100.14	100.37	100.48	100.46
V	74	100	95	69	68	108	122	93	72
Cr	29	48	41	30	32	135	188	95	32
Ni	12	18	16	15	15	42	74	31	13
Zn	85	74	59	81	86	84	74	83	84
Zr	313	215	222	307	313	247	224	271	312
Nb	16	11	9	15	14	13	13	15	14
Ba	644	849	469	658	650	499	456	569	636
La	40	37	36	35	39	30	22	29	29
Ce	93	70	57	99	73	55	57	68	102
Nd	54	46	29	39	37	41	32	27	47
Ga	20	20	17	20	21	20	19	19	21
Pb	21	13	19	20	20	15	12	16	21
Rb	131	191	85	137	193	110	48	85	185
Sr	239	301	335	231	248	213	230	240	250
Th	14	19	16	14	15	11	7	12	13
Y	45	31	22	42	44	38	34	41	44

Field No.	**MS-82**	**MS-85**	**MS-87**	**MS-92**	**MS-93**	**MS-96**	**MS-99**	**MS-105**	**MS-106b**
UOC Sample No.	32868A	32869A	32870A	32871A	32442A	33243A	32436A	32872A	32443A
SiO_2	60.99	59.84	60.44	63.17	55.79	55.61	74.4	55.60	57.63
TiO_2	1.30	1.11	1.11	1.15	1.09	1.03	0.1	1.08	1.08
Al_2O_3	15.62	15.97	16.01	15.58	16.01	15.79	12.3	15.99	15.67
FeO_t	7.45	7.06	6.93	6.88	7.99	8.11	1.61	8.10	7.68
MnO	0.13	0.11	0.11	0.06	0.16	0.13	0.02	0.16	0.1
MgO	2.42	3.70	3.70	1.53	6.44	6.75	0.06	6.55	6.17
CaO	5.04	5.88	5.56	3.54	7.7	7.59	0.9	7.64	6.64
Na_2O	3.57	3.47	3.15	3.29	2.96	2.94	3.3	2.92	2.88
K_2O	2.15	1.87	2.66	3.38	1.25	1.10	4.28	1.14	1.93
P_2O_5	0.28	0.23	0.23	0.29	0.19	0.18	0.03	0.19	0.21
LOI	1.25	0.74	0.37	1.2	0.75	1.25	3.21	0.86	0.47
Total	100.2	99.98	100.27	100.07	100.33	100.48	100.21	100.23	100.46
V	74	95	102	62	128	129	12	132	125
Cr	26	98	106	21	279	288	9	277	287
Ni	14	34	37	9	111	119	<3	109	83
Zn	88	80	80	87	73	77	54	73	75
Zr	320	263	262	337	204	194	141	205	232
Nb	15	14	13	16	11	10	13	10	13
Ba	679	528	532	675	402	344	433	388	409
La	36	27	29	41	15	39	58	19	16
Ce	67	60	64	82	51	50	120	47	61
Nd	44	37	38	43	31	26	60	37	29
Ga	20	19	20	22	19	18	20	19	19
Pb	21	16	16	22	12	14	34	12	12
Rb	195	130	117	147	95	102	249	107	84
Sr	258	260	226	249	246	217	57	229	214
Th	14	10	11	16	6	13	24	9	8
Y	44	36	39	43	31	35	35	32	33

Field No.	**MS-118**	**MS-126**	**MS-134**	**MS-137**	**MS-138**	**MS-140**	**MS-141**	**MS-146**	**MS-162**
UOC Sample No.	33244A	33245A	32873A	32874A	32875A	32444A	33246A	33247A	32437A
SiO_2	55.93	61.68	61.65	61.75	58.65	61.37	71.59	61.79	62.05
TiO_2	1.07	1.21	1.28	1.21	1.14	1.2	0.55	1.25	1.25
Al_2O_3	15.93	15.41	15.71	15.41	15.98	15.46	13.01	15.43	15.72
FeO_t	8.03	6.91	7.28	6.93	7.47	6.9	4.12	7.06	7.16
MnO	0.13	0.10	0.10	0.10	0.12	0.1	0.06	0.11	0.12
MgO	6.32	2.25	2.33	2.20	4.34	2.23	1.47	2.21	2.25
CaO	7.57	4.61	3.79	4.62	6.54	4.58	2.46	4.83	4.67
Na_2O	2.96	3.49	3.73	3.15	3.33	4.01	3.71	3.86	3.2
K_2O	1.34	2.31	3.41	2.9	1.79	1.61	1.57	1.89	3.14
P_2O_5	0.18	0.26	0.28	0.27	0.22	0.27	0.16	0.27	0.28
LOI	0.94	1.93	0.66	1.64	0.64	2.64	1.80	1.31	0.53
Total	100.4	100.16	100.22	100.18	100.22	100.37	100.5	100.01	100.37
V	129	68	79	68	107	68	94	68	77
Cr	276	30	33	29	134	28	38	28	31
Ni	110	13	15	13	37	12	15	14	12
Zn	74	87	86	84	80	85	55	88	88
Zr	205	309	304	313	246	309	193	315	319
Nb	10	15	14	15	13	15	8	15	16
Ba	363	631	710	701	485	686	507	630	671
La	33	37	36	31	25	36	32	40	36
Ce	54	84	72	73	58	88	53	79	96
Nd	25	45	51	42	36	47	44	44	51
Ga	18	21	21	21	19	21	15	22	21
Pb	15	22	21	21	16	19	17	21	21
Rb	92	139	146	148	116	166	62	178	101
Sr	217	236	203	233	273	256	303	243	260
Th	15	18	13	14	12	11	16	20	15
Y	32	45	53	43	36	47	23	44	46

Field No.	**MS-165**	**MS-170**	**MS-183**	**MS-184**	**MS-189**	**MS-191**	**MS-192**	**MS-193**	**MS-194**
UOC Sample No.	32445A	32876A	32446A	32877A	32878A	32438A	32879A	32880A	32447A
SiO_2	62.16	59.98	62.14	57.94	60.88	56.63	55.36	57.04	55.68
TiO_2	1.23	1.10	1.26	1.21	1.25	1.05	1.07	1.07	1.08
Al_2O_3	15.54	15.86	15.63	16.21	15.58	15.85	16.00	15.76	16.09
FeO_t	7	7.01	7.11	7.58	7.58	7.72	7.99	7.84	8.02
MnO	0.1	0.10	0.11	0.14	0.11	0.11	0.13	0.12	0.14
MgO	2.28	4.20	2.25	4.40	2.21	6.08	6.41	5.75	6.5
CaO	4.73	5.42	4.75	6.79	4.51	7.66	7.71	6.94	7.66
Na_2O	3.61	3.09	3.43	3.47	3.54	2.77	3.07	2.86	2.98
K_2O	2.35	2.6	2.59	1.52	2.28	1.24	1.02	2.08	1.25
P_2O_5	0.27	0.22	0.27	0.21	0.29	0.18	0.18	0.19	0.19
LOI	1.19	0.72	0.78	0.72	1.76	1.08	1.31	0.69	0.83
Total	100.46	100.3	100.32	100.19	99.99	100.37	100.25	100.34	100.42
V	70	113	71	128	66	131	130	137	128
Cr	32	181	28	104	24	296	278	300	282
Ni	15	42	13	32	8	113	115	113	109
Zn	82	82	87	82	90	71	73	76	74
Zr	307	243	317	245	323	196	201	202	200
Nb	15	13	16	12	15	11	10	10	12
Ba	694	493	724	466	615	334	364	378	411
La	33	29	36	29	36	15	31	20	27
Ce	91	56	77	62	76	66	45	43	47
Nd	33	47	48	43	54	37	40	20	31
Ga	21	19	21	19	22	18	17	18	18
Pb	18	17	21	13	22	11	11	12	13
Rb	151	120	184	125	167	51	107	96	80
Sr	241	206	241	255	247	221	211	183	222
Th	11	14	13	13	15	10	7	10	9
Y	43	39	45	35	43	30	38	31	31

Field No.	**MS-198**	**MS-205**	**MS-206**	**MS-208**	**MS-209**	**MS-212**	**MS-213**	**MS-215**	**MS-216b**
UOC Sample No.	32448A	32881A	32882A	32883A	32884A	32506A	32507A	32508A	32509A
SiO_2	61.72	58.82	59.03	58.27	55.91	56.81	60.12	59.5	74.54
TiO_2	1.25	1.13	1.23	1.15	1.06	1.11	1.11	1.2	0.1
Al_2O_3	15.43	15.95	15.89	15.85	15.88	16.07	15.98	16.06	12.41
FeO_t	7.05	7.43	7.58	7.46	8.04	8.04	6.92	7.02	1.49
MnO	0.1	0.12	0.11	0.11	0.12	0.17	0.11	0.12	0.01
MgO	2.19	4.40	3.83	5.23	6.57	5.79	3.74	3.82	<0.05
CaO	4.68	6.34	6.43	6.30	7.62	6.83	5.49	5.88	0.9
Na_2O	3.26	3.19	3.18	3.02	2.9	2.92	3.04	3.29	2.96
K_2O	2.81	1.57	2.05	2.23	1.23	1.95	2.91	2.26	4.74
P_2O_5	0.27	0.23	0.25	0.22	0.17	0.2	0.23	0.24	0.03
LOI	1.72	1.12	0.74	0.6	0.91	0.41	0.65	0.89	3.02
Total	100.48	100.3	100.32	100.44	100.41	100.3	100.3	100.28	100.2
V	68	100	97	117	134	121	97	101	15
Cr	26	130	94	214	280	198	101	83	4
Ni	12	40	31	70	112	71	39	31	4
Zn	86	83	80	77	75	77	80	81	52
Zr	313	250	265	243	202	227	259	280	139
Nb	16	13	14	13	10	13	14	14	14
Ba	711	493	540	466	370	435	559	513	488
La	35	26	25	28	22	23	32	29	50
Ce	74	57	55	51	49	64	67	77	96
Nd	40	30	26	27	10	34	34	29	59
Ga	21	19	20	19	17	18	20	20	20
Pb	19	15	16	13	10	12	17	14	35
Rb	137	144	107	105	96	57	122	123	241
Sr	232	243	253	223	223	234	226	240	56
Th	14	13	14	11	9	7	10	11	25
Y	44	40	38	35	36	33	41	37	36

Field No.	**MS-217**	**MS-218**	**MS-219**	**MS-220**	**MS-221**	**MS-222**	**MS-223**	**MS-226**
UOC Sample No.	32510A	32511A	32885A	32886A	32887A	32888A	32889A	32890A
SiO_2	58.77	76.26	74.86	76.46	76.96	76.40	76.72	76.83
TiO_2	1.36	0.11	0.10	0.10	0.10	0.11	0.11	0.10
Al_2O_3	16.09	13.51	12.47	12.83	12.62	12.68	12.60	12.65
FeO_t	8.62	1.28	1.22	1.35	1.33	1.85	1.35	1.42
MnO	0.11	<0.01	0.01	0.01	0.01	0.02	<0.01	0.01
MgO	3.2	0.06	0.06	0.06	0.09	0.06	<0.05	<0.05
CaO	6.03	0.13	0.95	0.89	0.84	0.78	0.84	0.88
Na_2O	3.33	1.46	3.18	3.06	2.95	2.89	3	3.04
K_2O	2.41	5.43	4.49	5.03	4.96	4.93	4.99	4.92
P_2O_5	0.29	0.03	0.03	0.04	0.03	0.04	0.03	0.03
LOI	0.12	2.01	3.09	0.34	0.44	0.51	0.34	0.38
Total	100.33	100.28	100.46	100.17	100.33	100.27	99.98	100.26
V	82	14	6	6	6	7	7	4
Cr	20	<3	5	<3	5	4	5	3
Ni	9	4	<3	<3	<3	<3	<3	<3
Zn	87	38	52	76	41	60	61	49
Zr	317	149	146	152	149	149	147	146
Nb	14	16	14	14	13	14	14	14
Ba	590	474	456	477	463	487	457	447
La	30	57	52	48	69	64	52	49
Ce	76	86	97	94	112	108	93	93
Nd	47	56	47	46	68	76	58	44
Ga	21	23	21	20	21	21	21	20
Pb	17	36	36	36	36	37	37	36
Rb	103	265	242	248	247	249	246	244
Sr	318	40	65	58	57	53	54	56
Th	9	26	26	26	25	27	28	26
Y	41	30	37	31	34	33	30	29

McQueens Valley Samples

Field No.	**MV-4**	**MV-5**	**MV-7**	**MV-8**	**MV-9**	**MV-11**	**MV-12**	**MV-13**	**MV-17**
UOC Sample No.	32449A	32450A	32451A	32452B	32518A	32519A	32520A	32521A	32522A
SiO_2	66.63	64.64	64.27	72.63	60.27	59.7	64.04	76.61	77.08
TiO_2	0.81	0.69	0.85	0.18	1.38	1.39	0.75	0.1	0.31
Al_2O_3	16.44	15.25	15.5	12.96	15.77	15.74	15.2	12.53	12.82
FeO_t	3.15	5.29	6.15	1.85	7.11	7.45	5.84	1.57	0.71
MnO	0.03	0.09	0.11	0.02	0.12	0.11	0.09	<0.01	<0.01
MgO	0.25	0.76	0.98	0.1	3.1	3.03	0.84	<0.05	0.34
CaO	2.48	2.57	3.06	0.63	5.47	5.47	2.81	0.29	0.31
Na_2O	4.61	4.16	4.41	3.02	3.4	3.36	4.12	3.9	1.58
K_2O	4.27	4.61	3.91	4.25	2.34	2.37	4.43	4.78	5.36
P_2O_5	0.25	0.2	0.25	0.02	0.25	0.25	0.23	0.04	0.03
LOI	1.25	1.67	0.72	4.1	1.11	1.55	1.77	0.45	1.85
Total	100.17	99.93	100.21	99.76	100.32	100.42	100.12	100.27	100.39
V	43	34	43	10	105	99	39	22	16
Cr	7	4	<3	3	47	41	4	4	24
Ni	4	5	4	3	15	15	4	<3	3
Zn	74	91	101	84	90	107	94	74	43
Zr	560	496	526	382	258	265	549	207	309
Nb	46	40	44	13	13	13	43	65	18
Ba	961	948	858	833	545	553	887	75	1035
La	69	55	59	64	34	31	52	53	64
Ce	132	116	125	127	77	81	121	94	110
Nd	45	52	55	61	40	51	61	66	72
Ga	27	26	26	21	20	21	26	28	20
Pb	20	21	18	36	17	17	19	28	26
Rb	146	153	131	451	188	200	141	252	221
Sr	278	239	275	63	232	232	255	10	60
Th	18	18	16	22	9	13	18	32	22
Y	46	42	43	74	37	44	43	43	30

Field No.	**MV-19**
UOC Sample No.	32792A
SiO_2	78.17
TiO_2	0.16
Al_2O_3	11.38
FeO_t	1.19
MnO	<0.01
MgO	<0.05
CaO	0.24
Na_2O	2.2
K_2O	4.91
P_2O_5	0.02
LOI	1.41
Total	99.68
V	6
Cr	4
Ni	<3
Zn	24
Zr	347
Nb	15
Ba	980
La	43
Ce	88
Nd	38
Ga	18
Pb	30
Rb	216
Sr	27
Th	21
Y	33

Gawler Downs Samples

Field No.	**GD-2**	**GD-4**	**GD-6**	**GD-10**	**GD-13**	**GD-15**	**GD-16**	**GD-17**	**GD-19**
UOC Sample No.	32523A	32524A	32525A	32790A	32526A	32527A	32528A	32529A	32530A
SiO_2	60.95	63.44	67.00	73.77	67.64	68.15	63.08	65.52	64.85
TiO_2	1.09	1.13	0.78	0.81	0.84	0.96	1.33	1.08	1.15
Al_2O_3	16.07	15.75	15.31	13.56	15.14	16.54	16.38	15.52	16.07
FeO_t	6.51	6.23	4.30	1.85	4.78	2.64	5.96	5.60	5.00
MnO	0.12	0.09	0.07	<0.01	0.04	0.02	0.07	0.06	0.03
MgO	3.25	1.9	0.76	0.21	0.95	0.42	1.46	1.54	1.23
CaO	5.27	3.96	2.80	1.82	2.93	2.72	4.35	3.40	3.87
Na_2O	3.33	3.19	3.55	2.31	3.34	3.22	3.39	3.28	3.37
K_2O	2.48	3.08	3.47	3.64	3.99	3.95	3.2	3.54	3.46
P_2O_5	0.23	0.27	0.25	0.2	0.27	0.26	0.28	0.27	0.28
LOI	0.78	1.08	1.87	1.5	0.48	1.38	0.83	0.61	1.01
Total	100.08	100.12	100.16	99.67	100.4	100.26	100.33	100.42	100.32
V	89	66	36	43	44	57	74	64	72
Cr	81	27	9	16	12	18	28	26	31
Ni	31	10	6	6	25	10	14	13	14
Zn	81	79	65	42	144	83	99	85	89
Zr	261	314	361	312	368	359	315	334	329
Nb	15	16	15	14	16	16	17	16	16
Ba	571	724	796	717	789	868	711	730	757
La	34	38	58	69	48	45	35	39	42
Ce	76	85	117	108	90	87	74	85	85
Nd	44	48	63	67	59	50	45	56	47
Ga	21	21	21	18	21	22	22	21	21
Pb	17	23	29	23	27	28	22	26	25
Rb	143	170	194	149	169	168	134	150	146
Sr	229	238	219	168	225	239	229	232	255
Th	12	11	16	13	19	18	14	16	14
Y	37	42	50	53	53	38	41	45	38

Field No.	**GD-18**	**GD-20**	**GD-21**	**GD-22**	**GD-26**	**GD-28**	**GD-29**	**GD-30**
UOC Sample No.	33251A	32531A	32532A	33252A	32533A	32534A	32535A	32791A
SiO_2	68.13	64.68	64.15	63.94	58.12	74.97	77.36	64.28
TiO_2	0.64	1.14	1.12	1.09	1.35	0.10	0.11	1.16
Al_2O_3	14.75	15.45	15.76	15.53	16.22	12.35	12.95	15.84
FeO_t	4.29	6.30	6.18	6.43	7.76	1.53	0.79	5.74
MnO	0.06	0.09	0.05	0.08	0.18	0.02	<0.01	0.05
MgO	1.51	1.87	1.27	1.43	4.05	0.12	0.06	1.37
CaO	2.94	3.80	3.65	3.60	6.42	0.88	0.74	3.60
Na_2O	3.39	3.27	3.46	3.48	3.39	2.84	2.8	3.11
K_2O	2.45	3.3	3.49	3.02	2.17	4.74	5.2	3.37
P_2O_5	0.16	0.26	0.3	0.29	0.25	0.02	0.03	0.27
LOI	2.08	0.31	0.95	1.49	0.48	2.82	0.13	1.13
Total	100.4	100.47	100.38	100.38	100.39	100.39	100.17	99.92
V	93	65	62	57	108	15	14	63
Cr	42	27	17	20	60	4	<3	30
Ni	18	11	14	10	23	<3	<3	10
Zn	59	84	99	94	86	57	27	93
Zr	248	321	338	336	269	143	141	326
Nb	9	16	17	16	15	15	15	16
Ba	578	743	724	721	493	444	516	758
La	31	42	46	54	27	43	68	43
Ce	63	79	90	106	71	89	108	63
Nd	28	49	62	61	36	58	82	57
Ga	17	22	23	22	21	20	22	21
Pb	18	25	20	24	14	34	35	25
Rb	91	142	152	152	94	234	251	146
Sr	285	240	259	250	238	55	58	231
Th	16	16	16	20	10	23	26	16
Y	21	47	48	45	39	35	29	41

Rangitata Gorge Samples

Field No.	**RG-2**	**RG-3**	**RG-4**	**RG-5**	**RG-7**	**RG-10**	**RG-11**	**RG-13**	**RG-14**
UOC Sample No.	33248A	32771A	33249A	32772A	32773A	32774A	33250A	32775A	32776A
SiO_2	56.95	62.46	71.66	62.98	60.90	57.57	57.75	62.27	63.05
TiO_2	1.09	1.17	0.47	1.14	1.27	1.10	1.08	1.15	1.15
Al_2O_3	15.88	15.36	14.00	15.35	15.64	15.78	15.63	15.41	15.14
FeO_t	7.49	7.18	3.95	6.16	7.68	7.40	7.74	7.10	7.07
MnO	0.20	0.09	0.05	0.09	0.10	0.13	0.13	0.10	0.11
MgO	6.13	1.92	1.32	1.54	2.58	5.63	5.55	1.81	1.67
CaO	7.23	3.73	1.05	3.99	4.58	6.20	7.09	3.57	3.64
Na_2O	2.92	3.34	5.05	3.72	3.31	2.91	2.79	3.48	3.5
K_2O	1.61	3.25	0.89	2.56	2.94	2.13	1.70	3.53	3.31
P_2O_5	0.19	0.3	0.12	0.29	0.28	0.21	0.21	0.29	0.29
LOI	0.61	0.59	1.67	1.79	0.79	0.89	0.64	1.17	0.63
Total	100.3	99.39	100.23	99.61	100.07	99.95	100.31	99.88	99.56
V	131	62	68	55	78	133	121	67	71
Cr	271	21	25	18	34	233	215	34	24
Ni	107	7	17	8	15	81	81	12	10
Zn	79	91	66	93	92	78	78	85	82
Zr	219	331	141	335	307	233	231	326	323
Nb	12	15	8	14	15	11	12	15	15
Ba	393	654	205	668	586	408	398	658	670
La	20	31	6	35	28	18	24	34	37
Ce	59	76	36	76	71	46	68	76	72
Nd	34	44	24	47	31	19	25	50	44
Ga	18	22	13	22	22	19	18	22	21
Pb	14	21	10	22	21	15	15	23	23
Rb	78	142	47	242	130	104	41	178	148
Sr	209	247	211	264	239	210	250	213	224
Th	16	13	13	16	13	10	16	16	14
Y	34	42	13	43	42	34	35	45	47

Field No.	**RG-16**	**RG-18**	**RG-21**	**RG-25**	**RG-30**	**RG-32**	**RG-33**	**RG-34**	**RG-37**
UOC Sample No.	32777A	32778A	32779A	32780A	32781A	32782A	32783A	32784A	32785A
SiO_2	71.22	73.82	71.78	72.75	62.50	57.26	67.94	56.27	60.26
TiO_2	0.25	0.24	0.25	0.24	1.17	1.12	0.54	1.14	1.26
Al_2O_3	14.18	14.00	14.32	13.99	15.42	15.83	15.17	16.40	15.65
FeO_t	2.99	0.88	2.44	1.34	7.09	7.83	3.81	7.91	7.54
MnO	0.06	0.03	0.07	0.03	0.11	0.13	0.06	0.14	0.12
MgO	0.32	<0.05	0.17	0.06	1.90	5.52	1.42	5.74	2.43
CaO	1.14	1.12	1.25	1.11	4.05	6.79	2.08	7.12	5.20
Na_2O	3.43	3.45	3.41	3.17	3.88	3.39	3.5	2.78	3.4
K_2O	5.1	5.36	5.17	5.45	2.22	1.2	3.2	1.72	2.32
P_2O_5	0.08	0.08	0.08	0.08	0.29	0.2	0.14	0.21	0.28
LOI	0.89	0.24	0.71	0.97	0.8	0.65	1.88	0.68	1.78
Total	99.66	99.22	99.65	99.19	99.43	99.92	99.74	100.11	100.24
V	5	5	6	3	60	124	80	129	80
Cr	<3	<3	4	<3	21	213	28	206	32
Ni	5	3	3	<3	8	73	9	77	15
Zn	71	85	71	33	91	79	53	78	91
Zr	371	360	352	362	340	234	267	241	309
Nb	16	16	16	16	16	12	11	12	14
Ba	1279	1382	1397	1298	682	417	647	463	567
La	64	64	65	62	32	19	30	34	40
Ce	115	119	120	117	84	55	68	57	67
Nd	71	67	62	69	36	22	20	40	54
Ga	24	19	21	16	22	18	15	20	21
Pb	37	32	31	31	23	13	15	14	20
Rb	202	216	204	219	204	103	123	35	190
Sr	114	147	149	165	264	231	390	248	275
Th	23	21	24	23	15	9	14	11	13
Y	64	55	55	58	14	33	25	43	43

Field No.	**RG-38**	**RG-39**
UOC Sample No.	32786A	32787A
SiO_2	72.32	70.70
TiO_2	0.25	0.25
Al_2O_3	14.62	14.19
FeO_t	1.70	3.47
MnO	0.01	0.05
MgO	<0.05	0.22
CaO	1.31	0.81
Na_2O	3.1	3.33
K_2O	5.52	5.38
P_2O_5	0.08	0.09
LOI	0.97	1.1
Total	99.88	99.59
V	7	4
Cr	4	4
Ni	5	4
Zn	53	62
Zr	372	353
Nb	16	16
Ba	1349	1278
La	64	60
Ce	128	113
Nd	76	69
Ga	21	24
Pb	37	38
Rb	224	212
Sr	133	129
Th	25	20
Y	65	60

Malvern Hills Samples

Field No.	**MH-1**	**MH-3**	**MH-5**	**MH-6**	**MH-7**	**MH-8**	**MH-11**	**MH-12**	**MH-13**
UOC Sample No.	32512A	32513A	32514A	32515A	32516A	32517A	32793A	32794A	32795A
SiO_2	46.14	75.95	73.85	75.45	78.25	78.02	52.94	73.52	72.18
TiO_2	2.55	0.20	0.16	0.22	0.14	0.16	1.39	0.17	0.19
Al_2O_3	12.30	13.48	12.78	13.42	11.48	12.16	17.17	12.71	13.27
FeO_t	13.38	0.92	1.99	1.19	0.83	0.91	13.09	1.76	1.91
MnO	0.18	<0.01	0.01	<0.01	<0.01	<0.01	0.10	0.01	0.01
MgO	10.67	0.15	0.24	0.14	0.10	0.09	2.69	0.23	0.16
CaO	9.78	0.78	0.87	0.71	0.48	0.70	5.47	0.88	0.92
Na_2O	3.49	2.89	3.96	3.11	2.19	3.01	3.15	4.2	3.96
K_2O	1.31	5.36	2.54	5.47	5.94	5.01	0.86	2.46	3.07
P_2O_5	0.65	0.1	0.09	0.13	0.07	0.09	0.28	0.09	0.1
LOI	-0.53	0.46	3.85	0.57	0.55	0.32	2.86	4.2	3.96
Total	99.92	100.29	100.34	100.41	100.03	100.47	100	100.23	99.73
V	188	14	14	17	16	16	74	6	6
Cr	290	4	4	<3	<3	4	23	5	9
Ni	267	4	4	4	<3	3	16	5	5
Zn	117	47	74	47	38	68	231	75	74
Zr	229	195	161	203	133	153	352	164	202
Nb	58	20	19	26	18	20	20	20	20
Ba	343	1097	625	699	609	643	608	663	998
La	26	56	44	47	44	43	47	44	56
Ce	70	105	102	101	83	100	69	81	102
Nd	41	48	50	54	45	39	50	52	60
Ga	20	20	20	20	18	18	24	20	21
Pb	1	34	30	31	30	31	15	34	35
Rb	23	199	253	178	213	195	86	234	220
Sr	682	83	98	63	62	59	361	95	86
Th	6	21	18	18	15	18	14	16	20
Y	28	20	15	16	14	14	67	14	20

Field No.	**MH-14**	**MH-15**	**MH-16**	**MH-17**	**MH-20**	**MH-21**	**MH-22**	**MH-26**	**MH-28**
UOC Sample No.	32796A	32797A	32798A	32799A	32800A	32801A	32802A	32803A	32804A
SiO_2	58.64	58.62	74.64	74.47	58.73	58.78	67.73	69.24	77.30
TiO_2	1.30	1.37	0.18	0.22	1.44	1.44	0.18	0.58	0.18
Al_2O_3	15.80	15.81	12.15	14.24	16.09	16.05	12.04	15.90	11.42
FeO_t	8.34	8.55	1.02	1.04	7.95	8.39	0.93	3.22	0.55
MnO	0.12	0.14	0.01	<0.01	0.17	0.15	0.02	0.03	<0.01
MgO	3.69	3.27	0.12	0.13	3.29	3.02	0.10	0.62	0.06
CaO	5.64	5.64	1.04	0.53	5.94	5.75	5.90	1.21	0.39
Na_2O	3.06	3.37	1.13	2.3	3.72	3.53	1.41	2.84	0.66
K_2O	2.51	1.48	6.29	5.39	1.47	1.98	5.33	4.05	8.4
P_2O_5	0.28	0.28	0.09	0.08	0.29	0.29	0.09	0.23	0.07
LOI	0.49	1.48	2.89	1.53	0.85	0.57	6.31	2.32	0.8
Total	99.87	100.01	99.56	99.93	99.94	99.95	100.04	100.24	99.83
V	95	88	5	7	89	87	6	52	7
Cr	48	30	4	5	29	30	5	23	4
Ni	23	15	4	6	15	15	<3	7	<3
Zn	97	96	32	46	96	100	62	50	11
Zr	293	298	194	235	304	307	195	341	183
Nb	17	17	17	20	18	18	18	25	16
Ba	544	569	1645	1351	601	560	903	978	632
La	19	22	45	60	28	27	42	78	44
Ce	59	68	85	104	62	53	86	91	81
Nd	28	44	52	60	35	38	30	63	39
Ga	19	21	19	22	21	21	17	21	17
Pb	15	16	34	34	13	15	30	26	21
Rb	181	136	268	198	137	114	182	157	251
Sr	226	252	366	106	265	235	358	156	89
Th	10	10	16	23	10	11	20	17	17
Y	39	47	15	22	45	47	18	40	17

Field No.	**MH-29**	**MH-30**	**MH-32**	**MH-33**	**MH-34**	**MH-36**	**MH-39**	**MH-40**	**MH-42**
UOC Sample No.	32805A	32806A	32807A	32808A	32809A	32810A	32811A	32812A	32814A
SiO_2	71.93	71.90	74.16	70.04	73.28	77.22	72.18	74.53	72.72
TiO_2	0.20	0.20	0.20	0.74	0.25	0.15	0.43	0.35	0.36
Al_2O_3	13.34	13.25	13.60	14.33	14.22	12.34	15.35	13.77	14.59
FeO_t	1.92	2.10	2.21	4.09	1.99	1.15	1.50	1.21	2.22
MnO	0.02	0.01	<0.01	0.06	0.01	<0.01	0.02	0.02	0.02
MgO	0.21	0.27	0.18	0.55	0.19	0.12	0.33	0.15	0.32
CaO	0.92	1.01	0.30	1.40	0.59	0.60	1.02	0.72	0.71
Na_2O	3.64	3.83	1.94	2.59	2.69	2.86	3	2.59	2.53
K_2O	3	2.79	5.22	3.84	5.2	5.24	4.83	5.75	5
P_2O_5	0.1	0.1	0.08	0.21	0.14	0.07	0.21	0.19	0.15
LOI	4.55	4.58	1.6	2.04	1.3	0.68	1.27	0.82	1.6
Total	99.83	100.04	99.49	99.89	99.86	100.43	100.14	100.1	100.22
V	5	6	7	70	10	6	26	18	17
Cr	6	6	6	30	5	8	11	10	10
Ni	3	<3	4	13	<3	<3	5	3	6
Zn	76	77	94	84	67	45	56	38	44
Zr	203	207	216	312	223	150	322	270	263
Nb	18	20	20	21	25	21	24	23	25
Ba	1121	1078	1196	953	827	623	1265	859	888
La	55	54	56	38	41	42	64	50	110
Ce	102	103	100	82	78	71	118	92	103
Nd	77	60	56	34	35	49	64	40	81
Ga	21	21	21	18	20	19	20	17	20
Pb	34	34	36	26	32	40	28	26	29
Rb	279	234	202	144	172	205	158	182	169
Sr	120	136	55	145	64	50	145	86	88
Th	20	22	22	15	19	18	21	18	20
Y	23	19	21	35	12	13	48	23	36

Field No.	**MH-45**	**MH-46**	**MH-47**	**MH-49**	**MH-50**	**MH-54**	**MH-55**	**MH-56**	**MH-59**
UOC Sample No.	32815A	32816A	32817A	32818A	32819A	32820A	32821A	32822A	32823A
SiO_2	48.76	67.75	76.71	72.78	72.30	74.79	74.62	73.60	48.42
TiO_2	1.43	0.65	0.22	0.22	0.25	0.19	0.22	0.23	3.09
Al_2O_3	10.62	14.93	12.62	13.71	14.05	13.75	13.41	13.28	17.45
FeO_t	12.42	4.21	0.52	2.45	2.97	1.50	1.62	2.93	11.57
MnO	0.16	0.06	<0.01	0.01	0.01	<0.01	<0.01	<0.01	0.33
MgO	13.17	1.83	<0.05	0.25	0.31	0.19	0.16	0.15	3.64
CaO	8.38	2.61	0.18	0.23	0.40	0.56	0.64	0.75	8.58
Na_2O	2.07	3.52	1.21	2.27	2.36	2.9	2.74	2.9	3.74
K_2O	0.55	2.72	7.77	6.72	6.27	4.93	5.43	5.3	1.12
P_2O_5	0.22	0.17	0.12	0.08	0.1	0.13	0.12	0.14	0.57
LOI	2.71	1.58	1.02	1.28	1.03	1.28	1.33	1.06	1.21
Total	100.49	100.03	100.37	100	100.05	100.22	100.29	100.34	99.72
V	144	98	11	9	10	9	9	10	208
Cr	497	46	5	5	5	6	6	6	11
Ni	364	13	<3	4	4	4	4	5	44
Zn	125	70	24	89	76	43	51	57	136
Zr	98	283	198	210	215	163	197	201	330
Nb	16	10	23	24	25	31	24	24	34
Ba	218	650	691	1645	1441	278	676	671	357
La	11	48	40	39	41	29	41	42	21
Ce	32	80	83	89	84	61	80	79	57
Nd	16	36	55	33	42	31	41	46	34
Ga	16	18	15	23	23	22	18	18	24
Pb	9	16	31	33	32	33	34	35	5
Rb	15	101	217	233	217	203	180	176	23
Sr	336	521	78	59	76	42	52	62	374
Th	4	16	19	20	21	16	19	19	5
Y	18	26	13	18	18	8	12	13	50

Field No.	**MH-60**	**MH-61**	**MH-62**	**MH-63**	**MH-65**	**MH-66**	**MH-69**	**MH-70**	**MH-71**
UOC Sample No.	32824A	32825A	32826A	32827A	32828A	32829A	32830A	32831A	32832A
SiO_2	74.59	76.35	71.62	71.64	70.94	76.65	60.26	74.39	72.60
TiO_2	0.23	0.20	0.35	0.35	0.33	0.25	1.49	0.21	0.21
Al_2O_3	14.24	12.78	14.54	14.42	15.21	13.21	16.61	13.37	13.40
FeO_t	0.92	0.69	2.68	2.82	2.82	0.64	7.31	2.02	2.09
MnO	<0.01	<0.01	0.02	0.01	0.01	<0.01	0.11	<0.01	0.01
MgO	0.13	0.15	0.25	0.31	0.23	<0.05	1.72	0.16	0.25
CaO	0.38	0.46	1.00	1.02	0.54	0.21	5.36	0.32	0.99
Na_2O	2.28	2.19	3.18	3.21	2.41	1.37	3.28	1.89	3.57
K_2O	6.06	6.51	5.02	4.89	5.46	5.57	2.76	6.14	2.23
P_2O_5	0.14	0.14	0.19	0.21	0.18	0.15	0.3	0.1	0.1
LOI	1.24	0.72	1.25	1.29	1.73	2.12	0.93	1.64	4.4
Total	100.21	100.19	100.1	100.17	99.86	100.17	100.13	100.24	99.85
V	9	10	21	25	20	12	93	6	4
Cr	4	5	8	12	6	7	37	4	7
Ni	5	5	8	8	11	4	14	<3	<3
Zn	42	50	77	68	94	12	94	75	76
Zr	214	186	275	267	266	235	312	213	214
Nb	25	24	23	24	23	22	17	19	20
Ba	903	412	1283	1044	1418	837	537	1192	1285
La	54	35	60	49	52	49	32	46	64
Ce	100	68	97	94	84	91	69	96	115
Nd	34	30	39	36	57	54	58	69	64
Ga	20	19	20	21	23	19	22	22	21
Pb	32	34	31	28	33	26	12	29	34
Rb	197	215	160	166	175	177	150	219	204
Sr	57	50	121	110	90	296	248	66	752
Th	21	19	27	24	27	24	10	19	21
Y	13	10	19	20	18	15	58	21	22

Mandamus Igneous Complex Samples

Field No.	**M-2**	**M-3**	**M-6**	**M-8**	**M-9**	**M-12**	**M-16**	**M-22**	**M-23**
UOC Sample No.	32833A	32834A	32835A	32836A	33253A	32837A	32838A	33254A	32839A
SiO_2	55.51	43.33	44.61	47.50	47.14	47.37	63.20	70.92	60.91
TiO_2	1.35	3.17	4.25	2.70	3.22	3.47	0.47	0.62	1.10
Al_2O_3	15.48	14.81	15.33	15.67	10.62	13.98	16.69	14.50	17.92
FeO_t	8.34	10.52	12.45	10.52	12.10	10.79	5.19	4.16	4.55
MnO	0.12	0.21	0.18	0.14	0.17	0.15	0.25	0.04	0.08
MgO	1.94	3.23	3.75	4.36	10.10	8.20	0.22	1.56	1.44
CaO	4.74	10.77	7.72	6.02	11.59	11.73	0.30	0.22	2.63
Na_2O	3.65	3.29	3.69	3.9	2.36	2.74	6.16	4.06	6.74
K_2O	3.05	1.69	1.65	2.5	1.24	0.7	5.22	2.32	3.99
P_2O_5	0.63	1.07	0.81	0.99	0.50	0.26	0.08	0.12	0.32
LOI	4.92	7.26	1.98	5.34	0.77	0.74	2.19	1.80	0.35
Total	99.73	99.35	96.42	99.64	99.81	100.13	99.97	100.32	100.03
V	96	203	291	133	235	216	<3	97	47
Cr	12	85	21	<3	551	345	<3	49	7
Ni	6	51	41	<3	227	131	<3	16	5
Zn	124	226	129	115	99	72	72	44	45
Zr	488	449	393	536	279	157	1164	204	631
Nb	86	113	85	140	59	47	252	8	149
Ba	783	512	488	562	208	255	153	482	737
La	52	55	31	81	49	10	120	21	89
Ce	119	136	97	145	81	47	215	48	165
Nd	78	91	63	108	67	27	116	28	68
Ga	24	23	25	23	18	19	35	16	29
Pb	9	36	20	2	6	<1	20	11	5
Rb	77	30	38	59	31	10	110	86	102
Sr	610	1359	846	773	564	821	44	260	523
Th	14	12	9	14	10	3	31	14	30
Y	40	37	36	43	28	18	74	17	42

Field No.	**M-32**	**M-35**	**M-37**	**M-40**	**M-41**	**M-42**	**M-43**	**M-49**	**M-50**
UOC Sample No.	32840A	32841A	32842A	32843A	32844A	32845A	32846A	32847A	32848A
SiO_2	46.70	61.24	44.99	43.76	62.56	45.64	62.74	59.98	63.57
TiO_2	3.34	0.89	4.39	3.47	0.87	3.36	0.81	0.88	0.72
Al_2O_3	16.21	17.64	14.27	15.77	18.43	14.79	18.06	17.36	15.72
FeO_t	11.22	4.83	14.42	10.99	3.68	12.13	4.84	6.32	6.36
MnO	0.26	0.16	0.33	0.15	0.03	0.34	0.06	0.18	0.19
MgO	3.96	0.48	5.06	5.23	0.66	3.74	0.12	0.76	0.53
CaO	8.78	0.53	8.47	6.16	0.39	6.91	0.25	1.40	0.65
Na_2O	3.51	6.33	3.9	3.68	6.83	4.16	7.02	7.3	6.84
K_2O	2.29	5.71	1.95	5.34	5.5	2.04	5.21	4.37	5
P_2O_5	1.13	0.05	1.06	1.03	0.24	1.02	0.19	0.21	0.12
LOI	2.21	-3.56	-0.54	3.5	0.6	5.25	0.63	1.31	0.22
Total	99.61	94.3	98.3	99.08	99.79	99.38	99.93	100.07	99.92
V	187	<3	283	227	<3	209	<3	<3	<3
Cr	56	<3	<3	61	3	<3	4	<3	6
Ni	17	<3	<3	32	<3	4	<3	<3	<3
Zn	123	56	214	170	40	122	114	135	160
Zr	460	493	285	432	494	401	728	711	1222
Nb	130	175	75	110	137	100	174	166	266
Ba	675	302	357	535	1288	386	683	806	49
La	69	77	40	61	66	59	64	88	121
Ce	134	141	93	121	127	113	128	144	247
Nd	98	73	68	70	77	78	60	84	111
Ga	24	31	23	25	26	23	32	30	37
Pb	2	13	20	15	9	<1	10	9	16
Rb	44	150	81	239	110	72	79	96	129
Sr	1067	79	827	642	131	627	42	125	11
Th	12	14	7	12	12	11	18	20	31
Y	41	41	40	36	27	45	47	54	68

Field No.	**M-59**	**M-60**	**M-61**	**M-62**	**M-64**	**M-66**	**M-67**	**M-68**	**M-71**
UOC Sample No.	32849A	32850A	32851A	32852A	32853A	32854A	32855A	32856A	33255A
SiO_2	47.23	60.82	65.23	49.02	61.27	58.55	46.35	49.18	65.57
TiO_2	3.34	1.01	0.51	2.78	0.58	1.42	3.03	2.95	0.69
Al_2O_3	15.04	17.07	17.54	14.66	17.40	16.62	10.97	17.74	16.64
FeO_t	12.54	6.66	2.10	10.77	6.42	8.14	12.15	11.48	4.48
MnO	0.13	0.10	0.07	0.19	0.19	0.15	0.18	0.12	0.04
MgO	3.51	0.80	0.24	3.19	0.45	1.62	11.32	2.88	1.97
CaO	5.94	0.54	0.57	5.33	0.66	4.04	11.38	5.56	1.57
Na_2O	3.77	7	6.82	5.7	7.03	5.71	2	5.13	3.82
K_2O	4.64	5.04	5.69	3.67	4.96	3.09	1.44	3.18	4.25
P_2O_5	0.99	0.26	0.08	1.09	0.16	0.45	0.53	1.09	0.15
LOI	2.53	0.75	0.38	3.25	0.69	0.16	0.7	0.1	0.88
Total	99.66	100.05	99.23	99.65	99.81	99.95	100.05	99.41	100.06
V	193	<3	<3	148	<3	26	261	98	112
Cr	<3	<3	<3	<3	<3	<3	568	<3	50
Ni	<3	<3	<3	<3	<3	<3	260	<3	20
Zn	150	108	21	222	133	93	120	59	31
Zr	424	467	2037	452	1227	302	259	582	191
Nb	105	113	477	114	304	93	54	160	11
Ba	472	1925	41	478	174	1106	225	338	645
La	51	49	132	151	194	60	15	69	22
Ce	124	116	260	156	298	123	65	147	67
Nd	73	44	118	138	148	79	59	92	42
Ga	24	27	40	23	37	24	17	26	20
Pb	6	7	10	<1	14	4	10	<1	8
Rb	234	111	180	141	149	96	44	136	169
Sr	641	58	20	582	34	817	494	705	258
Th	9	11	32	12	99	12	5	14	16
Y	50	40	87	135	68	36	27	48	26

Field No.	**M-77**	**M-78**	**M-80**	**M-83**	**M-84**	**M-86**	**M-87**	**M-88**	**M-89**
UOC Sample No.	32857A	32858A	33256A	32859A	32860A	32861A	32862A	32863A	32864A
SiO_2	42.55	58.24	63.81	50.65	52.11	40.53	49.69	48.84	46.88
TiO_2	3.39	1.24	0.88	1.85	1.48	4.60	2.06	2.70	2.77
Al_2O_3	14.91	16.51	16.49	18.37	19.63	12.16	17.55	16.66	15.72
FeO_t	13.37	7.51	5.73	7.09	6.54	15.28	8.73	11.72	11.92
MnO	0.36	0.20	0.03	0.14	0.19	0.24	0.18	0.11	0.27
MgO	5.40	1.42	1.72	2.02	1.27	7.99	3.27	4.25	3.69
CaO	9.90	2.70	1.70	5.03	3.95	12.57	6.49	6.53	5.71
Na_2O	3.02	6.54	5.09	6.38	8.75	1.54	5.48	3.27	4.69
K_2O	2.73	4.36	3.50	3.42	3.94	1.01	2.43	1.74	3.67
P_2O_5	0.64	0.32	0.19	0.51	0.37	0.62	0.58	0.68	0.78
LOI	3.5	0.78	1.16	4.16	0.71	3.4	3.1	3.68	3.13
Total	99.77	99.82	100.3	99.62	98.94	99.94	99.56	100.18	99.23
V	277	16	130	64	32	445	94	242	215
Cr	48	7	49	8	<3	279	51	81	87
Ni	44	3	16	6	<3	136	31	50	41
Zn	176	145	27	122	131	115	120	94	151
Zr	275	606	390	777	719	317	764	345	371
Nb	74	165	9	196	224	77	184	67	82
Ba	217	877	648	1166	1364	397	929	321	1119
La	30	87	24	89	106	36	92	35	37
Ce	76	152	59	162	173	87	160	96	98
Nd	32	72	43	73	84	45	82	67	54
Ga	20	29	20	24	28	22	25	25	24
Pb	4	5	7	<1	2	<1	<1	6	9
Rb	96	84	165	97	95	18	57	26	148
Sr	542	255	391	1280	1221	688	1836	706	885
Th	7	19	19	20	21	6	20	10	6
Y	28	55	25	36	38	31	37	34	32

Appendix 4: ICP-MS Analytical Procedures and data set

The analyses were undertaken with the assistance of Dr D. Garbe-Schönberg at the Institute of Geosciences, Christian-Albrechts University of Kiel, Germany; using an upgraded VG Plasmaquad PQ1 Inductively Coupled Plasma-Mass Spectrometer (ICP-MS) (Garbe-Schönberg, 1993). The sample preparation was undertaken by myself with the assistance of Mrs H. Blaschek.

A4.1 Analytical Procedures

Each sample was crushed coarsely, washed in distilled water, cleaned ultrasonically and dried overnight at 50ºC. The rock chips were hand-picked using a binocular microscope to select the freshest chips. The chips were then milled in an agate ring mill to a fine powder.

4ml HF, 3ml HCl and 1ml HNO_3 were added to 250mg of rock powder. The mixture was heated overnight (12 hours) at 160ºC. The following day, 1ml HCl was added to each beaker before the mixture was evaporated at 180ºC (3-4 hours). When evaporated a mixutre of 2:1 HNO_3 : distilled water was added to each beaker until each beaker was half full. The mixtures were heated at 160ºC for 1-2 hours before being left to stand overnight. The following day the solutions were evaporated at 180ºC (2-3 hours). Once evaporated 1ml HNO_3 and 5ml distilled water were added to each beaker and heated for 1-2 hours. The samples were completely dissolved with with no sediment visible. The samples were placed in cleaned large beakers ready for analysis and diluted with distilled water until the solution weighed 50g. Evolved samples which contain resilient minerals such as zircon were made into glass fusion beads before undergoing the dissolution procedure.

Precision of analytical results as estimated from duplicate measurements was generally better than 3 %. Details of the analytical procedure have been described by Garbe-Schönberg, 1993. Blanks and international standards, AGV-1, BHVO-1 and BR were analysed with the samples in order to to evaluate the precision and accuracy of the measurements.

A4.2 Data Set

Field No.	MS-34	MS-93	MS-75	MS-162	MS-126	MS-68	MS-29
Th	7.16	6.70	7.48	11.21	10.94	11.02	13.71
U	1.81	1.87	2.18	3.17	3.13	3.16	3.97
Nb	10.77	9.97	10.89	15.61	15.09	15.47	17.15
Ta	0.79	0.69	0.76	1.07	1.03	1.06	1.16
La	21.48	20.98	25.22	34.98	35.32	34.12	41.21
Ce	46.75	45.48	54.25	75.97	75.91	74.38	90.13
Pb	11.73	11.84	13.38	21.42	20.89	21.17	24.63
Nd	22.77	21.74	25.62	35.09	35.35	34.48	41.36
Sm	5.28	4.93	5.75	7.67	7.71	7.50	8.85
Hf	4.72	4.59	5.21	7.20	6.84	7.13	8.18
Eu	1.16	1.12	1.21	1.39	1.36	1.36	1.49
Gd	5.07	4.84	5.68	7.32	7.21	7.06	7.93
Tb	0.84	0.80	0.92	1.18	1.16	1.15	1.25
Dy	5.11	4.82	5.54	7.06	6.92	6.86	7.23
Er	2.86	2.77	3.17	3.98	3.87	3.84	3.88
Tm	0.41	0.40	0.46	0.57	0.55	0.55	0.54
Yb	2.68	2.58	2.91	3.68	3.53	3.53	3.45
Lu	0.39	0.38	0.43	0.54	0.52	0.52	0.49
Y	29.59	29.57	35.76	42.83	41.30	40.83	42.07

MS-99	MS-42-JR	MS-226	MS-37	MS-65a	RG-34	Field No.	RG-32	RG-18
22.60	24.55	20.06	9.69	9.48	7.92	**Th**	7.73	20.38
5.00	4.73	4.41	1.98	2.02	2.14	**U**	2.23	4.20
14.37	16.88	12.84	10.78	8.87	11.79	**Nb**	12.03	16.67
1.15	1.28	1.12	0.75	0.63	0.80	**Ta**	0.82	1.20
55.36	86.34	49.41	23.26	30.94	25.99	**La**	24.82	64.40
111.26	149.28	100.38	48.05	62.08	58.04	**Ce**	54.33	135.77
35.44	36.79	36.65	17.31	17.43	13.84	**Pb**	14.17	34.50
48.17	72.51	43.29	22.65	26.15	27.33	**Nd**	25.57	55.04
9.99	13.62	9.14	5.04	5.20	6.18	**Sm**	5.71	10.97
4.92	8.15	4.68	4.68	6.03	5.41	**Hf**	5.42	9.51
0.51	1.06	0.48	0.94	1.08	1.26	**Eu**	1.21	1.22
7.94	11.03	7.31	3.92	4.41	5.78	**Gd**	5.48	8.80
1.19	1.53	1.04	0.69	0.64	0.95	**Tb**	0.90	1.34
6.07	9.88	5.45	3.89	3.69	5.70	**Dy**	5.43	8.37
2.19	5.36	2.02	2.12	2.04	3.13	**Er**	3.06	4.97
0.26	0.77	0.24	0.31	0.28	0.45	**Tm**	0.44	0.75
1.51	4.58	1.42	1.97	1.87	2.96	**Yb**	2.85	4.50
0.19	0.61	0.18	0.31	0.28	0.42	**Lu**	0.41	0.65
30.76	64.09	29.50	22.99	23.68	32.15	**Y**	32.35	51.00

RG-4	RG-3	MV-9	MV-19	MH-21	MH-8	GD-17	GD-13	M-12
9.69	12.48	9.68	16.09	8.94	16.87	12.21	14.71	3.19
1.90	3.61	2.83	2.80	2.52	3.31	3.39	4.10	0.64
9.21	15.98	13.09	15.19	17.23	19.20	15.88	16.49	47.92
0.61	1.08	0.90	1.00	1.16	1.23	1.09	1.12	2.92
19.16	38.30	30.02	37.21	31.10	43.08	36.97	44.88	17.98
40.40	82.71	65.01	87.03	68.08	94.85	80.65	95.68	39.24
7.67	22.37	17.03	26.34	14.74	32.35	23.83	26.49	2.50
16.86	37.75	30.23	32.34	31.97	39.35	36.45	42.79	20.87
3.65	8.02	6.65	6.80	7.11	8.42	7.86	8.99	4.71
4.93	7.40	5.91	9.02	6.69	4.86	5.84	6.94	3.89
0.81	1.44	1.29	0.82	1.54	0.57	1.34	1.34	1.98
2.86	7.24	6.14	5.56	7.05	5.99	7.23	8.03	4.18
0.44	1.15	0.97	0.83	1.18	0.75	1.17	1.27	0.61
2.90	6.72	5.67	4.80	7.16	3.04	6.97	7.43	3.20
1.78	3.71	3.07	2.82	4.15	0.77	3.89	4.07	1.41
0.25	0.53	0.43	0.42	0.60	0.05	0.56	0.59	0.18
1.80	3.43	2.76	2.73	3.90	0.39	3.65	3.85	1.12
0.27	0.49	0.40	0.41	0.57	0.05	0.54	0.58	0.16
18.58	39.63	32.71	29.37	43.97	14.16	41.53	44.66	15.44

M-67	M-40	Field No.	M-84	M-78	M-80	M-66	M-86
4.22	7.34	**Th**	18.00	13.74	12.99	13.09	6.04
0.82	2.17	**U**	4.88	3.67	2.44	2.22	1.82
47.37	89.38	**Nb**	188.54	127.50	12.46	74.76	69.53
2.82	5.05	**Ta**	10.34	7.26	0.88	4.28	4.53
33.48	60.49	**La**	115.61	86.21	27.93	80.68	48.01
73.15	126.75	**Ce**	213.98	172.20	50.38	161.97	102.51
8.24	10.89	**Pb**	8.90	7.43	3.93	7.80	2.85
37.25	59.01	**Nd**	70.98	66.51	23.13	69.58	52.96
7.80	11.56	**Sm**	11.80	12.66	4.64	12.91	10.86
2.84	5.21	**Hf**	10.09	11.86	9.78	2.34	7.62
2.26	3.35	**Eu**	3.54	3.50	1.09	4.32	3.30
6.83	9.59	**Gd**	8.57	10.10	3.77	10.56	9.30
0.97	1.34	**Tb**	1.28	1.61	0.56	1.50	1.34
4.99	6.77	**Dy**	6.78	8.70	3.52	7.86	7.03
2.14	2.90	**Er**	3.10	4.45	2.21	3.57	2.98
0.27	0.36	**Tm**	0.42	0.63	0.32	0.45	0.37
1.59	2.07	**Yb**	2.49	3.82	2.15	2.72	2.23
0.21	0.27	**Lu**	0.33	0.58	0.35	0.37	0.31
23.99	32.94	**Y**	39.06	49.97	24.76	41.04	31.51

Appendix 5: Radiogenic isotope geochemistry – Analytical techniques and data set

This appendix provides a brief overview of the preparatory and analytical procedures employed in the TIMS analysis of radiogenic isotopes Sr, Nd and Pb.

A5.1 Sample Preparation

These procedures were followed whilst undertaking a 6 month analytical research period at GEOMAR, Kiel, Germany.

The samples chosen for isotope analyses also needed to be analysed for the full range of trace elements by ICP-MS analysis. Particular attention was given to the samples to ensure that the material analysed was of optimal quality. The procedure outlined below relates to the procedure employed at GEOMAR for all samples analysed by ICP-MS and TIMS.

A5.1.1 General Procedure

1. Crushing using a jaw crusher to reduce the short axis of the particles to <5mm.
2. Seiving to remove the <1mm fraction.
3. Rinsing in distilled water
4. Placing in an ultra-sound bath for 10 mins to remove loose material and general cleaning.
5. Drying overnight in a warm oven.
6. Picking of only the freshest material using binocular microscope.
7. Milling in an agate mill to reduce the size of fractions to fine sand.
8. Further milling in either an agate ring mill if sufficient material or in a small agate mill with agitating agate spheres to reduce the sand to a fine powder.

A5.1.2 General cleanliness and contamination avoidance measures

All crushing devices were cleaned thoroughly before use. The normal combination of cleaning is distilled water, high pressure air gun and P2 propenol/distilled water. The propenol/distilled water mixture is usually the final cleaning stage due to its evaporation properties.

The isotope separation procedures were undertaken in clean-room conditions.

A5.2 Analytical Procedure

All measured $^{87}Sr/^{86}Sr$ ratios are corrected for fractionation effects in the mass spectrometer. Unleached powders were dissolved in a hot HF-HNO_3 mixture followed by ion exchange procedures (Hoernle & Tilton, 1991). Isotopic ratios were determined on a Finnigan MAT262 RPQ^{2+} Thermal Ionization Mass Spectrometer (TIMS) at GEOMAR, operating in static mode for Sr and Pb and in multidynamic mode for Nd. Sr and Nd isotopic ratios are normalized within run to $^{86}Sr/^{88}Sr=0.1194$ and $^{146}Nd/^{144}Nd=0.7219$ respectively and all errors are 2 sigma. Over the course of this study NBS987 gave $^{87}Sr/^{86}Sr = 0.710208 \pm 0.000030$ (N=30), $^{143}Nd/^{144}Nd = 0.511710 \pm 0.000011$ (N=16) for the in-house monitor SPEX. $^{87}Sr/^{86}Sr$ ratios are normalized to $^{87}Sr/^{86}Sr=0.71025$. NBS981 (N= 25) gave $^{206}Pb/^{204}Pb = 36.520 \pm 0.027$, $^{207}Pb/^{204}Pb = 15.434 \pm 0.008$, $^{208}Pb/^{204}Pb = 16.897 \pm 0.007$ and corrected to the NBS 981 values given in (Todt *et al.*, 1996). The chemistry blanks for Sr, Nd and Pb ranged from 89pg to 730pg for the evolved samples and are thus considered negligible.

Pb replicate analyses were performed on all samples except MS-99 and the variance between samples is generally (19 of 22) better than 0.04% per a.m.u (atomic mass unit). MS-34 was reproduced within 0.09% per a.m.u., M-78 within0.06% per a.m.u. and M-67 within 0.05% per a.m.u.

A5.3 Data Set

Please see the following pages for the complete data set from the MSVG and MIC.

Sample	Rock Type	Age (Ma)	Rb (ppm)	Sr (ppm)	$^{87}Sr/^{86}Sr_m$	$^{87}Sr/^{86}Sr_{in}$	Sm (ppm)	Nd (ppm)	$^{147}Sm/^{144}Nd$	$^{143}Nd/^{144}Nd_m$	$^{143}Nd/^{144}Nd_{in}$	εNd_{in}	U (ppm)	Th (ppm)	Pb (ppm)	$^{206}Pb/^{204}Pb_m$	$^{207}Pb/^{204}Pb_m$	$^{208}Pb/^{204}Pb_m$	$^{206}Pb/^{204}Pb_{in}$	$^{207}Pb/^{204}Pb_{in}$	$^{208}Pb/^{204}Pb_{in}$	$^{238}U/^{204}Pb$ (μ)
M-12	Gabb	97.5	10	821	0.703322(6)	0.703273	4.71	20.87	0.136	0.512793(8)	0.512706	3.78	0.64	3.91	2.50	19.692	15.673	39.410	19.437	15.661	38.898	16.73
M-40	P-Teph	97.5	239	642	0.704529(7)	0.703037	11.56	59.01	0.118	0.512812(4)	0.512737	4.37	2.17	8.1	10.89	19.800	15.685	39.505	19.600	15.675	39.261	13.11
M-66	Sy-Dio	97.5	96	817	0.704084(9)	0.703613	12.91	69.58	0.112	0.512755(8)	0.512684	3.34	2.22	13.82	7.80	19.509	15.672	39.467	19.225	15.658	38.889	18.60
M-67	Basalt	97.5	44	494	0.703664(7)	0.703307	7.80	37.25	0.126	0.512796(8)	0.512716	3.96	0.82	4.98	8.24	19.395	15.671	39.201	19.296	15.667	39.004	6.50
M-78	Sye	97.5	84	255	0.704284(8)	0.702964	12.83	68.22	0.113	0.512821(8)	0.512749	4.61	3.39	13.74	23.83	20.428	15.714	40.134	20.283	15.707	39.942	9.50
M-80	Sed	97.5	169	401	0.707721(7)	0.706032	4.15	21.01	0.119	0.512558(8)	0.512482	-0.59	2.44	12.99	3.93	19.532	15.673	39.664	18.913	15.644	38.581	40.64
M-84	T-Pho	97.5	96	987	0.703299(8)	0.702909	11.49	69.63	0.099	0.512807(9)	0.512744	4.51	5.79	18.00	8.90	20.923	15.729	40.457	20.253	15.697	39.775	43.92
M-86	P-Bas	97.5	18	688	0.703283(7)	0.703178	10.86	52.96	0.123	0.512806(8)	0.512727	4.19	1.82	6.04	2.85	20.328	15.705	40.004	19.680	15.674	39.299	42.51
MS-34	B-And	97.5	99	222	0.707632(8)	0.705845	5.28	22.77	0.140	0.512584(7)	0.512495	-0.34	1.81	7.93	11.73	18.937	15.640	38.821	18.787	15.633	38.604	9.89
MS-75	B-And	97.5	48	230	0.707001(7)	0.706165	5.75	25.62	0.135	0.512564(7)	0.512478	-0.68	2.18	8.21	13.38	18.946	15.641	38.817	18.786	15.633	38.620	10.46
RG-34	B-And	97.5	35	248	0.706759(9)	0.706193	6.18	27.33	0.136	0.512573(6)	0.512486	-0.52	2.14	8.68	13.84	18.942	15.655	38.855	18.791	15.647	38.654	9.96
MS-68	And	97.5	147	234	0.709454(7)	0.706936	7.50	34.48	0.131	0.512516(6)	0.512432	-1.56	3.16	11.79	21.19	18.932	15.641	38.801	18.785	15.634	38.622	9.60
MS-126	And	97.5	139	236	0.709574(8)	0.707213	7.71	35.35	0.131	0.512516(8)	0.512432	-1.57	3.13	11.70	20.89	18.945	15.654	38.844	18.798	15.647	38.664	9.65
MV-9	And	97.5	188	232	0.709696(8)	0.706447	6.65	30.23	0.132	0.512533(8)	0.512449	-1.25	2.83	10.46	17.03	18.993	15.655	38.895	18.830	15.647	38.697	10.69
MH-21	And	97.5	141	238	0.707921(9)	0.705546	7.11	31.97	0.134	0.512623(5)	0.512538	0.49	2.52	9.69	14.74	18.947	15.636	38.830	18.779	15.628	38.619	11.00
MS-29	Dac	97.5	158	266	0.710334(9)	0.707953	8.85	41.36	0.129	0.512487(8)	0.512405	-2.10	3.97	14.47	24.63	18.968	15.645	38.834	18.810	15.637	38.645	10.38
GD-17	Dac	97.5	151	236	0.710270(9)	0.707705	7.86	36.45	0.130	0.512483(8)	0.512400	-2.19	3.39	12.96	23.83	18.927	15.640	38.796	18.788	15.634	38.621	9.14
MS-99	Pitch	97.5	249	57	0.726057(7)	0.708515	9.74	46.13	0.127	0.512470(8)	0.512389	-2.41	5.95	22.60	35.44	18.996	15.654	38.881	18.831	15.646	38.676	10.82
MS-42-JR	Rhy	97.5	188	101	0.717511(7)	0.710042	12.32	66.15	0.112	0.512469(7)	0.512397	-2.25	5.08	9.74	36.79	18.946	15.646	38.825	18.810	15.640	38.739	8.88
MH-8	Rhy	97.5	162	60	0.720262(7)	0.709426	8.05	38.63	0.125	0.512575(6)	0.512495	-0.34	3.92	16.87	32.35	18.893	15.632	38.745	18.775	15.626	38.578	7.78
MS-37	Sed	97.5	149	142	0.716306(5)	0.712097	4.94	22.79	0.130	0.512381(9)	0.512298	-4.19	2.35	9.69	17.31	18.904	15.649	38.771	18.771	15.643	38.592	8.73
MS-65a	Sed	97.5	85	335	0.708917(8)	0.707900	5.01	25.45	0.118	0.512377(9)	0.512301	-4.12	2.22	24.21	17.43	18.964	15.653	38.853	18.839	15.647	38.406	8.20
RG-4	Sed	97.5	47	211	0.709724(7)	0.708831	3.07	15.24	0.121	0.512388(9)	0.512311	-3.94	2.08	9.69	7.67	19.371	15.677	39.214	19.103	15.664	38.803	17.59

Appendix 6: Geochronology – Analytical techniques and data set

This appendix provides a brief overview of the procedures employed in the U-Pb (SHRIMP) analysis of zircon crystals from the MSVG and the Ar-Ar analysis of single crystals from the MSVG and MIC.

SHRIMP (Sensitive High Resolution Ion Micro Probe) anlayses were undertaken at the Research School of Earth Sciences, ANU, Canberra using SHRIMP II. The SHRIMP machine is an adapted secondary ion mass spectrometer, the main application of which has been U-Pb dating of zircon crystals.

The Ar-Ar analyses were undertaken by Dr. P. van den Bogaard at GEOMAR Research Institute, Kiel, Germany.

A6.1 SHRIMP Geochronology

A6.1.1 Sample preparation and analytical procedure

Trevor Ireland, pers. comm

Zircons were separated from the rock samples using standard crushing and heavy-liquid techniques, mounted in epoxy, and polished to reveal their mid-sections. U-Th-Pb isotopes were analysed in-situ on small areas within single zircon crystals. The advantage of this method over conventional U-Pb zircon dating is that petrographically selected areas of zircon can be analysed enabling the determination of the crystallisation age of a rock, as well as identification and dating of inherited zircon crystals, and older cores within magmatic crystals. Furthermore, the reliability of any given age determination can be assessed through standard statistical techniques in the pooling of data. If all data lie within the error of the mean then good confidence can be placed in this age determination. If the data are not well grouped then the population can be examined for the effects of Pb loss and/or inheritance.

A mass filtered O_2^- primary beam was focussed to sputter a 30μm diameter area. Pb isotopic ratios were taken as measured; no corrections have been applied for isotopic mass fractionation of Pb hybrid interferences; any corrections would have a negligible effect on this data set because the ages are determined primarily from the $^{238}U/^{206}Pb$ ratios. The Pb/U in the samples was calibrated using an empirical quadratic relationship between $^{206}Pb^+/U^+$ and UO^+/U^+ and then normalised to the Pb/U pf the standard zircon measured with the unknowns. Two standards were used during the course of this work. TEMORA and FC1 were measured at regular intervals (every 4 anlayses) to maintain accuracy controls.

The Temora standard is 417 Ma and FC-1 is 1099Ma. A 1% uncertainty was summed in quadrature to the measured Pb/U as the minimum Pb/U covariance for any analysis (calibration error).

The contribution of common Pb to the measured Pb/U is assessed from the measured $^{207}Pb/^{206}Pb$ ratio, rather than the more generally used method (in conventional isotope dilution U-Pb analyses) based on the $^{204}Pb/^{206}Pb$ ratio. Because of the low levels of ^{204}Pb in zircon, the error in its measurement causes large propagated uncertainties on the low abundance ^{207}Pb peak and so the $^{207}Pb^*/^{206}Pb^*$ ratio is often an insensitive determinant of age in Phanerozoic zircons. For this work, the measured $^{207}Pb/^{206}Pb$ ratio was used to estimate the common Pb. Since the radiogenic $^{207}Pb/^{206}Pb$ ratio in Phanerozoic systems is less than c. 0.06, and common Pb has a $^{207}Pb/^{206}Pb$ ratio of c. 0.9, the measured $^{207}Pb/^{206}Pb$ ratio from zircon is quite sensitive to the presence of even a small component of common Pb. The fraction of common ^{206}Pb, *f*, is given by:

$$f = \frac{(^{207}Pb/^{206}Pb)_{tot} - (^{207}Pb/^{206}Pb)_{rad}}{(^{207}Pb/^{206}Pb)_{init} - (^{207}Pb/^{206}Pb)_{rad}}$$

The subscripts, *tot*, refers to the total measured Pb isotopic composition, *rad* refers to the inferred radiogenic composition, and *init* refers to the initial, or common Pb isotopic composition. This equation can be solved iteratively for each point, and because the radiogenic composition changes only slowly with time in the Phanerozoic, it rapidly converges. The initial common Pb composition is taken as model growth Pb (Cumming &

Richards, 1975), and so it too can be included in the time iteration. Graphically on a Tera-Wasserburg concordia plot (Tera & Wasserburg, 1972). This method assumes that a given analysis is a simple mixture of radiogenic and common Pb and the radiogenic $^{238}U/^{206}Pb$ is the extrapolation from the common Pb through the measured point to concordia. As such, the Tera-Wasserburg plots in this work show uncorrected Pb isotopic compositions and concordance is an indicator of common Pb contribution as well as of equal ages for ^{235}U and ^{238}U systems. A point on a Tera-Wasserburg plot will only be concordant if the two U decay schemes agree and there is no initial Pb in the system.

The analyses for a given sample are combined to assess whether they belong to a single population. The mean square of the weighted deviates (MSWD) of the 206Pb*/238U ages is used to test whether the dispersion of the data is consistent with the errors of the individual points. If the MSWD exceeds the appropriate critical value, proportional to the number of analyses in the population, then the population is examined for outliers. Such outliers are typically ascribed to inheritance (older ages) or Pb loss (younger ages). While the treatment is statistical to avoid bias in selection of outliers, most outliers detected in this work are clearly removed from the main population and user selection cannot be arbitrary. However, when inherited populations become close to the inferred magmatic age, or only a small degree of Pb loss is present in some grains, then the selection can become subjective and more rigorous approaches can be adopted (Sambridge & Compston, 1994).

The final age is the weighted mean of the analyses' contribution to the population. The error in the mean of that population is reported in the results section at the 1σ level. The age is based on the Pb/U measured relative to the mean of the standards and so the uncertainty in the mean of the standards must be included in the final error of the unknown.

A6.1.2 SHRIMP Data Set

	U	Th	Th/U	$^{204}Pb/^{206}Pb$	$f206$ (%)	$^{207}Pb/^{206}Pb$	$^{238}U/^{206}Pb$	Age (Ma)
A115 MV-19								
1.1	161	89	0.56	0.00001 ± 0.01467	0.53 ± 0.29	0.0521 ± 0.0023	66.85 ± 1.48	95 ± 2
2.1	199	112	0.56	0.00039 ± 0.00043	0.32 ± 0.26	0.0505 ± 0.0020	64.28 ± 1.23	99 ± 1
3.1	536	447	0.83	0.00024 ± 0.00015	0.39 ± 0.37	0.0510 ± 0.0029	66.04 ± 1.20	96 ± 1
4.1	127	57	0.45	0.00001 ± 0.00038	0.20 ± 0.47	0.0495 ± 0.0037	67.24 ± 1.43	94 ± 2
5.1	447	378	0.85	0.00014 ± 0.00028	0.62 ± 0.24	0.0529 ± 0.0019	64.04 ± 1.08	99 ± 1
6.1	699	711	1.02	0.00098 ± 0.00029	1.21 ± 0.15	0.0575 ± 0.0012	65.29 ± 1.00	96 ± 1
6.2	546	492	0.90	0.00001 ± 0.00011	0.22 ± 0.23	0.0498 ± 0.0018	62.79 ± 0.96	101 ± 1
7.1	155	76	0.49	0.00100 ± 0.00087	0.66 ± 0.31	0.0531 ± 0.0024	65.74 ± 1.25	96 ± 1
8.1	550	522	0.95	0.00001 ± 0.00014	0.10 ± 0.17	0.0488 ± 0.0013	66.51 ± 1.13	96 ± 1
9.1	743	687	0.93	0.00025 ± 0.00020	0.21 ± 0.15	0.0496 ± 0.0012	66.08 ± 1.30	96 ± 1
10.1	615	461	0.75	0.00011 ± 0.00017	<0.15	0.0471 ± 0.0012	63.80 ± 0.93	100 ± 1
11.1	569	455	0.80	0.00018 ± 0.00020	<0.20	0.0472 ± 0.0016	64.56 ± 1.03	99 ± 1
12.1	496	553	1.12	0.00047 ± 0.00036	0.23 ± 0.17	0.0498 ± 0.0014	65.03 ± 1.02	98 ± 1
A117 MH-8								
1.1	660	119763	181.34	0.00000 ± 0.00033	4.54 ± 0.31	0.0875 ± 0.0025	25.03 ± 0.57	241 ± 5
2.1	32	6	0.21	0.00008 ± 0.00016	0.24 ± 0.25	0.0498 ± 0.0020	67.91 ± 1.63	94 ± 2
3.1	15	2	0.14	0.00001 ± 0.00027	0.07 ± 0.31	0.0485 ± 0.0025	63.79 ± 1.31	100 ± 2
4.1	18	25	1.34	0.00001 ± 0.00032	0.61 ± 0.30	0.0527 ± 0.0023	67.60 ± 1.79	94 ± 2
5.1	60	31	0.51	0.00000 ± 0.00006	<0.21	0.0476 ± 0.0016	48.47 ± 0.66	131 ± 1
6.1	11	7	0.71	0.00002 ± 0.50281	0.78 ± 0.34	0.0542 ± 0.0027	63.93 ± 1.30	99 ± 2
7.1	15	9	0.60	0.00001 ± 241.32001	0.71 ± 0.36	0.0549 ± 0.0029	39.80 ± 0.82	158 ± 3
8.1	14	2	0.17	0.00055 ± 0.00065	0.24 ± 0.30	0.0499 ± 0.0024	65.13 ± 1.26	97 ± 1
9.1	28	35	1.26	0.00001 ± 0.01014	0.34 ± 0.26	0.0506 ± 0.0021	67.73 ± 1.84	94 ± 2
9.2	22	24	1.08	0.00001 ± 0.00020	0.05 ± 0.27	0.0484 ± 0.0021	64.99 ± 1.33	98 ± 2
10.1	27	18	0.67	0.00001 ± 0.00682	0.38 ± 0.16	0.0538 ± 0.0012	27.82 ± 0.42	226 ± 3
10.2	29	19	0.67	0.00004 ± 0.00007	<0.22	0.0500 ± 0.0018	28.07 ± 0.47	225 ± 3
11.1	161	69	0.43	0.00078 ± 0.00055	0.58 ± 0.57	0.0526 ± 0.0045	65.87 ± 1.65	96 ± 2
12.1	253	131	0.52	0.00041 ± 0.00065	0.46 ± 0.22	0.0516 ± 0.0018	66.56 ± 1.11	95 ± 1
13.1	250	315	1.26	0.00001 ± 0.00025	0.14 ± 0.33	0.0491 ± 0.0026	65.15 ± 1.66	98 ± 2
A118 MS-226								
1.1	297	170	0.57	0.00001 ± 5.21160	0.18 ± 0.21	0.0493 ± 0.0017	66.30 ± 1.42	96 ± 2
2.1	625	139	0.22	0.00000 ± 0.00015	<0.19	0.0474 ± 0.0015	63.54 ± 1.04	100 ± 1
3.1	276	191	0.69	0.00042 ± 0.00035	0.24 ± 0.28	0.0498 ± 0.0022	65.72 ± 1.12	97 ± 1
4.1	362	242	0.67	0.00001 ± 0.00028	0.58 ± 0.30	0.0525 ± 0.0024	64.68 ± 1.09	98 ± 1
5.1	2273	579	0.25	0.00006 ± 0.00005	0.01 ± 0.07	0.0481 ± 0.0006	61.64 ± 0.78	103 ± 1
6.1	504	199	0.40	0.00007 ± 0.00012	0.16 ± 0.26	0.0492 ± 0.0020	64.22 ± 1.19	99 ± 1
7.1	231	108	0.47	0.00000 ± 0.00011	<0.16	0.0520 ± 0.0013	16.72 ± 0.28	375 ± 6
7.2	880	23	0.03	0.00006 ± 0.00003	<0.09	0.0519 ± 0.0007	16.39 ± 0.20	382 ± 4
8.1	249	150	0.61	0.00100 ± 0.00047	0.93 ± 0.34	0.0554 ± 0.0027	63.59 ± 1.27	99 ± 2
9.1	1425	823	0.58	0.00000 ± 0.00410	0.21 ± 0.10	0.0497 ± 0.0008	62.51 ± 0.76	102 ± 1
10.1	279	203	0.73	0.00056 ± 0.00047	0.39 ± 0.35	0.0510 ± 0.0028	67.53 ± 1.63	94 ± 2
11.1	397	167	0.42	0.00007 ± 0.00013	0.31 ± 0.19	0.0504 ± 0.0015	65.88 ± 1.02	96 ± 1
12.1	2063	914	0.44	0.00000 ± 0.00002	0.04 ± 0.12	0.0483 ± 0.0009	65.26 ± 0.78	98 ± 1
13.1	341	175	0.51	0.00018 ± 0.00023	0.15 ± 0.25	0.0491 ± 0.0019	67.69 ± 1.52	94 ± 2
14.1	203	101	0.50	0.00091 ± 0.00079	0.43 ± 0.43	0.0513 ± 0.0034	66.88 ± 1.17	95 ± 1

A6.2 Ar-Ar Geochronology

A6.2.1 Sample Preparation and analytical procedure

Each sample was crushed and sieved to separate different size fractions. K-bearing inclusion-free crystal phases were separated (plagioclase, alkali feldspar, biotite, amphibole) using a fine moistened paintbrush and binocular microscope. Individual crystals were weighed and the appropriate number collected in each weight range (as specified by the Ar-Ar laboratory).

The amphibole and feldspar crystals were etched in 5% HF solution and rinsed with distilled water. The water was then evaporated off using heat lamps.

The crystals were cleaned ultrasonically in distilled water before being packaged and sent off for analysis.

The samples were sent to GEOMAR Tephrachronology Laboratory where they were prepared (sent away for irradiation) and purified gas samples were anlysed using a 25W Spectra Physics argon ion laser and a MAP 216 series mass spectrometer fitted with a Baur-Signer ion source and a Johnston electron multiplier (secondary electron multiplier).

The Ar-Ar analyses involved fusing single crystals of biotite and feldspar phenocrysts as well as glass and matrix chips in a single step or by laser-stepheating analysis as necessary. Raw mass spectrometer peaks were corrected for mass discrimination, background and blank values determined every fifth analysis. The neutron flux was monitored using TCR sanidine (Taylor Creek Rhyolite, 27.92 Ma (Duffield & Dalrymple, 1990)). The primary K-Ar standard to calibrate TCR was Interlaboratory biotite standard SB-3 (162.9 Ma (Lanphere & Dalrymple, 2000))

The analyses were performed by Dr P. van den Bogaard.

A6.2.2 Ar-Ar data

	Sample No.	Single crystal or whole-rock	No. of analyses	Age (Ma)	Error (2 Sigma)	MSWD
MSVG	MS-126	Feldspar	13	90.2	2.2	6.12
	MS-146	Feldspar	12	90.7	1.6	2.31
	MS-165	Feldspar	12	85.4	2.0	5.83
	MS-29	Feldspar	12	93.4	0.8	0.60
	MS-36	Feldspar	24	92.3	1.6	0.86
	MS-40	Feldspar	13	93.4	1.2	0.82
	MS-68	Feldspar	24	88.4	1.4	2.34
	MS-96	Feldspar	11	92.7	1.8	0.45
	MH-12	Biotite	2	96.7	3.6	
	MH-12	Feldspar	2	93.5	0.6	
	MH-29	Feldspar	13	93.6	0.8	2.04
	MH-7	Biotite	13	94.2	0.8	1.66
	MV-11	Feldspar	13	91.0	2.6	0.87
	MV-4	K-feldspar	12	11.59	0.08	0.49
	MV-9	Feldspar	2	88.0	6	
	RG-11	Feldspar	13	95.7	1.8	0.77
	RG-2	Feldspar	13	94.1	2.2	1.96
	GD-22	Matrix stepheat (61% plateau)		90.7	0.4	
	GD-2	Matrix stepheat (40% plateau)		86.1	0.6	
MIC	M-12	Biotite	11	95.1	0.8	1.47
	M-23	Biotite	11	91.2	1.8	3.62
	M-66	Biotite	7	94.0	1.4	2.71
	M-77	Feldspar	10	90.0	2.4	2.86
	M-9	Biotite	13	94.8	0.6	0.72

The above table lists the complete Ar-Ar data set. The samples not considered in chapter 6 are those with: MSWD >3, Small number of samples analysed e.g. MH-12 and the stepheat samples GD-22 and GD-2, which produced questionable plateaux, especially GD-2 which gave only a 40% plateau. Sample MV-4 was dated to confirm whether the flows are of

Cretaceous or Tertiary age. The 11.59 Ma age is consistent with the conclusions reached during the course of mapping that these flows are actually of Tertiary age and overlie the Cretaceous volcanics in McQueens Valley. The geological map (Chapter 4) has been adjusted accordingly.

	U	Th	Th/U	$^{204}Pb/^{206}Pb$	$f206$ (%)	$^{207}Pb/^{206}Pb$	$^{238}U/^{206}Pb$	Age (Ma)
A115 MV-19								
1.1	161	89	0.56	0.00001 ± 0.01467	0.53 ± 0.29	0.0521 ± 0.0023	66.85 ± 1.48	95 ± 2
2.1	199	112	0.56	0.00039 ± 0.00043	0.32 ± 0.26	0.0505 ± 0.0020	64.28 ± 1.23	99 ± 1
3.1	536	447	0.83	0.00024 ± 0.00015	0.39 ± 0.37	0.0510 ± 0.0029	66.04 ± 1.20	96 ± 1
4.1	127	57	0.45	0.00001 ± 0.00038	0.20 ± 0.47	0.0495 ± 0.0037	67.24 ± 1.43	94 ± 2
5.1	447	378	0.85	0.00014 ± 0.00028	0.62 ± 0.24	0.0529 ± 0.0019	64.04 ± 1.08	99 ± 1
6.1	699	711	1.02	0.00098 ± 0.00029	1.21 ± 0.15	0.0575 ± 0.0012	65.29 ± 1.00	96 ± 1
6.2	546	492	0.90	0.00001 ± 0.00011	0.22 ± 0.23	0.0498 ± 0.0018	62.79 ± 0.96	101 ± 1
7.1	155	76	0.49	0.00100 ± 0.00087	0.66 ± 0.31	0.0531 ± 0.0024	65.74 ± 1.25	96 ± 1
8.1	550	522	0.95	0.00001 ± 0.00014	0.10 ± 0.17	0.0488 ± 0.0013	66.51 ± 1.13	96 ± 1
9.1	743	687	0.93	0.00025 ± 0.00020	0.21 ± 0.15	0.0496 ± 0.0012	66.08 ± 1.30	96 ± 1
10.1	615	461	0.75	0.00011 ± 0.00017	<0.15	0.0471 ± 0.0012	63.80 ± 0.93	100 ± 1
11.1	569	455	0.80	0.00018 ± 0.00020	<0.20	0.0472 ± 0.0016	64.56 ± 1.03	99 ± 1
12.1	496	553	1.12	0.00047 ± 0.00036	0.23 ± 0.17	0.0498 ± 0.0014	65.03 ± 1.02	98 ± 1
A117 MH-8								
1.1	660	119763	181.34	0.00000 ± 0.00033	4.54 ± 0.31	0.0875 ± 0.0025	25.03 ± 0.57	241 ± 5
2.1	32	6	0.21	0.00008 ± 0.00016	0.24 ± 0.25	0.0498 ± 0.0020	67.91 ± 1.63	94 ± 2
3.1	15	2	0.14	0.00001 ± 0.00027	0.07 ± 0.31	0.0485 ± 0.0025	63.79 ± 1.31	100 ± 2
4.1	18	25	1.34	0.00001 ± 0.00032	0.61 ± 0.30	0.0527 ± 0.0023	67.60 ± 1.79	94 ± 2
5.1	60	31	0.51	0.00000 ± 0.00006	<0.21	0.0476 ± 0.0016	48.47 ± 0.66	131 ± 1
6.1	11	7	0.71	0.00002 ± 0.50281	0.78 ± 0.34	0.0542 ± 0.0027	63.93 ± 1.30	99 ± 2
7.1	15	9	0.60	0.00001 ± 241.32001	0.71 ± 0.36	0.0549 ± 0.0029	39.80 ± 0.82	158 ± 3
8.1	14	2	0.17	0.00055 ± 0.00065	0.24 ± 0.30	0.0499 ± 0.0024	65.13 ± 1.26	97 ± 1
9.1	28	35	1.26	0.00001 ± 0.01014	0.34 ± 0.26	0.0506 ± 0.0021	67.73 ± 1.84	94 ± 2
9.2	22	24	1.08	0.00001 ± 0.00020	0.05 ± 0.27	0.0484 ± 0.0021	64.99 ± 1.33	98 ± 2
10.1	27	18	0.67	0.00001 ± 0.00682	0.38 ± 0.16	0.0538 ± 0.0012	27.82 ± 0.42	226 ± 3
10.2	29	19	0.67	0.00004 ± 0.00007	<0.22	0.0500 ± 0.0018	28.07 ± 0.47	225 ± 3
11.1	161	69	0.43	0.00078 ± 0.00055	0.58 ± 0.57	0.0526 ± 0.0045	65.87 ± 1.65	96 ± 2
12.1	253	131	0.52	0.00041 ± 0.00065	0.46 ± 0.22	0.0516 ± 0.0018	66.56 ± 1.11	95 ± 1
13.1	250	315	1.26	0.00001 ± 0.00025	0.14 ± 0.33	0.0491 ± 0.0026	65.15 ± 1.66	98 ± 2
A118 MS-226								
1.1	297	170	0.57	0.00001 ± 5.21160	0.18 ± 0.21	0.0493 ± 0.0017	66.30 ± 1.42	96 ± 2
2.1	625	139	0.22	0.00000 ± 0.00015	<0.19	0.0474 ± 0.0015	63.54 ± 1.04	100 ± 1
3.1	276	191	0.69	0.00042 ± 0.00035	0.24 ± 0.28	0.0498 ± 0.0022	65.72 ± 1.12	97 ± 1
4.1	362	242	0.67	0.00001 ± 0.00028	0.58 ± 0.30	0.0525 ± 0.0024	64.68 ± 1.09	98 ± 1
5.1	2273	579	0.25	0.00006 ± 0.00005	0.01 ± 0.07	0.0481 ± 0.0006	61.64 ± 0.78	103 ± 1
6.1	504	199	0.40	0.00007 ± 0.00012	0.16 ± 0.26	0.0492 ± 0.0020	64.22 ± 1.19	99 ± 1
7.1	231	108	0.47	0.00000 ± 0.00011	<0.16	0.0520 ± 0.0013	16.72 ± 0.28	375 ± 6
7.2	880	23	0.03	0.00006 ± 0.00003	<0.09	0.0519 ± 0.0007	16.39 ± 0.20	382 ± 4
8.1	249	150	0.61	0.00100 ± 0.00047	0.93 ± 0.34	0.0554 ± 0.0027	63.59 ± 1.27	99 ± 2
9.1	1425	823	0.58	0.00000 ± 0.00410	0.21 ± 0.10	0.0497 ± 0.0008	62.51 ± 0.76	102 ± 1
10.1	279	203	0.73	0.00056 ± 0.00047	0.39 ± 0.35	0.0510 ± 0.0028	67.53 ± 1.63	94 ± 2
11.1	397	167	0.42	0.00007 ± 0.00013	0.31 ± 0.19	0.0504 ± 0.0015	65.88 ± 1.02	96 ± 1
12.1	2063	914	0.44	0.00000 ± 0.00002	0.04 ± 0.12	0.0483 ± 0.0009	65.26 ± 0.78	98 ± 1
13.1	341	175	0.51	0.00018 ± 0.00023	0.15 ± 0.25	0.0491 ± 0.0019	67.69 ± 1.52	94 ± 2
14.1	203	101	0.50	0.00091 ± 0.00079	0.43 ± 0.43	0.0513 ± 0.0034	66.88 ± 1.17	95 ± 1

Appendix 7: Stable oxygen isotope analyses: Analytical techniques and data set

This appendix provides a brief overview of the procedures employed in the analysis of single crystal phases and whole-rocks for stable oxygen isotope data.

A7.1 Sample Preparation

Quartz and garnet crystals were picked from manually crushed pitchstone samples using a binocular microscope and fine paint brush. From the mineral separates clean crystals, free of groundmass were selected for analysis.

A7.2 Analytical Procedure

Oxygen was extracted from quartz for isotope analyses using a CO_2 laser and BrF_5, similar to the method described by Sharp (1990). In the case of whole rock, meta-sediments oxygen was extracted from samples using the conventional BrF_5, Ni-rod method (Clayton & Mayeda, 1963). Samples were crushed to a fine powder using a tungsten carbide ring mill, out-gassed under vacuum at 200ºC for at least 12 hours and pretreated with BrF_5 at room temperature for 2 minutes. Samples were reacted with BrF_5 at 550ºC overnight to extract oxygen from samples. All sample results were normalized to the quartz standard NBS-28 using a value of +9.6‰, relative to V-SMOW. Values for four NBS-28 analyzed with the samples had values that varied by less than 0.1‰.

A7.3 Data Set

Listed below are the data for the samples analysed from the MSVG and the Rakaia terrane (as shown in Chapter 7).

Sample Number	**Mineral**	**$\delta^{18}O$ ‰ VSMOW**	**Average $\delta^{18}O$ (‰)**	**Replication difference**
GD-28 (pitchstone)	Quartz	10.7, 10.6	10.7	± 0.05
MS-99 (pitchstone)	Quartz	9.9, 10.6	10.3	± 0.35
MH-12 (pitchstone)	Quartz Garnet	11.4, 11.5 8.7, 8.9	11.5 8.8	± 0.05 ± 0.1
RG-4 Rakaia terrane	Whole-rock	10.0, 9.4, 9.3	9.6	± 0.4
M-65a Rakaia terrane	Whole-rock	9.6, 9.6	9.6	Nil
MS-37 Rakaia terrane	Whole-rock	9.7, 9.6	9.7	± 0.05
M-80 Pahau terrane	Whole-rock	2.9, 2.9, 3.0	2.9	± 0.1

Table A7.1 Oxygen isotope data

A7.4 Geothermometry

Crystallisation temperatures can be made based upon the $\delta^{18}O$ of co-existing mineral phases. For sample MH-12 both quartz and garnet data are available. The general equation used to calculate temperature is:

$$10^3 \ln\alpha_{a\text{-}b} = \frac{A \times 10^6}{T^2} + B \qquad [1]$$

Where a and b are the concentrations of ^{18}O in the two mineral phases and A and B are constants, derived from experimental determination.

The temperature dependence of the fractionation of ^{18}O between quartz and garnet (A) is 2.88 (Bottinga & Javoy, 1975). B is considered to be zero.

Where a and b are <10‰, $10^3 \ln\alpha_{a\text{-}b}$ can be approximated to $\delta^{18}O_{quartz} - \delta^{18}O_{garnet.}$ However, because $\delta^{18}O_{quartz}$ for sample MH-12 = 11.5, $\alpha_{a\text{-}b}$ must be resolved:

$$\alpha_{a\text{-}b} = \frac{1000 + \delta^{18}O_{quartz}}{1000 + \delta^{18}O_{garnet}} \qquad [2]$$

$$\alpha_{a\text{-}b} = 1.00268 \qquad [3]$$

Substituting [3] into [1] and inserting the value of A (2.88) gives:

$$10^3 \ln_{1.00268} = \frac{2.88 \times 10^6}{T^2} \qquad [4]$$

Resolving [4] gives: **T = 1037 K or 764ºC**

Appendix 8: AFC Modelling parameters

The AFC modelling was based upon the AFC equation of DePaolo (1981):

$$\frac{C_L}{C_O} = f' + \frac{r}{(r-1+D)} \times \frac{C_A}{C_O}(1-f')$$

Where:

C_L / C_O = Ratio of the concentration of a trace element in a remaining liquid to the concentration in the parental liquid

r = Ratio of assimilation rate to the fractionation rate

D = Bulk Distribution Co-efficient

C_A = Concentration of a trace element in the wallrock being assimilated during AFC

f´ = the fraction of melt remaining in the AFC process given by the equation:

$$f' = F^{-(r-1+D)/(r-1)}$$

F = Fraction of melt remaining

Basaltic-Andesite mineral phase proportions and Bulk Partition Co-efficients (Bulk P.C.):

Element	**Plag (66%)**	**Opx (33%)**	**Fe-Ti oxide (0.2%)**	**Cpx (0.7)**	**Bulk P.C.**
Ba	0.23[1]	0.013[1]	-	0.026[1]	**0.16**
Rb	0.071[1]	0.022[1]	-	0.031[1]	**0.05**
La	0.1477[2]	-	1.5[3]	0.056[4]	**0.10**
Y	0.03[1]	0.18[1]	0.2[1]	0.9[1]	**0.09**
Th	0.01[1]	-	-	0.03[1]	**0.01**

Andesite mineral phase proportions and Bulk Partition Co-efficients (Bulk P.C.):

Element	**Plag (69%)**	**Opx (17%)**	**Fe-Ti oxide (9%)**	**Cpx (5%)**	**BULK P.C.**
Ba	0.16[5]	0.013[6]	0.01[5]	0.02[5]	**0.11**
Rb	0.07[5]	0.022[6]	0.01[5]	0.02[5]	**0.05**
La	0.302[4]	0.031[4]	-	0.047[4]	**0.22**
Y	0.06[7]	0.45[7]	0.5[7,5]	1.5[7]	**0.24**
Th	0.01[5]	0.05[5]	0.1[5]	0.01[5]	**0.02**

Dacite mineral phase proportions and Bulk Partition Co-efficients (Bulk P.C.):

Element	**Plag (46%)**	**Opx (18%)**	**Ilm (11.75%)**	**Cpx (12%)**	**A-fsp (9%)**	**Gnt (0.25%)**	**Qz (3%)**	**Bulk P.C.**
Ba	0.36[8]	0.003[8]	-	0.131[8]	6.12[8]	0.017[8]	0.022[9]	**0.73**
Rb	0.048[8]	0.003[8]	-	0.032[8]	0.34[8]	0.009[8]	0.041[9]	**0.06**
La	0.38[9]	0.015[4]	2.5[9]	0.015[4]	0.08[9]	0.39[10]	0.015[9]	**0.48**
Y	0.1[7]	1.0[7]	-	4.0[7]	-	35.0[8]	-	**0.79**
Th	0.048[9]	0.13[9]	5.0[9]	0.15[9]	0.023[9]	-	0.009[9]	**0.65**

Rhyolite mineral phase proportions and Bulk Partition Co-efficients (Bulk P.C.):

Element	**Qz (50%)**	**Plag (13.5)**	**Ilm (1%)**	**Opx (0.3%)**	**Gnt (3%)**	**A-fsp (25%)**	**Biot (7%)**	**Zircon (0.2%)**	**Bulk P.C.**
Ba	0.022[9]	0.308[8]	-	0.003[8]	0.017[8]	4.3[11]	5.367[11]	-	**1.5**
Rb	0.041[9]	0.041[8]	-	0.003[8]	0.009[8]	0.34[8]	2.24[8]	-	**0.27**
La	0.015[9]	0.38[9]	1.223[9]	0.78[9]	0.39[10]	0.08[9]	5.713[9]	16.9[11]	**0.54**
Y	-	0.13[9]	-	1.0[7]	30.0[8]	-	0.03[7]	-	**0.92**
Th	0.009[9]	0.048[9]	7.0[9]	0.13[9]	-	0.023[9]	1.227[11]	76.8[11]	**0.33**

The superscript numbers refer to the source of the data and are listed as follows:

1 Compilation (Arth, 1976; Dostal *et al.*, 1983; Fujimaki *et al.*, 1984; Green *et al.*, 1989; Henderson, 1982; Pearce & Norry, 1979; Schock, 1979).

2 mean of two basaltic andesites SiO_2 55% and 57% (Fujimaki *et al.*, 1984)

3 (Schock, 1979)

4 (Fujimaki *et al.*, 1984)

5 Compilation (Gill, 1981)

6 (Philpotts & Schnetzler, 1970)

7 (Pearce & Norry, 1979)

8 (Arth, 1976)

9 (Nash & Crecraft, 1985)

10 (Irving & Frey, 1978)

11 (Mahood & Hildreth, 1983)

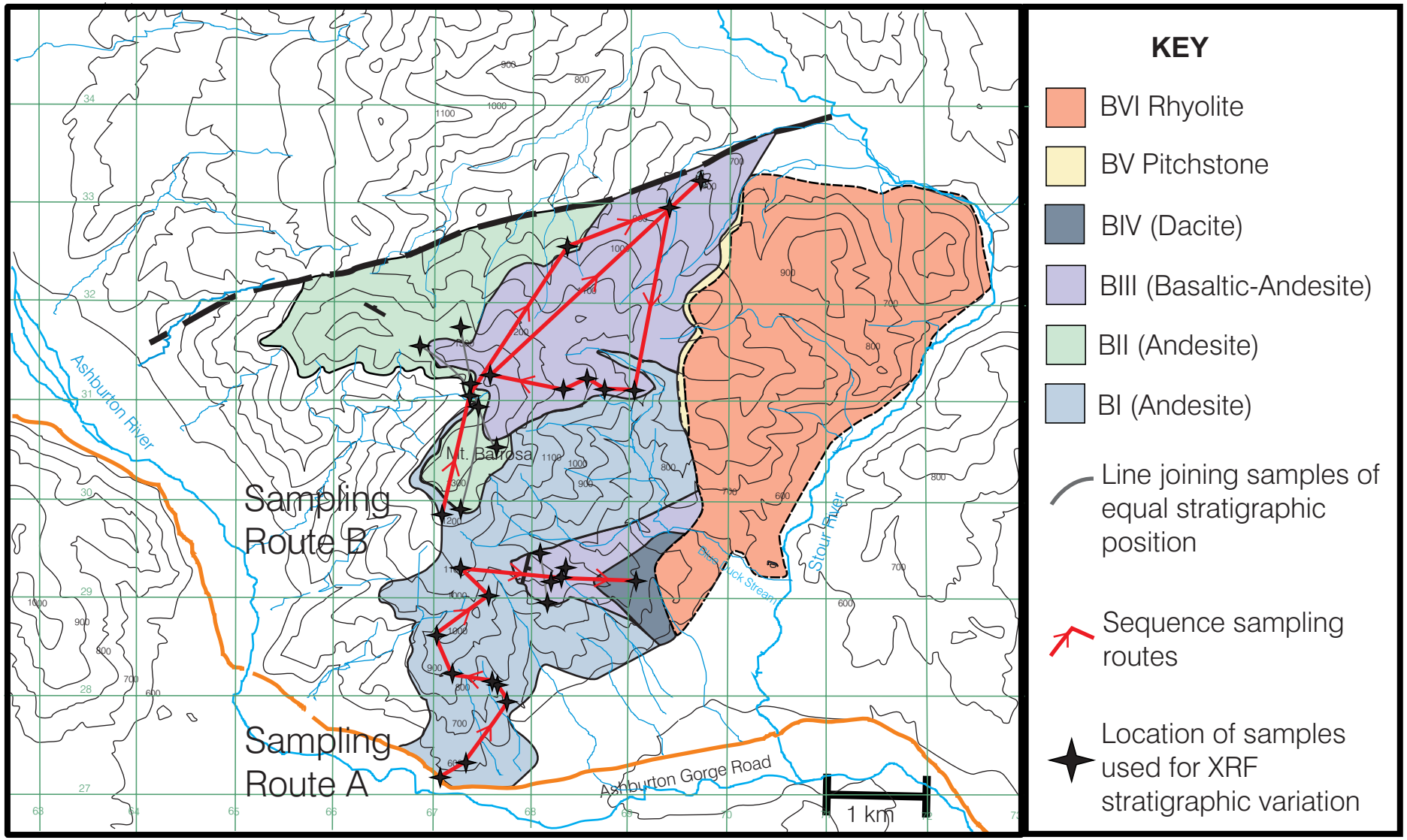

Fig.7.5 Map of Barrosa showing the up-sequence sampling routes

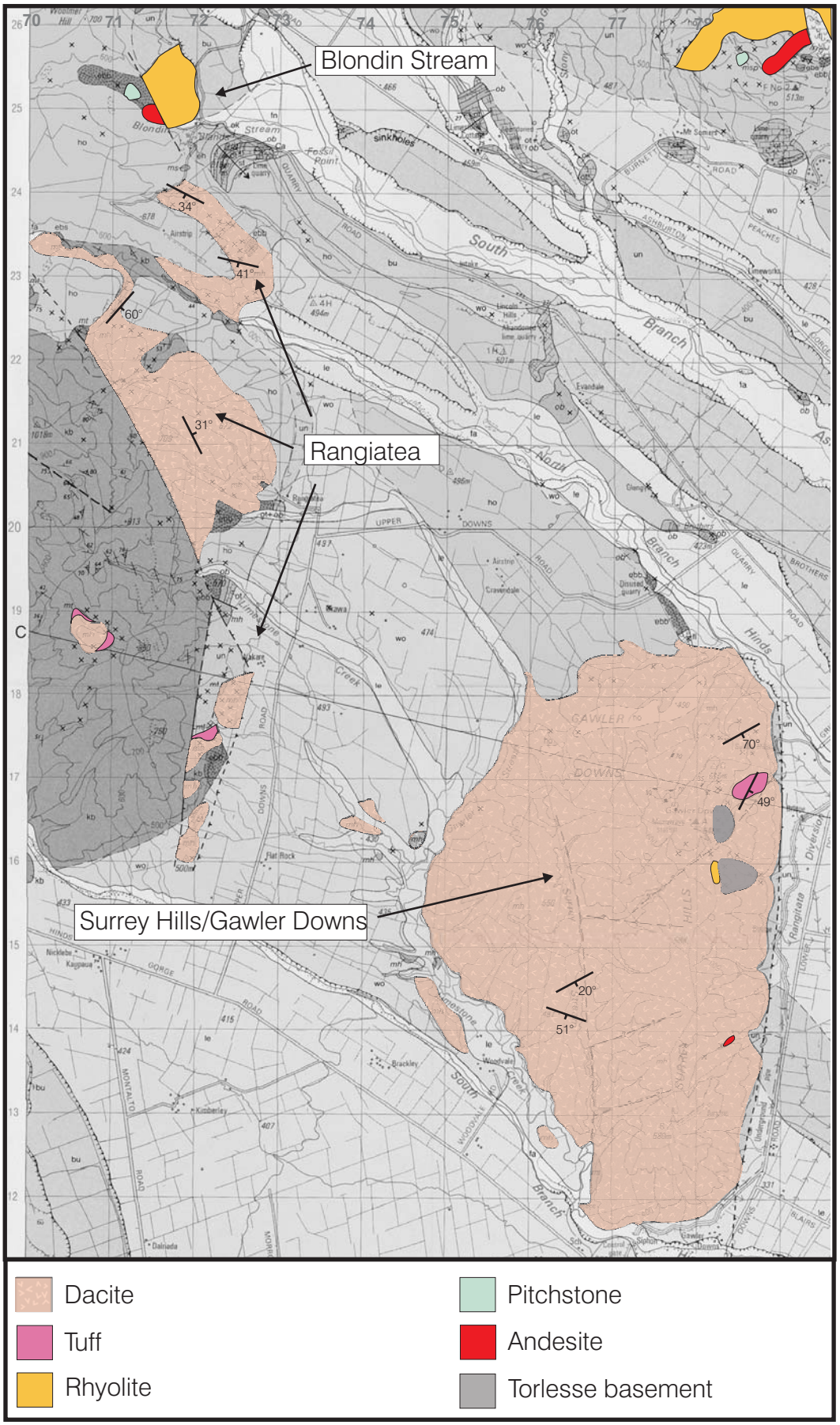

Fig.4.18 Geological Map of the Gawler Downs field area, adapted from Oliver & Keene (1989). Strike and dip symbols indicate flow directions.

Fig.4.1 Geological Map of Mt Barrosa

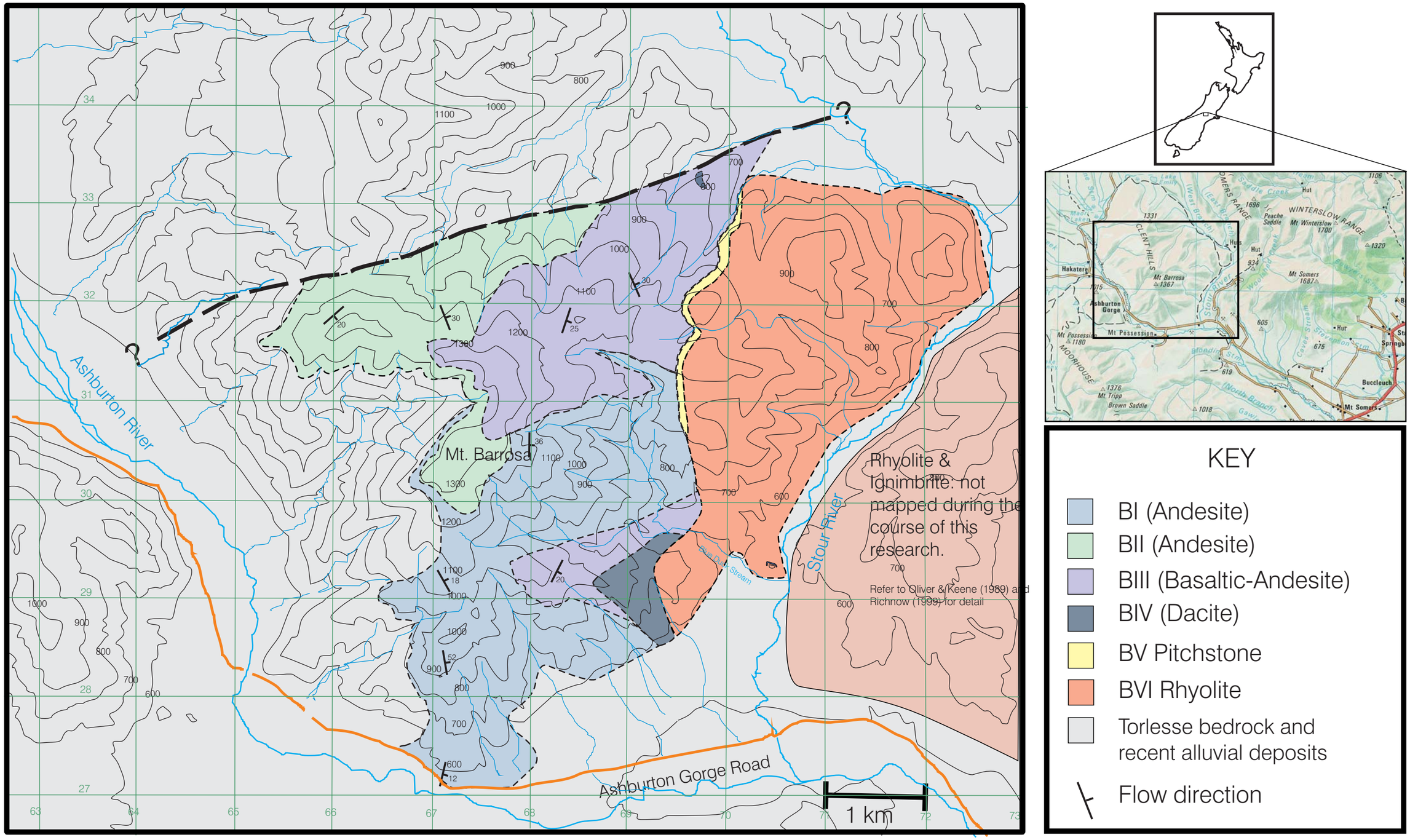

Fig. 4.22 Volcanic Geology of the Malvern Hills

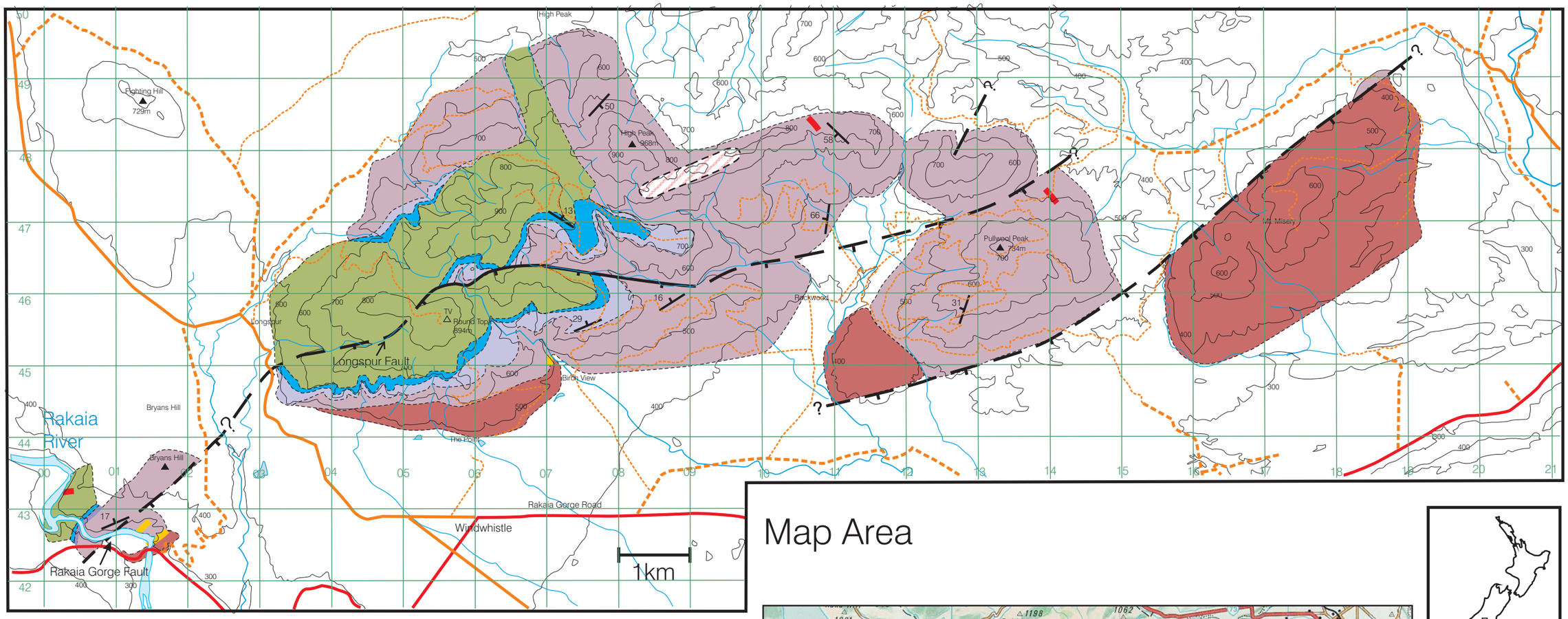

KEY

- Round Top Andesite
- Glassy Ignimbrite (upper)
- Glassy Ignimbrite (lower)
- Rockwood Ignimbrite
- Iron Bridge Rhyolite
- Faults (teeth to downthrown block)
- Mafic Dykes
- Pitchstone Dykes
- Rhyolite fissure dyke
- State Highway 77
- Minor Road
- Gravel Road
- Minor trail/Forestry Track
- Streams

Map Area

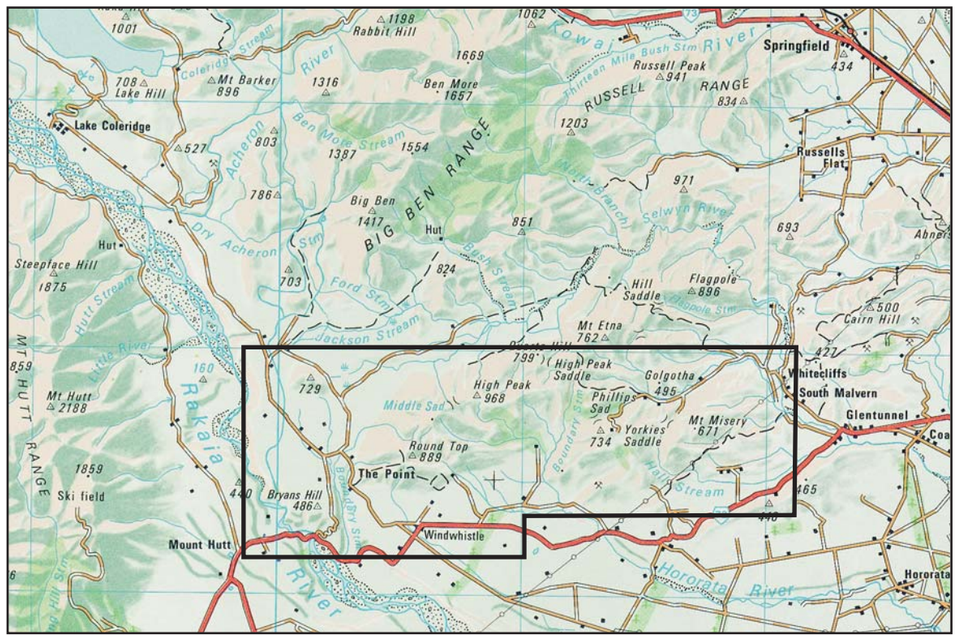

Fig.5.7 Cross-section A-B

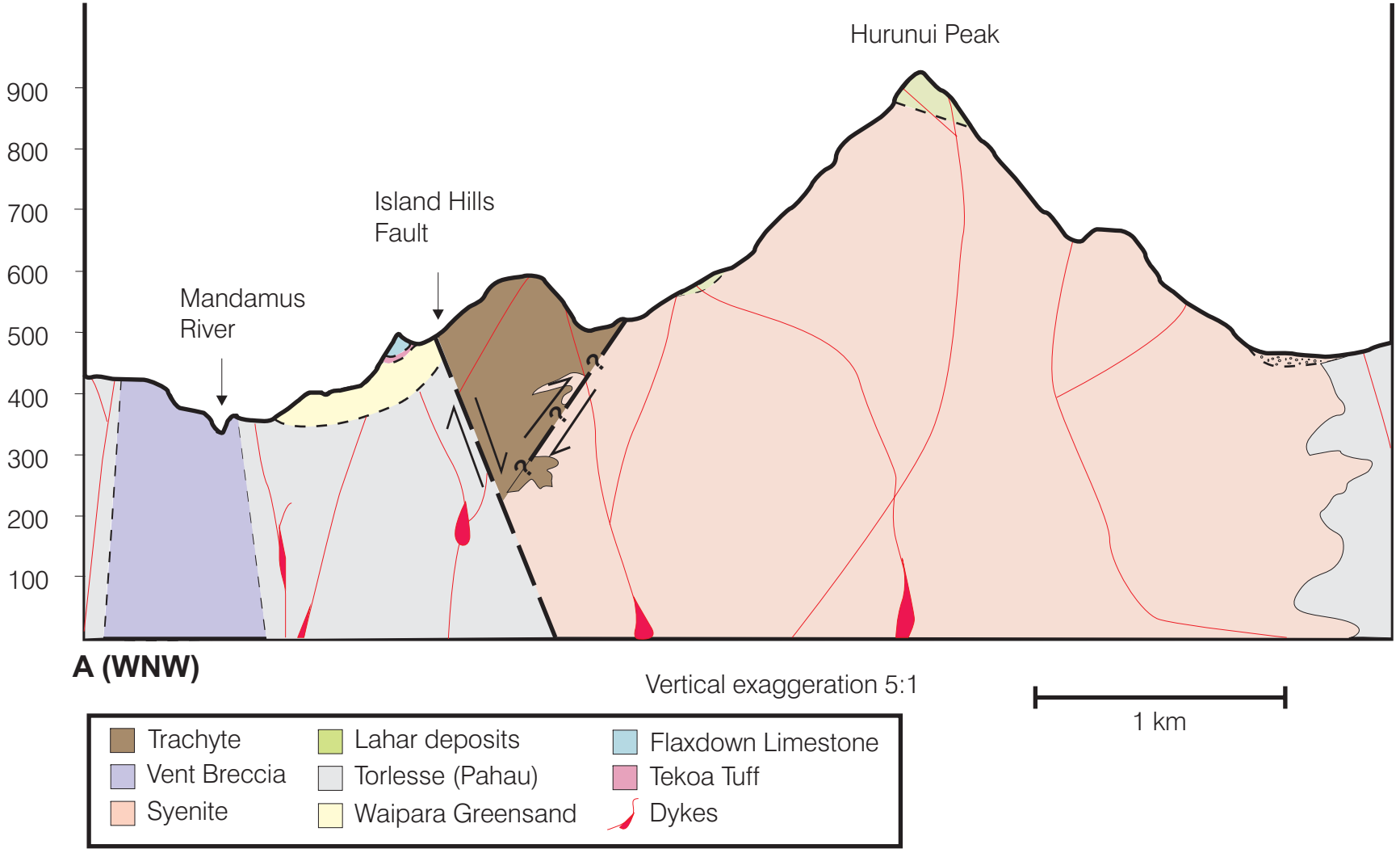

Fig. 5.6 Geological Map of the Mandamus Valley

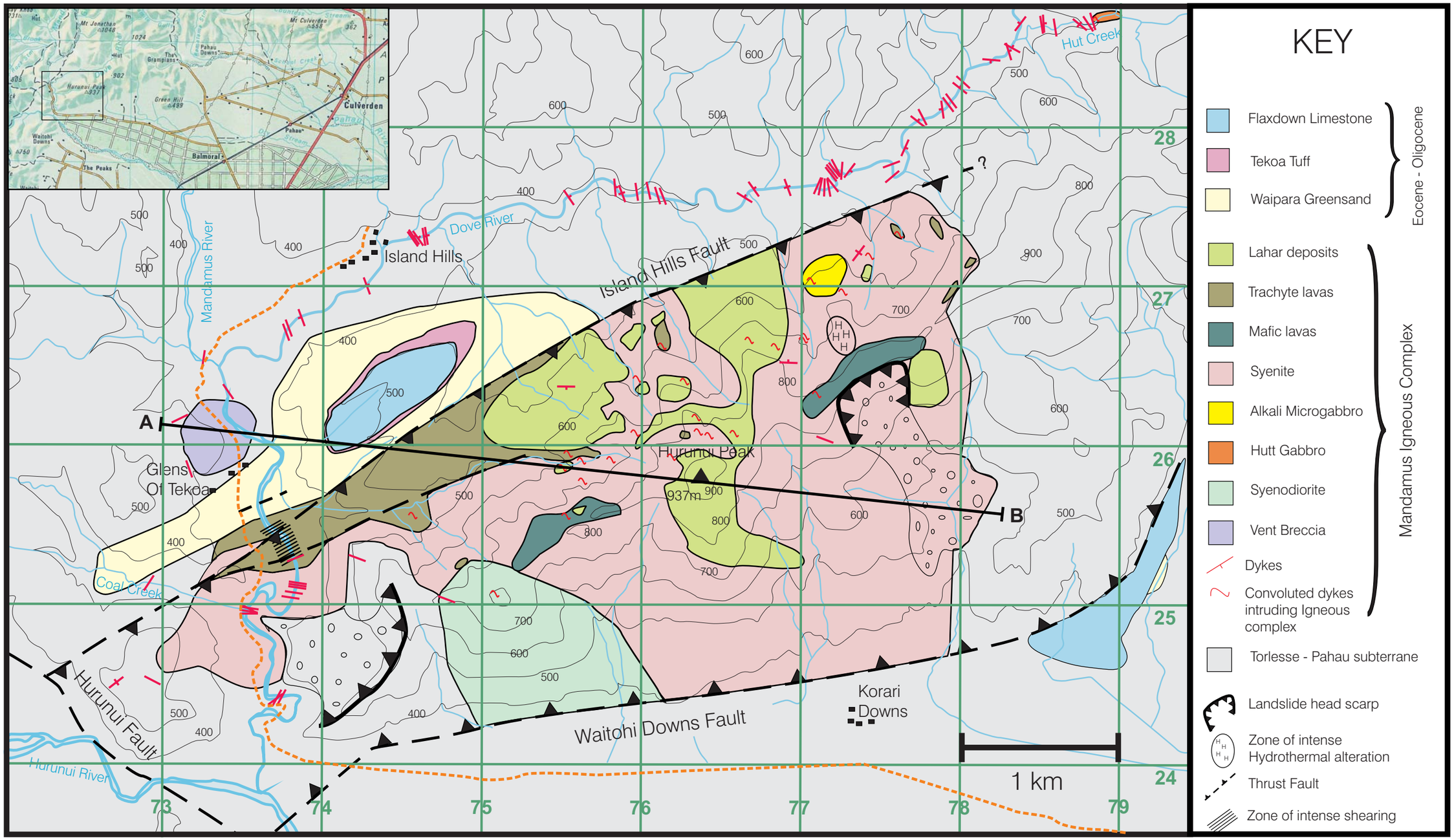

Tertiary stratigraphy and Waitohi Downs Fault position after Mould (1992)

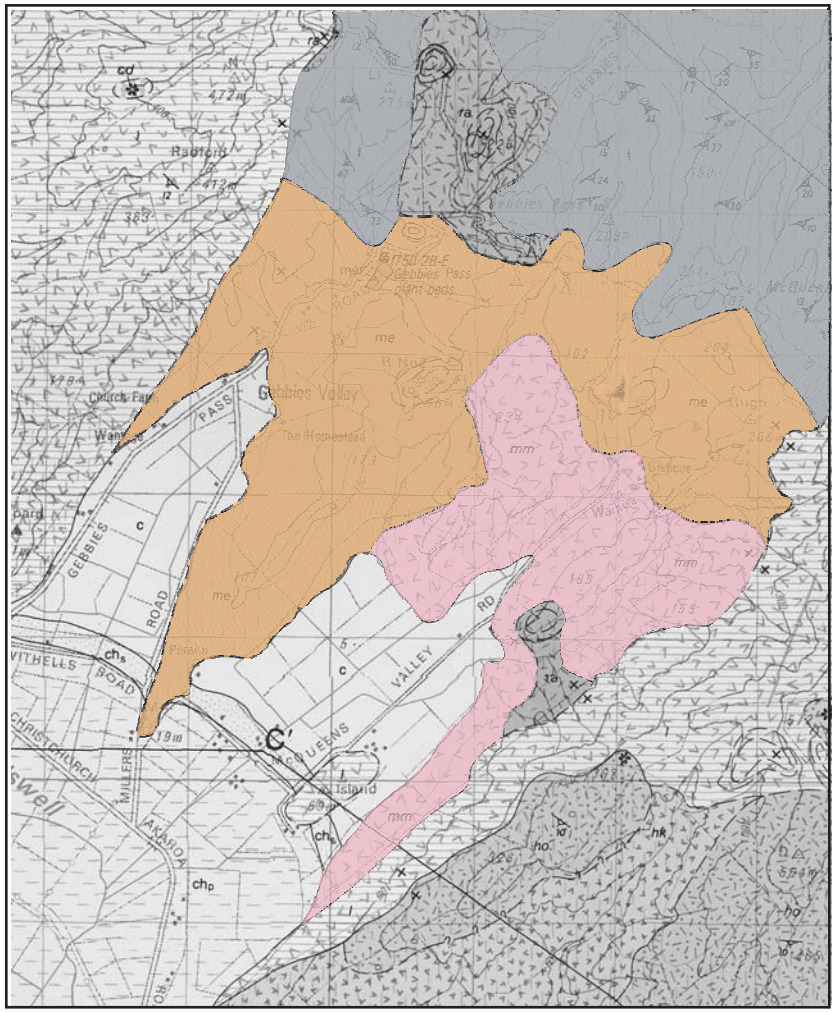

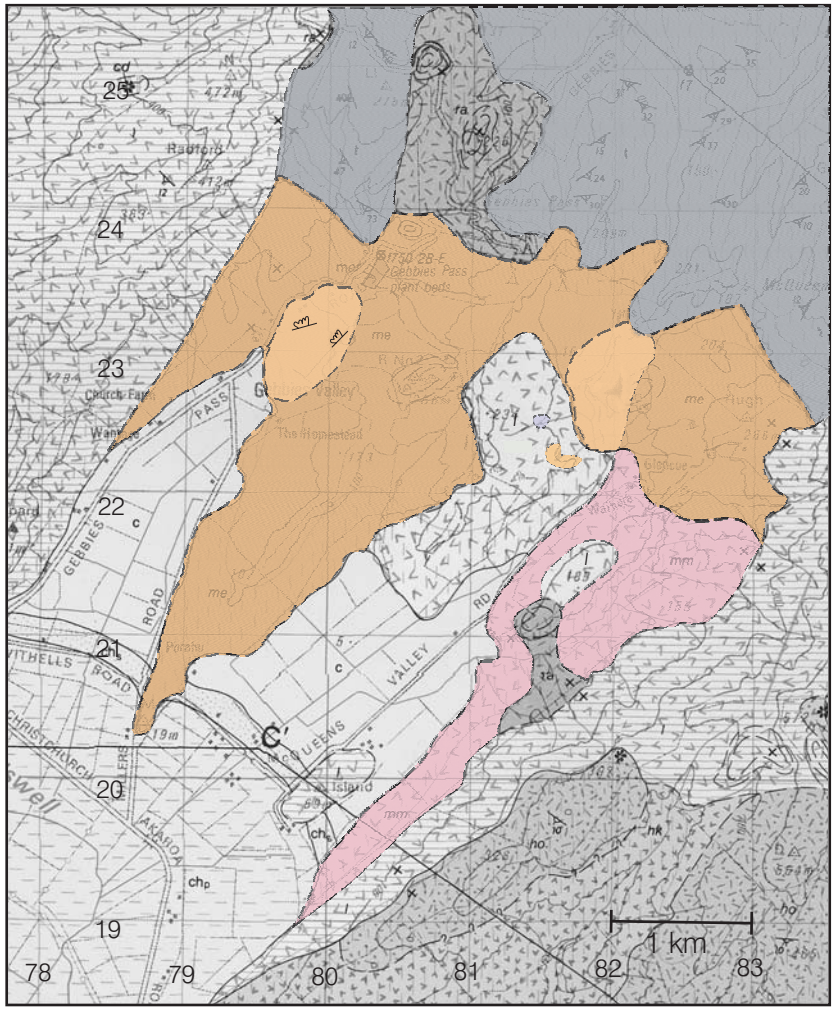

Gebbies Rhyolite Gebbies Ignimbrite Gebbies Pitchstone McQueen's Andeiste Torlesse basement

Fig.4.39a Original Geological map of McQueens Valley, adapted from Sewell *et al* (1988). Grey-scale features are Tertiary volcanics and gravel sequences

Fig.4.39b New Geological map of McQueens Valley, based on the original map of Sewell *et al* (1988).

Fig.4.43 Geological Map of the Rangitata Gorge field area, adapted from Oliver & Keene (1990)